

Национальный исследовательский университет ИТМО

(Университет ИТМО)



На правах рукописи

Тофтул Иван Дмитриевич

**Передача импульса и углового момента поля
субволновым рассеивателям в опто- и
акустомеханике**

Диссертация на соискание учёной степени

кандидата физико-математических наук

Национальный исследовательский университет ИТМО
(Университет ИТМО)



На правах рукописи

Тофтул Иван Дмитриевич

**Передача импульса и углового момента поля
субволновым рассеивателям в опто- и
акустомеханике**

Специальность 1.3.6.

«Оптика (физико-математические науки)»

Диссертация на соискание учёной степени
кандидата физико-математических наук

Научный руководитель:
PhD,
физико-математические науки
Петров Михаил Игоревич

Диссертация подготовлена в: федеральное государственное автономное образовательное учреждение высшего образования «Национальный исследовательский университет ИТМО».

Научный руководитель: PhD, физико-математические науки
Петров Михаил Игоревич

Официальные оппоненты: Булгаков Евгений Николаевич, доктор физико-математических наук, доцент, Институт физики имени Л. В. Киренского СО РАН, Ведущий научный сотрудник, Лаборатория теории нелинейных процессов

Родригес-Фортуно Франциско Хосе, PhD, Королевский колледж Лондона, Лектор факультета естественных, математических и технических наук

Защита диссертации состоится в удаленном интерактивном режиме 07.11.2022 г. в 15:00 ссылка на публичную трансляцию защиты: <https://youtu.be/B7C1Qejg8vA>.

С диссертацией можно ознакомиться в библиотеке Университета ИТМО по адресу: Санкт-Петербург, ул. Ломоносова, д. 9 и на сайте <https://dissovet.itmo.ru>.

Ученый секретарь диссертационного совета 05.22.00 Университета ИТМО, кандидат физико-математических наук, доцент, Старовойтов Антон Андреевич.

ITMO University



As a manuscript

Toftul Ivan Dmitrievich

**Transfer of linear and angular momentum to
subwavelength scatterers in opto- and
acoustomechanics**

Speciality 1.3.6.
Optics (Physics and Mathematics)

Academic dissertation candidate of physics and mathematics

Supervisor:
PhD
Petrov Mihail Igorevich

The research was carried out at: ITMO University.

Supervisor: PhD
Petrov Mihail Igorevich

Official opponents: Bulgakov Evgeny Nikolaevich, doctor of Physical and Mathematical Sciences, Kirensky Institute of Physics, Leading Researcher, Laboratory of the Theory of Nonlinear Processes

Rodriguez-Fortuno Francisco Jose, PhD, King's College London,
Lecturer faculty of Natural, Mathematical & Engineering Sciences

The defense will be held on 07.11.2022 at 15:00 at the meeting of the ITMO University Dissertation Council 05.22.01, <https://youtu.be/B7CIQejg8vA>.

The thesis is available in the Library of ITMO University, Lomonosova St. 9, Saint-Petersburg, Russia and on <https://dissovet.itmo.ru> website.

Science Secretary of the ITMO University Dissertation Council 05.22.00, PhD in Physics and Mathematics,
Starovoytov Anton A.

Table of contents

Peþepar	10
Synopsis	39
Introduction	65
Background and motivation	65
Scientific statements	65
Structure of this thesis	66
 Chapter 1. Optical forces and torques: theory overview	 68
1.1 Maxwell stress tensor approach	68
1.2 Subwavelength limit	70
1.3 Small particles as a measure of canonical momenta of light	73
1.4 (Bi-)anisotropic particles	75
1.4.1 Chiral particles	75
1.4.2 Geometric anisotropy and particles made of anisotropic crystals	78
1.5 Bichromatic force	80
1.6 Dynamics simulation with a stochastic force	81
1.7 Acoustic force and torque	83
1.7.1 Rigorous approach for the force	83
1.7.2 Rigorous approach for the torque	84
1.7.3 Acoustic pressure from a plane wave on a sphere	85
 Chapter 2. Spin and orbital angular momenta of sphere and cylindrical waveguide modes	 86
2.1 Spherical resonator	86
2.1.1 Canonical field properties and eigen modes of a sphere	88
2.1.2 Angular momenta of eigen modes of a sphere	93
2.2 Fiber mode profiles	97
2.2.1 Electric field structure and mode designations	99
2.2.2 Mode polarizations and Stokes vector	100

2.2.3	Evanescent mode field intensity	104
2.2.4	Angular momentum of dielectric step-index fiber modes . . .	105
Chapter 3. Transverse optical binding via waveguide mode		111
3.1	General idea	111
3.2	Optical binding near a single-mode nanofiber	113
3.3	Stability of the trapping	116
3.4	Nanoparticle binding in a multi-mode regime	118
3.5	Radial and azimuthal binding of nanoparticles	119
3.6	Two beam trapping by phase tuning	121
3.7	Validity of the dipole model	121
3.8	A scientific statement	124
Chapter 4. Spin and orbital momenta transfer from light to nanoparticles		125
4.1	Orbital angular momenta transfer	125
4.2	A scientific statement	133
4.3	Spin angular momenta transfer	133
4.3.1	Torque from the arbitrary polarized plane wave using Stokes parameters	134
4.3.2	The critical angle	136
4.3.3	Rotation dynamics	137
4.3.4	Case of two beams	138
4.3.5	Taking into account chirality	141
4.3.6	Rotation of chiral particle in the field of HE_{11}	142
4.3.7	Torque on a small isotropic dipole particle and dipole approximation problems	144
4.3.8	Some useful decompositions	147
4.4	Spin angular momenta transfer: non-linear regime	147
4.5	A scientific statement	151
Chapter 5. Momentum transfer from an acoustic wave to scatterer		152
5.1	Main acoustics equations and variables	152
5.1.1	Spin and orbital angular momentum of acoustic waves	154
5.2	Mie scattering problem	154
5.2.1	General solution and the dispersion equation	154

5.2.2	Sphere resonances	156
5.2.3	Cross sections	158
5.2.4	Decomposition of the scattering coefficient in Taylor series . .	161
5.3	Monopole and dipole polarizability and its connection with scattering coefficients	161
5.3.1	Monopole polarizability	161
5.3.2	Dipole polarizability	163
5.4	Acoustic force and torque	164
5.4.1	Limit for the small particles. Connection with canonical momenta	164
5.4.2	Evanescent wave. Complex angle approach	167
5.5	Green's function	168
5.6	A scientific statement	169
Conclusion		170
List of figures		171
List of tables		181
References		182
Acknowledgements		219
Appendix A. Helpful math identities		220
Appendix B. Electric and magnetic dipole polarizabilities		222
B.1	Definitions	222
B.2	More on Mie	224
B.3	Comments on the connection with the literature	225
B.4	Dipole approximation for the scattering cross section	228
Appendix C. Fiber Green's tensor		230
Appendix D. Effective polarizability. General case		235
Appendix E. Canonical properties for complex frequency domain .		236
E.1	Mean of an arbitrary quadratic form	236

E.2	Poynting vector	236
E.3	Canonical spin angular momenta density	237
E.4	Canonical linear momentum density	237
E.5	Energy density	237
Appendix F. Photon wave function		238
Appendix G. Mie coefficients and dispersion equations		239
Appendix H. Derivation of Optical force from Maxwell stress tensor		241
H.1	Helpful identities	241
H.2	Calculating \mathbf{F}_{mix}	242
H.3	Calculating \mathbf{F}_{self}	243
Appendix I. Complex Vector Spherical Harmonics		245
I.1	Explicit form	245
I.2	Orthogonality	247
I.3	Connection to the other sources	248
I.4	Helpful math identities with vector spherical functions	252
Appendix J. Explicit form of j^2 for several first multipoles		254
Appendix K. Integrated values of the square of kinetic AM		255
Appendix L. Fundamental connection between diffusion and friction coefficients		256
Appendix M. (mandatory) Texts of author's key publications		258

To my grandfather Yuri Aleksandrovich Nechaev.

Реферат

Краткое содержание диссертации

Актуальность

Диссертация развивает фундаментальные знания в области исследований опто- и акустомеханики. Большой технический прогресс в оптической и акустической манипуляции объектами на субволновом уровне сделал ее доступной в многочисленных приложениях: 3D объемные дисплеи [1; 2], улавливание одиночных атомов [3; 4], инвазивное манипулирование биочастицами [5] и многие другие [6]. Быстрое развитие этой области требует как новых подходов к манипулированию субволновыми объектами, так и более глубокого понимания фундаментальных аспектов. Среди последних выделяется вопрос “*Как именно происходит передача линейного и углового моментов от полей к веществу вблизи нанофотонных структур?*” выделяется и становится одной из центральных проблем, рассматриваемых в данной диссертации.

Цель и задачи

Целью данной диссертации является углубление понимания передачи линейного и углового момента в опто- и акустомеханике, в частности, в нанофотонных и акустических геометриях. Были решены следующие конкретные **задачи**:

- сделан подробный обзор основ оптических сил и моментов, а также канонических свойств света был сделан;
- было предложено оптическое связывание с дальнодействием через волноводные моды нановолокна с использованием поперечной накачки;

- описана передача спинового и орбитального момента света к веществу вблизи бесконечного цилиндра и идеальной сферы;
- была установлена связь между оптомеханическими и акустомеханическими эффектами при рассеянии волн на субволновых объектах.

Научные положения

1. Массив субволновых частиц над волноводом может образовывать стабильную конфигурацию в поле линейно поляризованной плоской волны, падающей перпендикулярно оси волновода. Жесткость связи между частицами линейно растёт с ростом числа частиц.
2. Для орбитального вращения частицы вокруг диэлектрического волновода в вязкой жидкости, вызванного распространяющейся циркулярно поляризованной фундаментальной модой волновода, существует оптимальный радиус частицы, для которого орбитальная частота максимальна. Положение этого максимума не совпадает с максимумом канонической плотности полного углового момента.
3. Для непоглощающей частицы, геометрия которой осесимметрична относительно направления падающей волны, может возникнуть механический вращающий момент, связанный с генерацией второй гармоники. Возникновение вращающего момента оказывается связанным с ненулевым угловым моментом генерируемого поля второй гармоники, который строго связан с симметрией кристаллической решетки наночастицы.
4. Акустическая сила, действующая на субволновые частицы, прямо пропорциональна сумме плотности линейного канонического момента и градиента плотности энергии. Акустический крутящий момент на субволновые частицы пропорционален плотности канонического спинового момента.

Научная новизна

Несмотря на то, что перенос линейного и углового моментов является центральной проблемой оптомеханики с первых лет ее существования, с развитием методов и геометрии субволновых манипуляций возникают новые вопросы, требующие детального теоретического анализа. Результаты, полученные в рамках задач настоящей диссертации, вносят особую новизну в данную область, а именно:

- впервые теоретически было показано, что массив субволновых частиц около волновода может образовывать устойчивую конфигурацию в поле линейно поляризованной плоской волны, падающей перпендикулярно оси волновода. Жесткость связи между частицами линейно увеличивается с ростом числа частиц;
- впервые автором продемонстрировано, что для орбитального движения частицы вокруг диэлектрического волновода в вязкой жидкости, индуцированного циркулярно поляризованной основной модой, существует оптимальный радиус частицы, для которого орбитальная частота максимальна. Положение этого максимума точно не совпадает с максимумом канонической плотности полного углового момента;
- впервые теоретически доказано, что для непоглощающей частицы, геометрия которой осесимметрична под направлением падающей волны, может возникать механический момент, связанный с генерацией излучения на удвоенной частоте. Возникновение вращающего момента оказывается связанным с ненулевым угловым моментом генерируемого поля на второй гармонике, который возникает из-за специфической структуры кристаллической решетки наночастицы;
- впервые было показано, что акустическая сила, действующая на субволновые частицы, прямо пропорциональна сумме линейной канонической плотности импульса и градиента плотности энергии, а акустический импульс пропорционален канонической плотности спинового импульса.

Практическая значимость

Область оптомеханики постоянно требует новых инструментов для достижения более высокой степени контроля и манипуляций над нанообъектами. Оптические нановолокна являются прекрасным примером надежной платформы для изучения взаимодействия света и материи. В диссертации представлен ряд важных результатов, которые помогают понять основы захвата наночастиц и манипуляций вблизи диэлектрического нановолокна, предлагая новые подходы для вращения и удержания нанообъектов. Эти результаты также могут быть распространены на манипуляции с квантовыми системами, такими как ультрахолодные атомы. Более того, полученные результаты могут помочь в разработке новых методов манипуляции на основе резонансных диэлектрических рассеивателей Ми, локальные поля которых, описываемые в терминах мультиполей, могут позволить себе универсальный инструмент для наноразмерного пинцета. Наконец, мы укрепляем связь разработанных подходов в оптомеханике с акустомеханикой, позволяя эффективно перенести хорошо зарекомендовавшие себя подходы оптических манипуляций в акустику.

Таким образом, результаты работы могут найти применение в областях, где в настоящее время активно используются оптические и акустические пинцеты, таких как биология, нанотехнологии, квантовые манипуляции и вычисления, и многих других.

Практическая значимость работы заключается в потенциальном увеличении числа степеней свободы при манипулировании нано- и микрообъектами. Например, в дополнение к распространенной сейчас трехпозиционной манипуляции добавляется еще одна степень свободы — вращательная (орбитальная и спиновая). Последнее становится возможным благодаря более глубокому пониманию механизма передачи светового углового момента.

Достоверность

Достоверность полученных результатов обеспечивается, прежде всего, подтверждением теоретических выводов численными экспериментами, а также реальным экспериментом, где это было возможно. Кроме того, все основные результаты были опубликованы в высокоцитируемых журналах и успешно представлены на международных конференциях.

Апробация работы

Основные результаты исследований были доложены на следующих конференциях:

- [METANANO 2021 VI International Conference on Metamaterials and Nanophotonics](#). Total angular momenta quantization of dielectric sphere modes. Saint-Petersburg, Russia / Online. September 13–17, 2021.
- [APS March Meeting 2021](#). Directional scattering reinforced by acoustic bianisotropy and related acousto-mechanical effects. Online. March 15–19, 2021.
- [Quantum Nanophotonics \(Benasque\)](#). Stable Self-trapping Of Nanoparticles Via Waveguide Modes Of A Nanofiber. Online. Feb 28 – Mar 05, 2021.
- [METANANO 2020. V International Conference on Metamaterials and Nanophotonics](#). Saint-Petersburg, Russia / Online. Sep 14-18, 2020. 2 talks:
 - Optical binding of nanoparticles near a nanofiber waveguide;
 - Acoustic forces and torques: directional scattering and acoustic spin.
- [ONNA: Optical Nanofiber Applications](#). Self-induced anisotropy of spherical nanoparticle near a nanofiber and related optomechanical effects. Okinawa, Japan. Jul 3-6, 2019.
- [Conference on Nanophotonics: Foundations & Applications](#). Acoustic force and torque in connection with canonical momentum and spin: an optical approach. Sep 1-6, 2019. Ascona, Switzerland.

- [Okinawa School in Physics: Coherent Quantum Dynamics](#). Self-trapping of submicron particles near a nanofiber. Okinawa, Japan. Sep 25 - Oct 4, 2018.
- [JSAP photonics annual meeting](#). Dipole nanoparticles with induced anisotropy as point detectors of the angular momentum of light. Okinawa, Japan. Nov 30 - Dec 1, 2018.

Личный вклад автора

Вклад автора в данную работу заключается в построении теоретических моделей, получении аналитических результатов, таких как формулы и графики, анализе полученных результатов, объяснении соответствующей физики, а также в проведении численных расчетов. Автор внес значительный вклад не только в решение рассматриваемых задач, но и в их формулировку, поскольку это большая часть работы исследователя.

Вклад автора по всем главам следующий:

- В Главе **1** автор представил свою собственную уникальную точку зрения на оптические силы и крутящие моменты.
- В Главе **2** автор провел анализ собственных мод сферического и цилиндрического резонаторов.
- В Главе **3** автор нашел стабильную конфигурацию конечного массива наночастиц, удерживающихся с помощью поперечной накачки, и связанных дальнедействующим взаимодействием через волноводные моды нановолокна. Автор выполнил все основные теоретические и численные расчёты.
- В Главе **4** автор выполнил только теоретическую часть работы, а эксперимент был проведен Георгием Ткаченко в группе профессора Síle Nic Chormaic в OIST.
- В Главе **5** автор в сотрудничестве с Константином Блюхом нашел способ связать акустические силу и момент с каноническими моментами акустических полей. Автор также выполнил все теоретические и численные расчеты.

Объем и структура работы

Диссертация состоит из введения, 5 глав, заключения и 13 приложений. Полный объем диссертации составляет 282 страницы, включая 60 рисунков и 6 таблиц. Список литературы содержит 364 наименования.

В Главе 1 представлены основы оптических сил и моментов, а также последние достижения в этой области. Глава 2 посвящена спиновым и орбитальным угловым моментам собственных мод сферы и бесконечного цилиндра. В Главе 3 представлена теория оптического связывания рядом с волноводом. Глава 4 посвящена передаче линейного и углового моментов света веществу, а также теоретическому описанию орбитального движения наночастицы вокруг сверхтонкого одномодового оптического волокна. Наконец, в Главе 5 подробно описывается тесная связь между оптикой и линейной акустикой. Мы показываем, как субволновые акустические частицы могут быть мерой канонических моментов падающего поля.

Основное содержание работы

Растущий интерес к оптическим манипуляциям различного рода стимулируется огромным успехом в доступных экспериментальных реализациях. Неинвазивное манипулирование частицами является важной и неотъемлемой техникой в исследовании нано- и микрообъектов. Механические манипуляции часто неприемлемы, поскольку они могут потенциально разрушить исследуемый объект.

Чтобы подчеркнуть важность этой отрасли науки, упомянем, что несколько ученых были удостоены Нобелевской цены за достижения в области оптической манипуляции. Среди них Артур Эшкин в 2018 году “за оптический пинцет и его применение в биологических системах”; Стивен Чу, Клод Коэн-Таннуджи и Уильям Дэниел Филлипс в 1997 году “за разработку методов охлаждения и ловушки атомов с помощью лазерного излучения”. На этом фоне только недавно акустические системы захвата частиц начали приближаться к такому же уровню контроля. Например, первая реализация акустического пинцета с помощью *одного* пучка, аналогичного стандартному оптическому пинцету, была продемонстрирована только в 2016 году [7]. В таблице 1 приведена краткая сводка доступных размеров частиц и требуемых мощностей пучка на сегодняшний день.

Table 1 — Сравнение типичных размеров и мощности оптического и акустического пинцетов. Данные взяты из [5].

Метод	Размер частиц	Мощность (Вт/см ²)
Акустический пинцет	100 нм – 10 мм	$10^{-2} - 10^1$
Оптический пинцет	10 нм – 1 мм	$10^6 - 10^7$

Данная диссертация углубляется в фундаментальные явления в этой области. Центральным вопросом является то, как именно передача импульса и углового момента связана с опто- и акустомеханикой. На протяжении всей работы одной из основных идей является то, что малые частицы субволновой длины действуют как измерительные инструменты для электромагнитного или акустического поля, что кратко представлено на рисунке 1. Далее приводится краткое содержание каждой главы без излишних технических подробностей.

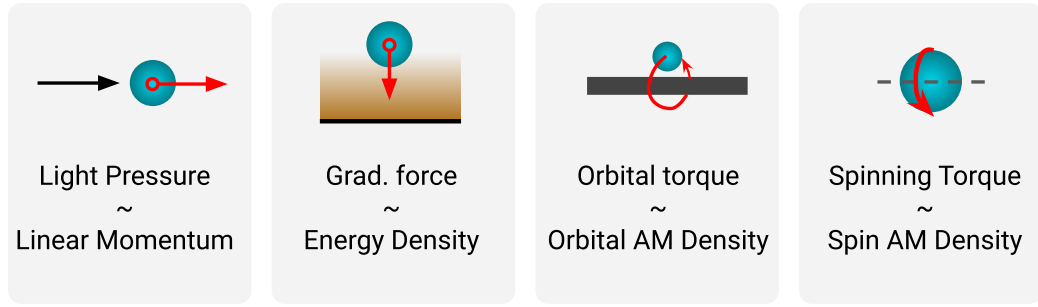


Figure 1 — Концепция связи между каноническими свойствами электромагнитного поля и оптомеханикой для частиц субволновой длины. Существует также полная аналогия для акустических полей и акустомеханики

В **Главе 1** мы подробно обсуждаем весь формализм, лежащий в основе вычисления оптических и акустических сил. Самый общий способ нахождения силы и момента за период колебаний заключается в нахождении изменения потока линейного импульса (или тензора напряжений Максвелла) и потока углового импульса полного поля. Формально это можно сделать следующим образом:

$$\mathbf{F} = \oint_{\Sigma} \langle \hat{\mathcal{T}} \rangle \mathbf{n} d\Sigma, \quad \mathbf{T} = \oint_{\Sigma} \langle \hat{\mathcal{M}} \rangle \mathbf{n} d\Sigma \quad (1)$$

где тензоры потоков для однородной изотропной среды с ϵ и μ даны в виде [8]

$$\langle \hat{\mathcal{T}} \rangle = \frac{1}{2} \text{Re} \left[\epsilon \epsilon_0 \mathbf{E}^* \cdot \mathbf{E} + \mu \mu_0 \mathbf{H}^* \cdot \mathbf{H} - \hat{\mathbf{I}} \left(\epsilon \epsilon_0 |\mathbf{E}|^2 + \mu \mu_0 |\mathbf{H}|^2 \right) \right], \quad (2)$$

$$\langle \mathcal{M}_{ij} \rangle = \epsilon_{ikl} r_k \langle \mathcal{T}_{lj} \rangle \quad (3)$$

Обычно именно эти выражения используются в полных численных расчетах.

Для того, чтобы подступиться аналитически к практически любой задаче с оптическими силами, очень удобным может оказываться рассмотреть предел субволновых частиц. Наиболее важным безразмерным параметром здесь является ka , где $k = n\omega/c$ — длина волны в среде с показателем преломления n , а a — характерный радиус частицы.

В пределе $ka \ll 1$ мы можем заменить частицу точечным электрическим диполем \mathbf{p} и точечным магнитным диполем \mathbf{m} . После этого можно взять интеграл в (1) (см. Приложение H) и получить выражения для силы и момента

$$\mathbf{F}_{ka \ll 1} = \mathbf{F}^{(e)} + \mathbf{F}^{(m)} + \mathbf{F}^{(e-m)}$$

$$= \underbrace{\frac{1}{2} \text{Re}(\mathbf{p}^* \cdot (\nabla) \mathbf{E})}_{\sim (ka)^3} + \underbrace{\frac{\mu \mu_0}{2} \text{Re}(\mathbf{m}^* \cdot (\nabla) \mathbf{H})}_{\sim (ka)^5 \text{ for } \mu_p = \mu} - \underbrace{\frac{k^4}{12\pi} \sqrt{\frac{\mu \mu_0}{\epsilon \epsilon_0}} \text{Re}(\mathbf{p}^* \times \mathbf{m})}_{\sim (ka)^8 \text{ for } \mu_p = \mu} \quad (4)$$

где обозначение, впервые введенное Берри [9], “ $\cdot(\nabla)$ ” следует понимать как $\mathbf{A} \cdot (\nabla)\mathbf{B} \equiv \sum_{\alpha} \sum_{i=x,y,z} A_i \hat{\mathbf{e}}_{\alpha} \nabla_{\alpha} B_i$, где α индекс произвольной ортогональной системы координат (декартовой, цилиндрической, сферической и т.д.). Подчеркнем, что суммирование ведется по декартовым координатам (про другие системы координат см. в Приложении A).

Оптический момент будет

$$\mathbf{T}_{ka \ll 1} = \mathbf{T}^{(e)} + \mathbf{T}^{(m)}, \quad (5a)$$

$$\mathbf{T}^{(e)} = \mathbf{T}_0^{(e)} + \mathbf{T}_s^{(e)} = \frac{1}{2} \operatorname{Re} [\mathbf{p}^* \times \mathbf{E}] - \frac{k^3}{12\pi\epsilon\epsilon_0} \operatorname{Im} [\mathbf{p}^* \times \mathbf{p}], \quad (5b)$$

$$\mathbf{T}^{(m)} = \mathbf{T}_0^{(m)} + \mathbf{T}_s^{(m)} = \frac{1}{2} \operatorname{Re} [\mu\mu_0 \mathbf{m}^* \times \mathbf{H}] - \frac{k^3 \mu\mu_0}{12\pi} \operatorname{Im} [\mathbf{m}^* \times \mathbf{m}], \quad (5c)$$

где электрическая и магнитная компоненты связаны с взаимодействием с электрическим $\mathbf{p} = \alpha_e \mathbf{E}$ и магнитным $\mathbf{m} = (\mu\mu_0)^{-1} \alpha_m \mathbf{H}$ диполя соответственно. Присутствие членов рассеяния $\mathbf{T}_s^{(e,m)}$ имеет решающее значение для непоглощающих частиц. Например, для маленькой непоглощающей сферы крутящий момент должен быть равен нулю [10; 11], поскольку в силу соображений азимутальной симметрии не происходит изменения углового момента при рассеянии. Единственный возможный способ получить этот ноль — учесть поправку на рассеяние в (5) (подробнее см. в Приложении 4.3.7).

Наконец, после введения электрической α_e и магнитной α_m поляризуемости мы можем явно связать силу и момент с каноническими свойствами поля: плотность электромагнитной энергии $W = W^{(e)} + W^{(m)}$, плотность линейного импульса $\mathbf{P} = \mathbf{P}^{(e)} + \mathbf{P}^{(m)}$, плотность спинового углового момента $\mathbf{S} = \mathbf{S}^{(e)} + \mathbf{S}^{(m)}$, комплексный поток энергии (или комплексный вектор Пойнтинга) $\mathbf{\Pi}_{\operatorname{Im}}^{\operatorname{Re}} = \frac{1}{2} \frac{\operatorname{Re}}{\operatorname{Im}} (\mathbf{E}^* \times \mathbf{H})$ [12–14],[15, § 6. 9],[16, § 2.20],[17, § 12.5] как

$$\mathbf{F} = \mathbf{F}^{(e)} + \mathbf{F}^{(m)} + \mathbf{F}^{(e-m)}, \quad (6a)$$

$$\mathbf{F}^{(e)} = \underbrace{(\frac{\epsilon\epsilon_0}{\mu\mu_0})^{-1} \operatorname{Re}[\alpha_e] \nabla W^{(e)}}_{\text{conservative}} + \underbrace{2 \frac{c}{n} \sigma_{\operatorname{ext}}^{(e)} \mathbf{P}^{(e)}}_{\text{non-conservative}} \quad (6b)$$

$$\mathbf{F}^{(e-m)} = -\frac{c^2 k^4}{6\pi} \frac{c}{n} \left[\operatorname{Re}(\alpha_e \alpha_m^*) \frac{1}{n^2} \left(\mathbf{P} + \frac{1}{2} \nabla \times \mathbf{S} \right) + \operatorname{Im}(\alpha_e \alpha_m^*) \frac{1}{c^2} \mathbf{\Pi}^{\operatorname{Im}} \right] \quad (6c)$$

Для случая $\mathbf{S}^{(e)} = \mathbf{S}^{(m)}$ (например, для эллиптически поляризованной плоской волны) вращающий момент будет равен

$$\mathbf{T} = 2 \frac{c}{n} \left(\sigma_{\operatorname{abs}}^{(e)} \mathbf{S}^{(e)} + \sigma_{\operatorname{abs}}^{(m)} \mathbf{S}^{(m)} \right) = \frac{c}{n} \sigma_{\operatorname{abs}} \mathbf{S} \quad (7)$$

Здесь $\sigma_{\text{ext}}^{(e,m)} = \sigma_{\text{sc}}^{(e,m)} + \sigma_{\text{abs}}^{(e,m)}$ — это электрическая и магнитная части сечений экстинкции, поглощения и рассеяния частицы. Они связаны с поляризуемостями (см. Приложение В.4).

Манипулируемые частицы могут иметь сложную *внутреннюю* структуру с точки зрения электромагнитного отклика [18; 19]. Очень ярким примером таких частиц являются жидкие кристаллы, которые широко обсуждаются в [20]. Наиболее общий случай бианизотропных сред может быть полностью описан конститутивными соотношениями [21–24]

$$\begin{pmatrix} \mathbf{D} \\ \mathbf{B} \end{pmatrix} = \begin{pmatrix} \varepsilon \varepsilon_0 & i\mathbf{\kappa}/c \\ -i\mathbf{\kappa}^T/c & \mu \mu_0 \end{pmatrix} \begin{pmatrix} \mathbf{E} \\ \mathbf{H} \end{pmatrix} \quad (8)$$

где ε , μ , κ — комплексно оцененные тензоры 3×3 . Здесь мы также приняли во внимание, что среда является взаимно обратимой, поэтому диагональные элементы в Ур. (8) связаны. Для невзаимных сред мы рекомендуем прочитать ссылки. [21; 22]. Когда речь идет о малых частицах, можно получить дипольные поляризабельности $(\alpha_e, \alpha_m, \alpha_c)$ из объемных параметров $(\varepsilon, \mu, \kappa)$. Это приводит к [25; 26]

$$\begin{pmatrix} \mathbf{p} \\ \mu \mu_0 \mathbf{m} \end{pmatrix} = \begin{pmatrix} \alpha_e & i\alpha_c \\ -i\alpha_c^T & \alpha_m \end{pmatrix} \begin{pmatrix} \mathbf{E} \\ \mathbf{H} \end{pmatrix} \quad (9)$$

где α_e , α_m , α_c — в общем случае комплексно значные 3×3 тензоры. Мы подчеркиваем, что $\alpha_{e,m,c}$, являются функциями ε , μ и κ (явные выражения см. в Приложении В). Поправки на перестройку и оптическая теорема для бианизотропных частиц обсуждаются в [27, § II.C].

Сила на хиральной изотропной частице будет [18; 23; 24; 26; 28–31] (однако, не в каждой ссылке учитывается слагаемое $\mathbf{F}^{(e-m)}$)

$$\mathbf{F} = \mathbf{F}^{\text{non-chiral}} + \frac{\omega}{n} \text{Re}(\alpha_c) \nabla \mathcal{G} + \omega \gamma_{\text{abs},c}^{\text{Re}} \mathbf{S} - \text{Im}(\alpha_c) \nabla \times \mathbf{\Pi}^{\text{Re}} - \frac{k^4 c}{6\pi n} |\alpha_c|^2 \mathbf{\Pi}^{\text{Re}}. \quad (10)$$

Здесь $\mathbf{F}^{\text{non-chiral}}$ — сила из (6b), а α_e и α_m — функции $(\varepsilon, \mu, \kappa)$ (см. Приложение В). Мы также использовали следующее тождество: $\omega^2 \mathbf{S} - \frac{1}{2} \nabla \times \mathbf{\Pi}^{\text{Re}} = -\frac{1}{4} \text{Re}(\mathbf{H}^* \cdot (\nabla) \mathbf{E} - \mathbf{E}^* \cdot (\nabla) \mathbf{H})$ [23; 24]. Подставляя (9) в (5), получаем крутящий момент, действующий на хиральную изотропную частицу [32; 33]

$$\mathbf{T} = \frac{c}{n} \sigma_{\text{abs},c} \mathbf{S} + \frac{1}{\omega} \gamma_{\text{abs},c}^{\text{Re}} \mathbf{\Pi}^{\text{Re}} + \frac{1}{\omega} \gamma_{\text{abs},c}^{\text{Im}} \mathbf{\Pi}^{\text{Im}}. \quad (11)$$

Обобщенные хиральные сечения поглощения имеют вид

$$\sigma_{\text{abs},c} = \sigma_{\text{abs},c}^{(e)} + \sigma_{\text{abs},c}^{(m)}, \quad (12a)$$

$$\sigma_{\text{abs},c}^{(e)} = \frac{k}{\varepsilon \varepsilon_0} (\text{Im}(\alpha_e) - g_e |\alpha_e|^2 - g_m |\alpha_c|^2), \quad (12b)$$

$$\sigma_{\text{abs},c}^{(m)} = \frac{k}{\varepsilon \varepsilon_0} (\text{Im}(\alpha_m) - g_m |\alpha_m|^2 - g_e |\alpha_c|^2), \quad (12c)$$

$$\gamma_{\text{abs},c}^{\text{Re}} = 2\omega \text{Im}(\alpha_c) - 2\omega g_e \text{Re}(\alpha_e \alpha_c^*) - 2\omega g_m \text{Re}(\alpha_m \alpha_c^*), \quad (12d)$$

$$\gamma_{\text{abs},c}^{\text{Im}} = 2\omega g_m \text{Im}(\alpha_m \alpha_c^*) - 2\omega g_e \text{Im}(\alpha_e \alpha_c^*), \quad (12e)$$

где определены константы $g_e = \frac{k^3}{6\pi\varepsilon\varepsilon_0}$ и $g_m = \frac{k^3}{6\pi\mu\mu_0}$. Отметим, что для хиральной частицы без потерь с $\text{Im}(\varepsilon) = \text{Im}(\mu) = \text{Im}(\kappa) = 0$ момент равен нулю, поэтому никакой угловой момент не может быть передан от любого падающего оптического поля к такой частице. Стоит отметить, что вышеприведенный вывод справедлив и для любой хиральной сферы без потерь любого размера [32, Ур. (9)]. Это альтернативно следует из оптической теоремы для хиральных частиц [34], подробнее см. упр. (B.30) в Приложении B. Альтернативное разложение можно найти в [31, Ур. (7)].

Удивительно, но в субволновом приближении для частиц с потерями, благодаря симметрии уравнений, существует простое замкнутое соотношение между диссипативной частью силы и скручиванием хиральной и нехиральной частей момента, что открывает прямой путь измерения хиральной части поляризуемости, потока энергии и плотности спинового углового момента [24, eqs. (15, 16)]

$$\mathbf{F}_{\text{diss}}^{(e,m)} + \frac{1}{2} \nabla \times \mathbf{T}^{(e,m)} = \frac{n}{c} \sigma_{\text{abs}} \mathbf{\Pi}^{\text{Re}} \quad (13a)$$

$$\mathbf{F}_{\text{diss}}^{(c)} + \frac{1}{2} \nabla \times \mathbf{T}^{(c)} = 2\omega^2 \text{Im}(\alpha_c) \mathbf{S} \quad (13b)$$

где для малых поглощающих частиц с $\sigma_{\text{ext}} \approx \sigma_{\text{abs}}$ мы имеем $\mathbf{F}_{\text{diss}} = \mathbf{F}_{\text{diss}}^{(e,m)} + \mathbf{F}_{\text{diss}}^{(c)} = \frac{c}{n} \sigma_{\text{abs}} \mathbf{P} + 2 \text{Im}(\alpha_c) (\omega^2 \mathbf{S} - \frac{1}{2} \nabla \times \mathbf{\Pi}^{\text{Re}})$ - диссипативная (или неконсервативная) часть силы и момента, равная $\mathbf{T} = \mathbf{T}^{(e,m)} + \mathbf{T}^{(c)} = \frac{c}{n} \sigma_{\text{abs}} \mathbf{S} + 2 \text{Im}(\alpha_c) \mathbf{\Pi}^{\text{Re}}$. Здесь мы использовали $\mathbf{\Pi}^{\text{Re}} = \frac{c^2}{n^2} (\mathbf{P} + \frac{1}{2} \nabla \times \mathbf{S})$ и предположили, что $\mathbf{P}^{(e)} = \mathbf{P}^{(m)}$ и $\mathbf{S}^{(e)} = \mathbf{S}^{(m)}$. Заметим, что это соотношение написано для дипольных частиц с потерями, для которых можно пренебречь поправочными членами отдачи (рассеяния) в силе и моменте.

Также есть много сходств с теорией линейной субволновой акустотехники, которая обсуждается в разделе 1.7 и в главе 5. Наконец, в разделе 1.6 мы также

сделаем краткий обзор стохастического моделирования, которое крайне важно учитывать, когда речь идет о реальных системах.

Наконец, в разделе 1.6 мы также сделаем краткий обзор стохастического моделирования, которое крайне важно учитывать, когда речь идет о реальных системах.

Проведение экспериментов по изучению оптических сил и моментов в реальном мире всегда сопровождается броуновскими силами или *стохастическими силами* \mathbf{F}_{st} . Природа этой силы заложена в огромном количестве столкновений с более мелкими частицами вмещающей жидкости. Одним из возможных безразмерных параметров для определения потенциального влияния стохастических сил является соотношение между энергией частиц U (кинетической, например, обусловленной оптическим давлением или локальной глубиной потенциального колодца оптической ловушки) и энергией теплового движения [6; 35; 36]:

$$\gamma = \frac{U}{k_{\text{B}}T}, \quad \begin{cases} \gamma \lesssim 1 & - \mathbf{F}_{\text{st}} \text{ has to be considered} \\ \gamma \gg 1 & - \mathbf{F}_{\text{st}} \text{ is negligible} \end{cases} \quad (14)$$

где k_{B} — постоянная Больцмана, а T — абсолютная температура вмещающей среды. Оценка для энергии U зависит от доминирующего типа оптической силы: консервативной (градиентная сила) или неконсервативной (оптическое давление) [6; 37–40][41, § 3]. В дипольном приближении два различных вклада можно увидеть из уравнения (6b).

Если консервативная сила доминирует, то потенциальная глубина оптической ловушки для электрической дипольной частицы может быть оценена как $U = U_{\text{tr}} = \langle \mathbf{p} \cdot \mathcal{E} \rangle = \frac{1}{2} \text{Re}(\alpha_{\text{e}}) |\mathbf{E}|^2$. Поскольку вблизи точки равновесия сила линейна по отношению к перемещению, можно ввести эффективную жесткость в виде $F \approx -\kappa \Delta r$, таким образом потенциальная энергия будет равна $U_{\text{tr}} = \frac{1}{2} \kappa \overline{\Delta r}^2$ [6; 36], где $\overline{\Delta r}$ — средняя ширина потенциального колодца в реальном пространстве. Следует подчеркнуть, что такой анализ справедлив только в том случае, если консервативная часть оптических сил доминирует. В противном случае, если доминируют неконсервативные силы, то кинетическая энергия должна быть помещена в Ур. (1.41). Например, для давления плоской волны это будет $U = U_{\text{kin}} = \frac{m \langle \mathbf{v} \rangle^2}{2}$, где средняя скорость частицы может быть получена из равенства оптической

силы давления и силы трения (закон Стокса [42]) $\langle v \rangle = \sigma_{\text{ext}}^{(e)} \frac{1}{2} \varepsilon \varepsilon_0 |\mathbf{E}|^2 / (6\pi\nu a)$, где ν — динамическая вязкость вмещающей жидкости, а a — радиус частицы.

Как только стохастическая сила должна быть учтена, уравнение Ланжевена должно быть решено численно, чтобы достичь правильного моделирования динамики. Конечно, для проведения дальнейшего статистического анализа потребуется множество реализаций одного и того же численного эксперимента. Уравнение движения будет иметь вид

$$m\ddot{\mathbf{r}} = -\zeta\dot{\mathbf{r}} + \mathbf{F}_{\text{st}} + \mathbf{F} \quad \text{or} \quad \begin{cases} \dot{\mathbf{r}} = \mathbf{v} \\ \dot{\mathbf{v}} = -\frac{\zeta}{m}\mathbf{v} + \frac{1}{m}(\mathbf{F}_{\text{st}} + \mathbf{F}) \end{cases} \quad (15)$$

где m — масса частиц, ζ — коэффициент тяги (для сферы применим закон Стокса, поэтому $\zeta = 6\pi\nu a$, где a и ν — стороны частиц и динамическая вязкость вмещающей жидкости), \mathbf{F} — оптическая сила, а \mathbf{F}_{st} — дельта-коррелированная стохастическая сила с нулевым средним, так что она удовлетворяет $\langle \mathbf{F}_{\text{st}}(t) \rangle_t = 0$ и $\langle F_{\text{st},\alpha}(t) F_{\text{st},\beta}(t + \tau) \rangle_t = 2D\delta_{\alpha\beta}\delta(\tau)$. Важно понимать, что трение и стохастические силы связаны друг с другом на фундаментальном уровне. Это означает, что коэффициент трения ζ связан с коэффициентом автокорреляции D стохастических сил как $D = k_{\text{B}}T\zeta$ [43] (доказательство см. в Приложении L).

Уравнение (15) может быть переписано как система двух дифференциальных уравнений первого порядка относительно \mathbf{r} и \mathbf{v} , и решено любой стандартной численной процедурой, такой как семейство методов Эйлера, методы Рунге-Кутты или любой другой [44], с некоторым специальным подходом к стохастическому члену \mathbf{F}_{st} [43]. Все эти методы основаны на дескритизации временной линии $t \rightarrow \{t_i\}$ с шагом Δt . Интегрирование (15), т.е. $\int_{t_i}^{t_{i+1}} (1.42) dt$, будет иметь препятствия, поскольку $\int_{t_i}^{t_{i+1}} \mathbf{F}_{\text{st}}(t) dt \neq \mathbf{F}_{\text{st}}(t_i)\Delta t$. Хитрость заключается в том, чтобы ввести новую переменную $\int_{t_i}^{t_{i+1}} dt \mathbf{F}_{\text{st}}(t) \equiv \mathbf{W}_i$. со свойствами, которые следуют из свойств белозумности \mathbf{F}_{st} : $\langle \mathbf{W}_i \rangle = 0$ и $\langle \mathbf{W}_i \cdot \mathbf{W}_j \rangle = \delta_{ij} \cdot 6k_{\text{B}}T\zeta\Delta t = \delta_{ij} \cdot 3\sigma_{W_\alpha}^2$ с $\alpha = x, y, z$, заметим, что последнее является фактически дисперсией нормально распределенной случайной величины W_α . Таким образом, для простого метода Эйлера конечная система будет иметь вид

$$\begin{cases} \mathbf{r}(t_{i+1}) = \mathbf{r}(t_i) + \Delta t \mathbf{v}(t_i), \\ \mathbf{v}(t_{i+1}) = \mathbf{v}(t_i) - \Delta t \frac{\zeta}{m} \mathbf{v}(t_i) + \frac{1}{m} \mathbf{W}_i \end{cases}, \quad \begin{cases} \sigma_{W_\alpha} = \sqrt{2k_{\text{B}}T\zeta\Delta t} \\ \alpha = x, y, z \end{cases} \quad (16)$$

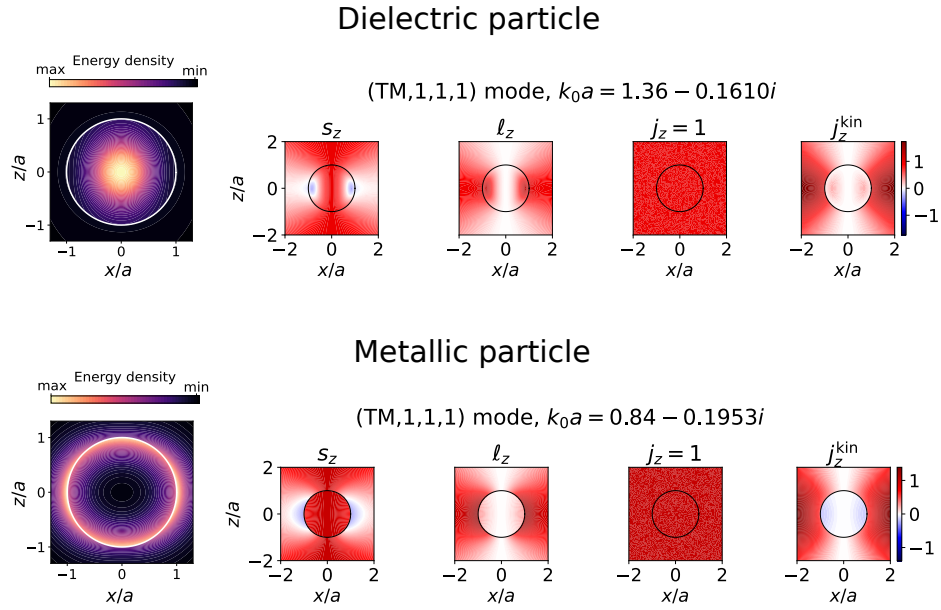


Figure 2 — Распределение плотности углового момента для дипольных мод для диэлектрических и металлических частиц

Мы подчеркиваем, что дисперсия (или квадратичное отклонение) зависит от временного шага дескритизации Δt .

В **Главе 2** проводится анализ собственных мод двух аналитически решаемых геометрий: сферы и бесконечного цилиндра. В случае сферы, собственные моды описываются векторными сферическими гармониками (VSH) и их собственные частоты всегда комплексные, так как это открытая система, поэтому

$$\omega = \omega' - i\delta \quad (17)$$

где $\delta/2$ показывает обратное среднее время жизни режима. В конечном итоге, структура собственных мод диэлектрической сферы напоминает электрическое и магнитное поле одиночного фотона с определенным угловым моментом.

Мы анализируем собственные моды, используя канонические свойства поля, введенные недавно в работе [45] для, вообще говоря, дисперсионных сред, что имеет решающее значение для случая металлических частиц. Энергия Бриллюэна W , линейный импульс \mathbf{P} , спин \mathbf{S} , орбитальный \mathbf{L} и полный угловой момент \mathbf{J} могут быть сформулированы в манере квантовой механики

следующим образом [15; 45; 46]

$$W = \langle \psi | \omega | \psi \rangle = \frac{1}{4} (\tilde{\epsilon} \epsilon_0 |\mathbf{E}|^2 + \tilde{\mu} \mu_0 |\mathbf{H}|^2), \quad (18)$$

$$\mathbf{P} = \langle \psi | \hat{\mathbf{p}} | \psi \rangle = \frac{1}{4\omega'} \text{Im} (\tilde{\epsilon} \epsilon_0 \mathbf{E}^* \cdot (\nabla) \mathbf{E} + \tilde{\mu} \mu_0 \mathbf{H}^* \cdot (\nabla) \mathbf{H}), \quad (19)$$

$$(20)$$

$$\mathbf{S} = \langle \psi | \hat{\mathbf{S}} | \psi \rangle = \frac{1}{4\omega'} \text{Im} (\tilde{\epsilon} \epsilon_0 \mathbf{E}^* \times \mathbf{E} + \tilde{\mu} \mu_0 \mathbf{H}^* \times \mathbf{H}), \quad (21)$$

$$\mathbf{L} = \mathbf{r} \times \mathbf{P}, \quad \mathbf{J} = \mathbf{L} + \mathbf{S}, \quad (22)$$

и квадратичная форма квадрата полного углового момента, обозначаемого как $[\mathbf{J}^2]$, дается как

$$[\mathbf{J}^2] = \langle \psi | (\hat{\mathbf{L}} + \hat{\mathbf{S}})^2 | \psi \rangle = \frac{1}{4\omega'} \text{Re} \tilde{\epsilon} \epsilon_0 \left[r^2 \sum_{i=x,y,z} E_i^* \Delta_\Omega E_i + 2(\mathbf{E}^* \cdot \nabla)(\mathbf{r} \cdot \mathbf{E}) \right] + (\text{магнитная часть: } \begin{matrix} \mathbf{E} \rightarrow \mathbf{H} \\ \tilde{\epsilon} \epsilon_0 \rightarrow \tilde{\mu} \mu_0 \end{matrix}). \quad (23)$$

которая, насколько нам известно, была написана в явном виде впервые. Каждая из компонент может быть естественным образом разложена на электрическую и магнитную части. Здесь $(\tilde{\epsilon}, \tilde{\mu}) = (\epsilon, \mu) + \omega \partial_\omega (\epsilon, \mu)$, электромагнитная 6-компонентная “волновая функция” дается $|\psi\rangle = \sqrt{g/2} (\sqrt{\tilde{\epsilon} \epsilon_0} \mathbf{E}, \sqrt{\tilde{\mu} \mu_0} \mathbf{H})^T$ [45; 47–51], где константа g зависит от системы единиц: $g^{\text{Gaussian}}_{\text{SI units}} = \left(\frac{(2\omega)^{-1}}{(8\pi\omega)^{-1}} \right)$. Эта волновая функция фотона записывается в виде Шредингероподобной формулировки уравнений Максвелла. В литературе существует и другой способ записи волновой функции фотона, который основан на Диракоподобной формулировке уравнений Максвелла [52–57]. Как утверждают Vialynicki-Birula [53; 57] и Sipe [54], для фотонов лучше всего принять волновую функцию, модуль квадрата которой является средней плотностью энергии фотона, а не плотностью вероятности положения, как в случае с электронами [58], что верно для обеих формулировок.

Мы построили график плотности канонических угловых моментов и показали, что она является целочисленной величиной, если найти полный угловой момент на один фотон (рис. 2). Таким образом, это открывает путь к исследованию структуры электрического поля одиночных фотонов путем изучения структуры собственных мод сферы. Далее мы также подробно анализируем направляемые моды диэлектрического волновода. В частности, мы показываем, что, как и в случае сферы, каноническая полная плотность

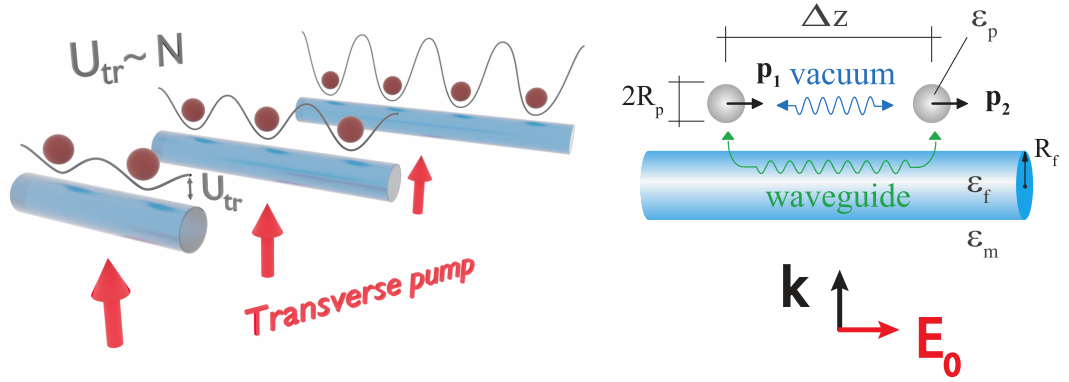


Figure 3 — Основная идея главы 3: массив субволновых частиц вблизи нановолокна с поперечной накачкой. Потенциал захвата вдоль оси волокна растет линейно с числом частиц в цепи. Дальнее взаимодействие достигается за счет взаимодействия через волноводную моду

угловых моментов на один фотон собственных мод квантуется

$$\mathbf{E}(\mathbf{r}) \sim e^{im\varphi} \quad \rightarrow \quad j_z = \frac{\omega' J_z}{W} = \frac{\omega(rP_\varphi + S_z)}{W} = m. \quad (24)$$

В Главе 3 мы рассматриваем очень своеобразную и богатую физикой систему. Оказывается, что конечное множество мелких частиц может быть захвачено во всех трех направлениях *одиночным* пучком (см. рисунок 3).

Большинство методов оптического захвата и манипулирования основаны на формировании интенсивности светового поля с помощью оптических систем, таких как пространственный модулятор света, который обеспечивает формирование дипольного потенциала захвата. Этот подход был эффективно использован для манипулирования объектами в различных средах, таких как воздух, вода и вакуум. Однако альтернативный метод манипулирования и упорядочения больших ансамблей основан на подходе самосборки[59]. Полевая картина интенсивности формируется за счет рассеяния оптических полей объектами, что приводит к эффективным диполь-дипольным взаимодействиям и последующему структурированию больших ансамблей. Типичным примером такого эффекта является поперечное оптическое связывание [60; 61], когда наночастица может образовывать связанные состояния при однородном освещении. Хотя оптические диполь-дипольные взаимодействия довольно слабы, они могут быть усилены и модифицированы с помощью вспомогательных фотонных структур [62], таких как метаматериалы[63; 64] и метаповерхности[65], плазмонные структуры[66; 67], фотонные кристаллические полые волокна[68], а также диэлектрические

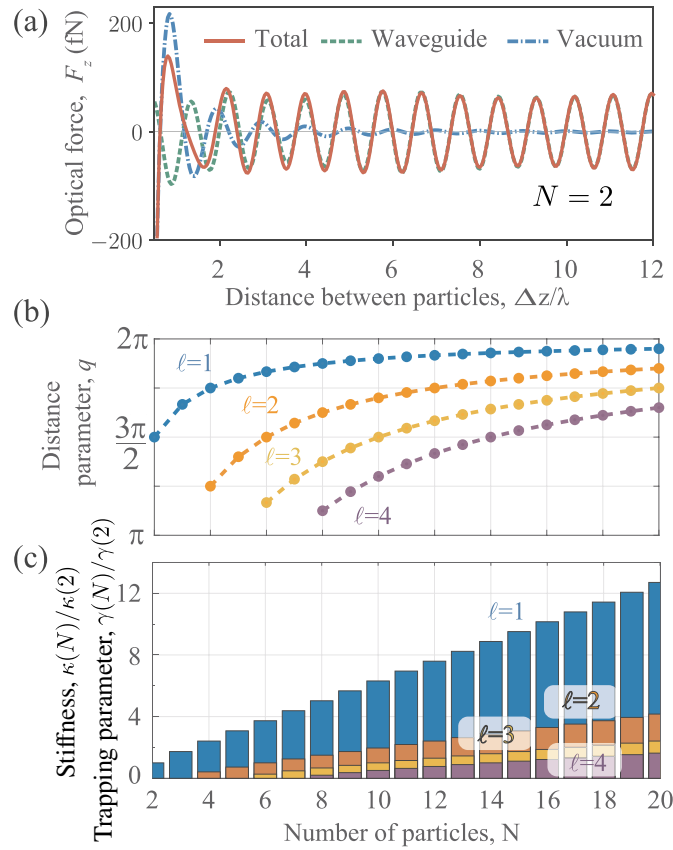


Figure 4 — (a) Продольная сила F_z в одномодовом режиме, действующая на одну из двух частиц в зависимости от расстояния вдоль оси нановолокна Δz . Красная сплошная линия показывает полную оптическую силу, которая учитывает взаимодействие как через свободное пространство, так и через волокно ($\hat{\mathbf{G}}_s + \hat{\mathbf{G}}_0$), зеленая пунктирная линия показывает только взаимодействие через волокно ($\hat{\mathbf{G}}_s$) и синяя пунктирная линия показывает только взаимодействие в свободном пространстве ($\hat{\mathbf{G}}_0$). (b) Равновесные решения. Первые три ветви решения для расстояния между двумя ближайшими частицами $q = \Delta z\beta$ в отношении общего числа частиц в цепочке N . (c) Параметр ловушки γ , который равен эффективной потенциальной глубине ловушки, деленной на тепловую энергию вмещающей среды kT , и нормированная жесткость ловушки по отношению к числу частиц в цепочке N

нановолокна[69]. Последнее представляет собой универсальную платформу[70] для изучения взаимодействия света с наночастицами[71; 72] и атомами[73–75], расположенными близко к его поверхности. Использование одномодовых дальнедействующих диполь-дипольных взаимодействий, обеспечиваемых волноводными системами, уже было предложено для самоорганизации атомов и наночастиц в волноводных системах[68; 76; 77].

Мы предлагаем геометрию массива наночастиц, расположенных вблизи ультратонкого волокна и освещаемых плоской волной, распространяющейся в изотропной среде перпендикулярно оси волокна, как показано на рис. 3.2. Такая конфигурация позволяет использовать преимущества эффекта поперечного оптического связывания [61; 78]. Связывание происходит из-за интерференции полей, рассеиваемых наночастицами, и было применено для самоорганизации ансамблей наночастиц при внешнем монохроматическом освещении [79–81], включая частичное связывание у металлической поверхности вблизи поверхностного плазмон-поляритонного резонанса (ППП) [82]. В литературе поперечное связывание наблюдалось в большом ансамбле диэлектрических субмикронных сфер [83] и нанопроводов [84; 85] с сильными коллективными взаимодействиями через вакуум.

Направленные моды нановолокна позволяют накапливать дальние взаимодействия между удаленными наночастицами благодаря чрезвычайно низким потерям, что приводит к увеличению жесткости частиц с ростом длины цепочки наночастиц. Более того, в нашей конкретной геометрии связывания вблизи нановолокна, мы также предполагаем захват наночастиц в радиальном направлении вблизи поверхности волокна с помощью двух встречно распространяющихся плоских волн и использования преимуществ фотонной струи нановолокна или эффекта линзирования [86]. В этом эффекте при поперечном возбуждении диэлектрическое нановолокно начинает действовать как фокусирующая линза. Таким образом, мы предлагаем геометрию системы, которая позволяет немедленно проверить заявленный эффект в конкретной экспериментальной установке с использованием оптических нановолокон.

При возбуждении плоской волной наночастицы формируют устойчивый самоорганизованный периодический массив вдоль оси волновода за счет эффекта поперечного связывания. Мы показали, что из-за дальнего взаимодействия между наночастицами потенциал захвата для каждой наночастицы в цепи линейно возрастает с увеличением размера системы, что делает образование длинных цепей более благоприятным. Мы показали, что для оптической нановолоконной платформы энергия связи двух наночастиц находится в диапазоне $9 \div 13 k_B T$, достигая значения $110 k_B T$ при увеличении размера цепи до 20 наночастиц (рис. 4). Мы также предлагаем геометрию возбуждения двух встречно распространяющихся

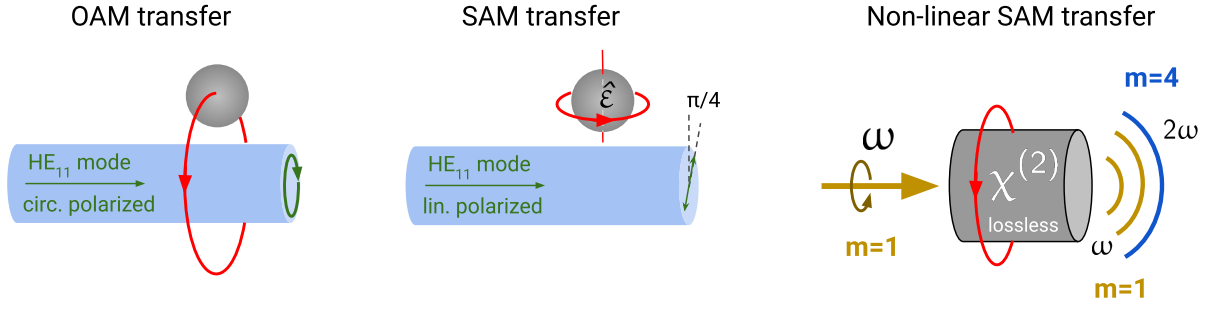


Figure 5 — В **Главе 4** рассмотрены три основные системы, в которых происходит передача спинового и орбитального угловых моментов (SAM и OAM). Слева направо: передача OAM от круговой поляризованной основной направляющей волны HE_{11} ; передача SAM от поперечного спина, который исходит от линейно поляризованной моды HE_{11} к анизотропным частицам; нелинейная передача SAM от плоской круговой поляризованной волны через процесс генерации второй гармоники, наличие момента объясняется из закона сохранения АМ

плоских волн, которая позволит удерживать наночастицы вблизи оптического нановолокна, обеспечивая эффективное взаимодействие между наночастицами и нановолокном.

В **Главе 4** рассматриваются три различные системы, в которых происходит передача углового момента от электромагнитного поля к субволновым частицам (рисунок 5):

1. **Передача орбитального углового момента.** Для иллюстрации переноса орбитального углового момента мы рассмотрим орбитальную микрочастицу вокруг нановолокна, в котором распространяется круговая поляризованная плоская волна. Мы показываем, что существует ненулевая плотность OAM, которая в конечном итоге проявляется в орбитальном движении частицы. Результаты этого раздела подтверждаются экспериментальными данными. В дипольном приближении мы можем записать орбитальный (внешний) момент в виде

$$T_{\text{orb}} = rF_{\varphi} \propto L_z \propto \ell|\mathbf{E}|^2 \quad (25)$$

где r —расстояние до оси волокна, F_{φ} — азимутальная оптическая сила на частице, а ℓ — азимутальное “квантовое” число моды. Для фундаментальной моды $HE_{\ell m}$ мы имеем $\ell = m = 1$. Также

были проанализированы оптические параметры волокна и радиусы частикул.

2. **Передача спинового углового момента.** В этой части обсуждается концепция поперечных спиновых угловых моментов. Анализ плотности SAM линейно поляризованной моды HE_{11} показывает, что при определенных азимутальных углах существует максимум радиальной плотности SAM. Здесь мы предлагаем геометрию, в которой этот поперечный SAM может проявить себя. Для этого мы анализируем вращательную динамику (спиннинг-динамику) анизотропной частицы, которая описывается тензором проницаемости $\hat{\epsilon}$. Выбор анизотропной частицы обусловлен желанием уменьшить возможные тепловые потери, которые усиливают броуновское движение, но при этом иметь значительный крутящий момент. Мы пришли к выводу, что вращающий момент в дипольном приближении может быть записан как

$$\mathbf{T} = \mathbf{T}_{\text{anis}} + \mathbf{T}_{\text{alignment}} + \mathbf{T}_{\text{losses}} \quad (26)$$

где $\mathbf{T}_{\text{anis}} \propto \mathbf{S}$ — вращающий момент, который всегда стремится повернуть частицу вокруг собственной оси в том же направлении, что и плотность SAM; $\mathbf{T}_{\text{alignment}}$ — выравнивающий момент, который стремится совместить главную ось тензора проницаемости с полуосями главного эллипса поляризации.

3. **Нелинейная передача спинового углового момента.** Начнем с модельной задачи о рассеянии циркулярно поляризованной плоской волны с частотой ω на диэлектрическом рассеивателе с симметрией цилиндра (см. Рис. 6). Плоская волна падает вдоль оси цилиндра и несет световой импульс \hbar фотона. Тогда, в силу симметрии задачи, оптический момент в линейном режиме $\mathbf{T}^{(\omega)}$, действующий на частицу, точно пропорционален сечению поглощения [10; 11] и, в терминах канонической плотности спиновых угловых моментов, можно написать $\mathbf{T}^{(\omega)} = c/n_0 \cdot \sigma_{\text{abs}} \mathbf{S}^{(\omega)}$, где $\mathbf{S}^{(\omega)} = m_{\text{inc}}/(2\omega) \cdot \epsilon \epsilon_0 [E_0^{(\omega)}]^2 \mathbf{e}_z$ — это каноническая плотность спиновых угловых моментов [45] с азимутальным числом $m_{\text{inc}} = \pm 1$ для правой (левой) круговой поляризации и $n_0 = \sqrt{\epsilon \mu}$ — показатель преломления вмещающей среды. Теперь, когда длина волны возбуждения выбрана из полосы поглощения материала, можно пренебречь потерями, что логически

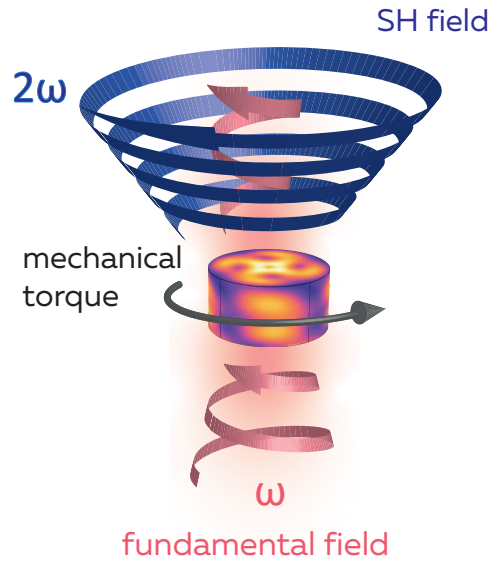


Figure 6 — Механизм нелинейного крутящего момента. Циркулярно поляризованная плоская волна с частотой ω падает на цилиндр без потерь, последняя генерирует вторую гармонику с ненулевым угловым моментом, который определяется правилами отбора. Вследствие сохранения углового момента существует ненулевой механический момент

обеспечивает условие нулевого крутящего момента. Однако далее мы покажем, что при учете оптических процессов высшего порядка может возникнуть ненулевой нелинейный оптический момент даже в геометрии, рассмотренной на рис. 6. Далее мы ограничимся рассмотрением процесса генерации второй гармоники (SHG), который является доминирующим нелинейным процессом во многих оптических материалах [87]. Он проявляется в преобразовании двух фотонов с частотой ω на основной гармонике (ФН) в один фотон на второй гармонике (SH) с частотой 2ω , отсюда две компоненты оптического нелинейного момента

$$\mathbf{T} = \mathbf{T}^{(\omega)} + \mathbf{T}^{(2\omega)} \quad (27)$$

где $\mathbf{T}^{(\omega)}$ и $\mathbf{T}^{(2\omega)}$ — оптические моменты на основной и второй гармониках, которые, как оказалось, прекрасно связаны через те же коэффициенты рассеяния, как мы покажем ниже.

Наконец, в **Главе 5** мы исследуем силу акустического излучения и крутящий момент на маленькой (субволновой) поглощающей изотропной частице, погруженной в монохроматическое (но в целом неоднородное) поле

звуковых волн. Основными уравнениями являются линеаризованное уравнение Навье-Стокса и уравнение неразрывности:

$$\begin{cases} \rho_0 \partial_t \mathbf{v} = -\nabla p & \text{1-й порядок Н.-С.} \\ \beta_0 \partial_t p = -\nabla \cdot \mathbf{v} & \text{1-й порядок ур-я неразрывности} \\ p = c_s^2 \rho & \text{ур-е состояния} \end{cases} \quad (28)$$

Где $c_s = 1/\sqrt{\rho_0 \beta_0}$ - скорость звука. Из сказанного выше также следует, что векторное поле удовлетворяет

$$\nabla \times \mathbf{v} = 0. \quad (29)$$

Среда описывается двумя основными величинами: *(i)* плотностью ρ_0 , $[\rho_0] = [\text{kg} \cdot \text{m}^{-3}]$ и *(ii)* сжимаемостью $\beta_0 = -\frac{1}{V} \frac{\partial V}{\partial p}$, $[\beta_0] = [\text{m}^2 \cdot \text{N}^{-1}]$. Связь со скоростью звука дана через $c_s = 1/\sqrt{\rho_0 \beta_0}$.

Объект внутри этой среды может быть описан собственной плотностью ρ_1 и сжимаемостью β_1 . Удобно использовать нормированные безразмерные параметры [88–90]: *(i)* нормализованную плотность $\bar{\rho}_1 = \rho_1/\rho_0$ и *(ii)* нормализованную сжимаемость $\bar{\beta}_1 = \beta_1/\beta_0$. После введения этих нормированных квантов, я могу записать волновой вектор внутри объекта как

$$k_1 = k_0 \sqrt{\bar{\rho}_1 \bar{\beta}_1}. \quad (30)$$

Обычно потери в линейной акустике определяются как мнимый член, если волновой вектор $k_1 = k'_1 + i\delta_1$. *Пористые* материалы являются отличным примером материи с потерями в линейной акустике [89–92]. Однако использование относительной плотности и сжимаемости позволяет ввести потери, как это делается в оптике, так что для $\text{Im}(\bar{\rho}_1) > 0$, $\text{Im}(\bar{\beta}_1) > 0$ получается частица с потерями, а для $\text{Im}(\bar{\rho}_1) < 0$, $\text{Im}(\bar{\beta}_1) < 0$ получается частица с усилением (для выбора $e^{-i\omega t}$).

Удобно рассмотреть комплексные амплитуды для монохроматических полей $A(\mathbf{r}, t) = \text{Re}(A(\mathbf{r})e^{-i\omega t})$, где $A = p, \rho, \mathbf{v}$.

Плотность энергии и канонические моменты акустической монохроматической волны можно записать как [93]

$$W = \frac{1}{4} (\beta_0 |p|^2 + \rho_0 |\mathbf{v}|^2) \equiv W^{(p)} + W^{(\mathbf{v})}, \quad (31a)$$

$$\mathbf{P} = \frac{1}{4\omega} \text{Im} [\beta_0 p^* \nabla p + \rho_0 \mathbf{v}^* \cdot (\nabla) \mathbf{v}] \equiv \mathbf{P}^{(p)} + \mathbf{P}^{(\mathbf{v})}, \quad (31b)$$

$$\mathbf{L} = \mathbf{r} \times \mathbf{P}, \quad (31c)$$

$$\mathbf{S} = \frac{\rho_0}{2\omega} \text{Im} \mathbf{v}^* \times \mathbf{v}, \quad \mathbf{J} = \mathbf{L} + \mathbf{S}, \quad (31d)$$

где W — плотность энергии, \mathbf{P} — каноническая плотность линейного момента, \mathbf{L} , \mathbf{S} и \mathbf{J} — плотности орбитального, спинового и полного углового моментов, соответственно. Здесь я использовал нотацию Берри $\mathbf{v}^* \cdot (\nabla) \mathbf{v} \equiv \sum_{i=x,y,z} v_i^* \nabla v_i$ [9].

Мы показываем, что если ввести монопольную и дипольную поляризуемости частицы, то проблема может быть рассмотрена аналогично хорошо изученным оптическим силам и моментам на дипольных частицах Рэлея. Мы получаем простые аналитические выражения для акустической силы (включая градиентную силу и силу рассеяния) и крутящего момента:

$$\mathbf{F}^{\text{acoustic}} = \underbrace{-\frac{1}{2} \text{Re} \left[\frac{i}{\omega} M^* \nabla p - \rho \mathbf{D}^* \cdot (\nabla) \mathbf{v} \right]}_{\mathbf{F}_M + \mathbf{F}_D} - \underbrace{\frac{\rho k^3}{12\pi} \text{Im} [M^* \mathbf{D}]}_{\mathbf{F}_{\text{self}}} \quad (32)$$

и

$$\mathbf{T}^{\text{acoustic}} = \frac{\rho}{2} \text{Re} (\mathbf{D}^* \times \mathbf{v}) - \frac{\rho k^3}{24\pi} \text{Im} (\mathbf{D}^* \times \mathbf{D}) \quad (33)$$

где M - акустический монополь, а \mathbf{D} - акустический диполь. В терминах сечения поглощения и канонической плотности спинового углового момента момент будет равен

$$\mathbf{T}^{\text{acoustic}} = c_s \sigma_{\text{abs}}^D \mathbf{S}^{\text{acoustic}} \quad (34)$$

где c_s - скорость звука в принимающей среде. Насколько известно, уравнения (33) и (34) написаны впервые и имеют много общего с уравнениями в оптике [94].

Используя поляризуемости, определяемые как $M = -i\omega\beta\alpha_M p$ и $\mathbf{D} = \alpha_D \mathbf{v}$, мы связываем действие поля на маленькую частицу с каноническими свойствами акустической падающей волны:

$$\mathbf{F}^{\text{acoustic}} = \mathbf{F}^{\text{grad}} + \mathbf{F}^{\text{scat}} + \mathbf{F}^{\text{recoil}}. \quad (35)$$

Здесь части градиента и рассеяния связаны с действительной и мнимой частями поляризацій частиц:

$$\mathbf{F}^{\text{grad}} = \text{Re}(\alpha_M) \nabla W^{(p)} + \text{Re}(\alpha_D) \nabla W^{(v)}, \quad (36)$$

$$\mathbf{F}^{\text{scat}} = 2\omega \left[\text{Im}(\alpha_M) \mathbf{P}^{(p)} + \text{Im}(\alpha_D) \mathbf{P}^{(v)} \right] \quad (37)$$

$$\mathbf{F}^{\text{recoil}} = \frac{k^4}{6\pi c_s} \left(\text{Re}(\alpha_M \alpha_d^*) \mathbf{\Pi}^{\text{Re}} + \text{Im}(\alpha_M \alpha_D^*) \mathbf{\Pi}^{\text{Im}} \right) \quad (38)$$

Важно отметить, что эти выражения обнаруживают тесную связь с фундаментальными полевыми свойствами, недавно введенными для акустических полей: каноническим импульсом и плотностью спинового углового момента. Мы сравниваем наши аналитические результаты с предыдущими расчетами и точным численным моделированием. Мы также рассматриваем важный пример частицы в испаряющейся акустической волне, которая проявляет взаимно ортогональные силы рассеяния (радиационного давления), градиентную силу и момент от поперечного спина поля.

Важно отметить, что мы также приводим решение ряда полезных задач, таких как задача рассеяния Ми и приближение комплексного угла в акустике.

Рассеяние плоской волны на сфере может быть решено точно (задача рассеяния Ми). Это решение стало чрезвычайно популярным в оптике, но еще не в акустике. Здесь мы вновь обратимся к этому решению. Падающее поле может быть разложено как [95]

$$p^i = p_0 e^{ikr \cos \theta} = \sum_{n=0}^{\infty} p_n j_n(kr) P_n(\cos \theta), \quad (39)$$

где $p_n = p_0 i^n (2n + 1)$.

Любое излучение от тела, расположенного в начале координат, может быть охарактеризовано суммами мультиполей:

$$p(\mathbf{r}, \omega) = \sum_{n=0}^{\infty} \sum_{m=-n}^n A_{mn}(\omega) z_n(kr) Y_n^m(\theta, \varphi) \quad (40)$$

Где $z_n = j_n, h_n^{(1)}$ — радиально зависимые функции, которая обычно является одной из сферических функций Бесселя в зависимости от граничных условий, а $\psi_{mn}(\mathbf{r}) = z_n(kr) Y_n^m(\theta, \varphi)$ — *моды сферы*. Далее, система обладает симметрией над φ , поэтому

$$p(\mathbf{r}, \omega) = \sum_{n=0}^{\infty} A_n(\omega) z_n(kr) P_n(\cos \theta). \quad (41)$$

Частица с радиусом a описывается ρ_1 и β_1 и находится в жидкости с ρ_0 и β_0 . Граничные условия следующие

$$\begin{cases} p^i + p^s = p^{\text{in}} \\ v_r^i + v_r^s = v_r^{\text{in}} \end{cases} \quad (42)$$

где $\mathbf{v} = \frac{1}{i\omega\rho_0}\nabla p$, поэтому второе уравнение трансформируется в $\partial_r p^i + \partial_r p^s = \frac{\rho_0}{\rho_1}\partial_r p^{\text{in}}$. Разложения для рассеянного поля и поля внутри частицы имеют вид

$$p^s(\mathbf{r}, \omega) = \sum_{n=0}^{\infty} p_n a_n(\omega) h_n^{(1)}(kr) P_n(\cos \theta), \quad (43)$$

$$p^{\text{in}}(\mathbf{r}, \omega) = \sum_{n=0}^{\infty} p_n c_n(\omega) j_n(k_1 r) P_n(\cos \theta), \quad (44)$$

где $p_n = p_0 i^n (2n + 1)$. Граничные условия дают явные выражения для коэффициентов a_n и c_n :

$$c_n = \frac{i/(ka)^2}{j_n(k_1 a) h_n^{(1)'}(ka) - \gamma j_n'(k_1 a) h_n^{(1)}(ka)}, \quad (45)$$

$$a_n = \frac{\gamma j_n'(k_1 a) j_n(ka) - j_n(k_1 a) j_n'(ka)}{j_n(k_1 a) h_n^{(1)'}(ka) - \gamma j_n'(k_1 a) h_n^{(1)}(ka)}, \quad (46)$$

где $k_1 = k\sqrt{\bar{\rho}_1\beta_1}$ и $\gamma = \frac{k_1\rho_0}{k\rho_1} = \sqrt{\bar{\beta}_1/\bar{\rho}_1}$. Эти коэффициенты находятся в согласии с коэффициентами A_n и B_n из [96]: $a_n = A_n$ и $c_n = -\bar{\rho}_1 B_n$ (похоже, в [96] есть опечатка, c_n в данной рукописи удовлетворяет предельному случаю $p^{\text{in}}(\bar{\rho}_1 = \bar{\beta}_1 = 1) = p^i$).

Можно также найти сечение корсов рассеяния, экстинкции и поглощения. Окончательный ответ будет следующим

$$\sigma_{\text{ext}} = \sigma_{\text{abs}} + \sigma_{\text{sc}}, \quad (47)$$

где после интегрирования мы получаем выражение, очень похожее на аналогичное в задаче электромагнитного рассеяния Ми [97]:

$$\sigma_{\text{sc}} = \frac{4\pi}{k^2} \sum_{n=0}^{\infty} (2n + 1) |a_n|^2, \quad (48)$$

$$\sigma_{\text{ext}} = -\frac{4\pi}{k^2} \sum_{n=0}^{\infty} (2n + 1) \text{Re}(a_n), \quad (49)$$

$$\sigma_{\text{abs}} = -\frac{4\pi}{k^2} \sum_{n=0}^{\infty} (2n + 1) \left(|a_n|^2 + \text{Re}(a_n) \right) \quad (50)$$

Мы также приводим таблицу сечений для различных комбинаций популярных акустических материалов, которая должна помочь найти подходящий резонансный материал: воздух, вода, пористый кремний, эпоксидная смола и аэрогель (рис. 5.4 в основном тексте). Общее правило заключается в том, что акустический коэффициент преломления должен быть $n_{\text{acoustic}} = c_s^{\text{host}}/c_s^{\text{particle}} = \sqrt{\bar{\rho}_1\bar{\beta}_1} \gtrsim 1$.

Рассмотрим случай малых частиц. В терминах монопольной и дипольной поляризуемостей, которые определены в разделе 5.3, мы можем переписать это как:

$$\sigma_{\text{ext}} = k (\text{Im}(\alpha_M) + \text{Im}(\alpha_D)), \quad (51)$$

$$\sigma_{\text{sc}} = \frac{k^4}{4\pi} \left(|\alpha_M|^2 + \frac{1}{3} |\alpha_D|^2 \right), \quad (52)$$

$$\sigma_{\text{abs}} = \underbrace{k \text{Im} \alpha_M - \frac{k^4}{4\pi} |\alpha_M|^2}_{\sigma_{\text{abs}}^M} + \underbrace{k \text{Im} \alpha_D - \frac{k^4}{12\pi} |\alpha_D|^2}_{\sigma_{\text{abs}}^D} \quad (53)$$

Поскольку поляризуемости масштабируются как объем частицы $\alpha_M, \alpha_D \sim a^3$, мы можем заключить, что для частиц с потерями ($\text{Im}(\bar{\rho}), \text{Im}(\bar{\beta}) \sim 1$) на субволновых размерах $\sigma_{\text{abs}} \sim a^3 \gg \sigma_{\text{sc}} \sim a^6$. Другими словами, маленькие частицы лучше поглощают, чем рассеивают. Однако, для больших частиц рассеяние становится более доминирующим.

Наконец, для изучения резонанса Ми в акустике полезно использовать подход комплексного угла, который помогает найти силу и момент в расширяющемся поле с помощью полуаналитического подхода. Падающая плоская волна $p^{\text{p.w.}}(\mathbf{r}) = p_0 e^{ikz}$ может быть преобразована в эванесцентную волну путем поворота ее аргумента на комплексный угол

$$p^{\text{evan}}(\mathbf{r}) = p^{\text{p.w.}}(\hat{R}(i\alpha)\mathbf{r}) = p_0 e^{ik \cosh(\alpha)z} e^{-k \sinh(\alpha)x}, \quad (54)$$

где $\hat{R}(i\alpha) = \begin{pmatrix} \cosh(\alpha) & 0 & -i \sinh(\alpha) \\ 0 & 1 & 0 \\ i \sinh(\alpha) & 0 & \cosh(\alpha) \end{pmatrix}$.

Оператор Ми также является линейным, поэтому мы знаем рассеянное поле в случае исчезающей падающей волны для любой сферы

$$p^s(\mathbf{r}) \rightarrow p^s(\hat{R}(i\alpha)\mathbf{r}) \quad (55)$$

поэтому $x \rightarrow x' = x \cosh(\alpha) - iz \sinh(\alpha)$, $y \rightarrow y' = y$, $z \rightarrow z' = ix \sinh(\alpha) + z \cosh(\alpha)$ или для сферических координат $r \rightarrow r' = r$, $\theta \rightarrow \theta' = \cos^{-1} \frac{z'}{r}$, и

$\varphi \rightarrow \varphi' = \text{tg}^{-1} \frac{y}{x'}$. А скорость всегда определяется как $\mathbf{v} = \frac{1}{i\omega\rho} \nabla p$. Поскольку мы знаем все поля, мы можем численно проинтегрировать (1.47с). Результат расчета представлен на рис. 5.6 в основном тексте. Заметим, что возможны силы отталкивания и притяжения к поверхности.

Основные публикации по теме диссертации

Основные результаты по теме диссертации изложены в 9 публикациях, из них 8 публикаций находятся в изданиях, рецензируемых Web of Science и Scopus.

В международных изданиях, индексируемых в базах данных Web of Science и Scopus:

1. Optical binding via surface plasmon polariton interference / N. Kostina [et al.] // Phys. Rev. B. — 2019. — Mar. — Vol. 99, no. 12. — P. 125416. — URL: <https://doi.org/10.1103/PhysRevB.99.125416>.
2. Acoustic Radiation Force and Torque on Small Particles as Measures of the Canonical Momentum and Spin Densities / I. D. Toftul [et al.] // Phys. Rev. Lett. — 2019. — Oct. — Vol. 123, no. 18. — P. 183901. — URL: <https://doi.org/10.1103/PhysRevLett.123.183901>.
3. Light-induced rotation of dielectric microparticles around an optical nanofiber / G. Tkachenko [et al.] // Optica. — 2020. — Jan. — Vol. 7, no. 1. — P. 59–62. — URL: <https://doi.org/10.1364/OPTICA.374441>.
4. *Toftul I. D., Kornovan D. F., Petrov M. I.* Self-Trapped Nanoparticle Binding via Waveguide Mode // ACS Photonics. — 2020. — Jan. — Vol. 7, no. 1. — P. 114–119. — URL: <https://doi.org/10.1021/acsp Photonics.9b01157>.
5. *Toftul I., Bliokh K., Petrov M.* Acoustic forces and torques: Directional scattering and acoustic spin // AIP Conf. Proc. — 2020. — Dec. — Vol. 2300, no. 1. — P. 020127. — URL: <https://doi.org/10.1063/5.0032100>.
6. Detection of the transverse spin of light by twisting anisotropic particles near an optical nanofiber waveguide / G. Tkachenko [et al.] // Proceedings Volume 11926, Optical Manipulation and Structured Materials Conference 2021. Vol.

11926. — SPIE, 10/2021. — P. 69–71. — URL: <https://doi.org/10.1117/12.2616130>.
7. *Toftul I., Frizyuk K., Petrov M.* Total angular momenta quantization of dielectric sphere modes // J. Phys. Conf. Ser. — 2021. — Nov. — Vol. 2015, no. 1. — P. 012152. — URL: <https://doi.org/10.1088/1742-6596/2015/1/012152>.
 8. Orbiting of dielectric particles around a single-mode ultrathin fiber waveguide / G. Tkachenko [et al.] // Proceedings Volume 11522, Optical Manipulation and Structured Materials Conference 2020. Vol. 11522. — SPIE, 06/2020. — P. 38–40. — URL: <https://doi.org/10.1117/12.2573514>.

В иных изданиях:

1. Angular momenta and negative azimuthal forces induced on a particle via guided light in ultrathin optical fibers / V. G. Truong [et al.] // Optica Publishing Group. — 2019. — Apr. — AM3E.5. — URL: <https://doi.org/10.1364/OMA.2019.AM3E.5>.

Synopsis

General thesis summary

Relevance

The Thesis advances the fundamental knowledge in the research area of opto- and acoustomechanics. The great technical progress in optical and acoustical manipulation of objects at the subwavelength scale made it accessible in the numerous applications: 3D volumetric displays [1; 2], single atom trapping [3; 4], invasive manipulation of bio-particles [5], and many more [6]. The rapid development of this area requires both novel approaches to subwavelength object manipulation and deeper understanding of fundamental aspects. Among the latter ones, the question “*How exactly is linear and angular momenta is transferred from fields to matter close to nanophotonic structures?*” stands out and becomes one of the central problems under consideration in this dissertation.

The goal and tasks

The **goal** of this Thesis is to deepen the understanding of linear and angular momenta transfer in opto- and acoustomechanics in particular nanophotonic and acoustic geometries. The following particular **tasks** were accomplished:

- a deep overview of fundamentals of optical forces and torques, as well as canonical properties of light was provided;
- a long-range optical binding via waveguided mode of a nanofiber using transverse pump was proposed;
- the transfer of spin and angular momenta from light to matter near infinity cylinder and ideal sphere described;
- the connection between the optomechanical and acoustomechanical effects during waves scattering at subwavelength objects was established.

Scientific statements

1. An array of subwavelength particles above the waveguide can form a stable in-line configuration in the field of a linearly polarized plane wave incident perpendicular to the waveguide axis. The binding stiffness between particles increases linearly with the number of particles.
2. For an orbiting motion of particle around a dielectric waveguide in a viscous fluid induced by circular polarized fundamental mode there is an optimal particle radius for which orbiting frequency is maximal. The position of this maxima does not coincide with the maximum of the canonical total angular momentum density.
3. For a non-absorbing particle geometry of which is axially symmetric with respect to the direction of incident wave, the mechanical spinning torque associated with the generation of second harmonic radiation can arise. The appearance of the spinning torque turns out to be associated with a nonzero angular momentum of the generated second harmonic field, which appears due to the specific structure of the crystal lattice of the nanoparticle.
4. The acoustic force acting on subwavelength particles are directly proportional to the sum of the density of the linear canonical momenta and the gradient of the energy density. The acoustic torque on subwavelength particles is proportional to the canonical spin momentum density.

Scientific novelty

Despite that the linear and angular momenta transfer has been the central problem of optomechanics since its yearly years, with the development of subwavelength manipulations methods and geometries new questions arise which require detailed theoretical analysis. The results obtained within the tasks of this thesis bring carry particular novelty to the field, namely:

- it was shown theoretically for the first time that an array of subwavelength particles over a waveguide can form a stable configuration in the field of a linearly polarized plane wave incident perpendicular to the waveguide axis.

The stiffness of the coupling between particles increases linearly with the number of particles;

- for the first time the author has demonstrated that for orbital motion of a particle around a dielectric waveguide in a viscous fluid induced by circularly polarized main mode, there is an optimal radius of the particle for which the orbital frequency is maximum. The position of this maximum does not coincide with the maximum of the canonical total angular momentum density;
- for the first time it has been theoretically proved that for a non-absorbing particle, geometry of which is axisymmetrical under the direction of incident wave, there can appear a mechanical torque related with generation of second harmonic radiation. The appearance of the rotating moment turns out to be related to the nonzero angular momentum of the generated second harmonic field, which appears due to the specific structure of the crystal lattice of the nanoparticle;
- it was shown for the first time that the acoustic force acting on subwavelength particles is directly proportional to the sum of linear canonical momentum density and energy density gradient, and the acoustic momentum is proportional to the canonical spin momentum density.

The practical significance

The field of optomechanics constantly requires novel tools for achieving higher degree of control and manipulations over the nanoobjects. Optical nanofibers is an excellent example of a reliable platform for studying the light matter interactions. The Thesis provides a number of significant results which help understanding the basics of nanoparticle trapping and manipulations close to a dielectric nanofiber suggesting novel approaches for rotating and arranging nanoobjects. These result can be also extended to manipulation of quantum systems such as ultracold atoms. Moreover, the obtained results can help developing novel methods of manipulation basing on resonant dielectric Mie scatterers, which local fields described in terms of multipoles, can afford a versatile tool for nanoscale tweezing. Finally, we advance the

link the developed field of optomechanics with the acoustomechanics allowing immediate transfer of well-established approaches of optical manipulations to acoustics.

Thus, the results of the work can find their application in the areas where optical and acoustical tweezers are actively used now such as biology, nanotechnology, quantum manipulations and computing, and many others.

The **practical significance** of the work lies in the potential increase in degrees of freedom when manipulating nano- and micro-objects. For example, in addition to the now common three-position manipulation, another degree of freedom is added — rotational (orbiting and spinning). The latter becomes possible due to a deeper understanding of the mechanism of light angular momentum transfer.

Reliability and the validity

The validity of the results obtained is ensured primarily by the confirming the theoretical findings with the numerical experiments, as well as with the real experiment, where it was possible to do it. In addition, all key results have been published in highly cited journals and successfully presented at the international conferences.

Approbation of research results

- Key research results were presented and discussed at the following conferences:
- [METANANO 2021 VI International Conference on Metamaterials and Nanophotonics](#). Total angular momenta quantization of dielectric sphere modes. Saint-Petersburg, Russia / Online. September 13–17, 2021.
 - [APS March Meeting 2021](#). Directional scattering reinforced by acoustic bianisotropy and related acousto-mechanical effects. Online. March 15–19, 2021.
 - [Quantum Nanophotonics \(Benasque\)](#). Stable Self-trapping Of Nanoparticles Via Waveguide Modes Of A Nanofiber. Online. Feb 28 – Mar 05, 2021.

- [METANANO 2020. V International Conference on Metamaterials and Nanophotonics](#). Saint-Petersburg, Russia / Online. Sep 14-18, 2020. 2 talks:
 - Optical binding of nanoparticles near a nanofiber waveguide;
 - Acoustic forces and torques: directional scattering and acoustic spin.
- [ONNA: Optical Nanofibre Applications](#). Self-induced anisotropy of spherical nanoparticle near a nanofiber and related optomechanical effects. Okinawa, Japan. Jul 3-6, 2019.
- [Conference on Nanophotonics: Foundations & Applications](#). Acoustic force and torque in connection with canonical momentum and spin: an optical approach. Sep 1-6, 2019. Ascona, Switzerland.
- [Okinawa School in Physics: Coherent Quantum Dynamics](#). Self-trapping of submicron particles near a nanofiber. Okinawa, Japan. Sep 25 - Oct 4, 2018.
- [JSAP photonics annual meeting](#). Dipole nanoparticles with induced anisotropy as point detectors of the angular momentum of light. Okinawa, Japan. Nov 30 - Dec 1, 2018.

Author contribution

The author's contribution to this work consists in constructing theoretical models, obtaining analytical results such as formulas and plots, analyzing the obtained results, explaining the corresponding physics behind, and also in performing the numerical calculations. The author not only contributed significantly to the solution of the problems under consideration, but also to their formulation as it is a big part of the researcher's work.

Author contribution among all the chapters is the following:

- In Chapter 1 author presented his own unique point of view on optical forces and torques.
- In Chapter 2 author performed all the analyses of the eigen modes of a spherical and cylindrical resonators.

- In Chapter 3 author with his colleagues Mihail Petrov and Daniil Kornovan found a stable configuration of the finite array of nanoparticles trapped by a transverse pump and bound by a long-range interaction through the waveguided mode. Author did the main theoretical and numerical work.
- In Chapter 4 author performed only the theoretical part of the work, while the experiment was performed in the group of prof. Sile Nic Chormaic at OIST by Georgiy Tkachenko.
- In Chapter 5 author in collaboration with Konstantin Bliokh has found a way how to connect acoustic force and torque with canonical momenta of acoustic fields. Author also did all the theoretical and numerical calculations.

Thesis structure and number of pages

Thesis consists of the introduction, 5 chapter, conclusion and 13 appendix. Thesis is 282 pages long, including 60 figure and 6 table. Bibliography consists of 364 items.

The thesis consists of introduction, four chapters, conclusion, list of references, and several appendices. In Chapter 1 we present the fundamentals of the optical forces and torques, as well as the most recent achievements in the field. Chapter 2 is devoted to the spin and orbital angular momenta of eigen modes of a sphere and an infinite cylinder. In Chapter 3 theory of optical binding next to a waveguide is presented. Chapter 4 is devoted to the linear and angular momenta transfer of light to matter, as well as theoretical description of the orbiting motion of a nanoparticle around the ultra-thin single mode optical fiber. Finally, in Chapter 5 the close connection between optics and linear acoustics is described in details. We show how subwavelength acoustic particles could be a measure of canonical momenta of the incident field.

Main contents of the work

Increasing interest in optical manipulation of various kind has been stimulated by a huge success in accessible experimental realizations. Non-invasive particle manipulation is an important and integral technique in the study of nano- and micro-objects. Mechanical manipulation is often unacceptable because it can potentially destroy the object under study.

To highlight the importance of this branch of science, we mention that several scientists were awarded the Nobel prizes for their achievements in the optical tweezing and optical manipulation. Among them are Arthur Ashkin in 2018 “for the optical tweezers and their application to biological systems”; Steven Chu, Claude Cohen-Tannoudji, and William Daniel Phillips in 1997 for “for development of methods to cool and trap atoms with laser light”. Against this background, only recently have acoustic particle-capture systems begun to approach the same level of control. For example, the first implementation of acoustic tweezers in a *single beam*, similar to the standard optical tweezers, was demonstrated only in 2016 [7]. In the Table 2 a short summary of accessible particle sizes and required beam powers are shown as of today.

Table 2 — Comparison of typical sized and powers of optical and acoustical tweezers. Data is from [5].

Method	Particle size	Power (Wt/cm ²)
Acoustic tweezer	100 nm – 10 mm	10 ⁻² – 10 ¹
Optical tweezer	10 nm – 1 mm	10 ⁶ – 10 ⁷

This dissertation goes deeper in the fundamental direction in this field. The central question is how exactly the transfer of linear and angular momenta is connected to the opto- and acoustomechanics. Through out this work once of the main ideas to convey is that small subwavelength particles act as a measurement tools of the electromagnetic or acoustic field, which is summarized in Figure A. Below we provide a short summary of each chapter without way too much technical details.

In **Chapter 1** we discuss in great details all the formalism and math behind optical and acoustical force and torque calculation. The most general way of finding the *average* over oscillation period force and torque is to find the change of the linear momentum flux (or Maxwell stress tensor) and angular momentum flux of the total

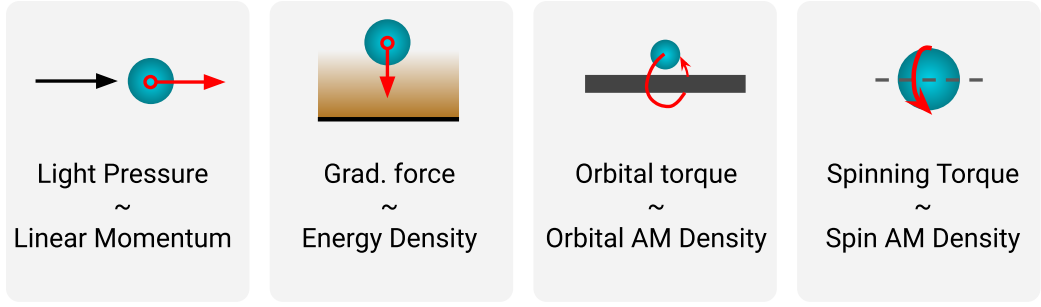


Figure A — Concept of the connection between electromagnetic field properties and optomechanics for subwavelength particles. There is also a full analogy for the acoustic fields and acoustomechanics

field. The way to do this formally is the following:

$$\mathbf{F} = \oint_{\Sigma} \langle \hat{\mathcal{T}} \rangle \mathbf{n} d\Sigma, \quad \mathbf{T} = \oint_{\Sigma} \langle \hat{\mathcal{M}} \rangle \mathbf{n} d\Sigma \quad (56)$$

where the flux tensors for the homogeneous isotropic medium with ε and μ are given by [8]

$$\langle \hat{\mathcal{T}} \rangle = \frac{1}{2} \text{Re} \left[\varepsilon \varepsilon_0 \mathbf{E}^* \mathbf{E} + \mu \mu_0 \mathbf{H}^* \mathbf{H} - \hat{\mathbf{I}} \left(\varepsilon \varepsilon_0 |\mathbf{E}|^2 + \mu \mu_0 |\mathbf{H}|^2 \right) \right], \quad (57)$$

$$\langle \mathcal{M}_{ij} \rangle = \varepsilon_{ikl} r_k \langle \mathcal{T}_{lj} \rangle. \quad (58)$$

Usually, exactly these expressions are used in the full numerical calculations.

To approach any problem analytically, the subwavelength limit can be very handy. The most important dimensionless parameter here is going to be so-called size parameter ka where $k = n\omega/c$ is the wavenumber in media with refractive index n and a is the typical radius of the particle.

In the limit $ka \ll 1$ we safely replace the particle by point electric dipole \mathbf{p} and point magnetic dipole \mathbf{m} . Once it is done, the integral in Eq. (56) can be taken (see Appendix H) and the expressions for the force and torque are going to be

$$\begin{aligned} \mathbf{F}_{ka \ll 1} &= \mathbf{F}^{(e)} + \mathbf{F}^{(m)} + \mathbf{F}^{(e-m)} \\ &= \underbrace{\frac{1}{2} \text{Re}(\mathbf{p}^* \cdot (\nabla) \mathbf{E})}_{\sim (ka)^3} + \underbrace{\frac{\mu \mu_0}{2} \text{Re}(\mathbf{m}^* \cdot (\nabla) \mathbf{H})}_{\sim (ka)^5 \text{ for } \mu_p = \mu} - \underbrace{\frac{k^4}{12\pi} \sqrt{\frac{\mu \mu_0}{\varepsilon \varepsilon_0}} \text{Re}(\mathbf{p}^* \times \mathbf{m})}_{\sim (ka)^8 \text{ for } \mu_p = \mu} \end{aligned} \quad (59)$$

where the notation, first introduced by Berry [9], “ $\cdot(\nabla)$ ” should be read as $\mathbf{A} \cdot (\nabla) \mathbf{B} \equiv \sum_{\alpha} \sum_{i=x,y,z} A_i \hat{\mathbf{e}}_{\alpha} \nabla_{\alpha} B_i$ with α being any coordinate system index (Cartesian, cylindrical, spherical, etc). We stress that the summation is taken over Cartesian coordinates (see Appendix A for other coordinate systems).

The optical torque is going to be [98]

$$\mathbf{T}_{ka \ll 1} = \mathbf{T}^{(e)} + \mathbf{T}^{(m)}, \quad (60a)$$

$$\mathbf{T}^{(e)} = \mathbf{T}_0^{(e)} + \mathbf{T}_s^{(e)} = \frac{1}{2} \operatorname{Re} [\mathbf{p}^* \times \mathbf{E}] - \frac{k^3}{12\pi\epsilon\epsilon_0} \operatorname{Im} [\mathbf{p}^* \times \mathbf{p}], \quad (60b)$$

$$\mathbf{T}^{(m)} = \mathbf{T}_0^{(m)} + \mathbf{T}_s^{(m)} = \frac{1}{2} \operatorname{Re} [\mu\mu_0 \mathbf{m}^* \times \mathbf{H}] - \frac{k^3 \mu\mu_0}{12\pi} \operatorname{Im} [\mathbf{m}^* \times \mathbf{m}], \quad (60c)$$

where electric and magnetic components are associated with the interaction with electric $\mathbf{p} = \alpha_e \mathbf{E}$ and magnetic $\mathbf{m} = (\mu\mu_0)^{-1} \alpha_m \mathbf{H}$ dipole respectively. The presence of the scattering terms $\mathbf{T}_s^{(e,m)}$ is crucial for the non absorbing particles. For example, for a small non-absorbing sphere torque has to be zero [10; 11] since no change of the angular momenta occurs due to the axial symmetry considerations. Exact cancellation of two terms in Eq. (60) happens once the scattering correction to the polarizabilities are properly taken into account (see Appendix 4.3.7 for more details).

Finally, after introducing electric α_e and magnetic α_m polarizabilities we can explicitly connect force and torque with the canonical field properties: electromagnetic energy density $W = W^{(e)} + W^{(m)}$, linear momentum density $\mathbf{P} = \mathbf{P}^{(e)} + \mathbf{P}^{(m)}$, spin angular momentum density $\mathbf{S} = \mathbf{S}^{(e)} + \mathbf{S}^{(m)}$, complex energy flow (or complex Poynting vector) $\mathbf{\Pi}^{\operatorname{Re}} = \frac{1}{2} \operatorname{Re} (\mathbf{E}^* \times \mathbf{H})$ [12–14],[15, § 6.9],[16, § 2.20],[17, § 12.5] as

$$\mathbf{F} = \mathbf{F}^{(e)} + \mathbf{F}^{(m)} + \mathbf{F}^{(e-m)}, \quad (61a)$$

$$\mathbf{F}^{(e)} = \underbrace{\left(\frac{\epsilon\epsilon_0}{\mu\mu_0} \right)^{-1} \operatorname{Re} [\alpha_e] \nabla W^{(e)}}_{\text{conservative}} + \underbrace{2 \frac{c}{n} \sigma_{\text{ext}}^{(e)}}_{\text{non-conservative}} \mathbf{P}^{(e)} \quad (61b)$$

$$\mathbf{F}^{(e-m)} = -\frac{c^2 k^4}{6\pi} \frac{c}{n} \left[\operatorname{Re} (\alpha_e \alpha_m^*) \frac{1}{n^2} \left(\mathbf{P} + \frac{1}{2} \nabla \times \mathbf{S} \right) + \operatorname{Im} (\alpha_e \alpha_m^*) \frac{1}{c^2} \mathbf{\Pi}^{\operatorname{Im}} \right] \quad (61c)$$

Torque for the case of $\mathbf{S}^{(e)} = \mathbf{S}^{(m)}$ (i.g. for an elliptically polarized plane wave) the torque is going to be

$$\mathbf{T} = 2 \frac{c}{n} \left(\sigma_{\text{abs}}^{(e)} \mathbf{S}^{(e)} + \sigma_{\text{abs}}^{(m)} \mathbf{S}^{(m)} \right) = \frac{c}{n} \sigma_{\text{abs}} \mathbf{S} \quad (62)$$

Here $\sigma_{\text{ext}}^{(e,m)} = \sigma_{\text{sc}}^{(e,m)} + \sigma_{\text{abs}}^{(e,m)}$ are the electric and magnetic parts of extinction, absorption, and scattering cross sections of the particle. Those are connected with the polarizabilities (see Appendix B.4).

Manipulated particles can have a complex *internal* structure in terms of electromagnetic response [18; 19]. A very distinguished example of such particles are

liquid crystals which are greatly discussed in [20]. The most general case is the bi-anisotropic media can be fully described by constitutive relations [21–24]

$$\begin{pmatrix} \mathbf{D} \\ \mathbf{B} \end{pmatrix} = \begin{pmatrix} \varepsilon\varepsilon_0 & i\boldsymbol{\kappa}/c \\ -i\boldsymbol{\kappa}^T/c & \boldsymbol{\mu}\boldsymbol{\mu}_0 \end{pmatrix} \begin{pmatrix} \mathbf{E} \\ \mathbf{H} \end{pmatrix} \quad (63)$$

where ε , $\boldsymbol{\mu}$, $\boldsymbol{\kappa}$ are generally complex valued 3×3 tensors. Here we also took in account that the medium is reciprocal, so diagonal elements in Eq. (63) are connected. For non-reciprocal media we encourage to read Refs. [21; 22]. When it comes for the small particles, it is possible to get dipolar polarizabilities ($\boldsymbol{\alpha}_e, \boldsymbol{\alpha}_m, \boldsymbol{\alpha}_c$) from the bulk parameters ($\varepsilon, \boldsymbol{\mu}, \boldsymbol{\kappa}$). That brings to [25; 26]

$$\begin{pmatrix} \mathbf{p} \\ \boldsymbol{\mu}\boldsymbol{\mu}_0\mathbf{m} \end{pmatrix} = \begin{pmatrix} \boldsymbol{\alpha}_e & i\boldsymbol{\alpha}_c \\ -i\boldsymbol{\alpha}_c^T & \boldsymbol{\alpha}_m \end{pmatrix} \begin{pmatrix} \mathbf{E} \\ \mathbf{H} \end{pmatrix} \quad (64)$$

where $\boldsymbol{\alpha}_e, \boldsymbol{\alpha}_m, \boldsymbol{\alpha}_c$ are generally complex valued 3×3 tensors. We stress that $\boldsymbol{\alpha}_{e,m,c}$, are all functions of $\varepsilon, \boldsymbol{\mu}$, and $\boldsymbol{\kappa}$ (see Appendix B for the explicit expressions). The radiation corrections and optical theorem for bi-anisotropic particles is discussed in [27, § II.C].

Force on chiral isotropic particle is going to be [18; 23; 24; 26; 28–31] (however, not in every reference the $\mathbf{F}^{(e-m)}$ is taken into account)

$$\mathbf{F} = \mathbf{F}^{\text{non-chiral}} + \frac{\omega}{n} \text{Re}(\boldsymbol{\alpha}_c) \nabla \mathcal{G} + \omega \gamma_{\text{abs},c}^{\text{Re}} \mathbf{S} - \text{Im}(\boldsymbol{\alpha}_c) \nabla \times \boldsymbol{\Pi}^{\text{Re}} - \frac{k^4 c}{6\pi n} |\boldsymbol{\alpha}_c|^2 \boldsymbol{\Pi}^{\text{Re}}. \quad (65)$$

Here $\mathbf{F}^{\text{non-chiral}}$ is the force from (61b) but with $\boldsymbol{\alpha}_e$ and $\boldsymbol{\alpha}_m$ are being functions of ($\varepsilon, \boldsymbol{\mu}, \boldsymbol{\kappa}$) (see Appendix B). We also have used the following identity: $\omega^2 \mathbf{S} - \frac{1}{2} \nabla \times \boldsymbol{\Pi}^{\text{Re}} = -\frac{1}{4} \text{Re}(\mathbf{H}^* \cdot (\nabla) \mathbf{E} - \mathbf{E}^* \cdot (\nabla) \mathbf{H})$ [23; 24]. Substituting (64) in (60) we get the torque on a chiral isotropic particle [32; 33]

$$\mathbf{T} = \frac{c}{n} \boldsymbol{\sigma}_{\text{abs},c} \mathbf{S} + \frac{1}{\omega} \gamma_{\text{abs},c}^{\text{Re}} \boldsymbol{\Pi}^{\text{Re}} + \frac{1}{\omega} \gamma_{\text{abs},c}^{\text{Im}} \boldsymbol{\Pi}^{\text{Im}}. \quad (66)$$

The generalized chiral absorption cross sections are

$$\boldsymbol{\sigma}_{\text{abs},c} = \boldsymbol{\sigma}_{\text{abs},c}^{(e)} + \boldsymbol{\sigma}_{\text{abs},c}^{(m)}, \quad (67a)$$

$$\boldsymbol{\sigma}_{\text{abs},c}^{(e)} = \frac{k}{\varepsilon\varepsilon_0} (\text{Im}(\boldsymbol{\alpha}_e) - g_e |\boldsymbol{\alpha}_e|^2 - g_m |\boldsymbol{\alpha}_c|^2), \quad (67b)$$

$$\boldsymbol{\sigma}_{\text{abs},c}^{(m)} = \frac{k}{\varepsilon\varepsilon_0} (\text{Im}(\boldsymbol{\alpha}_m) - g_m |\boldsymbol{\alpha}_m|^2 - g_e |\boldsymbol{\alpha}_c|^2), \quad (67c)$$

$$\gamma_{\text{abs},c}^{\text{Re}} = 2\omega \text{Im}(\boldsymbol{\alpha}_c) - 2\omega g_e \text{Re}(\boldsymbol{\alpha}_e \boldsymbol{\alpha}_c^*) - 2\omega g_m \text{Re}(\boldsymbol{\alpha}_m \boldsymbol{\alpha}_c^*), \quad (67d)$$

$$\gamma_{\text{abs},c}^{\text{Im}} = 2\omega g_m \text{Im}(\boldsymbol{\alpha}_m \boldsymbol{\alpha}_c^*) - 2\omega g_e \text{Im}(\boldsymbol{\alpha}_e \boldsymbol{\alpha}_c^*) \quad (67e)$$

with $g_e = \frac{k^3}{6\pi\epsilon\epsilon_0}$ and $g_m = \frac{k^3}{6\pi\mu\mu_0}$. We note that for lossless chiral particle with $\text{Im}(\epsilon) = \text{Im}(\mu) = \text{Im}(\kappa) = 0$ torque is equal to zero, so no momentum can be transferred from any incident optical fields to the particle. It is worth noting that the above conclusion is also valid to any lossless chiral sphere of any size [32, see Eq. (9)]. This alternatively follows from the optical theorem for chiral particles [34], for details see Eq. (B.30) in Appendix B. Alternative decomposition can be found in [31, Eq. (7)].

Surprisingly, in the lower approximation for the lossy particles, due to the symmetry of the equations, there are simple closed relation between dissipative part of the force and curl of the chiral and non-chiral parts of the torque which reveals the direct way of measuring the chiral part of the polarizability, energy flow, and spin angular momentum density [24, eqs. (15, 16)]

$$\mathbf{F}_{\text{diss}}^{(e,m)} + \frac{1}{2}\nabla \times \mathbf{T}^{(e,m)} = \frac{n}{c}\sigma_{\text{abs}}\mathbf{\Pi}^{\text{Re}} \quad (68a)$$

$$\mathbf{F}_{\text{diss}}^{(c)} + \frac{1}{2}\nabla \times \mathbf{T}^{(c)} = 2\omega^2 \text{Im}(\alpha_c)\mathbf{S} \quad (68b)$$

where for the small absorbing particles with $\sigma_{\text{ext}} \approx \sigma_{\text{abs}}$ we have $\mathbf{F}_{\text{diss}} = \mathbf{F}_{\text{diss}}^{(e,m)} + \mathbf{F}_{\text{diss}}^{(c)} = \frac{c}{n}\sigma_{\text{abs}}\mathbf{P} + 2\text{Im}(\alpha_c)(\omega^2\mathbf{S} - \frac{1}{2}\nabla \times \mathbf{\Pi}^{\text{Re}})$ is the dissipative (or non-conservative) part of the force and torque being $\mathbf{T} = \mathbf{T}^{(e,m)} + \mathbf{T}^{(c)} = \frac{c}{n}\sigma_{\text{abs}}\mathbf{S} + 2\text{Im}(\alpha_c)\mathbf{\Pi}^{\text{Re}}$. Here we have used $\mathbf{\Pi}^{\text{Re}} = \frac{c^2}{n^2}(\mathbf{P} + \frac{1}{2}\nabla \times \mathbf{S})$ and assumed that $\mathbf{P}^{(e)} = \mathbf{P}^{(m)}$ and $\mathbf{S}^{(e)} = \mathbf{S}^{(m)}$. We note that this relation is written for lossy dipole particles for which it is possible to neglect the correction recoil (scattering) terms in force and torque.

Also there are many similarities with the theory of linear subwavelength acoustomechanics which is discussed in Section 1.7 and in Chapter 5.

Finally, we also make a short overview of the stochastic simulations in Section 1.6 which is crucial to consider when real systems are involved.

Performing experiments on optical forces and torques in the real world is always accompanied with a Brownian forces or *stochastic forces* \mathbf{F}_{st} . The nature of this force is laying in huge amount of collisions with smaller particles of a host fluid. One of the possible dimensionless parameters to identify the potential impact of the stochastic forces is the relation between particle energy U (kinetic, e.g. due to the optical pressure or local depth of the potential well of an optical trap) and the energy of thermal motion [6; 35; 36]:

$$\gamma = \frac{U}{k_B T}, \quad \begin{cases} \gamma \lesssim 1 & - \mathbf{F}_{\text{st}} \text{ has to be considered} \\ \gamma \gg 1 & - \mathbf{F}_{\text{st}} \text{ is negligible} \end{cases} \quad (69)$$

where k_B is the Boltzmann constant and T is the absolute temperature of the host media. The estimation for the energy U depends on the dominant type of optical force: conservative (gradient force) or non-conservative (optical pressure) [6; 37–40][41, § 3]. In the dipole approximation two different contributions can be seen from Eq. (61b).

Once conservative force is dominant then the potential depth of the optical trap for electric dipole particle can be estimated as $U = U_{\text{tr}} = \langle \mathbf{p} \cdot \mathcal{E} \rangle = \frac{1}{2} \text{Re}(\alpha_e) |\mathbf{E}|^2$. Since near the equilibrium point force is linear with respect to the displacement it is possible to introduce effective stiffness as $F \approx -\kappa \Delta r$ thus the potential energy is going to be $U_{\text{tr}} = \frac{1}{2} \kappa \overline{\Delta r}^2$ [6; 36], where $\overline{\Delta r}$ is the average potential well width in real space. We have to stress that such analyses is valid only if the conservative part of optical forces is dominant. Otherwise, if non-conservative forces is dominant then kinetic energy should be placed in Eq. (1.41). For example, for the plane wave pressure it is going to be $U = U_{\text{kin}} = \frac{m \langle \mathbf{v} \rangle^2}{2}$, where average velocity of the particle can be obtained from the equality of optical pressure force and friction force (Stokes' law [42]) $\langle v \rangle = \sigma_{\text{ext}}^{(e)} \frac{1}{2} \epsilon \epsilon_0 |\mathbf{E}|^2 / (6\pi \nu a)$, where ν is the dynamic viscosity of the host fluid and a is the particle radius.

Once stochastic force has to be considered, *Langevin equation* has to be solved numerically to achieve a proper dynamics simulation. For sure, many realization of the same numeric experiment are needed to perform further statistical analyses. The equation of motion is going to be

$$m \ddot{\mathbf{r}} = -\zeta \dot{\mathbf{r}} + \mathbf{F}_{\text{st}} + \mathbf{F} \quad \text{or} \quad \begin{cases} \dot{\mathbf{r}} = \mathbf{v} \\ \dot{\mathbf{v}} = -\frac{\zeta}{m} \mathbf{v} + \frac{1}{m} (\mathbf{F}_{\text{st}} + \mathbf{F}) \end{cases} \quad (70)$$

where m is the mass of the particles, ζ is the friction coefficient (for a sphere the Stokes' law is applicable, so $\zeta = 6\pi \nu a$ with a and ν being particles radius and dynamic viscosity of the host fluid), \mathbf{F} is the optical force, and \mathbf{F}_{st} is delta correlated stochastic force with zero average, so it satisfies $\langle \mathbf{F}_{\text{st}}(t) \rangle_t = 0$ and $\langle F_{\text{st},\alpha}(t) F_{\text{st},\beta}(t + \tau) \rangle_t = 2D \delta_{\alpha\beta} \delta(\tau)$. It is important to understand that friction and stochastic forces are connected with each other on the fundamental level. It means that the friction coefficient ζ is connected to the auto-correlation coefficient D of the stochastic forces as $D = k_B T \zeta$ [43] (see Appendix L for the proof).

Equation (70) can be rewritten as a system of two first order differential equations with respect to \mathbf{r} and \mathbf{v} , and solved by any standart numerical procedure such as family of Euler methods, Runge–Kutta methods or any other [44],

with some special treatment to the stochastic term \mathbf{F}_{st} [43]. All these methods rely on discretization of the time line $t \rightarrow \{t_i\}$ with a step Δt . Integration of (70), i.e. $\int_{t_i}^{t_{i+1}} (1.42)dt$, is going to have obstacles since $\int_{t_i}^{t_{i+1}} \mathbf{F}_{\text{st}}(t)dt \neq \mathbf{F}_{\text{st}}(t_i)\Delta t$. The trick is to introduce a new variable $\int_{t_i}^{t_{i+1}} dt\mathbf{F}_{\text{st}}(t) \equiv \mathbf{W}_i$ with properties which follows from the properties of the white-noise nature of the \mathbf{F}_{st} : $\langle \mathbf{W}_i \rangle = 0$ and $\langle \mathbf{W}_i \cdot \mathbf{W}_j \rangle = \delta_{ij} \cdot 6k_{\text{B}}T\zeta\Delta t = \delta_{ij} \cdot 3\sigma_{W_\alpha}^2$ with $\alpha = x, y, z$, we note that the later one is actually a dispersion of normally distributed random value W_α . So for the simple Euler method the final system is going to be

$$\begin{cases} \mathbf{r}(t_{i+1}) = \mathbf{r}(t_i) + \Delta t\mathbf{v}(t_i), \\ \mathbf{v}(t_{i+1}) = \mathbf{v}(t_i) - \Delta t\frac{\zeta}{m}\mathbf{v}(t_i) + \frac{1}{m}\mathbf{W}_i \end{cases}, \quad \begin{cases} \sigma_{W_\alpha} = \sqrt{2k_{\text{B}}T\zeta\Delta t} \\ \alpha = x, y, z \end{cases} \quad (71)$$

We stress that dispersion (or quadratic deviation) depends on the discretization time step Δt .

In **Chapter 2** there is an analyses of the eigen modes of two analytically solved geometries: sphere and infinite cylinder. In the case of a sphere, the eigen modes are described by the vector spherical harmonics (VSH) and their eigen frequency are always complex since it is an open system, so

$$\omega = \omega' - i\delta \quad (72)$$

where $\delta/2$ shows the inverse average life time of the mode. Eventually, the structure of the eigen modes of a dielectric sphere resembles the electric and magnetic field of a single photon with a particular angular momenta.

We analyze the eigen modes using canonical properties of the field introduced recently in Ref. [45] for the, generally, dispersive media, which is crucial for the case of metallic particles. The Brillouin energy W , linear momentum \mathbf{P} , spin \mathbf{S} , orbital \mathbf{L} , and total \mathbf{J} angular momentum can be formulated in the manner of quantum mechanics as follows [15; 45; 46]

$$W = \langle \psi | \omega | \psi \rangle = \frac{1}{4} (\tilde{\epsilon}\epsilon_0 |\mathbf{E}|^2 + \tilde{\mu}\mu_0 |\mathbf{H}|^2), \quad (73)$$

$$\mathbf{P} = \langle \psi | \hat{\mathbf{p}} | \psi \rangle = \frac{1}{4\omega'} \text{Im} (\tilde{\epsilon}\epsilon_0 \mathbf{E}^* \cdot (\nabla)\mathbf{E} + \tilde{\mu}\mu_0 \mathbf{H}^* \cdot (\nabla)\mathbf{H}), \quad (74)$$

$$\mathbf{S} = \langle \psi | \hat{\mathbf{S}} | \psi \rangle = \frac{1}{4\omega'} \text{Im} (\tilde{\epsilon}\epsilon_0 \mathbf{E}^* \times \mathbf{E} + \tilde{\mu}\mu_0 \mathbf{H}^* \times \mathbf{H}), \quad (75)$$

$$\mathbf{L} = \mathbf{r} \times \mathbf{P}, \quad \mathbf{J} = \mathbf{L} + \mathbf{S}, \quad (76)$$

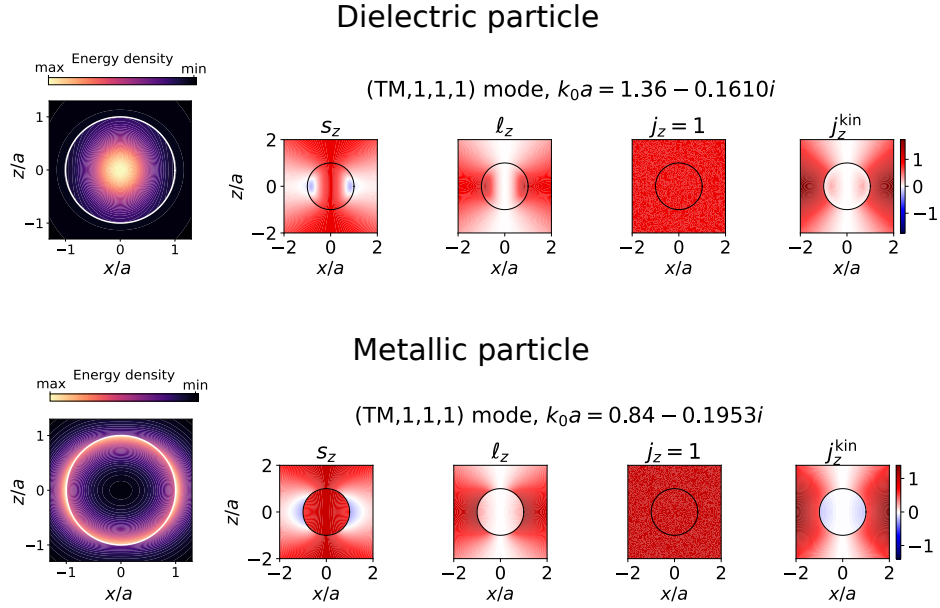


Figure B – Angular momenta density distribution for the dipole modes for dielectric and metallic particles

and the quadratic form of a square of total angular momenta denoted as $[\mathbf{J}^2]$ is given by

$$\begin{aligned}
 [\mathbf{J}^2] = \langle \psi | (\hat{\mathbf{L}} + \hat{\mathbf{S}})^2 | \psi \rangle &= \frac{1}{4\omega'} \text{Re} \tilde{\epsilon} \epsilon_0 \left[r^2 \sum_{i=x,y,z} E_i^* \Delta_\Omega E_i + 2(\mathbf{E}^* \cdot \nabla)(\mathbf{r} \cdot \mathbf{E}) \right] \\
 &+ (\text{magnetic part: } \begin{matrix} \mathbf{E} \rightarrow \mathbf{H} \\ \tilde{\epsilon} \epsilon_0 \rightarrow \tilde{\mu} \mu_0 \end{matrix}). \quad (77)
 \end{aligned}$$

which was explicitly written for the first time for the best of our knowledge. Each of the components can be naturally decomposed into the electric and magnetic parts. Here $(\tilde{\epsilon}, \tilde{\mu}) = (\epsilon, \mu) + \omega \partial_\omega (\epsilon, \mu)$, the electromagnetic 6-component “wave function” is given by $|\psi\rangle = \sqrt{g/2} (\sqrt{\tilde{\epsilon} \epsilon_0} \mathbf{E}, \sqrt{\tilde{\mu} \mu_0} \mathbf{H})^T$ [45; 47–51], where the constant g depends on the unit system: $g^{\text{(Gaussian)}}_{\text{SI units}} = \left(\frac{(2\omega)^{-1}}{(8\pi\omega)^{-1}} \right)$. This photon wave function is written in the manner of Shrodinger-like formulation of the Maxwell equations. In literature there is another way of how the photon wave function may written which is based on Dirac-like formulation of Maxwell equations [52–57]. As well argued by Bialynicki-Birula [53; 57] and by Sipe [54], for photons it is best to adopt a wave function whose modulus squared is the photon’s mean energy density, rather than being a position probability density, as is the case for electrons [58] which is true for the both formulations.

We plot the canonical angular momenta density and show that it is an integer value if ones find the total angular momentum per one photon (Fig. B). Thus, it opens a door to the investigation of the electric field structure of a single photons

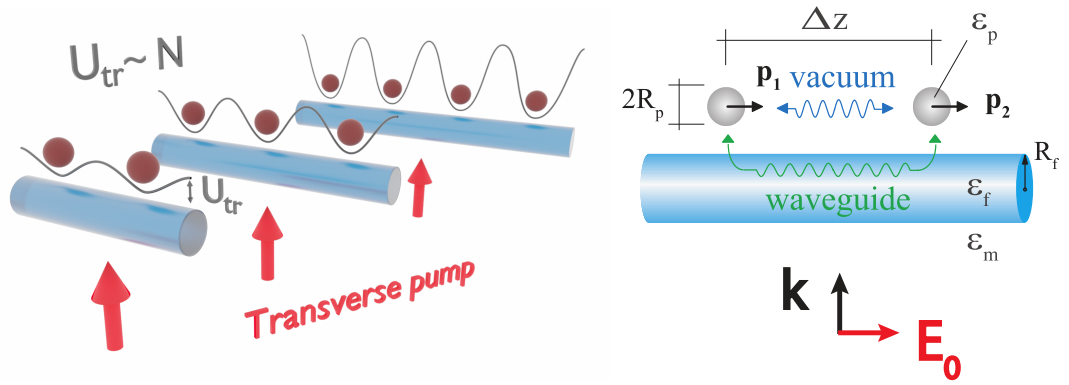


Figure C — The main concept of Chapter 3: an inline array of subwavelength particles near a nanofiber with transverse illumination. The trapping potential along the fiber axis growth linearly with the number of particles in the chain. The long-range interaction is achieved via the interaction through the guided mode

by examining the structure of the eigen modes of a sphere. Next, we also analyze in deep details the guided modes of the dielectric waveguide. In particular, we show that, as it was with the sphere, the canonical total angular momenta density per one photon of eigen modes is quantized

$$\mathbf{E}(\mathbf{r}) \sim e^{im\varphi} \quad \rightarrow \quad j_z = \frac{\omega' J_z}{W} = \frac{\omega(rP_\varphi + S_z)}{W} = m. \quad (78)$$

In **Chapter 3** we consider a very peculiar and physics-rich system. It appears that the finite array of small particles can be trapped in all three directions by a *single* beam (see Figure C).

The majority of the optical trapping and manipulation methods are based on shaping the light field intensity with optical systems such as spatial light modulator which provides formation of the dipole trapping potential. This approach has been effectively used for manipulation of objects in different environment such as air, water, and vacuum. However, an alternative method of large ensembles manipulation and ordering bases on self-assembly approach[59]. The field intensity pattern forms due to rescattering of the optical fields by the objects resulting in effective dipole-dipole interactions and consequent structuring of large ensembles. A typical example of such effect is transverse optical binding [60; 61] where the nanoparticle can form bounded states under homogeneous illumination. Though the optical dipole-dipole interactions are quite weak, they can be enhanced and modified with auxiliary photonic structures [62] such as metamaterials[63; 64] and metasurfaces[65], plasmonic structures[66; 67], photonic crystal hollow fibers [68] as well as dielectric nanofibers[69]. The latter one represents a versatile platform[70] for

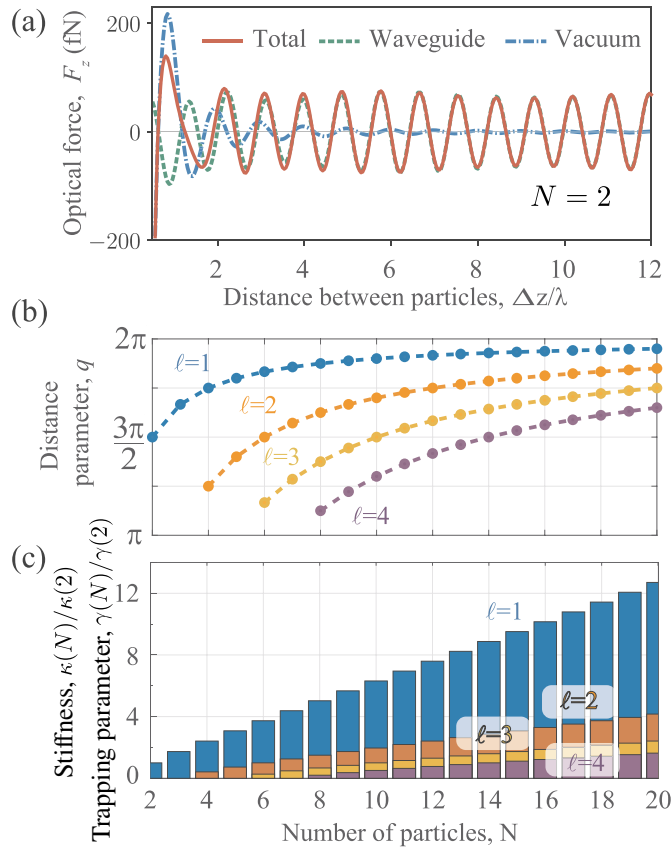


Figure D — (a) Longitudinal force F_z in a single mode regime acting on one of two particles as a function of distance along the nanofiber axis Δz . Red solid line shows total optical force which takes into account interaction through both free space and fiber ($\hat{\mathbf{G}}_s + \hat{\mathbf{G}}_0$), green dashed line shows only interaction through the fiber ($\hat{\mathbf{G}}_s$) and blue dash-and-dot line shows only free space interaction ($\hat{\mathbf{G}}_0$). (b) Equilibrium solutions. First three branches of the solution for the distance between the two closest particles $q = \Delta z \beta$ with respect to the total number of particles in a chain N . (c) Trapping parameter γ , which equals to the effective potential depth of the trap divided by a thermal energy of the host media kT , and normalized stiffness of the trap with respect to the number of particles in a chain N

studying light interaction with nanoparticles[71; 72] and atoms[73–75] placed close to its surface. Utilization of a single mode long-range dipole-dipole interactions provided by waveguiding systems has already been suggested for self-organization of atoms and nanoparticles in waveguiding systems[68; 76; 77].

We propose a geometry of an array of nanoparticles placed close to the ultra-thin fiber and illuminated by a plane wave propagating in the isotropic host media perpendicularly to the fiber axis as it is shown in Fig. 3.2. Such configuration allows to take the advantage of the transverse optical binding effect [61; 78]. The binding happens due to the interference of the fields scattered by the nanoparti-

cles, and it has been applied for self-organization of nanoparticle ensembles under the external monochromatic illumination [79–81], including particle binding near a metallic surface near surface plasmon polariton resonance (SPP) [82]. In the literature, a transverse binding has been observed in a large ensemble of dielectric sub-micron spheres [83] and nanowires [84; 85] with the strong collective interactions through the vacuum.

The nanofiber guided modes allow for accumulation of long-range interactions between distant nanoparticles due to their extremely low losses, which results in the increasing particles stiffness with the growth of the nanoparticle chain length. Moreover, in our particular geometry of binding near a nanofiber, we also suggest a trapping of the nanoparticles in the radial direction close to the fiber surface by using two counter propagating plane waves and taking the advantage of nanofiber photonic jet or lensing effect [86]. In this effect during the transverse excitation dielectric nanofiber start to act as focusing lens. Thus, we propose a geometry of the system that allows us to immediately test the claimed effect in a specific experimental setup using optical nanofibers.

Under the plane wave excitation the nanoparticles form a stable self-organized periodic array along waveguide axis through the transverse binding effect. We show that owing to the long-range interaction between the nanoparticles the trapping potential for each nanoparticle in the chain increases linearly with the system size, making the formation of long chains more favourable. We show that for an optical nanofiber platform the binding energy for two nanoparticles is in the range of $9 \div 13 k_B T$ reaching the value of $110 k_B T$ when the chain size is increased to 20 nanoparticles (Fig. D). We also suggest the geometry of the two counter-propagating plane waves excitation, which will allow trapping the nanoparticles close to the optical nanofiber providing efficient interaction between the nanoparticles and the nanofiber.

In **Chapter 4** three different systems are considered where the transfer of angular momenta from electromagnetic field to subwavelength particles is occurring (Figure F):

1. **OAM transfer.** To illustrate the orbital angular momentum transfer we consider an orbiting microparticle around a nanofiber in which the circular polarized plane wave propagates. We show that there is a non-zero OAM density which eventually shows itself in the orbiting motion of the particle. The result of this section are supported by the experimental data. In the

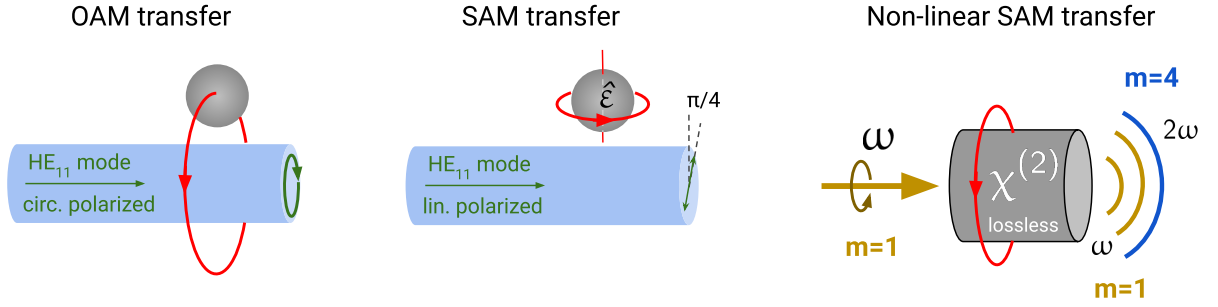


Figure F — Three main systems considered in Chapter 4 where the spin and orbital angular momenta (SAM and OAM) is transferred. From left to right: OAM transfer from the circular polarized fundamental waveguided mode HE_{11} ; SAM transfer from the transverse spin which comes from the linearly polarized HE_{11} mode to the anisotropic particles; non-linear SAM transfer from a plane circular polarized wave via second harmonic generation process, the presence of torque is explained from the AM conservation law

dipole approximation we can write the orbiting (extrinsic) torque as

$$T_{\text{orb}} = rF_{\varphi} \propto L_z \propto \ell|\mathbf{E}|^2 \quad (79)$$

where r is the distance to the fiber axis, F_{φ} is the azimuthal optical force on the particle, and ℓ is the azimuthal “quantum” number of the mode. For the fundamental mode $HE_{\ell m}$ we have $\ell = m = 1$. The optical parameters of the fiber and particle radii have been analyzed as well.

2. **SAM transfer.** The concept of the transverse spin angular momenta is discussed in this part. The analyses of the SAM density of the linearly polarized HE_{11} mode shows that at a particular azimuthal angles there is a maxima of the radial SAM densities. Here we propose a geometry where this transverse SAM can show yourself. For this we analyze the rotational dynamics (spinning dynamics) of an anisotropic particle which is described by a permittivity tensor $\hat{\epsilon}$. The choice of anisotropic particle is motivated by the desire to reduce any possible heat losses which enhances the Brownian motion but still have a significant torque. We come to the conclusion that the torque in the dipole approximation can be written as

$$\mathbf{T} = \mathbf{T}_{\text{anis}} + \mathbf{T}_{\text{alignment}} + \underbrace{\mathbf{T}_{\text{losses}}}_{=0} \quad (80)$$

where $\mathbf{T}_{\text{anis}} \propto \mathbf{S}$ is the spinning torque which always tend to rotate the particle around it’s own axis in the same direction as the SAM density;

$\mathbf{T}_{\text{alignment}}$ is the alignment torque which tends to align the principle axis of the permittivity tensor with the main polarization ellipse semi-axes.

3. **Non-linear SAM transfer.** We start with a model problem of scattering of a circularly polarized plane wave with frequency ω on a dielectric scatterer with cylinder symmetry (see Fig. G). The plane wave is incident along the axis of the cylinder and carries the momentum of light of \hbar photon. Then, due to the symmetry of the problem the optical torque in the linear regime $\mathbf{T}^{(\omega)}$ acting on the particle is exactly proportional to the absorption cross section [10; 11] and, in terms of canonical spin angular momenta density one can write $\mathbf{T}^{(\omega)} = c/n_0 \cdot \sigma_{\text{abs}} \mathbf{S}^{(\omega)}$, where $\mathbf{S}^{(\omega)} = m_{\text{inc}}/(2\omega) \cdot \epsilon \epsilon_0 [E_0^{(\omega)}]^2 \mathbf{e}_z$ is the canonical spin angular momenta density [45] with azimuthal number $m_{\text{inc}} = \pm 1$ for right(left) circular polarization and $n_0 = \sqrt{\epsilon \mu}$ is the refractive index of the host media. Now, once the excitation wavelength is tuned out of the absorption band of the material, one can neglect losses, which logically provides the condition of zero torque. However, in the following we will show that once the higher order optical processes are accounted there can appear non-zero nonlinear optical torque even in the geometry considered in Fig. G. In the following, we first restrict the consideration to the process of second-harmonic generation (SHG) which is a dominant nonlinear process in many optical materials [87]. It manifests in conversion of two photons with frequency ω at the fundamental harmonic (FH) to one photon at the second harmonic (SH) with frequency 2ω , hence there two components of the optical nonlinear torque

$$\mathbf{T} = \mathbf{T}^{(\omega)} + \mathbf{T}^{(2\omega)} \quad (81)$$

where $\mathbf{T}^{(\omega)}$ and $\mathbf{T}^{(2\omega)}$ are the optical torques at the fundamental and second harmonics, which are appeared to be beautifully connected via the same scattering coefficients as we show below.

Finally, in **Chapter 5** we examine acoustic radiation force and torque on a small (subwavelength) absorbing isotropic particle immersed in a monochromatic (but generally inhomogeneous) sound-wave field. Master equations are linearised

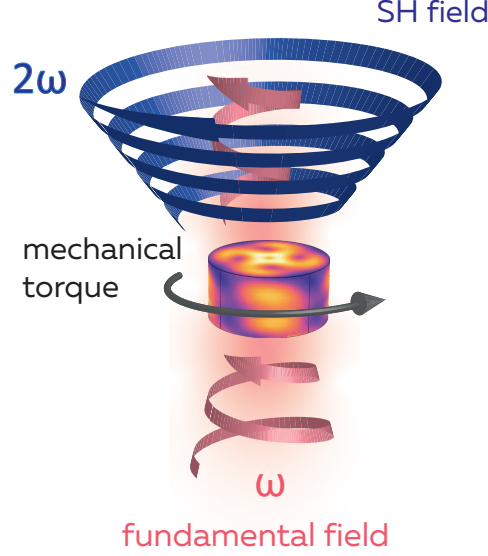


Figure G — The mechanism of the non-linear torque. Circularly polarized plane wave with frequency ω wave is incident on a lossless cylinder, the latter one generates second harmonic with non-zero angular momentum which is defined by selection rules. Due to the conservation of the angular momenta there is a non-zero mechanical torque

Navie-Stokes equation and continuity equation:

$$\begin{cases} \rho_0 \partial_t \mathbf{v} = -\nabla p & \text{1st order N.-S.} \\ \beta_0 \partial_t p = -\nabla \cdot \mathbf{v} & \text{1st order c.e.} \\ p = c_s^2 \rho & \text{state eq.} \end{cases} \quad (82)$$

Where $c_s = 1/\sqrt{\rho_0 \beta_0}$ is the speed of sound. From above it also follows that vector field is curl-free

$$\nabla \times \mathbf{v} = 0. \quad (83)$$

Media is described by two main quantities: (i) density ρ_0 , $[\rho_0] = [\text{kg} \cdot \text{m}^{-3}]$ and (ii) compressibility $\beta_0 = -\frac{1}{V} \frac{\partial V}{\partial p}$, $[\beta_0] = [\text{m}^2 \cdot \text{N}^{-1}]$. Connection with the speed of sound is given by $c_s = 1/\sqrt{\rho_0 \beta_0}$.

Object inside this media can be described by its own density ρ_1 and compressibility β_1 . It is convenient to use normalized dimensionless parameters [88–90]: (i) normalized density $\bar{\rho}_1 = \rho_1/\rho_0$ and (ii) normalized compressibility $\bar{\beta}_1 = \beta_1/\beta_0$. After introducing these normalized quantities, I can write the wavevector inside the object as

$$k_1 = k_0 \sqrt{\bar{\rho}_1 \bar{\beta}_1}. \quad (84)$$

Usually, losses in linear acoustics are defined as an imaginary term if the wave vector $k_1 = k'_1 + i\delta_1$. *Porous* materials are the great example of lossy matter in linear acoustics [89–92]. However, using relative density and compressibility allows to introduce losses as it is done in optics, so for $\text{Im}(\bar{\rho}_1) > 0$, $\text{Im}(\bar{\beta}_1) > 0$ one gets a lossy particle, and for $\text{Im}(\bar{\rho}_1) < 0$, $\text{Im}(\bar{\beta}_1) < 0$ one gets a particle with gain (for the $e^{-i\omega t}$ choice).

It is convenient to consider complex amplitudes for the monochromatic fields $A(\mathbf{r}, t) = \text{Re}(A(\mathbf{r})e^{-i\omega t})$ where $A = p, \rho, \mathbf{v}$.

Energy density and canonical momenta of an acoustic monochromatic wave can be written as [93]

$$W = \frac{1}{4} (\beta_0 |p|^2 + \rho_0 |\mathbf{v}|^2) \equiv W^{(p)} + W^{(\mathbf{v})}, \quad (85a)$$

$$\mathbf{P} = \frac{1}{4\omega} \text{Im} [\beta_0 p^* \nabla p + \rho_0 \mathbf{v}^* \cdot (\nabla) \mathbf{v}] \equiv \mathbf{P}^{(p)} + \mathbf{P}^{(\mathbf{v})}, \quad (85b)$$

$$\mathbf{L} = \mathbf{r} \times \mathbf{P}, \quad (85c)$$

$$\mathbf{S} = \frac{\rho_0}{2\omega} \text{Im} \mathbf{v}^* \times \mathbf{v}, \quad \mathbf{J} = \mathbf{L} + \mathbf{S}, \quad (85d)$$

where W is the energy density, \mathbf{P} is the canonical linear momenta density, \mathbf{L} , \mathbf{S} , and \mathbf{J} are the orbital, spin, and total angular momentum densities, respectively. Here I have used Berry's notation $\mathbf{v}^* \cdot (\nabla) \mathbf{v} \equiv \sum_{i=x,y,z} v_i^* \nabla v_i$ [9].

We show that by introducing the monopole and dipole polarizabilities of the particle, the problem can be treated in a way similar to the well-studied optical forces and torques on dipole Rayleigh particles. We derive simple analytical expressions for the acoustic force (including both the gradient and scattering forces) and torque:

$$\mathbf{F}^{\text{acoustic}} = \underbrace{-\frac{1}{2} \text{Re} \left[\frac{i}{\omega} M^* \nabla p - \rho \mathbf{D}^* \cdot (\nabla) \mathbf{v} \right]}_{\mathbf{F}_M + \mathbf{F}_D} - \underbrace{\frac{\rho k^3}{12\pi} \text{Im} [M^* \mathbf{D}]}_{\mathbf{F}_{\text{self}}} \quad (86)$$

and

$$\mathbf{T}^{\text{acoustic}} = \frac{\rho}{2} \text{Re} (\mathbf{D}^* \times \mathbf{v}) - \frac{\rho k^3}{24\pi} \text{Im} (\mathbf{D}^* \times \mathbf{D}) \quad (87)$$

where M is the acoustic monopole, and \mathbf{D} is the acoustic dipole. In terms of absorption cross section and canonical spin angular momentum density the torque is going to be

$$\mathbf{T}^{\text{acoustic}} = c_s \sigma_{\text{abs}}^D \mathbf{S}^{\text{acoustic}} \quad (88)$$

where c_s is the speed of sound in the host media. To the best of knowledge, eqs. (87) and (88) are written the first time and have lots of similarities with the ones in optics [94].

Using polarizabilities, defined as $M = -i\omega\beta\alpha_M p$ and $\mathbf{D} = \alpha_D \mathbf{v}$, we connect the field action on a small particle with the canonical properties of the acoustic incident wave:

$$\mathbf{F}^{\text{acoustic}} = \mathbf{F}^{\text{grad}} + \mathbf{F}^{\text{scat}} + \mathbf{F}^{\text{recoil}}. \quad (89)$$

Here the gradient and scattering parts are related to the real and imaginary parts of the particle polarizabilities:

$$\mathbf{F}^{\text{grad}} = \text{Re}(\alpha_M) \nabla W^{(p)} + \text{Re}(\alpha_D) \nabla W^{(v)}, \quad (90)$$

$$\mathbf{F}^{\text{scat}} = 2\omega \left[\text{Im}(\alpha_M) \mathbf{P}^{(p)} + \text{Im}(\alpha_D) \mathbf{P}^{(v)} \right] \quad (91)$$

$$\mathbf{F}^{\text{recoil}} = \frac{k^4}{6\pi c_s} \left(\text{Re}(\alpha_M \alpha_D^*) \mathbf{\Pi}^{\text{Re}} + \text{Im}(\alpha_M \alpha_D^*) \mathbf{\Pi}^{\text{Im}} \right) \quad (92)$$

Importantly, these expressions reveal intimate relations to the fundamental field properties introduced recently for acoustic fields: the canonical momentum and spin angular momentum densities. We compare our analytical results with previous calculations and exact numerical simulations. We also consider an important example of a particle in an evanescent acoustic wave, which exhibits the mutually orthogonal scattering (radiation-pressure) force, gradient force, and torque from the transverse spin of the field.

Importantly, we also provide a solution to a number of helpful problems such as Mie scattering problem and complex angle approach in acoustics.

Scattering of a plane wave on a sphere can be solved exactly (Mie scattering problem). This solution become extremely popular in optics, but not in acoustics yet. Here we revisit this solution as well. Incident field can be decomposed as [95]

$$p^i = p_0 e^{ikr \cos \theta} = \sum_{n=0}^{\infty} p_n j_n(kr) P_n(\cos \theta), \quad (93)$$

where $p_n = p_0 i^n (2n + 1)$.

Any radiation from a body located at the origin can be characterized by sums of multipoles:

$$p(\mathbf{r}, \omega) = \sum_{n=0}^{\infty} \sum_{m=-n}^n A_{mn}(\omega) z_n(kr) Y_n^m(\theta, \varphi) \quad (94)$$

Where $z_n = j_n, h_n^{(1)}$ are the radial dependent functions which is usually one of the spherical Bessel functions depending on the boundary conditions, and $\psi_{mn}(\mathbf{r}) = z_n(kr)Y_n^m(\theta, \varphi)$ are *the modes of the sphere*. Next, system has symmetry over φ , so

$$p(\mathbf{r}, \omega) = \sum_{n=0}^{\infty} A_n(\omega) z_n(kr) P_n(\cos \theta). \quad (95)$$

Particle with radius a is described by ρ_1 and β_1 and located in a fluid with ρ_0 and β_0 . Boundary conditions are

$$\begin{cases} p^i + p^s = p^{\text{in}} \\ v_r^i + v_r^s = v_r^{\text{in}} \end{cases} \quad (96)$$

where $\mathbf{v} = \frac{1}{i\omega\rho_0} \nabla p$, so the second equations transforms to $\partial_r p^i + \partial_r p^s = \frac{\rho_0}{\rho_1} \partial_r p^{\text{in}}$. Decompositions for scattered field and field inside the particle are

$$p^s(\mathbf{r}, \omega) = \sum_{n=0}^{\infty} p_n a_n(\omega) h_n^{(1)}(kr) P_n(\cos \theta), \quad (97)$$

$$p^{\text{in}}(\mathbf{r}, \omega) = \sum_{n=0}^{\infty} p_n c_n(\omega) j_n(k_1 r) P_n(\cos \theta), \quad (98)$$

where $p_n = p_0 i^n (2n + 1)$. Boundary conditions give explicit expressions for a_n and c_n coefficients:

$$c_n = \frac{i/(ka)^2}{j_n(k_1 a) h_n^{(1)'}(ka) - \gamma j_n'(k_1 a) h_n^{(1)}(ka)}, \quad (99)$$

$$a_n = \frac{\gamma j_n'(k_1 a) j_n(ka) - j_n(k_1 a) j_n'(ka)}{j_n(k_1 a) h_n^{(1)'}(ka) - \gamma j_n'(k_1 a) h_n^{(1)}(ka)}, \quad (100)$$

where $k_1 = k\sqrt{\bar{\rho}_1 \bar{\beta}_1}$ and $\gamma = \frac{k_1 \rho_0}{k \rho_1} = \sqrt{\bar{\beta}_1 / \bar{\rho}_1}$. These coefficient are in the agreement with coefficients A_n and B_n from [96]: $a_n = A_n$ and $c_n = -\bar{\rho}_1 B_n$ (it seems there is a typo in [96], c_n in this work satisfies the limiting case $p^{\text{in}}(\bar{\rho}_1 = \bar{\beta}_1 = 1) = p^i$).

It is possible also to find scattering, extinction, and absorption cross section. The final answer is the following

$$\sigma_{\text{ext}} = \sigma_{\text{abs}} + \sigma_{\text{sc}}, \quad (101)$$

where after integration we get expression very similar to the identical ones in the electromagnetic Mie scattering problem [97]:

$$\sigma_{\text{sc}} = \frac{4\pi}{k^2} \sum_{n=0}^{\infty} (2n+1) |a_n|^2, \quad (102)$$

$$\sigma_{\text{ext}} = -\frac{4\pi}{k^2} \sum_{n=0}^{\infty} (2n+1) \text{Re}(a_n), \quad (103)$$

$$\sigma_{\text{abs}} = -\frac{4\pi}{k^2} \sum_{n=0}^{\infty} (2n+1) \left(|a_n|^2 + \text{Re}(a_n) \right) \quad (104)$$

We also provide a table of cross sections for various combination of popular acoustic materials which is about to help to find a proper resonant material: air, water, porous silicon, epoxy resin, and aerogel (fig. 5.4 in the main text). The general rule of thumb is that the acoustic refractive index should be $n_{\text{acoustic}} = c_s^{\text{host}}/c_s^{\text{particle}} = \sqrt{\bar{\rho}_1 \bar{\beta}_1} \gtrsim 1$.

Let us consider the case of small particles. In terms of monopole and dipole polarizabilities, which are defined in Sec. 5.3, we can rewrite it as:

$$\sigma_{\text{ext}} = k (\text{Im}(\alpha_M) + \text{Im}(\alpha_D)), \quad (105)$$

$$\sigma_{\text{sc}} = \frac{k^4}{4\pi} \left(|\alpha_M|^2 + \frac{1}{3} |\alpha_D|^2 \right), \quad (106)$$

$$\sigma_{\text{abs}} = \underbrace{k \text{Im} \alpha_M - \frac{k^4}{4\pi} |\alpha_M|^2}_{\sigma_{\text{abs}}^M} + \underbrace{k \text{Im} \alpha_D - \frac{k^4}{12\pi} |\alpha_D|^2}_{\sigma_{\text{abs}}^D} \quad (107)$$

Since polarizabilities are scaled as the volume of the particle $\alpha_M, \alpha_D \sim a^3$, we can conclude that for lossy ($\text{Im}(\bar{\rho}), \text{Im}(\bar{\beta}) \sim 1$) subwavelength particles $\sigma_{\text{abs}} \sim a^3 \gg \sigma_{\text{sc}} \sim a^6$. In other words, small particles absorb better than scatter. However, for bigger particles scattering become more dominant.

Finally, for to study Mie resonances in acoustics, it helpful to implement the complex angle approach which help to find force and torque in the evanescent field using semi-analytical approach. The incident plane wave $p^{\text{p.w.}}(\mathbf{r}) = p_0 e^{ikz}$ can be transformed to the evanescent wave by the rotation its argument on the complex angle

$$p^{\text{evan}}(\mathbf{r}) = p^{\text{p.w.}}(\hat{R}(i\alpha)\mathbf{r}) = p_0 e^{ik \cosh(\alpha)z} e^{-k \sinh(\alpha)x}, \quad (108)$$

where $\hat{R}(i\alpha) = \begin{pmatrix} \cosh(\alpha) & 0 & -i \sinh(\alpha) \\ 0 & 1 & 0 \\ i \sinh(\alpha) & 0 & \cosh(\alpha) \end{pmatrix}$.

Mie operator is also linear so we know the scattered field in the case of evanescent incident wave for any sphere

$$p^s(\mathbf{r}) \rightarrow p^s(\hat{R}(i\boldsymbol{\alpha})\mathbf{r}) \quad (109)$$

so $x \rightarrow x' = x \cosh(\boldsymbol{\alpha}) - iz \sinh(\boldsymbol{\alpha})$, $y \rightarrow y' = y$, $z \rightarrow z' = ix \sinh(\boldsymbol{\alpha}) + z \cosh(\boldsymbol{\alpha})$ or for spherical coordinates $r \rightarrow r' = r$, $\theta \rightarrow \theta' = \cos^{-1} \frac{z'}{r}$, and $\varphi \rightarrow \varphi' = \text{tg}^{-1} \frac{y}{x'}$. And the velocity is always defined as $\mathbf{v} = \frac{1}{i\omega\rho} \nabla p$. Since we know all the fields, we can numerically integrate (1.47c). The result of calculation is presented in Fig. 5.6 in the main text. Note that repulsion and attraction forces to the surface are possible.

Publications relevant to this thesis

Key results of research are described in 9 publications. Among them 8 are published in a journal indexed by Scopus and Web of Science and 1 is published in other sources.

Publications in international journals indexed by Scopus and Web of Science:

1. Optical binding via surface plasmon polariton interference / N. Kostina [et al.] // Phys. Rev. B. — 2019. — Mar. — Vol. 99, no. 12. — P. 125416. — URL: <https://doi.org/10.1103/PhysRevB.99.125416>.
2. Acoustic Radiation Force and Torque on Small Particles as Measures of the Canonical Momentum and Spin Densities / I. D. Toftul [et al.] // Phys. Rev. Lett. — 2019. — Oct. — Vol. 123, no. 18. — P. 183901. — URL: <https://doi.org/10.1103/PhysRevLett.123.183901>.
3. Light-induced rotation of dielectric microparticles around an optical nanofiber / G. Tkachenko [et al.] // Optica. — 2020. — Jan. — Vol. 7, no. 1. — P. 59–62. — URL: <https://doi.org/10.1364/OPTICA.374441>.
4. *Toftul I. D., Kornovan D. F., Petrov M. I.* Self-Trapped Nanoparticle Binding via Waveguide Mode // ACS Photonics. — 2020. — Jan. — Vol. 7, no. 1. — P. 114–119. — URL: <https://doi.org/10.1021/acsp Photonics.9b01157>.
5. *Toftul I., Bliokh K., Petrov M.* Acoustic forces and torques: Directional scattering and acoustic spin // AIP Conf. Proc. — 2020. — Dec. — Vol. 2300, no. 1. — P. 020127. — URL: <https://doi.org/10.1063/5.0032100>.

6. Detection of the transverse spin of light by twisting anisotropic particles near an optical nanofiber waveguide / G. Tkachenko [et al.] // Proceedings Volume 11926, Optical Manipulation and Structured Materials Conference 2021. Vol. 11926. — SPIE, 10/2021. — P. 69–71. — URL: <https://doi.org/10.1117/12.2616130>.
7. *Toftul I., Frizyuk K., Petrov M.* Total angular momenta quantization of dielectric sphere modes // J. Phys. Conf. Ser. — 2021. — Nov. — Vol. 2015, no. 1. — P. 012152. — URL: <https://doi.org/10.1088/1742-6596/2015/1/012152>.
8. Orbiting of dielectric particles around a single-mode ultrathin fiber waveguide / G. Tkachenko [et al.] // Proceedings Volume 11522, Optical Manipulation and Structured Materials Conference 2020. Vol. 11522. — SPIE, 06/2020. — P. 38–40. — URL: <https://doi.org/10.1117/12.2573514>.

From other sources:

1. Angular momenta and negative azimuthal forces induced on a particle via guided light in ultrathin optical fibers / V. G. Truong [et al.] // Optica Publishing Group. — 2019. — Apr. — AM3E.5. — URL: <https://doi.org/10.1364/OMA.2019.AM3E.5>.

Introduction

Background and motivation

The topic of this dissertation is devoted to the field of optical forces and torques, as well as transfer of linear and orbital momenta to matter.

The optical manipulation provides unique opportunities for controlling micro and nanoobjects, as well as single atoms, at the remarkable level of precision. This field has passed through ages starting from the early astronomical studies by I. Kepler, to formulation of electro-dynamical grounds in works of J.C. Maxwell [99] and later experimental verification independently by Russian physicist P. N. Lebedev [100] and by American physicists Nichols and Hull [101; 102]. Notably, the final results from Nichols and Hull agreed with Maxwell's theory to better than 1%. The modern age of optical forces and manipulation has started after early works by A. Ashkin [103], where he proposed the basic concept of optical manipulation of microobjects, which later led to a revolution in atomic cooling and trapping [104; 105]. Today the standard methods of optomechanical control with spatial modulation of electromagnetic field intensity [106] allows one to manipulate single biomolecules [107] and sort biological cells [108; 109]. Besides, it can be precise enough to visualize the spin to orbital light momentum conversion [110]. The optical manipulation provides a bridge between classical and quantum physics on the way of cooling of trapped microscale objects down to the temperature of quantized mechanical motion [111; 112]. On the other hand, the quantum physics has already gained a lot due to progress in optical manipulation allowing to trap and study single atoms [113] or two-dimensional[114] and three-dimensional[115; 116] atomic lattices providing a reliable platform for studying many-body quantum physics.

Scientific statements

The scientific statements presented for the defence are:

1. An array of subwavelength particles above the waveguide can form a stable in-line configuration in the field of a linearly polarized plane wave incident perpendicular to the waveguide axis. The binding stiffness between particles increases linearly with the number of particles.
2. For an orbiting motion of particle around a dielectric waveguide in a viscous fluid induced by circular polarized fundamental mode there is an optimal particle radius for which orbiting frequency is maximal. The position of this maxima does not coincide with the maximum of the canonical total angular momentum density.
3. For a non-absorbing particle geometry of which is axially symmetric with respect to the direction of incident wave, the mechanical spinning torque associated with the generation of second harmonic radiation can arise. The appearance of the spinning torque turns out to be associated with a nonzero angular momentum of the generated second harmonic field, which appears due to the specific structure of the crystal lattice of the nanoparticle.
4. The acoustic force acting on subwavelength particles are directly proportional to the sum of the density of the linear canonical momenta and the gradient of the energy density. The acoustic torque on subwavelength particles is proportional to the canonical spin momentum density.

Structure of this thesis

This thesis consists of the introduction, 5 chapters, conclusion and 13 appendixes. The thesis is 282 pages long, including 60 figures and 6 tables. Bibliography consists of 364 items.

In Chapter 1 we present the fundamentals of the optical forces and torques, as well as the most recent achievements in the field. Chapter 2 is devoted to the spin and orbital angular momenta of eigen modes of a sphere and an infinite cylinder. In Chapter 3 theory of optical binding next to a waveguide is presented. Chapter 4 is devoted to the linear and angular momenta transfer of light to matter, as well as the theoretical description of the orbiting motion of a nanoparticle around the ultra-thin single mode optical fiber. Finally, in Chapter 5 the close connection between optics

and linear acoustics is described in details. We show how subwavelength acoustic particles could be a measure of canonical momenta of the incident field.

Chapter 1. Optical forces and torques: theory overview

In this chapter, we give a structured overview on how to calculate force and torque in electromagnetic and acoustics systems, which is tightly related all other chapters of the thesis.

1.1 Maxwell stress tensor approach

When it comes to describe the optical force from the electromagnetic field, in the core we have nothing but a Lorentz force acting on a single charge q which moves with a velocity \mathbf{v} :

$$\mathbf{f}(\mathbf{r}, t) = \rho\mathcal{E}(\mathbf{r}, t) + \mathbf{j}(\mathbf{r}, t) \times \mathcal{B}(\mathbf{r}, t), \quad \mathbf{F} = \int_{\text{particle}} \mathbf{f}dV \quad (1.1)$$

where \mathcal{E} and \mathcal{B} are the observable electric and magnetic fields. This law can be actually considered as a definition of electric and magnetic fields [15; 117]. Here ρ is the distribution of charges and currents \mathbf{j} satisfying continuity equation $\nabla \cdot \mathbf{j} + \partial_t \rho = 0$. However, such a straightforward approach is hardly applicable once we have a complex distribution of the charges and currents, including the displacement current. To overcome this computation obstacle we can calculate the difference of the linear and angular momenta of light before and after scattering on some finite-sized object. Combining Eq. (1.1) rewritten for the density distributions with the Maxwell equations we come to the following expression for the force and torque [8; 15; 30; 118; 119]

$$\mathbf{F}(\mathbf{r}, t) = \oint_{\Sigma} \hat{\mathcal{T}} \cdot \mathbf{n}d\Sigma - \frac{d}{dt} \int \mathcal{P}^{\text{field}}dV, \quad \mathbf{T}(\mathbf{r}, t) = \oint_{\Sigma} \hat{\mathcal{M}} \cdot \mathbf{n}d\Sigma - \frac{d}{dt} \int \mathbf{r} \times \mathcal{P}^{\text{field}}dV \quad (1.2)$$

where \mathbf{n} is the outer unit normal vector to the surface Σ , and $\hat{\mathcal{T}}$ and $\hat{\mathcal{M}}$ is the *Maxwell stress tensor* (momentum-flux) and AM-flux tensors given, correspondingly. The last term is the time derivative of the kinetic momenta of the field $\mathcal{P}^{\text{field}} = \frac{1}{c^2}\mathcal{E}(\mathbf{r}, t) \times \mathcal{H}(\mathbf{r}, t)$. [8; 120–122]. An integration should be performed over an arbitrary *closed* surface Σ with the outer normal \mathbf{n} , which surrounds the particle. Generally, this force is a consequence of a change in momentum carried by photons [35; 103; 121].

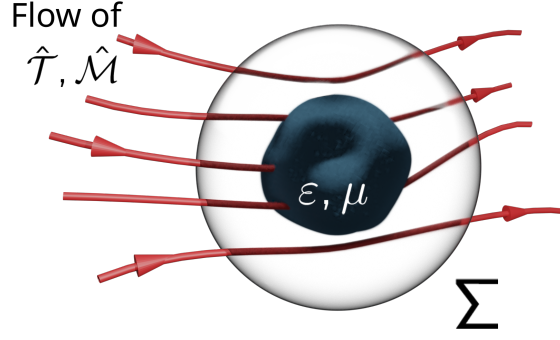


Figure 1.1 — The change in the flux of the momentum energy tensor and the flux of the angular momentum density during integration through the closed surface Σ shows what force and torque acts on the particle with the parameters ε and μ

In real life application the most common source of the electromagnetic fields are the monochromatic fields oscillating with frequency ω for which the description via complex amplitudes are the most common and handy. The connection between real observable fields $\mathcal{E}(\mathbf{r}, t)$, $\mathcal{H}(\mathbf{r}, t)$ and their complex amplitudes $\mathbf{E}(\mathbf{r}, \omega)$, $\mathbf{H}(\mathbf{r}, \omega)$ are given as

$$\mathcal{E}(\mathbf{r}, t) = \text{Re} [\mathbf{E}(\mathbf{r}, \omega)e^{-i\omega t}], \quad \mathcal{H}(\mathbf{r}, t) = \text{Re} [\mathbf{H}(\mathbf{r}, \omega)e^{-i\omega t}] \quad (1.3)$$

and the same for any other time-dependent value. A time average of a product of any two real valued functions expressed via its complex amplitudes can be written as follows $\langle A(\mathbf{r}, t)B(\mathbf{r}, t) \rangle = \frac{1}{2} \text{Re} [A^*(\mathbf{r}, \omega)B(\mathbf{r}, \omega)]$.

The time average force for the monochromatic case is going to be

$$\langle \mathbf{F} \rangle = \oint_{\Sigma} \langle \hat{\mathcal{T}} \rangle \mathbf{n} d\Sigma, \quad \langle \mathbf{T} \rangle = \oint_{\Sigma} \langle \hat{\mathcal{M}} \rangle \mathbf{n} d\Sigma \quad (1.4)$$

where the flux tensors for the homogeneous isotropic medium with ε and μ are given by [8]

$$\langle \hat{\mathcal{T}} \rangle = \frac{1}{2} \text{Re} \left[\varepsilon \varepsilon_0 \mathbf{E}^* \mathbf{E} + \mu \mu_0 \mathbf{H}^* \mathbf{H} - \frac{\hat{\mathbf{I}}}{2} \left(\varepsilon \varepsilon_0 |\mathbf{E}|^2 + \mu \mu_0 |\mathbf{H}|^2 \right) \right], \quad (1.5)$$

$$\langle \mathcal{M}_{ij} \rangle = \varepsilon_{ikl} r_k \langle \mathcal{T}_{lj} \rangle \quad (1.6)$$

In the case of full numerical calculations via formulas (1.4) the best results are usually achieved by creating a closed surface right next to the scatterer (even with the same shape) to maximize the number of integration point to enhance the accuracy. We note that force can be rewritten in terms of the far-field calculations as $\langle \mathbf{F} \rangle = -\frac{\sqrt{\varepsilon\mu}}{c} \oint_{\Sigma_{\infty}} \langle \mathbf{\Pi} - \mathbf{\Pi}^{(i)} \rangle d\Sigma$ [123].

Once the integration surface is chosen to be a sphere, expressions above could be simplified as [124–128]

$$\langle \mathbf{F} \rangle = \frac{r^2}{2} \operatorname{Re} \int_{4\pi} d\Omega \left[\epsilon \epsilon_0 E_r^* \mathbf{E} + \mu \mu_0 H_r^* \mathbf{H} - \frac{1}{2} (\epsilon \epsilon_0 |\mathbf{E}|^2 + \mu \mu_0 |\mathbf{H}|^2) \hat{\mathbf{e}}_r \right] \quad (1.7)$$

$$\langle \mathbf{T} \rangle = -\frac{r^3}{2} \operatorname{Re} \int_{4\pi} d\Omega \left[(\epsilon \epsilon_0 E_r^* E_\varphi + \mu \mu_0 H_r^* H_\varphi) \hat{\mathbf{e}}_\vartheta - (\epsilon \epsilon_0 E_r^* E_\vartheta + \mu \mu_0 H_r^* H_\vartheta) \hat{\mathbf{e}}_\varphi \right] \quad (1.8)$$

where $\int_{4\pi} d\Omega = \int_0^{2\pi} d\varphi \int_0^\pi \sin \vartheta d\vartheta$. We emphasize that the result does not depend on the radius of the control sphere r . Later on in the work we will omit the $\langle \dots \rangle$ assuming only time-averaged values.

There is a long-lasting debate on how to calculate momentum of light inside medium. We are not going to go deep into this topic since it is out of scope this dissertation. However, we present some main points.

Initially it was started by Abraham [129; 130] and Minkowski [131; 132] in their classical works. It is considered that Minkowsky tensor is responsible for the mechanical action.

Fundamentally optical force and torque is caused by the change of linear or angular momenta of scattered photon. A major part of main pioneer experiments on optical manipulation were performed with suspended particles in fluids. The well established theory for the free space [133] met obstacles when question “*what is the momentum of a photon in a bulk medium?*” had been raised [46; 134–136]. The situation gained much in complexity when the effects of dispersive medium came into the play [45; 46; 137–139] and even dispersive bianisotropic medium [140].

Eventually, in the optical force community, the Minkowsky form is chosen for the vast majority of applications [121]. For example, in [141] Sukhov used Minkowsky tensor to calculate force on a floating particle. However, using any approach the correct answer to the force can be obtained once all the correct contributions are considered.

1.2 Subwavelength limit

Optomechanics deals with scatterers of various sizes. Depending on the size of a sphere various approaches can be implemented. In this section, we will focus on

the subwavelength limit of such scatterers. Equation (1.4) is a convenient way to calculate force and torque numerically. However, it is usually too complex for the elegant short analytic answers. The situation is different once we apply a multipole decomposition to the incident and scattered fields [142–145].

We start from the simple isotropic small particle with dominant electric \mathbf{p} and magnetic \mathbf{m} dipoles. The general small parameter here is the so-called *size parameter* ka , where $k = \sqrt{\epsilon\mu}\frac{\omega}{c}$ is the wavenumber in the host media and a is the radius of the particle. There are very distinguished limits for different cases:

$$\begin{cases} ka \ll 1 & \text{— dipole approximation} \\ ka \sim 1 & \text{— Mie resonant regime} \\ ka \gg 1 & \text{— ray approximation} \end{cases} \quad (1.9)$$

Sufficiently small particles with $ka \ll 1$ possess only electric and magnetic dipole responses. For isotropic particles electric \mathbf{p} and magnetic \mathbf{m} dipole moments depend on linear functions of incident electric and magnetic fields (see Appendix B)

$$\mathbf{p} = \alpha_e \mathbf{E}, \quad \mathbf{m} = (\mu\mu_0)^{-1} \alpha_m \mathbf{H}. \quad (1.10)$$

All the electromagnetic response properties of the particles can be conveniently hidden in the polarizabilities α_e and α_m . Here we have used slightly different definition for the polarizability to get more symmetric further answers, see comments on the connection with the literature in Appendix B. For spherical particles in free space Mie theory gives the exact answer for the n -pole polarizability [30; 146–151]. For the case of small particles we can write $\alpha_e = 4\pi\epsilon_0 \cdot i\frac{3\epsilon}{3k^3}a_1 \approx \alpha_e^{(0)} + i\frac{k^3}{6\pi\epsilon\epsilon_0} \left| \alpha_e^{(0)} \right|^2$ and $\alpha_m = 4\pi\mu_0 \cdot i\frac{3\mu}{3k^3}b_1 \approx \alpha_m^{(0)} + i\frac{k^3}{6\pi\mu\mu_0} \left| \alpha_m^{(0)} \right|^2$, where $\alpha_e^{(0)} \approx \frac{4\pi\epsilon\epsilon_0}{k^3} \frac{\epsilon_p - \epsilon}{\epsilon_p + 2\epsilon} (ka)^3$ and $\alpha_m^{(0)} \approx 4\pi\mu\mu_0 a^3 \frac{\mu_p - \mu}{\mu_p + 2\mu} + \mathcal{O}((ka)^5) \approx \frac{4\pi\mu_0}{k^3} \frac{\epsilon_p - \epsilon}{30\epsilon} (ka)^5 \Big|_{\mu=\mu_p=1}$ are the electrostatic electric and magnetic polarizabilities (see Appendix B for more general case and more details).

Expression (1.6) contains the full field, which can be decomposed into incident and scattered as $\mathbf{E} = \mathbf{E}_0 + \mathbf{E}_{sc}$ (see Appendix H for a detailed derivation). The surface integral can be taken in the limit of subwavelength particles such that only electric and magnetic dipoles are excited. As a result, we get the force [121;

142–145; 152; 153]

$$\begin{aligned}
\mathbf{F}_{ka \ll 1} &= \mathbf{F}^{(e)} + \mathbf{F}^{(m)} + \mathbf{F}^{(e-m)} \\
&= \underbrace{\frac{1}{2} \operatorname{Re}(\mathbf{p}^* \cdot (\nabla) \mathbf{E})}_{\sim (ka)^3} + \underbrace{\frac{\mu\mu_0}{2} \operatorname{Re}(\mathbf{m}^* \cdot (\nabla) \mathbf{H})}_{\sim (ka)^5 \text{ for } \mu_p = \mu} - \underbrace{\frac{k^4}{12\pi} \sqrt{\frac{\mu\mu_0}{\varepsilon\varepsilon_0}} \operatorname{Re}(\mathbf{p}^* \times \mathbf{m})}_{\sim (ka)^8 \text{ for } \mu_p = \mu}
\end{aligned} \tag{1.11}$$

where a very handy notation $\cdot(\nabla)$ should be read as $\mathbf{A} \cdot (\nabla) \mathbf{B} \equiv \sum_{\alpha} \sum_{i=x,y,z} A_i \hat{\mathbf{e}}_{\alpha} \nabla_{\alpha} B_i$ with α being any coordinate system index (Cartesian, cylindrical, spherical, etc). We stress that the summation is taken over Cartesian coordinates (see Appendix A for other coordinate systems). It was initially introduced by Berry in Ref. [9]. The optical torque can be decomposed as follows [98]

$$\mathbf{T} = \mathbf{T}^{(e)} + \mathbf{T}^{(m)}, \tag{1.12}$$

where electric and magnetic components are associated with the interaction with electric $\mathbf{p} = \alpha_e \mathbf{E}$ and magnetic $\mathbf{m} = (\mu\mu_0)^{-1} \alpha_m \mathbf{H}$ dipole respectively

$$\mathbf{T}^{(e)} = \mathbf{T}_0^{(e)} + \mathbf{T}_s^{(e)} = \frac{1}{2} \operatorname{Re}[\mathbf{p}^* \times \mathbf{E}] - \frac{k^3}{12\pi\varepsilon\varepsilon_0} \operatorname{Im}[\mathbf{p}^* \times \mathbf{p}], \tag{1.13a}$$

$$\mathbf{T}^{(m)} = \mathbf{T}_0^{(m)} + \mathbf{T}_s^{(m)} = \frac{1}{2} \operatorname{Re}[\mu\mu_0 \mathbf{m}^* \times \mathbf{H}] - \frac{k^3 \mu\mu_0}{12\pi} \operatorname{Im}[\mathbf{m}^* \times \mathbf{m}], \tag{1.13b}$$

Here $k = \frac{\omega}{c} \sqrt{\varepsilon\mu}$. We define magnetic polarizability α_m in a manner of Bekshaev et al. [120; 121; 154] in contrast to some conventional definitions [143; 150; 155; 156] to achieve more symmetric final expressions. Second term \mathbf{T}_s is responsible for the re-radiation or recoil or scattering torque. Once the particle is significantly lossy, one can omit the recoil term as it is done in many works [8; 15; 120]. Otherwise, is it vital important to consider the recoil term to obtain the correct answers. In particular, in the case of homogeneous small sphere torque will be proportional to the absorption but not the extinction cross section as it should be [157]. It is impossible to transfer any spin momentum to the *lossless* homogeneous sphere and hence the torque is zero $\mathbf{T} \equiv 0$. We note that there are also gradient terms of the torque [98] which are not discussed here.

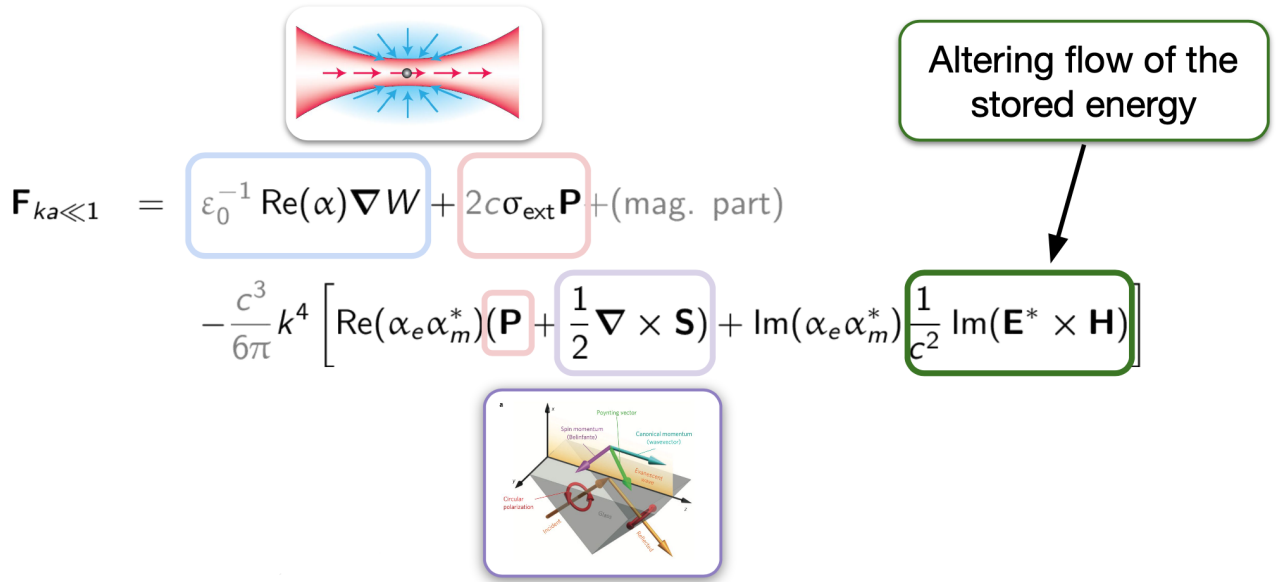


Figure 1.2 — Artistic view of the optical force decomposition for the small particles

1.3 Small particles as a measure of canonical momenta of light

Small subwavelength particles serve as a universal tool for detecting local field properties [158–167]. The main canonical properties of the fields for the case of monochromatic fields are as follows [45; 46; 168]

$$W = W^{(e)} + W^{(m)} = \frac{1}{4} (\varepsilon \varepsilon_0 |\mathbf{E}|^2 + \mu \mu_0 |\mathbf{H}|^2), \quad (1.14)$$

$$\mathbf{P} = \mathbf{P}^{(e)} + \mathbf{P}^{(m)} = \frac{1}{4\omega} \operatorname{Im} [\varepsilon \varepsilon_0 \mathbf{E}^* \cdot (\nabla) \mathbf{E} + \mu \mu_0 \mathbf{H}^* \cdot (\nabla) \mathbf{H}], \quad (1.15)$$

$$\mathbf{S} = \mathbf{S}^{(e)} + \mathbf{S}^{(m)} = \frac{1}{4\omega} \operatorname{Im} [\varepsilon \varepsilon_0 \mathbf{E}^* \times \mathbf{E} + \mu \mu_0 \mathbf{H}^* \times \mathbf{H}], \quad (1.16)$$

$$\mathbf{L} = \mathbf{L}^{(e)} + \mathbf{L}^{(m)} = \mathbf{r} \times \mathbf{P}, \quad (1.17)$$

$$\mathfrak{S} = \frac{n}{2\omega} \operatorname{Im}(\mathbf{H}^* \cdot \mathbf{E}), \quad (1.18)$$

where W is the energy density [15, § 6.8], [169, § 80] (the so-called Brillouin formula), \mathbf{P} is the canonical linear momentum, and \mathbf{S} , \mathbf{L} are the canonical spin and orbital momenta; \mathfrak{S} is the helicity [49]. The case of dispersive media is greatly discussed in Refs. [45; 170].

It is often convenient to write optical force and torque in terms of the canonical properties of the fields defined above [45; 46; 154]. This can be achieved by allocating terms which are proportional to the real and imaginary parts of the polarizabilities.

The force is going to be

$$\mathbf{F} = \mathbf{F}^{(e)} + \mathbf{F}^{(m)} + \mathbf{F}^{(e-m)}, \quad (1.19a)$$

$$\mathbf{F}^{(e)} = \underbrace{(\frac{\varepsilon\varepsilon_0}{\mu\mu_0})^{-1} \text{Re}[\alpha_m^{(e)}] \nabla W^{(e)}}_{\text{conservative}} + \underbrace{2\frac{c}{n}\sigma_{\text{ext}}^{(e)} \mathbf{P}^{(e)}}_{\text{non-conservative}} \quad (1.19b)$$

$$\mathbf{F}^{(e-m)} = -\frac{c^2 k^4 c}{6\pi n} \left[\text{Re}(\alpha_e \alpha_m^*) \frac{1}{n^2} \left(\mathbf{P} + \frac{1}{2} \nabla \times \mathbf{S} \right) + \text{Im}(\alpha_e \alpha_m^*) \frac{1}{c^2} \mathbf{\Pi}^{\text{Im}} \right] \quad (1.19c)$$

Here we have used a decomposition of the kinetic field momentum $\mathcal{P}^{\text{field}} = \frac{1}{c^2} \mathbf{\Pi}^{\text{Re}} = \frac{1}{n^2} (\mathbf{P} + \frac{1}{2} \nabla \times \mathbf{S})$ [9; 24; 171], where $\mathbf{\Pi}^{\text{Re}} = \frac{1}{2} \text{Re} (\mathbf{E}^* \times \mathbf{H})$ is the complex Poynting vector [12–14],[15, § 6.9],[16, § 2.20],[17, § 12.5]. The divergence of $\mathbf{\Pi}^{\text{Im}}$ is equal to 2ω times the difference of the mean values of magnetic and electric densities which follows from the complex Poynting theorem, so $\mathbf{\Pi}^{\text{Im}}$ describes the alternating flow of the stored energy [15, § 6.9]. Next, torque for the case of $\mathbf{S}^{(e)} = \mathbf{S}^{(m)}$ (i.g. for an elliptically polarized plane wave) the torque is going to be

$$\mathbf{T} = 2\frac{c}{n} \left(\sigma_{\text{abs}}^{(e)} \mathbf{S}^{(e)} + \sigma_{\text{abs}}^{(m)} \mathbf{S}^{(m)} \right) = \frac{c}{n} \sigma_{\text{abs}} \mathbf{S} \quad (1.20)$$

Here $\sigma_{\text{ext}}^{(e,m)} = \sigma_{\text{sc}}^{(e,m)} + \sigma_{\text{abs}}^{(e,m)}$ are the electric and magnetic parts of extinction, absorption, and scattering cross sections of the particle. Those are connected with the polarizabilities as (see Appendix B and B.4)

$$\sigma_{\text{ext}} = \sigma_{\text{ext}}^{(e)} + \sigma_{\text{ext}}^{(m)} = \frac{k}{\varepsilon\varepsilon_0} \text{Im}(\alpha_e) + \frac{k}{\mu\mu_0} \text{Im}(\alpha_m) \quad (1.21)$$

$$\sigma_{\text{sc}} = \sigma_{\text{sc}}^{(e)} + \sigma_{\text{sc}}^{(m)} = \frac{k^4}{6\pi(\varepsilon\varepsilon_0)^2} |\alpha_e|^2 + \frac{k^4}{6\pi(\mu\mu_0)^2} |\alpha_m|^2 \quad (1.22)$$

and the electric and magnetic absorption cross sections $\sigma_{\text{abs}} = \sigma_{\text{abs}}^{(e)} + \sigma_{\text{abs}}^{(m)}$ are

$$\sigma_{\text{abs}}^{(e)} = \frac{k}{\varepsilon\varepsilon_0} \left[\text{Im}(\alpha_e) - \frac{k^3}{6\pi\varepsilon\varepsilon_0} |\alpha_e|^2 \right], \quad \sigma_{\text{abs}}^{(m)} = \frac{k}{\mu\mu_0} \left[\text{Im}(\alpha_m) - \frac{k^3}{6\pi\mu\mu_0} |\alpha_m|^2 \right] \quad (1.23)$$

We remind that in this work polarizabilities are defined as $\mathbf{p} = \alpha_e \mathbf{E}$ and $\mathbf{m} = (\mu\mu_0)^{-1} \alpha_m \mathbf{H}$. We note that Eq. (1.20) is the exact answer for the spherical particles of any size. It is possible to show that $\sigma_{\text{abs}}^{(e)} \sim \text{Im}(\varepsilon)$ and $\sigma_{\text{abs}}^{(m)} \sim \text{Im}(\mu)$ [144; 145; 172]. At this step it is crucial to take into account the correction terms in the expression of the torque (1.13a) and (1.13b). It means that for azimuthally isotropic particles in linear regime with $\text{Im}(\varepsilon) = \text{Im}(\mu) = 0$ spinning torque is going to be

zero, i.e. $\mathbf{T} = 0$. A similar decomposition to relate canonical properties of the fields and mechanical action was also made in acoustics [173].

In the literature different decomposition of the optical force (1.19b) can be found [121; 143; 174; 175]: $\mathbf{F}^{(e)} = (\frac{\epsilon\epsilon_0}{\mu\mu_0})^{-1} \text{Re}[\alpha^{(e)}] \nabla W^{(e)} + \sigma_{\text{ext}}^{(e)} \frac{n}{c} \mathbf{\Pi}^{\text{Re}} - \sigma_{\text{ext}}^{(e)} \frac{c}{n} \nabla \times \mathbf{S}^{(e)}$, where $n = \sqrt{\epsilon\mu}$ is the refractive index, and $\mathbf{\Pi}^{\text{Re}} = \frac{1}{2} \text{Re} \mathbf{E}^* \times \mathbf{H}$ is the Poynting vector which can be decomposed as $\frac{1}{c^2} \mathbf{\Pi}^{\text{Re}} = \frac{1}{n^2} (\mathbf{P} + \frac{1}{2} \nabla \times \mathbf{S})$ due to the non-uniform helicity [9; 154] with $\frac{1}{c^2} \mathbf{\Pi}^{\text{Re}} = \mathcal{P}^{\text{field}}$ is being the *kinetic field momentum* [168]. This decomposition is greatly analyzed in [175]. Here we want to stress that the non-conservative part of the dipole force ($\mathbf{F}^{(e)}$ and $\mathbf{F}^{(m)}$) is always colinear with the canonical linear momenta \mathbf{P} but not with the kinetic momentum density $\mathcal{P}^{\text{field}} = \frac{1}{c^2} \mathbf{\Pi}^{\text{Re}}$. To observe the curl-spin contribution *experimentally* one needs to consider higher order corrections which is present in $\mathbf{F}^{(e-m)}$. The simplest configuration to get the non-uniform helicity is to create an evanescent wave via circularly polarized plane wave by total internal reflection. In such geometry the lateral curl-spin force arises [176]. However, lowest dipole order is not sufficient since there is going to be the exact lateral component from Poynting vector contribution but with different sign. To get first non-zero lateral contribution one needs to consider $\mathbf{F}^{(e-m)}$ term. In 2014, the experimental scheme [120] was proposed, and already in 2016 the experimental result [13] was published.

1.4 (Bi-)anisotropic particles

1.4.1 Chiral particles

Manipulated particles can have a complex *internal* structure in terms of electromagnetic response [18; 19]. A very distinguished example of such particles are liquid crystals which are greatly discussed in [20]. The most general case is the bi-anisotropic media can be fully described by constitutive relations [21–24]

$$\begin{pmatrix} \mathbf{D} \\ \mathbf{B} \end{pmatrix} = \begin{pmatrix} \epsilon\epsilon_0 & i\kappa/c \\ -i\kappa^T/c & \mu\mu_0 \end{pmatrix} \begin{pmatrix} \mathbf{E} \\ \mathbf{H} \end{pmatrix} \quad (1.24)$$

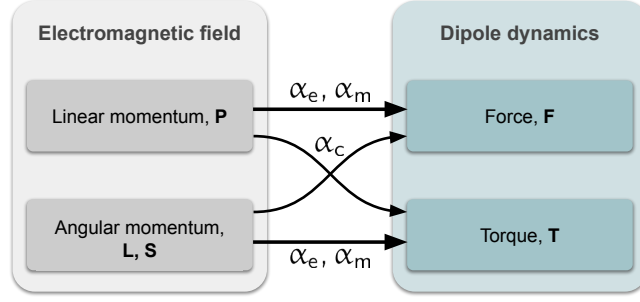


Figure 1.3 — Schematic of the “direct” and “crossed” momentum transfer interpretation of optical forces and torques applied to a chiral dipole. The nonchiral component α_e, α_m of the dissipative force (the torque) couples the linear (angular) momentum of the light to the linear (angular) momentum of the particle, while the chiral component α_c of the dissipative force and of the torque cross-couples linear to angular momenta in both directions. Adopted from [24]. The explicit dependency is written in eqs. (1.26) and (1.27)

where ε , μ , κ are generally complex valued 3×3 tensors. Here we also took in account that the medium is reciprocal, so diagonal elements in Eq. (1.24) are connected. For non-reciprocal media we encourage to read Refs. [21; 22]. When it comes for the small particles, it is possible to get dipolar polarizabilities ($\alpha_e, \alpha_m, \alpha_c$) from the bulk parameters (ε, μ, κ). That brings to [25; 26]

$$\begin{pmatrix} \mathbf{p} \\ \mu\mu_0\mathbf{m} \end{pmatrix} = \begin{pmatrix} \alpha_e & i\alpha_c \\ -i\alpha_c^T & \alpha_m \end{pmatrix} \begin{pmatrix} \mathbf{E} \\ \mathbf{H} \end{pmatrix} \quad (1.25)$$

where $\alpha_e, \alpha_m, \alpha_c$ are generally complex valued 3×3 tensors. We stress that $\alpha_{e,m,c}$, are all functions of ε, μ , and κ (see Appendix B for the explicit expressions). The radiation corrections and optical theorem for bi-anisotropic particles is discussed in [27, § II.C].

Force on chiral isotropic particle is going to be [18; 23; 24; 26; 28–31] (however, not in every reference the $\mathbf{F}^{(e-m)}$ is taken into account)

$$\mathbf{F} = \mathbf{F}^{\text{non-chiral}} + \frac{\omega}{n} \text{Re}(\alpha_c) \nabla \mathcal{G} + \omega \gamma_{\text{abs},c}^{\text{Re}} \mathbf{S} - \text{Im}(\alpha_c) \nabla \times \mathbf{\Pi}^{\text{Re}} - \frac{k^4 c}{6\pi n} |\alpha_c|^2 \mathbf{\Pi}^{\text{Re}}. \quad (1.26)$$

Here $\mathbf{F}^{\text{non-chiral}}$ is the force from (1.19b) but with α_e and α_m are being functions of (ε, μ, κ) (see Appendix B). We also have used the following identity: $\omega^2 \mathbf{S} - \frac{1}{2} \nabla \times \mathbf{\Pi}^{\text{Re}} = -\frac{1}{4} \text{Re}(\mathbf{H}^* \cdot (\nabla) \mathbf{E} - \mathbf{E}^* \cdot (\nabla) \mathbf{H})$ [23; 24]. Substituting (1.25) in (1.12) we get the torque on a chiral isotropic particle [32; 33]

$$\mathbf{T} = \frac{c}{n} \sigma_{\text{abs},c} \mathbf{S} + \frac{1}{\omega} \gamma_{\text{abs},c}^{\text{Re}} \mathbf{\Pi}^{\text{Re}} + \frac{1}{\omega} \gamma_{\text{abs},c}^{\text{Im}} \mathbf{\Pi}^{\text{Im}}. \quad (1.27)$$

The generalized chiral absorption cross sections are

$$\sigma_{\text{abs,c}} = \sigma_{\text{abs,c}}^{(e)} + \sigma_{\text{abs,c}}^{(m)}, \quad (1.28a)$$

$$\sigma_{\text{abs,c}}^{(e)} = \frac{k}{\varepsilon \varepsilon_0} \left(\text{Im}(\alpha_e) - g_e |\alpha_e|^2 - g_m |\alpha_c|^2 \right), \quad (1.28b)$$

$$\sigma_{\text{abs,c}}^{(m)} = \frac{k}{\varepsilon \varepsilon_0} \left(\text{Im}(\alpha_m) - g_m |\alpha_m|^2 - g_e |\alpha_c|^2 \right), \quad (1.28c)$$

$$\gamma_{\text{abs,c}}^{\text{Re}} = 2\omega \text{Im}(\alpha_c) - 2\omega g_e \text{Re}(\alpha_e \alpha_c^*) - 2\omega g_m \text{Re}(\alpha_m \alpha_c^*), \quad (1.28d)$$

$$\gamma_{\text{abs,c}}^{\text{Im}} = 2\omega g_m \text{Im}(\alpha_m \alpha_c^*) - 2\omega g_e \text{Im}(\alpha_e \alpha_c^*) \quad (1.28e)$$

with $g_e = \frac{k^3}{6\pi\varepsilon\varepsilon_0}$ and $g_m = \frac{k^3}{6\pi\mu\mu_0}$. We note that for lossless chiral particle with $\text{Im}(\varepsilon) = \text{Im}(\mu) = \text{Im}(\kappa) = 0$ torque is equal to zero, so no momentum can be transferred from any incident optical fields to the particle. It is worth noting that the above conclusion is also valid to any lossless chiral sphere of any size [32, see eq. (9)]. This alternatively follows from the optical theorem for chiral particles [34], for details see eq. (B.30) in Appendix B. Alternative decomposition can be found in [31, eq. (7)].

Surprisingly, in the lower approximation for the lossy particles, due to the symmetry of the equations, there are simple closed relation between dissipative part of the force and curl of the chiral and non-chiral parts of the torque which reveals the direct way of measuring the chiral part of the polarizability, energy flow, and spin angular momentum density [24, eqs. (15, 16)]

$$\mathbf{F}_{\text{diss}}^{(e,m)} + \frac{1}{2} \nabla \times \mathbf{T}^{(e,m)} = \frac{n}{c} \sigma_{\text{abs}} \mathbf{\Pi}^{\text{Re}} \quad (1.29a)$$

$$\mathbf{F}_{\text{diss}}^{(c)} + \frac{1}{2} \nabla \times \mathbf{T}^{(c)} = 2\omega^2 \text{Im}(\alpha_c) \mathbf{S} \quad (1.29b)$$

where for the small absorbing particles with $\sigma_{\text{ext}} \approx \sigma_{\text{abs}}$ we have $\mathbf{F}_{\text{diss}} = \mathbf{F}_{\text{diss}}^{(e,m)} + \mathbf{F}_{\text{diss}}^{(c)} = \frac{c}{n} \sigma_{\text{abs}} \mathbf{P} + 2 \text{Im}(\alpha_c) \left(\omega^2 \mathbf{S} - \frac{1}{2} \nabla \times \mathbf{\Pi}^{\text{Re}} \right)$ is the dissipative (or non-conservative) part of the force and torque being $\mathbf{T} = \mathbf{T}^{(e,m)} + \mathbf{T}^{(c)} = \frac{c}{n} \sigma_{\text{abs}} \mathbf{S} + 2 \text{Im}(\alpha_c) \mathbf{\Pi}^{\text{Re}}$. Here we have used $\mathbf{\Pi}^{\text{Re}} = \frac{c^2}{n^2} \left(\mathbf{P} + \frac{1}{2} \nabla \times \mathbf{S} \right)$ and assumed that $\mathbf{P}^{(e)} = \mathbf{P}^{(m)}$ and $\mathbf{S}^{(e)} = \mathbf{S}^{(m)}$. We note that this relation is written for lossy dipole particles for which it is possible to neglect the correction recoil (scattering) terms in force and torque.

1.4.2 Geometric anisotropy and particles made of anisotropic crystals

To identify the electric and magnetic dipole polarizabilities of the uniaxial sphere in a simple way, we need to visualize the electric and magnetic modes in terms of its electric field.

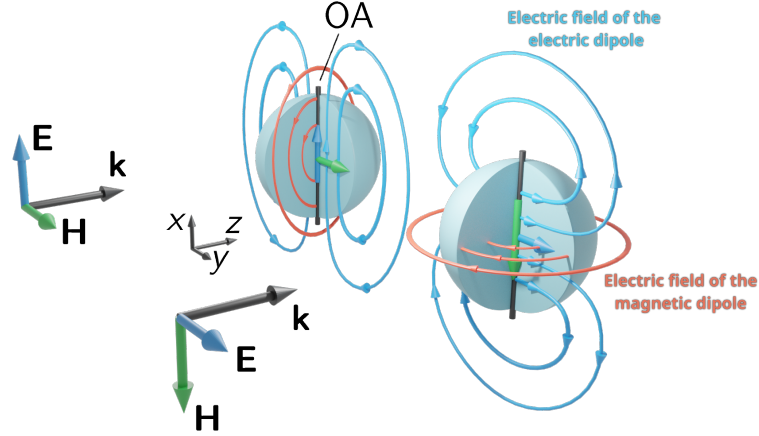


Figure 1.4 — Simplification of the anisotropic bipolar sphere. We take into account only electric p and magnetic m dipole moments, and also neglect the bipolar structure of the anisotropy. For this geometry $\epsilon_{xx} = \epsilon_{\parallel} > \epsilon_{yy,zz} = \epsilon_{\perp}$

We suppose that the permittivity of the particle is given by

$$\hat{\epsilon} = \begin{pmatrix} \epsilon_{xx} & 0 & 0 \\ 0 & \epsilon_{yy} & 0 \\ 0 & 0 & \epsilon_{zz} \end{pmatrix}, \quad \epsilon_{xx} > \epsilon_{yy} = \epsilon_{zz}, \quad \mu = 1$$

and, hence, the optical axis (OA) is along x-axes.

Since we want to achieve simple result which can be analyzed analytically rather than purely numerically [20; 124–126; 177–196], we assume that the field in the particle is almost homogeneous, so the electric field "feels" only one or another component (or its average) of the particle permittivity $\hat{\epsilon}$. This assumption could lead to the errors for the bigger particle once higher order dipole moment components are arose, such as toroidal dipole moment [197; 198].

We fix the orientation of the principal axes of the particle which are codirectional with xyz-axes. This leads to the electric dipole polarizability components as

$$\alpha_{xx}^{(e)} = \alpha_{xx}^{(e)}(\epsilon_{xx}), \quad \alpha_{yy}^{(e)} = \alpha_{yy}^{(e)}(\epsilon_{yy})$$

and magnetic dipole polarizability components as

$$\alpha_{xx}^{(m)} = \alpha_{xx}^{(m)}(\varepsilon_{yy}), \quad \alpha_{yy}^{(m)} = \alpha_{yy}^{(m)}\left(\frac{\varepsilon_{xx} + \varepsilon_{yy}}{2}\right)$$

which seems to be a very counterintuitive results but still holds true. To the best of our knowledge such simple and elegant expressions for the magnetic dipole moments haven't been published in the literature. The effect of elongation of the mode profile, as shown on the figure above, is indeed takes place for the bipolar droplets (e.g. see [190, fig. 3]).

Material anisotropy and geometrical anisotropy

The problem is solved analytically in the Bohren & Huffmann book in the electrostatics approximation. Let us compare an isotropic ellipsoid and an anisotropic sphere. The polarizability of both particles is a tensor, so in the diagonal form they are (here we are talking only about electric polarizabilities)

$$\alpha_j^{(e),\text{ellipsoid}} = 4\pi\varepsilon\varepsilon_0 abc \frac{\varepsilon_p - \varepsilon}{3\varepsilon + 3L_j(\varepsilon_p - \varepsilon)} \quad (1.30)$$

$$\alpha_j^{(e),\text{anis.sph.}} = 4\pi a^3 \frac{\varepsilon_{p,j} - \varepsilon}{\varepsilon_{p,j} + 2\varepsilon} \quad (1.31)$$

where a, b, c are the ellipsoid semi axes, and L_j are the geometric factors

$$L_1 = \frac{abc}{2} \int_0^\infty \frac{dq}{(a^2 + q)f(q)}, \quad (1.32)$$

$$L_2 = \frac{abc}{2} \int_0^\infty \frac{dq}{(b^2 + q)f(q)}, \quad (1.33)$$

$$L_3 = \frac{abc}{2} \int_0^\infty \frac{dq}{(c^2 + q)f(q)}, \quad (1.34)$$

where $f(q) = \sqrt{(q + a^2)(q + b^2)(q + c^2)}$. Although there are similarities between the two types of particle, *they are not completely equivalent*: given an anisotropic sphere in a particular medium, there does not exist, in general, an equal volume ellipsoid with the same polarizability. That can be understood from the following facts. Anisotropic sphere is defined by *six* independent parameters (real and imaginary parts of $\varepsilon_{p,j}$), while there are only *four* parameters for an isotopic ellipsoid:

the real and imaginary parts of ε_p together with two geometrical factors. In the special case of a nonabsorbing sphere or when two principal values of the permittivity tensor are equal an isotropic ellipsoid can be found – theoretically, at least – with the same polarizability tensor.

Finally, the case of anisotropic ellipsoid the axes of which coincide with the principal axes of its permittivity tensor can be described as

$$\alpha_j^{(e),\text{anis.ellip.}} = 4\pi\varepsilon\varepsilon_0 abc \frac{\varepsilon_{p,j} - \varepsilon}{3\varepsilon + 3L_j(\varepsilon_{p,j} - \varepsilon)} \quad (1.35)$$

The most general case of anisotropic ellipsoid is considered in [199].

1.5 Bichromatic force

The concept of the bichromatic force is well developed in the area of atom trapping community [200–209], where light scattering on quantum system is considered. However, here we focus only on the classical electrodynamics.

Suppose we have two real fields A and B . For each of them we have two contributions at different frequencies, so

$$A(t) = \text{Re}[A_0^{(\omega_1)} e^{-i\omega_1 t}] + \text{Re}[A_0^{(\omega_2)} e^{-i\omega_2 t}] \quad (1.36)$$

$$B(t) = \text{Re}[B_0^{(\omega_1)} e^{-i\omega_1 t}] + \text{Re}[B_0^{(\omega_2)} e^{-i\omega_2 t}] \quad (1.37)$$

Force is a quadratic function of the fields. We are interested in the time average force which is going to have beatings at the slow frequency once frequencies are close:

$$\begin{aligned} \langle AB \rangle_{\text{fast time}} &\approx \frac{1}{2} \text{Re} \left[\bar{A}_0^{(\omega_1)} B_0^{(\omega_1)} \right] + \frac{1}{2} \text{Re} \left[\bar{A}_0^{(\omega_2)} B_0^{(\omega_2)} \right] \\ &\quad + \frac{1}{2} \text{Re} \left[\left(\bar{A}_0^{(\omega_2)} B_0^{(\omega_1)} + A_0^{(\omega_1)} \bar{B}_0^{(\omega_2)} \right) e^{-i\Delta\omega t} \right] \end{aligned} \quad (1.38)$$

where $\Delta\omega t = (\omega_1 - \omega_2)t$ is the so-called slow time in the system.

Averaging only by the fast time will leave the last term in the (1.2), so it is helpful to know

$$\left\langle \frac{d}{dt} AB \right\rangle_{\text{fast time}} = -\frac{\Delta\omega}{2} \text{Im} \left[e^{-i\Delta\omega t} \left(\bar{A}_0^{(\omega_2)} B_0^{(\omega_1)} + A_0^{(\omega_1)} \bar{B}_0^{(\omega_2)} \right) \right] \quad (1.39)$$

In the dipole approximation, starting from [8, Eq. 13.30] we have

$$\begin{aligned}
\langle \mathbf{F} \rangle_{\text{fast time}} &= \left\langle \mathbf{p}_i \nabla \mathcal{E}_i + \frac{d}{dt} \mathbf{p} \times \mathcal{H} \right\rangle_{\text{fast time}} \\
&= \frac{1}{2} \text{Re} \left[p_i^{*(1)} \nabla E_i^{(1)} + p_i^{*(2)} \nabla E_i^{(2)} \right] \\
&\quad + \frac{1}{2} \text{Re} \left[e^{-i\Delta\omega t} \left(p_i^{*(2)} \nabla E_i^{(1)} + p_i^{(1)} \nabla E_i^{*(2)} \right) \right] \\
&\quad - \frac{\Delta\omega}{2} \mu\mu_0 \text{Im} \left[e^{-i\Delta\omega t} \left(\mathbf{p}^{*(2)} \times \mathbf{H}^{(1)} + \mathbf{p}^{*(1)} \times \mathbf{H}^{*(2)} \right) \right] \quad (1.40)
\end{aligned}$$

1.6 Dynamics simulation with a stochastic force

Performing experiments on optical forces and torques in the real world is always accompanied with a Brownian forces or *stochastic forces* \mathbf{F}_{st} . The nature of this force is laying in huge amount of collisions with smaller particles of a host fluid. One of the possible dimensionless parameters to identify the potential impact of the stochastic forces is the relation between particle energy U (kinetic, e.g. due to the optical pressure or local depth of the potential well of an optical trap) and the energy of thermal motion [6; 35; 36]:

$$\gamma = \frac{U}{k_{\text{B}}T}, \quad \begin{cases} \gamma \lesssim 1 & - \mathbf{F}_{\text{st}} \text{ has to be considered} \\ \gamma \gg 1 & - \mathbf{F}_{\text{st}} \text{ is negligible} \end{cases} \quad (1.41)$$

where k_{B} is the Boltzmann constant and T is the absolute temperature of the host media. The estimation for the energy U depends on the dominant type of optical force: conservative (gradient force) or non-conservative (optical pressure) [6; 37–40][41, § 3]. In the dipole approximation two different contributions can be seen from Eq. (1.19b).

Once conservative force is dominant then the potential depth of the optical trap for electric dipole particle can be estimated as $U = U_{\text{tr}} = \langle \mathbf{p} \cdot \mathcal{E} \rangle = \frac{1}{2} \text{Re}(\alpha_{\text{e}}) |\mathbf{E}|^2$. Since near the equilibrium point force is linear with respect to the displacement it is possible to introduce effective stiffness as $F \approx -\kappa \Delta r$ thus the potential energy is going to be $U_{\text{tr}} = \frac{1}{2} \kappa \overline{\Delta r}^2$ [6; 36], where $\overline{\Delta r}$ is the average potential well width in real space. We have to stress that such analyses is valid only if the conservative part of optical forces is dominant. Otherwise, if non-conservative forces is dominant

then kinetic energy should be placed in Eq. (1.41). For example, for the plane wave pressure it is going to be $U = U_{\text{kin}} = \frac{m\langle \mathbf{v} \rangle^2}{2}$, where average velocity of the particle can be obtained from the equality of optical pressure force and friction force (Stokes' law [42]) $\langle v \rangle = \sigma_{\text{ext}}^{(e)} \frac{1}{2} \epsilon \epsilon_0 |\mathbf{E}|^2 / (6\pi \nu a)$, where ν is the dynamic viscosity of the host fluid and a is the particle radius.

Once stochastic force has to be considered, *Langevin equation* has to be solved numerically to achieve a proper dynamics simulation. For sure, many realization of the same numeric experiment are needed to perform further statistical analyses. The equation of motion is going to be

$$m\ddot{\mathbf{r}} = -\zeta\dot{\mathbf{r}} + \mathbf{F}_{\text{st}} + \mathbf{F} \quad \text{or} \quad \begin{cases} \dot{\mathbf{r}} = \mathbf{v} \\ \dot{\mathbf{v}} = -\frac{\zeta}{m}\mathbf{v} + \frac{1}{m}(\mathbf{F}_{\text{st}} + \mathbf{F}) \end{cases} \quad (1.42)$$

where m is the mass of the particles, ζ is the friction coefficient (for a sphere the Stokes' law is applicable, so $\zeta = 6\pi\nu a$ with a and ν being particles radius and dynamic viscosity of the host fluid), \mathbf{F} is the optical force, and \mathbf{F}_{st} is delta correlated stochastic force with zero average, so it satisfies $\langle \mathbf{F}_{\text{st}}(t) \rangle_t = 0$ and $\langle F_{\text{st},\alpha}(t) F_{\text{st},\beta}(t + \tau) \rangle_t = 2D\delta_{\alpha\beta}\delta(\tau)$. It is important to understand that friction and stochastic forces are connected with each other on the fundamental level. It means that the friction coefficient ζ is connected to the auto-correlation coefficient D of the stochastic forces as $D = k_{\text{B}}T\zeta$ [43] (see Appendix L for the proof).

Equation (1.42) can be rewritten as a system of two first order differential equations with respect to \mathbf{r} and \mathbf{v} , and solved by any standard numerical procedure such as family of Euler methods, Runge–Kutta methods or any other [44], with some special treatment to the stochastic term \mathbf{F}_{st} [43]. All these methods rely on discretization of the time line $t \rightarrow \{t_i\}$ with a step Δt . Integration of (1.42), i.e. $\int_{t_i}^{t_{i+1}} (1.42) dt$, is going to have obstacles since $\int_{t_i}^{t_{i+1}} \mathbf{F}_{\text{st}}(t) dt \neq \mathbf{F}_{\text{st}}(t_i)\Delta t$. The trick is to introduce a new variable

$$\int_{t_i}^{t_{i+1}} dt \mathbf{F}_{\text{st}}(t) \equiv \mathbf{W}_i \quad (1.43)$$

with properties which follows from the properties of the white-noise nature of the \mathbf{F}_{st} : $\langle \mathbf{W}_i \rangle = 0$ and $\langle \mathbf{W}_i \cdot \mathbf{W}_j \rangle = \delta_{ij} \cdot 6k_{\text{B}}T\zeta\Delta t = \delta_{ij} \cdot 3\sigma_{W_\alpha}^2$ with $\alpha = x, y, z$, we note that the later one is actually a dispersion of normally distributed random value

W_α . So for the simple Euler method the final system is going to be

$$\begin{cases} \mathbf{r}(t_{i+1}) = \mathbf{r}(t_i) + \Delta t \mathbf{v}(t_i), \\ \mathbf{v}(t_{i+1}) = \mathbf{v}(t_i) - \Delta t \frac{\zeta}{m} \mathbf{v}(t_i) + \frac{1}{m} \mathbf{W}_i \end{cases}, \quad \begin{aligned} \sigma_{W_\alpha} &= \sqrt{2k_B T \zeta \Delta t} \\ \alpha &= x, y, z \end{aligned} \quad (1.44)$$

We stress that dispersion (or quadratic deviation) depends on the discretization time step Δt .

In literature a different but *equal* approach can be seen [210]. It appears that it is possible to integrate the equation of motion as

$$\int_{t_i}^{t_{i+1}} dt \mathbf{F}(t) \equiv \mathbf{R}_i \Delta t, \quad (1.45)$$

where \mathbf{R}_i is a normally distributed random function with the dispersion $\sigma_R^2 = \langle \mathbf{R}_i \cdot \mathbf{R}_i \rangle$ which depends *differently* on the time discretization step $\langle \mathbf{R}_i \cdot \mathbf{R}_j \rangle = \delta_{ij} \cdot \frac{2k_B T \zeta}{\Delta t}$. We emphasize that this approach gives exactly the same result as mentioned above. For the exact derivation the reader is encourage to go through the reference [211].

1.7 Acoustic force and torque

A big part of this work is dedicated to acoustomechanical effects, and thus, here we provide a brief overview of forces and torques acting on acoustic scatters and will provide the full analogy with the optomechanics.

1.7.1 Rigorous approach for the force

The most general approach to the force generated by an acoustic wave is given by the integration of the *momentum flux density tensor* of the sound field $\Pi_{ji} = p\delta_{ji} + \rho \mathbf{v}_j \mathbf{v}_i$ though the surface Σ enclosing the object [212; 213]:

$$F_j = - \oint_{\Sigma} dS \Pi_{ji} n_i, \quad (1.46)$$

where \mathbf{n} is the outer normal unit vector. The cycle average force up to the second order can be written as [214–217]

$$\langle F_j \rangle = - \oint_{\Sigma} dS \left(\left[\frac{\beta_0}{2} \langle p^2 \rangle - \frac{\rho_0}{2} \langle v^2 \rangle \right] \delta_{ji} + \rho_0 \langle v_j v_i \rangle \right) n_i \quad (1.47a)$$

$$= - \oint_{\Sigma} dS \langle \Pi_{ji}^{(\text{mix})} \rangle n_i - \oint_{\Sigma} dS \langle \Pi_{ji}^{(\text{self})} \rangle n_i \quad (1.47b)$$

$$= - \oint_{\Sigma} dS \left([\beta_0 \langle p^i p^s \rangle - \rho_0 \langle v_k^i v_k^s \rangle] \delta_{ji} + \rho_0 \langle v_j^s v_i^i + v_j^i v_i^s \rangle \right) n_i - \\ - \lim_{R \rightarrow \infty} \oint_{\Sigma} dS \rho_0 \langle v_j^s v_i^s \rangle n_i, \quad (1.47c)$$

where $(p, \mathbf{v}) = (p, \mathbf{v})^i + (p, \mathbf{v})^s$ are the total fields outside the object. Expression (1.47c) is true only for the limit of the infinite radius of the integration sphere Σ (see details in Ref. [214]). In other words, one uses the relation

$$- \oint_{\Sigma} dS \Pi_{ji}^{(\text{self})} n_i = - \oint_{\Sigma} dS \left(\left[\frac{\beta_0}{2} \langle p_s^2 \rangle - \frac{\rho_0}{2} \langle v_s^2 \rangle \right] \delta_{ji} + \rho_0 \langle v_j^s v_i^s \rangle \right) n_i \\ = - \lim_{R \rightarrow \infty} \oint_{\Sigma} dS \left(\left[\frac{\beta_0}{2} \langle p_s^2 \rangle - \frac{\rho_0}{2} \langle v_s^2 \rangle \right] \delta_{ji} + \rho_0 \langle v_j^s v_i^s \rangle \right) n_i \\ = - \lim_{R \rightarrow \infty} \oint_{\Sigma} dS \left(\rho_0 \langle v_j^s v_i^s \rangle \right) n_i \neq \oint_{\Sigma} dS \left(\rho_0 \langle v_j^s v_i^s \rangle \right) n_i, \quad (1.48)$$

which is more convenient for theoretical studies. However, eq. (1.47a) is still kept in this work, which is correct for the any surface radius R which contains the scatterer, since it is more suitable for the numeric computations.

1.7.2 Rigorous approach for the torque

In the similar manner to the force, the acoustical torque is defined by the flow of *flux density of angular momentum* $\mathcal{M}_{ji} = \varepsilon_{ikl} r_k \Pi_{lj}$ ($\hat{\mathcal{M}} = \mathbf{r} \times \hat{\mathbf{\Pi}}$) through the surface Σ enclosing the object [167; 212; 218–221]

$$T_i = - \oint_{\Sigma} dS \mathcal{M}_{ji} n_j, \quad (1.49)$$

where i, j represent Cartesian coordinates and \mathbf{n} is the outer unit normal vector to the Σ . The flux density of angular momentum obeys the conservation law $\partial_t(\rho \mathbf{r} \times$

$\mathbf{v})_i + \nabla_j \cdot \mathcal{M}_{ij} = 0$ and for the monochromatic fields of the nonviscous fluid it is divergenceless $\nabla \cdot \langle \hat{\mathcal{M}} \rangle = 0$ [221].

Since one is free to choose the integration surface, we choose sphere with radius $R \geq a$ centered at the origin where the particle is, which simplifies expression for the torque to

$$\langle \mathbf{T} \rangle = -\frac{\rho_0}{2} R^3 \operatorname{Re} \oint_{4\pi} d\Omega (\mathbf{n} \cdot \mathbf{v}^*) \times \mathbf{n} \mathbf{v}, \quad (1.50)$$

where $d\Omega = \sin \theta d\varphi d\theta$, $\mathbf{v} = \mathbf{v}^i + \mathbf{v}^s$ is the total velocity field, and assumption of monochromatic fields is used.

1.7.3 Acoustic pressure from a plane wave on a sphere

An illustrative example is the derivation of acoustic pressure from a plane wave $p^i = p_0 e^{ikr \cos \theta}$ acting on a sphere with ρ_1 and β_1 . Using solutions (5.11)–(43) obtained above and good amount of recursion relations of the special functions I get

$$F^{\text{press}} = -\frac{2\pi p_0^2 \beta_0}{k^2} \sum_{n=0}^{\infty} \left[(2n+1) \operatorname{Re}(a_n) + 2(n+1) \operatorname{Re}(a_n^* a_{n+1}) \right]$$

This expression supports imaginary parameters of the particle, i.e. it can take into account absorption. It was successfully verified by numerical evaluation of the initial expression (1.47c). Moreover, F^{press} is always positive for any ρ_1 and β_1 (without gain). Decomposition for the small *absorbing* particle gives us

$$F_{ka \ll 1}^{\text{press}} = \frac{2\pi \beta_0 (ka)^3}{3k^2} \left(\operatorname{Im}(\bar{\beta}_1) + 9 \frac{\operatorname{Im}(\bar{\rho}_1)}{|2\bar{\rho}_1 + 1|^2} \right) + \mathcal{O}((ka)^6) \quad (1.51)$$

Here only a_0 and a_1 terms are considered since they have the order of $(ka)^3$ and discarded the interference term since it is the order of $(ka)^6$ for the absorbing particle. In the case of non-absorbing particle with $\operatorname{Im}(\bar{\rho}_1) = \operatorname{Im}(\bar{\beta}_1) = 0$ the interference term is not negligible anymore and the expression becomes

$$F_{ka \ll 1}^{\text{press}} = \frac{2\pi \beta_0 (ka)^6}{3k^2} \left(\frac{1}{9} (\bar{\beta}_1 - 1)^2 + \frac{1}{3} \frac{(\bar{\rho}_1 - 1)^2}{(2\bar{\rho}_1 + 1)^2} - \frac{1}{6} (\bar{\beta}_1 - 1) \frac{\bar{\rho}_1 - 1}{2\bar{\rho}_1 + 1} \right) \quad (1.52)$$

Later on, in Chapter 5 we consider the subwavelength limit of the force for the general case. We show that it is going to be also proportional to the canonical momenta of acoustic fields.

Chapter 2. Spin and orbital angular momenta of sphere and cylindrical waveguide modes

In this chapter we will consider the eigen modes of an infinite cylinder and of a finite sphere and introduce the canonical values of linear and angular momentum densities.

2.1 Spherical resonator

Spherical particles both dielectric and metallic are essential building blocks in nanophotonics. During recent rapid development of *Mie-tronic* [222–224] which uses heavily the phenomena of Mie — nanophotonics devices heavily using various features of the Mie-resonances — the deep fundamental investigation of the eigen modes of such particles by using novel computational tools is still relevant and currently important. Moreover, eigen modes of a sphere are closely related to the *Vector Spherical Harmonics* (VSH) which are widely used in the multipolar decomposition to analyze less symmetric structures. In this work we study in details the *canonical spin and angular momenta* (AM), helicity and other properties of the eigen modes of dielectric (nondispersive) and metallic (dispersive) spheres. We compare results with the conventional kinetic (Abraham-type) approach. We show that canonical momentum *density* of the AM as quantized and has a close relation to the quantum picture of a single photon. In this study, we provide a solid platform for future studies and applications of the AM transfer from near fields of spherical particles to the matter in its vicinity.

Canonical properties of light — linear momenta, spin and orbital angular momenta, energy density, helicity — have a great importance in the field of light and matter interactions as well as optical manipulation via optical forces and torques [45]. Spin and orbital angular momenta (SAM and OAM) of light are well-established concepts as of today [225–229]. It is of high interest to search various way to control the exact AM of electromagnetic field. Alongside to the beam optics [230–233] there is another way — utilizing the properties of near fields of eigen modes of different structures [234]. The most conventional way among those is to use modes of a dielectric

or metallic circular waveguide (or a nanofiber) [235–237]. On the other side, one can utilize Mie resonances [238] in a single particles and/or collective resonances metasurfaces to boost the particular effect.

The challenge is to overcome the problem of precise analyses of spin-orbital content of a particular fields. We focus of the eigen fields of a spherical resonator made of a dielectric (non-dispersive) or a metal (dispersive). We apply the recently developed method [45] to find the projection of total angular momenta. We also find a way how to calculate the canonical square of total angular momenta to identify the total angular momentum number of the mode but only its projection. Another important challenge was to make a smooth transition between electromagnetic fields of a sphere and a field of a single photon [239].

Canonical momenta of an eigen mode can be quantized if one consider momenta per one photon. The effect of quantization of eigen modes of dielectric and metallic cylindrical waveguides was considered in [170; 240], as well as its consequences to the optical torques [241]. Some recent analyses of the OAM was done for the multilayered fiber in [242]. The analyses of AM of vector spherical harmonics was done for non-dispersive media and real valued eigen frequencies in [15; 239]. Multipolar decomposition into the series of Vector Spherical Harmonics harmonics shows its great power when it comes to the symmetry analyses of the studied structures [243; 244].

In this chapter we study in details the *canonical spin and angular momenta* (AM), helicity and other properties of the eigen modes of dielectric (nondispersive) and metallic (dispersive) spheres. We compare results with the conventional kinetic (Abraham-type) approach. We show that canonical momentum *density* of the AM as quantized and has a close relation to the quantum picture of a single photon. Our work provides a solid platform for future studies and applications of the AM transfer from near fields of spherical particles to the matter in its vicinity.

2.1.1 Canonical field properties and eigen modes of a sphere

Energy density, orbital and spin angular momenta, and square of total angular momenta

We analyze the eigen modes using canonical properties of the field introduced recently in Ref. [45] for the, generally, dispersive media, which is crucial for the case of metallic particles. The Brillouin energy W , linear momentum \mathbf{P} , spin \mathbf{S} , orbital \mathbf{L} , and total \mathbf{J} angular momentum can be formulated in the manner of quantum mechanics as follows [15; 45; 46]

$$W = \langle \psi | \omega | \psi \rangle = \frac{1}{4} (\tilde{\varepsilon} \varepsilon_0 |\mathbf{E}|^2 + \tilde{\mu} \mu_0 |\mathbf{H}|^2), \quad (2.1)$$

$$\mathbf{P} = \langle \psi | \hat{\mathbf{p}} | \psi \rangle = \frac{1}{4\omega'} \text{Im} (\tilde{\varepsilon} \varepsilon_0 \mathbf{E}^* \cdot (\nabla) \mathbf{E} + \tilde{\mu} \mu_0 \mathbf{H}^* \cdot (\nabla) \mathbf{H}), \quad (2.2)$$

$$\mathbf{S} = \langle \psi | \hat{\mathbf{S}} | \psi \rangle = \frac{1}{4\omega'} \text{Im} (\tilde{\varepsilon} \varepsilon_0 \mathbf{E}^* \times \mathbf{E} + \tilde{\mu} \mu_0 \mathbf{H}^* \times \mathbf{H}), \quad (2.3)$$

$$\mathbf{L} = \mathbf{r} \times \mathbf{P}, \quad \mathbf{J} = \mathbf{L} + \mathbf{S}, \quad (2.4)$$

and the quadratic form of a square of total angular momenta denoted as $[\mathbf{J}^2]$ is given by

$$[\mathbf{J}^2] = \langle \psi | (\hat{\mathbf{L}} + \hat{\mathbf{S}})^2 | \psi \rangle = \frac{1}{4\omega'} \text{Re} \tilde{\varepsilon} \varepsilon_0 \left[r^2 \sum_{i=x,y,z} E_i^* \Delta_\Omega E_i + 2(\mathbf{E}^* \cdot \nabla)(\mathbf{r} \cdot \mathbf{E}) \right] + (\text{magnetic part: } \begin{matrix} \mathbf{E} \rightarrow \mathbf{H} \\ \tilde{\varepsilon} \varepsilon_0 \rightarrow \tilde{\mu} \mu_0 \end{matrix}). \quad (2.5)$$

which was explicitly written for the first time for the best of our knowledge. Each of the components can be naturally decomposed into the electric and magnetic parts. Here $(\tilde{\varepsilon}, \tilde{\mu}) = (\varepsilon, \mu) + \omega \partial_\omega (\varepsilon, \mu)$, the electromagnetic 6-component “wave function” is given by $|\psi\rangle = \sqrt{g/2} (\sqrt{\tilde{\varepsilon} \varepsilon_0} \mathbf{E}, \sqrt{\tilde{\mu} \mu_0} \mathbf{H})^T$ [45; 47–51], where the constant g depends on the unit system: $g_{\text{SI units}}^{(\text{Gaussian})} = \left(\frac{(2\omega)^{-1}}{(8\pi\omega)^{-1}} \right)$. This photon wave function is written in the manner of Shrodinger-like formulation of the Maxwell equations. In literature there is another way of how the photon wave function may written which is based on Dirac-like formulation of Maxwell equations [52–57]. As well argued by Bialynicki-Birula [53; 57] and by Sipe [54], for photons it is best to adopt a wave function whose modulus squared is the photon’s mean energy density, rather than

being a position probability density, as is the case for electrons [58] which is true for the both formulations.

Here $\hat{\mathbf{L}} = \mathbf{r} \times \hat{\mathbf{p}} = -i\mathbf{r} \times \nabla$ is the orbital angular momenta operator, $\hat{\mathbf{S}}$ is the spin-1 operator (the generator of SO(3) vector rotations [52; 229]), which explicitly can be written as

$$\hat{\mathbf{S}} = -i \left(\begin{bmatrix} 0 & 0 & 0 \\ 0 & 0 & 1 \\ 0 & -1 & 0 \end{bmatrix}, \begin{bmatrix} 0 & 0 & -1 \\ 0 & 0 & 0 \\ 1 & 0 & 0 \end{bmatrix}, \begin{bmatrix} 0 & 1 & 0 \\ -1 & 0 & 0 \\ 0 & 0 & 0 \end{bmatrix} \right)^T, \quad \hat{S}_{i,jk} = -i\varepsilon_{ijk}. \quad (2.6)$$

where ε_{ijk} is the Levi-Civita tensor of the 3rd rang. for which we have $\hat{\mathbf{S}}^2 = 2\hat{\mathbf{I}} = s \cdot (s + 1)\hat{\mathbf{I}}|_{s=1}$, which emphasized that the spin of a photon is one.

In contrast, the kinetic (or Abraham-like) total angular momenta density is defined through the Poynting vector $\mathbf{\Pi}^{\text{Re}}$ as

$$\mathcal{P} = \frac{1}{c^2} \mathbf{\Pi}^{\text{Re}} = \frac{1}{2c^2} \text{Re} [\mathbf{E}^* \times \mathbf{H}], \quad \mathcal{J} = \mathbf{r} \times \mathcal{P}. \quad (2.7)$$

and the decomposition into spin and orbital parts is not obvious especially for the case of the dispersive media [46].

Finally, the electromagnetic helicity, which is related to the dual symmetry between electric and magnetic fields [168; 245–249] and is defined for generally dispersive media as [49]

$$\mathfrak{G} = \frac{1}{2\omega'} |\tilde{n}| \text{Im} (\mathbf{H}^* \cdot \mathbf{E}) = \frac{1}{4\omega'} \left| \tilde{\varepsilon} \varepsilon_0 \frac{\mu\mu_0}{\varepsilon\varepsilon_0} + \tilde{\mu}\mu_0 \frac{\varepsilon\varepsilon_0}{\mu\mu_0} \right| \text{Im} (\mathbf{H}^* \cdot \mathbf{E}) \quad (2.8)$$

where $\tilde{n} = \sqrt{\varepsilon\mu} + \omega\partial_\omega\sqrt{\varepsilon\mu}$ is the group refractive index of the medium. It can be also written in the operator form using $\hat{\mathfrak{G}} = \frac{\hat{\mathbf{S}} \cdot \hat{\mathbf{P}}}{|\tilde{n}|k_0}$ as $\mathfrak{G} = \langle \psi | \hat{\mathfrak{G}} | \psi \rangle$.

We consider only low dissipative modes, i.e. with $|\varepsilon| = \left| \frac{\gamma}{\omega_{\text{Re}}} \right| \ll 1$ for $\omega = \omega_{\text{Re}} - i\gamma$. Formulas in this section are written using this assumption. Otherwise, there should be some additional corrections. Further analyses can be found in the Appendix E.

Eigen modes of dielectric and metallic spheres

We consider dielectric particle of radius a placed at the origin, which can be formally defined as

$$\varepsilon(\mathbf{r}, \omega) = \begin{cases} \varepsilon_{\text{in}}(\omega) & \text{for } r \leq a \\ \varepsilon_{\text{out}} & \text{for } r > a \end{cases} \quad \text{and} \quad \mu(\mathbf{r}, \omega) = \begin{cases} \mu_{\text{in}}(\omega) & \text{for } r \leq a \\ \mu_{\text{out}} & \text{for } r > a \end{cases} \quad (2.9)$$

The eigen modes of a sphere is defined by a Helmholtz equation, which we rewrite in the form of eigen value problem

$$\hat{\mathbb{H}}\mathbf{E} = k_0^2\mathbf{E}. \quad (2.10)$$

Here operator $\hat{\mathbb{H}} = \varepsilon^{-1}\nabla \times \mu^{-1}\nabla \times$ contains all the information about the system, in particular all its symmetric properties. Wigner theorem states that eigen functions succeed all the symmetry properties of the $\hat{\mathbb{H}}$ [250; 251]. The solution is going to give the set of eigen modes with corresponding *complex* eigen frequencies $\omega = \omega_{\text{Re}} - i\gamma$, where γ is the dissipation rate. For the non-magnetic media with $\mu = 1$ we can rewrite Eq. (2.10) using Lagrange's formula $\nabla \times \nabla \times \mathbf{E} = \nabla(\nabla \cdot \mathbf{E}) - \nabla^2\mathbf{E} = -\nabla^2\mathbf{E}$ in a more conventional form as $-\varepsilon^{-1}\nabla^2\mathbf{E} = k_0^2\mathbf{E}$.

Let us describe the eigenmodes of a spherical particle. Two conditions for electric and magnetic fields of eigenmodes must be fulfilled: (i) they must obey Maxwell equations with frequency ω , and electric and magnetic permittivities ε and μ :

$$\nabla \times \mathbf{E} = i\omega\mu\mu_0\mathbf{H}, \quad \nabla \times \mathbf{H} = -i\omega\varepsilon\varepsilon_0\mathbf{E}. \quad (2.11)$$

and (ii) they must have a particular symmetry properties. Spherical particle has spherical symmetry, thus, the system operator $\hat{\mathbb{H}}$ is invariant under all symmetry transformations of the $O(3)$ group of a sphere. According to the Wigner theorem [244; 250; 251], the eigenfunctions of such operator should transform under the irreducible representations of $O(3)$ group. VSH denoted as \mathbf{N}_{mj} , \mathbf{M}_{mj} , and \mathbf{L}_{mj} (see Appendix I) check all the boxes. VSH with index j are basis functions of the $(2j + 1)$ -dimensional irreps of $O(3)$ group (numbered by index $m = -j, \dots, j$), it is quite natural that eigenmodes can be described by these functions, which indeed happens and is shown explicitly in Refs. [16; 252]. We also emphasize that according to the Wigner theorem the degeneracy of eigen values is equal to the dimension of the corresponding irreducible representation. It means that eigenvalues of eq. (2.10) $\omega_j^{(n)} = c\sqrt{[k_0^2]_j^{(n)}}$ can be numbered by a single index j and has $2j + 1$ degeneracy. Also, there are infinitely many different eigen values for each j numbered by n , each of them has a generacy described above (e.g. for $j = 1$ these are first, second, \dots , n -th dipole resonances).

There are two types of modes generally distinguished: transverse electric or TE mode ($\mathbf{r} \cdot \mathbf{E} = 0$) and transverse magnetic or TM mode ($\mathbf{r} \cdot \mathbf{H} = 0$):

$$\begin{aligned} \text{TE:} \quad & \begin{cases} \mathbf{E} = \text{const}_1(r) \cdot \mathbf{M}_{mj} \\ \mathbf{H} = -\text{const}_1(r) \cdot i\sqrt{\frac{\varepsilon\varepsilon_0}{\mu\mu_0}} \mathbf{N}_{mj} \end{cases} & \text{const}_1(r) = \begin{cases} A^{\text{TE}} & \text{if } r \leq a \\ B^{\text{TE}} & \text{if } r > a \end{cases} \\ \\ \text{TM:} \quad & \begin{cases} \mathbf{E} = \text{const}_2(r) \cdot \mathbf{N}_{mj} \\ \mathbf{H} = -\text{const}_2(r) \cdot i\sqrt{\frac{\varepsilon\varepsilon_0}{\mu\mu_0}} \mathbf{M}_{mj} \end{cases} & \text{const}_2(r) = \begin{cases} A^{\text{TM}} & \text{if } r \leq a \\ B^{\text{TM}} & \text{if } r > a \end{cases} \end{aligned} \quad (2.12)$$

Note, that we did not use the radial polarized harmonics \mathbf{L} as those come into play for the electrostatic solutions and, for example, resonant state expansion to form the full basis of vector fields. Up to now, we know everything about modes except normalization constants which comes from the boundary conditions. Here we use *complex* VSH due to the fact that we study circular polarized modes with non-zero angular momenta similar to [170]. The radial dependence in \mathbf{M} and \mathbf{N} depends on the domain

$$z_j = \begin{cases} j_j(n_{\text{in}}k_0r), & \text{for } r \leq a \\ h_j^{(1)}(n_{\text{out}}k_0r), & \text{for } r > a \end{cases} \quad (2.13)$$

The explicit form of the constants A and B depends on the normalization which is widely discussed in Ref. [252] for dielectrics and in Ref. [253] for the dispersive media such as metal particles. However, in this work this does not make any difference since the normalized values of the angular momenta are investigated, i.e. angular momentum per one photon.

All the eigen frequencies $\omega_j = ck_0^{(j)}$ can be identified as a poles of the scattering matrix of the systems. To be more precise, by the poles of the standard Mie scattering coefficients a_j and b_j which came from the plane wave scattering problem on a homogeneous sphere [172] (see Appendix G). Importantly, we find the relative values of the constants to be $A^{\text{TE}}/B^{\text{TE}} = \frac{h_j^{(1)}(n_{\text{out}}k_0a)}{j_j(n_{\text{in}}k_0a)}$ and $A^{\text{TM}}/B^{\text{TM}} = \sqrt{\frac{\varepsilon_{\text{out}}\mu_{\text{in}}}{\varepsilon_{\text{in}}\mu_{\text{out}}}} \frac{h_j^{(1)}(n_{\text{out}}k_0a)}{j_j(n_{\text{in}}k_0a)}$ which ensures the correct radial dependence.

All the eigen modes can be labeled by the set of three *quantum numbers* and a mode type

$$(\text{XX}, n, j, m) \quad (2.14)$$

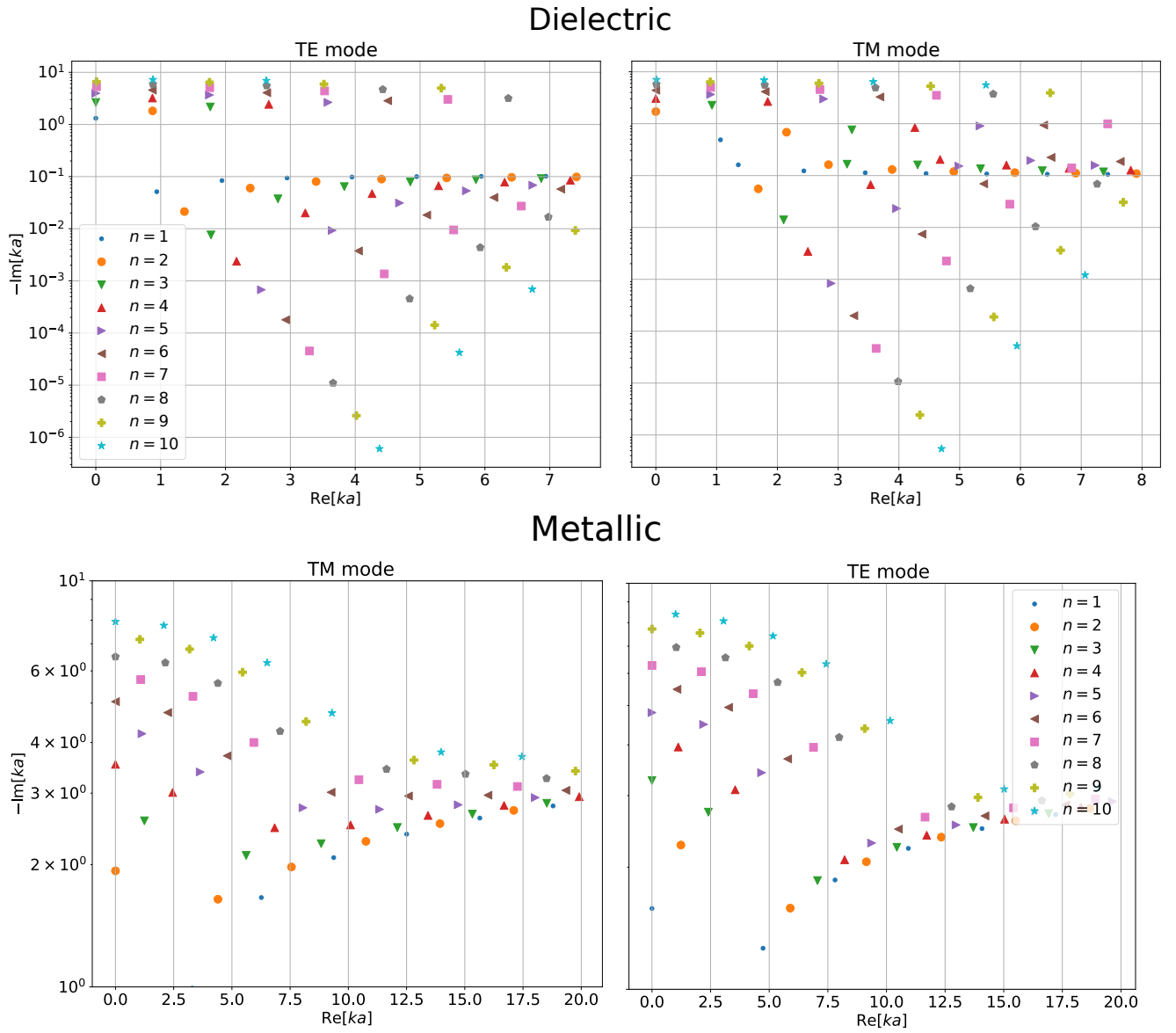


Figure 2.1 — Eigen modes for dielectric and metallic particles for the $n = 1, \dots, 10$. For dielectric particle: $a = 100$ nm, $\epsilon_p = 10$, $\mu_p = 1$. For metallic particle: $a = 50$ nm, Drude model $\epsilon_{\text{Drude}} = 1 - \omega_p^2 / (\omega^2 + i\Gamma\omega)$ for gold without losses with $\omega_p = 1.38 \cdot 10^{15} \frac{\text{rad}}{\text{s}}$ and $\Gamma = 0$

where $XX = \text{TE}, \text{TM}$ is the mode type, j is the total angular momenta quantum number, m is the projection of the total angular momenta number, and n is the radial quantum number.

2.1.2 Angular momenta of eigen modes of a sphere

Any axial symmetric system

The eigen modes of a sphere is defined by the Helmholtz equation

$$\nabla \times \mu^{-1} \nabla \times \mathbf{E} - k_0^2 \varepsilon \mathbf{E} = 0. \quad (2.15)$$

For the non-magnetic media with $\mu = 1$ we can rewrite (2.15) using Lagrange's formula $\nabla \times \nabla \times \mathbf{E} = \nabla(\nabla \cdot \mathbf{E}) - \nabla^2 \mathbf{E} = -\nabla^2 \mathbf{E}$ as

$$-\varepsilon^{-1} \nabla^2 \mathbf{E} = k_0^2 \mathbf{E}. \quad (2.16)$$

Operator $\hat{L} = -\varepsilon^{-1} \nabla^2$ contains all the information about the system, in particular all the symmetric properties. Wigner theorem states that eigen functions succeed all the symmetry properties of the \hat{L} [250; 251].

Next, we consider *any* axial symmetric system such as (in)finite cylinder, sphere, etc. The angular part of $-\varepsilon^{-1} \nabla^2$ leads to the known φ -dependence of eigen modes: $\mathbf{E}(\mathbf{r}) \sim e^{im\varphi}$ which is dictated by the condition $\mathbf{E}(\varphi + 2\pi N) = \mathbf{E}(\varphi)$ with N being an integer. Now, let us consider z -component of the total angular momenta in the cylindrical coordinate system

$$J_z = L_z + S_z = rP_\varphi + S_z, \quad (2.17)$$

where spin part is given by

$$S_z = \frac{1}{4\omega'} \text{Im} [\tilde{\varepsilon} \varepsilon_0 2i \text{Im} (E_r^* E_\varphi) + \tilde{\mu} \mu_0 2i \text{Im} (H_r^* H_\varphi)]. \quad (2.18)$$

The linear momenta needs extra attention since Eq. (2.2) is written in Cartesian system of coordinates. After some straightforward algebra we can get a general formula

$$\sum_{i=x,y,z} A_i^{\text{cart}} \nabla_\alpha B_i^{\text{cart}} = \sum_{i=r,\varphi,z} A_i^{\text{cyl}} \nabla_\alpha B_i^{\text{cyl}} + \delta_{\alpha\varphi} \frac{1}{r} (A_\varphi^{\text{cyl}} B_r^{\text{cyl}} - A_r^{\text{cyl}} B_\varphi^{\text{cyl}}) \quad (2.19)$$

Using this, we can write

$$P_\varphi = \frac{1}{4\omega' r} \text{Im} [\tilde{\varepsilon} \varepsilon_0 im |\mathbf{E}|^2 - \tilde{\varepsilon} \varepsilon_0 2i \text{Im} (E_r^* E_\varphi) + \tilde{\mu} \mu_0 im |\mathbf{H}|^2 - \tilde{\mu} \mu_0 2i \text{Im} (H_r^* H_\varphi)] \quad (2.20)$$

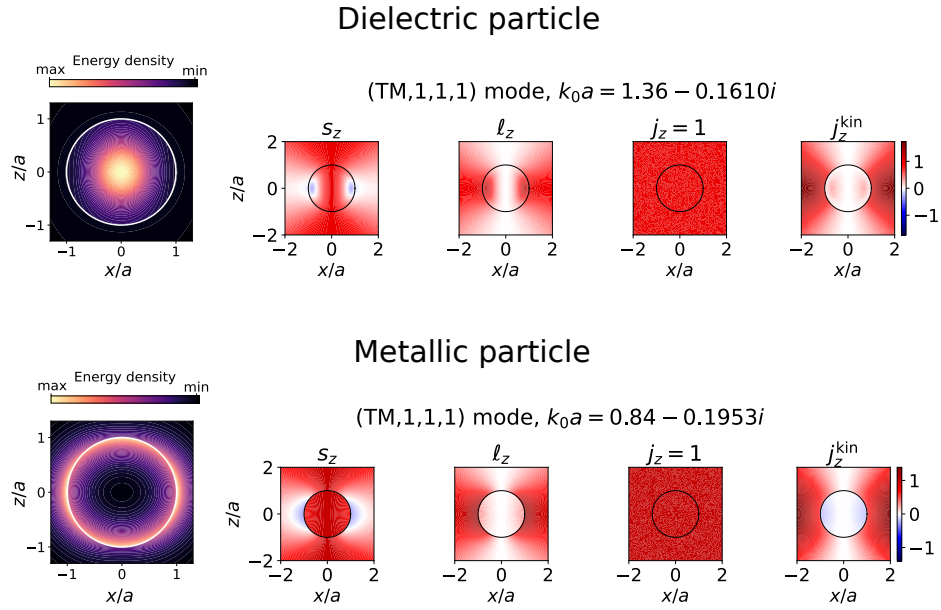


Figure 2.2 – Angular momenta density distribution for the dipole modes for dielectric and metallic particles

Where we have used $\nabla_\varphi = \frac{1}{r} \frac{\partial}{\partial \varphi}$ and $\frac{\partial}{\partial \varphi} \mathbf{E} = im\mathbf{E}$. Finally, normalizing total AM per one photon we can find that

$$\mathbf{E}(\mathbf{r}) \sim e^{im\varphi} \quad \rightarrow \quad j_z = \frac{\omega' J_z}{W} = \frac{\omega(rP_\varphi + S_z)}{W} = m. \quad (2.21)$$

Sphere

Canonical spin and orbital AM. The calculation of the canonical AM density per one photon for the modes of a sphere is identical to the general approach described above for a system of arbitrary symmetry. It means that for all eigen modes of a dielectric and metallic sphere modes labeled by (mj) one has

$$\frac{\omega' J_z}{W} = \frac{\omega' \langle J_z \rangle}{\langle W \rangle} = m, \quad (2.22)$$

so that total angular momenta projection on z -axis (density and integral values) is equal exactly to the azimuthal quantum number m .

The distribution of spin and orbital momentum are also worth attention. Since the total AM density is quantized, the distribution of the canonical spin and orbital momenta are not independent. We illustrate it for the dipole modes for the sake of simplicity but it also true for any other higher modes. The distribution is shown

in Figure 2.2 for the first dipole resonances of dielectric and metallic particles. Interesting to note that while total angular momenta of the dipole mode is positive ($m = +1$ in this case), local negative SAM is possible. At the same time, OAM can be locally larger than total AM. This reveals more opportunities in the light-matter interaction where local properties have greater importance.

Let us stress the differences in modes of dielectric and metallic spheres. First of all, for the dielectric particle field is localized in the volume of the particle, however, for the metallic particle electromagnetic energy density is localized near a surface, which is a general feature of surface plasmon modes.

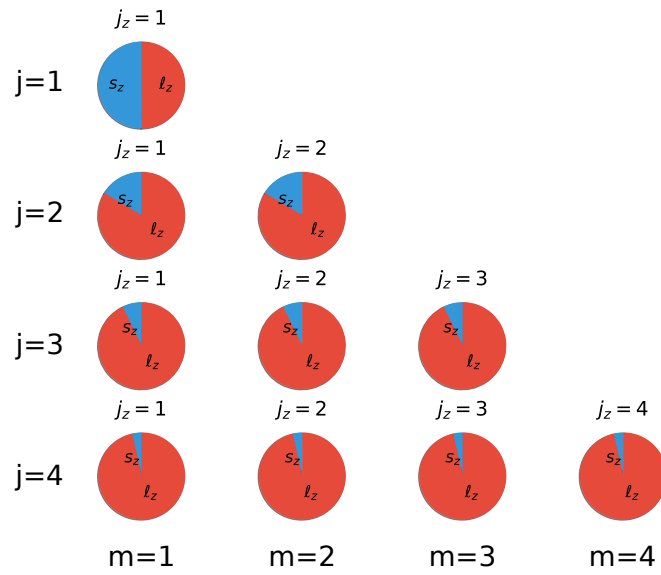


Figure 2.3 — Relation between integrated spin and orbital parts for all modes up to $j = 4$. Distribution stays the same for both dielectric and magnetic particles for TE and TM modes

Kinetic AM. In contrast to the canonical momenta, kinetic momenta tends to the m number only for integrated values:

$$\frac{\omega' \langle J_z^{\text{kin}} \rangle}{\langle W \rangle} = \frac{m \cdot \int_0^\infty dr \cdot 2r^2 |z_j|^2}{\int_0^\infty dr \cdot r^2 \left(|z_j|^2 + \frac{j+1}{2j+1} |z_{j-1}|^2 + \frac{j}{2j+1} |z_{j+1}|^2 \right)} = m \quad (2.23)$$

However, this answer is true only for low dissipative modes, i.e. for the modes with high Q -factor. The distribution of the kinetic AM density varies and is not constant in the space. The kinetic momentum density resembles more the canonical orbital momenta density with slight differences (see figure 2.2).

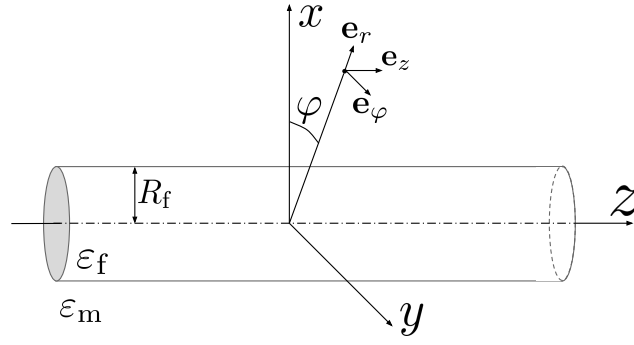


Figure 2.4 – Step-index fiber and cylindrical and Cartesian coordinates. In some cases cylindrical radial unit vector can be written as \mathbf{e}_ρ instead of \mathbf{e}_r in order not to mixed with spherical radial unit vector

Total canonical AM. Once we calculate the square of total angular momenta per photon, labeled as $\mathbf{j}^2 \equiv \langle \psi | (\hat{\mathbf{L}} + \hat{\mathbf{S}})^2 | \psi \rangle / \langle \psi | \psi \rangle$, we get the well know in quantum mechanics answer:

$$\mathbf{j}^2 = j(j + 1). \quad (2.24)$$

Helicity. For real frequencies helicity inside the particle are equal to zero identically. However, once there is a complex frequency, we have non-zero helicity inside the particle

$$\mathfrak{S} \sim \text{Im} (i\mathbf{N}_{jm}^* \cdot \mathbf{M}_{jm}) = -2 \text{Re} \left(Y_j^m \frac{d}{d\theta} Y_j^m \right) \frac{m}{\sin \theta} \text{Im} [(z_{j-1} - z_{j+1})^* z_j] \stackrel{r \lesssim a}{\approx} |kr|^{2j-1} \cdot \varepsilon + O(\varepsilon^2) \quad (2.25)$$

Here $\varepsilon = \omega''/\omega'$ is the small parameter for high- Q modes. We also omitted the angular dependence in the last equation.

The integral value of helicity is zero for any mode

$$\langle \mathfrak{S} \rangle = 0 \quad (2.26)$$

This can be formally shown using the orthognoality relations between VSH (see Appendix I).

2.2 Fiber mode profiles

Starting from the Maxwell equations

$$\begin{cases} \nabla \cdot \varepsilon \varepsilon_0 \mathbf{E} = 0, & \nabla \cdot \mu \mu_0 \mathbf{H} = 0 \\ \nabla \times \mathbf{E} = i\omega \mu \mu_0 \mathbf{H}, & \nabla \times \mathbf{H} = -i\omega \varepsilon \varepsilon_0 \mathbf{E} \end{cases} \quad (2.27)$$

and considering space with permittivities

$$\varepsilon(r) = \begin{cases} \varepsilon_f, & r \leq R_f \\ \varepsilon_m, & r > R_f \end{cases}, \quad \mu_m = \mu_f = 1, \quad n_{m,f} = \sqrt{\varepsilon_{m,f} \mu_{m,f}}, \quad (2.28)$$

where r is the radial coordinate in cylindrical coordinates (r, φ, z) (see Fig. 2.4). Due to the $z \rightarrow z + \Delta z, \forall \Delta z$ invariance and rotation symmetry of the fields results in a very simple z and φ dependence

$$\mathbf{E}, \mathbf{H} \sim e^{i\beta z} e^{i\ell\varphi}, \quad \ell = 0, 1, 2, \dots \quad (2.29)$$

where ℓ is the azimuthal mode number, and β is the propagation constant and defined by dispersion relation $\beta = \beta(\omega)$ which comes from the boundary conditions [235; 237]

$$\begin{aligned} \left[\frac{J'_\ell(hR_f)}{hR_f J_\ell(hR_f)} + \frac{K'_\ell(qR_f)}{qR_f K_\ell(qR_f)} \right] \left[\frac{n_f J'_\ell(hR_f)}{hR_f J_\ell(hR_f)} + \frac{n_m K'_\ell(qR_f)}{qR_f K_\ell(qR_f)} \right] = \\ = \ell^2 \frac{\beta^2}{k_0^2} \left(\frac{1}{h^2 R_f^2} + \frac{1}{q^2 R_f^2} \right), \end{aligned} \quad (2.30)$$

where $h = \sqrt{n_f k_0^2 - \beta^2}$ and $q = \sqrt{\beta^2 - n_m^2 k_0^2}$ are the transverse part of the wave vectors, which characterize the scales of the spatial variations of the field inside and outside the fiber, respectively. J_ℓ and K_ℓ stand for the Bessel function of the first kind and the modified Bessel functions of the second kind. Prime represents the derivatives with respect to the argument. When it comes to the numerical solution of (2.30) it is more convenient to split it to four different branches which solutions represent propagation constants of two hybrid modes (HE and EH) and

two transverse modes (TE and TM) with $\ell = 0$:

$$\ell = 0 \quad \text{TE:} \quad \frac{J_1(hR_f)}{hR_f J_0(hR_f)} = -\frac{K_1(qR_f)}{qR_f K_0(qR_f)}, \quad (2.31)$$

$$\ell = 0 \quad \text{TM:} \quad \frac{J_1(hR_f)}{hR_f J_0(hR_f)} = -\frac{n_m^2}{n_f^2} \frac{K_1(qR_f)}{qR_f K_0(qR_f)}, \quad (2.32)$$

$$\ell > 0 \quad \text{HE:} \quad \frac{J_{\ell-1}(hR_f)}{hR_f J_\ell(hR_f)} = -\frac{n_f^2 + n_m^2}{2n_f^2} \frac{K_\ell(qR_f)}{qR_f K_\ell(qR_f)} + \frac{\ell}{h^2 R_f} - D, \quad (2.33)$$

$$\ell > 0 \quad \text{EH:} \quad \frac{J_{\ell-1}(hR_f)}{hR_f J_\ell(hR_f)} = -\frac{n_f^2 + n_m^2}{2n_f^2} \frac{K_\ell(qR_f)}{qR_f K_\ell(qR_f)} + \frac{\ell}{h^2 R_f} + D, \quad (2.34)$$

where

$$D = \left[\left(\frac{n_f^2 - n_m^2}{2n_f^2} \right)^2 \left(\frac{K'_\ell(qR_f)}{qR_f K_\ell(qR_f)} \right) + \left(\frac{\ell\beta}{n_f k_0} \right)^2 \left(\frac{1}{q^2 R_f^2} + \frac{1}{h^2 R_f^2} \right)^2 \right]^{1/2}. \quad (2.35)$$

Equations (2.31) and (2.32) are obtained by putting $\ell = 0$ in (2.30). Equations (2.33) and (2.34) are obtained by solving (2.30) as a quadratic equation e.g. with respect to $\frac{J'_\ell(hR_f)}{hR_f J_\ell(hR_f)}$. A family of different solutions for fiber with $\varepsilon_f = 3.5$ in coordinates ω – β are shown in Fig. 2.5. It is also clear from the plot that

$$n_m k_0 < \beta < n_f k_0. \quad (2.36)$$

It means that for the real n_f and n_m transverse parts of wave vectors are also purely real $q, h \in \mathbb{R}$. In waveguide optics one may most likely find dispersion plotted in the different coordinates. For the quick reference we insert Fig. 2.8 taken from [254]. Author finds this plot very illustrative and helpful for theoretical investigations.

It is convenient to write the explicit expressions for the fields in the next manner

$$\mathbf{E}^{(\mu)}(\mathbf{r}) = \mathbf{e}^{(\mu)}(r) e^{if\beta z + ipl\varphi}, \quad \mathbf{H}^{(\mu)}(\mathbf{r}) = \mathbf{h}^{(\mu)}(r) e^{if\beta z + ipl\varphi}, \quad (2.37)$$

where $\mathbf{e}^{(\mu)}(r)$ and $\mathbf{h}^{(\mu)}(r)$ are more profile functions which are given in cylindrical coordinates (r, φ, z) as

$$\mathbf{e}^{(\mu)}(r) = \begin{pmatrix} e_r(r) \\ pe_\varphi(r) \\ fe_z(r) \end{pmatrix}, \quad \mathbf{h}^{(\mu)}(r) = \begin{pmatrix} fph_r(r) \\ fh_\varphi(r) \\ ph_z(r) \end{pmatrix}. \quad (2.38)$$

These mode profile functions depend on the different branch of solution of the Maxwell equations. The explicit expression for the mode profiles one can find in [235]. By index (μ) we denote all the mode parameters (which is slightly different from [235], where $(\mu) = (f\ell p)$):

$$(\mu) = \begin{pmatrix} \text{XX} \\ \ell \\ m \\ f \\ p \end{pmatrix}, \quad \text{XX} = \begin{cases} \text{HE, EH} & \text{hybrid modes: } e_z^{(\mu)} \neq 0 \\ \text{TE} & \text{transverse electric: } e_r^{(\mu)} = e_z^{(\mu)} = 0 \\ \text{TM} & \text{transverse magnetic: } h_r^{(\mu)} = h_z^{(\mu)} = 0 \end{cases} \quad (2.39)$$

where XX is the mode type, ℓ is the azimuthal number, m is the radial mode order, which, in particular, means that $|e_z^{(\mu)}(r, \varphi)|$ and $|h_z^{(\mu)}(r, \varphi)|$ have m maxima each in the radial direction, including the peak, if it exists, at the origin. Reader can notice this feature after careful investigation of Fig. 2.6. Practically, it is the m -th root in the corresponding solution branch of dispersion equation (2.30). Index $f = \pm 1$ represents positive ($+\mathbf{e}_z$) or negative ($-\mathbf{e}_z$) propagation direction which leads to the corresponding propagation phase factor of $e^{+i\beta z}$ or $e^{-i\beta z}$. Index $p = \pm 1$ corresponds to the counterclockwise or clockwise phase circulation, corresponding to the azimuthal phase factor of $e^{+i\ell\varphi}$ or $e^{-i\ell\varphi}$. With such choice we fix the signs of propagation constant $\beta > 0$ and azimuthal number $\ell \geq 0$.

2.2.1 Electric field structure and mode designations

In this thesis is used the standard way [237; 255] of labeling different modes:

$$\text{XX}_{\ell m} \quad (2.40)$$

where XX shows the type of the mode, e.g. hybrid (HE or EH) or transverse (TE or TM), ℓ is the azimuthal number and m is the radial mode order. Azimuthal mode number ℓ shows the amount of optical angular momentum [256; 257] which light carries since wavefront of the mode has an azimuthal phase dependence $e^{i\ell\varphi}$.

The structure of the mode may have dramatic changes. To illustrate this fact the electric field lines and intensity distributions of the first 12 modes was plotted on Fig. 2.6 using expressions from [258].

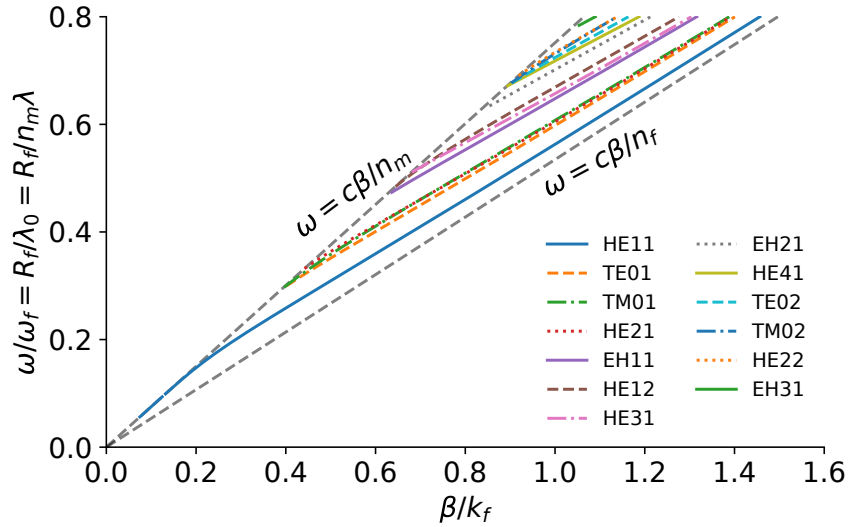


Figure 2.5 — Fiber dispersion. Propagation constants β as branch of solutions of the fiber dispersion equation (2.30). Here $k_f = 2\pi/R_f$, $\omega_f = 2\pi c/R_f$. Fiber material was chosen to be with $\varepsilon_f = 3.5$. It is clearly seen from this plot which values propagation constant can have: $n_m k_0 < \beta < n_f k_0$

2.2.2 Mode polarizations and Stokes vector

Fundamental solutions (2.37) are circularly polarized modes (except TE and TM). But in practice (by someone's need or due to experimental issues) people are often faced with custom polarized fields (linear, circular or elliptical). This section shows how can we connect custom polarization with obtained solutions above.

Fundamental hybrid mode solutions (HE and EH modes) have circular polarization. We can easily build a basis using right and left circular polarized modes which we denote as \mathbf{E}^+ ($p = +1$) and \mathbf{E}^- ($p = -1$) correspondingly. The main idea is a linear combination $\mathbf{E}^{\text{custom}} = C_1 \mathbf{E}^+ + C_2 \mathbf{E}^-$ with $C_1, C_2 \in \mathbb{C}$ can specify any desired polarization.

The closest conventional method is to use complex Jones vector $\mathbf{J} = (j_1, j_2)^T$. The only difference is that Jones vector formalism uses linear polarized basis \mathbf{E}_1 and \mathbf{E}_2 which can be written as

$$\mathbf{E}_1 = \frac{1}{\sqrt{2}} (\mathbf{E}^+ + \mathbf{E}^-), \quad \mathbf{E}_2 = \frac{1}{i\sqrt{2}} (\mathbf{E}^+ - \mathbf{E}^-). \quad (2.41)$$

so

$$\mathbf{E}^{\text{custom}} = j_1 \mathbf{E}_1 + j_2 \mathbf{E}_2. \quad (2.42)$$

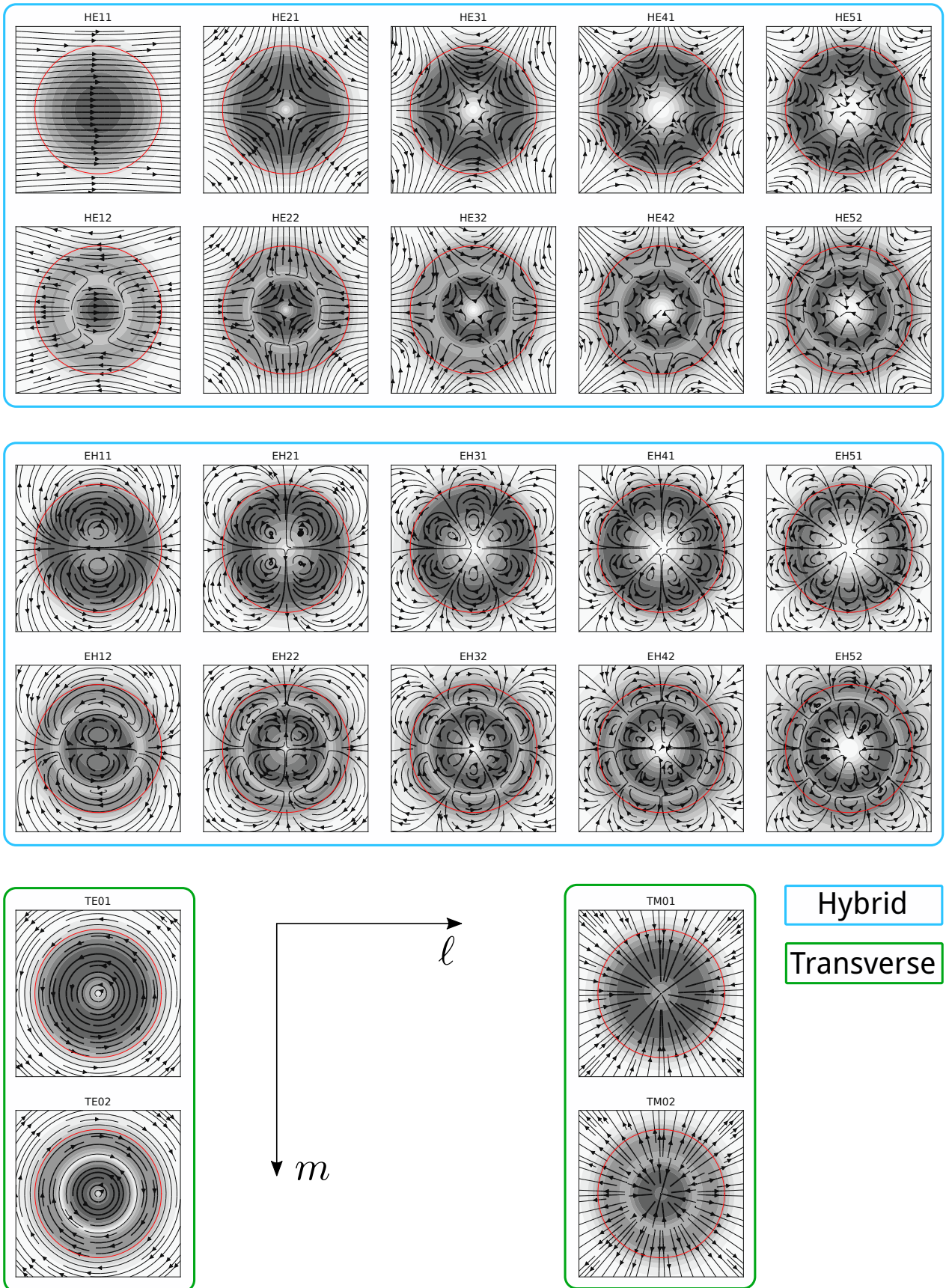


Figure 2.6 — Vector field (stream plot arrows) and intensity distributions (gray map) for the modes in a step index fiber. All modes are grouped by its families: HE, EH, TE and TM. Red circle represents the fiber border. Parameters: $n_m = 1$, $n_f = 1.45$, $k_0 R_f = 11.81$ (corresponds to $V = 12.46$)

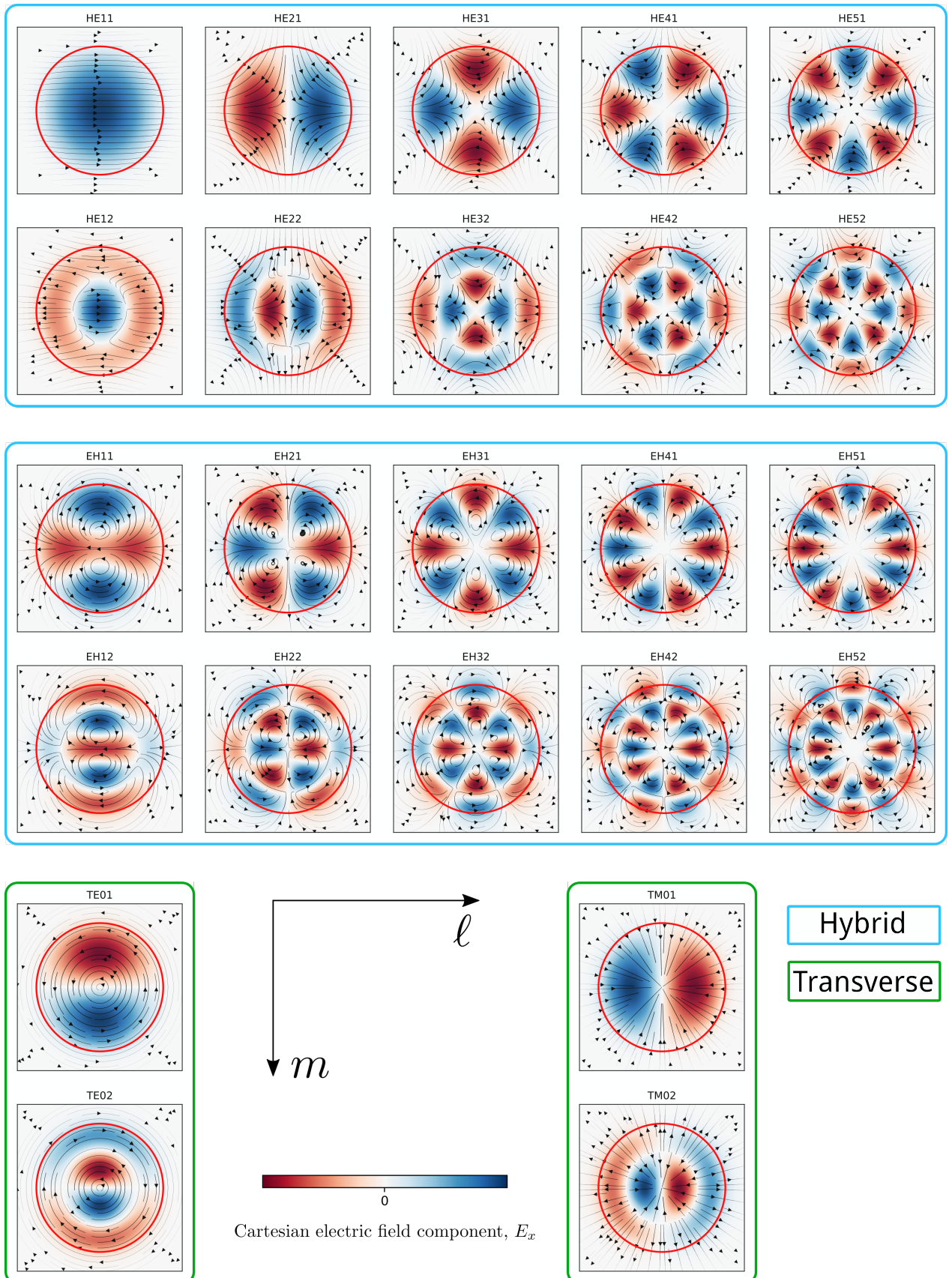


Figure 2.7 — Vector field (stream plot arrows) and Cartesian electric component \mathcal{E}_x (color map) for the modes in a step index fiber. All modes are grouped by its families: HE, EH, TE and TM. Red circle represents the fiber border. Parameters:

$$n_m = 1, n_f = 1.45, k_0 R_f = 11.81 \text{ (corresponds to } V = 12.46)$$

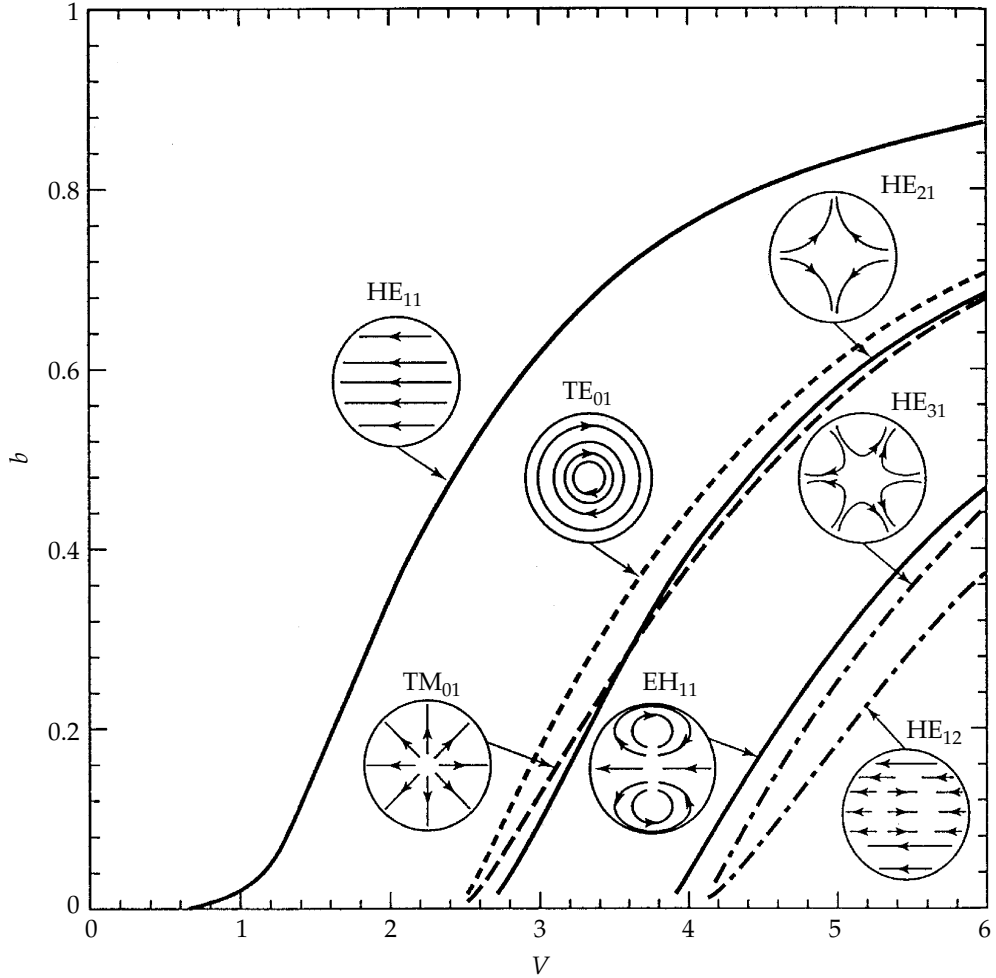


Figure 2.8 — Dispersion of a fiber with $(n_f - n_m)/n_f = 0.2$ and electric field lines of the first 7 modes. Here $b = \frac{N^2 - n_m^2}{n_f^2 - n_m^2}$, $\beta = k_0 N$, $V = k_0 R_f \sqrt{n_f^2 - n_m^2}$. Picture is taken from [254]

From the practical point of view it is more convenient to use Stokes vector $\mathbf{S} = (S_0, S_1, S_2, S_3)^T$ and Poincare sphere [259] which contains more information, e.g. non-coherent light (inside the Poincare Sphere). So Jones vector can only represent the perfectly polarized part of the Stokes vector. Because there is an arbitrary phase, there are an infinity of Jones' vectors that fit a given Stokes vector representation. Fixing that phase, we can build a method how to obtain Jones vector knowing the Stokes vector: $\mathbf{S} \rightarrow \mathbf{J}$.

The algorithm is the following. At first, we calculate the degree of polarization $\bar{p} = \sqrt{(S_1^2 + S_2^2 + S_3^2)/S_0}$, then we normalize Stokes vector $\tilde{\mathbf{S}} = \mathbf{S}/(S_0 \bar{p})$ and after

Table 3 — Connection between common values of Stokes vector and Jones vector

Polarization	Label	Stokes vector \mathbf{S}	Jones vector \mathbf{J}
Linearly polarized (horizontal)	H	$(1, +1, 0, 0)$	$(1, 0)$
Linearly polarized (vertical)	V	$(1, -1, 0, 0)$	$(0, 1)$
Linearly polarized ($+45^\circ$)	D	$(1, 0, +1, 0)$	$\frac{1}{\sqrt{2}}(1, +1)$
Linearly polarized (-45°)	A	$(1, 0, -1, 0)$	$\frac{1}{\sqrt{2}}(1, -1)$
Right-hand circularly polarized	R	$(1, 0, 0, +1)$	$\frac{1}{\sqrt{2}}(1, -i)$
Left-hand circularly polarized	L	$(1, 0, 0, -1)$	$\frac{1}{\sqrt{2}}(1, +i)$
Unpolarized	–	$(1, 0, 0, 0)$	–

that construct components of Jones vector

$$j_1 = S_0 \bar{p} \sqrt{\frac{1 + \tilde{S}_1}{2}}, \quad j_2 = S_0 \bar{p} \begin{cases} \frac{\tilde{S}_2}{2j_1} - i \frac{\tilde{S}_3}{2j_1}, & \text{if } j_1 \neq 0, \\ 1, & \text{if } j_1 = 0. \end{cases} \quad (2.43)$$

Using these components of Jones vector we can easily build $\mathbf{E}^{\text{custom}}$ by using (2.42) and (2.41).

It would be more precise to call these modes *quasi*-linear/circular/elliptical polarized since all hybrid modes has z component.

For a quick reference we write Jones and Stokes vectors for common polarizations below in Tab. 3.

2.2.3 Evanescent mode field intensity

The higher field intensity we have the higher dipole moment is induced since $\mathbf{p} = \alpha \mathbf{E}$ and stronger interaction we obtain. This behavior remain approximately the same beyond dipole approximation but with some unique feature as Mie resonances. The main message here is that we want to optimize the strength of a particular mode in the vicinity of the fiber.

Naive expectations that the thinner fiber¹ we have the higher evanescent field we would obtain are wrong. It appears [235; 260] that there is a maximum of inten-

¹Thinner fiber here means that we direct R_f to some critical fiber radius when desired modes still exists

Figure 2.9 — Electric field intensity in the vicinity of fiber as a function of fiber radius. Each mode carries the same amount of power. Behavior remains approximately the same for the bigger distance from vicinity. Parameters: $\lambda = 1064$ nm,

$$\epsilon_m^{\text{water}} = 1.77, \epsilon_m^{\text{air}} = 1.0, \epsilon_f = 2.1025,$$

sity and for each mode it is different which are clearly seen on Fig. 2.9. Interesting to notice that all the hybrid modes (HE and EH) starts from zero but transverse modes (TE and TM) has high starting point which is very close to maximum. One should pay attention to this behavior if there is a need to achieve the most efficient interaction through the evanescent field.

2.2.4 Angular momentum of dielectric step-index fiber modes

This approach was successfully implemented to describe angular momenta of dielectric-fiber and metallic-wire modes [170]. It was shown [170; 241] and verified in this work that *both the integral value and the density* of the total angular momentum per one photon is a quantized value

$$\frac{\omega \mathcal{J}_z}{W} = \frac{\omega \langle \mathcal{J}_z \rangle}{\langle W \rangle} = \ell, \quad \ell = 0, 1, 2, \dots \quad (2.44)$$

where $W = \frac{1}{4} (\epsilon_0 \tilde{\epsilon} |\mathbf{E}|^2 + \mu_0 \tilde{\mu} |\mathbf{H}|^2)$ is the Brillouin expression for the energy density [15; 169].

Direct application of (1.15)–(1.17) to step-index fiber modes gives its full canonical picture of AM analysis. Due to the fact that experimentally are only local densities are measured we bring forward of the AM densities but not integral values. On Fig. 2.10 and Fig. 2.11 there are maps in (R_f, r) parameter space. SAM and OAM are normalized as (2.44) so the sum of OAM and SAM at any point of the map gives azimuthal mode number ℓ . For the EH modes family S_z always has the opposite sign to the L_z outside the fiber

$$\text{sign } S_z^{\text{EH}} = - \text{sign } L_z^{\text{EH}}, \quad r > R_f. \quad (2.45)$$

This fact allows to obtain higher OAM for the lower ℓ numbers. Moreover, outside the fiber both S_z and L_z for HE and EH modes do not change its sign. Inside the

fiber S_z changes its sign $2(m - 1)$ times for HE modes and $2m - 1$ times for EH modes. Total AM density \mathcal{J}_z is normalized to the spin momentum of a circular polarized plane wave in free space $S_z^{\text{p.w.}} = \frac{\epsilon_0}{2\omega} E_0^2$ where $E_0^2 = \frac{Z_0 P}{2\pi R_f^2}$ is the field magnitude of a plane wave with carried power P (= power carried by the mode) normalized on the fiber cross section πR_f^2 and Z_0 is the vacuum impedance. Total AM decays with exponential rate and each mode has its own optimum fiber radius to observe maximum AM with fixed power carried by the mode.

Ratio between OAM and SAM can be shifted by changing ϵ_f which is shown for on Fig. 2.12–2.13. By increasing ϵ_f we engage field more inside the fiber and this always decrease the spin part of the total AM.

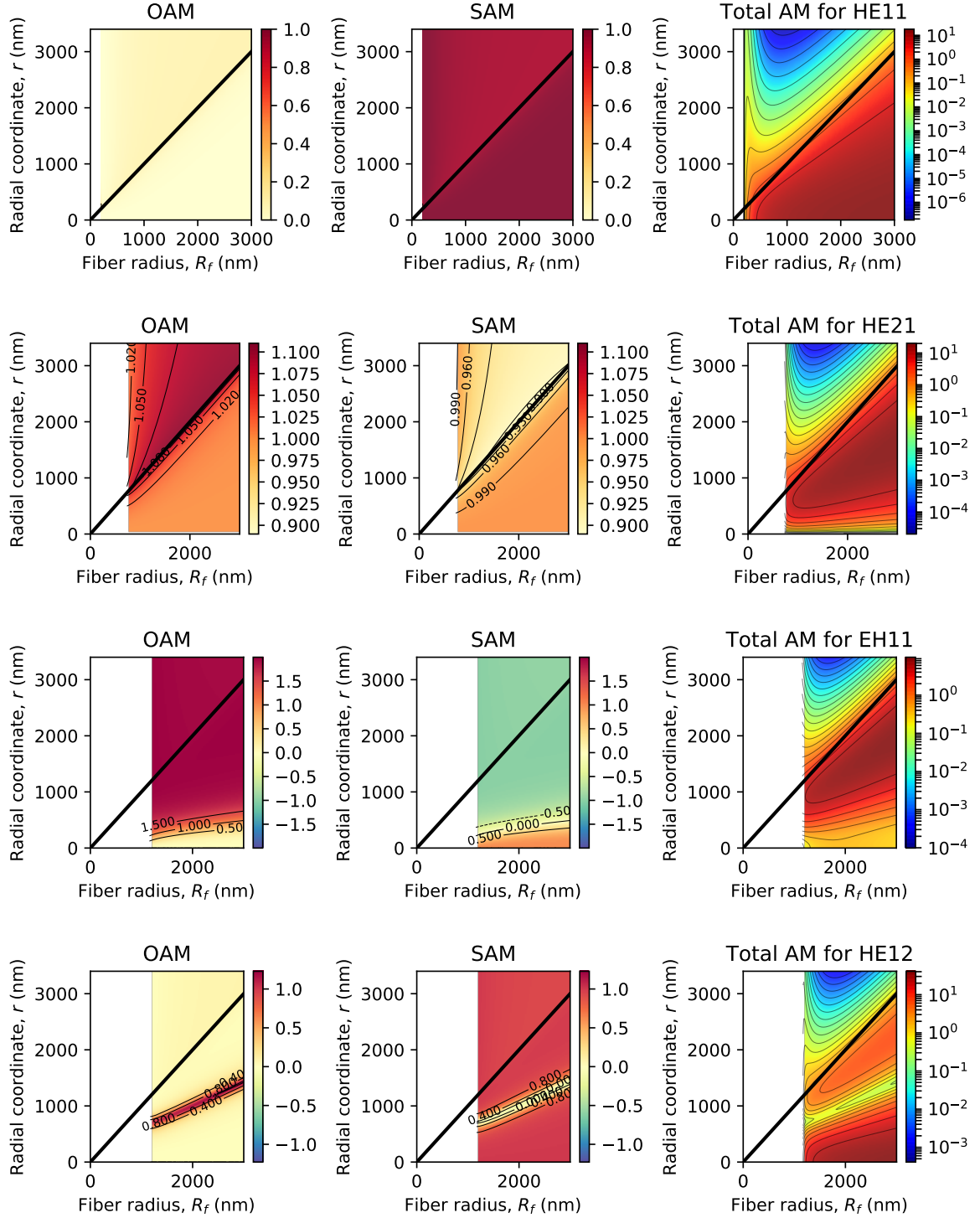


Figure 2.10 – Canonical OAM and SAM distributions for the first 4 dielectric fiber modes. Orbital and spin parts are normalized to the Brillouin energy as in (2.44). Total angular momentum is normalized to the spin momentum of a circular polarized plane wave in free space $S_z^{\text{p.w.}} = \frac{\epsilon_0}{2\omega} E_0^2$ where $E_0^2 = \frac{Z_0 P}{2\pi R_f^2}$ is the field magnitude of a plane wave with carried power P ($=$ power carried by the mode) normalized on the fiber cross section πR_f^2 , Z_0 is the vacuum impedance. $\lambda_0 = 1064$ nm, $\epsilon_f = 1.45^2$, $\epsilon_m = 1.77$.

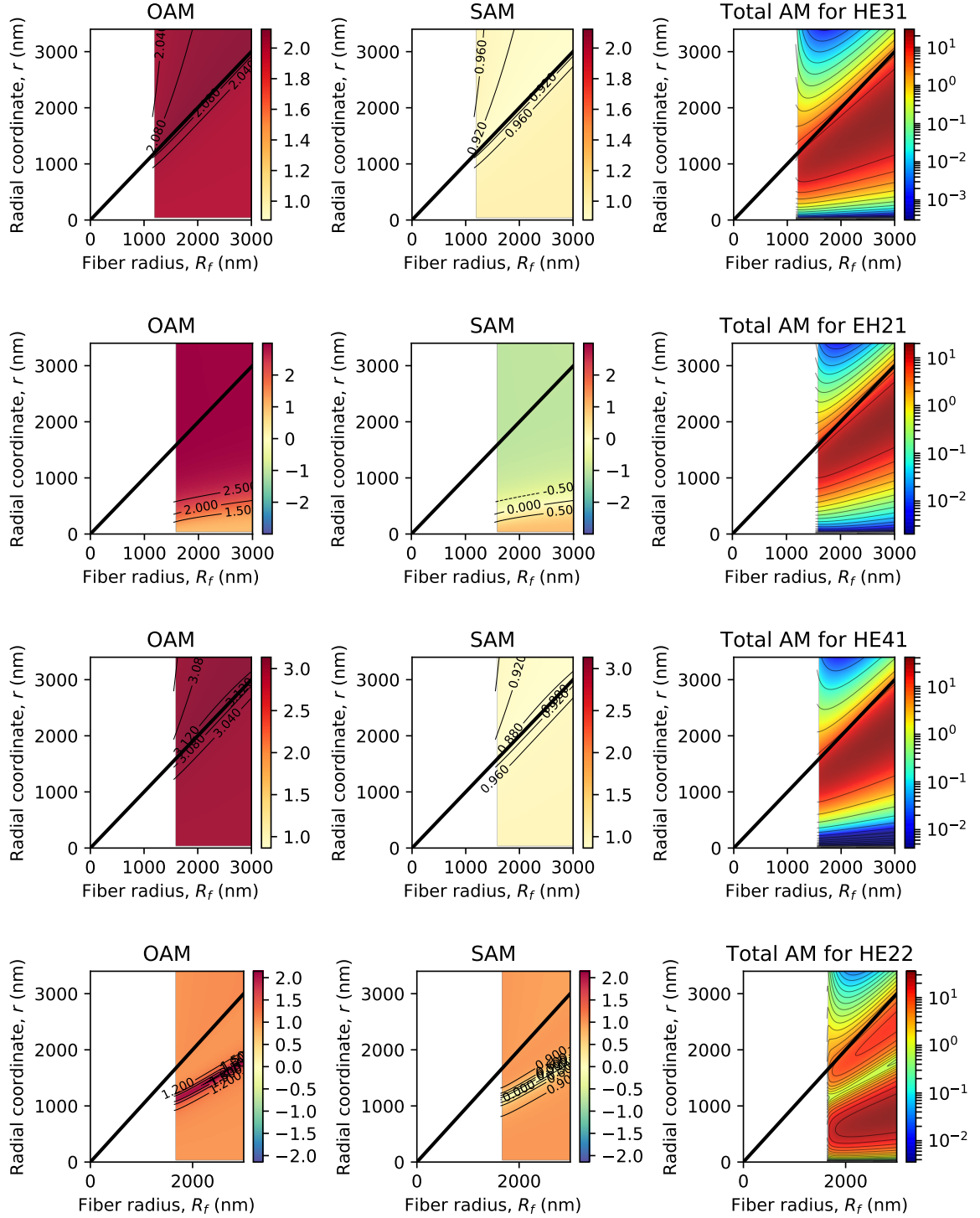


Figure 2.11 — Canonical OAM and SAM distributions for the second 4 dielectric fiber modes. Orbital and spin parts are normalized to the Brillouin energy as in (2.44). Total angular momentum is normalized to the spin momentum of a circular polarized plane wave in free space $S_z^{\text{p.w.}} = \frac{\epsilon_0}{2\omega} E_0^2$ where $E_0^2 = \frac{Z_0 P}{2\pi R_f^2}$ is the field magnitude of a plane wave with carried power P ($=$ power carried by the mode) normalized on the fiber cross section πR_f^2 , Z_0 is the vacuum impedance. $\lambda_0 = 1064$ nm, $\epsilon_f = 1.45^2$, $\epsilon_m = 1.77$.

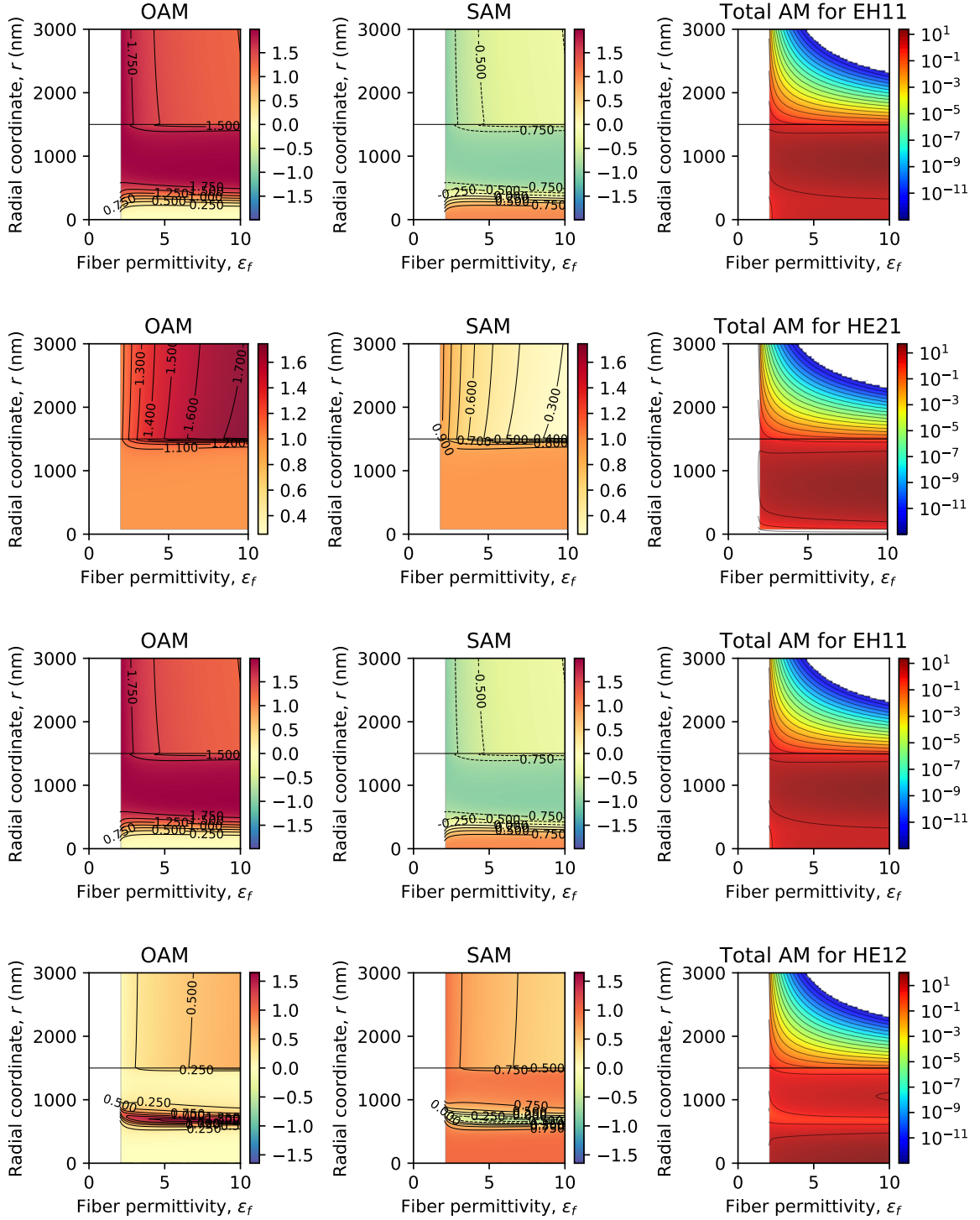


Figure 2.12 – Canonical OAM and SAM distributions for the first 4 dielectric fiber modes. Orbital and spin parts are normalized to the Brillouin energy as in (2.44). Total angular momentum is normalized to the spin momentum of a circular polarized plane wave in free space $S_z^{\text{p.w.}} = \frac{\epsilon_0}{2\omega} E_0^2$ where $E_0^2 = \frac{Z_0 P}{2\pi R_f^2}$ is the field magnitude of a plane wave with carried power P ($=$ power carried by the mode) normalized on the fiber cross section πR_f^2 , Z_0 is the vacuum impedance. $\lambda_0 = 1064$ nm, $\epsilon_f = 1.45^2$, $\epsilon_m = 1.77$

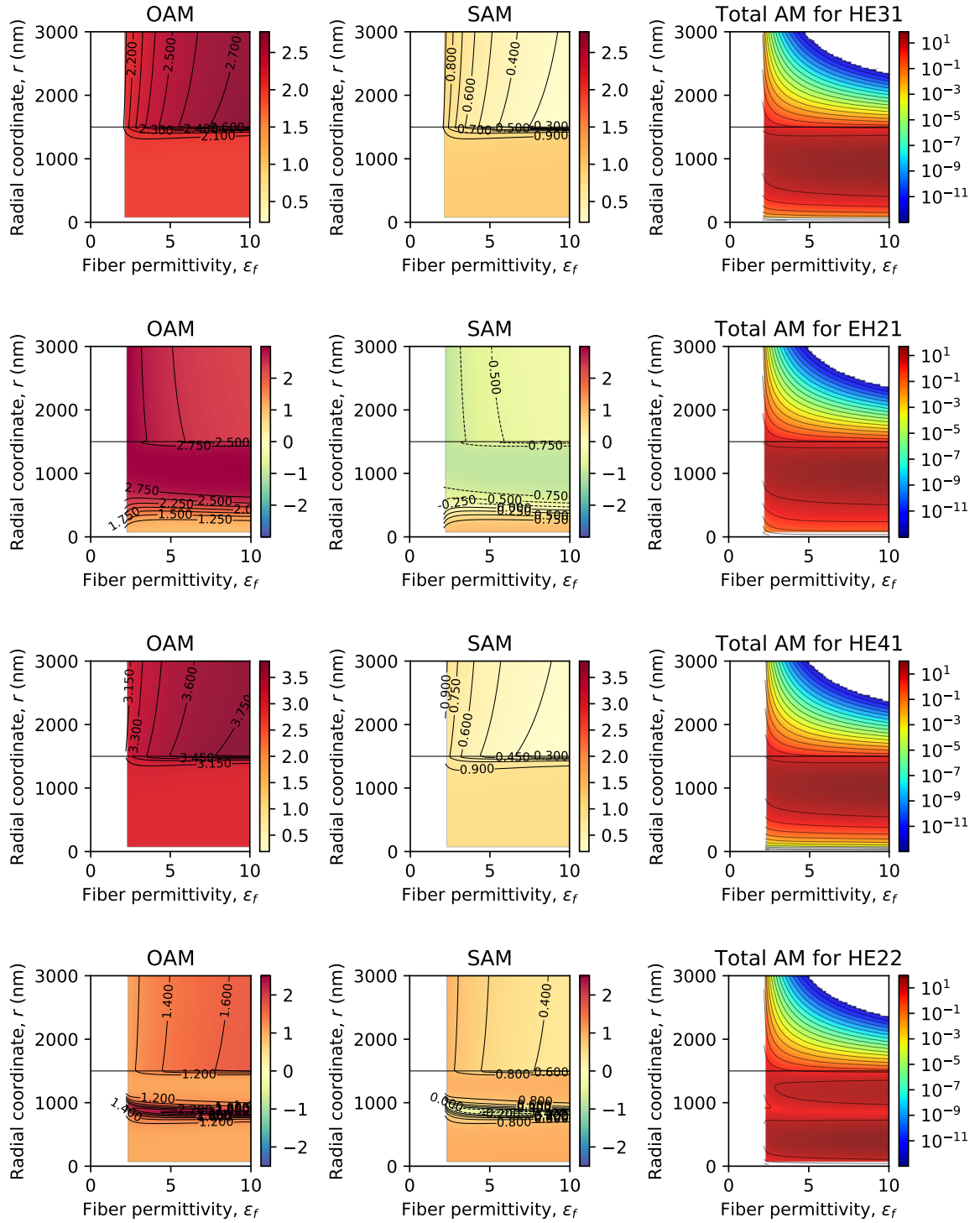


Figure 2.13 — Canonical OAM and SAM distributions for the second 4 dielectric fiber modes. Orbital and spin parts are normalized to the Brillouin energy as in (2.44). Total angular momentum is normalized to the spin momentum of a circular polarized plane wave in free space $S_z^{\text{p.w.}} = \frac{\epsilon_0}{2\omega} E_0^2$ where $E_0^2 = \frac{Z_0 P}{2\pi R_f^2}$ is the field magnitude of a plane wave with carried power P ($=$ power carried by the mode) normalized on the fiber cross section πR_f^2 , Z_0 is the vacuum impedance. $\lambda_0 = 1064$ nm, $\epsilon_f = 1.45^2$, $\epsilon_m = 1.77$

Chapter 3. Transverse optical binding via waveguide mode

In this chapter, we study a linear chain of subwavelength particles which are evenly coupled to a waveguided mode of a nanofiber. Interestingly, it is possible to make this system stable with only one beam (see Fig. 3.1). Under a transverse plane wave excitation nanoparticles form a stable self-organized periodic array along waveguide axis through the transverse binding effect. Another two degrees of freedom are ensured by a photonic jet effect. Most importantly, the depth of a trapping potential for each nanoparticle increases linearly with the system size, making the self-assembly of a longer chain more favourable. We estimate that for an optical nanofiber platform the binding energy for two nanoparticles is in the range of $9 \div 13 k_B T$ reaching the value of $110 k_B T$ when the chain size is increased up to 20 nanoparticles. Finally, we suggest the two counter-propagating plane waves excitation scheme, which will allow trapping the nanoparticles close to the optical nanofiber providing efficient interaction between the nanofiber and the nanoparticles.

3.1 General idea

The majority of the optical trapping and manipulation methods are based on shaping the light field intensity with optical systems such as spatial light modula-

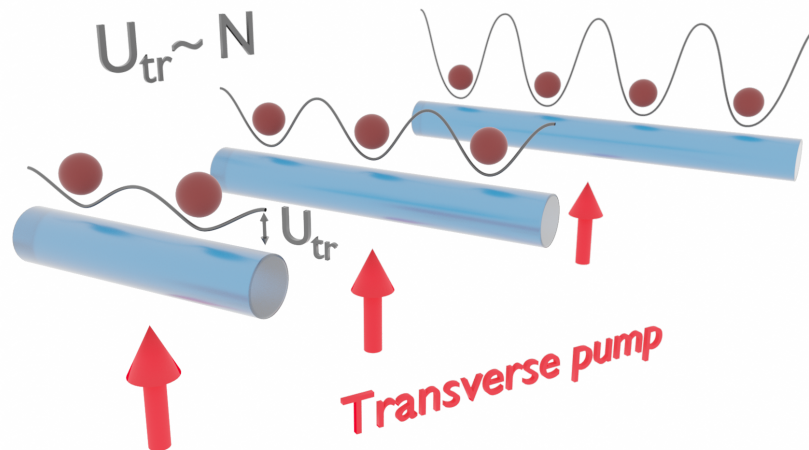


Figure 3.1 — The main concept of this chapter

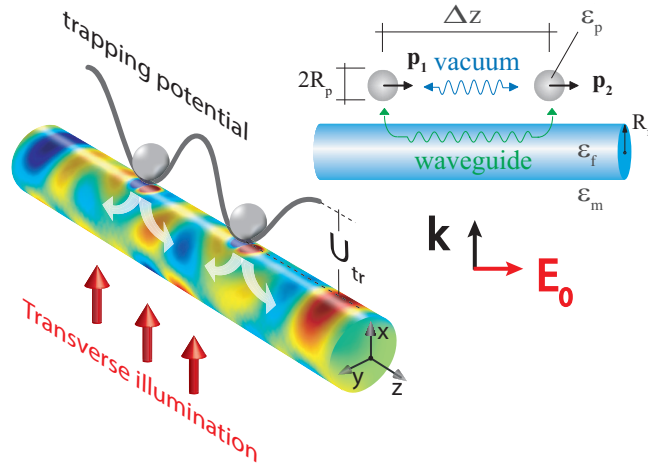


Figure 3.2 — The configuration of the system, which allows to achieve the stable binding of nanoparticles near the nanofiber in all 3 axis. The nanofiber adds a long range interaction channel of interaction

tor which provides formation of the dipole trapping potential. This approach has been effectively used for manipulation of objects in different environment such as air, water, and vacuum. However, an alternative method of large ensembles manipulation and ordering bases on self-assembly approach [59]. The field intensity pattern forms due to rescattering of the optical fields by the objects resulting in effective dipole-dipole interactions and consequent structuring of large ensembles. A typical example of such effect is transverse optical binding [60; 61] where the nanoparticle can form bounded states under homogeneous illumination. Though the optical dipole-dipole interactions are quite weak, they can be enhanced and modified with auxiliary photonic structures [62] such as metamaterials [63; 64] and metasurfaces [65], plasmonic structures [66; 67] and metals [261], photonic crystal hollow fibers [68] as well as dielectric nanofibers [69]. Binding also can be enhanced by going beyond the dipole approximation using higher resonances [262]. The latter one represents a versatile platform [70] for studying light interaction with nanoparticles [71; 72] and atoms [73–75] placed close to its surface. Utilization of a single mode long-range dipole-dipole interactions provided by waveguiding systems has already been suggested for self-organization of atoms and nanoparticles in waveguiding systems [68; 76; 77].

We propose a geometry of an array of nanoparticles placed close to the ultra-thin fiber and illuminated by a plane wave propagating in the isotropic host media perpendicularly to the fiber axis as it is shown in Fig. 3.2. Such configuration allows to take the advantage of the transverse optical binding effect [61; 78]. The

binding happens due to the interference of the fields scattered by the nanoparticles, and it has been applied for self-organization of nanoparticle ensembles under the external monochromatic illumination [79–81], including particle binding near a metallic surface near surface plasmon polariton resonance (SPP) [82]. In the literature, a transverse binding has been observed in a large ensemble of dielectric sub-micron spheres [83] and nanowires [84; 85] with the strong collective interactions through the vacuum.

The nanofiber guided modes allow for accumulation of long-range interactions between distant nanoparticles due to their extremely low losses, which results in the increasing particles stiffness with the growth of the nanoparticle chain length. Moreover, in our particular geometry of binding near a nanofiber, we also suggest a trapping of the nanoparticles in the radial direction close to the fiber surface by using two counter propagating plane waves and taking the advantage of nanofiber photonic jet or lensing effect [86]. In this effect during the transverse excitation dielectric nanofiber start to act as focusing lens. Thus, we propose a geometry of the system that allows us to immediately test the claimed effect in a specific experimental setup using optical nanofibers.

3.2 Optical binding near a single-mode nanofiber

The average optical force acting on a single point electric dipole \mathbf{p} placed in local electric field \mathbf{E}_{loc} is given by [263; 264] $\mathbf{F} = \frac{1}{2} \sum_{i=x,y,z} \text{Re } p_i^* \nabla E_{\text{loc},i}$. The latter one contains the incident plane wave field \mathbf{E}_{inc} , the field scattered by the nanofiber \mathbf{E}_{sc} , and the field scattered by other nanoparticles \mathbf{E}_p . The dipole moment of n -th particle then is defined through the local field strength $\mathbf{p}_i = \boldsymbol{\alpha}_0 \mathbf{E}_{\text{loc}}(\mathbf{r}_i) = \boldsymbol{\alpha}_0 (\mathbf{E}_0(\mathbf{r}_i) + \mathbf{E}_p(\mathbf{r}_i))$, where we defined $\mathbf{E}_0 = \mathbf{E}_{\text{inc}} + \mathbf{E}_{\text{sc}}$ as the external field, and $\boldsymbol{\alpha}_0$ is the exact dipole polarizability given by the Mie theory [265] (see Appendix B). The dipole field \mathbf{E}_p is the field generated by all other nanoparticles and can be expressed via Green's tensor formalism. For example, the field generated by the i -th particle at the position of j -th particle has the form $\mathbf{E}_{p,ij} = k_0^2 / \epsilon_0 \mathcal{G}(\mathbf{r}_i, \mathbf{r}_j) \mathbf{p}_j$, where $\hat{\mathbf{G}} = \hat{\mathbf{G}}_0 + \hat{\mathbf{G}}_s$ is the total Green's tensor which consists of two parts: free-space $\hat{\mathbf{G}}_0$ and scattered $\hat{\mathbf{G}}_s$, which appears due to the presence of the nanofiber (see Appendix C). Here k_0 is the vacuum wavenumber and ϵ_0 is the vacuum permittivity.

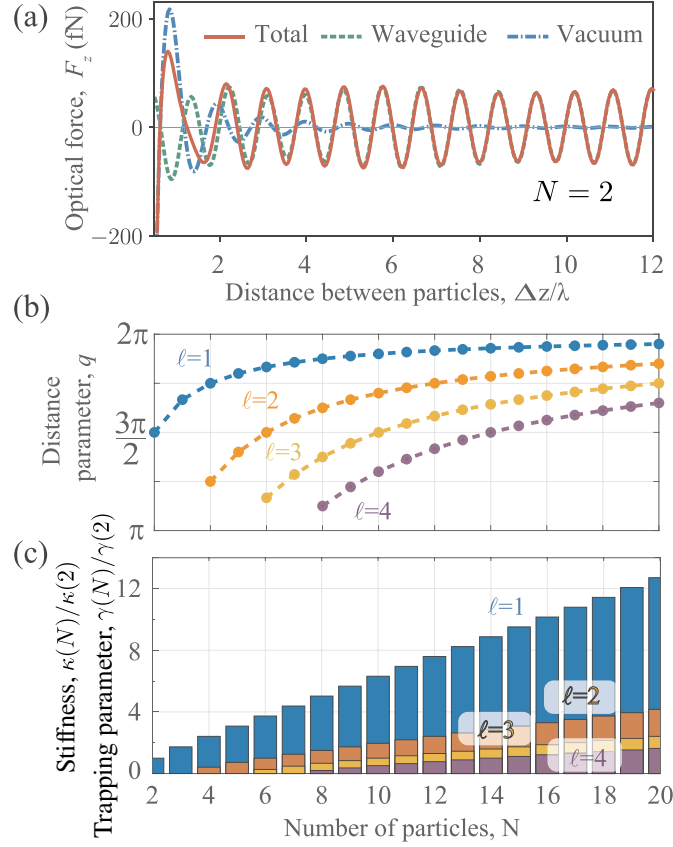


Figure 3.3 — (a) Longitudinal force F_z in a single mode regime acting on one of two particles as a function of distance along the nanofiber axis Δz . Red solid line shows total optical force which takes into account interaction through both free space and fiber ($\hat{\mathbf{G}}_s + \hat{\mathbf{G}}_0$), green dashed line shows only interaction through the fiber ($\hat{\mathbf{G}}_s$) and blue dash-and-dot line shows only free space interaction ($\hat{\mathbf{G}}_0$). (b) Equilibrium solutions. First three branches of the solution for the distance between the two closest particles $q = \Delta z\beta$ with respect to the total number of particles in a chain N . (c) Trapping parameter γ , which equals to the effective potential depth of the trap divided by a thermal energy of the host media kT , and normalized stiffness of the trap with respect to the number of particles in a chain N

The radius of a nanofiber can be chosen sufficiently small such that it supports only a single guided HE₁₁ mode [266] (SM-single mode regime). In this case we can expect almost periodical interaction strength between the nanoparticles with the inter-particle distance Δz . Indeed, in Fig. 3.3 a) the force between two nanoparticles that are located close to the nanofiber is shown as a function of the distance between them. The contributions of vacuum and nanofiber interaction channels are extracted by proper choosing the free-space $\hat{\mathbf{G}}_0$ or scattered $\hat{\mathbf{G}}_s$ part of Green's function. It can be seen that the force has a well-defined periodic character, which makes it possible to form a stable configuration of a system consisting of an arbitrary number of particles [77; 267]. The calculation of the optical force between the two particles was also performed using a complete numerical model in COMSOL Multiphysics, and a good agreement was obtained with the analytical dipole model (sec. 3.7).

In a single mode regime the Green's function of the waveguide can be reduced to $\hat{\mathbf{G}}_s^{\text{wg}}(\mathbf{r}; \mathbf{r}') = \hat{\mathcal{G}}_s^{\text{wg}}(\rho, \varphi; \rho', \varphi')e^{i\beta|\Delta z|}$, and $\hat{\mathbf{G}}_s^{\text{wg}}(\mathbf{r}; \mathbf{r})$ is purely imaginary for any waveguiding mode [268]. Here we neglect the contribution of the evanescent and leaky modes [266], since they fade significantly over long distances. In the field of a plane wave incident perpendicular to the nanofiber and polarized along the z axis (polarized TM), as shown in Fig. 3.2, the dipole moments will be aligned preferably along the nanofiber axis, thus having a dominant p_z -component, so $\mathbf{p}_i \approx \mathbf{n}_z p_i = \mathbf{n}_z \alpha_{\text{eff},zz} E_{0,z}$, (sec. D). TM excitation makes it possible to suppress the vacuum interaction channel, since the dipole emission along the nanofiber axis is weak. The force acting on a particle with the number n can be estimated as:

$$F_n^{\text{SM}} = \frac{|p|^2 k_0^3 \beta}{2\epsilon_0} \text{Im}(g_{zz}) \sum_{j \neq n}^N \cos(\beta|z_n - z_j|) \text{sign}(j - n). \quad (3.1)$$

Here N is the total number of particles in the chain, and we introduced the coupling constant $g_{zz}(\rho) = \hat{\mathcal{G}}_{s,zz}^{\text{wg}}(\rho, \varphi; \rho, \varphi)/k_0$, which depends only on the radial distance to the nanoparticle center in the geometry shown in Fig. 3.2. Within the framework of the considered approximations, the system has a stable equidistant configuration in which the distance between neighboring nanoparticles is constant [267]. In order to find it, one needs also to estimate the stiffness parameter κ , which determines the strength of the restoring force $F_z = -\kappa(z - z_0)$ acting on a single particle close to the equilibrium position z_0 . This approach is valid because the non-conservative part of the binding optical force is negligible. A stable configuration of

nanoparticles is observed if the separation distance between neighboring nanoparticles satisfies two conditions: (i) $F_{n,z} \propto \sum_{j \neq n}^N \cos(q|n-j|) \text{sign}(j-n) = 0$ and (ii) $\kappa_n \propto -\sum_{j \neq n}^N \sin(q|n-j|) > 0$ for all particles. Here $q = \beta \Delta z$ is the distance parameter and Δz is the distance between the neighbouring nanoparticles. After taking the sum in Eq. (3.1), the first condition provides us with the expression for the equidistant solution $Nq/2 = \pi/2 + \pi(N-\ell)$, where ℓ is an integer.

The stiffness of the n -th trap $\kappa_n = -\partial_{z_n} F_z$ in the chain of N particles can be estimated as follows:

$$\kappa_n^{\text{SM}} = -\frac{|p|^2 k_0^3 \beta^2}{2\epsilon_0} \text{Im}(g_{zz}) \sum_{j \neq n}^N \sin(q|n-j|), \quad (3.2)$$

and the summation is taken in order to take into account the interaction with all the nanoparticles in the chain. The stability condition requires that κ_n be positive for any particle in the chain. The analytical solution of the algebraic system shows that there are many stable configurations.

The separation distance q is 2π periodic in SM regime, so we analyze only the fundamental solution, which is $0 < q < 2\pi$. The distance between the particles q , which corresponds to $\ell = 1$, has a distance parameter [77] $q_1 = 2\pi - \pi/N$ (see the blue line in Fig. 3.3 (b)). Moreover, the stiffness parameter $\kappa_n = \kappa(N)$ is the same for any particle in the chain and increases with the total number of particles in the chain as $\kappa(N) \sim \text{ctg}(\pi/2N)$, which for $N \gg 1$ provides a linear increase in stiffness $\kappa(N) \sim N$, as shown in Fig. 3.3 (c). Other stable equidistant configurations correspond to other values of ℓ and have larger distance parameter $q = 2\pi - \ell\pi/N$, $\ell = 1, 2, \dots$ and $\ell \leq N/2$, as shown in Fig. 3.3 b) for $\ell = 2, 3, 4$. The κ_n values for these solutions also demonstrate the linear growth with N , however, with a smaller slope than for $\ell = 1$ (see Fig. 3.3 (c)).

3.3 Stability of the trapping

An increase in the stiffness of each nanoparticle trap mainly leads to an increase in the stability of the chain, which can be expressed in terms of the capture parameter $\gamma_{\text{tr}} = U_{\text{tr}}/kT$, where U_{tr} is the trapping potential separating the stable and unstable positions of each particle in the chain. It can be expressed as

Table 4 — Proposed system parameters

Parameter	Symbol	SM	MM
Fiber radius	R_f	300 nm	1000 nm
Wavelength	λ_0	1064 nm	
Particle radius	R_p	150 nm	
V -number	V	1.860	6.201
Distance to the fiber	d	45 nm	50 nm
Pump power	P	40 mW/ μm^2	
Pump field magnitude	E_0	$2.45 \cdot 10^6$ V/m	
Permittivity of	media	fiber	particle
	$\epsilon_m = 1$	$\epsilon_f = 1.45^2$	$\epsilon_p = 2.5$

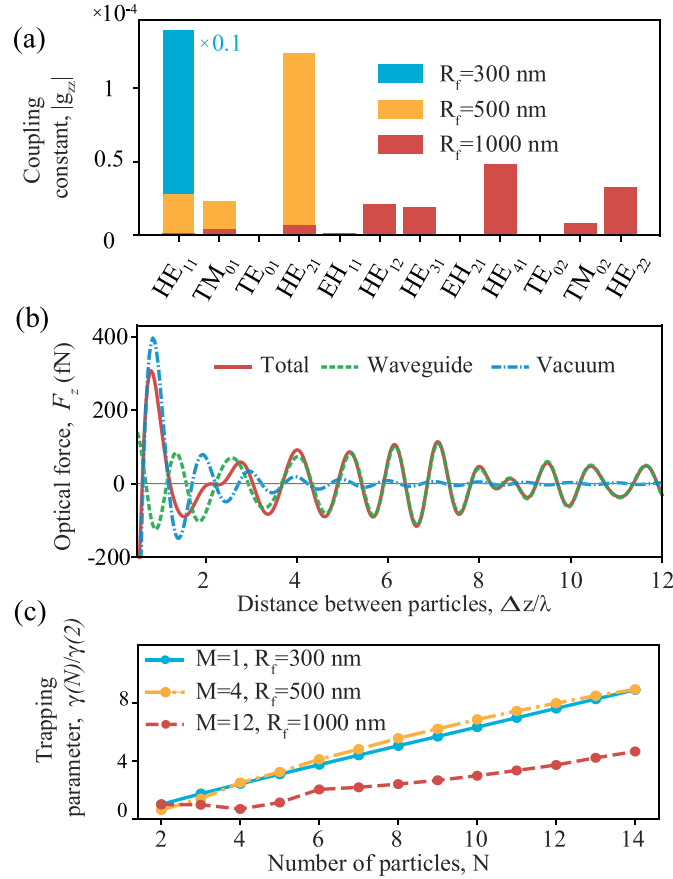


Figure 3.4 — (a) The amplitude of the coupling constant g_{zz} for different modes in single mode and multi-mode regimes for three different fiber radii: $R_f = 300, 500, 1000$ nm. (b) Longitudinal optical force F_z acting on one of the particles as a function of distance between the particles along the fiber axis Δz for multi-mode regime $R_f = 1000$ nm. (c) The trapping parameter of nanoparticles in a stable equidistant states as a function of the number of particles in multi-mode regime

$U_{\text{tr}}(N) = \kappa(N)\Delta(\pi/\beta)^2/2$, where π/β is the half distance between particles in the limit $N \gg 1$ and for $\ell = 1$. The trapping potential for the fundamental configuration with $\ell = 1$ then can be estimated in the single mode approximation as follows:

$$\gamma_{\text{tr}}^{\text{SM}}(N) = \frac{\pi^2 k_0^3 |p|^2}{4kT\epsilon_0} \text{Im}(g_{zz}^{\text{wg}}) \text{ctg}\left(\frac{\pi}{2N}\right) \propto N \quad (\text{for } N \gg 1). \quad (3.3)$$

This expression is one of the main results of the work, showing that the stability of the system under consideration increases linearly with an increase in the number of nanoparticles in the chain. This basically means that the self-ordering of nanoparticles in a longer chain will be more preferable and is actually limited only by the width of the exciting laser beam and the intensity of the light, since $\gamma_{\text{tr}} \sim |p|^2 \sim |E_0|^2$.

To confirm our analytical results and estimate the achievable values of the trapping potential, we used a complete model describing interacting dielectric nanoparticles located close to the nanofiber. We took into account the plane wave rescattering on the nanofiber, the nanoparticles self-polarization effect due to the nanofiber presence, as well nanoparticle cross polarization effects. For the set of parameters close to the experimental ones[269] and summarized in Table 4, the calculations give us the estimation of the binding parameter for two nanoparticles $\gamma(2) \approx 9$ at room temperature, which is a promising value for a potential experimental applications. Moreover, according to Fig. 3.3 in the chain consisting of $N = 20$ nanoparticles in the fundamental configuration one can expect $\gamma(20) \approx 110$, i.e. the trapping potential can be two-orders of magnitude higher than kT .

3.4 Nanoparticle binding in a multi-mode regime

With an increase in the radius of the nanofiber, the number of waveguide modes begins to increase rapidly, which significantly changes the picture of the interaction of nanoparticles. The coupling constants for each mode are shown in Fig. 3.4 (a). It can be seen that higher modes give a greater contribution to the coupling constant, since their penetration of the field beyond the waveguide is stronger. Simultaneous excitation of different modes provides a periodic interaction potential between two particles. Our computational model allows for a full modelling of multi-mode (MM) interaction between the nanoparticles, and the computed optical binding force is shown in Fig. 3.4 (b) for the parameters specified in Table 4. Our estimations of

the trapping parameter for MM regime give the value of $\gamma_{\text{tr}}^{\text{MM}}(2) \approx 13$ for the room temperature, which is higher than in a single mode regime due to larger number of modes and their stronger field penetration outside the waveguide [270].

Despite the aperiodic interaction, one still can expect the effect of self-induced organization of nanoparticles via transverse binding. In the MM regime Eq. (3.2) will gain another sum over many interaction channels corresponding to different waveguide modes:

$$\kappa_n^{\text{MM}} = -\frac{1}{2}|p|^2 \frac{k_0^3}{\epsilon_0} \sum_{\mu=1}^M \beta_{\mu}^2 \text{Im} \{g_{zz}^{\beta_{\mu}}\} \text{Im} \sum_{j=1}^N e^{i\beta_{\mu}|z_n - z_j|}, \quad (3.4)$$

where $\beta_{\mu} = \beta_{\text{HE}_{11}}, \beta_{\text{TM}_{01}}, \dots$ are the propagation constants of the allowed modes (see the dispersion curve in Fig. 1 in Supplementary materials), and M defines the number of the allowed waveguide modes. The stable configuration of the nanoparticle chain can be found through the maximization of Eq. (3.4). We applied a numerical optimization algorithm with proper constrains ($\kappa_n > 0$, $F_{n,z} = 0$ for any n) to identify the nanoparticles configuration and the stiffness of the trap. The optimization procedure started by a configuration of ordered chain separated with the distance $\Delta z \beta_{\text{max}} = 4\pi - \pi/N$, where β_{max} is the propagation constant corresponding to the dominant mode among all the excited ones (HE_{21} and HE_{41} for $R_f = 500$ nm and $R_f = 1000$ nm, respectively). The final result after the optimization procedure is the trapping parameter $\langle \gamma \rangle$ averaged over particles presented in Fig. 3.4 c). It can be seen that the system demonstrates a stable configuration in which the averaged capture parameter increases linearly with the size of N , similar to the case of SM.

3.5 Radial and azimuthal binding of nanoparticles

Finally, it is worth speculating about the potential mechanisms of capturing nanoparticles near the surface of nanofibers. We have not yet discussed the remaining two degrees of freedom of a nanoparticle: *radial* and *azimuthal*. It is known that particle can easily experience orbital motion around the nanofiber [271] and we need to embrace this motion as well. Illumination of the nanofiber by a plane wave forms an interference pattern in the vicinity of the nanofiber [86], which can act as a trapping potential for nanoparticles. However, single-laser illumination also provides a

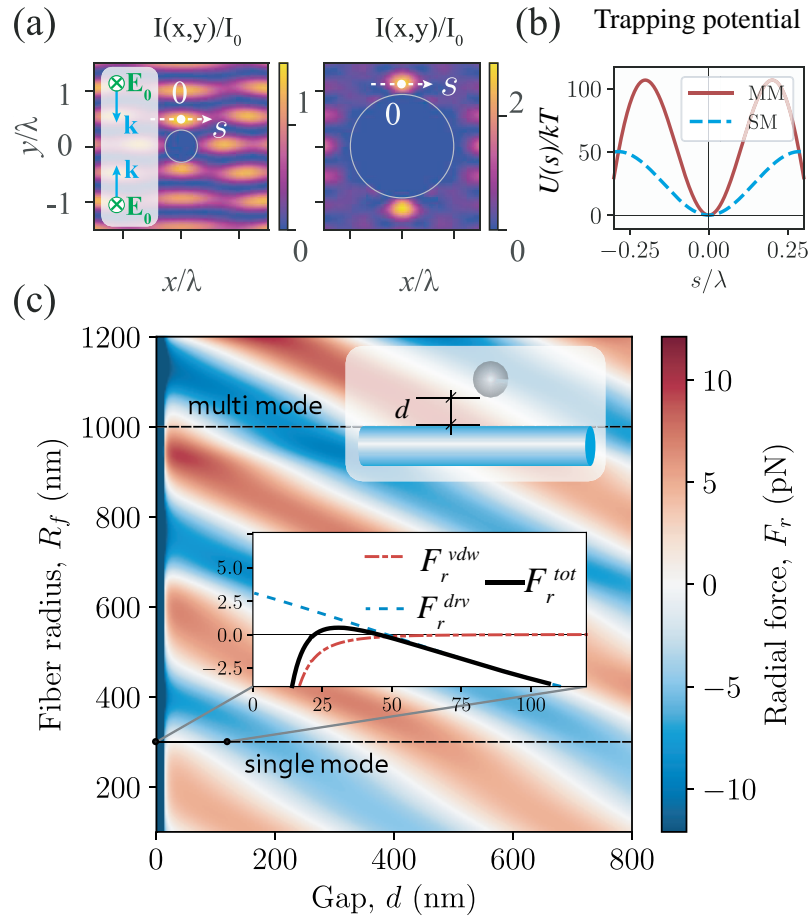


Figure 3.5 — (a) Normalized intensity of the total electric field for two different fiber radii: $R_f = 300$ nm and $R_f = 1000$ nm. (b) Potential energy of the transverse trap along the x axis normalized by kT . (c) Total radial force as a function of two parameters: the fiber radius R_f and the gap between fiber surface and particle's surface d . Two horizontal dashed black lines correspond to single mode and multi-mode fiber radii in Table 4. Inset: the force decomposition into optical force and van-der-Waals force. The equilibrium distances for single mode and multi-mode regimes are $d^{\text{SM}} = 45$ nm and $d^{\text{MM}} = 50$ nm

strong optical pressure acting on the particles, which prevents effective capture in the radial direction. We propose a geometry with two counter-propagating interfering beams that fully compensate for the optical pressure force and ensure strong binding of nanoparticles near the surface of the nanofiber. The formed potential trap provides both radial and azimuthal stability of nanoparticles. In Fig 3.5 (a) the field intensity distribution normalized by the intensity of the plane wave is shown around the SM and MM nanofibers providing stability of nanoparticles in the trap in the transverse direction along the s -axis. The trapping parameter cross section is depicted in Fig. 3.5 (b) demonstrating the values of 50 and 100 for a SM and MM nanofiber, respectively.

The radial stability of the particles is studied in Fig. 3.5 (c), where the radial force acting on the particle is shown as a function of the fiber-particle gap d and fiber radius R_f . Total radial force also includes the contribution from the van-der-Waals attractive force [272] \mathbf{F}^{vdW} , along with the driving force \mathbf{F}^{drv} . The white areas on the 2D map correspond to areas of zero optical strength and, thus, areas of radially stable configurations where the force changes sign from positive to negative with increasing clearance. Two dotted lines indicate the radii of the nanofibers SM and MM. In Fig. 3.5 (c) inset the cross section of the total radial force is shown for SM regime, demonstrating that a stable point at the gap distance of 45 nm can be achieved. Finally, it should be noted that by adding a phase difference between interfering beams propagating up and down, it is possible to gradually change the radial capture potential and fine-tune the position of radially stable points.

3.6 Two beam trapping by phase tuning

Using two beams instead of one gives several advantages. Firstly, the second beam suppresses the scattering pressure, which is able to overcome the gradient part of the force in the case of single-beam transverse pumping. Secondly, by adjusting the relative phase shift between two counter-propagating perpendicular beams, we can change the position of nodes and antinodes and, consequently, the position of the radial trapping (see Fig. 3.6).

3.7 Validity of the dipole model

Depending of the size parameter $x = k_p R_p = \sqrt{\epsilon_p} k_0 R_p$ a spherical particle can support different electric and magnetic modes [97] (dipole, quadrupole, octupole, etc) — the higher x , the richer multipole physics starts to play. The limit $x \ll 1$ stands for the pure dipole approximation, otherwise careful investigation is necessary. For each *multipole* it is possible to introduce polarizability. Particle response is defined by its scattering coefficients (Mie coefficients). Each Mie coefficient a_n

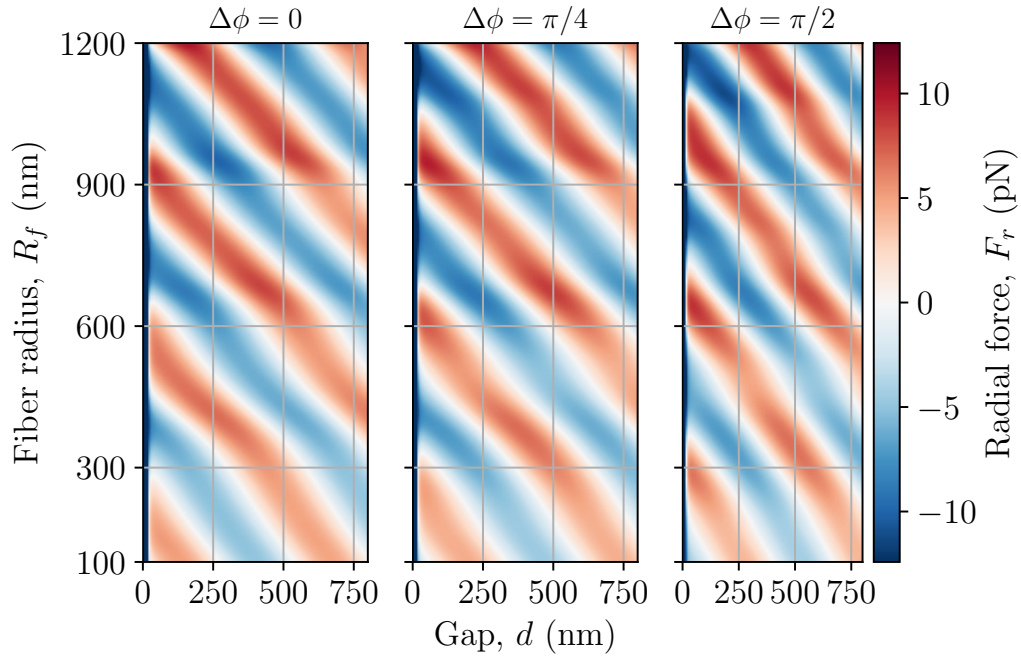


Figure 3.6 — The total radial force acting on a particle for the configuration of two oncoming beams depends on two parameters: the radius of the fiber and the gap between the fiber surface and the particle surface. A sequence of graphs for different phase shifts between two beams is shown, constructed to show how the equilibrium capture distance can be adjusted

(electric) and b_n (magnetic) is directly proportional with n -polar electric or magnetic polarizability [147].

It means that to estimate multipolar content of the particle it is sufficient to look only at the scattering coefficients and compare its magnitudes. From Fig. 3.7 one can note that electric dipole scattering coefficient a_1 dominates at the parameters of our choice.

To verify our dipole model we compared it with an exact numerical simulations performed in COMSOL Multiphysics. With the range of our parameters we got a very fine agreement between full numerical solution and dipole analytical model which is shown on Fig. 3.8.

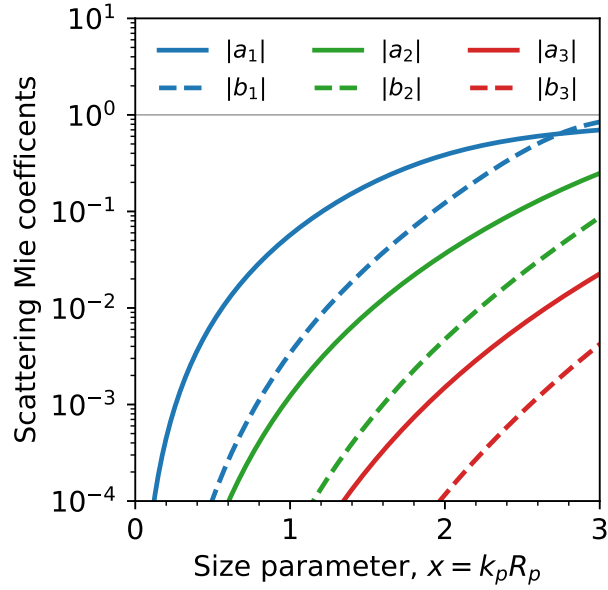


Figure 3.7 — First 3 electric a_n and magnetic b_n scattering Mie coefficients as a function of size parameter x . For the parameters of our choice we have $x \approx 1.4$ and dipole scattering coefficient $|a_1|$ dominates. Since n -polar polarizability is connected with n -th scattering coefficient, incident field mainly induce only dipole moment.

Here $k_p = \sqrt{\epsilon_p} k_0 = \sqrt{2.5} \frac{2\pi}{1064 \text{ nm}}$ and for $R_p = 150 \text{ nm}$ we have $x \approx 1.4$

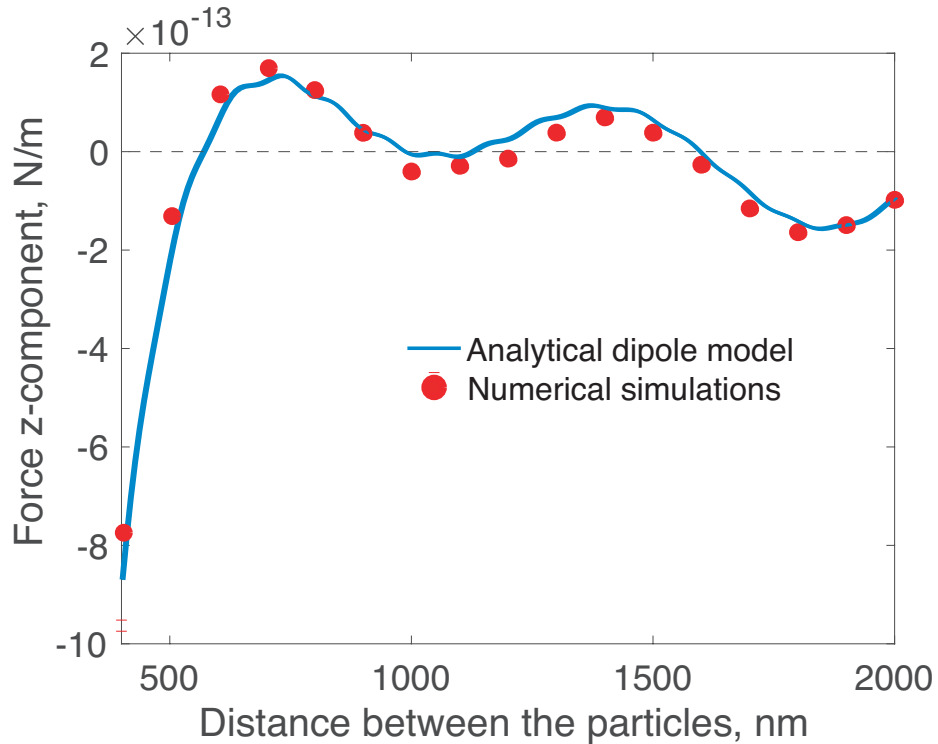


Figure 3.8 — Optical binding force between two particles with $R_p = 50 \text{ nm}$ over a single-mode $R_f = 300 \text{ nm}$ nanofiber under transverse pump illumination. Successful comparison of the full numerical solution and analytical dipole model

3.8 A scientific statement

First scientific statement

An array of subwavelength particles above the waveguide can form a stable in-line configuration in the field of a linearly polarized plane wave incident perpendicular to the waveguide axis. The binding stiffness between particles increases linearly with the number of particles.

Chapter 4. Spin and orbital momenta transfer from light to nanoparticles

In this chapter we are going to focus on the transfer of angular momenta of light from nanophotonics structures to matter. It is known that total angular momenta \mathbf{J} can be decomposed into the sum of spin and orbital components

$$\mathbf{J} = \mathbf{S} + \mathbf{L} \quad (4.1)$$

where \mathbf{S} is the spin angular momentum density and \mathbf{L} is the orbital angular momentum density. These components are not always independent due to the spin-orbit interaction of light [273]. However, the mechanical action of each component can be quite distinct. For subwavelength particle the answer is going to be simple and clear

$$T_z \sim S_z, \quad T_z^{\text{orb}} = rF_\varphi \sim L_z \quad (4.2)$$

However, for the case of Mie particle that is not always the case. As we will show in 4.1 particle of a size comparable with the wavelength might experience negative orbital torque.

While we do not discuss beams light beams since it is a very broad topic and goes out of scope this thesis, we could recommend to read the following Refs. [274–278].

4.1 Orbital angular momenta transfer

The spin angular momentum (SAM) carried by paraxial light rays in free space can be transferred to a material object, causing it to rotate around its axis if the object is absorbing or anisotropic [279]. On the contrary, the orbital angular momentum (ON) in beams with optical vortices can even cause isotropic, non-absorbing particles to rotate [280; 281]. In nonparaxial light, SAM and OAM can couple, leading to, for example, orbiting of isotropic particles trapped by a tightly focused, nonvortex beam [282] and to observable, spin-dependent, transverse shifts of the light itself [283; 284]. Symmetry breaking in a system consisting of a scattering particle at the interface between two media, under oblique illumination, produces an fascinating spin-dependent optomechanical effect [285].

The evanescent electromagnetic fields that accompany the total internal reflection and direction of light demonstrate even more complex spin–orbit interactions. In particular, in addition to the general axial SAM associated with polarization, such fields exhibit a SAM component perpendicular to the wave vector [286]. In addition, a material object in an evanescent field may experience a transverse force depending on light spin angular density, as demonstrated experimentally by means of a nanocantilever [287] or an optically trapped Mie scattering particle [288] placed near a total internal reflecting glass surface.

The evanescent field around an optical nanofiber [289] guiding a quasi-circularly polarized fundamental mode is also expected to carry significant OAM that is transferable to material objects [290]. In spite of numerous demonstrations of particle trapping, propulsion [260; 291; 292], and binding [293; 294] in the vicinity of optical nanofibers, orbital motion of particles in such systems has never been reported in the literature. The main reason for this lack of experimental evidence was the uncertainty about the polarization of light at the waist of a nanofiber waveguide. This uncertainty has been lifted only recently [295–297]. In this chapter, we present a demonstration of the SAM-dependent optical torque by means of light-induced rotation of isotropic microspheres around a single-mode optical nanofiber.

Let us start with a spherical, dielectric particle (of radius R_p) which is placed in the evanescent field of a single–mode optical fiber (of radius R_f), as shown in Fig. 4.1(a). The electric field of an *elliptically* polarized guided mode is given by

$$\mathcal{E} = \left(\sqrt{1 + \sigma} \mathcal{E}_{p=+1} + e^{i\varphi} \sqrt{1 - \sigma} \mathcal{E}_{p=-1} \right) / \sqrt{2} \quad (4.3)$$

where $\sigma \in [-1, 1]$ is the helicity parameter [284], $\varphi \in [0, 2\pi]$ determines the orientation of the symmetry axes of the polarization ellipse in the xy plane, and $\mathcal{E}_p = (e_r \hat{\mathbf{r}} + p e_\varphi \hat{\boldsymbol{\phi}} + e_z \hat{\mathbf{z}}) e^{i\beta z - ip\varphi}$ is the electric part of the *quasi-circularly* polarized guided mode with a polarization rotation index $p = \sigma/|\sigma| = \pm 1$ [298]. Here, β is the propagation constant, and e_r , e_φ , and e_z are the cylindrical components of the mode-profile function of \mathcal{E}_p with $p = +1$. The azimuthal component of the Poynting vector of the elliptically polarized guided mode is $\Pi_\varphi = \sigma (e_z h_r^* - e_r h_z^*) / 2$ where h_r and h_z are the components of the mode-profile function of the magnetic part, \mathcal{H}_p , of the guided mode with the polarization index $p = +1$. Since the longitudinal field components, e_z and h_z , are nonzero, we have $\Pi_\varphi^{(p)} \equiv \Pi_\varphi|_{\sigma=p} = p (e_z h_r^* - e_r h_z^*) / 2 \neq 0$. It has been shown that $\Pi_\varphi^{(p=+1)} > 0$ and $\Pi_\varphi^{(p=-1)} < 0$ outside the nanofiber [284].

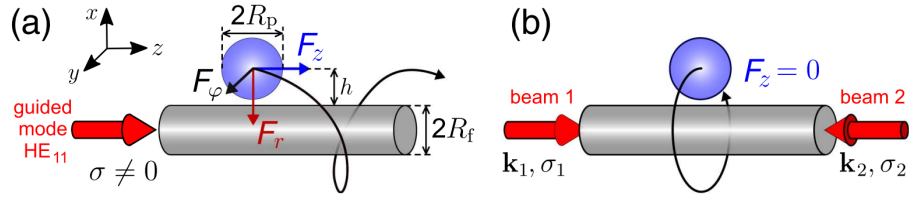


Figure 4.1 — (a) Isotropic, lossless dielectric particle in the evanescent field of an elliptically polarized, fundamental mode of an optical nanofiber. Due to the non-zero azimuthal component of optical force, F_ϕ , the particle can rotate around the fiber. (b) We eliminate axial motion by using two oncoming beams with the same intensity profiles and opposite helicities, $\sigma_1 = -\sigma_2$

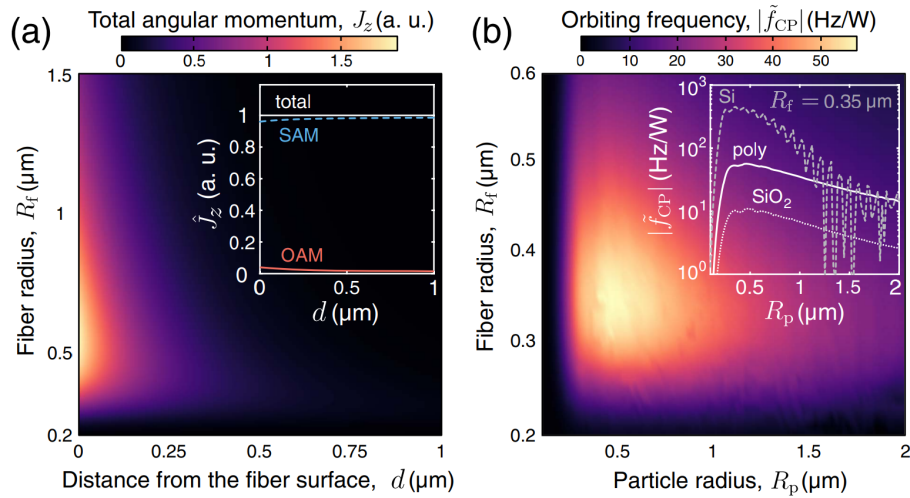


Figure 4.2 — Simulation results. (a) Density of the total angular momentum of light near a nanofiber (in water) guiding a fundamental mode with $\sigma = 1$. Inset shows total angular momentum normalized per photon and its spin and orbital contributions. (b) The orbiting frequency for a polystyrene particle, as a function of particle and fiber radii. Inset shows frequency at the optimum fiber radius ($R_f = 0.35 \mu\text{m}$) for three different particle materials: silica, silicon, and polystyrene

The force and torque induced by light on any object can be calculated if you know exactly the incident and scattered electromagnetic waves. In our problem, the incident wave (here, the evanescent field) is well known [235]. In order to approach to this problem semi-analytically, we implement the generalized Lorenz-Mie theory: in incident field can be decomposed into series of *vector spherical harmonics*, and the scattered fields are found by proper application of boundary conditions [299; 300]. Therefore, the force and torque, respectively, can be found by integrating the linear and angular momentum fluxes over the surface enclosing the object. Note that, although the Lorenz-Mie Theory is a generally accepted and fairly accurate semi-analytical approach to optomechanical calculations, it does not take into account multiple re-scattering in the light-matter system.

The optical force exerted on a scattering particle near a nanofiber can be decomposed into the longitudinal (F_z), radial (F_r), and azimuthal (F_φ) components [298] (see Fig. 4.1(a)). Under F_r , the particle is attracted to the fiber surface and stays at $r = \sqrt{x^2 + y^2} \geq (R_f + R_p)$ (the inequality being due to surface roughness and Brownian motion). Here, we aim at detection of the azimuthal force, F_φ , which sets the particle into orbital motion around the fiber. Since Brownian motion disrupts the mechanical contact between the particle and the fiber, it is expected that the contribution of the light-induced rotation of the particle to its azimuthal motion will be insignificant. According to our calculations, azimuthal component F_φ is much smaller than the longitudinal one, F_z . In order to study the azimuthal motion only, we eliminate the axial motion by launching a second counter-propagating HE₁₁ with a power equal to that of the initial mode (see Fig. 4.1(b)).

In principle, the rotation under F_φ could be studied if beam 1 were elliptically polarized ($\sigma_1 = \sigma \neq 0$) and beam 2 were linearly polarized ($\sigma_2 = 0$). However, such a beam 2 would produce an axially *asymmetric* intensity mode profile [301], and the particle would want to stop at the “hot spots” unless $|\sigma_1| \approx 1$. Since we consider all possible values of σ , we set the polarization of beam 2 to be also elliptical, with $\sigma_2 = -\sigma_1$. In such case, the total azimuthal force is the sum of the contributions from these two beams.

Once F_φ is known, the orbiting frequency of the particle at equilibrium can be easily calculated from the force balance equation, $F_\varphi + F_{\text{fr}} = 0$, where F_{fr} is the friction. In our experiments, the particle is immersed in water, which produces a friction of $F_{\text{fr}} = -\gamma v$, where v is the linear velocity of the particle’s center, and γ is the drag coefficient. As demonstrated by Marchington et al. [302], an appropriate

description of the friction for a microsphere in the evanescent field can be obtained using the lubrication correction [303] $\gamma = \gamma_0 [(8/15) \ln(h/R_p - 1) - 0.9588]$, where $\gamma_0 = 6\pi\eta R_p$ is the Stokes drag, η is the dynamic viscosity of the fluid ($\eta \approx 1$ mPas for water at room temperature), and the distance $h = r - R_f$ [see Fig. 4.1(a)] depends on the particle surface roughness. We note that the above formula for γ is valid only for large enough particles, $R_p > 0.25 \mu\text{m}$ [303]. The absolute value of the particle rotation frequency around a fiber when both beams are circularly polarized (CP) can thus be expressed as

$$|f_{\text{CP}}| = \frac{|v|}{2\pi(h + R_f)} = \frac{|F_\varphi|}{2\pi\gamma(h + R_f)}. \quad (4.4)$$

As follows from our simulations, in the general case of elliptical polarization (EP), the azimuthal force and the corresponding frequency, f_{EP} , are proportional to $\sigma = \sigma_1$, with opposite signs:

$$f_{\text{EP}} = -\sigma |f_{\text{CP}}|. \quad (4.5)$$

This result is consistent with the theoretical findings of Le Kien and Rauschenbeutel [298], for the relevant range of the size parameter, $n_m k R_p$, where n_m is the refractive index of the medium. For convenience, we normalize the rotation frequency by the total optical power, P .

Our theoretical findings are summarized in Fig. 4.2, where J_z is the z component of the total angular momentum carried by the field near an optical nanofiber. In order to better understand the structure of angular momentum, we calculated the SAM and OAM densities [see the inset in Fig. 4.2(a)] using the canonical expressions [45; 170]. Although most of J_z includes the spin part, both components of the total angular momentum can contribute to the orbital motion of particles near the nanofiber [241]. As shown in Fig. 4.2(b), the orbital frequency is expected to reach approximately 56 Hz/W for a polystyrene particle with a 1- μm diameter. As can be seen in the insert, the maximum frequency depends on the refractive index: it is equal to 11 Hz/W for silicon dioxide ($n = 1.45$) and 450 Hz/W for silicon ($n = 3.67$). In practice, one should also take into account Brownian motion, which is inversely proportional to R_p : smaller particles will exhibit longer thermal displacements and, consequently, weaker interaction with the damped field, which decreases sharply with distance from the fiber, d . As a reasonable compromise, we decided to use polystyrene spheres with a radius of $R_p = 1.5 \mu\text{m}$. For this parameters, the expected frequency for CP incident field is $\left| \tilde{f}_{\text{CP}} \right| \approx 21.3 \text{ Hz/W}$.

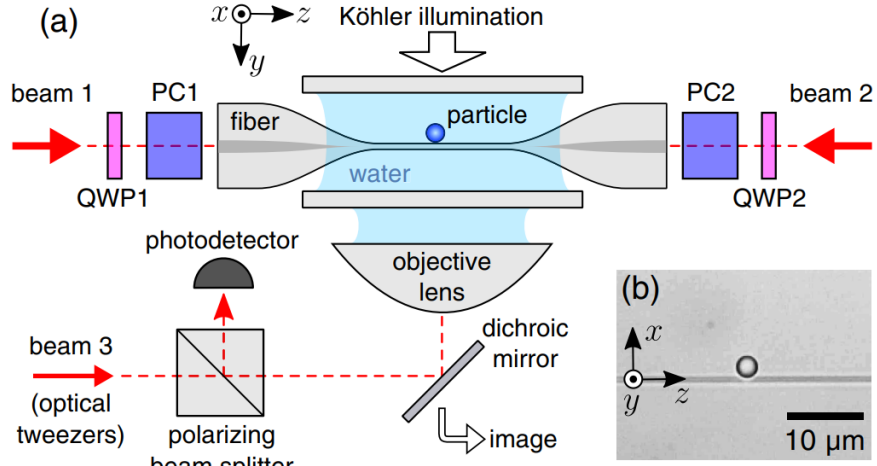


Figure 4.3 — (a) Experimental setup (not to scale): once the polarization transformations in the tapered fiber are reversed by the polarization compensators, PC1 and PC2, we set the values of σ_1 and $\sigma_2 = -\sigma_1$, by rotating the quarter-wave plates, QWP1 and QWP2. (b) Transmission image of a 3- μm polystyrene particle optically captured at the waist of a nanofiber

Our experimental setup is shown in Fig. 4.3(a). The nanofiber is made by controlled heating and pulling method [304]. The small tapering angles of 3 mrad provide adiabatic coupling [305; 306] between the fundamental modes in the fiber pigtailed and those in the 2-mm-long cylindrical waist region having a radius of $R_f = 0.33 \pm 0.04 \mu\text{m}$ (measured over a set of five nanofibers). The fiber pigtailed are coupled to laser beams 1 and 2 from the same source (Ventus, Laser Quantum Ltd., emission wavelength $\lambda = 1.064 \mu\text{m}$). The initial linear polarization of the beams (along x and y for beams 1 and 2, respectively) is changed into elliptical by means of two quarter-wave plates, QWP1 and QWP2, with their slow axes oriented at equal angles, $\theta_{\text{QWP1}} = \theta_{\text{QWP2}} = \theta$, with respect to x . This results in $\sigma = -S_3 = \sin 2\theta$, where S_3 is the third Stokes parameter in beam 1.

A nanofiber sample is immersed into 0.3 mL of deionized water with 3- μm polystyrene particles (Phosphorex, Inc.) and sandwiched between two glass cover slips separated by 1.5-mm-thick spacers. The sample is imaged by a video camera (DCC3240C by Thorlabs, Inc.) through a water-immersion objective lens (Zeiss Plan-Apochromat, 63 \times /1.00 w) under Köhler illumination [see Fig. 4.3(b)]. Individual particles are picked up from the bottom plate using optical tweezers, implemented by focusing a collimated beam 3 (from the same laser) using the same lens. The polarizing beam splitter cube transmits a y -polarized beam 3 and is

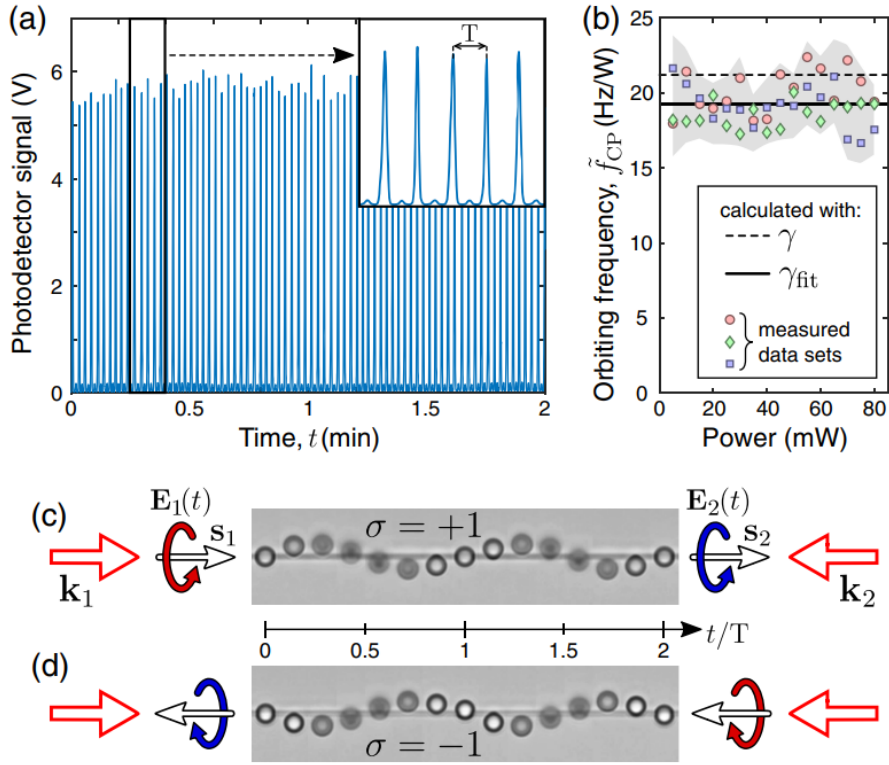


Figure 4.4 — Experimental results for a CP input (R = right, L = left). (a) Beatings in the detector signal acquired with an optical power of 15 mW in each beam. The zoomed-in view (inset) shows the local period, T . (b) Orbiting frequency versus power in each beam, at $\sigma = +1$. Markers: measured data sets for three samples; gray area: combined standard deviation range. Dashed line: frequency expected for the drag coefficient γ ; solid line: the best fit to the data with γ -fit. (c), (d) Time-lapse compilation of images for $\sigma = +1$ (c) and $\sigma = -1$ (d)

subsequently used to detect (PDA10A2 photodetector with Si amplification from Thorlabs, Inc.) laser light coming out of the nanofiber due to particle scattering.

Due to uncontrolled bends, twists or geometric inhomogeneities, the fiber does not support the polarization of directional light. To control the polarization state of the nanofiber waist, we reverse unknown polarization transformations for both beams using two free space compensators, PC1 and PC2. The compensation procedure described elsewhere [297] is based on self-scattering from the waist imaged by a second video camera, replacing the photodetector for this purpose.

The summary of experimental results for $|\sigma| = 1$ are shown in Fig. 4.4. The orbital motion of the particle around the fiber causes clear quasi-periodic fluctuations of the measured voltage [see Fig. 4.4(a)]. The orbiting frequency, \tilde{f}_{CP} , scales linearly with optical power, as can be seen in Fig. 4.4(b) for three different nanofibers. The

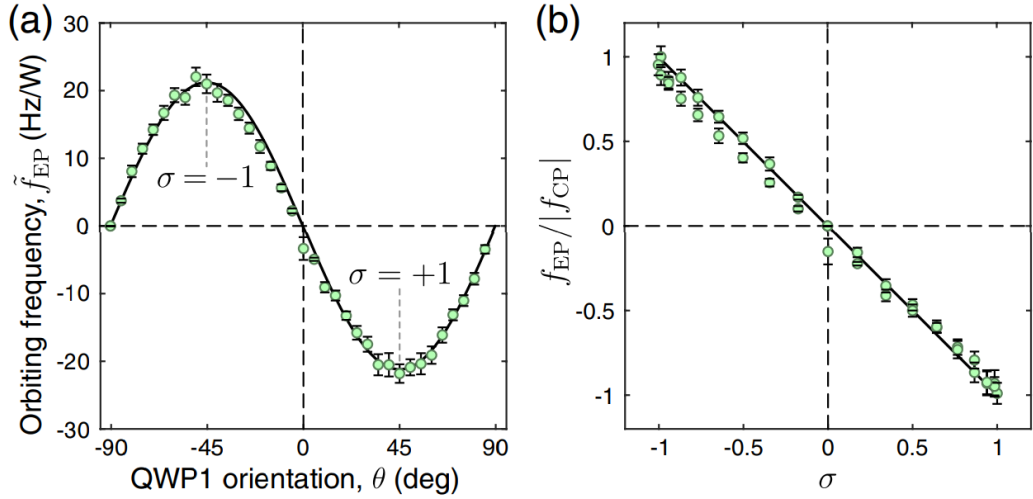


Figure 4.5 — Experimental results: (a) dependence of the measured orbiting frequency as a function of QWP1 orientation which controls the helicity and (b) the orbiting frequency versus the calculated helicity. Solid lines: simulation using Eq. (4.5), with $\sigma = \sin 2\theta$

data were fitted to Eq. (4.4) with an adjustable drag coefficient, γ -fit. The resulting frequency, \tilde{f}_{CP} , fit = 19.2 Hz/V, is about 9% lower than the expected value, a slight discrepancy, given the complexity of the hydrodynamic problem, the complete solution of which is beyond the scope of this study.

When the sign of σ is reversed, the particle rotates in the opposite direction, with nearly the same period, T (see visualizations in the Supplementary Materials to [307] and the corresponding time-lapse compilations of images in Figs. 4.4(c) and 4.4(d)), where $\mathbf{s}_{i=1,2} = \sigma_i \mathbf{k}_i / k_i$, and the curved arrows denote the rotation of the electric field vector, \mathbf{E} , in the xy plane for each beam, from the receiver’s point of view. These arrows also indicate the circulation direction of the energy flow (or Poynting vector) around the nanofiber [297].

The results for $\sigma \neq 1$ are summarized in Fig. 4.5, where solid lines show the simulated frequency, $\tilde{f}_{\text{EP}}(\sigma)$, and each error bar is the standard deviation range for at least $20T$ duration. Eqs. (4.5) and (4.4) were applied for this data set without any adjustable parameters. As one can see in Fig. 4.5(b), the transverse spin-dependent radiation force acting on the particle is proportional to the projection of SAM on the propagation direction, with opposite sign. The observed rotation caused by light is antiparallel to the azimuthal component of the Poynting vector around the nanofiber [297]. This counterintuitive “negative” radiation torque (OAM-induced) happens due to the dominant forward scattering. This is due to multipolar interfer-

ence when scattering from sufficiently large particles, $R_p > \lambda/(2\pi n_m) \approx 0.13 \mu\text{m}$. The related direct light scattering linked our results with previous demonstrations of the “negative” radiation forces [308–310].

Interestingly, σ affects not only the frequency, but also the trajectory of the particle. For CP input ($|\sigma| = 1$), it is close to a circle in the xy plane. When the polarization is elliptical ($|\sigma| < 1$), the trajectory takes the shape of an eight, with longer transitions along z for smaller $|\sigma|$. This distortion occurs due to the lack of axial symmetry in the intensity distribution for counter-propagating elliptically polarized modes [301]. Indeed, for the case of $|\sigma| \approx 0$, the intensity maxima for beams 1 and 2 are aligned parallel to the x and y axes, respectively. Therefore, the particle is pushed towards $z > 0$ or $z < 0$ when passing through the xz or yz planes.

4.2 A scientific statement

Second scientific statement

For an orbiting motion of particle around a dielectric waveguide in a viscous fluid induced by circular polarized fundamental mode there is an optimal particle radius for which orbiting frequency is maximal. The position of this maxima does not coincide with the maximum of the canonical total angular momentum density.

4.3 Spin angular momenta transfer

Now let us focus on the spin angular momenta transfer. In this section we will show that even if the particle is anisotropic, the rotational average spinning torque is also proportional to the spin angular momentum density.

4.3.1 Torque from the arbitrary polarized plane wave using Stokes parameters

The incoming wave is going to be written in the following form. We consider a polarized electromagnetic wave propagating along z -axis with the wave vector $k = \sqrt{\epsilon\mu}\frac{\omega}{c}$. The complex electric field can be written in Cartesian coordinates as

$$\mathbf{E} = E_0 \begin{pmatrix} e_x \\ e_y \\ 0 \end{pmatrix} e^{ikz}, \quad \mathbf{H} = \frac{E_0}{Z_0} \sqrt{\frac{\epsilon}{\mu}} \begin{pmatrix} -e_y \\ e_x \\ 0 \end{pmatrix} e^{ikz} \quad (4.6)$$

where $Z_0 = \sqrt{\mu_0/\epsilon_0}$ is the vacuum impedance and \mathbf{e} is the unit polarization vector. The reduced Stokes parameters [259] of the wave $s_i = S_i/S_0$ can be calculated as

$$s_1 = |e_x|^2 - |e_y|^2, \quad s_2 = 2 \operatorname{Re}(e_x^* e_y), \quad s_3 = 2 \operatorname{Im}(e_x^* e_y) \quad (4.7)$$

where $S_0 = |\mathbf{E}|^2$. The Stokes parameters are the measurable and convenient variables from the experimental perspective to identify the polarization of the beam, in contrast to the Jones vector [259].

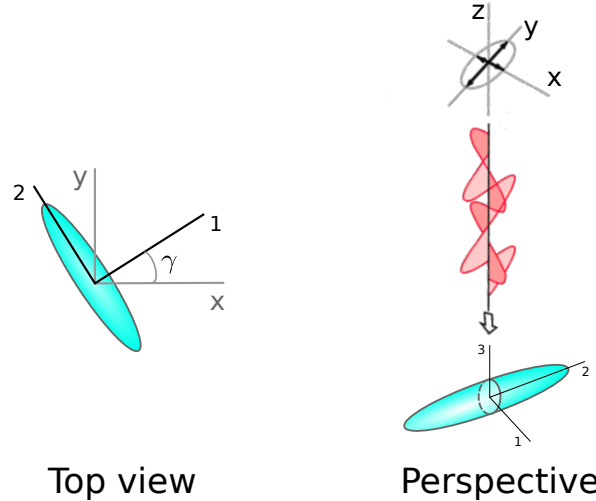


Figure 4.6 — Simple anisotropic particle in a field of an elliptically polarized light. Geometry of the problem. Blue ellipsoid represents the Fresnel ellipsoid

Next, we assume that the probe particle has anisotropy in the x - y plane as shown on Fig. 4.6. To write dipole moment in terms of polarizability $\mathbf{p} = \hat{\alpha}_e^{\text{cart}} \mathbf{E}$ and $\mathbf{m} = (\mu\mu_0)^{-1} \hat{\alpha}_m^{\text{cart}} \mathbf{H}$, we need to rotate to polarizability tensor $\hat{\alpha}$ to use it in Cartesian coordinates

$$\hat{\alpha}^{\text{cart}} = R(\gamma) \hat{\alpha} R^{-1}(\gamma), \quad (4.8)$$

where

$$R(\gamma) = \begin{pmatrix} \cos(\gamma) & -\sin(\gamma) & 0 \\ \sin(\gamma) & \cos(\gamma) & 0 \\ 0 & 0 & 1 \end{pmatrix}. \quad (4.9)$$

After some algebra we obtain $\mathbf{T} = (0, 0, T_z)^T$, where torque can be rewritten in terms of Stokes parameters (4.7) as

$$T_z = \frac{1}{2}E_0^2 \left[A_a^e - \frac{\varepsilon\varepsilon_0}{\mu\mu_0} A_a^m \right] \left(s_2 \cos(2\gamma) - s_1 \sin(2\gamma) \right) + \frac{1}{2}E_0^2 \left[A_s^e + \frac{\varepsilon\varepsilon_0}{\mu\mu_0} A_s^m \right] s_3, \quad (4.10)$$

where A_a^e and A_s^e ("a" for aligning and "s" for spinning) are the generalized anisotropic electric polarizabilities

$$A_a^e = \frac{1}{2} \operatorname{Re}(\alpha_1^e - \alpha_2^e) + \frac{k^3}{6\pi\varepsilon\varepsilon_0} \operatorname{Im}(\alpha_1^e \alpha_2^{e*}), \quad (4.11)$$

$$A_s^e = \frac{1}{2} \operatorname{Im}(\alpha_1^e + \alpha_2^e) - \frac{k^3}{6\pi\varepsilon\varepsilon_0} \operatorname{Re}(\alpha_1^e \alpha_2^{e*}) \quad (4.12)$$

and A_a^m and A_s^m are the generalized anisotropic magnetic polarizabilities

$$A_a^m = \frac{1}{2} \operatorname{Re}(\alpha_1^m - \alpha_2^m) + \frac{k^3}{6\pi\mu\mu_0} \operatorname{Im}(\alpha_1^m \alpha_2^{m*}), \quad (4.13)$$

$$A_s^m = \frac{1}{2} \operatorname{Im}(\alpha_1^m + \alpha_2^m) - \frac{k^3}{6\pi\mu\mu_0} \operatorname{Re}(\alpha_1^m \alpha_2^{m*}). \quad (4.14)$$

Here $k = \sqrt{\varepsilon\mu}k_0$. The spinning coefficients can be explicitly decomposed into the meaningful terms as

$$A_s = A_s^{\text{abs}} + A_s^{\text{anis}} \quad (4.15)$$

where the first terms is responsible for the absorbtion in the particle and the second term is responsible for the effects of the anisotropy. In the Rayleigh limit we can find that $A_s^{\text{abs}} \approx \frac{1}{2} \operatorname{Im}(\alpha_1^{\text{qs}} + \alpha_2^{\text{qs}})$ for (e) and (m), and $A_s^{(\text{e})\text{anis}} \approx \frac{k^3}{12\pi\varepsilon\varepsilon_0} \operatorname{Re}((\alpha_1^{(\text{e})\text{qs}} - \alpha_2^{(\text{e})\text{qs}})^2)$, $A_s^{(\text{m})\text{anis}} \approx \frac{k^3\mu\mu_0}{12\pi} \operatorname{Re}((\alpha_1^{(\text{m})\text{qs}} - \alpha_2^{(\text{m})\text{qs}})^2)$.

One can check that for the isotropic particle with $\alpha_1 = \alpha_2$ in terms of generalized polarizabilites we have

$$A_a^{e,m} \Big|_{\alpha_1=\alpha_2} = 0, \quad A_s^{e,m} \Big|_{\alpha_1=\alpha_2}^{ka \ll 1} = \operatorname{Im}(\alpha^{\text{rc}(e,m)}). \quad (4.16)$$

Here $\alpha^{\text{rc}(e,m)}$ is the quasi-statics approximation of the polazability which is given by the (B.4). This means that rotation of the isotropic particle is possible only in

the presence of losses. Which is a particular case of the fact that lossless isotropic sphere of any radius cannot be span by *any* incident field [10; 97; 127; 128].

We rewrite torque as the sum of three terms by its physical meanings as

$$T_z = T_z^{\text{alg}} + T_z^{\text{abs}} + T_z^{\text{anis}}. \quad (4.17)$$

Similar decomposition but with less detatails was given in [311]. Here T_z^{alg} is the alignment torque which is zero once we make the average on γ : $\langle T_z^{\text{alg}} \rangle_\gamma = 0$. Secondly, T_z^{abs} is the torque which is responsible to the ohmic losses and is eventually is proportional to the $\text{Im}(\varepsilon_p)$. In the case of small isotropic sphere torque is given only by this term $T_z^{\text{abs}} = \frac{1}{2} \text{Im}(\alpha^{\text{qs}}) S_3 = \frac{\varepsilon \varepsilon_0}{2k} \sigma_{\text{abs}} S_3$, where σ_{abs} is the absorption cross section. It is know that this holds true for the sphere of any radius [127; 128; 312]. More notes on this is given in the sec. 4.3.7. Lastly, T_z^{anis} is the torque which comes from the change of the momentum of the incident wave due to the scattering. For lossless anisotropic particle with $ka \ll 1$ in the circularly polarized plane wave we have only this component

$$\begin{aligned} T_z(s_3 = 1, \text{Im}(\varepsilon_{1,2}) = 0) &= T_z^{\text{anis}} = \\ &= E_0^2 \frac{k^3}{12\pi} \left[\frac{1}{\varepsilon \varepsilon_0} \text{Re} \left(\alpha_1^{\text{qs(e)}} - \alpha_2^{\text{qs(e)*}} \right)^2 + \frac{\varepsilon \varepsilon_0}{(\mu \mu_0)^2} \text{Re} \left(\alpha_1^{\text{qs(m)}} - \alpha_2^{\text{qs(m)*}} \right)^2 \right] \end{aligned} \quad (4.18)$$

Alignment and absorption torques are proportional to the canonical spin angular momentum density $\mathbf{S} = \mathbf{S}^{\text{el}} + \mathbf{S}^{\text{mag}} = \frac{1}{4\omega} \text{Im} [\varepsilon \varepsilon_0 \mathbf{E}^* \times \mathbf{E} + \mu \mu_0 \mathbf{H}^* \times \mathbf{H}]$, which is for the plane wave defined through (4.6) is going to be

$$S_z^{\text{el}} = \frac{\varepsilon \varepsilon_0 E_0^2}{4\omega} s_3. \quad (4.19)$$

4.3.2 The critical angle

The condition for the critical angle of the elliptically polarized light is given by the

$$\mathfrak{D}_{\text{QWP}}^{\text{cr}} : \quad T_z = 0 \quad \text{or} \quad T^{\text{alg}} = -T^{\text{spin}}, \quad (4.20)$$

where T^{alg} and T^{spin} are the first (γ -dependent) and the second (γ -independent) terms in (4.10). Polarization in the experiment is controlled by the rotation of the

quarter wave plate (QWP) on angle ϑ_{QWP} . On the Poincare sphere this rotation will induce 8-shaped curve and the corresponding stokes parameters are going to be [259; 313]

$$s_1 = \frac{1}{2} \sin 4\vartheta_{\text{QWP}}, \quad s_2 = \sin^2 2\vartheta_{\text{QWP}}, \quad s_3 = \cos 2\vartheta_{\text{QWP}}. \quad (4.21)$$

The related electric field is going to be

$$\mathbf{E} = \frac{E_0}{\sqrt{2}} \begin{pmatrix} c^2 + is^2 + (1-i)sc \\ s^2 + ic^2 + (1-i)sc \\ 0 \end{pmatrix} \quad (4.22)$$

Where $c \equiv \cos \vartheta_{\text{QWP}}$ and $s \equiv \sin \vartheta_{\text{QWP}}$. This can be found using Jones calculus formalism [259]. Condition (4.20) depends on two parameters: γ and ϑ_{QWP} . However, this can be reduced since for every ϑ_{QWP} there is one position of the optical axis (= one γ) for which T^{alg} is maximum. This condition leads to $\gamma = \vartheta_{\text{QWP}} - \pi/4$ for $\vartheta_{\text{QWP}} \in [0, \pi/2]$. Thus, we can finally find the critical angle of the QWP

$$\vartheta_{\text{QWP}}^{\text{cr}} = -\frac{1}{2} \text{atan} \frac{A_s^e + \frac{\varepsilon\varepsilon_0}{\mu\mu_0} A_s^m}{A_a^e - \frac{\varepsilon\varepsilon_0}{\mu\mu_0} A_a^m}. \quad (4.23)$$

This leads to the almost linear scaling due with the increase of the particle radius $\vartheta_{\text{QWP}}^{\text{cr}}(a) \propto \text{const}_1 - \text{const}_2 \cdot a$. This happens only after taking into account the magnetic dipole moment as illustrated on Fig. 4.7. In addition to this, we also find the limit for Reighley particles ($ka \ll 1$) to be

$$\vartheta_{\text{QWP}}^{\text{cr}} \Big|_{ka \ll 1} \approx -\frac{1}{2} \text{atan}(ka)^3 \frac{2\varepsilon(\varepsilon_{\parallel} - \varepsilon_{\perp})}{(\varepsilon_{\perp} + 2\varepsilon)(\varepsilon_{\parallel} + 2\varepsilon)} \quad (4.24)$$

4.3.3 Rotation dynamics

Once the spinning torque is larger than alignment torque particle may rotate with a frequency Ω which is limited by the viscosity of the host media. To study this process in details, we start from the second Newton's law for the rotation motion

$$J\ddot{\gamma} = T_z - \mu\dot{\gamma} \quad (4.25)$$

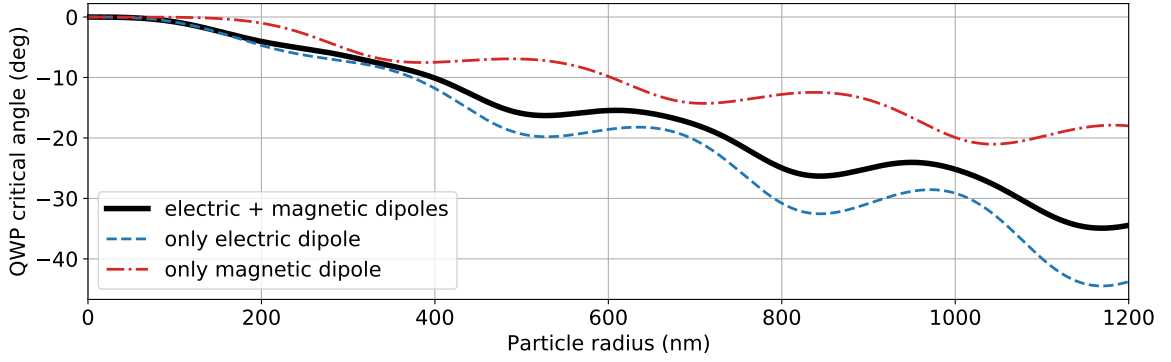


Figure 4.7 – The critical angle for the QWP to observe rotation of the uniaxial anisotropic particle. Calculated for $\varepsilon = 1.77$, $\varepsilon_{\parallel} = 2.9128$, $\varepsilon_{\perp} = 2.2641$ and $\lambda = 1064$ nm

where J is the moment of inertia, $\mu = 8\pi\nu a^3$ is the viscosity coefficient [314, ch. 2], where a is the particle radius, and ν is the dynamic viscosity.

The stationary rotation condition $\ddot{\gamma} = 0$, $\dot{\gamma} = \Omega$ and assuming the Stokes vector to be $\mathbf{s} = (1, 0, 0, 1)$ (circular polarized light) gives the expression for the rotation frequency

$$\Omega_0 = \frac{T_z}{\mu} = \frac{E_0^2}{16\pi\nu a^3} \left[A_s^e + \frac{\varepsilon\varepsilon_0}{\mu\mu_0} A_s^n \right] \propto \begin{cases} (ka)^3, & \text{for } ka \ll 1 \\ 1/(ka)^3, & \text{for } ka \gg 1 \end{cases}. \quad (4.26)$$

The limit for the $ka \gg 1$ is given regardless accidental periodic zeros. The scaling with the radius is shown on Fig. 4.8. However, solution for an arbitrary Stokes vector is anharmonic, which is clearly shown on Fig. 4.9. The typical "Bell" curve is shown on the Fig. 4.10.

4.3.4 Case of two beams

General results is the following. Torque is the quadratic function of fields, thus in the final expression for the torque from two beams with a total field given by $\mathbf{E}_{\text{tot}} = \mathbf{E}_1 + \mathbf{E}_2$ has three terms including the interference terms:

$$\langle T_z \rangle_{\gamma} = T_{1,z} + T_{2,z} + T_{\text{mix},z}, \quad (4.27)$$

where $T_{1,z} = T_{1,z}(\mathbf{E}_1)$, $T_{2,z} = T_{2,z}(\mathbf{E}_2)$, and $T_{\text{mix},z} = T_{\text{mix},z}(\mathbf{E}_1, \mathbf{E}_2)$. For incoherent beams we formally have to do the averaging over relative phase δ between \mathbf{E}_1 and

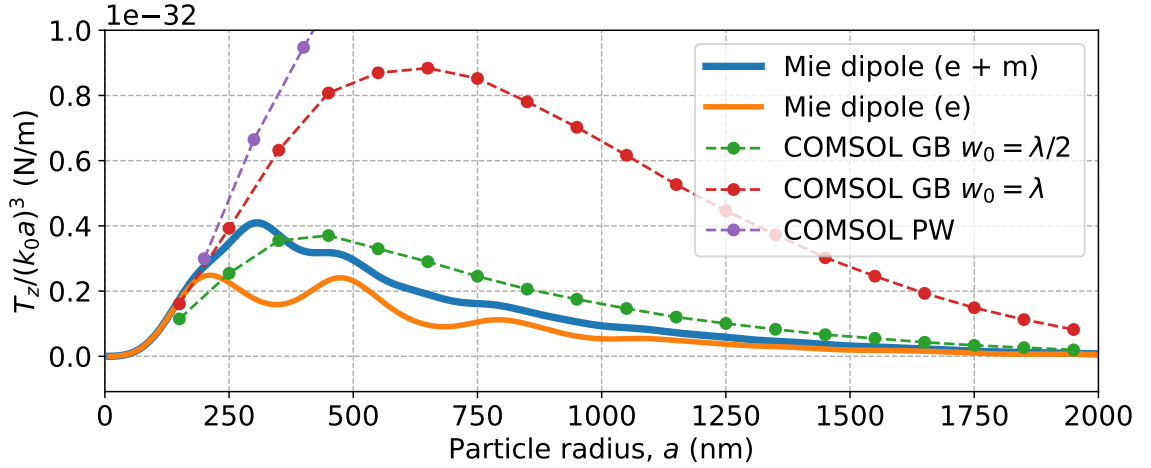


Figure 4.8 — Scaling of the rotational frequency with the particle radius. Results are compared the COMSOL simulations, where particle was illuminated by a gaussian beam (GB) with different waists w_0 and a plane wave (PW). Electric and magnetic dipoles are sufficient for the particle radius of $a < 300 - 400$ nm. For all lines the magnitude of electric field E_0 is constant

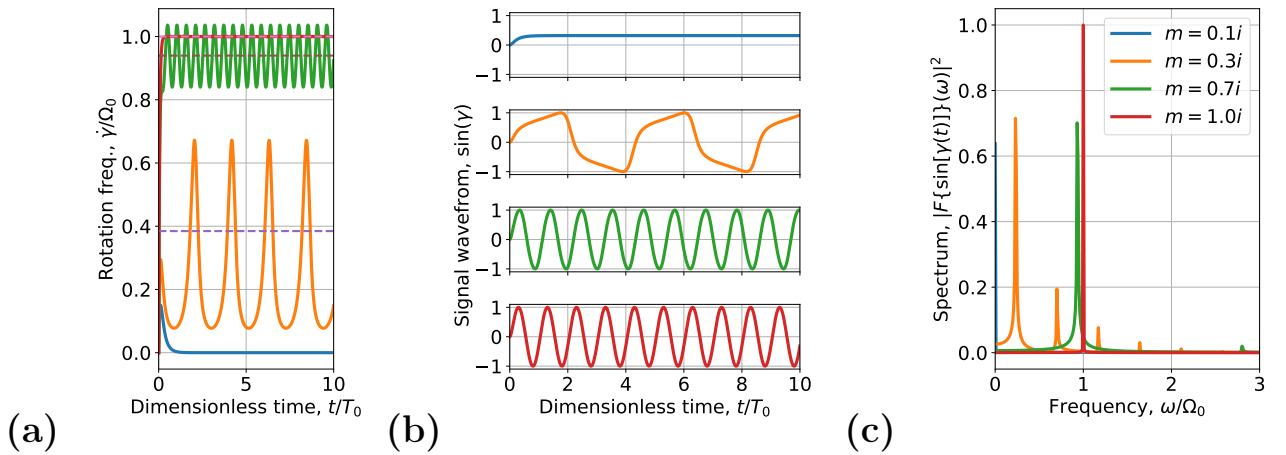


Figure 4.9 — Numerical solution of the system which describes the rotation dynamics of the anisotropic particle in the dipole approximation. **(a)** Instantaneous frequency exhibits oscillations on the double frequency due to the anisotropy; **(b)** Signal form $y(t) = \sin[\gamma(t)]$ and **(c)** its spectral representation. Solid lines show the numerical solution and dashed line is the first order approximated analytical solution. Signal is fully harmonic for the purely circular polarized light $m = \pm i$ and starts to be inharmonic close to the critical point. Here $T_0 = 2\pi/\Omega_0$. Other parameters are

$$E_0 = 4, \Delta = 0.1, \Gamma = 0.3, a = 1, \rho = 1, \text{ and } \nu = 0.1$$

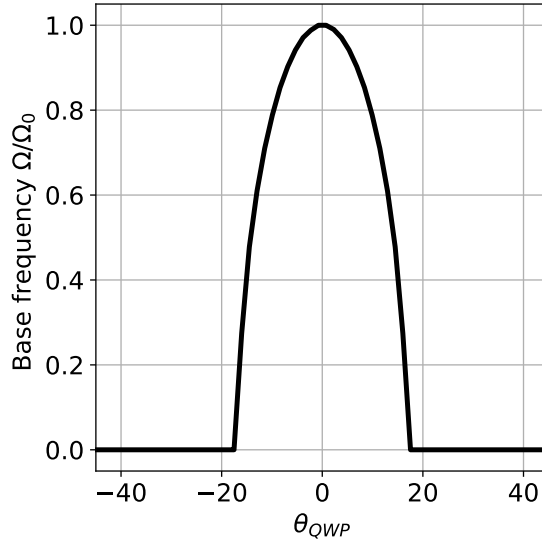


Figure 4.10 — Simple model solution for the base rotation frequency. Frequency is extracted numerically and normalized by Ω_0 which is defined by (4.26). This curve looks very similar to the one in literature [279]

\mathbf{E}_2 which gives zero:

$$\langle T_{\text{mix},z} \rangle_{\delta} = 0. \quad (4.28)$$

Hence, torque on a small particle in two beams is proportional to the sum of spin angular momenta of each beam without any interference terms.

Next, we consider a particular example of a small anisotropic particle $\hat{\boldsymbol{\alpha}}^{(e)}$ with electric dipole in the field of a plane wave and an evanescent wave. Fields are

$$\mathbf{E}_1 = \frac{E_{01}}{\sqrt{1 + |m_1|^2}} \begin{pmatrix} 1 \\ 0 \\ -m_1 \end{pmatrix} e^{iky}, \quad \mathbf{E}_2 = \frac{E_{02}}{\sqrt{2}} \begin{pmatrix} 1 \\ k/k_z \\ i\kappa/k_z \end{pmatrix} e^{ikz - \kappa x}. \quad (4.29)$$

Here $k_z - \kappa^2 = k^2$. It can be parametrised by a single real parameter θ : $k_z = k \cosh(\theta)$ and $\kappa = k \sinh(\theta)$. We assume that particle experience rotation around y axis and described by the polarizability tensor $\hat{\boldsymbol{\alpha}}_{\text{cart}}$. For this configuration with $m_1 = im_1''$ we have find torque averaged over particle rotation

$$\langle T_z \rangle_{\gamma} = T_{1,z} + T_{2,z} + T_{\text{mix},z}, \quad (4.30)$$

where

$$T_{1,z} = \frac{1}{2} S_3 A_s^e, \quad (4.31)$$

$$T_{2,z} = \frac{1}{2} E_{02}^2 e^{-2\kappa x} \frac{\kappa}{k_z} A_s^e, \quad (4.32)$$

$$T_z^{\text{mix}} = \frac{1}{2} E_{01} E_{02} e^{-\kappa x} \cos(\delta) \frac{\sqrt{2}}{\sqrt{|m_1|^2 + 1}} \left(m_1'' + \frac{\kappa}{k_z} \right) A_s^e \Big|_{\text{incoherent beams}}^{\langle \dots \rangle_\delta} = 0. \quad (4.33)$$

where $\delta = ky - k_z z$ is the interference phase. For incoherent beams this phase is random and, hence, $T_{\text{mix},z} = 0$ in average. This leads to an important yet simple consequence mentioned above: torque on a small particle in two beams is proportional to the sum of spin angular momenta of each beam without any interference terms.

4.3.5 Taking into account chirality

Chiral anisotropic particle is given by [24; 152]

$$\begin{bmatrix} \mathbf{p} \\ \mathbf{m} \end{bmatrix} = \begin{bmatrix} \hat{\alpha}_e & i \frac{\sqrt{\epsilon\mu}}{c} \hat{\alpha}_c \\ -i \frac{1}{\eta} \hat{\alpha}_c^T & \frac{1}{\mu\mu_0} \hat{\alpha}_m \end{bmatrix} \begin{bmatrix} \mathbf{E} \\ \mathbf{H} \end{bmatrix} \quad (4.34)$$

Here we define $\hat{\alpha}_c$ such that it has dimensionality of the volume, so $[\hat{\alpha}_c] = [\text{m}^3]$; $\eta = \sqrt{\frac{\mu\mu_0}{\epsilon\epsilon_0}}$ is the wave impedance. We start from the **tensor structure** of the $\hat{\alpha}_c$. Which acutally can be almost arbitrary. See many examples in [21; 22]. Let us consider the case of isotropic chirality, besides for this example we assume all other terms to be isotropic as well: $\hat{\alpha}_{e,m,c} = \hat{I} \alpha_{e,m,c}$, where \hat{I} is the unit dyadic. This case is partially was studied in [24] where it was shown that chirality reveals cross dependence of linear and angular momentum dependence between electromagnetic field properties and dipole dynamics. However, authors in [canaguier-durand2015ChiralRoutePulling] did not consider the correction term to the torque as we did here. This reveals new unique connection between optical torque and imaginary part of the Poynting vector. The example below illustrates this.

The total torque can be decomposed into the *chiral* and *non-chiral* parts

$$\mathbf{T} = \mathbf{T}^{\text{non-chiral}} + \mathbf{T}^{\text{chiral}}, \quad (4.35)$$

where

$$\mathbf{T}^{\text{non-chiral}} = \frac{2c}{\sqrt{\varepsilon\mu}} \left[\sigma_{\text{abs}}^{(e)} \mathbf{S}^{(e)} + \sigma_{\text{abs}}^{(m)} \mathbf{S}^{(m)} \right] \quad (4.36)$$

where $\sigma_{\text{abs}}^{(e)} = \frac{1}{4\pi\varepsilon\varepsilon_0} \cdot 4\pi k \left[\text{Im}(\alpha_e) - \frac{k^3}{6\pi\varepsilon\varepsilon_0} |\alpha_e|^3 \right]$ and $\sigma_{\text{abs}}^{(m)} = \frac{1}{4\pi\mu\mu_0} \cdot 4\pi k \left[\text{Im}(\alpha_m) - \frac{k^3}{6\pi\mu\mu_0} |\alpha_m|^3 \right]$ are the absorption cross sections. The chiral part is given by

$$\begin{aligned} \mathbf{T}^{\text{chiral}} = & 2\frac{\varepsilon\mu}{c} \text{Im}(\alpha_c) \mathbf{\Pi}^{\text{Re}} - \frac{k^3\omega}{3\pi} |\alpha_c|^2 \mathbf{S} \\ & - \frac{k^3}{3\pi} \text{Re} [\alpha_c^* (\eta\alpha_e + \eta^{-1}\alpha_m)] \mathbf{\Pi}^{\text{Re}} - \frac{k^3}{3\pi} \text{Im} [\alpha_c^* (\eta\alpha_e - \eta^{-1}\alpha_m)] \mathbf{\Pi}^{\text{Im}} \end{aligned} \quad (4.37)$$

where $\mathbf{\Pi}^{\text{Re}} = \frac{1}{2} \text{Re} [\mathbf{E}^* \times \mathbf{H}]$ and $\mathbf{\Pi}^{\text{Im}} = \frac{1}{2} \text{Im} [\mathbf{E}^* \times \mathbf{H}]$ are the real and imaginary parts of Poynting vector; $\mathbf{S} = \frac{1}{4\omega} \text{Im} [\varepsilon\varepsilon_0 \mathbf{E}^* \times \mathbf{E} + \mu\mu_0 \mathbf{H}^* \times \mathbf{H}] = \mathbf{S}^{(e)} + \mathbf{S}^{(m)}$ is the spin angular momentum density. Equations (4.35), (4.36) and (4.37) reveals the true connection between properties of the incident electromagnetic wave and dipole rotation dynamics. Chirality underpin possibilities of the direct measurements of the imaginary part of Poynting vector $\mathbf{\Pi}^{\text{Im}}$ which signifies the reactive power. For more theoretical insights see [315–317]. The imaginary Poynting vector was also measured experimentally via *optical force* [287] but not *optical torque*.

4.3.6 Rotation of chiral particle in the field of HE₁₁

The case of \mathbf{E} and \mathbf{H} being electric and magnetic fields of propagating fundamental linearly polarized mode HE₁₁^{lin.} simplifies expressions (4.36) and (4.37) for the torque. Besides, we also consider effects which are connected only with chirality, this leads to the $\alpha_c = \text{Re}(\alpha_c)$ in (4.34) [318].

Fields of HE₁₁^{lin.} are explicitly given in [235]

$$\mathbf{E}_{\text{lin.}}^{\text{HE}_{11}} = \sqrt{2} \begin{bmatrix} e_r \cos \varphi \\ ie_\varphi \sin \varphi \\ fe_z \cos \varphi \end{bmatrix} e^{if\beta z}, \quad \mathbf{H}_{\text{lin.}}^{\text{HE}_{11}} = \sqrt{2} \begin{bmatrix} ifh_r \sin \varphi \\ fh_\varphi \cos \varphi \\ ih_z \sin \varphi \end{bmatrix} e^{if\beta z} \quad (4.38)$$

We find that in cylindrical coordinates $(\hat{\mathbf{r}}, \hat{\boldsymbol{\phi}}, \hat{\mathbf{z}})$ spin angular momentum density is

$$\mathbf{S}^{(e)} = \frac{\varepsilon \varepsilon_0}{2\omega} f \begin{bmatrix} -\sin[2\boldsymbol{\varphi}] \operatorname{Re}(e_{\boldsymbol{\varphi}}^* e_z) \\ 2\cos^2(\boldsymbol{\varphi}) \operatorname{Im}(e_z^* e_r) \\ 0 \end{bmatrix}, \quad \mathbf{S}^{(m)} = \frac{\varepsilon \varepsilon_0}{2\omega} f \begin{bmatrix} \sin[2\boldsymbol{\varphi}] \operatorname{Re}(h_{\boldsymbol{\varphi}}^* h_z) \\ 2\sin^2(\boldsymbol{\varphi}) \operatorname{Im}(h_z^* h_r) \\ 0 \end{bmatrix}. \quad (4.39)$$

where $(e, h)_{r, \boldsymbol{\varphi}, z}$ are the mode profiles from [235, Appendix A], $f = \pm 1$ is responsible for the mode propagation direction along $\pm z$ correspondingly, and $\boldsymbol{\varphi} = \varphi - \varphi_{\text{pol}}$ is the polar angle with the φ_{pol} being the linear polarization angle of the mode. We emphasize the angular dependence by colors. The real and imaginary Poynting vectors are

$$\mathbf{\Pi}^{\text{Re}} = \begin{bmatrix} 0 \\ 0 \\ f \frac{1}{2} \sin(2\boldsymbol{\varphi}) \operatorname{Re}(e_z^* h_r - e_r^* h_z) \end{bmatrix}, \quad \mathbf{\Pi}^{\text{Im}} = \frac{1}{2} \begin{bmatrix} (1+c) \left[\frac{1-c}{1+c} - \cos(2\boldsymbol{\varphi}) \right] \operatorname{Im}(e_{\boldsymbol{\varphi}}^* h_z) \\ \sin[2\boldsymbol{\varphi}] \operatorname{Re}(e_z^* h_r - e_r^* h_z) \\ 0 \end{bmatrix} \quad (4.40)$$

Where $c = \operatorname{Im}(e_z^* h_{\boldsymbol{\varphi}}) / \operatorname{Im}(e_{\boldsymbol{\varphi}}^* h_z) = -s_2^{-1} \frac{(1-s_2)K_0 + (1+s_2)K_2}{(1-s)K_0 - (1+s)K_2}$. Here $K_n = K_n((\beta^2 - n_{\text{host}}^2 k_0^2)^{1/2} r)$ is the modified Bessel function of the second kind and parameters s and s_2 are given explicitly in [235; 290]. Interestingly, the $\mathbf{\Pi}^{\text{Im}}$ *does not depend on the propagation direction*, i.e. along $\pm z$. For the sake of convenience we plot (4.39) and (4.40) in Fig. 4.11.

Finally, the r - and $\boldsymbol{\varphi}$ -components of optical torque on chiral particle in the field of $\text{HE}_{11}^{\text{lin}}$ mode is given by

$$\mathbf{T}^{\text{chiral}} = -\frac{k^3 \omega}{3\pi} \alpha_c^2 \begin{bmatrix} S_r \\ S_{\boldsymbol{\varphi}} \\ 0 \end{bmatrix} - \frac{k^3}{3\pi} \alpha_c \operatorname{Re}[(\eta \alpha_e + \eta^{-1} \alpha_m)] \begin{bmatrix} 0 \\ 0 \\ \Pi_z^{\text{Re}} \end{bmatrix} - \frac{k^3}{3\pi} \alpha_c \operatorname{Im}[(\eta \alpha_e - \eta^{-1} \alpha_m)] \begin{bmatrix} 0 \\ 0 \\ \Pi_z^{\text{Im}} \end{bmatrix} \quad (4.41)$$

We also rewrite is in a simplified form to show the essential dependence:

$$T_r = \underbrace{T_r^{\text{tweezer}}}_{\text{const}(\boldsymbol{\varphi})} + \underbrace{\dots \cdot S_r^{(e)}}_{\sim \sin(2\boldsymbol{\varphi})} + \underbrace{\dots \cdot S_r^{(m)}}_{\sim -\sin(2\boldsymbol{\varphi})} + \underbrace{\dots \cdot \Pi_r^{\text{Im}}}_{\sim b - \cos(2\boldsymbol{\varphi})} \quad (4.42)$$

where $b = \frac{1-c}{1+c} = \frac{(ss_2-1)(K_0+K_2)}{(ss_2+1)(K_0+K_2)-2s_2(K_0-K_2)}$ and

$$T_{\boldsymbol{\varphi}} = \underbrace{T_{\boldsymbol{\varphi}}^{\text{tweezer}}}_{\text{const}(\boldsymbol{\varphi})} + \underbrace{\dots \cdot S_{\boldsymbol{\varphi}}^{(e)}}_{\sim \cos^2 \boldsymbol{\varphi}} + \underbrace{\dots \cdot S_{\boldsymbol{\varphi}}^{(m)}}_{\sim \sin^2 \boldsymbol{\varphi}} + \underbrace{\dots \cdot \Pi_{\boldsymbol{\varphi}}^{\text{Im}}}_{\sim \sin(2\boldsymbol{\varphi})} \quad (4.43)$$

This contribution caused by chirality **gives the shift** between measured orbiting frequency and spin angular momentum density.

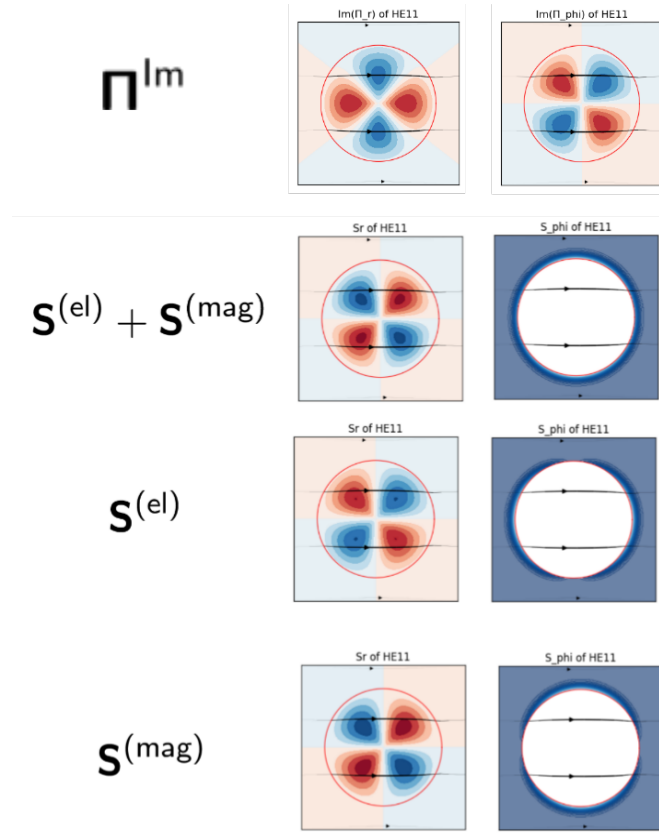


Figure 4.11 — Spin angular momentum density \mathbf{S} and imaginary Poynting vector $\mathbf{\Pi}^{\text{Im}}$ of $\text{HE}_{11}^{\text{lin}}$ mode. The black arrows represent the electric field lines

Some numerical results based on the dipole model are shown on Fig. 4.12 for non-chiral particle and on Fig. 4.13 for chiral particles with $\alpha_c = 0.001a^3$ and $\alpha_c = 0.1a^3$. In the case of high chirality radial component of the torque is almost entirely determined by the radial component of the imaginary Poynting vector $\mathbf{\Pi}_r^{\text{Im}}$ rather than radial spin angular momentum density S_r . This happens due to the fact that $S_r^{(\text{el})}$ and $S_r^{(\text{mag})}$ are out of phase as shown on Fig. 4.11 and derived in Eq. (4.39). Once particle supports *both* electric and magnetic dipoles, the total non-chiral radial torque is suppressed.

4.3.7 Torque on a small isotropic dipole particle and dipole approximation problems

Exact torque on a sphere is proportional to the absorption cross section [10]

$$T^{\text{exact}} = \frac{\Pi}{\omega} \sigma_{\text{abs}} = \frac{\Pi}{\omega} (\sigma_{\text{ext}} - \sigma_{\text{sc}}), \quad (4.44)$$

No chirality

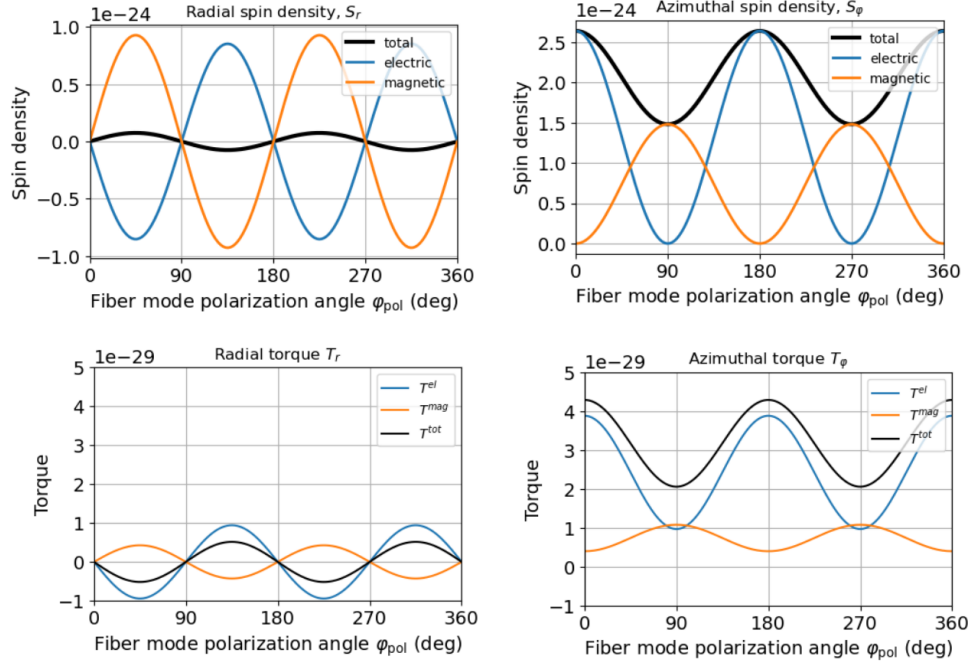


Figure 4.12 — Comparison of the optical torque and spin angular momentum density for a non-chiral particle

where Π is the average Poynting vector of the plane wave. In terms of Mie scattering coefficients [97] we have

$$T^{\text{exact}} \propto \sum_{n=1}^{\infty} (2n+1) [\text{Re}(a_n) - |a_n|^2 + \text{Re}(b_n) - |b_n|^2]. \quad (4.45)$$

For the dipole approximation we have only term a_1 . Expanding Mie coefficient in Taylor series over $x = k_0 a$ we have

$$a_1 \approx -i \frac{2(\varepsilon - 1)}{\varepsilon + 2} x^3 - i \frac{2(2 - 3\varepsilon + \varepsilon^2)}{5(2 + \varepsilon^2)^2} x^5 + \frac{4(\varepsilon - 1)^2}{9(\varepsilon + 2)^2} x^6 + \dots \quad (4.46)$$

Next, assuming particle to be lossless, e.g. $\text{Im}(\varepsilon) = 0$, we have

$$\text{Re}(a_n) - |a_n|^2 = \frac{4(\varepsilon - 1)^2}{9(\varepsilon + 2)^2} x^6 - \left| i \frac{2(\varepsilon - 1)}{\varepsilon + 2} \right|^2 x^6 + O(x^8) = 0. \quad (4.47)$$

Same is true for the b_n . So, in general, once $\text{Im}(\varepsilon) = 0$ we have identity

$$\text{Re}(a_n) - |a_n|^2 = 0, \quad \text{Re}(b_n) - |b_n|^2 = 0, \quad (4.48)$$

which is easy to check at least numerically.

Chiral

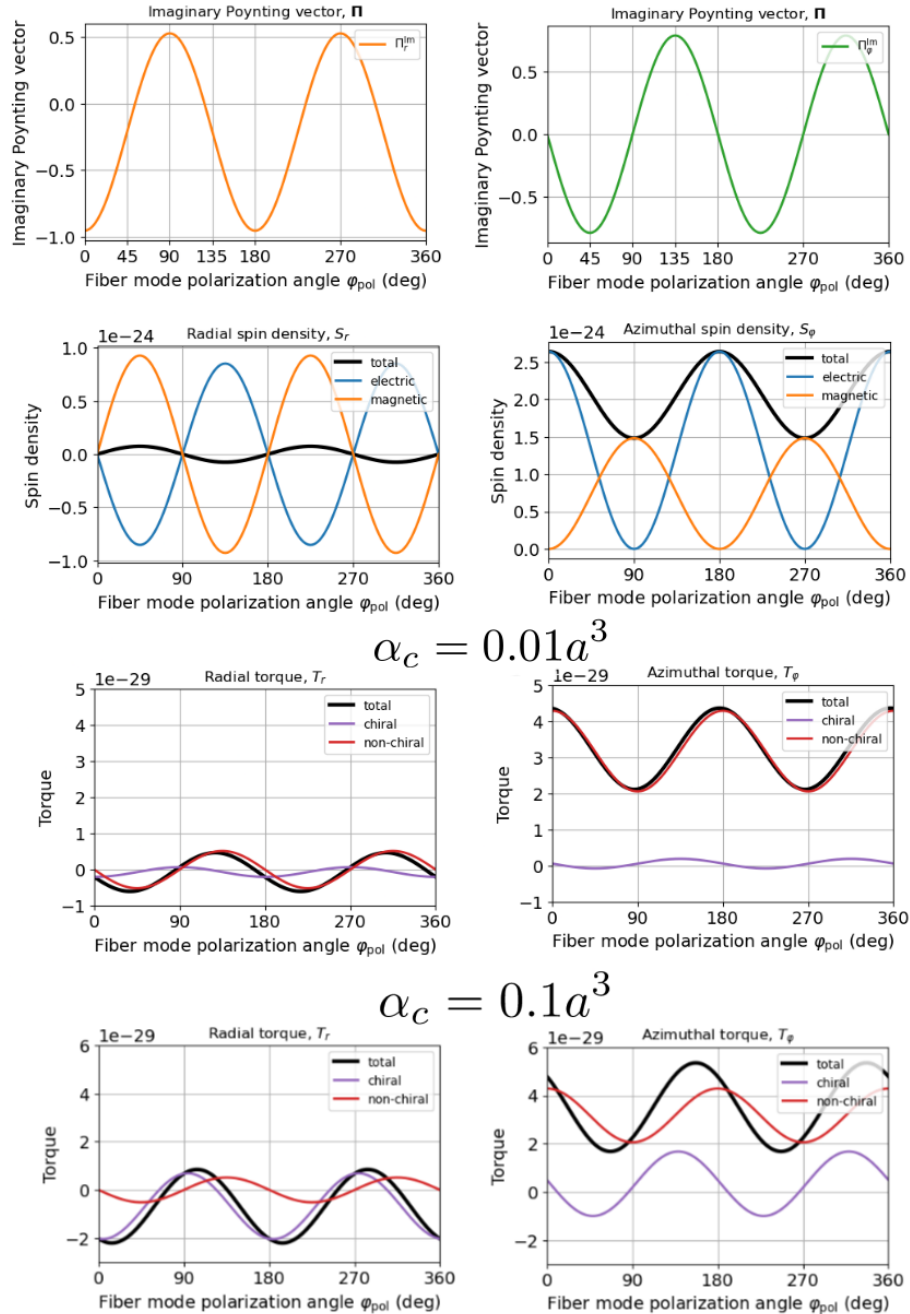


Figure 4.13 – Comparison of the optical torque and spin angular momentum density for a chiral particle with $\alpha_c = 0.001a^3$ and $\alpha_c = 0.1a^3$

On the other hand, for the case of lossy particle, complex ε , we have

$$\operatorname{Re}(a_n) - |a_n|^2 \approx \frac{2 \operatorname{Im}(\varepsilon)}{|2 + \varepsilon|^2} x^3 + \operatorname{Im}(\varepsilon) g(\varepsilon) x^5 - \frac{8 \operatorname{Im}(\varepsilon)^2}{|2 + \varepsilon|^4} x^6 + \dots \quad (4.49)$$

where $g(\varepsilon)$ some complicated real function of ε . This holds true for any order n and for b_n coefficients as well. From here we conclude

$$T = 0 \quad \Leftrightarrow \quad \operatorname{Im}(\varepsilon) = 0. \quad (4.50)$$

Classical formula $\mathbf{T} = 1/2 \operatorname{Re}[\mathbf{p}^* \times \mathbf{E}]$ gives only first term which is proportional to the $\operatorname{Im}(\alpha) \propto \operatorname{Re}\{a_1\}$ but not to $|a_n|^2$ in (4.47) and, hence, leads to the incorrect result. This happens due to the excess accuracy. That is why it is important to consider radiation corrections as well [145].

4.3.8 Some useful decompositions

Some decompositions might be helpful in the theoretical analyses:

$$\operatorname{Re}(\alpha_1 - \alpha_2) \approx \operatorname{Re}(\alpha_1^{\text{qs}} - \alpha_2^{\text{qs}}), \quad (4.51)$$

$$\operatorname{Im}(\alpha_1 + \alpha_2) \approx \underbrace{\operatorname{Im}(\alpha_1^{\text{qs}} + \alpha_2^{\text{qs}})}_{\text{losses}} + \frac{k^3}{6\pi\varepsilon\varepsilon_0} \operatorname{Re} [(\alpha_1^{\text{qs}})^2 + (\alpha_2^{\text{qs}})^2]. \quad (4.52)$$

and

$$\operatorname{Re}(\alpha_1 \alpha_2^*) \approx \operatorname{Re}(\alpha_1^{\text{qs}} \alpha_2^{\text{qs}*}), \quad (4.53)$$

$$\operatorname{Im}(\alpha_1 \alpha_2^*) \approx \operatorname{Im}(\alpha_1^{\text{qs}} \alpha_2^{\text{qs}*}) + \frac{k^3}{6\pi\varepsilon\varepsilon_0} \operatorname{Re} [(\alpha_1^{\text{qs}})^2 \alpha_2^{\text{qs}*} - \alpha_1^{\text{qs}} (\alpha_2^{\text{qs}*})^2] \quad (4.54)$$

where $k = k_0 \sqrt{\varepsilon}$. For the magnetic polarizability one needs to perform the substitution $\varepsilon\varepsilon_0 \rightarrow \mu\mu_0$.

4.4 Spin angular momenta transfer: non-linear regime

Light cannot exert an optical torque on a transparent object possessing continuous rotational symmetry, since photons scattered by such an object preserve

their angular momentum [319]. From this point of view, the phenomenon of optical torque is a consequence of broken rotational symmetry either geometrically (macroscopic symmetry breaking), either via crystal structure (microscopic symmetry breaking). In this work we show the mechanics and the particular example of torque generated by the microscopic symmetry breaking considering structure which generates higher harmonic.

Time averaged optical torque \mathbf{T} on a spherical non-absorbing particle on the first harmonic is equal to zero, since torque on an arbitrary sized sphere is proportional to the absorption cross section [10; 11], in terms of canonical spin angular momenta density we can write $\mathbf{T} = \frac{c}{n_0} \sigma_{\text{abs}} \mathbf{S}$, where \mathbf{S} is the canonical spin angular momenta density [45] and n_0 is the refractive index of the host media. Also we will fix the incident direction along z -axis, so $\mathbf{k}/k = \hat{\mathbf{e}}_z$ and $\mathbf{T} = T_z \hat{\mathbf{e}}_z$. This can be explained by the fact that in the linear scattering regime angular momenta of the scattered field is defined solely by the geometry of the scatterer. Sphere, in particular, has azimuthal symmetry, hence it cannot change angular momenta of the scattered field on the first harmonic and torque is going to be zero.

However, once this particle is made of non-centrosymmetric material (e.g. second order susceptibility tensor $\hat{\chi}^{(2)} \neq 0$) and the particle generates second harmonic the situation is going to be radically different due to the fact that crystal lattice of the particle adds additional azimuthal angular momentum number m , such that scattered field on second harmonic is $\mathbf{E}^{(2\omega)} \sim e^{im\varphi}$, where φ is the azimuthal angle. Angular momenta must conserve, hence once there is an additional momentum in the scattered field (which comes from the symmetry of the crystal lattice), particle must gain the same angular momenta with the same amplitude and different sign.

In the other words, time averaged optical torque on a *spherical* particle with non-zero susceptibility tensor $\hat{\chi}^{(2)}$ which is illuminated by a circular polarized plane wave can be written as

$$\mathbf{T} = \mathbf{T}^{(\omega)} + \mathbf{T}^{(2\omega)} \quad (4.55)$$

where $\mathbf{T}^{(\omega)}$ and $\mathbf{T}^{(2\omega)}$ are the optical torques on the first and second harmonics, respectively. Torque on the first harmonic on a *sphere* is proportional only to the losses in the particle. In our case — the case of lossless particle with non-zero $\hat{\chi}^{(2)}$ tensor — all the energy lost on the first harmonic is spent to the second harmonic generation, hence

$$T_z^{(\omega)} = \frac{c}{n_0} S_z^{(\omega)} \sigma_{\text{abs}} = \frac{c}{n_0} S_z^{(\omega)} \sigma_{\text{SHG}} \quad (4.56)$$

where $S_z^{(\omega)}$ is the canonical spin angular momenta [45] density of the incident wave. For a circular polarized plane wave we have $S_z^{(\omega)} = \mathfrak{S} \frac{1}{2\omega} \varepsilon \varepsilon_0 E_0^2$ with $\mathfrak{S} = -1(+1)$ for right (left) circular polarization. Within this convection field $\mathbf{E} = (1, -i, 0)^T e^{ikz}$ is RCP. Equation (4.56) shows first harmonic contribution of the torque mimics the spectrum of the SHG. Torque on the second harmonic can be defined by the scattered field on the second frequency $\mathbf{E}^{(2\omega)}$ as

$$\mathbf{T}^{(2\omega)} = \oint_{\Sigma} \hat{\mathcal{M}}^{(2\omega)} \cdot \mathbf{n} d\Sigma, \quad (4.57)$$

where $\hat{\mathcal{M}}^{(2\omega)}$ is the angular momentum flux tensor, which is the quadratic function of the fields on the second frequency; Σ is the closed surface which contains the scatterer, and \mathbf{n} is the outer normal to that surface.

It is possible to note some features of the torque on the first and second frequencies in advance. As we see from (4.56) particle gains torque from absorbing angular momenta from the field which energy goes for the second harmonic generation. Importantly, this part of the torque *does not* depend on the angular momenta of the scattered field. In contrast to this, torque contribution on the second frequency depends only on the angular momenta of the scattered field on the second frequency. It means that we in advance know that there is no contributions from the modes with total angular momenta zero, i.e. with $m = 0$ (which is explicitly shown later in eq. (4.59)). Other contributions with $m \neq 0$ or modes with non-zero angular momenta can be defined in advance from the symmetry analyses of the scattered lattice.

It appears that expressions (4.56) and (4.57) can be expressed through *the same scattering coefficients* as follows. The surface integral (4.57) can be taken once all the fields are decomposed in the complex vector spherical harmonics [97; 320]

$$\mathbf{E}^{(2\omega)} = E_0 \sum_{nm} [a_{mn}^s \mathbf{N}_{mn}(2\omega, \mathbf{r}) + b_{mn}^s \mathbf{M}_{mn}(2\omega, \mathbf{r})] \quad (4.58)$$

where $\sum_{mn} \equiv \sum_{n=1}^{\infty} \sum_{m=-n}^n$. The coefficients a_{mn} and b_{mn} implicitly contains information about $\chi^{(2)}$ tensor. The explicit connection with Wigner coefficients from [320] are written in the Supplementary Materials. Due to the orthogonality relations of the VSH it is possible to get to the answer [321–324]

$$T_z^{(2\omega)} = -\frac{1}{2} \frac{\varepsilon \varepsilon_0 E_0^2}{[k(2\omega)]^3} \sum_{mn} m \cdot n (n+1) [|a_{mn}^s|^2 + |b_{mn}^s|^2] \quad (4.59)$$

where n_0 is the refractive index of the surrounding medium. This expression is differs to the similar one in [321; 322] due the two factors: 1) there is no "incident"

wave on the second harmonic and 2) we define VSH with different normalization constant (see Supplementary Materials). It also coincides with the *scattering contribution* to the torque in the [323, eq. (32)]. On the other hand, cross section of the SHG is given by

$$\sigma_{\text{SHG}} = \frac{1}{[k(2\omega)]^2} \sum_{nm} n(n+1) \left[|a_{mn}^s|^2 + |b_{mn}^s|^2 \right] \quad (4.60)$$

where $k(2\omega) = n_0 \frac{2\omega}{c}$.

Finally, substituting (4.60) into the (4.56), and summing up contributions on both frequencies we come to the final answer

$$\begin{aligned} T_z &= T_z^{(\omega)} + T_z^{(2\omega)} \\ &= \frac{1}{2} \frac{\epsilon \epsilon_0 E_0^2}{[k(2\omega)]^3} \sum_{nm} (2\mathfrak{S} - m)n(n+1) \left[|a_{mn}|^2 + |b_{mn}|^2 \right] \end{aligned} \quad (4.61)$$

which is the central result of our work. Here $\mathfrak{S} = -1(+1)$ for right (left) circular polarization.

Moreover, there is one more thing we can say in advance even before any numerical calculations. We can identify the multipolar content of the torque on the second frequency by the *selection rules*. Indeed, the contribution to torque on the second frequency can be only from the modes with non-zero azimuthal numbers, i.e. $m \neq 0$. This can be understood in various ways. Firstly, this formally follows from the eq. (4.59). Second argument is in the physical interpretation of the eq. (4.57). Particle experience only recoil torque from those modes that have a non-zero angular momenta projection on the z axis. It can be shown that for the multipoles (or VSHs) total angular momenta per one photon is equal to its azimuthal quantum number m . It means that there is angular momenta only from the modes with non-zero m .

Next, the selection rules suggest what exactly azimuthal numbers are permitted in second harmonic. This is dictated by symmetry of the lattice (via $\hat{\chi}^{(2)}$ tensor), nanoparticle, and the incident field. It can be shown, that for spherical, cylindrical, and conical AlGaAs particles under left (right) circularly polarized plane wave only harmonics with $m = 0, +4$ for LCP and $m = 0, -4$ for RCP are allowed [320; 325]. The lattice orientation is also important, we have $[001] \parallel \hat{\mathbf{e}}_z$ in our case. Thus we expect to see only one peak in the second harmonic part of the torque spectrum $\mathbf{T}^{(2\omega)}$ exactly at the resonance with $m = \pm 4$. Alongside with this, the first harmonic part of the torque is directly proportional to the SHG spectrum as eq. (4.56) states. We are going to demonstrate this via numeric verification in the next section.

4.5 A scientific statement

Third scientific statement

For a non-absorbing particle geometry of which is axially symmetric with respect to the direction of incident wave, the mechanical spinning torque associated with the generation of second harmonic radiation can arise. The appearance of the spinning torque turns out to be associated with a nonzero angular momentum of the generated second harmonic field, which appears due to the specific structure of the crystal lattice of the nanoparticle.

Chapter 5. Momentum transfer from an acoustic wave to scatterer

Linear acoustics is an evolving field of science [5; 326]. It gained huge momentum in its development since experiments become very affordable and even bachelor students can assemble a simple acoustical tweezer setup. Moreover, many important concepts which are vital in optics are much easier to understand using the scalar fields in linear acoustics [327; 328].

5.1 Main acoustics equations and variables

Sound or an acoustic wave is alternating areas of compression and decompression which propagate in a medium with internal forces. The amplitude of the pressure of these oscillations is usually much lower than the background pressure, so perturbation theory can be easily applied. We limit to the case where only longitudinal waves are possible which is true for almost all soft bodies, liquids, and gases.

Decomposition up to a 3rd order of total pressure p_t , density ρ_t and velocity gives \mathbf{v}_t [215; 329; 330]

$$\begin{cases} p_t = p_0 + p + p'', \\ \rho_t = \rho_0 + \rho + \rho'', \\ \mathbf{v}_t = \mathbf{0} + \mathbf{v} + \mathbf{v}'', \quad |\mathbf{v}_t| \ll c_s. \end{cases} \quad (5.1)$$

Usually, in acoustics only 1st order disturbed values are sufficient to consider. Here we also assumed that the average displacement of individual molecules is much smaller than a wavelength. Master equations are linearised Navie-Stokes equation and continuity equation:

$$\begin{cases} \rho_0 \partial_t \mathbf{v} = -\nabla p & \text{1st order N.-S.} \\ \beta_0 \partial_t p = -\nabla \cdot \mathbf{v} & \text{1st order c.e.} \\ p = c_s^2 \rho & \text{state eq.} \end{cases} \quad (5.2)$$

Where $c_s = 1/\sqrt{\rho_0\beta_0}$ is the speed of sound. From above it is also follows that vector field is curl-free

$$\nabla \times \mathbf{v} = 0. \quad (5.3)$$

Media is described by two main quantities: (i) density ρ_0 , $[\rho_0] = [\text{kg} \cdot \text{m}^{-3}]$ and (ii) compressibility $\beta_0 = -\frac{1}{V} \frac{\partial V}{\partial p}$, $[\beta_0] = [\text{m}^2 \cdot \text{N}^{-1}]$. Connection with the speed of sound is given by $c_s = 1/\sqrt{\rho_0\beta_0}$.

Object inside this media can be described by its own density ρ_1 and compressibility β_1 . It is convenient to use normalized dimensionless parameters [88–90]: (i) normalized density $\bar{\rho}_1 = \rho_1/\rho_0$ and (ii) normalized compressibility $\bar{\beta}_1 = \beta_1/\beta_0$. After introducing these normalized quantities, we can write the wavevector inside the object as

$$k_1 = k_0 \sqrt{\bar{\rho}_1 \bar{\beta}_1}. \quad (5.4)$$

Usually, losses in linear acoustics are defined as an imaginary term if the wave vector $k_1 = k'_1 + i\delta_1$. *Porous* materials are the great example of lossy matter in linear acoustics [89–92]. However, using relative density and compressibility allows to introduce losses as it is done in optics, so for $\text{Im}(\bar{\rho}_1) > 0$, $\text{Im}(\bar{\beta}_1) > 0$ one gets a lossy particle, and for $\text{Im}(\bar{\rho}_1) < 0$, $\text{Im}(\bar{\beta}_1) < 0$ one gets a particle with gain (for the $e^{-i\omega t}$ choice).

It is convenient to consider complex amplitudes for the monochromatic fields $A(\mathbf{r}, t) = \text{Re}(A(\mathbf{r})e^{-i\omega t})$ where $A = p, \rho, \mathbf{v}$. The boundary conditions are shown in the Table 5.

Table 5 — Boundary conditions. Here Ω is the boundary surface, \mathbf{v}_n is the normal velocity component to the surface

Particle / Fluid	Viscous	Inviscid
Rigid and lossless	$\mathbf{v}(\mathbf{r} \in \Omega) = 0$	$\mathbf{v}_n = 0$
Compressible and lossy	\mathbf{v}_n, p continuous	\mathbf{v}_n, p continuous

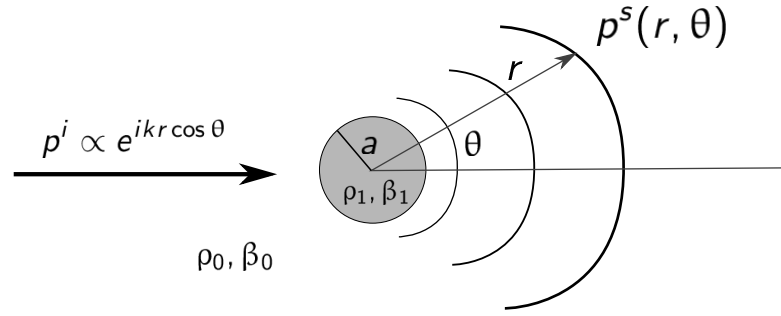


Figure 5.1 — Acoustic Mie scattering problem

5.1.1 Spin and orbital angular momentum of acoustic waves

Energy density and canonical momenta of an acoustic monochromatic wave can be written as [93]

$$W = \frac{1}{4} (\beta_0 |p|^2 + \rho_0 |\mathbf{v}|^2) \equiv W^{(p)} + W^{(\mathbf{v})} \quad (5.5a)$$

$$\mathbf{P} = \frac{1}{4\omega} \text{Im} [\beta_0 p^* \nabla p + \rho_0 \mathbf{v}^* \cdot (\nabla) \mathbf{v}] \equiv \mathbf{P}^{(p)} + \mathbf{P}^{(\mathbf{v})} \quad (5.5b)$$

$$\mathbf{L} = \mathbf{r} \times \mathbf{P} \quad (5.5c)$$

$$\mathbf{S} = \frac{\rho_0}{2\omega} \text{Im} \mathbf{v}^* \times \mathbf{v} \quad (5.5d)$$

where W is the energy density, \mathbf{P} is the canonical linear momenta density, \mathbf{L} and \mathbf{S} are the orbital and spin angular momentum densities, respectively. Here we have used Berry's notation $\mathbf{v}^* \cdot (\nabla) \mathbf{v} \equiv \sum_{i=x,y,z} v_i^* \nabla v_i$ [9].

5.2 Mie scattering problem

5.2.1 General solution and the dispersion equation

The geometry of the problem is shown in Fig. 5.1. Incident field can be decomposed as [95]

$$p^i = p_0 e^{ikr \cos \theta} = \sum_{n=0}^{\infty} p_n j_n(kr) P_n(\cos \theta), \quad (5.6)$$

where $p_n = p_0 i^n (2n + 1)$.

Any radiation from a body located at the origin can be characterized by sums of multipoles:

$$p(\mathbf{r}, \omega) = \sum_{n=0}^{\infty} \sum_{m=-n}^n A_{mn}(\omega) z_n(kr) Y_n^m(\theta, \varphi) \quad (5.7)$$

Where $z_n = j_n, h_n^{(1)}$ are the radial dependent functions which is usually one of the spherical Bessel functions depending on the boundary conditions, and $\Psi_{mn}(\mathbf{r}) = z_n(kr) Y_n^m(\theta, \varphi)$ are *the modes of the sphere*. Next, system has symmetry over φ , so

$$p(\mathbf{r}, \omega) = \sum_{n=0}^{\infty} A_n(\omega) z_n(kr) P_n(\cos \theta). \quad (5.8)$$

Particle with radius a is described by ρ_1 and β_1 and located in a fluid with ρ_0 and β_0 . Boundary conditions are

$$\begin{cases} p^i + p^s = p^{\text{in}} \\ v_r^i + v_r^s = v_r^{\text{in}} \end{cases} \quad (5.9)$$

where $\mathbf{v} = \frac{1}{i\omega\rho_0} \nabla p$, so the second equations transforms to $\partial_r p^i + \partial_r p^s = \frac{\rho_0}{\rho_1} \partial_r p^{\text{in}}$. Decompositions for scattered field and field inside the particle are

$$p^s(\mathbf{r}, \omega) = \sum_{n=0}^{\infty} p_n a_n(\omega) h_n^{(1)}(kr) P_n(\cos \theta), \quad (5.10)$$

$$p^{\text{in}}(\mathbf{r}, \omega) = \sum_{n=0}^{\infty} p_n c_n(\omega) j_n(k_1 r) P_n(\cos \theta), \quad (5.11)$$

where $p_n = p_0 i^n (2n + 1)$. Boundary conditions give explicit expressions for a_n and c_n coefficients:

$$c_n = \frac{i/(ka)^2}{j_n(k_1 a) h_n^{(1)'}(ka) - \gamma j_n'(k_1 a) h_n^{(1)}(ka)}, \quad (5.12)$$

$$a_n = \frac{\gamma j_n'(k_1 a) j_n(ka) - j_n(k_1 a) j_n'(ka)}{j_n(k_1 a) h_n^{(1)'}(ka) - \gamma j_n'(k_1 a) h_n^{(1)}(ka)}, \quad (5.13)$$

where $k_1 = k \sqrt{\bar{\rho}_1 \bar{\beta}_1}$ and $\gamma = \frac{k_1 \rho_0}{k \rho_1} = \sqrt{\bar{\beta}_1 / \bar{\rho}_1}$. These coefficient are in the agreement with coefficients A_n and B_n from [96]: $a_n = A_n$ and $c_n = -\bar{\rho}_1 B_n$ (it seems there is a typo in [96], c_n in this work satisfies the limiting case $p^{\text{in}}(\bar{\rho}_1 = \bar{\beta}_1 = 1) = p^i$).

Let us consider two general limits in acoustics:

1. **Rigid sphere.** For the absolute rigid sphere there is no radial velocity at the surface. This leads to the next boundary condition

$$\partial_r (p^i(r, \theta) + p^s(r, \theta)) \Big|_{r=a} = 0, \quad (5.14)$$

which results in

$$a_n^{\text{rigid}} = -\frac{j'_n(ka)}{h_n^{(1)'}(ka)}. \quad (5.15)$$

The same result can be obtained from (5.13) by taking limit $\beta_1 \rightarrow 0$ while $\rho_1 = \text{const.}$

2. **Pressure release sphere.** Total pressure at surface vanishes, so the boundary conditions come to

$$p^i(a, \theta) + p^s(a, \theta) = 0, \quad (5.16)$$

which leads to

$$a_n^{\text{p.r.}} = -\frac{j_n(ka)}{h_n^{(1)}(ka)}. \quad (5.17)$$

The same result can be obtained from (5.13) by taking limit $\beta_1 \rightarrow \infty$ while $\rho_1 = \text{const.}$

5.2.2 Sphere resonances

Resonant conditions is given by the zeros of the denominator of inner and scattering coefficient (5.12) and (5.13)

$$\Delta = j_n(k_1 a) h_n^{(1)'}(ka) - \gamma j'_n(k_1 a) h_n^{(1)}(ka) = 0, \quad (5.18)$$

where $k_1(\omega) = k(\omega) \sqrt{\bar{\rho}_1 \beta_1}$, $\gamma = \sqrt{\beta_1 / \bar{\rho}_1}$ and $k(\omega) = \omega/c$. Solution of this dispersion equation, in general, are the *complex* frequencies

$$\omega_n = \omega_{0n} - i\delta_n, \quad (5.19)$$

where $\tau = 1/2\delta_n$ is the mode lifetime. This happens because it is an open system and mode energy leaks to the free space. An example of the complex map to show approximate location of the roots for some random parameters are shown on Fig. 5.2. For the case of solid sphere with supports shear waves it is possible to realize bound

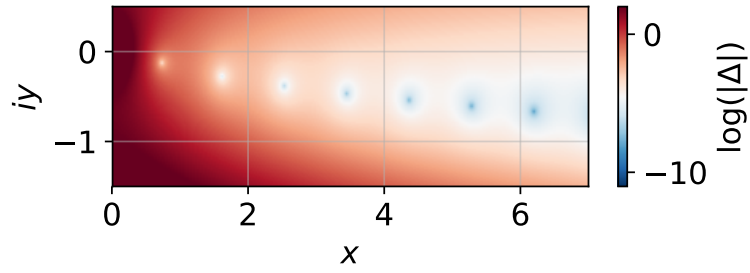
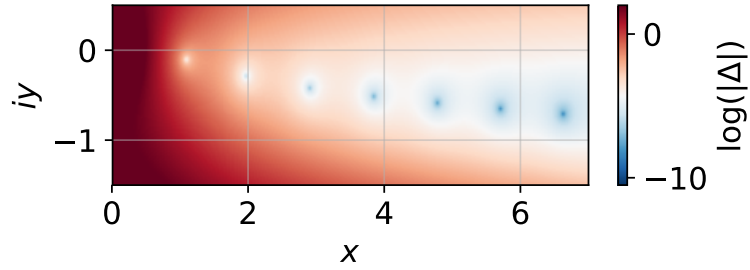
(a) $n = 0$ (b) $n = 1$

Figure 5.2 – An example of the complex roots of the acoustic dispersion equation with $n = 0$ and $n = 1$ for a sphere with $\bar{\rho}_1 = 3 + 0.1i$ and $\bar{\beta}_1 = 4 + 0.3i$. Here $x = \text{Re}(ka)$ and $y = \text{Im}(ka)$

state in the continuum with infinite Q -factor [331]. Otherwise, there always will be an finite lifetime for an open system.

Below we consider some particular cases.

Monopole resonance

For $n = 0$ dispersion equation (5.18) reduces to

$$q \sin(q)(ix - 1) = \gamma x (q \cos(q) - \sin(q)), \quad (5.20)$$

where $q = k_1(\omega)a$ and $x = k(\omega)a$.

Dipole resonance

For $n = 1$ dispersion equation (5.18) reduces to

$$\frac{q^2 \left(\frac{\sin(q)}{q} - \cos(q) \right)}{(q^2 - 2) \sin(q) + 2q \cos(q)} = -\frac{\gamma x(x + i)}{2x + 2i - ix^2} \quad (5.21)$$

5.2.3 Cross sections

We start with the absorption energy flow W which can be written as [97]

$$W_a = - \oint \mathbf{\Pi}^{\text{Re}} \cdot d\mathbf{S}, \quad (5.22)$$

where $\mathbf{\Pi}^{\text{Re}} = \frac{1}{2} \text{Re}(p^* \mathbf{v})$ is the energy flow or the acoustic analog of Poynting vector. If $W_a > 0$ energy is absorbed inside the integration sphere. Our fields are the sums of incident and scattered fields, so we have three types of terms: proportional only to the incident field, scattered field and interference term. The standard way of writing it is $W_a = W_i - W_s + W_{\text{ext}}$ where

$$W_i = -R^2 \int_{4\pi} d\Omega \frac{1}{2} \text{Re} p^{i*} v_r^i, \quad (5.23)$$

$$W_s = R^2 \int_{4\pi} d\Omega \frac{1}{2} \text{Re} p^{s*} v_r^s, \quad (5.24)$$

$$W_{\text{ext}} = -R^2 \int_{4\pi} d\Omega \frac{1}{2} \text{Re} (p^{s*} v_r^i + p^{i*} v_r^s), \quad (5.25)$$

where $R > a$ is any arbitrary radius of the integration sphere and $d\Omega = \sin\theta d\theta d\varphi$. $W_i = 0$ if the media is non-absorbing. Usually, W is normalized to the intensity of the incident wave $\sigma \equiv W/I_{\text{inc}}$. We can write

$$\sigma_{\text{ext}} = \sigma_{\text{abs}} + \sigma_{\text{sc}}, \quad (5.26)$$

where after integration we get expression very similar to the identical ones in the electromagnetic Mie scattering problem [97]:

$$\sigma_{\text{sc}} = \frac{4\pi}{k^2} \sum_{n=0}^{\infty} (2n+1) |a_n|^2, \quad (5.27)$$

$$\sigma_{\text{ext}} = -\frac{4\pi}{k^2} \sum_{n=0}^{\infty} (2n+1) \text{Re}(a_n), \quad (5.28)$$

$$\sigma_{\text{abs}} = -\frac{4\pi}{k^2} \sum_{n=0}^{\infty} (2n+1) \left(|a_n|^2 + \text{Re}(a_n) \right) \quad (5.29)$$

Plot for some artificial parameters on Fig. 5.3. We also provide a table of cross sections for various combination of popular acoustic materials which is about to help to find a proper resonant material: air, water, porous silicon, epoxy resin, and aerogel (fig. 5.4). The general rule of thumb is that the acoustic refractive index should be $n_{\text{acoustic}} = c_s^{\text{host}}/c_s^{\text{particle}} = \sqrt{\bar{\rho}_1 \bar{\beta}_1} \gtrsim 1$.

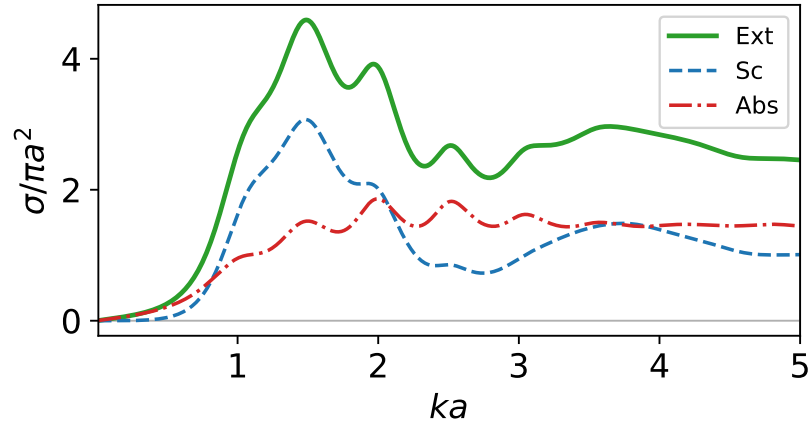


Figure 5.3 — Normalized acoustical cross sections for an absorbing sphere with $\bar{\rho}_1 = 3 + 0.1i$ and $\bar{\beta}_1 = 2 + 0.2i$

Let us consider the case of small particles. In terms of monopole and dipole polarizabilities, which are defined in Sec. 5.3, we can rewrite it as:

$$\sigma_{\text{ext}} = k (\text{Im}(\alpha_M) + \text{Im}(\alpha_D)), \quad (5.30)$$

$$\sigma_{\text{sc}} = \frac{k^4}{4\pi} \left(|\alpha_M|^2 + \frac{1}{3} |\alpha_D|^2 \right), \quad (5.31)$$

$$\sigma_{\text{abs}} = \underbrace{k \text{Im} \alpha_M - \frac{k^4}{4\pi} |\alpha_M|^2}_{\sigma_{\text{abs}}^M} + \underbrace{k \text{Im} \alpha_D - \frac{k^4}{12\pi} |\alpha_D|^2}_{\sigma_{\text{abs}}^D} \quad (5.32)$$

Since polarizabilities are scaled as the volume of the particle $\alpha_M, \alpha_D \sim a^3$, we can conclude that for lossy ($\text{Im}(\bar{\rho}), \text{Im}(\bar{\beta}) \sim 1$) subwavelength particles $\sigma_{\text{abs}} \sim a^3 \gg$

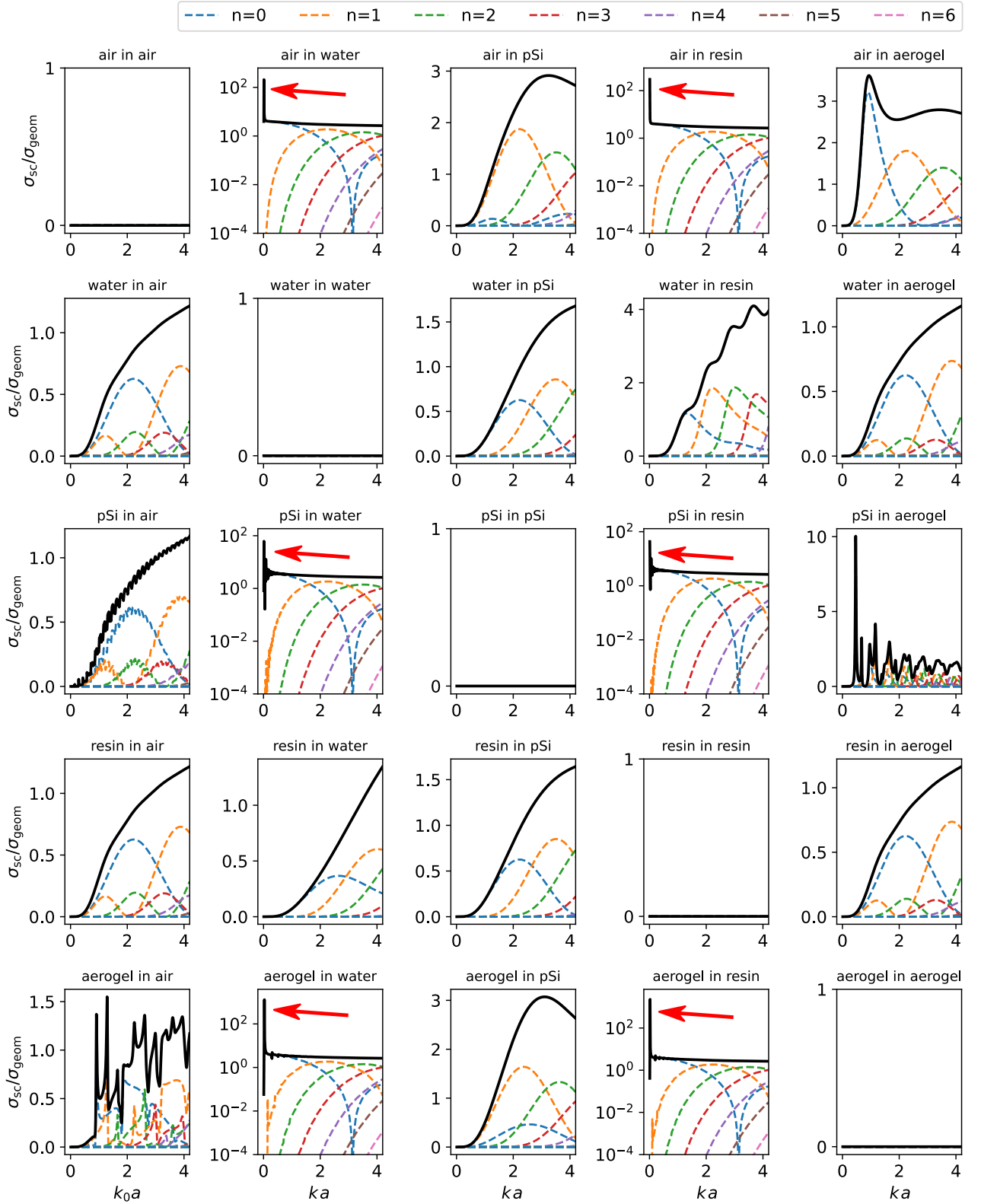


Figure 5.4 — Normalized scattering cross sections $\sigma_{sc}/\sigma_{geom}$ (with $\sigma_{geom} = \pi a^2$) for various materials versus size parameter ka , where k is the wavevector in the host media and a is a particle radius. For all materials we have artificially added small losses as $\bar{\rho}_1 \rightarrow \bar{\rho}_1(1+0.01i)$ and $\bar{\beta}_1 \rightarrow \bar{\beta}_1(1+0.01i)$ to remove some extremely sharp peaks which do not occur in real life. Red arrows show extremely sharp monopole resonances which occur for some particular combinations (log scale is applied for these plots). pSi is a shorthand for porous silicon, resin is a shorthand for epoxy resin

$\sigma_{sc} \sim a^6$. In other words, small particles absorb better than scatter. However, for bigger particles scattering become more dominant.

5.2.4 Decomposition of the scattering coefficient in Taylor series

Monopole coefficient:

$$a_0 = \frac{i}{3}x^3(\bar{\beta}_1 - 1) + \frac{i}{45}x^5(\bar{\beta}_1^2(\bar{\rho}_1 + 5) - 15\bar{\beta}_1 + 9) - \frac{1}{9}x^6(\bar{\beta}_1 - 1)^2 + \mathcal{O}(x^7) \quad (5.33)$$

Dipole coefficient:

$$a_1 = \frac{i}{3}x^3 \frac{\bar{\rho}_1 - 1}{2\bar{\rho}_1 + 1} + \frac{i}{5}x^5 \frac{\bar{\rho}_1^2(\bar{\beta}_1 - 1) - \bar{\rho}_1 + 1}{(2\bar{\rho}_1 + 1)^2} - \frac{1}{9}x^6 \left(\frac{\bar{\rho}_1 - 1}{2\bar{\rho}_1 + 1} \right)^2 + \mathcal{O}(x^7) \quad (5.34)$$

One of the important features of this decomposition is that for the case of real parameters $|a_n|^2 + \text{Re}(a_n) = 0$ for the all orders. This fact is important since exactly this combination presents in the absorption cross section in (??). It represents no losses for the *real* valued particle parameters ρ_1 and β_1 . The order of first non-zero terms in the decomposition of scalar Mie scattering coefficient are presented in Tab. 6.

5.3 Monopole and dipole polarizability and its connection with scattering coefficients

5.3.1 Monopole polarizability

The *monopole strength* M is by definition is the volume flow through the surface of the object per second [95; 334]. For the sphere of radius a it is given by

$$M(t) = \oint_{\text{particle}} \mathbf{v} \cdot d\mathbf{S} = 4\pi a^2 \langle v_r(a, t) \rangle_{\theta, \varphi}, \quad [M] = [\text{m}^3 \cdot \text{s}^{-1}], \quad (5.35)$$

where $\langle v_r(a, t) \rangle_{\theta, \varphi}$ is the average radial component of the velocity of the sphere surface. Radiation of the point monopole is given by [334] $p(r, t) = \frac{\rho_0 \dot{M}(t-r/c)}{4\pi r}$. For

Table 6 — Orders of first non-zero terms in decomposition of scattering coefficients. This decomposition is in consistent with [332]. Names of the multipoles are taken from [333]

Coefficient	a_n	$\mathcal{O}(\text{Re } a_n)$	$\mathcal{O}(\text{Im } a_n)$
Monopole	a_0	$\sim x^6$	$\sim x^3$
Dipole	a_1	$\sim x^6$	$\sim x^3$
Quadrupole	a_2	$\sim x^{10}$	$\sim x^5$
Octupole	a_3	$\sim x^{14}$	$\sim x^7$
Hexadecapole	a_4	$\sim x^{18}$	$\sim x^9$
Dotriacontapole	a_5	$\sim x^{22}$	$\sim x^{11}$
Tetrahexacontapole	a_6	$\sim x^{26}$	$\sim x^{13}$
Octacosahectapole	a_7	$\sim x^{30}$	$\sim x^{15}$
\vdots			
n -th multipole	a_n	$\sim x^{2(2n+1)}$	$\sim x^{2n+1}$

the monochromatic wave $p(\mathbf{r}, t) = \text{Re}(p(\mathbf{r})e^{-i\omega t})$ We have (the signs are defined opposite to those in [95; 334])

$$p_M(\mathbf{r}) = -\frac{\rho_0 c k^2}{4\pi} M \frac{e^{ikr}}{ikr}. \quad (5.36)$$

For the sake of convenience we also write velocity radiated by a monopole M in the far field (FF)

$$\mathbf{v}_M = \mathbf{n} \frac{ikM}{4\pi} \frac{e^{ikr}}{r} \left(1 - \frac{1}{ikr}\right) \stackrel{\text{FF}}{=} \mathbf{n} \frac{ikM}{4\pi} \frac{e^{ikr}}{r} \quad (5.37)$$

where $\mathbf{n} = \mathbf{r}/r$. Next, we define monopole polarizability as

$$M \equiv -i\omega\beta_0\alpha_M p, \quad (5.38)$$

where p is the total pressure field. By comparison (5.36) with the zero term ($n = 0$) of (5.10) and using definition (5.38) we find

$$\alpha_M = -\frac{4\pi i}{k^3} a_0 \approx \frac{4\pi}{3} a^3 (\bar{\beta} - 1), \quad (5.39)$$

where $Z_0 = \rho_0 c = \sqrt{\rho_0/\beta_0}$ is the impedance of the host media. And also helpful as a reference the explicit expressions for the real and imaginary parts in the lowest approximation $\text{Re}(\alpha_M) = \frac{4\pi}{3} a^3 \cdot (\text{Re}(\bar{\beta}_1) - 1)$ and $\text{Im}(\alpha_M) = \frac{4\pi}{3} a^3 \cdot \text{Im}(\bar{\beta}_1)$.

5.3.2 Dipole polarizability

The *dipole strength* by definition is given by [95]

$$\mathbf{D} = M\mathbf{d}, \quad [D] = [\text{m}^4 \cdot \text{s}^{-1}] \quad (5.40)$$

where \mathbf{d} is the vector which connects two opposite monopoles M . For the point dipole ($|\mathbf{d}| \rightarrow 0$) and monochromatic fields dipole radiation can be written in a vector form as (the signs are opposite to those in [95; 334])

$$p_{\text{D}}(\mathbf{r}) = i\rho_0ck(\mathbf{D} \cdot \nabla) \frac{e^{ikr}}{4\pi r} \quad (5.41)$$

or in spherical variables (r, θ, φ) as

$$p_{\text{D}}(\mathbf{r}) = \rho_0ck^2D \cos \theta \left(1 + \frac{i}{kr}\right) \frac{e^{ikr}}{4\pi r}. \quad (5.42)$$

For the sake of convenience we also write radiated velocity $\mathbf{v}_{\text{D}} = \frac{1}{i\omega\rho_0} \nabla p_{\text{D}}$ of a point acoustic dipole $\mathbf{D} = M\mathbf{d}$ in a vectorial form:

$$\begin{aligned} \mathbf{v}_{\text{D}}(\mathbf{r}) &= \frac{ik^2}{4\pi} \left(\mathbf{D} \frac{h'_0(kr)}{r} + (\mathbf{D} \cdot \mathbf{r}) \nabla \left[\frac{h'_0(kr)}{r} \right] \right) \\ &= \frac{ike^{ikr}}{4\pi r^2} \left[\mathbf{D} \left(1 + \frac{i}{kr}\right) + \mathbf{n}(\mathbf{D} \cdot \mathbf{n}) \left(ikr - 3 - \frac{3i}{kr}\right) \right] \end{aligned} \quad (5.43)$$

or in spherical coordinates

$$\mathbf{v}_{\text{D}}(r, \theta, \varphi) = \begin{pmatrix} v_r \\ v_\theta \\ v_\varphi \end{pmatrix} = \begin{pmatrix} k^2D \cos(\theta) \left(1 + \frac{2i}{kr} - \frac{2}{(kr)^2}\right) \frac{e^{ikr}}{4\pi r} \\ \frac{ikD}{r} \sin(\theta) \left(1 + \frac{i}{kr}\right) \frac{e^{ikr}}{4\pi r} \\ 0 \end{pmatrix}. \quad (5.44)$$

We define dipole polarizability as

$$\mathbf{D} \equiv \alpha_{\text{D}}\mathbf{v}, \quad (5.45)$$

where \mathbf{v} is the total complex velocity vector. To get the explicit expression for the α_{D} we do the same steps as we did for the α_{M} . After comparing (5.42) and first term ($n = 1$) of (5.10), using relation between pressure and velocity magnitudes $p_0 = \rho_0c|\mathbf{v}_0| = Z_0|\mathbf{v}_0|$, where Z_0 is the impedance of the host media, and assuming the particle is isotropic (i.e. $\mathbf{D} \parallel \mathbf{v}_0$), we come to the next expression

$$\alpha_{\text{D}} = -\frac{4\pi i}{k^3} 3a_1 \approx \frac{4\pi}{3} a_3^3 \frac{3(\bar{\rho} - 1)}{2\bar{\rho} + 1}. \quad (5.46)$$

And also helpful as a reference the explicit expressions for the real and imaginary parts in the lowest approximation $\text{Re}(\alpha_D) = 4\pi a^3 \frac{2|\bar{\rho}_1|^2 - \text{Re}(\bar{\rho}_1) - 1}{|2\bar{\rho}_1 + 1|^2}$ and $\text{Im}(\alpha_D) = 4\pi a^3 \frac{3\text{Im}(\bar{\rho}_1)}{|2\bar{\rho}_1 + 1|^2}$.

5.4 Acoustic force and torque

Let us go deeper into the acoustomechanics. Now, when acoustic polarizabilities are well defined, it is possible to write very clear expressions for the acoustic force and torque in the subwavelength regime.

5.4.1 Limit for the small particles. Connection with canonical momenta

Handwavy approach

Main idea of this approach:

$$\overrightarrow{\text{force}} = -\nabla(\text{interaction energy})$$

However, this approach cannot give non-cervative part of the force, but it still gives great amount of intuitive understanding.

Monopole force. Energy is proportional to the mass acceleration of the outgoing wave multiplied by the displacement magnitude which is proportional to the pressure, i.e. $E \propto \rho_0 \dot{Q}(t) \cdot p(\mathbf{r}, t)$. Since we are interested in the average quantities, we replace $\langle a(\mathbf{r}, t)b(\mathbf{r}, t) \rangle \rightarrow \frac{1}{2} \text{Re}(a^*(\mathbf{r})b(\mathbf{r}))$ and $\partial_t \rightarrow -i\omega$. The correct preconstant can be identified e.g. by the comparing with the plane wave pressure (1.51). Finally, the monopole force can be easily written as

$$\mathbf{F}_M = -\frac{1}{2\omega} \text{Im}(M^* \nabla p). \quad (5.47)$$

Dipole force. The dipole interaction energy can be written in the same manner as in electrodynamics, i.e. $E \propto \mathbf{D} \cdot \mathbf{v}$. Identifying the dimensional preconstant in the same way as it was done for the monopole, we come to

$$\mathbf{F}_D = -\frac{\rho_0}{2} \operatorname{Re} (\mathbf{D}^* \cdot (\nabla) \mathbf{v}). \quad (5.48)$$

where we have used Berry's notation $\mathbf{D}^* \cdot (\nabla) \mathbf{v} \equiv \sum_{i=x,y,z} D_i^* \nabla v_i$ [9].

Rigorous approach (integration of the stress tensor)

The most rigorous approach of the force calculation is based on the integration of the stress tensor (similarly to the Maxwell stress-tensor) $\Pi_{ij} = p\delta_{ij} + \rho v_i v_j$ over the surface enclosing the object [212; 213]: $\langle F_i \rangle = \oint_{\Sigma} d\Sigma \langle \Pi_{ij} \rangle n_j$, where angle brackets show time average. In the similar manner to the force, the acoustical torque is defined by the flow of *flux density of angular momentum* $\mathcal{M}_{ji} = \varepsilon_{ikl} r_k \Pi_{lj}$ ($\hat{\mathcal{M}} = \mathbf{r} \times \hat{\Pi}$) over the surface Σ enclosing the object [167; 212; 218–221]: $\langle T_i \rangle = -\oint_{\Sigma} d\Sigma \langle \hat{\mathcal{M}}_{ji} \rangle n_j$. To obtain a simple expression for small particles, we implemented the same approach used in optics [335]. We decompose the total field into incident and scattered parts $(p, \mathbf{v}) = (p, \mathbf{v})^{\text{inc}} + (p, \mathbf{v})^{\text{sc}}$. Since $\hat{\Pi}$ is quadratic with respect to the field, this gives us three types of terms: (1) $\hat{\Pi}_0$ which is proportional only to the incident field; (2) $\hat{\Pi}_{\text{self}}$ which is proportional only to the scattered field; and (3) $\hat{\Pi}_{\text{mix}}$ which consists of mix products. The terms involving the incident field only (as if the particle were not there) give no net contribution to the force and torque. Therefore we are left with the contribution to the force from the fields scattered by the monopole Q and dipole \mathbf{D} , and the contribution due to the cross terms involving both the scattered and incident fields. Integration of the mixed terms is convenient to perform in the near zone decomposing incident field, however $\hat{\Pi}_{\text{self}}$ is much easier to integrate in the far field. The result is the following [336; 337]:

$$\mathbf{F} = \underbrace{-\frac{1}{2} \operatorname{Re} \left[\frac{i}{\omega} M^* \nabla p - \rho \mathbf{D}^* \cdot (\nabla) \mathbf{v} \right]}_{\mathbf{F}_M + \mathbf{F}_D} - \underbrace{\frac{\rho k^3}{12\pi} \operatorname{Im} [M^* \mathbf{D}]}_{\mathbf{F}_{\text{self}}}. \quad (5.49)$$

Which is in consistent with the result obtained by the expanding the solutions of the general Lorentz-Mie solutions in acoustics [338]. We also introduce monopole

$\alpha_M = -\frac{4\pi i}{k^3} a_0 \approx \frac{4\pi}{3} a^3 (\bar{\beta} - 1)$ and dipole $\alpha_D = -\frac{4\pi i}{k^3} 3a_1 \approx \frac{4\pi}{3} a^3 \frac{3(\bar{\rho}-1)}{2\bar{\rho}+1}$ polarizabilities such that induced monopole and dipole moments are written as $M = -i\omega\beta\alpha_M p(\mathbf{r}_0)$ and $\mathbf{D} = \alpha_D \mathbf{v}(\mathbf{r}_0)$, where a_0, a_1 are the acoustic scattering Mie coefficients, \mathbf{r}_0 is the position of the particle. After that, it is possible to write a direct correspondence with the energy and canonical momentum densities [336].

Same approach is valid for the torque as well:

$$\mathbf{T} = \frac{\rho}{2} \text{Re}(\mathbf{D}^* \times \mathbf{v}) - \frac{\rho k^3}{24\pi} \text{Im}(\mathbf{D}^* \times \mathbf{D}) \quad (5.50)$$

or in terms of absorption cross section and canonical spin angular momentum density the torque is going to be

$$\mathbf{T} = c_s \sigma_{\text{abs}}^D \mathbf{S} \quad (5.51)$$

where c_s is the speed of sound in the host media. To the best of knowledge, eqs. (5.50) and (5.51) are written the first time and have lots of similarities with the ones in optics [94].

The last term of (5.49) is responsible for the recoil force, which is partially proportional to the radiated energy flow with the negative sign which can be seen from (5.57). Small particle characterized by the relative density $\bar{\rho}_1$ and compressibility $\bar{\beta}_1$ is in the field of an incident plane wave $p(\mathbf{r}) = p_0 e^{ikz}$. Monopole and dipole polarizabilities have the same scaling $\alpha_M, \alpha_D \sim (ka)^3$ [336] so the scattered intensity is comparable. The sum of a dipole and monopole radiation gives a directional scattering diagram (similarly to the Kerker effect in optics) [337; 339], which depends on the relative phase between Q and \mathbf{D} . This relative phase can be tuned by changing complex parameters of the particle $\{\bar{\rho}, \bar{\beta}\}$ [337].

A helpful reminder here of the polarizability definitions

$$\alpha_M = -\frac{4\pi i}{k^3} a_0 \approx \frac{4\pi}{3} a^3 (\bar{\beta} - 1), \quad M = -i\omega\beta\alpha_M p, \quad (5.52)$$

$$\alpha_D = -\frac{4\pi i}{k^3} 3a_1 \approx \frac{4\pi}{3} a^3 \frac{3(\bar{\rho} - 1)}{2\bar{\rho} + 1}, \quad \mathbf{D} = \alpha_D \mathbf{v}. \quad (5.53)$$

We need to mention that this expression depends only on the *incident* fields.

General notes about eqs. (5.49) and (5.50). Those equations support lossy particles. Also, for the case of lossless particles it is consistent with solutions of Gor'kov [213] and others [215; 340]. And it is totally consistent with eq. (5) from [341].

Using polarizabilities we connect the field action on a small particle with the canonical properties of the acoustic incident wave:

$$\mathbf{F} = \mathbf{F}^{\text{grad}} + \mathbf{F}^{\text{scat}} + \mathbf{F}^{\text{recoil}}. \quad (5.54)$$

Here the gradient and scattering parts are related to the real and imaginary parts of the particle polarizabilities:

$$\mathbf{F}^{\text{grad}} = \text{Re}(\alpha_M) \nabla W^{(p)} + \text{Re}(\alpha_D) \nabla W^{(v)}, \quad (5.55)$$

$$\mathbf{F}^{\text{scat}} = 2\omega \left[\text{Im}(\alpha_M) \mathbf{P}^{(p)} + \text{Im}(\alpha_D) \mathbf{P}^{(v)} \right] \quad (5.56)$$

$$\mathbf{F}^{\text{recoil}} = \frac{k^4}{6\pi c_s} \left(\text{Re}(\alpha_M \alpha_d^*) \mathbf{\Pi}^{\text{Re}} + \text{Im}(\alpha_M \alpha_D^*) \mathbf{\Pi}^{\text{Im}} \right) \quad (5.57)$$

These laconic expressions reveal the direct relation between the scattering force (which is associated with the absorption of phonons by the particle) and canonical momentum density of the acoustic field this is partially is published in [336; 337]. Such decomposition of the recoil part of the force is done first time to the best of my knowledge.

5.4.2 Evanescent wave. Complex angle approach

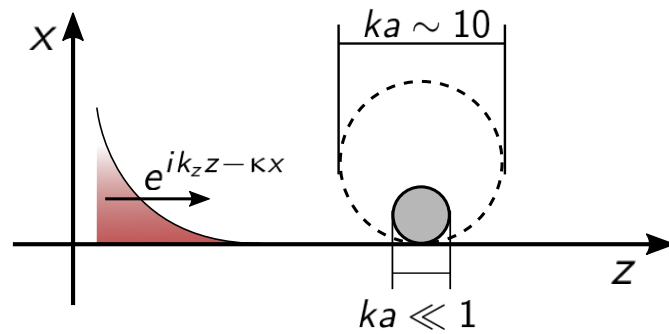


Figure 5.5 — Geometry of the problem. Similar approach to the [171, § 4]

As an example of the usage of optical method in acoustics let us consider a complex angle approach for an evanescent wave which first appeared in optics [171]. The incident plane wave $p^{\text{p.w.}}(\mathbf{r}) = p_0 e^{ikz}$ can be transformed to the evanescent wave by the rotation its argument on the complex angle

$$p^{\text{evan}}(\mathbf{r}) = p^{\text{p.w.}}(\hat{R}(i\alpha)\mathbf{r}) = p_0 e^{ik \cosh(\alpha)z} e^{-k \sinh(\alpha)x}, \quad (5.58)$$

where $\hat{R}(i\alpha) = \begin{pmatrix} \cosh(\alpha) & 0 & -i \sinh(\alpha) \\ 0 & 1 & 0 \\ i \sinh(\alpha) & 0 & \cosh(\alpha) \end{pmatrix}$.

Mie operator is also linear so we know the scattered field in the case of evanescent incident wave for any sphere

$$p^s(\mathbf{r}) \rightarrow p^s(\hat{R}(i\alpha)\mathbf{r}) \quad (5.59)$$

so $x \rightarrow x' = x \cosh(\alpha) - iz \sinh(\alpha)$, $y \rightarrow y' = y$, $z \rightarrow z' = ix \sinh(\alpha) + z \cosh(\alpha)$ or for spherical coordinates $r \rightarrow r' = r$, $\theta \rightarrow \theta' = \cos^{-1} \frac{z'}{r}$, and $\varphi \rightarrow \varphi' = \text{tg}^{-1} \frac{y}{x'}$. And the velocity is always defined as $\mathbf{v} = \frac{1}{i\omega\rho} \nabla p$. Since we know the all the fields, we can numerically integrate (1.47c). The result of calculation is presented in Fig. 5.6. Note that repulsion and attraction forces to the surface are possible.

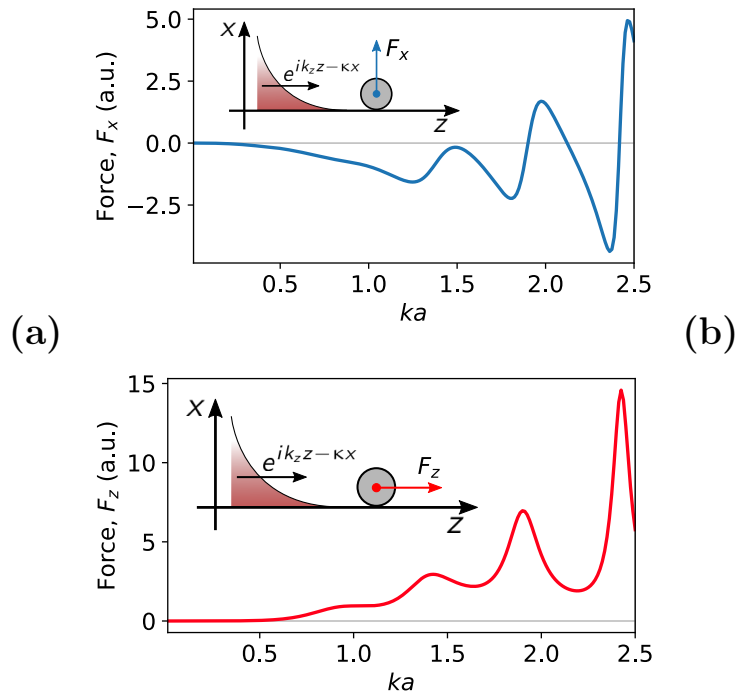


Figure 5.6 — Gradient force F_x (a) and pressure force F_z (b) for a lossless particle. With parameters $\bar{\beta}_1 = 3$, $\bar{\rho}_1 = 2$, and $\alpha = 0.8$

5.5 Green's function

Green's function method is powerful tool in various branches in physics such quantum mechanics, classical electrodynamics, and others. It is also well established in linear acoustics. Since Green's function is a solution of the delta perturbed master

equation, it shows how the simplest source radiates. For the case of acoustics, Green's functions shows the monopole radiation field. For a monopole M and a dipole \mathbf{D} located at \mathbf{r}_0 its radiated field can be expressed as [95, § 6.5]

$$p_M(\mathbf{r}) = -i\rho ckMG(\mathbf{r}, \mathbf{r}_0) \quad (5.60)$$

$$p_D(\mathbf{r}) = -\rho ck(\mathbf{D} \cdot \nabla_{\mathbf{r}_0})G(\mathbf{r}, \mathbf{r}_0)|_{\mathbf{r}_0=\mathbf{r}_0} \quad (5.61)$$

where for the free space Green's function is going to have a very simple form

$$G_0(\mathbf{r}, \mathbf{r}_0) = \frac{e^{ik|\mathbf{r}-\mathbf{r}_0|}}{4\pi|\mathbf{r}-\mathbf{r}_0|} \quad (5.62)$$

For any other geometries, all the complexity of the problem is going to be inside of a GF such as proper reflection coefficients and so on. Some simple geometries can be solved analytically such as infinite half space substrate [342, § 3].

5.6 A scientific statement

Fourth scientific statement

The acoustic force acting on subwavelength particles are directly proportional to the sum of the density of the linear canonical momenta and the gradient of the energy density. The acoustic torque on subwavelength particles is proportional to the canonical spin momentum density.

Conclusion

In this thesis we have solved several problems regarding optical and acoustical mechanical action. Here are the highlights of the most important results:

1. In Chapter 1 we have presented a consistent overview of the optical forces and torques. How it should be calculated in different approximations for various particle types such as isotropic, anisotropic, and chiral particles. We also showed the connection between canonical properties of light and optical forces. Finally, a brief overview of acoustical forces was also presented.
2. In Chapter 2 a complete picture of eigen modes analyses for spherical and cylindrical shapes was outlined.
3. In Chapter 3 the effect of stable optical binding of a linear array of nanoparticles trapped by a transverse pump near a nanofiber via photonic jet effect. The stability is achieved by long-range interaction by waveguided mode.
4. In Chapter 4 two scenarios of angular momenta transfer were analyzed: (1) transfer of orbiting motion of a microparticle around a nanofiber; (2) spinning motion of an anisotropic particle in a complex field. Finally, the non-linear effects were also considered. We have shown that it is possible to spin azimuthally symmetric objects via second-harmonic generation process.
5. In Chapter 5 we have illustrated and outlined in detail how one can successfully implement the well-established methods from optomechanics in the area of linear acoustomechanics. The main achievement in this chapter is the explicit connection between canonical momenta of acoustic fields and acoustomechanics action on a subwavelength particle.

List of figures

- 1 Концепция связи между каноническими свойствами электромагнитного поля и оптомеханикой для частиц субволновой длины. Существует также полная аналогия для акустических полей и акустомеханики 18
- 2 Распределение плотности углового момента для дипольных мод для диэлектрических и металлических частиц 24
- 3 Основная идея главы 3: массив субволновых частиц вблизи нановолокна с поперечной накачкой. Потенциал захвата вдоль оси волокна растет линейно с числом частиц в цепи. Дальнее взаимодействие достигается за счет взаимодействия через волноводную моду 26
- 4 (а) Продольная сила F_z в одномодовом режиме, действующая на одну из двух частиц в зависимости от расстояния вдоль оси нановолокна Δz . Красная сплошная линия показывает полную оптическую силу, которая учитывает взаимодействие как через свободное пространство, так и через волокно ($\hat{\mathbf{G}}_s + \hat{\mathbf{G}}_0$), зеленая пунктирная линия показывает только взаимодействие через волокно ($\hat{\mathbf{G}}_s$) и синяя пунктирная линия показывает только взаимодействие в свободном пространстве ($\hat{\mathbf{G}}_0$). (б) Равновесные решения. Первые три ветви решения для расстояния между двумя ближайшими частицами $q = \Delta z \beta$ в отношении общего числа частиц в цепочке N . (в) Параметр ловушки γ , который равен эффективной потенциальной глубине ловушки, деленной на тепловую энергию вмещающей среды kT , и нормированная жесткость ловушки по отношению к числу частиц в цепочке N . . . 27

5	В Главе 4 рассмотрены три основные системы, в которых происходит передача спинового и орбитального угловых моментов (SAM и OAM). Слева направо: передача OAM от круговой поляризованной основной направляющей волны HE_{11} ; передача SAM от поперечного спина, который исходит от линейно поляризованной моды HE_{11} к анизотропным частицам; нелинейная передача SAM от плоской круговой поляризованной волны через процесс генерации второй гармоники, наличие момента объясняется из закона сохранения AM	29
6	Механизм нелинейного крутящего момента. Циркулярно поляризованная плоская волна с частотой ω падает на цилиндр без потерь, последняя генерирует вторую гармонику с ненулевым угловым моментом, который определяется правилами отбора. Вследствие сохранения углового момента существует ненулевой механический момент	31
A	Concept of the connection between electromagnetic field properties and optomechanics for subwavelength particles. There is also a full analogy for the acoustic fields and acoustomechanics	46
B	Angular momenta density distribution for the dipole modes for dielectric and metallic particles	52
C	The main concept of Chapter 3 : an inline array of subwavelength particles near a nanofiber with transverse illumination. The trapping potential along the fiber axis growth linearly with the number of particles in the chain. The long-range interaction is achieved via the interaction through the guided mode	53

- D (a) Longitudinal force F_z in a single mode regime acting on one of two particles as a function of distance along the nanofiber axis Δz . Red solid line shows total optical force which takes into account interaction through both free space and fiber ($\hat{\mathbf{G}}_s + \hat{\mathbf{G}}_0$), green dashed line shows only interaction through the fiber ($\hat{\mathbf{G}}_s$) and blue dash-and-dot line shows only free space interaction ($\hat{\mathbf{G}}_0$). (b) Equilibrium solutions. First three branches of the solution for the distance between the two closest particles $q = \Delta z \beta$ with respect to the total number of particles in a chain N . (c) Trapping parameter γ , which equals to the effective potential depth of the trap divided by a thermal energy of the host media kT , and normalized stiffness of the trap with respect to the number of particles in a chain N 54
- F Three main systems considered in Chapter 4 where the spin and orbital angular momenta (SAM and OAM) is transferred. From left to right: OAM transfer from the circular polarized fundamental waveguided mode HE_{11} ; SAM transfer from the transverse spin which comes from the linearly polarized HE_{11} mode to the anisotropic particles; non-linear SAM transfer from a plane circular polarized wave via second harmonic generation process, the presence of torque is explained from the AM conservation law 56
- G The mechanism of the non-linear torque. Circularly polarized plane with frequency ω wave is incident on a lossless cylinder, the later one generates second harmonic with non-zero angular momentum which is defined by selection rules. Due to the conservation of the angular momenta there is a non-zero mechanical torque 58
- 1.1 The change in the flux of the momentum energy tensor and the flux of the angular momentum density during integration through the closed surface Σ shows what force and torque acts on the particle with the parameters ϵ and μ 69
- 1.2 Artistic view of the optical force decomposition for the small particles 73

1.3	Schematic of the “direct” and “crossed” momentum transfer interpretation of optical forces and torques applied to a chiral dipole. The nonchiral component α_e, α_m of the dissipative force (the torque) couples the linear (angular) momentum of the light to the linear (angular) momentum of the particle, while the chiral component α_c of the dissipative force and of the torque cross-couples linear to angular momenta in both directions. Adopted from [24]. The explicit dependency is written in eqs. (1.26) and (1.27)	76
1.4	Simplification of the anisotropic bipolar sphere. We take into account only electric p and magnetic m dipole moments, and also neglect the bipolar structure of the anisotropy. For this geometry $\epsilon_{xx} = \epsilon_{\parallel} > \epsilon_{yy,zz} = \epsilon_{\perp}$	78
2.1	Eigen modes for dielectric and metallic particles for the $n = 1, \dots, 10$. For dielectric particle: $a = 100$ nm, $\epsilon_p = 10, \mu_p = 1$. For metallic particle: $a = 50$ nm, Drude model $\epsilon_{\text{Drude}} = 1 - \omega_p^2 / (\omega^2 + i\Gamma\omega)$ for gold without losses with $\omega_p = 1.38 \cdot 10^{15} \frac{\text{rad}}{\text{s}}$ and $\Gamma = 0$	92
2.2	Angular momenta density distribution for the dipole modes for dielectric and metallic particles	94
2.3	Relation between integrated spin and orbital parts for all modes up to $j = 4$. Distribution stays the same for both dielectric and magnetic particles for TE and TM modes	95
2.4	Step-index fiber and cylindrical and Cartesian coordinates. In some cases cylindrical radial unit vector can be written as \mathbf{e}_ρ instead of \mathbf{e}_r in order not to mixed with spherical radial unit vector	96
2.5	Fiber dispersion. Propagation constants β as branch of solutions of the fiber dispersion equation (2.30). Here $k_f = 2\pi/R_f$, $\omega_f = 2\pi c/R_f$. Fiber material was chosen to be with $\epsilon_f = 3.5$. It is clearly seen from this plot which values propagation constant can have: $n_m k_0 < \beta < n_f k_0$	100
2.6	Vector field (stream plot arrows) and intensity distributions (gray map) for the modes in a step index fiber. All modes are grouped by its families: HE, EH, TE and TM. Red circle represents the fiber border. Parameters: $n_m = 1, n_f = 1.45, k_0 R_f = 11.81$ (corresponds to $V = 12.46$)	101

- 2.7 Vector field (stream plot arrows) and Cartesian electric component \mathcal{E}_x (color map) for the modes in a step index fiber. All modes are grouped by its families: HE, EH, TE and TM. Red circle represents the fiber border. Parameters: $n_m = 1$, $n_f = 1.45$, $k_0 R_f = 11.81$ (corresponds to $V = 12.46$) 102
- 2.8 Dispersion of a fiber with $(n_f - n_m)/n_f = 0.2$ and electric field lines of the first 7 modes. Here $b = \frac{N^2 - n_m^2}{n_f^2 - n_m^2}$, $\beta = k_0 N$, $V = k_0 R_f \sqrt{n_f^2 - n_m^2}$. Picture is taken from [254] 103
- 2.9 Electric field intensity in the vicinity of fiber as a function of fiber radius. Each mode carries the same amount of power. Behavior remains approximately the same for the bigger distance from vicinity. Parameters: $\lambda = 1064$ nm, $\epsilon_m^{\text{water}} = 1.77$, $\epsilon_m^{\text{air}} = 1.0$, $\epsilon_f = 2.1025$, 105
- 2.10 Canonical OAM and SAM distributions for the first 4 dielectric fiber modes. Orbital and spin parts are normalized to the Brillouin energy as in (2.44). Total angular momentum is normalized to the spin momentum of a circular polarized plane wave in free space $S_z^{\text{p.w.}} = \frac{\epsilon_0}{2\omega} E_0^2$ where $E_0^2 = \frac{Z_0 P}{2\pi R_f^2}$ is the field magnitude of a plane wave with carried power P (= power carried by the mode) normalized on the fiber cross section πR_f^2 , Z_0 is the vacuum impedance. $\lambda_0 = 1064$ nm, $\epsilon_f = 1.45^2$, $\epsilon_m = 1.77$ 107
- 2.11 Canonical OAM and SAM distributions for the second 4 dielectric fiber modes. Orbital and spin parts are normalized to the Brillouin energy as in (2.44). Total angular momentum is normalized to the spin momentum of a circular polarized plane wave in free space $S_z^{\text{p.w.}} = \frac{\epsilon_0}{2\omega} E_0^2$ where $E_0^2 = \frac{Z_0 P}{2\pi R_f^2}$ is the field magnitude of a plane wave with carried power P (= power carried by the mode) normalized on the fiber cross section πR_f^2 , Z_0 is the vacuum impedance. $\lambda_0 = 1064$ nm, $\epsilon_f = 1.45^2$, $\epsilon_m = 1.77$ 108

- 2.12 Canonical OAM and SAM distributions for the first 4 dielectric fiber modes. Orbital and spin parts are normalized to the Brillouin energy as in (2.44). Total angular momentum is normalized to the spin momentum of a circular polarized plane wave in free space $S_z^{\text{p.w.}} = \frac{\epsilon_0}{2\omega} E_0^2$ where $E_0^2 = \frac{Z_0 P}{2\pi R_f^2}$ is the field magnitude of a plane wave with carried power P (= power carried by the mode) normalized on the fiber cross section πR_f^2 , Z_0 is the vacuum impedance. $\lambda_0 = 1064$ nm, $\epsilon_f = 1.45^2$, $\epsilon_m = 1.77$ 109
- 2.13 Canonical OAM and SAM distributions for the second 4 dielectric fiber modes. Orbital and spin parts are normalized to the Brillouin energy as in (2.44). Total angular momentum is normalized to the spin momentum of a circular polarized plane wave in free space $S_z^{\text{p.w.}} = \frac{\epsilon_0}{2\omega} E_0^2$ where $E_0^2 = \frac{Z_0 P}{2\pi R_f^2}$ is the field magnitude of a plane wave with carried power P (= power carried by the mode) normalized on the fiber cross section πR_f^2 , Z_0 is the vacuum impedance. $\lambda_0 = 1064$ nm, $\epsilon_f = 1.45^2$, $\epsilon_m = 1.77$ 110
- 3.1 The main concept of this chapter 111
- 3.2 The configuration of the system, which allows to achieve the stable binding of nanoparticles near the nanofiber in all 3 axis. The nanofiber adds a long range interaction channel of interaction 112
- 3.3 (a) Longitudinal force F_z in a single mode regime acting on one of two particles as a function of distance along the nanofiber axis Δz . Red solid line shows total optical force which takes into account interaction through both free space and fiber ($\hat{\mathbf{G}}_s + \hat{\mathbf{G}}_0$), green dashed line shows only interaction through the fiber ($\hat{\mathbf{G}}_s$) and blue dash-and-dot line shows only free space interaction ($\hat{\mathbf{G}}_0$). (b) Equilibrium solutions. First three branches of the solution for the distance between the two closest particles $q = \Delta z \beta$ with respect to the total number of particles in a chain N . (c) Trapping parameter γ , which equals to the effective potential depth of the trap divided by a thermal energy of the host media kT , and normalized stiffness of the trap with respect to the number of particles in a chain N 114

- 3.4 (a) The amplitude of the coupling constant g_{zz} for different modes in single mode and multi-mode regimes for three different fiber radii: $R_f = 300, 500, 1000$ nm. (b) Longitudinal optical force F_z acting on one of the particles as a function of distance between the particles along the fiber axis Δz for multi-mode regime $R_f = 1000$ nm. (c) The trapping parameter of nanoparticles in a stable equidistant states as a function of the number of particles in multi-mode regime 117
- 3.5 (a) Normalized intensity of the total electric field for two different fiber radii: $R_f = 300$ nm and $R_f = 1000$ nm. (b) Potential energy of the transverse trap along the x axis normalized by kT . (c) Total radial force as a function of two parameters: the fiber radius R_f and the gap between fiber surface and particle's surface d . Two horizontal dashed black lines correspond to single mode and multi-mode fiber radii in Table 4. Inset: the force decomposition into optical force and van-der-Waals force. The equilibrium distances for single mode and multi-mode regimes are $d^{\text{SM}} = 45$ nm and $d^{\text{MM}} = 50$ nm 120
- 3.6 The total radial force acting on a particle for the configuration of two oncoming beams depends on two parameters: the radius of the fiber and the gap between the fiber surface and the particle surface. A sequence of graphs for different phase shifts between two beams is shown, constructed to show how the equilibrium capture distance can be adjusted 122
- 3.7 First 3 electric a_n and magnetic b_n scattering Mie coefficients as a function of size parameter x . For the parameters of our choice we have $x \approx 1.4$ and dipole scattering coefficient $|a_1|$ dominates. Since n -polar polarizability is connected with n -th scattering coefficient, incident field mainly induce only dipole moment. Here $k_p = \sqrt{\epsilon_p} k_0 = \sqrt{2.5} \frac{2\pi}{1064 \text{ nm}}$ and for $R_p = 150$ nm we have $x \approx 1.4$ 123
- 3.8 Optical binding force between two particles with $R_p = 50$ nm over a single-mode $R_f = 300$ nm nanofiber under transverse pump illumination. Successful comparison of the full numerical solution and analytical dipole model 123

- 4.1 (a) Isotropic, lossless dielectric particle in the evanescent field of an elliptically polarized, fundamental mode of an optical nanofiber. Due to the non-zero azimuthal component of optical force, F_φ , the particle can rotate around the fiber. (b) We eliminate axial motion by using two oncoming beams with the same intensity profiles and opposite helicities, $\sigma_1 = -\sigma_2$ 127
- 4.2 Simulation results. (a) Density of the total angular momentum of light near a nanofiber (in water) guiding a fundamental mode with $\sigma = 1$. Inset shows total angular momentum normalized per photon and its spin and orbital contributions. (b) The orbiting frequency for a polystyrene particle, as a function of particle and fiber radii. Inset shows frequency at the optimum fiber radius ($R_f = 0.35 \mu\text{m}$) for three different particle materials: silica, silicon, and polystyrene 127
- 4.3 (a) Experimental setup (not to scale): once the polarization transformations in the tapered fiber are reversed by the polarization compensators, PC1 and PC2, we set the values of σ_1 and $\sigma_2 = -\sigma_1$, by rotating the quarter-wave plates, QWP1 and QWP2. (b) Transmission image of a 3- μm polystyrene particle optically captured at the waist of a nanofiber 130
- 4.4 Experimental results for a CP input (R = right, L = left). (a) Beatings in the detector signal acquired with an optical power of 15 mW in each beam. The zoomed-in view (inset) shows the local period, T . (b) Orbiting frequency versus power in each beam, at $\sigma = +1$. Markers: measured data sets for three samples; gray area: combined standard deviation range. Dashed line: frequency expected for the drag coefficient γ ; solid line: the best fit to the data with γ -fit. (c), (d) Time-lapse compilation of images for $\sigma = +1$ (c) and $\sigma = -1$ (d) 131
- 4.5 Experimental results: (a) dependence of the measured orbiting frequency as a function of QWP1 orientation which controls the helicity and (b) the orbiting frequency versus the calculated helicity. Solid lines: simulation using Eq. (4.5), with $\sigma = \sin 2\theta$ 132
- 4.6 Simple anisotropic particle in a field of an elliptically polarized light. Geometry of the problem. Blue ellipsoid represents the Fresnel ellipsoid 134

- 4.7 The critical angle for the QWP to observe rotation of the uniaxial anisotropic particle. Calculated for $\varepsilon = 1.77$, $\varepsilon_{\parallel} = 2.9128$, $\varepsilon_{\perp} = 2.2641$ and $\lambda = 1064$ nm 138
- 4.8 Scaling of the rotational frequency with the particle radius. Results are compared the COMSOL simulations, where particle was illuminated by a gaussian beam (GB) with different waists w_0 and a plane wave (PW). Electric and magnetic dipoles are sufficient for the particle radius of $a < 300 - 400$ nm. For all lines the magnitude of electric field E_0 is constant 139
- 4.9 Numerical solution of the system which describes the rotation dynamics of the anisotropic particle in the dipole approximation. **(a)** Instantaneous frequency exhibits oscillations on the double frequency due to the anisotropy; **(b)** Signal form $y(t) = \sin[\gamma(t)]$ and **(c)** its spectral representation. Solid lines show the numerical solution and dashed line is the first order approximated analytical solution. Signal is fully harmonic for the purely circular polarized light $m = \pm i$ and starts to be inharmonic close to the critical point. Here $T_0 = 2\pi/\Omega_0$. Other parameters are $E_0 = 4$, $\Delta = 0.1$, $\Gamma = 0.3$, $a = 1$, $\rho = 1$, and $\nu = 0.1$. . . 139
- 4.10 Simple model solution for the base rotation frequency. Frequency is extracted numerically and normalized by Ω_0 which is defined by (4.26). This curve looks very similar to the one in literature [279] 140
- 4.11 Spin angular momentum density \mathbf{S} and imaginary Poynting vector $\mathbf{\Pi}^{\text{Im}}$ of $\text{HE}_{11}^{\text{lin}}$ mode. The black arrows represent the electric field lines 144
- 4.12 Comparison of the optical torque and spin angular momentum density for a non-chiral particle 145
- 4.13 Comparison of the optical torque and spin angular momentum density for a chiral particle with $\alpha_c = 0.001a^3$ and $\alpha_c = 0.1a^3$ 146
- 5.1 Acoustic Mie scattering problem 154
- 5.2 An example of the complex roots of the acoustic dispersion equation with $n = 0$ and $n = 1$ for a sphere with $\bar{\rho}_1 = 3 + 0.1i$ and $\bar{\beta}_1 = 4 + 0.3i$. Here $x = \text{Re}(ka)$ and $y = \text{Im}(ka)$ 157
- 5.3 Normalized acoustical cross sections for an absorbing sphere with $\bar{\rho}_1 = 3 + 0.1i$ and $\bar{\beta}_1 = 2 + 0.2i$ 159

5.4	Normalized scattering cross sections $\sigma_{sc}/\sigma_{geom}$ (with $\sigma_{geom} = \pi a^2$) for various materials versus size parameter ka , where k is the wavevector in the host media and a is a particle radius. For all materials we have artificially added small losses as $\bar{\rho}_1 \rightarrow \bar{\rho}_1(1 + 0.01i)$ and $\bar{\beta}_1 \rightarrow \bar{\beta}_1(1 + 0.01i)$ to remove some extremely sharp peaks which do not occur in real life. Red arrows show extremely sharp monopole resonances which occur for some particular combinations (log scale is applied for these plots). pSi is a shorthand for porous silicon, resin is a shorthand for epoxy resin	160
5.5	Geometry of the problem. Similar approach to the [171, § 4]	167
5.6	Gradient force F_x (a) and pressure force F_z (b) for a lossless particle. With parameters $\bar{\beta}_1 = 3$, $\bar{\rho}_1 = 2$, and $\alpha = 0.8$	168
B.1	Comparison of scattering cross sections between electric ($\epsilon_p = 16$, $\mu_p = 1$) and magnetic ($\epsilon_p = 1$, $\mu_p = 16$) particles in air ($\epsilon = \mu = 1$) to illustrate the symmetric properties of the Mie coefficients	225
B.2	Example of scattering cross sections for polysterene and silicon in water. Mie resonances give a huge enhancement in scattering only for sizes $x \sim 1 \div 3$	226
B.3	Absolute values of Mie coefficients for scattered field for silicon particle in water ($\epsilon_p = 11.5$, $\epsilon_m = 1.77$, $\mu_p = \mu_m = 1$)	227
E.1	An example of real and mean values of a product of two monochromatic functions with complex frequency	236

List of tables

1	Сравнение типичных размеров и мощности оптического и акустического пинцетов. Данные взяты из [5].	17
2	Comparison of typical sized and powers of optical and acoustical tweezers. Data is from [5].	45
3	Connection between common values of Stokes vector and Jones vector .	104
4	Proposed system parameters	117
5	Boundary conditions. Here Ω is the boundary surface, \mathbf{v}_n is the normal velocity component to the surface	153
6	Orders of first non-zero terms in decomposition of scattering coefficients. This decomposition is in consistent with [332]. Names of the multipoles are taken from [333]	162

References

1. A photophoretic-trap volumetric display / D. E. Smalley [et al.] // Nature. — 2018. — Vol. 553. — P. 486–490.
2. A volumetric display for visual, tactile and audio presentation using acoustic trapping / R. Hirayama [et al.] // Nature. — 2019. — Vol. 575. — P. 320–323.
3. Atom trapping and guiding with a subwavelength-diameter optical fiber / V. I. Balykin [et al.] // Phys. Rev. A. — 2004. — Vol. 70, no. 1. — P. 011401.
4. *Wieman C. E., Pritchard D. E., Wineland D. J.* Atom cooling, trapping, and quantum manipulation // Rev. Mod. Phys. — 1999. — Vol. 71, no. 2. — S253–S262.
5. Acoustic tweezers for the life sciences / A. Ozcelik [et al.] // Nat. Methods. — 2018. — Vol. 15. — P. 1021–1028.
6. Optical tweezers and their applications / P. Polimeno [et al.] // J. Quant. Spectrosc. Radiat. Transfer. — 2018. — Vol. 218. — P. 131–150. — URL: <https://www.sciencedirect.com/science/article/pii/S002240731830445X>.
7. *Baresch D., Thomas J.-L., Marchiano R.* Observation of a Single-Beam Gradient Force Acoustical Trap for Elastic Particles: Acoustical Tweezers // Phys. Rev. Lett. — 2016. — Vol. 116, no. 2. — P. 024301. — URL: <https://doi.org/10.1103/PhysRevLett.116.024301>.
8. *Novotny L., Hetch B.* Principles of Nano-Optics. Vol. 1. — 05/2010.
9. *Berry M. V.* Optical currents // J. Opt. A: Pure Appl. Opt. — 2009. — Vol. 11, no. 9. — P. 094001.
10. *Marston P. L., Crichton J. H.* Radiation torque on a sphere caused by a circularly-polarized electromagnetic wave // Phys. Rev. A. — 1984. — Vol. 30, no. 5. — P. 2508–2516. — URL: <https://doi.org/10.1103/PhysRevA.30.2508>.
11. Force and torque on an electric dipole by spinning light fields / A. Canaguier-Durand [et al.] // Phys. Rev. A. — 2013. — Vol. 88, no. 3. — P. 033831. — URL: <https://link.aps.org/doi/10.1103/PhysRevA.88.033831>.

12. Imaginary components of Poynting vector in rectangular waveguide. — 2022. — URL: <https://physics.stackexchange.com/questions/352261/imaginary-components-of-poynting-vector-in-rectangular-waveguide> ; [Online; accessed 24. Mar. 2022].
13. Direct Measurements of the Extraordinary Optical Momentum and Transverse Spin-Dependent Force Using a Nano-Cantilever / M. Antognozzi [et al.] // Nature Physics. — 2016. — Aug. — Vol. 12, no. 8. — P. 731–735. — URL: <http://www.nature.com/articles/nphys3732> (visited on 06/19/2019).
14. *Niziev V., Muys P.* Poynting vector and beam divergence // J. Opt. Soc. Am. A, JOSAA. — 2020. — Vol. 37, no. 11. — P. 1839–1844. — URL: <https://opg.optica.org/josaa/fulltext.cfm?uri=josaa-37-11-1839&id=442008>.
15. *Jackson J. D.* Classical Electrodynamics. Vol. 1. — 07/1998.
16. *Stratton J. A.* Electromagnetic Theory. — John Wiley & Sons, 2007.
17. *Haus H. A., Melcher J. R.* Electromagnetic fields and energy. Vol. 107. — Prentice Hall Englewood Cliffs, 1989. — URL: <http://uilis.unsyiah.ac.id/oer/files/original/14fee9185f9f8699325e0617fc3204d4.pdf>.
18. Chirality-assisted lateral momentum transfer for bidirectional enantioselective separation / Y. Shi [et al.] // Light Sci. Appl. — 2020. — Vol. 9, no. 62. — P. 1–12.
19. Extraordinary Multipole Modes and Ultra-Enhanced Optical Lateral Force by Chirality / T. Zhu [et al.] // PHYSICAL REVIEW LETTERS. — 2020. — P. 6.
20. *Brasselet E., Juodkazis S.* Optical Angular Manipulation of Liquid Crystal Droplets in Laser Tweezers // Journal of Nonlinear Optical Physics & Materials. — 2009. — June. — Vol. 18, no. 02. — P. 167–194. — URL: <https://www.worldscientific.com/doi/abs/10.1142/S0218863509004580> (visited on 03/12/2020).
21. *Caloz C., Sihvola A.* Electromagnetic Chirality, Part 1: The Microscopic Perspective [Electromagnetic Perspectives] // IEEE Antennas Propag. Mag. — 2020. — Vol. 62, no. 1. — P. 58–71. — URL: <https://ieeexplore.ieee.org/abstract/document/8982214>.

22. *Caloz C., Sihvola A.* Electromagnetic Chirality, Part 2: The Macroscopic Perspective [Electromagnetic Perspectives] // IEEE Antennas Propag. Mag. — 2020. — Vol. 62, no. 2. — P. 82–98. — URL: <https://ieeexplore.ieee.org/abstract/document/9051770>.
23. Mechanical separation of chiral dipoles by chiral light / A. Canaguier-Durand [et al.] // New J. Phys. — 2013. — Vol. 15, no. 12. — P. 123037. — URL: <http://dx.doi.org/10.1088/1367-2630/15/12/123037>.
24. *Canaguier-Durand A., Genet C.* Chiral route to pulling optical forces and left-handed optical torques // Phys. Rev. A. — 2015. — Oct. — Vol. 92, no. 4. — P. 043823. — URL: <https://doi.org/10.1103/PhysRevA.92.043823>.
25. *Wang S. B., Chan C. T.* Lateral Optical Force on Chiral Particles near a Surface // Nature Communications. — 2014. — Mar. 6. — Vol. 5, issue 1, no. 1. — P. 3307. — URL: <https://www.nature.com/articles/ncomms4307> (visited on 09/28/2020).
26. Realization of Optical Pulling Forces Using Chirality / K. Ding [et al.] // Physical Review A. — 2014. — June 27. — Vol. 89, no. 6. — P. 063825. — URL: <https://link.aps.org/doi/10.1103/PhysRevA.89.063825> (visited on 01/26/2021).
27. Magnetolectric point scattering theory for metamaterial scatterers / I. Sersic [et al.] // Phys. Rev. B. — 2011. — Vol. 83, no. 24. — P. 245102. — URL: <https://link.aps.org/doi/10.1103/PhysRevB.83.245102>.
28. *Fang L., Wang J.* Optical Trapping Separation of Chiral Nanoparticles by Subwavelength Slot Waveguides // Phys. Rev. Lett. — 2021. — Vol. 127, no. 23. — P. 233902.
29. *Genet C.* Chiral Light–Chiral Matter Interactions: an Optical Force Perspective // ACS Photonics. — 2022. — Vol. 9, no. 2. — P. 319–332.
30. Electromagnetic Chirality: From Fundamentals to Nontraditional Chiroptical Phenomena / J. Mun [et al.] // Light: Science & Applications. — 2020. — Vol. 9, no. 1. — P. 139. — URL: <https://www.nature.com/articles/s41377-020-00367-8> (visited on 02/09/2021).
31. Optical sorting of small chiral particles by tightly focused vector beams / M. Li [et al.] // Phys. Rev. A. — 2019. — Vol. 99, no. 3. — P. 033825. — URL: <https://link.aps.org/doi/10.1103/PhysRevA.99.033825>.

32. Optical Torque on Small Chiral Particles in Generic Optical Fields / H. Chen [et al.] // Optics Express. — 2017. — Dec. 25. — Vol. 25, no. 26. — P. 32867. — URL: <https://www.osapublishing.org/abstract.cfm?URI=oe-25-26-32867> (visited on 12/21/2019).
33. Optical forces in coupled chiral particles / K. J. Wo [et al.] // Phys. Rev. A. — 2020. — Vol. 102, no. 4. — P. 043526. — URL: <https://doi.org/10.1103/PhysRevA.102.043526>.
34. A condition imposed on the electromagnetic polarizability of a bianisotropic lossless scatterer / P. A. Belov [et al.] // Tech. Phys. Lett. — 2003. — Vol. 29, no. 9. — P. 718–720. — URL: <https://doi.org/10.1134/1.1615545>.
35. Observation of a single-beam gradient force optical trap for dielectric particles / A. Ashkin [et al.] // Opt. Lett. — 1986. — Vol. 11, no. 5. — P. 288–290. — URL: <https://opg.optica.org/ol/fulltext.cfm?uri=ol-11-5-288&id=8652>.
36. *Toftul I. D., Kornovan D. F., Petrov M. I.* Self-Trapped Nanoparticle Binding via Waveguide Mode // ACS Photonics. — 2020. — Jan. 15. — Vol. 7, no. 1. — P. 114–119. — URL: <https://pubs.acs.org/doi/10.1021/acsp Photonics.9b01157> (visited on 05/15/2020).
37. Direct Measurement of the Nonconservative Force Field Generated by Optical Tweezers / P. Wu [et al.] // Phys. Rev. Lett. — 2009. — Vol. 103, no. 10. — P. 108101. — URL: <https://link.aps.org/doi/10.1103/PhysRevLett.103.108101>.
38. *Volpe G., Petrov D.* Torque Detection using Brownian Fluctuations // Phys. Rev. Lett. — 2006. — Vol. 97, no. 21. — P. 210603. — URL: <https://link.aps.org/doi/10.1103/PhysRevLett.97.210603>.
39. Quantitative assessment of non-conservative radiation forces in an optical trap / G. Pesce [et al.] // Europhys. Lett. — 2009. — Vol. 86, no. 3. — P. 38002. — URL: <http://dx.doi.org/10.1209/0295-5075/86/38002>.
40. *Volpe G., Volpe G., Petrov D.* Brownian motion in a nonhomogeneous force field and photonic force microscope // Phys. Rev. E. — 2007. — Vol. 76, no. 6. — P. 061118. — URL: <https://link.aps.org/doi/10.1103/PhysRevE.76.061118>.

41. Optical tweezers — from calibration to applications: a tutorial / J. Gieseler [et al.] // *Adv. Opt. Photonics*. — 2021. — Vol. 13, no. 1. — P. 74–241. — URL: <https://opg.optica.org/aop/fulltext.cfm?uri=aop-13-1-74&id=448989>.
42. *Bird R. B., Stewart W. E., Lightfoot E. N.* Transport Phenomena, Revised 2nd Edition. — Hoboken, NJ, USA : John Wiley & Sons, Inc., 2006. — URL: <https://www.amazon.com/Transport-Phenomena-Revised-Byron-Bird/dp/0470115394>.
43. Stochastic Processes: Data Analysis and Computer Simulation. — 2021. — URL: https://www.edx.org/course/stochastic-processes-data-analysis-and-computer-si?source=aw&awc=6798_1637757482_dbe6399b19f1ac9d64ba4a94acca294f&utm_source=aw&utm_medium=affiliate_partner&utm_content=text-link&utm_term=101248_adgoal+GmbH+-+Content ; [Online; accessed 24. Nov. 2021].
44. *Lapidus L., Pinder G. F.* Numerical solution of partial differential equations in science and engineering. — John Wiley & Sons, 2011.
45. *Bliokh K. Y., Bekshaev A. Y., Nori F.* Optical Momentum, Spin, and Angular Momentum in Dispersive Media // *Phys. Rev. Lett.* — 2017. — Vol. 119, no. 7. — P. 073901. — URL: <https://doi.org/10.1103/PhysRevLett.119.073901>.
46. *Bliokh K. Y., Bekshaev A. Y., Nori F.* Optical momentum and angular momentum in complex media: from the Abraham–Minkowski debate to unusual properties of surface plasmon-polaritons // *New J. Phys.* — 2017. — Vol. 19, no. 12. — P. 123014. — URL: <https://doi.org/10.1088/1367-2630/aa8913>.
47. *De Nittis G., Lein M.* The Schrödinger formalism of electromagnetism and other classical waves—How to make quantum-wave analogies rigorous // *Ann. Phys.* — 2018. — Vol. 396. — P. 579–617. — URL: <https://doi.org/10.1016/j.aop.2018.02.019>.
48. *Silveirinha M. G., Maslovski S. I.* Exchange of momentum between moving matter induced by the zero-point fluctuations of the electromagnetic field // *Phys. Rev. A*. — 2012. — Vol. 86, no. 4. — P. 042118. — URL: <https://doi.org/10.1103/PhysRevA.86.042118>.

49. Electromagnetic Helicity in Complex Media / F. Alpegiani [et al.] // Phys. Rev. Lett. — 2018. — Vol. 120, no. 24. — P. 243605. — URL: <https://doi.org/10.1103/PhysRevLett.120.243605>.
50. *Silveirinha M. G.* Chern invariants for continuous media // Phys. Rev. B. — 2015. — Vol. 92, no. 12. — P. 125153. — URL: <https://doi.org/10.1103/PhysRevB.92.125153>.
51. *Gangaraj S. A. H., Silveirinha M. G., Hanson G. W.* Berry Phase, Berry Connection, and Chern Number for a Continuum Bianisotropic Material From a Classical Electromagnetics Perspective // IEEE J. Multiscale Multiphys. Comput. Tech. — 2017. — Vol. 2. — P. 3–17. — URL: <https://doi.org/10.1109/JMMCT.2017.2654962>.
52. *Akhiezer A., Berestetskii V.* Quantum Electrodynamics. — U.S. Atomic Energy Commission, 1953. — (Quantum Electrodynamics ; pt. 1). — URL: https://books.google.com.au/books?id=F%5C_9AAQAIAAJ.
53. *Białynicki-Birula I.* On the Wave Function of the Photon // Acta Phys. Pol. A. — 1994. — Vol. 1, no. 86. — P. 97–116. — URL: <https://www.infona.pl/resource/bwmeta1.element.bwnjournal-article-appv86z108kz>.
54. *Sipe J. E.* Photon wave functions // Phys. Rev. A. — 1995. — Vol. 52, no. 3. — P. 1875–1883. — URL: <https://doi.org/10.1103/PhysRevA.52.1875>.
55. *Cugnon J.* The photon wave function // Open Journal of Microphysics. — 2011. — Vol. 1. — P. 41–52. — URL: <https://orbi.uliege.be/bitstream/2268/138649/1/240.pdf>.
56. *Białynicki-Birula I.* Photon wave function. — 2005. — eprint: [quant-ph/0508202](https://arxiv.org/abs/quant-ph/0508202). — URL: <https://arxiv.org/abs/quant-ph/0508202v1> ; [Online; accessed 1. Dec. 2021].
57. *Białynicki-Birula I.* V Photon Wave Function // Progress in Optics. Vol. 36. — Waltham, MA, USA : Elsevier, 1996. — P. 245–294. — URL: [https://doi.org/10.1016/S0079-6638\(08\)70316-0](https://doi.org/10.1016/S0079-6638(08)70316-0).
58. *Smith B. J., Raymer M. G.* Photon wave functions, wave-packet quantization of light, and coherence theory // New J. Phys. — 2007. — Vol. 9, no. 11. — P. 414. — URL: <https://doi.org/10.1088/1367-2630/9/11/414>.

59. Multiple optical trapping and binding: new routes to self-assembly / T. Čižmar [et al.] // Journal of Physics B: Atomic, Molecular and Optical Physics. — 2010. — Vol. 43, no. 10. — P. 102001. — URL: <http://dx.doi.org/10.1088/0953-4075/43/10/102001>.
60. *Forbes K. A., Bradshaw D. S., Andrews D. L.* Optical binding of nanoparticles // Nanophotonics. — 2020. — Jan. — Vol. 9, no. 1. — P. 1–17. — URL: <https://doi.org/10.1515/nanoph-2019-0361>.
61. *Dholakia K., Zemanek P.* Colloquium: Grippled by light: Optical binding // Reviews of Modern Physics. — 2010. — Vol. 82, no. 2. — P. 1767–1791. — URL: <http://link.aps.org/doi/10.1103/RevModPhys.82.1767>.
62. Optical trapping and manipulation of nanostructures. / O. M. Maragò [et al.] // Nature Nanotechnology. — 2013. — Vol. 8, no. 11. — P. 807–19. — URL: <http://www.ncbi.nlm.nih.gov/pubmed/24202536>.
63. *Bogdanov A. A., Shalin A. S., Ginzburg P.* Optical forces in nanorod metamaterial // Scientific Reports. — 2015. — Vol. 5. — P. 15846. — URL: <http://dx.doi.org/10.1038/srep15846>;
<http://www.nature.com/articles/srep15846>.
64. Nano-scale tunable optical binding mediated by hyperbolic metamaterials / N. A. Kostina [et al.] // arXiv:1909.10265 [physics]. — 2019. — URL: <http://arxiv.org/abs/1909.10265> (visited on 12/07/2019) ; arXiv: 1909.10265.
65. Optomechanical Manipulation with Hyperbolic Metasurfaces / A. Ivinskaya [et al.] // ACS Photonics. — 2018. — Vol. 5. — P. 4371–4377. — arXiv: [1810.08856](https://arxiv.org/abs/1810.08856).
66. *Quidant R., Girard C.* Surface-plasmon-based optical manipulation // Laser and Photonics Reviews. — 2008. — Vol. 2, no. 1/2. — P. 47–57.
67. Plasmon-assisted optical trapping and anti-trapping / A. Ivinskaya [et al.] // Light: Science & Applications. — 2017. — Vol. 6, no. 5. — e16258–6. — URL: <http://dx.doi.org/10.1038/lsa.2016.258>.
68. Long-range optical trapping and binding of microparticles in hollow-core photonic crystal fibre / D. S. Bykov [et al.] // Light: Science & Applications. — 2018. — Vol. 7, no. 1. — P. 22. — URL: <http://www.nature.com/articles/s41377-018-0015-z> (visited on 07/31/2019).

69. Selective particle trapping and optical binding in the evanescent field of an optical nanofiber / M. C. Frawley [et al.] // *Optics Express*. — 2014. — Vol. 22, no. 13. — P. 16322.
70. *Daly M., Sergides M., Nic Chormaic S.* Optical trapping and manipulation of micrometer and submicrometer particles // *Laser & Photonics Reviews*. — 2015. — Vol. 9. — P. 309–329. — URL: <http://doi.wiley.com/10.1002/lpor.201500006>.
71. Nonlinear force dependence on optically bound micro-particle arrays in the evanescent fields of fundamental and higher order microfibre modes / A. Maimaiti [et al.] // *Scientific Reports*. — 2016. — Vol. 6, July. — P. 1–10. — URL: <http://dx.doi.org/10.1038/srep30131>.
72. Polarization Control of Linear Dipole Radiation Using an Optical Nanofiber / M. Joos [et al.] // *Physical Review Applied*. — 2018. — Vol. 9, no. 6. — P. 64035. — URL: <https://doi.org/10.1103/PhysRevApplied.9.064035>.
73. Optical Interface Created by Laser-Cooled Atoms Trapped in the Evanescent Field Surrounding an Optical Nanofiber / E. Vetsch [et al.] // *Physical Review Letters*. — 2010. — Vol. 104, no. 20. — P. 203603. — URL: <http://link.aps.org/doi/10.1103/PhysRevLett.104.203603>.
74. *Kornovan D. F., Sheremet A. S., Petrov M. I.* Collective polaritonic modes in an array of two-level quantum emitters coupled to optical nanofiber // *Physical Review B*. — 2016. — Vol. 94. — P. 245416.
75. Waveguide-coupled single collective excitation of atomic arrays / N. V. Corzo [et al.] // *Nature*. — 2019. — Vol. 566, no. 7744. — P. 359–362.
76. *Chang D. E., Cirac J. I., Kimble H. J.* Self-organization of atoms along a nanophotonic waveguide // *Physical Review Letters*. — 2013. — Vol. 110, no. 11. — P. 1–6.
77. *Holzmann D., Sonnleitner M., Ritsch H.* Self-ordering and collective dynamics of transversely illuminated point-scatterers in a 1D trap // *European Physical Journal D*. — 2014. — Vol. 68. — P. 352.
78. *Burns M. M., Fournier J. M., Golovchenko J. A.* Optical binding // *Physical Review Letters*. — 1989. — Vol. 63, no. 12. — P. 1233–1236.

79. *Chaumet P. C., Nieto-Vesperinas M.* Optical binding of particles with or without the presence of a flat dielectric surface // *Physical Review B*. — 2001. — Vol. 64, no. 3. — P. 035422. — URL: <http://link.aps.org/doi/10.1103/PhysRevB.64.035422>.
80. *Chvatal L., Brzobohaty O., Zemanek P.* Binding of a pair of Au nanoparticles in a wide Gaussian standing wave // *Optical Review*. — 2015. — Vol. 22, no. 1. — P. 157–161.
81. *Demergis V., Florin E. L.* Ultrastrong optical binding of metallic nanoparticles // *Nano Letters*. — 2012. — Vol. 12, no. 11. — P. 5756–5760.
82. Optical binding via surface plasmon polariton interference / N. Kostina [et al.] // *Physical Review B*. — 2019. — Vol. 99. — P. 125416. — arXiv: [1708.05471](https://arxiv.org/abs/1708.05471). — URL: <http://arxiv.org/abs/1708.05471>.
83. *Brzobohaty O., Chvatal L., Zemanek P.* Optomechanical properties of optically self-arranged colloidal waveguides // *Optics Letters*. — 2019. — Vol. 44, no. 3. — P. 707. — URL: <https://www.osapublishing.org/abstract.cfm?URI=ol-44-3-707> (visited on 07/19/2019).
84. Optical Binding of Nanowires / S. H. Simpson [et al.] // *Nano Letters*. — 2017. — June. — Vol. 17, no. 6. — P. 3485–3492. — URL: <https://doi.org/10.1021/acs.nanolett.7b00494> (visited on 11/29/2019).
85. Optical Trapping, Optical Binding, and Rotational Dynamics of Silicon Nanowires in Counter-Propagating Beams / M. G. Donato [et al.] // *Nano Letters*. — 2019. — Vol. 19, no. 1. — P. 342–352. — URL: <https://doi.org/10.1021/acs.nanolett.8b03978> (visited on 11/29/2019).
86. *Le Kien F., Hakuta K.* Microtraps for atoms outside a fiber illuminated perpendicular to its axis: Numerical results // *Physical Review A*. — 2009. — Vol. 80, no. 1. — P. 1–6.
87. *Ok K. M., Chi E. O., Halasyamani P. S.* Bulk characterization methods for non-centrosymmetric materials: second-harmonic generation, piezoelectricity, pyroelectricity, and ferroelectricity // *Chem. Soc. Rev*. — 2006. — July. — Vol. 35, no. 8. — P. 710–717. — URL: <https://doi.org/10.1039/B511119F>.
88. Deduction of Tortuosity and Porosity from Acoustic Reflection and Transmission Measurements on Thick Samples of Rigid-Porous Materials / O. Umnova [et al.] // *Applied Acoustics*. — 2005. — Vol. 66, no. 6. — P. 607–624.

89. Dynamic compressibility of air in porous structures at audible frequencies / D. Lafarge [et al.] // J. Acoust. Soc. Am. — 1998. — Vol. 102, no. 4. — P. 1995.
90. *Lauriks W., Boeckx L., Leclaire P.* Characterization of porous acoustic materials. — 12/2005. — URL: <https://hal.archives-ouvertes.fr/hal-01329870> ; [Online; accessed 14. Aug. 2022].
91. Deduction of tortuosity and porosity from acoustic reflection and transmission measurements on thick samples of rigid-porous materials / O. Umnova [et al.] // Appl. Acoust. — 2005. — Vol. 66, no. 6. — P. 607–624. — URL: <https://doi.org/10.1016/j.apacoust.2004.02.005>.
92. Evaluation of tortuosity in acoustic porous materials saturated by air / J. F. Allard [et al.] // Rev. Sci. Instrum. — 1994. — Vol. 65, no. 3. — P. 754–755.
93. *Bliokh K. Y., Nori F.* Spin and Orbital Angular Momenta of Acoustic Beams // arXiv. — 2019. — P. 1–14.
94. Optical manipulation with metamaterial structures / Y. Shi [et al.] // arXiv. — 2022. — eprint: [2204.02750](https://arxiv.org/abs/2204.02750).
95. *Williams E. G.* Fourier acoustics: sound radiation and nearfield acoustical holography. — Elsevier, 1999.
96. *Yosioka K., Kawasima Y.* Acoustic Radiation Pressure on a Compressible Sphere // Journal of Fluid Mechanics. — 1955. — Vol. 267, no. 1. — P. 1–22. — URL: <https://www.ingentaconnect.com/content/dav/aaua/1955/00000005/00000003/art00004>.
97. *Bohren C. F., Huffman D. R.* Absorption and scattering of light by small particles. — John Wiley & Sons, 2008.
98. *Wei L., Rodriguez-Fortuño F. J.* Optical multipolar torque in structured electromagnetic fields: On helicity gradient torque, quadrupolar torque, and spin of the field gradient // Phys. Rev. B. — 2022. — Mar. — Vol. 105, no. 12. — P. 125424. — URL: <https://doi.org/10.1103/PhysRevB.105.125424>.
99. *James Clerk M.* A treatise on electricity and magnetism. — 2010.
100. *Lebedew P.* Untersuchungen über die Druckkräfte des Lichtes // Annalen der Physik. — 1901.

101. *Nichols E. F., Hull G. F.* A Preliminary Communication on the Pressure of Heat and Light Radiation // *Phys. Rev. (Series I)*. — 1901. — Nov. — Vol. 13, no. 5. — P. 307–320. — URL: <https://doi.org/10.1103/PhysRevSeriesI.13.307>.
102. *Nichols E. F., Hull G. F.* The Pressure Due to Radiation. (Second Paper.) // *Phys. Rev. (Series I)*. — 1903. — Aug. — Vol. 17, no. 2. — P. 91–104. — URL: <https://doi.org/10.1103/PhysRevSeriesI.17.91>.
103. *Ashkin A.* Acceleration and Trapping of Particles by Radiation Pressure // *Phys. Rev. Lett.* — 1970. — Vol. 24, no. 4. — P. 156–159. — URL: <https://doi.org/10.1103/PhysRevLett.24.156>.
104. *Minogin V. G., Letokhov V. S.* Laser light pressure on atoms. — CRC Press, 1987.
105. *Phillips W. D.* Laser cooling and trapping of neutral atoms // *Reviews of Modern Physics*. — 1998. — Vol. 70, no. 3. — P. 721–741.
106. *Grier David G.* A revolution in optical manipulation // *Nature*. — 2003. — Vol. 24, August. — P. 810–816. — URL: <https://www.nature.com/articles/nature01935>.
107. *K. Neuman A. N., Neuman K. C., Nagy A.* Single-molecule force spectroscopy: optical tweezers, magnetic tweezers and atomic force microscopy // *Nature methods*. — 2008. — Vol. 5, no. 6. — P. 491–505. — arXiv: [NIHMS150003](https://arxiv.org/abs/NIHMS150003).
108. *Atajanov A., Zhbanov A., Yang S.* Sorting and manipulation of biological cells and the prospects for using optical forces // *Micro and Nano Systems Letters*. — 2018. — Vol. 6, no. 1. — URL: <https://doi.org/10.1186/s40486-018-0064-3>.
109. *Wyatt Shields IV C., Reyes C. D., Lopez G. P.* Microfluidic cell sorting: A review of the advances in the separation of cells from debulking to rare cell isolation // *Lab on a Chip*. — 2015. — Vol. 15, no. 5. — P. 1230–1249. — URL: <http://dx.doi.org/10.1039/C4LC01246A>.
110. Spin to orbital light momentum conversion visualized by particle trajectory / A. V. Arzola [et al.] // *Scientific Reports*. — 2019. — Vol. 9, no. 1. — P. 4127. — URL: <http://www.nature.com/articles/s41598-019-40475-z> (visited on 07/31/2019).

111. *Frimmer M., Gieseler J., Novotny L.* Cooling Mechanical Oscillators by Coherent Control // Physical Review Letters. — 2016. — Vol. 117. — P. 163601.
112. Cold Damping of an Optically Levitated Nanoparticle to Microkelvin Temperatures / F. Tebbenjohanns [et al.] // Physical Review Letters. — 2019. — Vol. 122, no. 22. — P. 223601. — URL: <https://doi.org/10.1103/PhysRevLett.122.223601>.
113. Trapping single atoms on a nanophotonic circuit with configurable tweezer lattices / M. E. Kim [et al.] // Nature Communications. — 2019. — Vol. 10, no. 1. — arXiv: [1810.08769](https://arxiv.org/abs/1810.08769). — URL: <http://dx.doi.org/10.1038/s41467-019-09635-7>.
114. *Gross C., Bloch I.* Quantum simulations with ultracold atoms in optical lattices // Science. — 2017. — Vol. 357, no. 6355. — P. 995–1001.
115. Sorting ultracold atoms in a three-dimensional optical lattice in a realization of Maxwell’s demon / A. Kumar [et al.] // Nature. — 2018. — Vol. 561, no. 7721. — P. 83–87. — URL: <http://dx.doi.org/10.1038/s41586-018-0458-7>.
116. Synthetic three-dimensional atomic structures assembled atom by atom / D. Barredo [et al.] // Nature. — 2018. — Vol. 561, no. 7721. — P. 79–82. — URL: <http://dx.doi.org/10.1038/s41586-018-0450-2>.
117. *Grant I. S., Phillips W. R.* Electromagnetism. — John Wiley & Sons, 2013.
118. *Ye Q., Lin H.* On deriving the Maxwell stress tensor method for calculating the optical force and torque on an object in harmonic electromagnetic fields // Eur. J. Phys. — 2017. — Vol. 38, no. 4. — P. 045202.
119. *Griffiths D. J.* Introduction to electrodynamics. — 2005.
120. *Bliokh K. Y., Bekshaev A. Y., Nori F.* Extraordinary Momentum and Spin in Evanescent Waves // Nature Communications. — 2014. — Vol. 5. — P. 1–8. — pmid: [24598730](https://pubmed.ncbi.nlm.nih.gov/24598730/).
121. Optical manipulation from the microscale to the nanoscale: fundamentals, advances and prospects - Light: Science & Applications / D. Gao [et al.] // Light Sci. Appl. — 2017. — Vol. 6, no. 9.

122. *Barnett S. M., Loudon R.* The Enigma of Optical Momentum in a Medium // Philosophical Transactions of the Royal Society A: Mathematical, Physical and Engineering Sciences. — 2010. — Vol. 368, no. 1914. — P. 927–939. — pmid: [20123741](#).
123. Unveiling the correlation between non-diffracting tractor beam and its singularity in Poynting vector / D. Gao [et al.] // Laser Photonics Rev. — 2015. — Vol. 9, no. 1. — P. 75–82. — URL: <https://doi.org/10.1002/lpor.201400071>.
124. Radiation Torque Exerted on a Uniaxial Anisotropic Sphere: Effects of Various Parameters / Z. Li [et al.] // Optics & Laser Technology. — 2014. — Dec. 1. — Vol. 64. — P. 269–277. — URL: <http://www.sciencedirect.com/science/article/pii/S0030399214001522> (visited on 12/14/2020).
125. *Li Z.-J., Wu Z.-S., Shang Q.-C.* Calculation of Radiation Forces Exerted on a Uniaxial Anisotropic Sphere by an Off-Axis Incident Gaussian Beam // Optics Express. — 2011. — Aug. 15. — Vol. 19, no. 17. — P. 16044–16057. — URL: <https://www.osapublishing.org/oe/abstract.cfm?uri=oe-19-17-16044> (visited on 12/14/2020).
126. Calculation of Radiation Force and Torque Exerted on a Uniaxial Anisotropic Sphere by an Incident Gaussian Beam with Arbitrary Propagation and Polarization Directions / Z.-J. Li [et al.] // Optics Express. — 2012. — July 16. — Vol. 20, no. 15. — P. 16421–16435. — URL: <https://www.osapublishing.org/oe/abstract.cfm?uri=oe-20-15-16421> (visited on 12/14/2020).
127. *Barton J. P., Alexander D. R., Schaub S. A.* Theoretical Determination of Net Radiation Force and Torque for a Spherical Particle Illuminated by a Focused Laser Beam // Journal of Applied Physics. — 1989. — Vol. 66, no. 10. — P. 4594–4602. — pmid: [17255001](#). — URL: <https://doi.org/10.1063/1.343813>.
128. *Barton J. P., Alexander D. R., Schaub S. A.* Internal and Near-Surface Electromagnetic Fields for a Spherical Particle Irradiated by a Focused Laser Beam // Journal of Applied Physics. — 1988. — Vol. 64, no. 4. — P. 1632–1639. — pmid: [3372545](#). — URL: <https://doi.org/10.1063/1.341811>.

129. *Abraham M.* On Minkowski's electrodynamics // Rend. Circ. Mat. Palermo. — 1910. — Vol. 30. — P. 33–46. — URL: http://neo-classical-physics.info/uploads/3/4/3/6/34363841/abraham_-_minkowski_ed.pdf.
130. *Abraham M.* On the electrodynamics of moving bodies // Rend. Circ. Mat. Palermo. — 1909. — Vol. 28. — P. 1–28. — URL: https://neo-classical-physics.info/uploads/3/4/3/6/34363841/abraham_-_ed_of_moving_bodies.pdf.
131. *Hilbert D., Minkowski H.* Gedächtnisrede // Math. Ann. — 1910. — Vol. 68. — P. 445–471.
132. *Minkowski H.* Die grundlagen für die elektromagnetischen vorgänge in bewegten körpern // Nachr. d. König. Gesellsch. d. Wiss. zu Gttingen, Math-phys. Klasse. — 1908. — Vol. 53. — P. 1978–1979.
133. *Griffiths D. J.* Resource Letter EM-1: Electromagnetic Momentum // Am. J. Phys. — 2011. — Vol. 80, no. 1. — P. 7.
134. *Kemp B. A., Grzegorzcyk T. M., Kong J. A.* Optical Momentum Transfer to Absorbing Mie Particles // Phys. Rev. Lett. — 2006. — Vol. 97, no. 13. — P. 133902.
135. *Barnett S. M., Loudon R.* The enigma of optical momentum in a medium // Philos. Trans. Royal Soc. A. — 2010. — Vol. 368, no. 1914. — P. 927–939. — URL: <https://doi.org/10.1098/rsta.2009.0207>.
136. *Chichkov N. B., Chichkov B. N.* On the origin of photon mass, momentum, and energy in a dielectric medium [Invited] // Optical Materials Express. — 2021. — Vol. 11, no. 8. — P. 2722–2729. — URL: <https://www.osapublishing.org/ome/abstract.cfm?uri=ome-11-8-2722>.
137. *Philbin T. G., Allanson O.* Optical Angular Momentum in Dispersive Media // Physical Review A - Atomic, Molecular, and Optical Physics. — 2012. — Vol. 86, no. 5. — P. 1–4. — arXiv: [1205.4929](https://arxiv.org/abs/1205.4929).
138. *Toptygin I., Levina K.* Energy—Momentum Tensor of the Electromagnetic Field in Dispersive Media // Uspekhi Fizicheskikh Nauk. — 2016. — Vol. 186, no. 2. — P. 146–158. — URL: <http://ufn.ru/ru/articles/2016/2/d/>.

139. Electromagnetic Helicity in Complex Media / F. Alpegiani [et al.] // Physical Review Letters. — 2018. — Vol. 120, no. 24. — P. 243605. — arXiv: [1802.09392](https://arxiv.org/abs/1802.09392).
140. Electromagnetic energy–momentum tensors in general dispersive bianisotropic media / R.-Y. Zhang [et al.] // J. Opt. Soc. Am. B, JOSAB. — 2021. — Vol. 38, no. 10. — P. 3135–3149.
141. Dynamic Consequences of Optical Spin–Orbit Interaction / S. Sukhov [et al.] // Nature Photonics. — 2015. — Dec. — Vol. 9, no. 12. — P. 809–812. — URL: <http://www.nature.com/articles/nphoton.2015.200> (visited on 11/24/2019).
142. *Chaumet P. C., Rahmani A.* Electromagnetic Force and Torque on Magnetic and Negative-Index Scatterers // Optics Express. — 2009. — Vol. 17, no. 4. — P. 2224.
143. Optical Forces on Small Magnetodielectric Particle / M. Nieto-Vesperinas [et al.] // Optics Express. — 2010. — Vol. 18, no. 11. — P. 11428.
144. *Nieto-Vesperinas M.* Optical Torque: Electromagnetic Spin and Orbital-Angular-Momentum Conservation Laws and Their Significance // Physical Review A. — 2015. — Oct. 30. — Vol. 92, no. 4. — P. 043843. — URL: <https://link.aps.org/doi/10.1103/PhysRevA.92.043843> (visited on 12/30/2019).
145. *Nieto-Vesperinas M.* Optical Torque on Small Bi-Isotropic Particles // Optics Letters. — 2015. — Vol. 40, no. 13. — P. 3021.
146. *Doyle W. T.* Optical Properties of a Suspension of Metal Spheres // Physical Review B. — 1989. — Vol. 39, no. 14. — P. 9852–9858.
147. *Le Ru E. C., Somerville W. R., Auguié B.* Radiative Correction in Approximate Treatments of Electromagnetic Scattering by Point and Body Scatterers // Physical Review A - Atomic, Molecular, and Optical Physics. — 2013. — Vol. 87, no. 1. — P. 1–12.
148. *Moroz A.* Depolarization Field of Spheroidal Particles // Journal of the Optical Society of America B. — 2009. — Vol. 26, no. 3. — P. 517.
149. Modeling of Isotropic Backward-Wave Materials Composed of Resonant Spheres / L. Jylhä [et al.] // Journal of Applied Physics. — 2006. — Vol. 99, no. 4.

150. Optical Response Features of Si-Nanoparticle Arrays / A. B. Evlyukhin [et al.] // Physical Review B. — 2010. — July 8. — Vol. 82, no. 4. — P. 045404. — URL: <https://link.aps.org/doi/10.1103/PhysRevB.82.045404> (visited on 11/25/2020).
151. Polarizabilities of Nonreciprocal Bianisotropic Particles / M. S. Mirmoosa [et al.] // Physical Review Applied. — 2014. — Vol. 1, no. 3. — P. 034005. — URL: <https://link.aps.org/doi/10.1103/PhysRevApplied.1.034005> (visited on 02/26/2021).
152. Electromagnetic chirality: from fundamentals to nontraditional chiroptical phenomena / J. Mun [et al.] // Light Sci. Appl. — 2020. — Vol. 9, no. 139. — P. 1–18. — URL: <https://doi.org/10.1038/s41377-020-00367-8>.
153. *Chaumet P. C., Nieto-Vesperinas M.* Time-averaged total force on a dipolar sphere in an electromagnetic field // Opt. Lett. — 2000. — Vol. 25, no. 15. — P. 1065–1067. — URL: <https://doi.org/10.1364/OL.25.001065>.
154. *Bekshaev A. Y.* Subwavelength Particles in an Inhomogeneous Light Field: Optical Forces Associated with the Spin and Orbital Energy Flows // Journal of Optics (United Kingdom). — 2013. — Vol. 15, no. 4.
155. *Gómez-Medina R., Nieto-Vesperinas M., Sáenz J. J.* Nonconservative Electric and Magnetic Optical Forces on Submicron Dielectric Particles // Physical Review A - Atomic, Molecular, and Optical Physics. — 2011. — Vol. 83, no. 3. — P. 1–7.
156. *Nieto-Vesperinas M., Gomez-Medina R., Saenz J. J.* Angle-Suppressed Scattering and Optical Forces on Submicrometer Dielectric Particles // Journal of the Optical Society of America A. — 2011. — Jan. 1. — Vol. 28, no. 1. — P. 54. — URL: <https://www.osapublishing.org/abstract.cfm?URI=josaa-28-1-54> (visited on 11/25/2020).
157. *Marston P. L., Crichton J. H.* Radiation Torque on a Sphere Caused by a Circularly-Polarized Electromagnetic Wave // Physical Review A. — 1984. — Nov. 1. — Vol. 30, no. 5. — P. 2508–2516. — URL: <https://link.aps.org/doi/10.1103/PhysRevA.30.2508> (visited on 12/30/2019).
158. *Jones R. V.* Pressure of Radiation // Nature. — 1953. — Vol. 171, no. 4364. — P. 1089–1093. — URL: <https://www.nature.com/articles/1711089a0> (visited on 02/17/2021).

159. Mechanical Evidence of the Orbital Angular Momentum to Energy Ratio of Vortex Beams / C. E. M. Demore [et al.] // *Phys. Rev. Lett.* — 2012. — Vol. 108, no. 19. — P. 194301. — URL: <https://doi.org/10.1103/PhysRevLett.108.194301>.
160. *Loudon R., Baxter C.* Contributions of John Henry Poynting to the Understanding of Radiation Pressure // *Proceedings of the Royal Society A: Mathematical, Physical and Engineering Sciences.* — 2012. — Vol. 468, no. 2143. — P. 1825–1838. — URL: <https://royalsocietypublishing.org/doi/10.1098/rspa.2011.0573> (visited on 02/17/2021).
161. *Brevik I.* Experiments in Phenomenological Electrodynamics and the Electromagnetic Energy-Momentum Tensor // *Physics Reports.* — 1979. — Vol. 52, no. 3. — P. 133–201. — URL: <https://www.sciencedirect.com/science/article/pii/0370157379900747> (visited on 02/17/2021).
162. Colloquium: Momentum of an Electromagnetic Wave in Dielectric Media / R. N. Pfeifer [et al.] // *Reviews of Modern Physics.* — 2007. — Vol. 79, no. 4. — P. 1197–1216. — arXiv: [0710.0461v2](https://arxiv.org/abs/0710.0461v2).
163. Direct Observation of Transfer of Angular Momentum to Absorptive Particles from a Laser Beam with a Phase Singularity / H. He [et al.] // *Physical Review Letters.* — 1995. — Vol. 75, no. 5. — P. 826–829. — URL: <https://link.aps.org/doi/10.1103/PhysRevLett.75.826> (visited on 02/17/2021).
164. Intrinsic and Extrinsic Nature of the Orbital Angular Momentum of a Light Beam / A. T. O’Neil [et al.] // *Physical Review Letters.* — 2002. — Vol. 88, no. 5. — P. 053601. — URL: <https://link.aps.org/doi/10.1103/PhysRevLett.88.053601> (visited on 02/17/2021).
165. Observation of the Transfer of the Local Angular Momentum Density of a Multiringed Light Beam to an Optically Trapped Particle / V. Garcés-Chavez [et al.] // *Physical Review Letters.* — 2003. — Vol. 91, no. 9. — P. 093602. — URL: <https://link.aps.org/doi/10.1103/PhysRevLett.91.093602> (visited on 02/17/2021).
166. *Volke-Sepulveda K., Santillan A. O., Boullosa R. R.* Transfer of Angular Momentum to Matter from Acoustical Vortices in Free Space // *Phys. Rev. Lett.* — 2008. — Vol. 100, no. 2. — P. 024302. — URL: <https://doi.org/10.1103/PhysRevLett.100.024302>.

167. *Zhang L., Marston P. L.* Angular momentum flux of nonparaxial acoustic vortex beams and torques on axisymmetric objects // *Phys. Rev. E.* — 2011. — Vol. 84, no. 6. — P. 065601.
168. *Bliokh K. Y., Bekshaev A. Y., Nori F.* Dual electromagnetism: helicity, spin, momentum and angular momentum // *New J. Phys.* — 2013. — Vol. 15, no. 3. — P. 033026. — URL: <https://doi.org/10.1088/1367-2630/15/3/033026>.
169. *Electrodynamics of Continuous Media* / L. D. Landau [et al.]. — Elsevier, 2013.
170. Angular momenta, helicity, and other properties of dielectric-fiber and metallic-wire modes / M. F. Picardi [et al.] // *Optica.* — 2018. — Vol. 5, no. 8. — P. 1016–1026. — URL: <https://doi.org/10.1364/OPTICA.5.001016>.
171. *Bekshaev A. Y., Bliokh K. Y., Nori F.* Mie scattering and optical forces from evanescent fields: A complex-angle approach // *Opt. Express.* — 2013. — Vol. 21, no. 6. — P. 7082–7095.
172. *Bohren C. F., Huffman D. R.* Absorbption and Scattering of Light by Small Particles. Vol. 1. — 09/1984.
173. Acoustic Radiation Force and Torque on Small Particles as Measures of the Canonical Momentum and Spin Densities / I. D. Toftul [et al.] // *Physical Review Letters.* — 2019. — Oct. 28. — Vol. 123, no. 18. — P. 183901. — URL: <https://link.aps.org/doi/10.1103/PhysRevLett.123.183901> (visited on 03/13/2020).
174. *Jones P. H., Maragò O. M., Volpe G.* Optical tweezers: Principles and applications. — Cambridge University Press, 2015.
175. Scattering Forces from the Curl of the Spin Angular Momentum of a Light Field / S. Albaladejo [et al.] // *Phys. Rev. Lett.* — 2009. — Vol. 102, no. 11. — P. 113602. — URL: <https://doi.org/10.1103/PhysRevLett.102.113602>.
176. Lateral forces on circularly polarizable particles near a surface / F. J. Rodriguez-Fortuño [et al.] // *Nat. Commun.* — 2015. — Nov. — Vol. 6, no. 8799. — P. 1–8. — URL: <https://doi.org/10.1038/ncomms9799>.

177. *Yuan Q.-k., Wu Z.-s., Li Z.-j.* Electromagnetic Scattering for a Uniaxial Anisotropic Sphere in an Off-Axis Obliquely Incident Gaussian Beam // *JOSA A*. — 2010. — June 1. — Vol. 27, no. 6. — P. 1457–1465. — URL: <https://www.osapublishing.org/josaa/abstract.cfm?uri=josaa-27-6-1457> (visited on 12/20/2020).
178. Analysis of the Radiation Force of a Laguerre Gaussian Vortex Beam Exerted on an Uniaxial Anisotropic Sphere / T. Qu [et al.] // *Journal of Quantitative Spectroscopy and Radiative Transfer*. — 2015. — Sept. 1. — Vol. 162. — P. 103–113. — (Laser-Light and Interactions with Particles 2014). — URL: <http://www.sciencedirect.com/science/article/pii/S0022407315001430> (visited on 12/14/2020).
179. Non-Mie Optical Resonances in Anisotropic Biomineral Nanoparticles / R. E. Noskov [et al.] // *Nanoscale*. — 2018. — Vol. 10, no. 45. — P. 21031–21040. — URL: <http://xlink.rsc.org/?DOI=C8NR07561A> (visited on 11/12/2020).
180. *Qiu C.-W., Luk'yanchuk B.* Peculiarities in Light Scattering by Spherical Particles with Radial Anisotropy // *Journal of the Optical Society of America A*. — 2008. — July 1. — Vol. 25, no. 7. — P. 1623. — URL: <https://www.osapublishing.org/abstract.cfm?URI=josaa-25-7-1623> (visited on 05/22/2020).
181. Mie Scattering by a Uniaxial Anisotropic Sphere / Y.-L. Geng [et al.] // *Physical Review E*. — 2004. — Nov. 17. — Vol. 70, no. 5. — P. 056609. — URL: <https://link.aps.org/doi/10.1103/PhysRevE.70.056609> (visited on 05/22/2020).
182. *Stout B., Nevière M., Popov E.* Mie Scattering by an Anisotropic Object Part I Homogeneous Sphere // *Journal of the Optical Society of America A*. — 2006. — May 1. — Vol. 23, no. 5. — P. 1111. — URL: <https://www.osapublishing.org/abstract.cfm?URI=josaa-23-5-1111> (visited on 05/22/2020).
183. *Savchenko A. Y., Tabiryán N. V., Zel'dovich B. Y.* Transfer of Momentum and Torque from a Light Beam to a Liquid // *Physical Review E*. — 1997. — Oct. 1. — Vol. 56, no. 4. — P. 4773–4779. — URL: <https://link.aps.org/doi/10.1103/PhysRevE.56.4773> (visited on 05/13/2020).

184. Radiation Torque on a Birefringent Sphere Caused by an Electromagnetic Wave / M. Liu [et al.] // *Physical Review E*. — 2005. — Nov. 23. — Vol. 72, no. 5. — P. 056610. — URL: <https://link.aps.org/doi/10.1103/PhysRevE.72.056610> (visited on 05/12/2020).
185. Optical Alignment and Spinning of Laser-Trapped Microscopic Particles / M. E. J. Friese [et al.] // *Nature*. — 1998. — July. — Vol. 394, no. 6691. — P. 348–350. — URL: <http://www.nature.com/articles/28566> (visited on 05/12/2020).
186. *Simpson S. H., Hanna S.* Optical Angular Momentum Transfer by Laguerre-Gaussian Beams // *Journal of the Optical Society of America A*. — 2009. — Mar. 1. — Vol. 26, no. 3. — P. 625. — URL: <https://www.osapublishing.org/abstract.cfm?URI=josaa-26-3-625> (visited on 03/24/2020).
187. The scattering properties of anisotropic dielectric spheres on electromagnetic / H. Chen [et al.] // *J. Phys.: Condens. Matter*. — 2003. — Dec. — Vol. 16, no. 1. — P. 165–179. — URL: <https://doi.org/10.1088/0953-8984/16/1/016>.
188. *Simpson S. H., Hanna S.* Optical Trapping of Spheroidal Particles in Gaussian Beams // *Journal of the Optical Society of America A*. — 2007. — Feb. 1. — Vol. 24, no. 2. — P. 430. — URL: <https://www.osapublishing.org/abstract.cfm?URI=josaa-24-2-430> (visited on 03/24/2020).
189. *Jánossy I.* Electromagnetic Torque and Force in Axially Symmetric Liquid-Crystal Droplets // *Optics Letters*. — 2008. — Oct. 15. — Vol. 33, no. 20. — P. 2371. — URL: <https://www.osapublishing.org/abstract.cfm?URI=ol-33-20-2371> (visited on 03/24/2020).
190. *Ding J., Yang Y.* Small Angle Light Scattering from Bipolar Nematic Droplets // *Molecular Crystals and Liquid Crystals Science and Technology. Section A. Molecular Crystals and Liquid Crystals*. — 1994. — Vol. 257, no. 1. — P. 63–87. — URL: https://www.tandfonline.com/doi/abs/10.1080/10587259408033765?casa_token=eL5aJxpaGGwAAAAA:QKWBxhk7Eawj30qZ-vuLVha6s_pqiaIAJMbWAKc41Po2L1PLJfmafT8m1U1Tkemm8D10VTe71MgMfNc.

191. *Žumer S., Doane J. W.* Light Scattering from a Small Nematic Droplet // Physical Review A. — 1986. — Oct. 1. — Vol. 34, no. 4. — P. 3373–3386. — URL: <https://link.aps.org/doi/10.1103/PhysRevA.34.3373> (visited on 03/17/2020).
192. *Wong K.-L., Chen H.-T.* Electromagnetic Scattering by a Uniaxially Anisotropic Sphere // IEE Proceedings H (Microwaves, Antennas and Propagation). — 1992. — Aug. 1. — Vol. 139, no. 4. — P. 314–318. — URL: <https://digital-library.theiet.org/content/journals/10.1049/ip-h-2.1992.0056> (visited on 12/15/2020).
193. *Doicu A., Wriedt T., Eremin Y. A.* Light Scattering by Systems of Particles: Null-Field Method with Discrete Sources: Theory and Programs. — Berlin, Germany : Springer, 2006. — URL: https://books.google.com.au/books/about/Light_Scattering_by_Systems_of_Particles.html?id=NXX7BQAAQBAJ&redir_esc=y.
194. *Doicu A.* Null-Field Method to Electromagnetic Scattering from Uniaxial Anisotropic Particles // Optics Communications. — 2003. — Mar. 15. — Vol. 218, no. 1. — P. 11–17. — URL: <http://www.sciencedirect.com/science/article/pii/S0030401803011647> (visited on 12/14/2020).
195. Light Scattering from an Optically Anisotropic Particle Illuminated by an Arbitrary Shaped Beam / J. J. Wang [et al.] // Journal of Quantitative Spectroscopy and Radiative Transfer. — 2015. — Dec. 1. — Vol. 167. — P. 135–144. — URL: <http://www.sciencedirect.com/science/article/pii/S0022407315300388> (visited on 12/14/2020).
196. Scattering of On-Axis Gaussian Beam by a Uniaxial Anisotropic Object / Z. Chen [et al.] // JOSA A. — 2014. — Nov. 1. — Vol. 31, no. 11. — P. 2545–2550. — URL: <https://www.osapublishing.org/josaa/abstract.cfm?uri=josaa-31-11-2545> (visited on 12/14/2020).
197. *Alaee R., Rockstuhl C., Fernandez-Corbaton I.* An electromagnetic multipole expansion beyond the long-wavelength approximation // Opt. Commun. — 2018. — Vol. 407. — P. 17–21. — URL: <https://www.sciencedirect.com/science/article/pii/S003040181730754X>.

198. Exact dipolar moments of a localized electric current distribution / I. Fernandez-Corbaton [et al.] // Opt. Express. — 2015. — Vol. 23, no. 26. — P. 33044–33064. — URL: <https://www.osapublishing.org/oe/fulltext.cfm?uri=oe-23-26-33044&id=333697>.
199. *Jones R. C.* A Generalization of the Dielectric Ellipsoid Problem // Phys. Rev. — 1945. — Vol. 68, no. 3/4. — P. 93–96. — URL: <https://doi.org/10.1103/PhysRev.68.93>.
200. *Romanenko V. I., Yatsenko L. P.* Evolution of the velocity distribution of atoms under the action of the bichromatic force // Phys. Rev. A. — 2021. — Vol. 103, no. 4. — P. 043104.
201. *Chieda M. A., Eyler E. E.* Prospects for rapid deceleration of small molecules by optical bichromatic forces // Phys. Rev. A. — 2011. — Vol. 84, no. 6. — P. 063401.
202. Bichromatic force on metastable argon for atom-trap trace analysis / Z. Feng [et al.] // Phys. Rev. A. — 2017. — Vol. 96, no. 1. — P. 013424.
203. Bichromatic force measurements using atomic beam deflections / M. R. Williams [et al.] // Phys. Rev. A. — 2000. — Vol. 61, no. 2. — P. 023408.
204. *Cashen M. T., Metcalf H.* Bichromatic force on helium // Phys. Rev. A. — 2001. — Vol. 63, no. 2. — P. 025406.
205. *Yatsenko L., Metcalf H.* Dressed-atom description of the bichromatic force // Phys. Rev. A. — 2004. — Vol. 70, no. 6. — P. 063402.
206. Measurement of the bichromatic optical force on Rb atoms / M. R. Williams [et al.] // Phys. Rev. A. — 1999. — Vol. 60, no. 3. — R1763–R1766(R).
207. Coherent Bichromatic Force Deflection of Molecules / I. Kozyryev [et al.] // Phys. Rev. Lett. — 2018. — Vol. 120, no. 6. — P. 063205.
208. *Aldridge L., Galica S. E., Eyler E. E.* Simulations of the bichromatic force in multilevel systems // Phys. Rev. A. — 2016. — Vol. 93, no. 1. — P. 013419.
209. Laser cooling without spontaneous emission using the bichromatic force / C. Corder [et al.] // J. Opt. Soc. Am. B, JOSAB. — 2015. — Vol. 32, no. 5. — B75–B83.

210. General principles of the crystallization of nanostructured disperse systems // S. V. Karpov [et al.] // *Colloid J.* — 2009. — Vol. 71, no. 3. — P. 313–328. — URL: <https://doi.org/10.1134/S1061933X09030053>.
211. *Heermann D. W.* Computer-Simulation Methods // *Computer Simulation Methods in Theoretical Physics.* — Berlin, Germany : Springer, 1990. — P. 8–12. — URL: https://doi.org/10.1007/978-3-642-75448-7_2.
212. *Landau L., Lifshitz E.* *Fluid Mechanics* Pergaman. — 1982.
213. *Gor'kov L. P.* On the forces acting on a small particle in an acoustical field in an ideal fluid // *Sov. Phys. Dokl.* Vol. 6. — 1962. — P. 773–775.
214. *Livett A. J., Emery E. W., Leeman S.* Acoustic Radiation Pressure // *Journal of Sound and Vibration.* — 1956. — Jan. — Vol. 29, no. 1. — P. 1–11. — URL: <http://asa.scitation.org/doi/10.1121/1.1908669>.
215. *Bruus H.* Acoustofluidics 7: The Acoustic Radiation Force on Small Particles // *Lab on a Chip.* — 2012. — Vol. 12, no. 6. — P. 1014–1021. — pmid: [22349937](https://pubmed.ncbi.nlm.nih.gov/22349937/).
216. *Westervelt P. J.* The Theory of Steady Forces Caused by Sound Waves // *The Journal of the Acoustical Society of America.* — 1951. — Vol. 23, no. 3. — P. 312–315.
217. *Silva G. T.* An Expression for the Radiation Force Exerted by an Acoustic Beam with Arbitrary Wavefront (L) // *The Journal of the Acoustical Society of America.* — 2011. — Vol. 130, no. 6. — P. 3541–3544.
218. *Silva G. T., Lobo T. P., Mitri F. G.* Radiation Torque Produced by an Arbitrary Acoustic Wave // *Epl.* — 2012. — Vol. 97, no. 5.
219. *Busse F. H., Wang T. G.* Torque Generated by Orthogonal Acoustic Waves—Theory // *The Journal of the Acoustical Society of America.* — 1981. — Vol. 69, no. 6. — P. 1634–1638.
220. *Zhang L., Marston P. L.* Acoustic radiation torque and the conservation of angular momentum (L) // *J. Acoust. Soc. Am.* — 2011. — Vol. 129, no. 4. — P. 1679. — URL: <https://doi.org/10.1121/1.3560916>.
221. *Maidanik G.* Torques due to acoustical radiation pressure // *The Journal of the Acoustical Society of America.* — 1958. — Vol. 30, no. 7. — P. 620–623.

222. *Bonod N., Kivshar Y.* All-Dielectric Mie-Resonant Metaphotonics // Comptes Rendus. Physique. — 2020. — Vol. 21, no. 4/5. — P. 425–442.
223. *Koshelev K., Kivshar Y.* Dielectric Resonant Metaphotonics // ACS Photonics. — 2021. — Vol. 8, no. 1. — P. 102–112.
224. *Won R.* Into the Mie-Tronic Era // Nature Photonics. — 2019. — Vol. 13, no. 9. — P. 585–587.
225. *Allen L., Barnett S. M., Padgett M. J.* Optical Angular Momentum. Vol. 1. — Institute of Physics Pub, 01/2003.
226. *Torres J. P., Torner L.* Twisted photons: applications of light with orbital angular momentum. — John Wiley & Sons, 2011.
227. *Andrews D. L., Babiker M.* The Angular Momentum of Light. Vol. 1. — 01/2012.
228. *Yao A. M., Padgett M. J.* Orbital Angular Momentum: Origins, Behavior and Applications // Advances in Optics and Photonics. — 2011. — Vol. 3, no. 2. — P. 161. — pmid: 9906912. — URL: <https://www.osapublishing.org/aop/abstract.cfm?uri=aop-3-2-161>.
229. *Bliokh K. Y., Nori F.* Transverse and longitudinal angular momenta of light // Phys. Rep. — 2015. — Vol. 592. — P. 1–38. — URL: <https://doi.org/10.1016/j.physrep.2015.06.003>.
230. Tuning the orbital angular momentum in optical vortex beams / C. H. J. Schmitz [et al.] // Opt. Express. — 2006. — Vol. 14, no. 15. — P. 6604–6612. — URL: <https://doi.org/10.1364/OE.14.006604>.
231. *Bliokh K. Y., Nori F.* Spatiotemporal vortex beams and angular momentum // Phys. Rev. A. — 2012. — Vol. 86, no. 3. — P. 033824. — URL: <https://doi.org/10.1103/PhysRevA.86.033824>.
232. *Yang Y., Qiu C.-W.* Generation of Optical Vortex Beams // Electromagnetic Vortices. — Chichester, England, UK : John Wiley & Sons, Ltd, 2021. — P. 223–244. — URL: <https://doi.org/10.1002/9781119662945.ch7>.
233. Recent advances on optical vortex generation / X. Wang [et al.] // Nanophotonics. — 2018. — Vol. 7, no. 9. — P. 1533–1556. — URL: <https://doi.org/10.1515/nanoph-2018-0072>.

234. *Bulgakov E., Sadreev A.* Trapping of light with angular orbital momentum above the light cone // AEM. — 2017. — Jan. — Vol. 6, no. 1. — P. 1–10. — URL: <https://doi.org/10.7716/aem.v6i1.423>.
235. Higher-order modes of vacuum-clad ultrathin optical fibers / F. Le Kien [et al.] // Phys. Rev. A. — 2017. — Vol. 96, no. 2. — P. 023835. — URL: <https://doi.org/10.1103/PhysRevA.96.023835>.
236. *Berglind E., Björk G.* Humblet's Decomposition of the Electromagnetic Angular Moment in Metallic Waveguides // IEEE Trans. Microwave Theory Tech. — 2014. — Vol. 62, no. 4. — P. 779–788. — URL: <https://doi.org/10.1109/TMTT.2014.2308891>.
237. *Okamoto K.* Fundamentals of Optical Waveguides. — Elsevier Science, 2021. — URL: <https://books.google.com.au/books?id=GCMZEAAAQBAJ>.
238. *Mie G.* Beiträge Zur Optik Trüber Medien, Speziell Kolloidaler Metallösungen // Annalen der Physik. — 1908. — Vol. 330, no. 3. — P. 377–445. — URL: <https://onlinelibrary.wiley.com/doi/abs/10.1002/andp.19083300302> (visited on 12/14/2020).
239. *Akhiezer A. I., Berestetsky V. B.* Quantum electrodynamics. Vol. 2876. — US Atomic Energy Commission, Technical Information Service Extension, 1957.
240. *Kien F. L., Balykin V. I., Hakuta K.* Angular Momentum of Light in an Optical Nanofiber // Physical Review A - Atomic, Molecular, and Optical Physics. — 2006. — Vol. 73, no. 5. — P. 1–7. — pmid: [23925241](https://pubmed.ncbi.nlm.nih.gov/23925241/).
241. *Le Kien F., Busch T.* Torque of guided light on an atom near an optical nanofiber // Opt. Express. — 2019. — Vol. 27, no. 10. — P. 15046–15061. — URL: <https://doi.org/10.1364/OE.27.015046>.
242. *Bhandari R.* Nature of the orbital angular momentum (OAM) fields in a multilayered fiber // OSA Continuum. — 2021. — Vol. 4, no. 6. — P. 1859–1874.
243. *Frizyuk K.* Second-harmonic generation in dielectric nanoparticles with different symmetries // J. Opt. Soc. Am. B, JOSAB. — 2019. — Vol. 36, no. 8. — F32–F37.
244. *Gladyshev S., Frizyuk K., Bogdanov A.* Symmetry analysis and multipole classification of eigenmodes in electromagnetic resonators for engineering their optical properties // Phys. Rev. B. — 2020. — Vol. 102, no. 7. — P. 075103.

245. *Afanasiev G. N., Stepanovsky Y. P.* The helicity of the free electromagnetic field and its physical meaning // Nuov. Cim. A. — 1996. — Vol. 109, no. 3. — P. 271–279. — URL: <https://doi.org/10.1007/BF02731014>.
246. Electromagnetic Duality Symmetry and Helicity Conservation for the Macroscopic Maxwell's Equations / I. Fernandez-Corbaton [et al.] // Phys. Rev. Lett. — 2013. — Vol. 111, no. 6. — P. 060401. — URL: <https://doi.org/10.1103/PhysRevLett.111.060401>.
247. *Kruining K. van, Götte J. B.* The conditions for the preservation of duality symmetry in a linear medium // J. Opt. — 2016. — Vol. 18, no. 8. — P. 085601. — URL: <https://doi.org/10.1088/2040-8978/18/8/085601>.
248. *Cameron R. P., Barnett S. M., Yao A. M.* Optical helicity, optical spin and related quantities in electromagnetic theory // New J. Phys. — 2012. — Vol. 14, no. 5. — P. 053050. — URL: <https://doi.org/10.1088/1367-2630/14/5/053050>.
249. *Trueba J. L., Rañada A. F.* The electromagnetic helicity // Eur. J. Phys. — 1996. — Vol. 17, no. 3. — P. 141–144. — URL: <https://doi.org/10.1088/0143-0807/17/3/008>.
250. *Petrashen M. I., Trifonov E. D., Chomet S.* Applications of group theory in quantum mechanics. — Courier Corporation, 2009.
251. *Solyom J.* Fundamentals of the Physics of Solids: Volume 1: Structure and Dynamics. Vol. 1. — Springer Science & Business Media, 2007.
252. *Doost M. B., Langbein W., Muljarov E. A.* Resonant-state expansion applied to three-dimensional open optical systems // Phys. Rev. A. — 2014. — Vol. 90, no. 1. — P. 013834.
253. *Sehmi H. S., Langbein W., Muljarov E. A.* Applying the resonant-state expansion to realistic materials with frequency dispersion // Phys. Rev. B. — 2020. — Vol. 101, no. 4. — P. 045304.
254. *Chen C.* Foundations for Guided-Wave Optics. — Wiley, 2006. — URL: <https://books.google.com.au/books?id=LxzWPsKhns0C>.
255. *Chen C.-L.* Foundations for Guided-Wave Optics. Vol. 1. — 12/2005.

256. Orbital angular momentum of light and the transformation of Laguerre-Gaussian laser modes / L. Allen [et al.] // Phys. Rev. A. — 1992. — Vol. 45, no. 11. — P. 8185–8189. — URL: <https://doi.org/10.1103/PhysRevA.45.8185>.
257. *Sukhov S., Dogariu A.* Non-conservative optical forces // Rep. Prog. Phys. — 2017. — Vol. 80, no. 11. — P. 112001. — URL: <https://doi.org/10.1088/1361-6633/aa834e>.
258. Higher-Order Modes of Vacuum-Clad Ultrathin Optical Fibers / F. Le Kien [et al.] // Physical Review A. — 2017. — Vol. 96, no. 2. — arXiv: [1703.00109](https://arxiv.org/abs/1703.00109).
259. *Collett E.* Field Guide to Polarization. — SPIE, 2005. — URL: <https://doi.org/10.1117/3.626141>.
260. Optical manipulation of microspheres along a subwavelength optical wire / G. Brambilla [et al.] // Opt. Lett. — 2007. — Vol. 32, no. 20. — P. 3041–3043. — URL: <https://doi.org/10.1364/OL.32.003041>.
261. *Bulgakov E., Pichugin K., Sadreev A.* Resonant binding of dielectric particles to a metal surface without plasmonics // Phys. Rev. A. — 2021. — May. — Vol. 103, no. 5. — P. L051501. — URL: <https://doi.org/10.1103/PhysRevA.103.L051501>.
262. *Bulgakov E. N., Bulgakov E. N., Sadreev A. F.* Resonant bending of silicon nanowires by incident light // Opt. Lett. — 2020. — Oct. — Vol. 45, no. 19. — P. 5315–5318. — URL: <https://doi.org/10.1364/OL.406109>.
263. *Chaumet P. C., Nieto-Vesperinas M.* Time averaged total force on a dipolar sphere in an electromagnetic field // Optics Letters. — 2000. — Vol. 25, no. 15. — P. 1065–1067. — URL: <http://arxiv.org/abs/physics/0305043>.
264. *Ranha Neves A. A., Cesar C. L.* Analytical calculation of optical forces on spherical particles in optical tweezers: tutorial // Journal of the Optical Society of America B. — 2019. — Vol. 36, no. 6. — P. 1525. — URL: <https://www.osapublishing.org/abstract.cfm?URI=josab-36-6-1525> (visited on 07/22/2019).
265. *Doyle W. T.* Optical properties of a suspension of metal spheres // Physical review B. — 1989. — Vol. 39, no. 14. — P. 9852.
266. *Marcuse D.* Light transmission optics. — Van Nostrand Reinhold New York, 1972.

267. *Holzmann D., Ritsch H.* Tailored Long Range Forces on Polarizable Particles by Collective Scattering of Broadband Radiation // *New Journal of Physics*. — 2016. — Vol. 18, no. 10.
268. *Yao P. J., Manga Rao V., Hughes S.* On-chip single photon sources using planar photonic crystals and single quantum dots // *Laser & Photonics Reviews*. — 2010. — Vol. 4, no. 4. — P. 499–516.
269. *Nieddu T., Gokhroo V., Chormaic S. N.* Optical nanofibres and neutral atoms // *Journal of Optics*. — 2016. — Vol. 18, no. 5. — P. 053001. — URL: <https://iopscience.iop.org/article/10.1088/2040-8978/18/5/053001/meta>.
270. Interaction of laser-cooled 87Rb atoms with higher order modes of an optical nanofibre / R. Kumar [et al.] // *New Journal of Physics*. — 2015. — Vol. 17, no. 1. — P. 013026. — URL: <https://iopscience.iop.org/article/10.1088/1367-2630/17/1/013026>.
271. Light-induced rotation of dielectric microparticles around an optical nanofiber / G. Tkachenko [et al.] // arXiv preprint arXiv:1907.13363. — 2019.
272. *Gu Y., Li D.* The van der Waals interaction between a spherical particle and a cylinder // *Journal of colloid and interface science*. — 1999. — Vol. 217, no. 1. — P. 60–69. — URL: <https://www.sciencedirect.com/science/article/pii/S002197979996349X>.
273. Spin-orbit interactions of light / K. Y. Bliokh [et al.] // *Nat. Photonics*. — 2015. — Dec. — Vol. 9. — P. 796–808. — URL: <https://doi.org/10.1038/nphoton.2015.201>.
274. *Kotlyar V. V., Nalimov A. G., Stafeev S. S.* Focusing a Vortex Laser Beam with Polarization Conversion // *Photonics*. — 2021. — Oct. — Vol. 8, no. 11. — P. 480. — URL: <https://doi.org/10.3390/photonics8110480>.
275. Exploiting the circular polarization of light to obtain a spiral energy flow at the subwavelength focus / V. V. Kotlyar [et al.] // *J. Opt. Soc. Am. B, JOSAB*. — 2019. — Oct. — Vol. 36, no. 10. — P. 2850–2855. — URL: <https://doi.org/10.1364/JOSAB.36.002850>.

276. *Nieminen T. A., Heckenberg N. R., Rubinsztein-dunlop H.* Optical measurement of microscopic torques // *J. Mod. Opt.* — 2001. — Mar. — Vol. 48, no. 3. — P. 405–413. — URL: <https://doi.org/10.1080/09500340108230922>.
277. Separation of chiral enantiomers by optical force and torque induced by tightly focused vector polarized hollow beams / X. Liu [et al.] // *Phys. Chem. Chem. Phys.* — 2019. — July. — Vol. 21, no. 28. — P. 15339–15345. — URL: <https://doi.org/10.1039/C9CP02101A>.
278. Optical force and torque on a dielectric Rayleigh particle by a circular Airy vortex beam / M. Chen [et al.] // *J. Quant. Spectrosc. Radiat. Transfer.* — 2018. — Mar. — Vol. 208. — P. 101–107. — URL: <https://doi.org/10.1016/j.jqsrt.2018.01.018>.
279. Optical alignment and spinning of laser-trapped microscopic particles / M. E. J. Friese [et al.] // *Nature.* — 1998. — Vol. 394. — P. 348–350. — URL: <https://doi.org/10.1038/28566>.
280. Intrinsic and Extrinsic Nature of the Orbital Angular Momentum of a Light Beam / A. T. O’Neil [et al.] // *Phys. Rev. Lett.* — 2002. — Vol. 88, no. 5. — P. 053601. — URL: <https://doi.org/10.1103/PhysRevLett.88.053601>.
281. Observation of the Transfer of the Local Angular Momentum Density of a Multiringed Light Beam to an Optically Trapped Particle / V. Garcés-Chavez [et al.] // *Phys. Rev. Lett.* — 2003. — Vol. 91, no. 9. — P. 093602. — URL: <https://doi.org/10.1103/PhysRevLett.91.093602>.
282. Spin-to-Orbital Angular Momentum Conversion in a Strongly Focused Optical Beam / Y. Zhao [et al.] // *Phys. Rev. Lett.* — 2007. — Vol. 99, no. 7. — P. 073901. — URL: <https://doi.org/10.1103/PhysRevLett.99.073901>.
283. *Baranova N., Savchenko A. Y., Zel’Dovich B. Y.* Transverse shift of a focal spot due to switching of the sign of circular polarization // *JETP Letters.* — 1994. — Vol. 59, no. 4. — P. 232–234. — URL: http://jetpletters.ru/ps/1298/article_19601.pdf.
284. Coriolis Effect in Optics: Unified Geometric Phase and Spin-Hall Effect / K. Y. Bliokh [et al.] // *Phys. Rev. Lett.* — 2008. — Vol. 101, no. 3. — P. 030404. — URL: <https://doi.org/10.1103/PhysRevLett.101.030404>.

285. Dynamic consequences of optical spin-orbit interaction / S. Sukhov [et al.] // Nat. Photonics. — 2015. — Vol. 9. — P. 809–812. — URL: <https://doi.org/10.1038/nphoton.2015.200>.
286. *Bliokh K. Y., Bekshaev A. Y., Nori F.* Extraordinary momentum and spin in evanescent waves // Nat. Commun. — 2014. — Vol. 5, no. 3300. — P. 1–8. — URL: <https://doi.org/10.1038/ncomms4300>.
287. Direct measurements of the extraordinary optical momentum and transverse spin-dependent force using a nano-cantilever / M. Antognozzi [et al.] // Nat. Phys. — 2016. — Vol. 12. — P. 731–735. — URL: <https://doi.org/10.1038/nphys3732>.
288. Three-Dimensional Measurement of the Helicity-Dependent Forces on a Mie Particle / L. Liu [et al.] // Phys. Rev. Lett. — 2018. — Vol. 120, no. 22. — P. 223901. — URL: <https://doi.org/10.1103/PhysRevLett.120.223901>.
289. Optical microfibers and nanofibers: A tutorial / L. Tong [et al.] // Opt. Commun. — 2012. — Vol. 285, no. 23. — P. 4641–4647. — URL: <https://doi.org/10.1016/j.optcom.2012.07.068>.
290. *Kien F. L., Balykin V. I., Hakuta K.* Angular momentum of light in an optical nanofiber // Phys. Rev. A. — 2006. — Vol. 73, no. 5. — P. 053823. — URL: <https://doi.org/10.1103/PhysRevA.73.053823>.
291. *Xu L., Li Y., Li B.* Size-dependent trapping and delivery of submicro-spheres using a submicrofibre // New J. Phys. — 2012. — Vol. 14, no. 3. — P. 033020. — URL: <https://doi.org/10.1088/1367-2630/14/3/033020>.
292. Higher order microfibre modes for dielectric particle trapping and propulsion / A. Maimaiti [et al.] // Sci. Rep. — 2015. — Vol. 5, no. 9077. — P. 1–8. — URL: <https://doi.org/10.1038/srep09077>.
293. Selective particle trapping and optical binding in the evanescent field of an optical nanofiber / M. C. Frawley [et al.] // Opt. Express. — 2014. — Vol. 22, no. 13. — P. 16322–16334. — URL: <https://doi.org/10.1364/OE.22.016322>.
294. Nonlinear force dependence on optically bound micro-particle arrays in the evanescent fields of fundamental and higher order microfibre modes / A. Maimaiti [et al.] // Sci. Rep. — 2016. — Vol. 6, no. 30131. — P. 1–10. — URL: <https://doi.org/10.1038/srep30131>.

295. Complete Polarization Control for a Nanofiber Waveguide Using Directional Coupling / F. Lei [et al.] // *Phys. Rev. Appl.* — 2019. — Vol. 11, no. 6. — P. 064041. — URL: <https://doi.org/10.1103/PhysRevApplied.11.064041>.
296. *Joos M., Bramati A., Glorieux Q.* Complete polarization control for a nanofiber waveguide using the scattering properties // *Opt. Express.* — 2019. — Vol. 27, no. 13. — P. 18818–18830. — URL: <https://doi.org/10.1364/OE.27.018818>.
297. *Tkachenko G., Lei F., Chormaic S. N.* Polarisation control for optical nanofibres by imaging through a single lens // *J. Opt.* — 2019. — Vol. 21, no. 12. — P. 125604. — URL: <https://doi.org/10.1088/2040-8986/ab5204>.
298. *Kien F. L., Rauschenbeutel A.* Negative azimuthal force of nanofiber-guided light on a particle // *Phys. Rev. A.* — 2013. — Vol. 88, no. 6. — P. 063845. — URL: <https://doi.org/10.1103/PhysRevA.88.063845>.
299. *Barton J. P., Alexander D. R., Schaub S. A.* Internal and near-surface electromagnetic fields for a spherical particle irradiated by a focused laser beam // *J. Appl. Phys.* — 1988. — Vol. 64, no. 4. — P. 1632–1639. — URL: <https://doi.org/10.1063/1.341811>.
300. *Almaas E., Brevik I.* Radiation forces on a micrometer-sized sphere in an evanescent field // *J. Opt. Soc. Am. B, JOSAB.* — 1995. — Vol. 12, no. 12. — P. 2429–2438. — URL: <https://doi.org/10.1364/JOSAB.12.002429>.
301. Field intensity distributions and polarization orientations in a vacuum-clad subwavelength-diameter optical fiber / F. L. Kien [et al.] // *Opt. Commun.* — 2004. — Vol. 242, no. 4. — P. 445–455. — URL: <https://doi.org/10.1016/j.optcom.2004.08.044>.
302. Optical deflection and sorting of microparticles in a near-field optical geometry / R. F. Marchington [et al.] // *Opt. Express.* — 2008. — Vol. 16, no. 6. — P. 3712–3726. — URL: <https://doi.org/10.1364/OE.16.003712>.
303. *Krishnan G. P., Leighton D. T.* Inertial lift on a moving sphere in contact with a plane wall in a shear flow // *Phys. Fluids.* — 1995. — Vol. 7, no. 11. — P. 2538–2545. — URL: <https://doi.org/10.1063/1.868755>.

304. Contributed Review: Optical micro- and nanofiber pulling rig / J. M. Ward [et al.] // *Rev. Sci. Instrum.* — 2014. — Vol. 85, no. 11. — P. 111501. — URL: <https://doi.org/10.1063/1.4901098>.
305. Tapered single-mode fibres and devices. Part 1: Adiabaticity criteria / J. D. Love [et al.] // *IEE Proceedings J (Optoelectronics)*. — 1991. — Vol. 138, no. 5. — P. 343–354. — URL: <https://doi.org/10.1049/ip-j.1991.0060>.
306. *Jung Y., Brambilla G., Richardson D. J.* Broadband single-mode operation of standard optical fibers by using a sub-wavelength optical wire filter // *Opt. Express*. — 2008. — Vol. 16, no. 19. — P. 14661–14667. — URL: <https://doi.org/10.1364/OE.16.014661>.
307. Light-induced rotation of dielectric microparticles around an optical nanofiber / G. Tkachenko [et al.] // *Optica*. — 2020. — Jan. — Vol. 7, no. 1. — P. 59–62. — URL: <https://doi.org/10.1364/OPTICA.374441>.
308. *Sukhov S., Dogariu A.* Negative Nonconservative Forces: Optical “Tractor Beams” for Arbitrary Objects // *Phys. Rev. Lett.* — 2011. — Vol. 107, no. 20. — P. 203602. — URL: <https://doi.org/10.1103/PhysRevLett.107.203602>.
309. Optical pulling force / J. Chen [et al.] // *Nat. Photonics*. — 2011. — Vol. 5. — P. 531–534. — URL: <https://doi.org/10.1038/nphoton.2011.153>.
310. Acoustic Tractor Beam / C. E. M. Demore [et al.] // *Phys. Rev. Lett.* — 2014. — Vol. 112, no. 17. — P. 174302. — URL: <https://doi.org/10.1103/PhysRevLett.112.174302>.
311. GHz Rotation of an Optically Trapped Nanoparticle in Vacuum / R. Reimann [et al.] // *Physical Review Letters*. — 2018. — July 20. — Vol. 121, no. 3. — P. 033602. — URL: <https://link.aps.org/doi/10.1103/PhysRevLett.121.033602> (visited on 02/13/2020).
312. *Chang S., Lee S. S.* Optical torque exerted on a homogeneous sphere levitated in the circularly polarized fundamental-mode laser beam // *J. Opt. Soc. Am. B, JOSAB*. — 1985. — Vol. 2, no. 11. — P. 1853–1860. — URL: <https://doi.org/10.1364/JOSAB.2.001853>.
313. *Kiselev A. D., Kesaev V. V.* Interferometric and Uhlmann phases of mixed polarization states // *Phys. Rev. A*. — 2018. — Vol. 98, no. 3. — P. 033816. — URL: <https://doi.org/10.1103/PhysRevA.98.033816>.

314. *Guazzelli E., Morris J. F., Pic S.* A Physical Introduction to Suspension Dynamics. — Cambridge, England, UK : Cambridge University Press, 2011. — URL: <https://doi.org/10.1017/CB09780511894671>.
315. *Xu X., Nieto-Vesperinas M.* Azimuthal Imaginary Poynting Momentum Density // *Phys. Rev. Lett.* — 2019. — Vol. 123, no. 23. — P. 233902. — URL: <https://doi.org/10.1103/PhysRevLett.123.233902>.
316. *Kaiser G.* Completing the complex Poynting theorem: Conservation of reactive energy in reactive time // *arXiv.* — 2014. — eprint: [1412.3850](https://arxiv.org/abs/1412.3850). — URL: <https://arxiv.org/abs/1412.3850v2>.
317. *Grimes D. M., Grimes C. A.* The complex Poynting theorem: reactive power, radiative Q, and limitations on electrically small antennas // *Proceedings of International Symposium on Electromagnetic Compatibility.* — IEEE, 1995. — P. 97–101. — URL: <https://doi.org/10.1109/ISEMC.1995.523526>.
318. *Ra'di Y., Asadchy V. S., Tretyakov S. A.* One-Way Transparent Sheets // *Physical Review B.* — 2014. — Vol. 89, no. 7. — P. 075109. — URL: <https://link.aps.org/doi/10.1103/PhysRevB.89.075109> (visited on 02/26/2021).
319. Negative Optical Torque - *Scientific Reports* / J. Chen [et al.] // *Sci. Rep.* — 2014. — Vol. 4, no. 6386. — P. 1–7.
320. Second-harmonic generation in Mie-resonant dielectric nanoparticles made of noncentrosymmetric materials / K. Frizyuk [et al.] // *Phys. Rev. B.* — 2019. — Vol. 99, no. 7. — P. 075425. — URL: <https://doi.org/10.1103/PhysRevB.99.075425>.
321. Radiation torque exerted on a uniaxial anisotropic sphere: Effects of various parameters / Z. Li [et al.] // *Opt. Laser Technol.* — 2014. — Vol. 64. — P. 269–277.
322. Calculation of radiation force and torque exerted on a uniaxial anisotropic sphere by an incident Gaussian beam with arbitrary propagation and polarization directions / Z.-J. Li [et al.] // *Opt. Express.* — 2012. — Vol. 20, no. 15. — P. 16421–16435.
323. Optical tweezers: theory and practice / G. Pesce [et al.] // *Eur. Phys. J. Plus.* — 2020. — Vol. 135, no. 12. — P. 949–38. — URL: <https://doi.org/10.1140/epjp/s13360-020-00843-5>.

324. Radiation torque on nonspherical particles in the transition matrix formalism / F. Borghese [et al.] // Opt. Express. — 2006. — Vol. 14, no. 20. — P. 9508–9521. — URL: <https://opg.optica.org/oe/abstract.cfm?uri=OE-14-20-9508>.
325. Nonlinear Circular Dichroism in Mie-Resonant Nanoparticle Dimers / K. Frizyuk [et al.] // Nano Lett. — 2021. — Vol. 21, no. 10. — P. 4381–4387.
326. Acoustic tweezers / L. Meng [et al.] // J. Phys. D: Appl. Phys. — 2019. — Vol. 52, no. 27. — P. 273001. — URL: <https://doi.org/10.1088/1361-6463/ab16b5>.
327. *Dholakia K., Drinkwater B. W., Ritsch-Marte M.* Comparing acoustic and optical forces for biomedical research // Nat. Rev. Phys. — 2020. — Vol. 2. — P. 480–491. — URL: <https://doi.org/10.1038/s42254-020-0215-3>.
328. Acoustic resonators: symmetry classification and multipolar content of the eigenmodes / M. Tsimokha [et al.] // arXiv. — 2021. — eprint: [2110.11220](https://arxiv.org/abs/2110.11220).
329. *Bruus H.* Acoustofluidics 1: Governing Equations in Microfluidics // Lab on a Chip. — 2011. — Vol. 11, no. 22. — P. 3742–3751. — pmid: [22011885](https://pubmed.ncbi.nlm.nih.gov/22011885/).
330. *Bruus H.* Acoustofluidics 2: Perturbation Theory and Ultrasound Resonance Modes // Lab on a Chip. — 2012. — Vol. 12, no. 1. — P. 20–28. — pmid: [22105715](https://pubmed.ncbi.nlm.nih.gov/22105715/).
331. Bound States in the Continuum in Compact Acoustic Resonators / I. Deriy [et al.] // Phys. Rev. Lett. — 2022. — Vol. 128, no. 8. — P. 084301.
332. *Silva G. T.* Acoustic radiation force and torque on an absorbing compressible particle in an inviscid fluid // J. Acoust. Soc. Am. — 2014. — Nov. — Vol. 136, no. 5. — P. 2405. — URL: <https://doi.org/10.1121/1.4895691>.
333. Character Table for Point Group C3v. — 2016. — URL: http://www.gernot-katzers-spice-pages.com/character_tables/C3v.html ; [Online; accessed 15. Apr. 2022].
334. *Blackstock D. T.* Fundamentals of physical acoustics. — ASA, 2001.
335. *Chaumet P. C., Rahmani A.* Electromagnetic force and torque on magnetic and negative-index scatterers // Optics express. — 2009. — Vol. 17, no. 4. — P. 2224–2234.

336. Acoustic radiation force and torque on small particles as measures of the canonical momentum and spin densities / I. Toftul [et al.] // Physical review letters. — 2019. — Vol. 123, no. 18. — P. 183901.
337. *Toftul I., Bliokh K., Petrov M.* Acoustic forces and torques: Directional scattering and acoustic spin // AIP Conf. Proc. — 2020. — Vol. 2300, no. 1. — P. 020127.
338. *Baresch D., Thomas J.-L., Marchiano R.* Observation of a single-beam gradient force acoustical trap for elastic particles: acoustical tweezers // Physical review letters. — 2016. — Vol. 116, no. 2. — P. 024301.
339. *Wei L., Rodriguez-Fortuño F. J.* Far-field and near-field directionality in acoustic scattering // arXiv preprint arXiv:2003.13292. — 2020.
340. *Settnes M., Bruus H.* Forces Acting on a Small Particle in an Acoustical Field in a Viscous Fluid // Physical Review E - Statistical, Nonlinear, and Soft Matter Physics. — 2012. — Vol. 85, no. 1. — P. 1–12.
341. *Karlsen J. T., Bruus H.* Forces Acting on a Small Particle in an Acoustical Field in a Thermoviscous Fluid // Physical Review E - Statistical, Nonlinear, and Soft Matter Physics. — 2015. — Vol. 92, no. 4. — pmid: [22400677](#).
342. A Short Survey on Green's Function for Acoustic Problems / A. R. Okoyenta [et al.] // J. Theor. Comp. Acout. — 2020. — Vol. 28, no. 02. — P. 1950025.
343. *Contributors to Wikimedia projects.* Del in cylindrical and spherical coordinates - Wikipedia. — 2022. — URL: https://en.wikipedia.org/w/index.php?title=Del_in_cylindrical_and_spherical_coordinates&oldid=1068192565 ; [Online; accessed 30. Mar. 2022].
344. *Contributors to Wikimedia projects.* Vector fields in cylindrical and spherical coordinates - Wikipedia. — 2022. — URL: https://en.wikipedia.org/w/index.php?title=Vector_fields_in_cylindrical_and_spherical_coordinates&oldid=1074404760 ; [Online; accessed 30. Mar. 2022].
345. *De Vries P., van Coevorden D. V., Lagendijk A.* Point Scatterers for Classical Waves // Reviews of Modern Physics. — 1998. — Vol. 70, no. 2. — P. 447–466. — pmid: [24335434](#). — URL: <https://link.aps.org/doi/10.1103/RevModPhys.70.447>.

346. Electromagnetic waves in chiral and bi-isotropic media / I. Lindell [et al.]. — Artech House, 1994. — URL: <https://research.aalto.fi/en/publications/electromagnetic-waves-in-chiral-and-bi-isotropic-media>.
347. *Wang S. B., Chan C. T.* Lateral optical force on chiral particles near a surface // Nat. Commun. — 2014. — Vol. 5, no. 3307. — P. 1–8. — URL: <https://doi.org/10.1038/ncomms4307>.
348. Tailoring azimuthal optical force on lossy chiral particles in Bessel beams / H. Chen [et al.] // Phys. Rev. A. — 2014. — Vol. 90, no. 4. — P. 043850. — URL: <https://link.aps.org/doi/10.1103/PhysRevA.90.043850>.
349. Selective trapping of chiral nanoparticles via vector Lissajous beams / H. Wu [et al.] // Opt. Express. — 2022. — Vol. 30, no. 3. — P. 3592–3600. — URL: <https://opg.optica.org/oe/fulltext.cfm?uri=oe-30-3-3592&id=468610>.
350. All-Optical Chirality-Sensitive Sorting via Reversible Lateral Forces in Interference Fields / T. Zhang [et al.] // ACS Nano. — 2017. — Vol. 11, no. 4. — P. 4292–4300. — URL: <https://doi.org/10.1021/acsnano.7b01428>.
351. Selectively transporting small chiral particles with circularly polarized Airy beams / W. Lu [et al.] // Opt. Lett. — 2018. — Vol. 43, no. 9. — P. 2086–2089. — URL: <https://opg.optica.org/ol/fulltext.cfm?uri=ol-43-9-2086&id=385815>.
352. *Chew W. C.* Waves and fields in inhomogeneous media. — Wiley-IEEE Press, 1999. — P. 632.
353. *Tai C.-T.* Dyadic Green functions in electromagnetic theory. — IEEE Press Series on Electromagnetic Waves, 1994. — P. 343.
354. *Novotny L., Hecht B.* Principles of nano-optics. — Cambridge university press, 2012.
355. *Bliokh K. Y., Dressel J., Nori F.* Conservation of the spin and orbital angular momenta in electromagnetism // New J. Phys. — 2014. — Vol. 16, no. 9. — P. 093037. — URL: <https://doi.org/10.1088/1367-2630/16/9/093037>.
356. *Markel V. A.* Pole expansion of the Lorenz-Mie coefficients // J. Nanophotonics. — 2010. — Vol. 4, no. 1. — P. 041555. — URL: <https://doi.org/10.1117/1.3332549>.

357. *Alù A., Engheta N.* Polarizabilities and effective parameters for collections of spherical nanoparticles formed by pairs of concentric double-negative, single-negative, and double-positive metamaterial layers // *J. Appl. Phys.* — 2005. — Vol. 97, no. 9. — P. 094310. — URL: <https://doi.org/10.1063/1.1884757>.
358. *Stout B., Colom R., McPhedran R. C.* Egocentric physics: Summing up Mie // *Wave Motion.* — 2018. — Vol. 83. — P. 173–187. — URL: <https://doi.org/10.1016/j.wavemoti.2018.09.001>.
359. *Lobanov S. V., Langbein W., Muljarov E. A.* Resonant-state expansion applied to three-dimensional open optical systems: Complete set of static modes // *Phys. Rev. A.* — 2019. — Vol. 100, no. 6. — P. 063811.
360. *Weisstein E. W.* Condon-Shortley Phase // Wolfram Research, Inc. — 2003. — URL: <https://mathworld.wolfram.com/Condon-ShortleyPhase.html>.
361. COMSOL Documentation. — 06/2021. — URL: https://doc.comsol.com/5.5/docserver/#!/com.comsol.help.comsol/comsol_ref_definitions.12.037.html ; [Online; accessed 2. Jun. 2021].
362. *De Witt C. M., Jensen J. H. D.* Über den Drehimpuls der Multipolstrahlung // *Zeitschrift für Naturforschung A.* — 1953. — Vol. 8, no. 4. — P. 267–270. — URL: <https://doi.org/10.1515/zna-1953-0409>.
363. *Varshalovich D. A., Moskalev A. N., Khersonskii V. K.* Quantum Theory of Angular Momentum. — Singapore : World Scientific Publishing Company, 1988.
364. DLMF: 14.5 Special Values. — 2021. — URL: <https://dlmf.nist.gov/14.5> ; [Online; accessed 14. Jul. 2021].

Acknowledgements

I would love to thank important people for me who inspired, supported, and helped me in direct or indirect way during my PhD at ITMO university. Among them are

- My grandfather Yuri Aleksandrovich Nechaev who inspired me to devote my life to science. He was the one who was never tired to answer trillion of questions when I was a child. I wish he could read this final manuscript but he lacked only a few months to witness it, unfortunately.
- My fiancée Liliia Kichigina who supported and loved me during all the hard times.
- My direct supervisor Mihail Petrov, who helped to manage important steps during my PhD such as two internships in Japan, he gave me motivation, and guidance along all the way.
- Kristina Frizyuk, a great friend of mine and my colleague. She is a great example of a true honest person and a talented inspiring researcher. We had endless scientific discussions along the way.
- Konstantin Bliokh with whom I had the honor to work together in RIKEN, Japan. From him I received plenty of valuable advice.
- All people from the prof. Sile Nic Chormaic unit at OIST for their hospitality and warm welcome. Especially, I would love to thank Georgy Tkachenko, Emi Nakamura, Sahar S. Hejazi, Fuchuan Lei, Fam Le Kien, Viet Giang Truong, Priscila Romagnoli, and prof. Sile Nic Chormaic herself. At this place I learned how to interact with experimentalists, and the role of the experiment in general. I also witnessed how high complexity of the modern physics experiments.

Without all these people this couldn't be possible.

Appendix A

Helpful math identities

Integrals with different number of \mathbf{n} :

$$\int_{4\pi} d\Omega n_i = 0, \quad \int_{4\pi} d\Omega n_i n_j n_k = 0, \quad \int_{4\pi} d\Omega (\text{odd number of } \mathbf{n}) = 0, \quad (\text{A.1})$$

$$\int_{4\pi} d\Omega n_i n_j = \frac{4\pi}{3} \delta_{ij}, \quad \int_{4\pi} d\Omega n_i n_j n_k n_\ell = \frac{4\pi}{15} (\delta_{ij} \delta_{kl} + \delta_{ik} \delta_{jl} + \delta_{il} \delta_{jk}), \quad (\text{A.2})$$

where $i, j, k, \ell = x, y, z$, $\mathbf{n} = (\sin \vartheta \cos \varphi, \sin \vartheta \sin \varphi, \cos \vartheta)^T$, and $\int_{4\pi} d\Omega = \int_0^\pi d\vartheta \sin \vartheta \int_0^{2\pi} d\varphi$.

As far as Berry notation $\mathbf{A} \cdot (\nabla) \mathbf{B} \equiv \sum_\alpha \sum_{i=x,y,z} A_i \hat{\mathbf{e}}_\alpha \nabla_\alpha B_i$ [9] appears quite often, we give some general rules. First of all, nabla operator should be just replaced to the corresponding nabla operator in desired coordinate system [343]. For the main coordinate systems we can write:

1. **Cylindrical coordinates.** For the cylindrical coordinates (r, φ, z) with $\nabla = (\frac{\partial}{\partial r}, \frac{\partial}{\partial \varphi}, \frac{\partial}{\partial z})^T$ this transformation can be written as

$$\sum_{i=x,y,z} A_i^{\text{cart}} \nabla_\alpha B_i^{\text{cart}} = \sum_{i=r,\varphi,z} A_i^{\text{cyl}} \nabla_\alpha B_i^{\text{cyl}} + \frac{1}{r} (A_\varphi^{\text{cyl}} B_r^{\text{cyl}} - A_r^{\text{cyl}} B_\varphi^{\text{cyl}}) \delta_{\alpha\varphi}. \quad (\text{A.3})$$

2. **Spherical coordinates.** For the spherical coordinates (r, ϑ, φ) , $\vartheta \in [0, \pi]$, $\varphi \in [0, 2\pi]$ with $\nabla = (\frac{\partial}{\partial r}, \frac{1}{r} \frac{\partial}{\partial \vartheta}, \frac{1}{r \sin \vartheta} \frac{\partial}{\partial \varphi})^T$ the rotation matrix is

$$\mathbf{A}^{\text{cart}} = R(\vartheta, \varphi) \mathbf{A}^{\text{sph}}, \quad (\text{A.4})$$

where [344]

$$R(\vartheta, \varphi) = \begin{pmatrix} \sin \vartheta \cos \varphi & \cos \vartheta \cos \varphi & -\sin \varphi \\ \sin \vartheta \sin \varphi & \cos \vartheta \sin \varphi & \cos \varphi \\ \cos \vartheta & -\sin \vartheta & 0 \end{pmatrix}, \quad R^{-1}(\vartheta, \varphi) = R^T(\vartheta, \varphi). \quad (\text{A.5})$$

After some algebra this transformation can be written as

$$\begin{aligned}
\sum_{i=x,y,z} A_i^{\text{cart}} \nabla_\alpha B_i^{\text{cart}} &= \sum_{i=r,\vartheta,\varphi} A_i^{\text{sph}} \nabla_\alpha B_i^{\text{sph}} + \delta_{\alpha\vartheta} \frac{1}{r} \mathbf{A}^{\text{sph}} Q^\vartheta \mathbf{B}^{\text{sph}} \\
&\quad + \delta_{\alpha\varphi} \frac{1}{r \sin \vartheta} \mathbf{A}^{\text{sph}} Q^\varphi \mathbf{B}^{\text{sph}}, \\
&= \sum_{i=r,\vartheta,\varphi} A_i^{\text{sph}} \nabla_\alpha B_i^{\text{sph}} + \delta_{\alpha\vartheta} \frac{1}{r} \left(B_r^{\text{sph}} A_\vartheta^{\text{sph}} - B_\vartheta^{\text{sph}} A_r^{\text{sph}} \right) \\
&\quad + \delta_{\alpha\varphi} \frac{A_\varphi^{\text{sph}} \left(B_r^{\text{sph}} \sin \vartheta + B_\vartheta^{\text{sph}} \cos \vartheta \right)}{r \sin \vartheta}, \\
&\quad - \delta_{\alpha\varphi} \frac{B_\varphi^{\text{sph}} \left(A_r^{\text{sph}} \sin \vartheta + A_\vartheta^{\text{sph}} \cos \vartheta \right)}{r \sin \vartheta}, \tag{A.6}
\end{aligned}$$

where

$$Q^\vartheta = R^{-1}(\vartheta, \varphi) \frac{\partial}{\partial \vartheta} R(\vartheta, \varphi) = \begin{pmatrix} 0 & -1 & 0 \\ 1 & 0 & 0 \\ 0 & 0 & 0 \end{pmatrix}, \tag{A.7}$$

$$Q^\varphi = R^{-1}(\vartheta, \varphi) \frac{\partial}{\partial \varphi} R(\vartheta, \varphi) = \begin{pmatrix} 0 & 0 & -\sin \vartheta \\ 0 & 0 & -\cos \vartheta \\ \sin \vartheta & \cos \vartheta & 0 \end{pmatrix}. \tag{A.8}$$

Unfortunately, this results is quite ugly compared to the result in cylindrical coordinates.

Appendix B

Electric and magnetic dipole polarizabilities

B.1 Definitions

In SI units we define electric and magnetic polarizabilities as

$$\mathbf{p} = \alpha_e \mathbf{E}, \quad \mathbf{m} = \frac{1}{\mu\mu_0} \alpha_m \mathbf{H}. \quad (\text{B.1})$$

This definition is different from [150], where $\mathbf{m} \equiv \alpha_m^{\text{from [150]}} \mathbf{H}$, so $\alpha_m^{\text{from [150]}} = \frac{1}{\mu\mu_0} \alpha_m^{\text{this work}}$. Exact electric and magnetic dipole polarizability for a sphere are given by:

$$\alpha_e = 4\pi\epsilon_0 \cdot i \frac{3\epsilon}{2k^3} a_1, \quad \alpha_m = 4\pi\mu_0 \cdot i \frac{3\mu}{2k^3} b_1. \quad (\text{B.2})$$

Here $k = \sqrt{\epsilon\mu} \frac{\omega}{c}$, ϵ and μ are the electric and magnetic permeabilities of the host medium, a_1 and b_1 are the first Mie coefficients [172]. Expanding in (ka) series [154; 172] we get first order correction to the electrostatic polarizabilities which satisfies the optical theorem [27; 147]:

$$\alpha_e = \frac{\alpha_e^{(0)}}{1 - i \frac{k^3}{6\pi\epsilon\epsilon_0} \alpha_e^{(0)}}, \quad \alpha_m = \frac{\alpha_m^{(0)}}{1 - i \frac{k^3}{6\pi\mu\mu_0} \alpha_m^{(0)}}, \quad (\text{B.3})$$

where the electrostatic polarizabilities (or to be more precise, first non-zero terms in Taylor series of a_1 and b_1) for the particle are defined by ϵ_p and μ_p are given by [120, see SM],[172, § 5.1]

$$\alpha_e^{(0)} = 4\pi\epsilon\epsilon_0 a^3 \frac{\epsilon_p - \epsilon}{\epsilon_p + 2\epsilon}, \quad (\text{B.4})$$

$$\alpha_m^{(0)} = 4\pi\mu\mu_0 a^3 \frac{\mu_p - \mu}{\mu_p + 2\mu} + \mathcal{O}((ka)^5) = \frac{4\pi\mu_0}{k^3} \frac{\epsilon_p - \epsilon}{30\epsilon} (ka)^5 \Big|_{\mu=\mu_p=1}. \quad (\text{B.5})$$

The Mie coefficients for the sphere with ε_p and μ_p in the host media with ε and μ are given as [172]

$$a_n = \frac{\mu m^2 j_n(mx) [x j_n(x)]' - \mu_p j_n(x) [mx j_n(mx)]'}{\mu m^2 j_n(mx) [x h_n^{(1)}(x)]' - \mu_p h_n^{(1)}(x) [mx j_n(mx)]'}, \quad (\text{B.6})$$

$$b_n = \frac{\mu_p j_n(mx) [x j_n(x)]' - \mu j_n(x) [mx j_n(mx)]'}{\mu_p j_n(mx) [x h_n^{(1)}(x)]' - \mu h_n^{(1)}(x) [mx j_n(mx)]'} \quad (\text{B.7})$$

Here, $x = nk_0 a$ is the normalized particle radius; $k_0 = \omega/c$ is the wave vector in vacuum, with ω being the angular frequency and c being light velocity in vacuum; $m = n_p/n = \sqrt{\varepsilon_p \mu_p} / \sqrt{\varepsilon \mu}$ is the relative refractive index of the particle. j_n and $h_n^{(1)}$ are the spherical Bessel and Hankel functions of order n (which is an integer from 1 to infinite). The derivations are performed with respect to the argument, e.g., $j_n(nx)' \equiv d[j_n(nx)] / d(nx)$.

Radiative correction (B.3) can be also found via renormalization procedure [345]. The dipole radiation can change its own dipole moment, formally it be written via free space Greens tensor as $\mathbf{p} = \alpha_e^{(0)} (\mathbf{E} + \mathbf{E}_{\text{self}}) = \alpha_e^{(0)} \left(\mathbf{E} + (\varepsilon \varepsilon_0)^{-1} k^2 \hat{\mathbf{G}}_0(\mathbf{r}_0, \mathbf{r}_0) \mathbf{p} \right)$, where \mathbf{r}_0 is the location of the dipole. The main obstacle here is to find the free space Green tensor at the origin. The real part diverges, so $\text{Re } \hat{\mathbf{G}}_0(\mathbf{r}_0, \mathbf{r}_0) \rightarrow \infty$ but imaginary part is finite $\text{Im } \hat{\mathbf{G}}_0(\mathbf{r}_0, \mathbf{r}_0) = \frac{k}{6\pi} \hat{\mathbf{I}}$, so $\alpha_e = \left(1 - \alpha_e^{(0)} \frac{k^2}{\varepsilon \varepsilon_0} i \text{Im } \hat{\mathbf{G}}_0(\mathbf{r}_0, \mathbf{r}_0) \right)^{-1} \alpha_e^{(0)}$.

For a particle made of chiral media with bulk parameters $\eta = (\varepsilon, \mu, \kappa)$, polarizabilities are defined as

$$\begin{pmatrix} \mathbf{p} \\ \mu \mu_0 \mathbf{m} \end{pmatrix} = \begin{pmatrix} \alpha_e(\eta) & i \alpha_c(\eta) \\ -i \alpha_c^T(\eta) & \alpha_m(\eta) \end{pmatrix} \begin{pmatrix} \mathbf{E} \\ \mathbf{H} \end{pmatrix} \quad (\text{B.8})$$

and can be found rigorously for a spherical particle from bi-anisotropic material with constitutive relations by solving Mie scattering problem [346, § 6.1.1][347, SM][24; 31–33; 348–351]

$$\alpha_e = i \frac{6\pi \varepsilon \varepsilon_0}{k^3} a_1 \approx 4\pi \varepsilon \varepsilon_0 a^3 \frac{(\varepsilon_r - 1)(\mu_r + 2) - \kappa^2}{(\varepsilon_r + 2)(\mu_r + 2) - \kappa^2}, \quad (\text{B.9})$$

$$\alpha_m = i \frac{6\pi \mu \mu_0}{k^3} b_1 \approx 4\pi \mu \mu_0 a^3 \frac{(\mu_r - 1)(\varepsilon_r + 2) - \kappa^2}{(\mu_r + 2)(\varepsilon_r + 2) - \kappa^2}, \quad (\text{B.10})$$

$$\alpha_c = \frac{6\pi n}{ck^3} c_1 \approx 12\pi \frac{n}{c} a^3 \frac{\kappa}{(\varepsilon_r + 2)(\mu_r + 2) - \kappa^2} \quad (\text{B.11})$$

where $\varepsilon_r = \varepsilon_p/\varepsilon$ and $\mu_r = \mu_p/\mu$. Correct imaginary part of the approximate values can be found via optical theorem for chiral dipole particles, see eq. (B.30). The Mie coefficients for the chiral sphere are

$$a_n = \frac{V_n(R)A_n(L) + V_n(L)A_n(R)}{W_n(L)V_n(R) + W_n(R)V_n(L)} \quad (\text{B.12})$$

$$b_n = \frac{W_n(L)B_n(R) + W_n(R)B_n(L)}{W_n(L)V_n(R) + W_n(R)V_n(L)} \quad (\text{B.13})$$

$$c_n = i \frac{W_n(R)A_n(L) - W_n(L)A_n(R)}{W_n(L)V_n(R) + W_n(R)V_n(L)} \quad (\text{B.14})$$

with

$$W_n(J) = m\psi_n(m_Jx)\xi'_n(x) - \xi_n(x)\psi'_n(m_Jx) \quad (\text{B.15})$$

$$V_n(J) = \psi_n(m_Jx)\xi'_n(x) - m\xi_n(x)\psi'_n(m_Jx) \quad (\text{B.16})$$

$$A_n(J) = m\psi_n(m_Jx)\psi'_n(x) - \psi_n(x)\psi'_n(m_Jx) \quad (\text{B.17})$$

$$B_n(J) = \psi_n(m_Jx)\psi'_n(x) - m\psi_n(x)\psi'_n(m_Jx) \quad (\text{B.18})$$

here $J = R, L$, $x = ka = \sqrt{\varepsilon\mu}\frac{\omega}{c}$, $\psi_n(\rho) = \rho j_n(\rho)$, $\xi_n(\rho) = \rho h_n^{(1)}(\rho)$ with j_n is being the spherical Bessel function and $h_n^{(1)}$ is being the spherical Hankel function of the first kind. The relative indices m_L , m_R and the mean refractive index m take expressions of $m_{L,R} = (\sqrt{\varepsilon_p\mu_p} \pm \kappa) / \sqrt{\varepsilon\mu}$ and $m = (m_L + m_R)/2$.

B.2 More on Mie

Some properties of the Mie coefficients

1. Mie coefficients are symmetric:

$$a_n(\varepsilon_r, \mu_r) = b_n(\mu_r, \varepsilon_r) \quad (\text{B.19})$$

where where $\varepsilon_r = \varepsilon_p/\varepsilon$ and $\mu_r = \mu_p/\mu$ are the relative permittivity and permeability. See Fig. B.1 for an example. However, this is not the case for the acoustics.

2. Mie resonances are relevant only for particle sizes around $kR_p \sim 1$, otherwise it does not give any significant increase in scattering (Fig B.2).
3. Plot of first several Mie coefficients is shown in Fig. B.3.

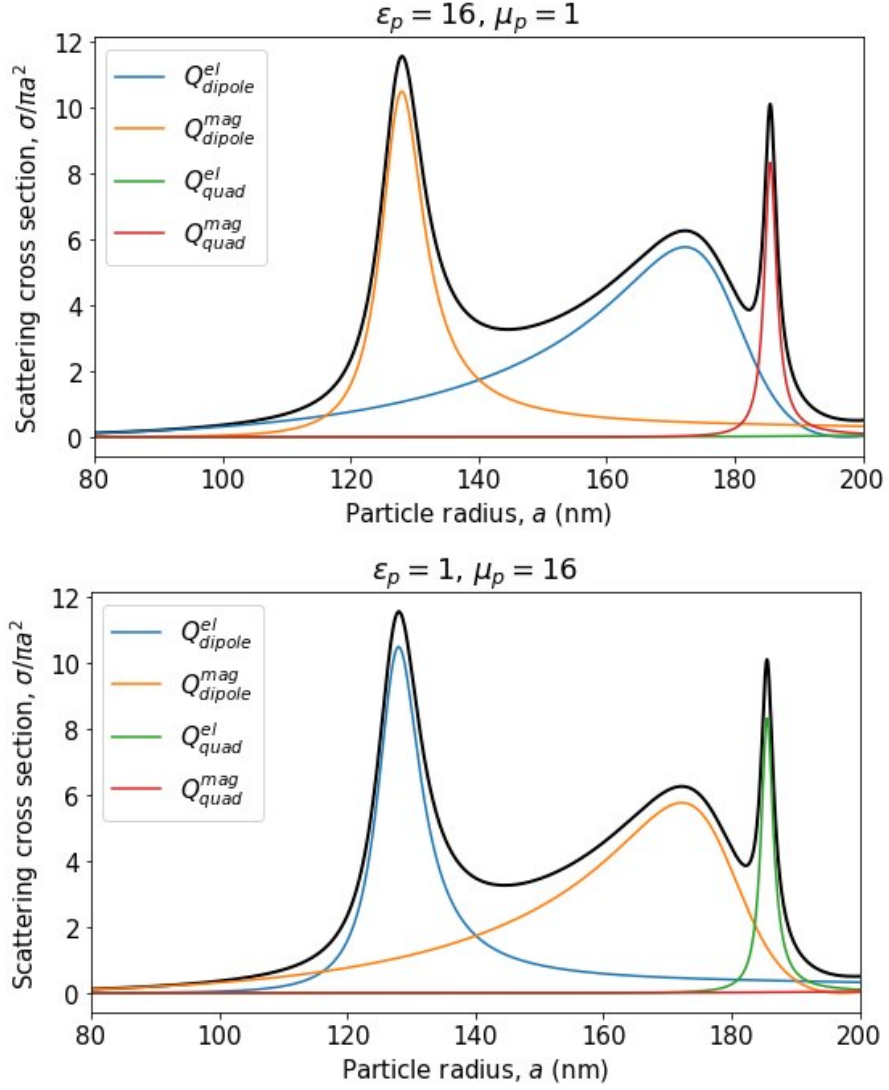


Figure B.1 — Comparison of scattering cross sections between electric ($\epsilon_p = 16$, $\mu_p = 1$) and magnetic ($\epsilon_p = 1$, $\mu_p = 16$) particles in air ($\epsilon = \mu = 1$) to illustrate the symmetric properties of the Mie coefficients

B.3 Comments on the connection with the literature

Usually polarizabilities are written in Gaussian units. Moreover, for the magnetic polarizability are at least two conventions:

1. Nieto et al. [143; 155; 156] (Gaussian units)

$$\mathbf{m} = \alpha_m \mathbf{B} \quad (\text{B.20})$$

2. Bekshaev et al. [120; 154] (Gaussian units)

$$\mathbf{m} = \mu^{-1} \alpha_m \mathbf{H} \quad (\text{B.21})$$

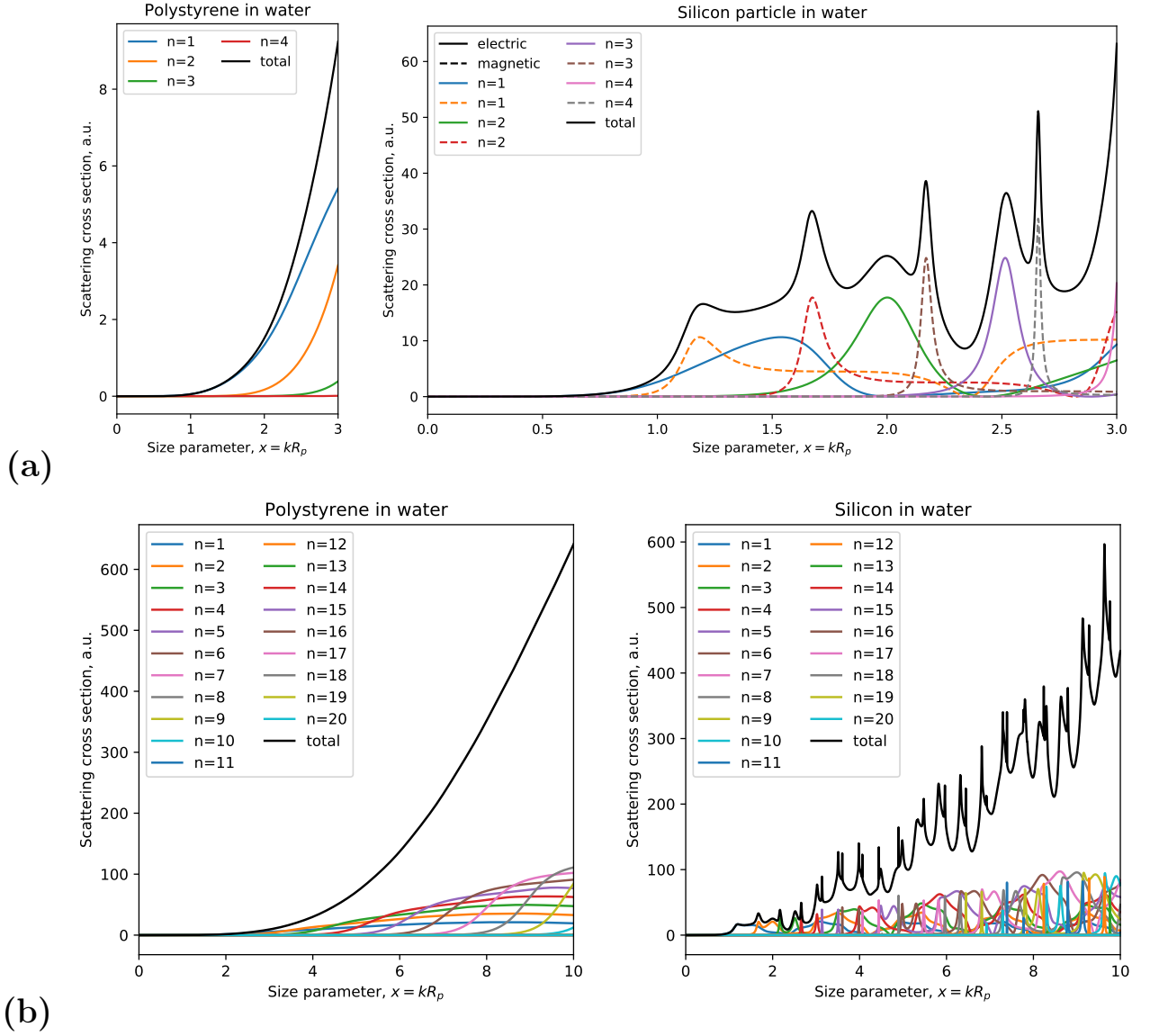


Figure B.2 — Example of scattering cross sections for polysterene and silicon in water. Mie resonances give a huge enhancement in scattering only for sizes $x \sim 1 \div 3$

This was done in order to obtain more symmetric expressions in [154]. Bekshaev explicitly notice the difference with the other sources [143; 155; 156].

If one expands both expressions, then everything converges to the same thing, *there are no contradictions!* Two formalisms are connected in the Gaussian system as

$$\alpha_m^{\text{Nieto}} \mu^2 = \alpha_m^{\text{Bekshaev}} \quad (\text{B.22})$$

Also, in [24] magnetic dipole moment is defined slightly different such that

$$\mathbf{m}^{\text{from [24]}} \approx 4\pi\mu\mu_0 a^3 \frac{\mu_p - \mu}{\mu_p + 2\mu} \mathbf{H}, \quad \mathbf{m}^{\text{this work}} \approx 4\pi a^3 \frac{\mu_p - \mu}{\mu_p + 2\mu} \mathbf{H} \quad (\text{B.23})$$

so $\mathbf{m}^{\text{from [24]}} = \mu\mu_0 \mathbf{m}^{\text{this work}}$ and hence have different dimension.

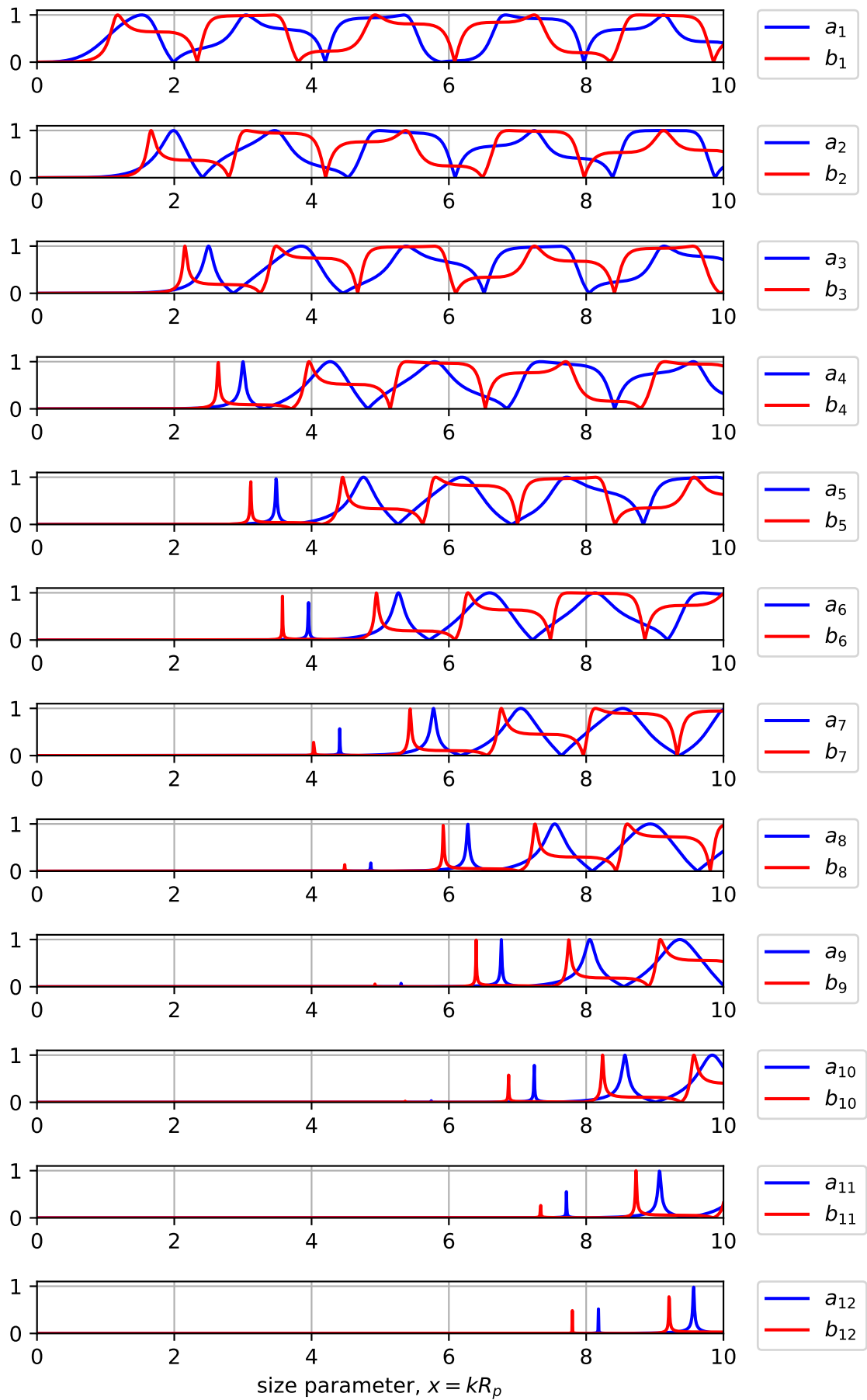


Figure B.3 — Absolute values of Mie coefficients for scattered field for silicon particle in water ($\epsilon_p = 11.5$, $\epsilon_m = 1.77$, $\mu_p = \mu_m = 1$)

B.4 Dipole approximation for the scattering cross section

Let us assume that particle support only electric and magnetic dipole modes with polarizabilities ($\mathbf{p} = \alpha_e \mathbf{E}$ and $\mathbf{m} = (\mu\mu_0)^{-1} \alpha_m \mathbf{H}$) expressed through the Mie coefficients as stated by (B.2). Then the cross sections are going to be

$$\sigma_{\text{ext}} = \sigma_{\text{ext}}^{(e)} + \sigma_{\text{ext}}^{(m)} = \frac{1}{4\pi\epsilon\epsilon_0} \cdot 4\pi k \text{Im}(\alpha_e) + \frac{1}{4\pi\mu\mu_0} \cdot 4\pi k \text{Im}(\alpha_m) \quad (\text{B.24})$$

$$\sigma_{\text{sc}} = \sigma_{\text{sc}}^{(e)} + \sigma_{\text{sc}}^{(m)} = \frac{1}{(4\pi\epsilon\epsilon_0)^2} \cdot \frac{8\pi}{3} k^4 |\alpha_e|^2 + \frac{1}{(4\pi\mu\mu_0)^2} \cdot \frac{8\pi}{3} k^4 |\alpha_m|^2 \quad (\text{B.25})$$

and, finally, the electric and magnetic absorption cross sections $\sigma_{\text{abs}} = \sigma_{\text{abs}}^{(e)} + \sigma_{\text{abs}}^{(m)}$ are

$$\sigma_{\text{abs}}^{(e)} = \frac{k}{\epsilon\epsilon_0} \left[\text{Im}(\alpha_e) - \frac{k^3}{6\pi\epsilon\epsilon_0} |\alpha_e|^2 \right] \quad (\text{B.26})$$

and

$$\sigma_{\text{abs}}^{(m)} = \frac{k}{\mu\mu_0} \left[\text{Im}(\alpha_m) - \frac{k^3}{6\pi\mu\mu_0} |\alpha_m|^2 \right] \quad (\text{B.27})$$

For the case of no-inside-gain particle, i.e. there no energy is emitted by the particle internally ($\sigma_{\text{abs}} > 0$), we have a particular case of the optical theorem

$$\frac{1}{4\pi\epsilon\epsilon_0} \text{Im}(\alpha_e) + \frac{1}{4\pi\mu\mu_0} \text{Im}(\alpha_m) \geq \frac{2k^3}{3} \left[\frac{|\alpha_e|^2}{(4\pi\epsilon\epsilon_0)^2} + \frac{|\alpha_m|^2}{(4\pi\mu\mu_0)^2} \right] \quad (\text{B.28})$$

The sign of equality is achieved for non-absorbing particles, i.e. for $\text{Im}(\epsilon) = \text{Im}(\mu) = 0$.

For chiral particles (B.8) with

$$\begin{pmatrix} \mathbf{p} \\ \mu\mu_0 \mathbf{m} \end{pmatrix} = \overline{\overline{\boldsymbol{\alpha}}} \begin{pmatrix} \mathbf{E} \\ \mathbf{H} \end{pmatrix}, \quad \overline{\overline{\boldsymbol{\alpha}}} = \begin{pmatrix} \alpha_e & i\alpha_c \\ -i\alpha_c^T & \alpha_m \end{pmatrix} \quad (\text{B.29})$$

The generalization of the optical theorem is going to be the following [27, eq. (13)][34]

$$\frac{1}{2i} \left(\overline{\overline{\boldsymbol{\alpha}}}^{-1} - \left(\overline{\overline{\boldsymbol{\alpha}}}^{-1} \right)^\dagger \right) \geq -\frac{k^3}{6\pi} \begin{pmatrix} \hat{\mathbf{I}}/(\epsilon\epsilon_0) & 0 \\ 0 & \hat{\mathbf{I}}/(\mu\mu_0) \end{pmatrix} \quad (\text{B.30})$$

The sign of equality is achieved for non-absorbing particles, i.e. for $\text{Im}(\epsilon) = \text{Im}(\mu) = \text{Im}(\kappa) = 0$. We note that it is equivalent to the (B.28) in case of $\kappa = 0$. The cross

sections for scalar case are [26; 31; 349]

$$\sigma_{\text{ext}}^{(e)} = \frac{k}{\varepsilon \varepsilon_0} \text{Im}(\alpha_e), \quad \sigma_{\text{ext}}^{(m)} = \frac{k}{\varepsilon \varepsilon_0} \text{Im}(\alpha_m) \quad (\text{B.31})$$

$$\sigma_{\text{ext}} = \sigma_{\text{ext}}^{(e)} + \sigma_{\text{ext}}^{(m)} - \frac{c^2 k^4}{6\pi n^2} (\text{Re}(\alpha_e \alpha_m^*) + |\alpha_c|^2) \quad (\text{B.32})$$

$$\sigma_{\text{abs,c}} = \sigma_{\text{abs,c}}^{(e)} + \sigma_{\text{abs,c}}^{(m)} \quad (\text{B.33})$$

$$\sigma_{\text{abs,c}}^{(e)} = \frac{k}{\varepsilon \varepsilon_0} (\text{Im}(\alpha_e) - g_e |\alpha_e|^2 - g_m |\alpha_c|^2) \quad (\text{B.34})$$

$$\sigma_{\text{abs,c}}^{(m)} = \frac{k}{\varepsilon \varepsilon_0} (\text{Im}(\alpha_m) - g_m |\alpha_m|^2 - g_e |\alpha_c|^2) \quad (\text{B.35})$$

$$\gamma_{\text{abs,c}}^{\text{Re}} = 2\omega \text{Im}(\alpha_c) - 2\omega g_e \text{Re}(\alpha_e \alpha_c^*) - 2\omega g_m \text{Re}(\alpha_m \alpha_c^*) \quad (\text{B.36})$$

$$\gamma_{\text{abs,c}}^{\text{Im}} = 2\omega g_m \text{Im}(\alpha_m \alpha_c^*) - 2\omega g_e \text{Im}(\alpha_e \alpha_c^*) \quad (\text{B.37})$$

with $g_e = \frac{k^3}{6\pi\varepsilon\varepsilon_0}$ and $g_m = \frac{k^3}{6\pi\mu\mu_0}$.

Appendix C

Fiber Green's tensor

The classical electromagnetic Green's tensor of our system can be found from the vector Helmholtz equation:

$$\left[-\frac{\omega^2}{c^2} \boldsymbol{\varepsilon}(\mathbf{r}, \omega) + \nabla \times \nabla \times \right] \mathbf{G}(\mathbf{r}, \mathbf{r}', \omega) = \mathbf{I} \delta(\mathbf{r} - \mathbf{r}'), \quad (\text{C.1})$$

where $\boldsymbol{\varepsilon}(\mathbf{r}, \omega)$ is the complex dielectric function and \mathbf{I} is the unit dyad. In our case, we consider a dielectric cylindrical waveguide of radius ρ_c and dielectric permittivity ε being constant inside the cylinder. To find the solution we apply the scattering superposition method [352; 353], which allows to expand the Green's tensor into the homogeneous and inhomogeneous terms:

$$\mathbf{G}(\mathbf{r}, \mathbf{r}', \omega) = \mathbf{G}_0(\mathbf{r}, \mathbf{r}', \omega) + \mathbf{G}_s(\mathbf{r}, \mathbf{r}', \omega). \quad (\text{C.2})$$

As soon as we consider dielectric particles in the vicinity of the waveguide, so that \mathbf{r}, \mathbf{r}' are outside the cylinder, the homogeneous term is always present and describes the field directly generated at the field point \mathbf{r} by the source placed at the point \mathbf{r}' . This term can be obtained analytically from the Green tensor written in cartesian coordinates using the transformation from cartesian to cylindrical coordinates $\mathbf{S}(\varphi) \mathbf{G}_0^{Cart}(\mathbf{r}, \mathbf{r}', \omega) \mathbf{S}^T(\varphi')$, where \mathbf{G}_0^{Cart} has an analytic expression [354] and is given by

$$\mathbf{G}_0^{Cart}(\mathbf{r}, \mathbf{r}', \omega) = \left(\mathbf{I} + \frac{1}{k^2} \nabla \otimes \nabla \right) G_0(\mathbf{r}, \mathbf{r}', \omega), \quad (\text{C.3})$$

here $G_0(\mathbf{r}, \mathbf{r}', \omega) = e^{ik|\mathbf{r}-\mathbf{r}'|}/4\pi|\mathbf{r}-\mathbf{r}'|$ is the Green's function of the scalar Helmholtz equation.

The scattering term can be calculated via the integral representation of the homogeneous part. To obtain this representation we apply the method of vectorial wave function (VWF) explained in details in Ref. [352; 353], here we cover only the basic ideas and provide the final expressions. To find the solution of the vector Helmholtz equation (C.1) we introduce the scalar Helmholtz equation and the

solution of this equation in the cylindrical coordinates:

$$\begin{aligned}\nabla^2 \varphi(\mathbf{k}, \mathbf{r}) + k^2 \varphi(\mathbf{k}, \mathbf{r}) &= 0, \\ \varphi_n(k_z, \mathbf{r}) &= J_n(k_\rho \rho) e^{in\varphi + ik_z z},\end{aligned}\quad (\text{C.4})$$

here $J_n(x)$ is the Bessel function of the first kind, $\mathbf{r} = (\rho, \varphi, z)$ are the cylindrical coordinates and k_ρ, k_z are the projections of the wavevector \mathbf{k} . The solution of the vector Helmholtz equation may be written in terms of the following vector wavefunctions:

$$\begin{aligned}\mathbf{M}_n(k_z, \mathbf{r}) &= \nabla \times [\varphi_n(k_z, \mathbf{r}) \mathbf{e}_z] \\ \mathbf{N}_n(k_z, \mathbf{r}) &= \frac{1}{k} \nabla \times \mathbf{M}_n(k_z, \mathbf{r})\end{aligned}\quad (\text{C.5})$$

where \mathbf{e}_z is the so-called pilot vector, the unit vector pointing in the z direction. These VWFs $\mathbf{M}_n(k_z, \mathbf{r}), \mathbf{N}_n(k_z, \mathbf{r})$ correspond to TE/TM modes of the field.

One can show [352] that the homogeneous part of the Green's function can be expanded in terms of these vector wavefunction in the following way:

$$\mathbf{G}_0(\mathbf{r}, \mathbf{r}', \omega) = -\frac{\mathbf{e}_\rho \mathbf{e}_\rho}{k_0^2} \delta(\mathbf{r} - \mathbf{r}') + \frac{i}{8\pi} \sum_{n=-\infty}^{\infty} \int_{-\infty}^{\infty} \frac{dk_z}{k_{0\rho}^2} \mathbf{F}_n(k_z, \mathbf{r}, \mathbf{r}') \quad (\text{C.6})$$

and the $\mathbf{F}_n(k_z, \mathbf{r}, \mathbf{s})$ function is given by

$$\begin{cases} \mathbf{M}_n^{(1)}(k_z, \mathbf{r}) \overline{\mathbf{M}}_n(k_z, \mathbf{r}') + \mathbf{N}_n^{(1)}(k_z, \mathbf{r}) \overline{\mathbf{N}}_n(k_z, \mathbf{r}') \\ \mathbf{M}_n(k_z, \mathbf{r}) \overline{\mathbf{M}}_n^{(1)}(k_z, \mathbf{r}') + \mathbf{N}_n(k_z, \mathbf{r}) \overline{\mathbf{N}}_n^{(1)}(k_z, \mathbf{r}') \end{cases} \quad (\text{C.7})$$

here the first line holds for $\rho_r > \rho_{r'}$ while the second one for $\rho_r < \rho_{r'}$, and $k_0 = \omega/c$, $k_{0\rho} = \sqrt{k_0^2 - k_z^2}$ and the superscript (1) in vector wave functions denotes that the Bessel function of the first kind $J_n(k_\rho \rho)$ should be replaced with the Hankel function

of the first kind $H_n^{(1)}(k_\rho \rho)$. Here we provide the explicit form of VWF:

$$\mathbf{M}_n(k_z, \mathbf{r}) = \begin{pmatrix} \frac{in}{\rho} J_n(k_{0\rho} \rho) \\ -k_{0\rho} (J_n(k_{0\rho} \rho))' \\ 0 \end{pmatrix} e^{in\varphi + ik_z z}, \quad (\text{C.8})$$

$$\mathbf{N}_n(k_z, \mathbf{r}) = \begin{pmatrix} \frac{ik_z k_{0\rho}}{k} (J_n(k_{0\rho} \rho))' \\ -\frac{nk_z}{\rho k} J_n(k_{0\rho} \rho) \\ \frac{k_{0\rho}^2}{k} J_n(k_{0\rho} \rho) \end{pmatrix} e^{in\varphi + ik_z z} \quad (\text{C.9})$$

$$\overline{\mathbf{M}}_n(k_z, \mathbf{r}') = \begin{pmatrix} -\frac{in}{\rho'} J_n(k_{0\rho} \rho') \\ -k_{0\rho} (J_n(k_{0\rho} \rho'))' \\ 0 \end{pmatrix}^T e^{-in\varphi' - ik_z z'}, \quad (\text{C.10})$$

$$\overline{\mathbf{N}}_n(k_z, \mathbf{r}') = \begin{pmatrix} -\frac{ik_z k_{0\rho}}{k} (J_n(k_{0\rho} \rho'))' \\ -\frac{nk_z}{\rho' k} J_n(k_{0\rho} \rho') \\ \frac{k_{0\rho}^2}{k} J_n(k_{0\rho} \rho') \end{pmatrix}^T e^{-in\varphi' - ik_z z'} \quad (\text{C.11})$$

where $J_n(k_\rho \rho)'$ means derivative with respect to the dimensionless argument.

Now having the integral representation of the homogeneous term of the Green's function, we can construct the scattering term in a similar fashion. Let us denote the medium outside the dielectric cylinder as 1 and the medium inside as 2. The particular form of the Green's tensor depends on the position of a source point \mathbf{r}' : whether it is inside or outside the cylinder. As soon as we are interested in a situation, when both source and receiver are outside the cylinder and in the latter we consider only the second case. Thus, the total Green's tensor can be written as:

$$\begin{cases} \mathbf{G}^{11}(\mathbf{r}, \mathbf{r}', \omega) = \mathbf{G}_0^{11}(\mathbf{r}, \mathbf{r}', \omega) + \mathbf{G}_s^{11}(\mathbf{r}, \mathbf{r}', \omega), \\ \mathbf{G}^{21}(\mathbf{r}, \mathbf{r}', \omega) = \mathbf{G}_s^{21}(\mathbf{r}, \mathbf{r}', \omega), \end{cases} \quad (\text{C.12})$$

here two superscripts denote position of the receiver the source point respectively and the two scattering parts of the Green's tensor has the following form:

$$\begin{aligned}
\mathbf{G}_s^{11}(\mathbf{r}, \mathbf{r}', \omega) &= \frac{i}{8\pi} \sum_{n=-\infty}^{\infty} \int_{-\infty}^{\infty} \frac{dk_z}{k_{\rho 1}^2} \mathbf{F}_{\mathbf{M};n,1}^{11(1)}(k_z, \mathbf{r}) \overline{\mathbf{M}}_{n,1}^{(1)}(k_z, \mathbf{r}') \\
&\quad + \mathbf{F}_{\mathbf{N};n,1}^{11(1)}(k_z, \mathbf{r}) \overline{\mathbf{N}}_{n,1}^{(1)}(k_z, \mathbf{r}'), \\
\mathbf{F}_{\mathbf{M};n,1}^{11(1)}(k_z, \mathbf{r}) &= R_{MM}^{11} \mathbf{M}_{n,1}^{(1)}(k_z, \mathbf{r}) + R_{NM}^{11} \mathbf{N}_{n,1}^{(1)}(k_z, \mathbf{r}), \\
\mathbf{F}_{\mathbf{N};n,1}^{11(1)}(k_z, \mathbf{r}) &= R_{MN}^{11} \mathbf{M}_{n,1}^{(1)}(k_z, \mathbf{r}) + R_{NN}^{11} \mathbf{N}_{n,1}^{(1)}(k_z, \mathbf{r}). \tag{C.13}
\end{aligned}$$

$$\begin{aligned}
\mathbf{G}_s^{21}(\mathbf{r}, \mathbf{r}', \omega) &= \frac{i}{8\pi} \sum_{n=-\infty}^{\infty} \int_{-\infty}^{\infty} \frac{dk_z}{k_{\rho 1}^2} \mathbf{F}_{\mathbf{M};n,2}^{21}(k_z, \mathbf{r}) \overline{\mathbf{M}}_{n,1}^{(1)}(k_z, \mathbf{r}') \\
&\quad + \mathbf{F}_{\mathbf{N};n,1}^{21}(k_z, \mathbf{r}) \overline{\mathbf{N}}_{n,1}^{(1)}(k_z, \mathbf{r}'), \\
\mathbf{F}_{\mathbf{M};n,2}^{21}(k_z, \mathbf{r}) &= R_{MM}^{21} \mathbf{M}_{n,2}(k_z, \mathbf{r}) + R_{NM}^{21} \mathbf{N}_{n,2}(k_z, \mathbf{r}), \\
\mathbf{F}_{\mathbf{N};n,2}^{21}(k_z, \mathbf{r}) &= R_{MN}^{21} \mathbf{M}_{n,2}(k_z, \mathbf{r}) + R_{NN}^{21} \mathbf{N}_{n,2}(k_z, \mathbf{r}), \tag{C.14}
\end{aligned}$$

here the scattering Fresnel coefficients R_{AB}^{ij} are introduced and the second subscript in the VWFs denotes that k and k_{ρ} should be replaced with their values inside the corresponding media $k_i = \sqrt{\varepsilon_i(\mathbf{r}, \omega)} k_0$, $k_{\rho i} = \sqrt{k_i^2 - k_z^2}$ and also $k_{0\rho}$ becomes $k_{\rho i}$. We should notice that unlike the case of the homogeneous term, here we have products of \mathbf{M} and \mathbf{N} , which is due to the fact that the normal modes in our case have hybrid nature.

The form of the Fresnel coefficients mentioned above can be found by imposing the boundary conditions on the Green's tensor at the surface of the cylinder

$$\begin{cases} \mathbf{e}_{\rho} \times [\mathbf{G}^{11}(\mathbf{r}, \mathbf{r}', \omega) - \mathbf{G}^{21}(\mathbf{r}, \mathbf{r}', \omega)]|_{\rho_r=\rho_c} = 0, \\ \mathbf{e}_{\rho} \times \nabla_{\mathbf{r}} \times [\mathbf{G}^{11}(\mathbf{r}, \mathbf{r}', \omega) - \mathbf{G}^{21}(\mathbf{r}, \mathbf{r}', \omega)]|_{\rho_r=\rho_c} = 0. \end{cases} \tag{C.15}$$

Solving for this, we can find the Fresnel coefficients R_{AB}^{ij} and, finally, construct the scattering part of the Green's tensor $\mathbf{G}_s(\mathbf{r}, \mathbf{r}', \omega)$. We provide the explicit expressions

for the Fresnel coefficients below:

$$\begin{aligned}
DT(k_z) &= -\left(\frac{1}{k_{\rho 2}^2} - \frac{1}{k_{\rho 1}^2}\right)^2 k_z^2 n^2 + \left(\frac{(J_n(k_{\rho 2}\rho_c))'}{k_{\rho 2}J_n(k_{\rho 2}\rho_c)} - \frac{(H_n^{(1)}(k_{\rho 1}\rho_c))'}{k_{\rho 1}H_n^{(1)}(k_{\rho 1}\rho_c)}\right) \times \\
&\quad \left(\frac{(J_n(k_{\rho 2}\rho_c))'k_2^2}{k_{\rho 2}J_n(k_{\rho 2}\rho_c)} - \frac{(H_n^{(1)}(k_{\rho 1}\rho_c))'k_1^2}{k_{\rho 1}H_n^{(1)}(k_{\rho 1}\rho_c)}\right) \rho_c^2 \\
R_{MM}^{11}(k_z) &= \frac{J_n(k_{\rho 1}\rho_c)}{H_n^{(1)}(k_{\rho 1}\rho_c)} \left[\left(\frac{1}{k_{\rho 2}^2} - \frac{1}{k_{\rho 1}^2}\right)^2 k_z^2 n^2 - \left(\frac{(J_n(k_{\rho 2}\rho_c))'}{k_{\rho 2}J_n(k_{\rho 2}\rho_c)} - \frac{(J_n(k_{\rho 1}\rho_c))'}{k_{\rho 1}J_n(k_{\rho 1}\rho_c)}\right) \times \right. \\
&\quad \left. \left(\frac{(J_n(k_{\rho 2}\rho_c))'k_2^2}{k_{\rho 2}J_n(k_{\rho 2}\rho_c)} - \frac{(H_n^{(1)}(k_{\rho 1}\rho_c))'k_1^2}{k_{\rho 1}H_n^{(1)}(k_{\rho 1}\rho_c)}\right) \rho_c^2 \right] \frac{1}{DT(k_z)} \\
R_{NM}^{11}(k_z) &= \frac{J_n(k_{\rho 1}\rho_c)}{H_n^{(1)}(k_{\rho 1}\rho_c)} \frac{1}{k_{\rho 1}} \left(\frac{1}{k_{\rho 1}^2} - \frac{1}{k_{\rho 2}^2}\right) \left(\frac{(J_n(k_{\rho 1}\rho_c))'}{J_n(k_{\rho 1}\rho_c)} - \frac{(H_n^{(1)}(k_{\rho 1}\rho_c))'}{H_n^{(1)}(k_{\rho 1}\rho_c)}\right) \frac{k_1 k_z n \rho_c}{DT(k_z)} \\
R_{MN}^{11}(k_z) &= R_{NM}^{11}(k_z) \\
R_{NN}^{11}(k_z) &= \frac{J_n(k_{\rho 1}\rho_c)}{H_n^{(1)}(k_{\rho 1}\rho_c)} \left[\left(\frac{1}{k_{\rho 2}^2} - \frac{1}{k_{\rho 1}^2}\right)^2 k_z^2 n^2 - \left(\frac{(J_n(k_{\rho 2}\rho_c))'}{k_{\rho 2}J_n(k_{\rho 2}\rho_c)} - \frac{(H_n^{(1)}(k_{\rho 1}\rho_c))'}{k_{\rho 1}H_n^{(1)}(k_{\rho 1}\rho_c)}\right) \times \right. \\
&\quad \left. \left(\frac{(J_n(k_{\rho 2}\rho_c))'k_2^2}{k_{\rho 2}J_n(k_{\rho 2}\rho_c)} - \frac{(J_n(k_{\rho 1}\rho_c))'k_1^2}{k_{\rho 1}J_n(k_{\rho 1}\rho_c)}\right) \rho_c^2 \right] \frac{1}{DT(k_z)} \tag{C.16}
\end{aligned}$$

Appendix D

Effective polarizability. General case

The effective polarizability of a nanoparticle placed in the vicinity of a nanofiber waveguide and accounted for the interaction with another particle can be expressed as follows:

$$\hat{\boldsymbol{\alpha}}_{\text{eff}}^{(i)} = \left[\hat{\mathbf{I}} - \left(\frac{k^2}{\varepsilon_0} \right)^2 \hat{\boldsymbol{\alpha}}_s^{(i)} \hat{\mathbf{G}}^{ij} \hat{\boldsymbol{\alpha}}_s^{(j)} \hat{\mathbf{G}}^{ji} \right]^{-1} \hat{\boldsymbol{\alpha}}_s^{(i)} \left(\hat{\mathbf{I}} + \frac{k^2}{\varepsilon_0} \hat{\mathbf{G}}^{ij} \hat{\boldsymbol{\alpha}}_s^{(j)} \right), \quad (\text{D.1})$$

where $i = 1, 2$ and $j = 1 \cdot \delta_{i2} + 2 \cdot \delta_{i1}$, $\hat{\mathbf{G}} = \hat{\mathbf{G}}_0 + \hat{\mathbf{G}}_s$ and

$$\hat{\boldsymbol{\alpha}}_s^{(j)} = \alpha_0 \left(\hat{\mathbf{I}} - \alpha_0 \frac{k^2}{\varepsilon_0} \hat{\mathbf{G}}_s^{jj} \right)^{-1}. \quad (\text{D.2})$$

Here we consider the polarizability for the case when $\mathbf{E}_0(\mathbf{r}_1) \neq \mathbf{E}_0(\mathbf{r}_2)$. Hence, it follows that it is impossible to factor out the external field \mathbf{E}_0 to obtain an expression as $\mathbf{p} = \hat{\boldsymbol{\alpha}}_{\text{eff}} \mathbf{E}_0$. Yet we can still introduce the effective polarizability tensor if we convert it into an operator by introducing a *shifting operator*. The obtained operator of the effective polarizability will have a form:

$$\hat{\boldsymbol{\alpha}}_{\text{eff}}^{(i)} = \left[\hat{\mathbf{I}} - \left(\frac{k^2}{\varepsilon_0} \right)^2 \hat{\boldsymbol{\alpha}}_s^{(i)} \hat{\mathbf{G}}^{ij} \hat{\boldsymbol{\alpha}}_s^{(j)} \hat{\mathbf{G}}^{ji} \right]^{-1} \hat{\boldsymbol{\alpha}}_s^{(i)} \left(\hat{\mathbf{I}} + \frac{k^2}{\varepsilon_0} \hat{\mathbf{G}}^{ij} \hat{\boldsymbol{\alpha}}_s^{(j)} e^{(\mathbf{r}_i - \mathbf{r}_j) \cdot \nabla} \right), \quad (\text{D.3})$$

where $i = 1, 2$ and $j = 1 \cdot \delta_{i2} + 2 \cdot \delta_{i1}$, $\hat{\mathbf{G}} = \hat{\mathbf{G}}_0 + \hat{\mathbf{G}}_s$, $e^{(\mathbf{r}_2 - \mathbf{r}_1) \cdot \nabla}$ is the shifting operator. Using (D.3) we can calculate the dipole moment in a straightforward way as

$$\mathbf{p}_i = \hat{\boldsymbol{\alpha}}_{\text{eff}}^{(i)} \mathbf{E}(\mathbf{r}_i). \quad (\text{D.4})$$

We also need to note, that this expression is a generalization of what was used in this paper, as we considered that all the particles are placed in the same external field $\mathbf{E}_0(\mathbf{r}_1) = \mathbf{E}_0(\mathbf{r}_2)$.

Appendix E

Canonical properties for complex frequency domain

E.1 Mean of an arbitrary quadratic form

Let us have two monochromatic real functions $\mathcal{A}(t)$ and $\mathcal{B}(t)$ defined through its complex amplitudes A and B as $\mathcal{A}(t) = \text{Re} [Ae^{-i\omega t}]$ and $\mathcal{B}(t) = \text{Re} [Be^{-i\omega t}]$. We let frequency be complex-valued, so $\omega = \omega' + i\omega''$. Now we find the time-average value of its product

$$\langle \mathcal{A}\mathcal{B} \rangle_{\text{fast time}} = \frac{1}{2} \text{Re} [A^* B] e^{2\omega'' t} + O(\varepsilon) \quad (\text{E.1})$$

For the next calculations we denote observable electric and magnetic fields as

$$\mathcal{E}(t) = \text{Re} [\mathbf{E}e^{-i\omega t}], \quad \mathcal{H}(t) = \text{Re} [\mathbf{H}e^{-i\omega t}] \quad (\text{E.2})$$

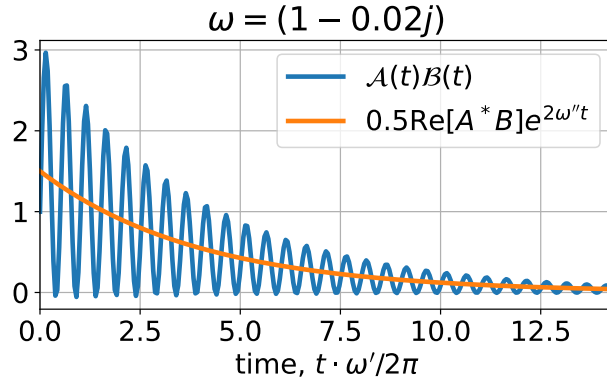


Figure E.1 — An example of real and mean values of a product of two monochromatic functions with complex frequency

E.2 Poynting vector

The mean value of Poynting vector is going to be

$$\langle \mathbf{\Pi} \rangle = \langle \mathcal{E} \times \mathcal{H} \rangle = \frac{1}{2} \text{Re} [\mathbf{E}^* \times \mathbf{H}] e^{2\omega'' t} \quad (\text{E.3})$$

E.3 Canonical spin angular momenta density

Using expression from the field theory, the SAM density (its electric part) can be written through the vector potential \mathcal{A} as $\mathcal{S}^{(\text{el})} = \mathcal{E} \times \mathcal{A}$ [168; 355]. The mean value is going to be

$$\begin{aligned} \mathbf{S} &= \langle \mathcal{S}^{(\text{el})} \rangle = \frac{1}{2} \text{Re} [\mathbf{E}^* \times \mathbf{A}] e^{2\omega''t} = \frac{1}{2} \text{Re} \left[\mathbf{E}^* \times \frac{-i}{\omega} \mathbf{E} \right] e^{2\omega''t} \\ &\approx \frac{1}{2\omega'} \text{Im} [\mathbf{E}^* \times \mathbf{E}] e^{2\omega''t} + O(\varepsilon^2), \end{aligned} \quad (\text{E.4})$$

here we have used $1/\omega \approx \frac{1}{\omega'}(1 - i\varepsilon) + O(\varepsilon^2)$ and the fact that $\text{Re}[\mathbf{E}^* \times \mathbf{E}] = 0$. Here $\varepsilon = \frac{\omega''}{\omega'}$.

E.4 Canonical linear momentum density

Using the same approach we have

$$\begin{aligned} \mathbf{P}^{(\text{el})} &= \langle \mathcal{P}^{(\text{el})} \rangle = \frac{1}{2} \text{Re} [\mathbf{E} \cdot (\nabla) \mathbf{A}^*] e^{2\omega''t} = \frac{1}{2} \text{Re} \left[\mathbf{E}^* \cdot (\nabla) \frac{-i}{\omega} \mathbf{E} \right] e^{2\omega''t} \\ &\approx \frac{1}{2\omega'} \text{Im} [\mathbf{E}^* \cdot (\nabla) \mathbf{E}] e^{2\omega''t} - \varepsilon \cdot \frac{1}{2\omega'} \text{Re} [\mathbf{E}^* \cdot (\nabla) \mathbf{E}] e^{2\omega''t} + O(\varepsilon^2) \end{aligned} \quad (\text{E.5})$$

E.5 Energy density

Electromagnetic energy density gains just an exponent factor

$$W = \langle \mathcal{W} \rangle = \frac{1}{4} (|\mathbf{E}|^2 + |\mathbf{H}|^2) e^{2\omega''t} \quad (\text{E.6})$$

Appendix F

Photon wave function

It is possible to rewrite Maxwell equations as

$$\underbrace{\begin{pmatrix} & i\nabla\times \\ -i\nabla\times & \end{pmatrix}}_{\hat{\mathbf{N}}}\underbrace{\begin{pmatrix} \mathbf{E} \\ \mathbf{H} \end{pmatrix}}_{\mathbf{f}} = i\partial_t \underbrace{\begin{pmatrix} \epsilon\epsilon_0 & \\ & \mu\mu_0 \end{pmatrix}}_{\hat{\mathbf{M}}}\begin{pmatrix} \mathbf{E} \\ \mathbf{H} \end{pmatrix} \quad (\text{F.1})$$

or

$$\hat{\mathbf{H}}\mathbf{f} = i\partial_t\mathbf{f} \quad (\text{F.2})$$

where

$$\hat{\mathbf{H}} = \hat{\mathbf{M}}^{-1}\hat{\mathbf{N}} \quad (\text{F.3})$$

Operator $\hat{\mathbf{H}}$ is hermitian for the scalar product defined as

$$(\mathbf{f}_1, \mathbf{f}_2) \equiv \int d^3\mathbf{r}\mathbf{f}_1^\dagger\hat{\mathbf{M}}\mathbf{f}_2 \quad (\text{F.4})$$

so

$$(\mathbf{f}_1, \hat{\mathbf{H}}\mathbf{f}_2) = (\hat{\mathbf{H}}\mathbf{f}_1, \mathbf{f}_2) \quad (\text{F.5})$$

It is possible to redefine the wave function as

$$\psi = \sqrt{\frac{1}{4\omega}}\hat{\mathbf{M}}^{-\frac{1}{2}}\begin{pmatrix} \mathbf{E} \\ \mathbf{H} \end{pmatrix} \quad (\text{F.6})$$

And after all the quantum mechanics formalism will work as expected.

Appendix G

Mie coefficients and dispersion equations

To find the dispersion equations we need to apply boundary conditions, namely $(\mathbf{E}^{\text{in}} - \mathbf{E}^{\text{out}}) \times \hat{\mathbf{e}}_r$ and $(\mathbf{H}^{\text{in}} - \mathbf{H}^{\text{out}}) \times \hat{\mathbf{e}}_r$ at the boundary $r = a$ for all ϑ and φ . Technically it is sufficient to consider only ϑ -components of the fields, i.e. for TE mode

$$\begin{cases} A^{\text{TE}} M_{\vartheta}^{\text{in}} \Big|_{r=a} = B^{\text{TE}} M_{\vartheta}^{\text{out}} \Big|_{r=a} \\ -i \sqrt{\frac{\epsilon_{\text{in}} \epsilon_0}{\mu_{\text{in}} \mu_0}} A^{\text{TE}} N_{\vartheta}^{\text{in}} \Big|_{r=a} = -i \sqrt{\frac{\epsilon_{\text{out}} \epsilon_0}{\mu_{\text{out}} \mu_0}} B^{\text{TE}} N_{\vartheta}^{\text{out}} \Big|_{r=a} \end{cases} \quad (\text{G.1})$$

Here superscript “in” shows that $z_j \rightarrow j_j(n_{\text{in}} k_0 r)$ and “out” shows that $z_j \rightarrow h_j^{(1)}(n_{\text{out}} k_0 r)$. System (G.1) can be written as $[\cdot \cdot] \begin{bmatrix} A^{\text{TE}} \\ B^{\text{TE}} \end{bmatrix} = 0$ which gives us the dispersion equation as $\det [\cdot \cdot] = 0$. In a similar way one can perform this procedure for the TM modes. The final answer is

$$\text{dispersion eq. for TE:} \quad \frac{\mu_{\text{in}}}{\mu_{\text{out}}} \left(1 + n_{\text{out}} z \frac{h_j^{(1)'}(n_{\text{out}} z)}{h_j^{(1)}(n_{\text{out}} z)} \right) = 1 + n_{\text{in}} z \frac{j_j'(n_{\text{in}} z)}{j_j(n_{\text{in}} z)} \quad (\text{G.2})$$

$$\text{dispersion eq. for TM:} \quad \frac{\epsilon_{\text{in}}}{\epsilon_{\text{out}}} \left(1 + n_{\text{out}} z \frac{h_j^{(1)'}(n_{\text{out}} z)}{h_j^{(1)}(n_{\text{out}} z)} \right) = 1 + n_{\text{in}} z \frac{j_j'(n_{\text{in}} z)}{j_j(n_{\text{in}} z)} \quad (\text{G.3})$$

Here $z = k_0 a = \frac{\omega}{c} a \in \mathbb{Z}$ is the dimensionless complex frequency. For $\mu_{\text{out}} = \mu_{\text{in}} = 1$ is in consistency with [252]. We note that the zeros of denominator of Mie coefficients a_n and b_n are exactly zeros of the dispersion equations for TM (G.3) and TE modes (G.2), respectively (see Appendix G). Also, we do not include extra zeros which may appear on the real axis, i.e. with $\text{Im } z_n = 0$. The most robust way to search for the roots is to look at the poles of the Mie scattering coefficients [356–358].

Importantly, we find the relative values of the constants to be

$$A^{\text{TE}}/B^{\text{TE}} = \frac{h_j^{(1)}(n_{\text{out}} k_0 a)}{j_j(n_{\text{in}} k_0 a)} \quad (\text{G.4})$$

and

$$A^{\text{TM}}/B^{\text{TM}} = \sqrt{\frac{\epsilon_{\text{out}} \mu_{\text{in}}}{\epsilon_{\text{in}} \mu_{\text{out}}}} \frac{h_j^{(1)}(n_{\text{out}} k_0 a)}{j_j(n_{\text{in}} k_0 a)} \quad (\text{G.5})$$

which ensures the correct radial dependence.

The Mie coefficients for the sphere with ε_p and μ_p in the host media with ε and μ are given as [172]

$$a_j = \frac{\mu m^2 j_j(mx) [x j_j(x)]' - \mu_p j_j(x) [m x j_j(mx)]'}{\mu m^2 j_j(mx) [x h_j^{(1)}(x)]' - \mu_p h_j^{(1)}(x) [m x j_j(mx)]'}, \quad (\text{G.6})$$

$$b_j = \frac{\mu_p j_j(mx) [x j_j(x)]' - \mu j_j(x) [m x j_j(mx)]'}{\mu_p j_j(mx) [x h_j^{(1)}(x)]' - \mu h_j^{(1)}(x) [m x j_j(mx)]'} \quad (\text{G.7})$$

Here, $x = nk_0 r$ is the normalized particle radius; $k_0 = \omega/c$ is the wave vector in vacuum, with ω being the angular frequency and c being light velocity in vacuum; $m = n_p/n = \sqrt{\varepsilon_p \mu_p} / \sqrt{\varepsilon \mu}$ is the relative refractive index of the particle. j_j and $h_j^{(1)}$ are the spherical Bessel and Hankel functions of order j (which is an integer from 1 to infinite). The derivations are performed with respect to the argument, e.g., $j_j(nx)' \equiv d[j_j(nx)] / d(nx)$.

We note that the roots of denominators of a_j and b_j are exactly the roots of (G.3) and (G.2) correspondingly:

$$\text{den}[a_j] = 0 \quad \longleftrightarrow \quad \text{Dispersion Eq. (G.3) for TM mode} \quad (\text{G.8})$$

$$\text{den}[b_j] = 0 \quad \longleftrightarrow \quad \text{Dispersion Eq. (G.2) for TE mode} \quad (\text{G.9})$$

Appendix H

Derivation of Optical force from Maxwell stress tensor

We follow the work [142] by Chaumet, Patrick C. and Rahmani, Adel. However, here we write a more detailed derivation. We consider only electric and magnetic dipoles in vacuum with $\varepsilon = \mu = 1$.

Force is given by (cgs units)

$$\mathbf{F} = \text{Re} r^2 \int_{4\pi} d\Omega \frac{1}{8\pi} \underbrace{\left\{ (\mathbf{E} \cdot \mathbf{n})\mathbf{E}^* + (\mathbf{H} \cdot \mathbf{n})\mathbf{H}^* - \mathbf{n} \frac{1}{2} (|\mathbf{E}|^2 + |\mathbf{H}|^2) \right\}}_{\hat{\mathcal{T}} \cdot \mathbf{n}} \quad (\text{H.1})$$

Maxwell stress tensor can be decomposed using

$$\mathbf{E}(\mathbf{r}) = \mathbf{E}_0(\mathbf{r}) + \mathbf{E}_d(\mathbf{r}), \quad \mathbf{H}(\mathbf{r}) = \mathbf{H}_0(\mathbf{r}) + \mathbf{H}_d(\mathbf{r}). \quad (\text{H.2})$$

Thus

$$\hat{\mathcal{T}} = \underbrace{\hat{\mathcal{T}}_0}_{\sim E_0^2, \text{ no contribution}} + \underbrace{\hat{\mathcal{T}}_{\text{mix}}}_{\sim E_0 E_d, \text{ gives } \mathbf{F}_{\text{mix}}} + \underbrace{\hat{\mathcal{T}}_{\text{self}}}_{\sim E_d^2, \text{ gives } \mathbf{F}_{\text{self}}} \quad (\text{H.3})$$

Where

$$\mathbf{F} = \mathbf{F}_{\text{mix}} + \mathbf{F}_{\text{self}} = \frac{1}{2} \text{Re} [p_i^* \nabla E_{0i} + m_i^* \nabla H_{0i}] - \frac{k^4}{3} \text{Re} [\mathbf{p} \times \mathbf{m}^*] \quad (\text{H.4})$$

H.1 Helpful identities

The electric and magnetic fields from electric and magnetic dipoles in free space are

$$\mathbf{E}_d = e^{ikr} \left[(3\mathbf{n}(\mathbf{n} \cdot \mathbf{p}) - \mathbf{p}) \left(\frac{1}{r^3} - \frac{ik}{r^2} \right) + \frac{k^2}{r} (\mathbf{n} \times \mathbf{p}) \times \mathbf{n} - k^2 (\mathbf{n} \times \mathbf{m}) \left(\frac{1}{r} + \frac{i}{kr^2} \right) \right] \quad (\text{H.5})$$

$$\mathbf{H}_d = e^{ikr} \left[(3\mathbf{n}(\mathbf{n} \cdot \mathbf{m}) - \mathbf{m}) \left(\frac{1}{r^3} - \frac{ik}{r^2} \right) + \frac{k^2}{r} (\mathbf{n} \times \mathbf{m}) \times \mathbf{n} + k^2 (\mathbf{n} \times \mathbf{p}) \left(\frac{1}{r} + \frac{i}{kr^2} \right) \right] \quad (\text{H.6})$$

with $\mathbf{n} = \mathbf{r}/r$.

Integrals with different number of \mathbf{n} :

$$\int_{4\pi} d\Omega n_i = 0, \quad \int_{4\pi} d\Omega n_i n_j n_k = 0, \quad \int_{4\pi} d\Omega (\text{odd number of } \mathbf{n}) = 0, \quad (\text{H.7})$$

$$\int_{4\pi} d\Omega n_i n_j = \frac{4\pi}{3} \delta_{ij}, \quad \int_{4\pi} d\Omega n_i n_j n_k n_\ell = \frac{4\pi}{15} (\delta_{ij} \delta_{kl} + \delta_{ik} \delta_{j\ell} + \delta_{i\ell} \delta_{jk}), \quad (\text{H.8})$$

where $i, j, k, \ell = x, y, z$, $\mathbf{n} = (\sin \vartheta \cos \varphi, \sin \vartheta \sin \varphi, \cos \vartheta)^T$, and $\int_{4\pi} d\Omega = \int_0^\pi d\vartheta \sin \vartheta \int_0^{2\pi} d\varphi$.

For two Levi-Civita symbols we have

$$\varepsilon_{ijk} \varepsilon_{imn} = \delta_{jm} \delta_{kn} - \delta_{jn} \delta_{km}. \quad (\text{H.9})$$

In the free space without charges we have

$$\nabla \cdot \mathbf{E}_0 = 0 \quad (\text{H.10})$$

Also helpful will be

$$\nabla \times \mathbf{E} = ik\mathbf{H} \quad (\text{H.11})$$

H.2 Calculating \mathbf{F}_{mix}

From (H.1) for cross terms we have

$$\mathbf{F}_{\text{mix}} = \frac{1}{8\pi} \text{Re} r^2 \int_{4\pi} d\Omega \left\{ (\mathbf{E}_d \cdot \mathbf{n}) \mathbf{E}_0^* + (\mathbf{E}_0^* \cdot \mathbf{n}) \mathbf{E}_d + (\mathbf{H}_d \cdot \mathbf{n}) \mathbf{H}_0^* + (\mathbf{H}_0^* \cdot \mathbf{n}) \mathbf{H}_d - \mathbf{n} [(\mathbf{E}_d \cdot \mathbf{E}_0^*) + (\mathbf{H}_d \cdot \mathbf{H}_0^*)] \right\} \quad (\text{H.12})$$

The next important step is to take this integral in the **near field (NF)**. Suppose we have only electric dipole \mathbf{p} then

$$\begin{cases} \mathbf{E}_0(\mathbf{r}) \approx \mathbf{E}_0 + r(\mathbf{n} \cdot \nabla) \mathbf{E}_0, \\ \mathbf{H}_0(\mathbf{r}) \approx \mathbf{H}_0 + r(\mathbf{n} \cdot \nabla) \mathbf{H}_0, \end{cases} \quad \begin{cases} \mathbf{E}_d \stackrel{\text{NF}}{=} \frac{3\mathbf{n}(\mathbf{n} \cdot \mathbf{p}) - \mathbf{p}}{r^3}, \\ \mathbf{H}_d \stackrel{\text{NF}}{=} i \frac{k}{r^2} \mathbf{n} \times \mathbf{p} \end{cases} \quad (\text{H.13})$$

We consider different terms separately

$$r^2 \int_{4\pi} d\Omega (\mathbf{E}_d \cdot \mathbf{n}) \mathbf{E}_0^* \stackrel{(\text{H.7}) \text{ and } (\text{H.13})}{=} \int_{4\pi} d\Omega 2(\mathbf{n} \cdot \mathbf{p})(\mathbf{n} \cdot \nabla) \mathbf{E}_0^* \stackrel{(\text{H.8})}{=} \frac{8\pi}{3} (\mathbf{p} \cdot \nabla) \mathbf{E}_0^* \quad (\text{H.14})$$

$$\begin{aligned} r^2 \int_{4\pi} d\Omega (\mathbf{E}_0^* \cdot \mathbf{n}) \mathbf{E}_d &\stackrel{(\text{H.13})}{=} r^2 \int_{4\pi} d\Omega [\mathbf{E}_0^* + r(\mathbf{n} \cdot \nabla)(\mathbf{E}_0^* \cdot \mathbf{n})] \frac{3\mathbf{n}(\mathbf{n} \cdot \mathbf{p}) - \mathbf{p}}{r^3} \\ &\stackrel{(\text{H.7})}{=} \int_{4\pi} d\Omega [3(\mathbf{n} \cdot \nabla)(\mathbf{E}_0^* \cdot \mathbf{n})(\mathbf{n} \cdot \mathbf{p})\mathbf{n} - (\mathbf{n} \cdot \nabla)(\mathbf{E}_0^* \cdot \mathbf{n})\mathbf{p}] \\ &\stackrel{(\text{H.8}) \text{ and } (\text{H.10})}{=} \frac{4\pi}{5} (\mathbf{p} \cdot \nabla) \mathbf{E}_0^* + \frac{4\pi}{5} p_j \nabla E_{0j} \end{aligned} \quad (\text{H.15})$$

$$-r^2 \int_{4\pi} d\Omega (\mathbf{E}_d \cdot \mathbf{E}_0) \mathbf{n} = -\frac{4\pi}{5} p_j \nabla E_{0j}^* - \frac{4\pi}{5} (\mathbf{p} \cdot \nabla) \mathbf{E}_0^* + \frac{4\pi}{3} p_j \nabla E_{0j}^* \quad (\text{H.16})$$

$$-r^2 \int_{4\pi} d\Omega (\mathbf{H}_d \cdot \mathbf{H}_0^*) \mathbf{n} = ik \frac{4\pi}{3} \varepsilon_{\ell ik} H_{0i}^* p_k \stackrel{(\text{H.11}) \text{ and } (\text{H.9})}{=} \frac{4\pi}{3} p_j \nabla E_{0j}^* - \frac{4\pi}{3} (\mathbf{p} \cdot \nabla) \mathbf{E}_0^* \quad (\text{H.17})$$

$$r^2 \int_{4\pi} d\Omega (\mathbf{H}_0^* \cdot \mathbf{n}) \mathbf{H}_d = ik \frac{4\pi}{3} \varepsilon_{\ell ik} H_{0i}^* p_k \stackrel{(\text{H.11}) \text{ and } (\text{H.9})}{=} \frac{4\pi}{3} p_j \nabla E_{0j}^* - \frac{4\pi}{3} (\mathbf{p} \cdot \nabla) \mathbf{E}_0^* \quad (\text{H.18})$$

Other terms does not contribute to the electric dipole force. After summing everything up we have

$$\mathbf{F}_{\text{mix}}^{(\text{el})} = \frac{1}{2} \text{Re} [p_j \nabla E_{0j}^*] \quad (\text{H.19})$$

Analogously, we can get force on the magnetic dipole m so

$$\mathbf{F}_{\text{mix}} = \frac{1}{2} \text{Re} [p_j \nabla E_{0j}^* + m_j \nabla H_{0j}^*]. \quad (\text{H.20})$$

H.3 Calculating \mathbf{F}_{self}

From (H.1) for self-action terms only we have

$$\mathbf{F}_{\text{self}} = \frac{1}{8\pi} \text{Re} r^2 \int_{4\pi} d\Omega \left\{ \underbrace{(\mathbf{E}_d \cdot \mathbf{E}_d^*) + (\mathbf{H}_d \cdot \mathbf{H}_d^*)}_{\text{does not contribute (e.g. consider NF using (H.7))}} - \mathbf{n} \frac{1}{2} (|\mathbf{E}_d|^2 + |\mathbf{H}_d|^2) \right\} \quad (\text{H.21})$$

$$= -\frac{1}{16\pi} \text{Re} r^2 \int_{4\pi} d\Omega (|\mathbf{E}_d|^2 + |\mathbf{H}_d|^2) \mathbf{n} \quad (\text{H.22})$$

We will integrate this in the **far field (FF)**, then for \mathbf{p} and \mathbf{m} we have

$$\begin{cases} \mathbf{E}_d \stackrel{\text{FF}}{=} e^{ikr} \frac{k^2}{r} [\mathbf{n} \times \mathbf{p} \times \mathbf{n} - \mathbf{n} \times \mathbf{m}] \\ \mathbf{H}_d \stackrel{\text{FF}}{=} e^{ikr} \frac{k^2}{r} [\mathbf{n} \times \mathbf{m} \times \mathbf{n} + \mathbf{n} \times \mathbf{p}] \end{cases} \quad (\text{H.23})$$

Consider different terms separately

$$\begin{aligned} r^2 \int_{4\pi} d\Omega |\mathbf{H}_d|^2 \mathbf{n} &\stackrel{\text{FF}}{=} k^4 \int_{4\pi} d\Omega (\mathbf{n} \times \mathbf{m} \times \mathbf{n} + \mathbf{n} \times \mathbf{p}) \cdot (\mathbf{n} \times \mathbf{m}^* \times \mathbf{n} + \mathbf{n} \times \mathbf{p}^*) \mathbf{n} \\ &\stackrel{(\text{H.7})}{=} k^4 \int_{4\pi} d\Omega 2 \text{Re} [(\mathbf{n} \times \mathbf{p}) \cdot (\mathbf{n} \times \mathbf{m}^* \times \mathbf{n})] \mathbf{n} \\ &\stackrel{\mathbf{b}(\mathbf{a}\cdot\mathbf{c})-\mathbf{c}(\mathbf{a}\cdot\mathbf{b}) \text{ and } (\text{H.8})}{=} \frac{4\pi}{3} 2k^4 \text{Re} [\mathbf{p} \times \mathbf{m}^*] \end{aligned} \quad (\text{H.24})$$

$$r^2 \int_{4\pi} d\Omega |\mathbf{E}_d|^2 \mathbf{n} = \frac{4\pi}{3} 2k^4 \text{Re} [\mathbf{p} \times \mathbf{m}^*] \quad (\text{H.25})$$

And finally

$$\mathbf{F}_{\text{self}} = -\frac{k^4}{3} \text{Re} [\mathbf{p} \times \mathbf{m}^*] \quad (\text{H.26})$$

The total force in the dipole approximation will be

$$\mathbf{F} = \mathbf{F}_{\text{mix}} + \mathbf{F}_{\text{self}} = \frac{1}{2} \text{Re} [p_i^* \nabla E_{0i} + m_i^* \nabla H_{0i}] - \frac{k^4}{3} \text{Re} [\mathbf{p} \times \mathbf{m}^*] \quad (\text{H.27})$$

This derivation is done for the point electric and magnetic dipoles in vacuum with $\epsilon = \mu = 1$.

Appendix I

Complex Vector Spherical Harmonics

I.1 Explicit form

We define complex vector spherical harmonics in the similar way to the classical Bohren & Huffman book [172]. We stick to the already build-in functions in most popular scientific packages such as SciPy, Wolfram Mathematica, and others. So, the only difference with [172] is the we use spherical functions instead of associated Legendre polynomials, i.e. $\begin{pmatrix} \cos m\varphi \\ \sin m\varphi \end{pmatrix} P_j^m(\cos \varphi) \rightarrow Y_j^m(\vartheta, \varphi)$ which means that there are no even or odd harmonics. The usage of spherical harmonic ensures us the symmetry with $m \rightarrow -m$ with no additional rules. This is similar to the basis change from linear to circular functions.

We start from the solution of the scalar Helmholtz equation which has all the symmetries of the problem. In our case we have spherical symmetry and the scalar function is going to be

$$\psi_{mj}(\rho, \vartheta, \varphi) = z_j(\rho) Y_j^m(\vartheta, \varphi), \quad \rho = kr = \sqrt{\epsilon\mu} \frac{\omega}{c} r \quad (\text{I.1})$$

Here $z_j(\rho) = j_j(\rho), y_n(\rho), h_j^{(1)}(\rho), h_j^{(2)}(\rho)$ is spherical Bessel of the 1st and 2nd kind, spherical Hankel functions of the 1st and 2nd kind, respectively, and $\rho = kr$ with $k = \sqrt{\epsilon\mu} \frac{\omega}{c}$ being the wavevector in media. Next, we follow the standard procedure as in Bohren & Huffman book and define vector harmonics as

$$\mathbf{M}_{mj} = \nabla \times (\mathbf{r}\psi_{mj}), \quad \mathbf{N}_{mj} = \frac{1}{k} \nabla \times \mathbf{M}_{mj}, \quad \mathbf{L}_{mj} = \frac{1}{k} \nabla \psi_{mj}. \quad (\text{I.2})$$

Note that in other sources \mathbf{L} such as [172] is defined to be dimensional but not in this work. There an alternative form of the \mathbf{M} harmonic as $\mathbf{M}_{mj} = -i\hat{\mathbf{L}}\psi_{mj}$, where $\hat{\mathbf{L}} = -i\mathbf{r} \times \nabla$ is the orbital angular momentum operator. In the spherical

coordinate system $(\hat{\mathbf{r}}, \hat{\boldsymbol{\theta}}, \hat{\boldsymbol{\varphi}})$ this leads to

$$\begin{aligned} \mathbf{M}_{mj} &= \begin{bmatrix} 0 \\ \frac{im}{\sin \theta} z_j(kr) Y_j^m(\theta, \varphi) \\ -z_j(kr) \frac{d}{d\theta} Y_j^m(\theta, \varphi) \end{bmatrix}, & \mathbf{N}_{mj} &= \begin{bmatrix} j(j+1) \frac{z_j(kr)}{kr} Y_j^m(\theta, \varphi) \\ \frac{1}{kr} \frac{d}{dr} [r z_j(kr)] \frac{d}{d\theta} Y_j^m(\theta, \varphi) \\ \frac{im}{\sin \theta} \frac{1}{kr} \frac{d}{dr} [r z_j(kr)] Y_j^m(\theta, \varphi) \end{bmatrix}, \\ \mathbf{L}_{mj} &= \begin{bmatrix} z_j'(kr) Y_j^m(\theta, \varphi) \\ \frac{z_j(kr)}{kr} \frac{d}{d\theta} Y_j^m(\theta, \varphi) \\ \frac{im}{\sin \theta} \frac{z_j}{kr} Y_j^m(\theta, \varphi) \end{bmatrix}. \end{aligned} \quad (\text{I.3})$$

One of the important properties is that VSH are connected with each other through curl operation:

$$\mathbf{N}_{mj} = \frac{1}{k} \nabla \times \mathbf{M}_{mj}, \quad \mathbf{M}_{mj} = \frac{1}{k} \nabla \times \mathbf{N}_{mj} \quad (\text{I.4})$$

It means that if e.g. electric field is given by the \mathbf{N} harmonic then magnetic field is automatically is given by the \mathbf{M} harmonics and vice versa.

Any vector field can be decomposed into the series of complex vector spherical harmonics as

$$\mathbf{A} = \sum_{j=0}^{\infty} \sum_{m=-j}^j A_{mj} \mathbf{N}_{mj} + B_{mj} \mathbf{M}_{mj} + C_{mj} \mathbf{L}_{mj} \quad (\text{I.5})$$

In the case of sphere, omitting the electrostatic modes described by the \mathbf{L} harmonics, we get (longitudinal harmonics are used for the electrostatics, anisotropic structures and RSE applications to name a few [252; 253; 359]).

Some properties:

1. \mathbf{M} and \mathbf{N} are the solutions of the Helmholtz equation

$$\nabla \times \mathbf{N} = \frac{1}{k} \nabla \times \nabla \times \mathbf{M} = k\mathbf{M}, \quad (\text{I.6})$$

2. \mathbf{M} and \mathbf{N} are solenoidal,

$$\nabla \cdot \mathbf{M} = \nabla \cdot \mathbf{N} = 0, \quad (\text{I.7})$$

3. \mathbf{L} is potential,

$$\nabla \times \mathbf{L} = 0. \quad (\text{I.8})$$

To complete the picture with all the explicit definitions we also write the definition of the spherical function

$$Y_j^m(\vartheta, \varphi) = \sqrt{\frac{2j+1}{4\pi} \frac{(j-m)!}{(j+m)!}} P_j^m(\cos \vartheta) e^{im\varphi}, \quad (\text{I.9})$$

and associated Legendre polynomials with Condon-Shortley Phase [360] included

$$P_j^m(x) = (-1)^m (1-x^2)^{m/2} \frac{d^m}{dx^m} P_j(x), \quad (\text{I.10})$$

$$P_j^{-m} = (-1)^m \frac{(j-m)!}{(j+m)!} P_j^m, \quad (\text{I.11})$$

where the Legendre polynomials are defined as

$$P_j(x) = \frac{1}{2^j j!} \frac{d^j}{dx^j} (x^2 - 1)^j. \quad (\text{I.12})$$

All the equations (I.9, I.10, I.12) are *already* coded in most math packages such as SciPy and Wolfram Mathematica. It can be shown that

$$Y_j^{-m}(\theta, \varphi) = (-1)^m Y_j^{m*}(\theta, \varphi), \quad (\text{I.13})$$

so

$$\mathbf{M}_{-mj} = (-1)^m \mathbf{M}_{mj}^*, \quad \mathbf{N}_{-mj} = (-1)^m \mathbf{N}_{mj}^*, \quad \mathbf{L}_{-mj} = (-1)^m \mathbf{L}_{mj}^*. \quad (\text{I.14})$$

only for real valued $z_j(kr)$.

I.2 Orthogonality

Spherical functions are orthogonal

$$\int_{4\pi} d\Omega Y_{j'}^{m'*} Y_j^m = \delta_{jj'} \delta_{mm'}. \quad (\text{I.15})$$

The orthogonality of vector spherical functions is more complicated [16, p. 418]:

$$\int d\Omega |\mathbf{M}_{mj}|^2 = j(j+1) |z_j(kr)|^2 \quad (\text{I.16})$$

$$\int d\Omega |\mathbf{N}_{mj}|^2 = \frac{j(j+1)}{2j+1} [(j+1) |z_{j-1}(kr)|^2 + j |z_{j+1}(kr)|^2] \quad (\text{I.17})$$

$$\int d\Omega |\mathbf{L}_{mj}|^2 = \frac{1}{2j+1} [j |z_{j-1}(kr)|^2 + (j+1) |z_{j+1}(kr)|^2] \quad (\text{I.18})$$

$$\int d\Omega \mathbf{L}_{mj}^* \cdot \mathbf{N}_{mj} = \frac{j(j+1)}{2j+1} (|z_{j-1}(kr)|^2 - |z_{j+1}(kr)|^2) \quad (\text{I.19})$$

All other combinations are zeros.

I.3 Connection to the other sources

COMSOL Multiphysics

In COMSOL Multiphysics spherical harmonics defined as [361]

$$\text{COMSOL } Y_n^m(\boldsymbol{\theta}, \boldsymbol{\varphi}) = \begin{cases} (-1)^m \sqrt{\frac{(2n+1)(n-m)!}{4\pi(n+m)!}} \sin(\boldsymbol{\theta})^m \frac{d^m}{d(\cos(\boldsymbol{\theta}))^m} (P_n(\cos(\boldsymbol{\theta}))) e^{im\boldsymbol{\varphi}} & m > 0 \\ P_n(\cos(\boldsymbol{\theta})) & m = 0 \\ \sqrt{\frac{(2n+1)(n-|m|)!}{4\pi(n+|m|)!}} \sin(\boldsymbol{\theta})^{|m|} \frac{d^{|m|}}{d(\cos(\boldsymbol{\theta}))^{|m|}} (P_n(\cos(\boldsymbol{\theta}))) e^{im\boldsymbol{\varphi}} & m < 0 \end{cases} \quad (\text{I.20})$$

The only difference with (I.9) is the case of $m = 0$, e.g.

$$Y_j^m(\boldsymbol{\theta}, \boldsymbol{\varphi}) = \text{COMSOL } Y_{n=j}^m(\boldsymbol{\theta}, \boldsymbol{\varphi}) \quad \text{for } m \neq 0 \quad (\text{I.21})$$

and

$$Y_j^{m=0}(\boldsymbol{\theta}, \boldsymbol{\varphi}) = \sqrt{\frac{2n+1}{4\pi}} \cdot \text{COMSOL } Y_{n=j}^{m=0}(\boldsymbol{\theta}, \boldsymbol{\varphi}) \quad \text{for } m = 0 \quad (\text{I.22})$$

Jackson. Classical electrodynamics

Jackson defines his own vector harmonics as [15, § 9.7]

$$\mathbf{X}_{lm} = \frac{1}{\sqrt{l(l+1)}} \hat{\mathbf{L}} Y_{j=l}^m(\boldsymbol{\vartheta}, \boldsymbol{\varphi}), \quad (\text{I.23})$$

where $\hat{\mathbf{L}} = -i\mathbf{r} \times \nabla$ is the \hbar^{-1} times angular momentum operator. \mathbf{X}_{lm} is defined to be zero for $l = 0$. Explicitly it can be written as

$$\mathbf{X}_{lm} = \frac{-1}{\sqrt{l(l+1)}} \begin{bmatrix} 0 \\ \frac{m}{\sin \boldsymbol{\vartheta}} Y_{j=l}^m \\ i \frac{d}{d\boldsymbol{\vartheta}} Y_{j=l}^m \end{bmatrix} \quad (\text{I.24})$$

Definition of $Y_{lm}(\boldsymbol{\theta}, \boldsymbol{\varphi})$ from Jacskon's book is identical to (I.9) with $j \rightarrow l$. The relation between \mathbf{M} harmonics can be written explicitly

$$\mathbf{M}_{mj}(\boldsymbol{\rho}, \boldsymbol{\vartheta}, \boldsymbol{\varphi}) = -i\sqrt{j(j+1)} \cdot z_j(\boldsymbol{\rho})\mathbf{X}_{l=j,m}(\boldsymbol{\vartheta}, \boldsymbol{\varphi}) \quad (\text{I.25})$$

So, it means that Jackson harmonics \mathbf{X} are in fact the radius independent part of \mathbf{M} harmonic.

de Witt & Jensen. Über den Drehimpuls der Multipolstrahlung

De Witt in [362] also uses functions very close to VSH which he calls $\mathfrak{F}_{LMk,0}$ and $\mathfrak{F}_{LMk,1}$. They are connected as

$$\mathbf{M}_{mj} = -i\mathfrak{F}_{L=j,M=m,k,0} \quad (\text{I.26})$$

for $f_{Lk}(r)$ from [362] being $j_j(kr)$.

Bohren & Huffmann. Absorbtion and scattering of light by Small Particles

Bohren & Huffmann [172] use linear polarized-like basis, i.e. real valued VSH. Because of that there two types of harmonics: even and odd. Instead of (I.1) they have chosen

$$\psi_{\varepsilon mn}^{\text{B\&H}} = \frac{\cos(m\varphi)}{\sin(m\varphi)} \cdot P_n^m(\cos \boldsymbol{\vartheta})z_n(\boldsymbol{\rho}) \quad (\text{I.27})$$

and VSH are defined as

$$\mathbf{M} = \nabla \times (\mathbf{r}\psi^{\text{B\&H}}), \quad \mathbf{N} = \frac{1}{k}\nabla \times \mathbf{M}, \quad \mathbf{L} = \nabla\psi^{\text{B\&H}}. \quad (\text{I.28})$$

The explicit view of harmonics is

$$\mathbf{M}_{emn}^{\text{B\&H}} = \begin{bmatrix} 0 \\ \frac{-m}{\sin \vartheta} \sin(m\varphi) P_n^m(\cos \vartheta) z_n(\rho) \\ -\cos(m\varphi) \frac{d}{d\vartheta} P_n^m(\cos \vartheta) z_n(\rho) \end{bmatrix}, \quad (\text{I.29})$$

$$\mathbf{M}_{omn}^{\text{B\&H}} = \begin{bmatrix} 0 \\ \frac{m}{\sin \vartheta} \cos(m\varphi) P_n^m(\cos \vartheta) z_n(\rho) \\ -\sin(m\varphi) \frac{d}{d\vartheta} P_n^m(\cos \vartheta) z_n(\rho) \end{bmatrix} \quad (\text{I.30})$$

$$\mathbf{N}_{emn}^{\text{B\&H}} = \begin{bmatrix} \frac{z_n(\rho)}{\rho} \cos(m\varphi) n(n+1) P_n^m(\cos \vartheta) \\ \cos(m\varphi) \frac{dP_n^m(\cos \vartheta)}{d\vartheta} \frac{1}{\rho} \frac{d}{d\rho} [\rho z_n(\rho)] \\ -m \sin(m\varphi) \frac{P_n^m(\cos \vartheta)}{\sin \vartheta} \frac{1}{\rho} \frac{d}{d\rho} [\rho z_n(\rho)] \end{bmatrix}, \quad (\text{I.31})$$

$$\mathbf{N}_{omn}^{\text{B\&H}} = \begin{bmatrix} \frac{z_n(\rho)}{\rho} \sin(m\varphi) n(n+1) P_n^m(\cos \vartheta) \\ \sin(m\varphi) \frac{dP_n^m(\cos \vartheta)}{d\vartheta} \frac{1}{\rho} \frac{d}{d\rho} [\rho z_n(\rho)] \\ m \cos(m\varphi) \frac{P_n^m(\cos \vartheta)}{\sin \vartheta} \frac{1}{\rho} \frac{d}{d\rho} [\rho z_n(\rho)] \end{bmatrix} \quad (\text{I.32})$$

$$\mathbf{L}_{emn}^{\text{B\&H}} = k \begin{bmatrix} z_n'(\rho) P_n^m(\cos \vartheta) & \cos(m\varphi) \\ \frac{1}{\rho} z_n(\rho) \frac{dP_n^m(\cos \vartheta)}{d\vartheta} & \sin(m\varphi) \\ -1 \cdot \frac{m}{\rho \sin \vartheta} z_n(\rho) P_n^m(\cos \vartheta) & \sin(m\varphi) \\ +1 \cdot \frac{m}{\rho \sin \vartheta} z_n(\rho) P_n^m(\cos \vartheta) & \cos(m\varphi) \end{bmatrix} \quad (\text{I.33})$$

The connection with VSH of this work for $m \geq 0$ is given by

$$\mathbf{M}_{mj} = \sqrt{\frac{2j+1}{4\pi} \frac{(j-m)!}{(j+m)!}} \cdot (\mathbf{M}_{e,m,n=j}^{\text{B\&H}} + i\mathbf{M}_{o,m,n=j}^{\text{B\&H}}), \quad (\text{I.34})$$

$$\text{for } m \geq 0: \quad \mathbf{N}_{mj} = \sqrt{\frac{2j+1}{4\pi} \frac{(j-m)!}{(j+m)!}} \cdot (\mathbf{N}_{e,m,n=j}^{\text{B\&H}} + i\mathbf{N}_{o,m,n=j}^{\text{B\&H}}), \quad (\text{I.35})$$

$$\mathbf{L}_{mj} = \sqrt{\frac{2j+1}{4\pi} \frac{(j-m)!}{(j+m)!}} \cdot \frac{1}{k} (\mathbf{L}_{e,m,n=j}^{\text{B\&H}} + i\mathbf{L}_{o,m,n=j}^{\text{B\&H}}). \quad (\text{I.36})$$

Note that VSH from Bohren & Huffmann book does not follow (I.14) due to the convention (I.11) on associated Legendre polynomials. One should use (I.14) to calculate the case of $m < 0$ if using B&H functions.

Stratton. Electromagnetic theory

Same as Bohren & Huffmann.

Varshalovich, Moskalev, and Khersonskii. Quantum theory of angular momentum

Spherical tensor \mathbf{Y}_{JM}^{LS} which is defined [363] to be such that

$$\hat{\mathbf{J}}^2 \mathbf{Y}_{JM}^{LS} = J(J+1) \mathbf{Y}_{JM}^{LS}, \quad (\text{I.37})$$

$$\hat{J}_z \mathbf{Y}_{JM}^{LS} = M \mathbf{Y}_{JM}^{LS}, \quad (\text{I.38})$$

$$\hat{\mathbf{L}}^2 \mathbf{Y}_{JM}^{LS} = L(L+1) \mathbf{Y}_{JM}^{LS}, \quad (\text{I.39})$$

$$\hat{\mathbf{S}}^2 \mathbf{Y}_{JM}^{LS} = S(S+1) \mathbf{Y}_{JM}^{LS} \quad (\text{I.40})$$

Vector spherical harmonics are closely connected to this spherical tensor \mathbf{Y}_{JM}^{LS} which is defined to be with rank $S = 1$ which are $\mathbf{Y}_{JM}^{L1} \equiv \mathbf{Y}_{JM}^L$:

$$\mathbf{Y}_{JM}^L = \sum_{m,\sigma} C_{Lm\ 1\sigma}^{JM} Y_{Lm}(\vartheta, \varphi) \hat{\mathbf{e}}_\sigma. \quad (\text{I.41})$$

In particular, it is connected with spherical vectors $\mathbf{Y}_{JM}^{(\lambda)}$ where $\lambda = 0, \pm 1$. These vectors are **not** eigen functions of $\hat{\mathbf{L}}^2$, however they have a very helpful property with respect to the unit orth $\mathbf{n} = \mathbf{r}/r$ as

$$\mathbf{n} \cdot \mathbf{Y}_{JM}^{(1)} = \mathbf{n} \cdot \mathbf{Y}_{JM}^{(0)} = 0, \quad \mathbf{n} \times \mathbf{Y}_{JM}^{(-1)} = 0. \quad (\text{I.42})$$

Which are connected with the spherical tensors \mathbf{Y}_{JM}^{LS} as

$$\begin{aligned} \mathbf{Y}_{JM}^{(1)}(\vartheta, \varphi) &= \sqrt{\frac{J+1}{2J+1}} \mathbf{Y}_{JM}^{J-1,1}(\vartheta, \varphi) + \sqrt{\frac{J}{2J+1}} \mathbf{Y}_{JM}^{J+1,1}(\vartheta, \varphi) \\ \mathbf{Y}_{JM}^{(0)}(\vartheta, \varphi) &= \mathbf{Y}_{JM}^{J1}(\vartheta, \varphi) \end{aligned} \quad (\text{I.43})$$

$$\mathbf{Y}_{JM}^{(-1)}(\vartheta, \varphi) = \sqrt{\frac{J}{2J+1}} \mathbf{Y}_{JM}^{J-1,1}(\vartheta, \varphi) - \sqrt{\frac{J+1}{2J+1}} \mathbf{Y}_{JM}^{J+1,1}(\vartheta, \varphi)$$

Connections with the Jackson's \mathbf{X} is given by

$$\mathbf{X}_{\ell m}(\vartheta, \varphi) = \mathbf{Y}_{J=\ell, M=m}^{(0)}(\vartheta, \varphi) = \mathbf{Y}_{J=\ell, M=m}^{L=\ell}(\vartheta, \varphi) \quad (\text{I.44})$$

The explicit connection with complex vector harmonics used in this paper are the following:

$$\mathbf{M}_{mj}^{(1)}(\rho, \vartheta, \varphi) = -i \sqrt{j(j+1)} j_j(\rho) \mathbf{Y}_{J=j, M=m}^{L=j}(\vartheta, \varphi) \quad (\text{I.45})$$

$$\mathbf{N}_{mj}^{(1)}(\rho, \vartheta, \varphi) = -\sqrt{\frac{j(j+1)}{2j+1}} \left[\sqrt{j} \cdot j_{j+1}(\rho) \mathbf{Y}_{J=j, M=m}^{L=j+1}(\vartheta, \varphi) \quad (\text{I.46}) \right.$$

$$\left. -\sqrt{j+1} \cdot j_{j-1}(\rho) \mathbf{Y}_{J=j, M=m}^{L=j-1}(\vartheta, \varphi) \right] \quad (\text{I.47})$$

Here $\rho = n_{\text{in}}k_0r$, $(\vartheta, \varphi) = \mathbf{r}/r$.

I.4 Helpful math identities with vector spherical functions

Decomposition of the plane wave [52, Eq. (2.2.27)]

$$e^{i\mathbf{k}\cdot\mathbf{r}} = 4\pi \sum_{nm} i^n j_n(kr) Y_n^{m*} \left(\frac{\mathbf{k}}{k} \right) Y_n^m \left(\frac{\mathbf{r}}{r} \right) \quad (\text{I.48})$$

Connection between real and \mathbf{k} -space arguments of vector spherical functions

$$\int d\Omega_{\mathbf{k}} \mathbf{Y}_{JM}^L \left(\frac{\mathbf{k}}{k} \right) e^{i\mathbf{k}\cdot\mathbf{r}} = g_L(kr) \mathbf{Y}_{JM}^L \left(\frac{\mathbf{r}}{r} \right) \quad (\text{I.49})$$

Where $g_L(kr) = 4\pi i^L j_L(kr)$.

Since the eigen modes in \mathbf{k} -space is proportional to the spherical tensors $\mathbf{L}_{JM}^L(\mathbf{k}/k)$ it is usefull to write a transformation of $\hat{\mathbf{J}}_{\mathbf{k}}^2 \mathbf{L}_{JM}^L(\mathbf{k}/k) = J(J+1) \mathbf{L}_{JM}^L(\mathbf{k}/k)$ with $\hat{\mathbf{J}}_{\mathbf{k}} = -i\mathbf{k} \times \nabla_{\mathbf{k}} + \hat{\mathbf{S}}$ to real space:

$$\int d\Omega_{\mathbf{k}} e^{i\mathbf{k}\cdot\mathbf{r}} \hat{\mathbf{J}}_{\mathbf{k}}^2 \mathbf{L}_{JM}^L(\mathbf{k}/k) = \int d\Omega_{\mathbf{k}} e^{i\mathbf{k}\cdot\mathbf{r}} J(J+1) \mathbf{L}_{JM}^L(\mathbf{k}/k) \quad (\text{I.50})$$

$$\int d\Omega_{\mathbf{k}} e^{i\mathbf{k}\cdot\mathbf{r}} \hat{\mathbf{J}}_{\mathbf{k}}^2 \mathbf{L}_{JM}^L(\mathbf{k}/k) = J(J+1) g_L(kr) \mathbf{L}_{JM}^L(\mathbf{r}/r) \quad (\text{I.51})$$

Lets proof that $g_\ell \mathbf{Y}_{jM}^\ell$ with $g_\ell = g_\ell(kr)$ being any function of $r = |\mathbf{r}|$, is the eigen function of $\hat{\mathbf{J}}^2$. Action of the $\hat{\mathbf{J}}^2$ in the real space

$$\hat{\mathbf{J}}^2 [g_\ell \mathbf{Y}_{jM}^\ell] = \hat{\mathbf{L}}^2 [g_\ell \mathbf{Y}_{jM}^\ell] + \hat{\mathbf{S}}^2 [g_\ell \mathbf{Y}_{jM}^\ell] + 2(\hat{\mathbf{S}} \cdot \hat{\mathbf{L}}) [g_\ell \mathbf{Y}_{jM}^\ell] = j(j+1) g_\ell \mathbf{Y}_{jM}^\ell \quad (\text{I.52})$$

here we have used that $\hat{\mathbf{S}}^2 = s(s+1) = 2$, $\hat{\mathbf{L}}^2 \mathbf{Y}_{jM}^\ell = \ell(\ell+1) \mathbf{Y}_{jM}^\ell$, and the fact that orbital angular momenta operator acts only on the angular part, since it can be rewritten as

$$\hat{\mathbf{L}} = i \left(\hat{\boldsymbol{\vartheta}} \frac{1}{\sin(\vartheta)} \frac{\partial}{\partial \varphi} - \hat{\boldsymbol{\varphi}} \frac{\partial}{\partial \vartheta} \right) \quad (\text{I.53})$$

$$\begin{aligned} &= i \hat{\mathbf{x}} \left(\sin(\varphi) \frac{\partial}{\partial \vartheta} + \text{ctg}(\vartheta) \cos(\varphi) \frac{\partial}{\partial \varphi} \right) \\ &\quad + i \hat{\mathbf{y}} \left(-\cos(\varphi) \frac{\partial}{\partial \vartheta} + \text{ctg}(\vartheta) \sin(\varphi) \frac{\partial}{\partial \varphi} \right) - i \hat{\mathbf{z}} \frac{\partial}{\partial \varphi} \end{aligned} \quad (\text{I.54})$$

and identity for vector spherical harmonic [363, eq. (67)]

$$(\hat{\mathbf{S}} \cdot \hat{\mathbf{L}}) \mathbf{Y}_{jL}^\ell = \frac{1}{2} [j(j+1) - \ell(\ell+1) - 2] \quad (\text{I.55})$$

For general purpose we also write $\hat{\mathbf{S}}_i^{\text{sph}} = \mathbf{R}^{-1} \hat{\mathbf{S}}_i \mathbf{R}$ for $i = x, y, z$ which acts on a vector in a spherical basis. Here

$$\hat{\mathbf{S}}_{\{i\}_{\text{cart}}\{jk\}_{\text{sph}}} = -i \begin{pmatrix} \begin{bmatrix} 0 & -\sin \varphi & -\cos \vartheta \cos \varphi \\ \sin \varphi & 0 & \sin \vartheta \cos \varphi \\ \cos \vartheta \cos \varphi & -\sin \vartheta \cos \varphi & 0 \end{bmatrix} \\ \begin{bmatrix} 0 & \cos \varphi & -\cos \vartheta \sin \varphi \\ -\cos \varphi & 0 & \sin \vartheta \sin \varphi \\ \cos \vartheta \sin \varphi & -\sin \vartheta \sin \varphi & 0 \end{bmatrix} \\ \begin{bmatrix} 0 & 0 & \sin \vartheta \\ 0 & 0 & \cos \vartheta \\ -\sin \vartheta & -\cos \vartheta & 0 \end{bmatrix} \end{pmatrix}. \quad (\text{I.56})$$

and

$$R = \begin{pmatrix} \sin \vartheta \cos \varphi & \cos \vartheta \cos \varphi & -\sin \varphi \\ \sin \vartheta \sin \varphi & \cos \vartheta \sin \varphi & \cos \varphi \\ \cos \vartheta & -\sin \vartheta & 0 \end{pmatrix} \quad (\text{I.57})$$

Appendix J

Explicit form of \mathbf{j}^2 for several first multipoles

For total angular momentum per one photon $\mathbf{j} = \frac{\omega \mathbf{J}}{W}$ we find a general form

$$\mathbf{j}_{mn}^2(\mathbf{r}) = \frac{4 [m \operatorname{cosec} \vartheta [P_n^m]_{\vartheta}' P_n^m]^2 + \operatorname{cosec}^2 \vartheta \left[m \left([m \operatorname{cosec} \vartheta P_n^m]^2 + ([P_n^m]_{\vartheta}')^2 \right) + 2m \operatorname{ctg} \vartheta [P_n^m]_{\vartheta}' P_n^m \right]^2}{\left[(m \operatorname{cosec} \vartheta P_n^m)^2 + \operatorname{cosec}^2 \vartheta \left((1+n) \cos \vartheta P_n^m + (m-n-1) P_{n+1}^m \right)^2 \right]^2}. \quad (\text{J.1})$$

We note that it does not depend on r and φ . For the first several n and m we find:

$$\mathbf{j}_{m=-1,1}^2 = \frac{10 + 2 \cos 2\vartheta}{(3 + \cos 2\vartheta)^2} \quad (\text{J.2})$$

$$\mathbf{j}_{m=-1,1}^2 = \frac{\sin^2(4\vartheta) \operatorname{cosec}^2(\vartheta) + \operatorname{ctg}^2(\vartheta) (\sin(4\vartheta) \operatorname{cosec}(\vartheta) - 2(\cos(3\vartheta) + \sec(\vartheta)))^2}{4(\cos^2(\vartheta) + \cos^2(2\vartheta))^2} \quad (\text{J.3})$$

$$\mathbf{j}_{m=-2,2}^2 = -\frac{2(\cos(2\vartheta) - 10 \operatorname{cosec}^2(\vartheta) + 2 \cos(\vartheta)(\cos(2\vartheta) + 3) \operatorname{ctg}(\vartheta) \operatorname{cosec}(\vartheta) + 9)}{(\cos^2(\vartheta) + 1)^2} \quad (\text{J.4})$$

$$\mathbf{j}_{m=-1,1}^2 = \frac{16 \cos^2(\vartheta) (20 \cos(2\vartheta) + 75 \cos(4\vartheta) + 33)^2 + 4 \sin^2(\vartheta) (60 \cos(2\vartheta) - 75 \cos(4\vartheta) + 143)^2}{16(\cos^2(\vartheta)(15 \cos(2\vartheta) - 7)^2 + (5 \cos(2\vartheta) + 3)^2)^2} \quad (\text{J.5})$$

$$\mathbf{j}_{m=-2,2}^2 = \frac{2(936 \cos(2\vartheta) + 332 \cos(4\vartheta) + 24 \cos(6\vartheta) - 27 \cos(8\vartheta) + 783) \operatorname{cosec}^2(\vartheta)}{(28 \cos(2\vartheta) + 9(\cos(4\vartheta) + 3))^2} \quad (\text{J.6})$$

$$\mathbf{j}_{m=-3,3}^2 = \frac{\operatorname{cosec}^6(\vartheta) \left(-\frac{48(\cos(2\vartheta)+3) \operatorname{ctg}^2(\vartheta) |\sin(\vartheta)|^3}{\sqrt{\sin^2(\vartheta)}} + 124 \cos(2\vartheta) + 9 \cos(4\vartheta) + 187 \right)}{8(\operatorname{ctg}^2(\vartheta) + \operatorname{cosec}^2(\vartheta))^2} \quad (\text{J.7})$$

It can be shown using these known relations of associated Legendre polynomials at zero [364]

$$P_n^m(0) = \frac{2^m \pi^{1/2}}{\Gamma(\frac{1}{2}n - \frac{1}{2}m + 1) \Gamma(\frac{1}{2} - \frac{1}{2}n - \frac{1}{2}m)}, \quad (\text{J.8})$$

$$\left. \frac{dP_n^m(x)}{dx} \right|_{x=0} = \frac{2^{m+1} \pi^{1/2}}{\Gamma(\frac{1}{2}n - \frac{1}{2}m + \frac{1}{2}) \Gamma(-\frac{1}{2}n - \frac{1}{2}m)} \quad (\text{J.9})$$

where $\Gamma(z)$ is the gamma function, that

$$\mathbf{j}^2(\vartheta = 0) = m^2. \quad (\text{J.10})$$

Appendix K

Integrated values of the square of kinetic AM

Jackson in his fundamental book Classical Electrodynamics made wonder on angular momenta calculation of the multipoles in § 9.8. Using kinetic approach for the AM calculation (i.e. using Poynting vector)

$$\mathbf{J}_{\text{kin}} = \frac{1}{2c^2} \text{Re} [\mathbf{r} \times (\mathbf{E} \times \mathbf{H}^*)] \quad (\text{K.1})$$

where $\mathbf{H} = \text{const} \cdot \mathbf{X}_{lm} h_l^{(1)}(kr)$. In the far field zone (for $kr \gg 1$) we have used a different approach

$$\text{our approach:} \quad \frac{\omega^2 \langle \mathbf{J}_{\text{kin}}^2 \rangle_{4\pi}}{\langle W \rangle_{4\pi}^2} = m^2 \cdot 8\pi^2 \int_0^\pi d\vartheta \frac{1}{\sin \vartheta} |Y_n^m|^4 \quad (\text{K.2})$$

$$\text{from Jackson [15]:} \quad \frac{\omega^2 \left(\frac{d}{dr} \langle \mathbf{J}_{\text{kin}} \rangle_{4\pi} \right)^2}{\left(\frac{d}{dr} \langle W \rangle_{4\pi} \right)^2} = m^2 \quad (\text{K.3})$$

The answer (K.2) was obtained rigorously and verified by the numerical calculations. For some first multipoles we find $\langle \mathbf{j}_{\text{kin}}^2 \rangle \equiv \frac{\omega^2 \langle \mathbf{J}_{\text{kin}}^2 \rangle_{4\pi}}{\langle W \rangle_{4\pi}^2}$:

$$\langle \mathbf{j}_{\text{kin}}^2 \rangle_{(m=1)}^{(l=1)} = \frac{3}{2} = 1.5 \quad (\text{K.4})$$

$$\langle \mathbf{j}_{\text{kin}}^2 \rangle_{(m=1)}^{(l=2)} = \frac{45}{14} \approx 3.21 \quad (\text{K.5})$$

$$\langle \mathbf{j}_{\text{kin}}^2 \rangle_{(m=2)}^{(l=2)} = \frac{45}{7} \approx 6.43 \quad (\text{K.6})$$

$$\langle \mathbf{j}_{\text{kin}}^2 \rangle_{(m=1)}^{(l=3)} = \frac{63}{11} \approx 5.73 \quad (\text{K.7})$$

$$\langle \mathbf{j}_{\text{kin}}^2 \rangle_{(m=2)}^{(l=3)} = \frac{105}{11} \approx 9.55 \quad (\text{K.8})$$

$$\langle \mathbf{j}_{\text{kin}}^2 \rangle_{(m=3)}^{(l=3)} = \frac{175}{11} \approx 15.91 \quad (\text{K.9})$$

The result (K.2) was obtained using a number of recurrent relation. Especially helpful was to use [363]

$$\begin{aligned} -2m \text{ctg} \vartheta Y_{lm}(\vartheta, \varphi) &= \sqrt{l(l+1) - m(m+1)} e^{-i\varphi} Y_{l, m+1}(\vartheta, \varphi) \\ &+ \sqrt{l(l+1) - m(m-1)} e^{i\varphi} Y_{l, m-1}(\vartheta, \varphi). \end{aligned} \quad (\text{K.10})$$

Appendix L

Fundamental connection between diffusion and friction coefficients

Let us start with the Langevin equation

$$m\ddot{\mathbf{r}} = -\zeta\dot{\mathbf{r}} + \mathbf{F}_{\text{st}} \quad (\text{L.1})$$

All we know about stochastic force \mathbf{F}_{st} is that it is zero in average and each moment in time is independent from the past (white noise). Mathematically, it can be written as

$$\langle \mathbf{F}_{\text{st}}(t) \rangle_t = 0, \quad (\text{L.2})$$

$$\langle F_{\text{st},\alpha}(t)F_{\text{st},\beta}(t + \tau) \rangle_t = 2D\delta_{\alpha\beta}\delta(\tau), \quad (\text{L.3})$$

where $\alpha, \beta = x, y, z$ and $\langle f(t) \rangle_t \equiv \lim_{T \rightarrow \infty} \frac{1}{T} \int_{-T/2}^{T/2} dt f(t)$. Constant D is proportional to the diffusion constant and “2” is chosen for the sake of convenience.

Here we will show that

$$D = k_{\text{B}}T\zeta \quad (\text{L.4})$$

Equation (L.3) can be written in terms of *auto-correlation function* as

$$\varphi_F(\tau) = \langle \mathbf{F}_{\text{st}}(t) \cdot \mathbf{F}_{\text{st}}(t + \tau) \rangle_t = 6D\delta(\tau). \quad (\text{L.5})$$

Next, from a very general considerations we can write

$$D = D(\zeta, T). \quad (\text{L.6})$$

In order to find this dependency, some work needs to be done. One of the keys to the solution of this problem is thermodynamics.

At first, we find spectral density $S_F(\omega)$ of the stochastic force $\mathbf{F}_{\text{st}}(t)$ using Wiener-Khintchine theorem¹

$$S_F(\omega) = \int_{-\infty}^{\infty} dt e^{i\omega t} \varphi_F(t) = 6D. \quad (\text{L.7})$$

¹For a signal function $y(t)$ Wiener-Khintchine theorem reads as:

$$\varphi_y(\tau) = \int_{-\infty}^{\infty} \frac{d\omega}{2\pi} e^{-i\omega\tau} S_y(\omega).$$

It states that auto-correlation and spectral density functions are connected through Fourier transform.

Afterwards, we want to find the auto-correlation function of speed $\varphi_v(t)$, since it is connected with average kinetic energy $U_{\text{kin}} \propto \varphi_v(t=0)$. However, we don't know the exact time dependence $\mathbf{v}(t)$. We can work out this by finding $\mathbf{v}(\omega)$ using Fourier transform:

$$m\dot{\mathbf{v}} = -\zeta\mathbf{v} + \mathbf{F}_{\text{st}} \quad \xrightarrow{\mathcal{F}\{\dots\}} \quad \mathbf{v}(\omega) = \frac{\mathbf{F}_{\text{st}}(\omega)}{\zeta - i\omega m}. \quad (\text{L.8})$$

Spectral density of the velocity ²

$$S_v(\omega) = \lim_{T \rightarrow \infty} \frac{1}{T} |\mathbf{v}(\omega)|^2 = \frac{1}{\zeta^2 + m^2\omega^2} \lim_{T \rightarrow \infty} \frac{1}{T} |\mathbf{F}_{\text{st}}(\omega)|^2 = \frac{6D}{\zeta^2 + m^2\omega^2}. \quad (\text{L.9})$$

Applying Wiener-Khintchine theorem, we finally get

$$\varphi_v(t) = \int \frac{d\omega}{2\pi} e^{-i\omega t} S_v(\omega) = \frac{3D}{\zeta m} \exp\left(-\frac{\zeta}{m}|t|\right). \quad (\text{L.10})$$

As a final step here, we note that $\varphi_v(t=0) = \langle \mathbf{v}^2 \rangle$. In other words,

$$\langle U_{\text{kin}} \rangle = \frac{m \langle \mathbf{v}^2 \rangle}{2} = \left/ \text{from thermodynamics} \right/ = 3 \cdot \frac{kT}{2}, \quad (\text{L.11})$$

so we found the solution to the (L.6):

$$D = kT\zeta. \quad (\text{L.12})$$

²For a signal function $y(t)$ we have (proof of Wiener-Khintchine theorem)

$$\begin{aligned} \varphi_y(\tau) &\equiv \langle y(t)y(t+\tau) \rangle_t = \lim_{T \rightarrow \infty} \int_{-\infty}^{\infty} dt \left[y(t) \left(\int \frac{d\omega}{2\pi} e^{-i\omega(t+\tau)} y(\omega) \right) \right] = \\ &= \lim_{T \rightarrow \infty} \int_{-\infty}^{\infty} \frac{d\omega}{2\pi} \left[e^{-i\omega\tau} y(\omega) \int_{-\infty}^{\infty} dt (e^{-i\omega t} y(t)) \right] = \lim_{T \rightarrow \infty} \frac{1}{T} \int_{-\infty}^{\infty} \frac{d\omega}{2\pi} e^{-i\omega\tau} y(\omega) y^*(\omega) = \\ &= \int_{-\infty}^{\infty} \frac{d\omega}{2\pi} e^{-i\omega\tau} \underbrace{\left[\lim_{T \rightarrow \infty} \frac{1}{T} |y(\omega)|^2 \right]}_{\equiv S_y(\omega)} = \int_{-\infty}^{\infty} \frac{d\omega}{2\pi} e^{-i\omega\tau} S_y(\omega). \end{aligned}$$

Appendix M

(mandatory) Texts of author's key publications

Acoustic Radiation Force and Torque on Small Particles as Measures of the Canonical Momentum and Spin Densities

I. D. Toftul,^{1,2} K. Y. Bliokh^{1,3}, M. I. Petrov,² and F. Nori^{1,4}

¹Theoretical Quantum Physics Laboratory, RIKEN Cluster for Pioneering Research, Wako-shi, Saitama 351-0198, Japan

²ITMO University, Birzhevaya liniya 14, St.-Petersburg 199034, Russia

³Nonlinear Physics Centre, RSPE, The Australian National University, Canberra ACT 0200, Australia

⁴Physics Department, University of Michigan, Ann Arbor, Michigan 48109-1040, USA



(Received 29 May 2019; published 28 October 2019)

We examine acoustic radiation force and torque on a small (subwavelength) absorbing isotropic particle immersed in a monochromatic (but generally inhomogeneous) sound-wave field. We show that by introducing the monopole and dipole polarizabilities of the particle, the problem can be treated in a way similar to the well-studied optical forces and torques on dipole Rayleigh particles. We derive simple analytical expressions for the acoustic force (including both the gradient and scattering forces) and torque. Importantly, these expressions reveal intimate relations to the fundamental field properties introduced recently for acoustic fields: the canonical momentum and spin angular momentum densities. We compare our analytical results with previous calculations and exact numerical simulations. We also consider an important example of a particle in an evanescent acoustic wave, which exhibits the mutually orthogonal scattering (radiation-pressure) force, gradient force, and torque from the transverse spin of the field.

DOI: 10.1103/PhysRevLett.123.183901

Introduction.—Optical and acoustic radiation forces and torques are of great importance from both practical and fundamental points of view. On the one hand, these mechanical manifestations of the radiation power underpin optical and acoustic manipulations of small particles [1–6], atomic cooling [7–9], optomechanics [10], acoustofluidics [11,12], etc. On the other hand, radiation forces and torques reveal the fundamental momentum and angular-momentum properties of the optical and sound wave fields [13–23].

Since Kepler’s observation of the comet tail and early theoretical works by Euler and Poynting [13,14], the studies of optical and acoustic momentum and forces were developed in parallel ways. Remarkably, despite numerous works calculating radiation forces and torques acting on various small particles in optics [24–30] and acoustics [31–41], the explicit proportionality of the force and torque to the local wave momentum and spin angular momentum densities was properly established in optics only recently [42–51]. The reason for this is that, in generic inhomogeneous wave fields, the force and torque on an isotropic small absorbing particle are proportional to the canonical momentum and spin densities rather than the Poynting (kinetic) momentum and angular momentum commonly used for many decades [45–48,50,52–54].

In acoustics, such explicit connection between the radiation force (torque) and momentum (spin) in generic inhomogeneous fields has not been described so far. Moreover, the concepts of the canonical momentum and spin angular momentum densities in sound wave fields have been introduced only in very recent works [55–58].

In this Letter, we provide a simple yet accurate theory of acoustic forces and torques on small (subwavelength)

absorbing isotropic particles in generic monochromatic acoustic fields. By employing methods well-established in optics and involving the monopole and dipole polarizabilities of the particle (determined by the leading terms in the Mie scattering problem), we derive simple analytical expressions for the acoustic forces and torque. Most importantly, these expressions indeed expose the intimate relation to the canonical momentum and spin densities in the acoustic field. We show that our results agree with specific previous calculations and exact numerical simulations. We illustrate our general theory with an explicit example of the forces and torque on a small particle in an evanescent acoustic wave.

Properties of acoustic fields.—We will deal with monochromatic but arbitrarily inhomogeneous acoustic fields of frequency ω in a homogeneous dense medium (fluid or gas). The complex pressure and velocity fields, $p(\mathbf{r})$ and $\mathbf{v}(\mathbf{r})$, obey the wave equations [59]

$$i\omega\beta p = \nabla \cdot \mathbf{v}, \quad i\omega\rho\mathbf{v} = \nabla p, \quad (1)$$

where the medium is characterized by the compressibility β , the mass density ρ , and the speed of sound $c = 1/\sqrt{\rho\beta}$.

We will characterize the dynamical properties of the acoustic wave field by its energy, canonical momentum, and spin angular momentum densities. The energy density reads [59]:

$$W = \frac{1}{4}(\beta|p|^2 + \rho|\mathbf{v}|^2) \equiv W^{(p)} + W^{(v)}. \quad (2)$$

The canonical momentum and spin densities of acoustic fields were introduced very recently [56–58]:

$$\mathbf{P} = \frac{1}{4\omega} \text{Im}[\beta p^* \nabla p + \rho \mathbf{v}^* \cdot (\nabla) \mathbf{v}] \equiv \mathbf{P}^{(p)} + \mathbf{P}^{(v)}, \quad (3)$$

$$\mathbf{S} = \frac{\rho}{2\omega} \text{Im}(\mathbf{v}^* \times \mathbf{v}), \quad (4)$$

where $[\mathbf{v}^* \cdot (\nabla) \mathbf{v}]_i \equiv \Sigma_j v_j^* \nabla_i v_j$ [42].

The energy (2) and momentum (3) densities are represented as symmetric sums of the pressure- and velocity-related contributions, indicated by the corresponding superscripts. This is similar to the symmetric electric- and magnetic-field contributions in electromagnetism [42,45–48,52,54,60]. In contrast, the spin density (4) has only the velocity contribution because the scalar pressure field cannot generate any local vector rotation.

Note that the canonical momentum determines the orbital angular momentum density $\mathbf{L} = \mathbf{r} \times \mathbf{P}$ [45,48,52,53,58], and that the more familiar kinetic momentum density (the acoustic analog of the Poynting momentum) is given by $\mathbf{\Pi} = \mathbf{P} + \frac{1}{4} \nabla \times \mathbf{S} = (1/2c^2) \text{Re}(p^* \mathbf{v})$ [58,59]. The equivalence of the canonical and kinetic momentum and angular momentum quantities appears for their integral values for localized acoustic fields: $\langle \mathbf{P} \rangle = \langle \mathbf{\Pi} \rangle$ and $\langle \mathbf{S} \rangle + \langle \mathbf{L} \rangle = \langle \mathbf{r} \times \mathbf{\Pi} \rangle$ [45,48,52,53,58], where the angular brackets stand for spatial integration. However, here we are interested in local rather than integral field properties, which are very different in the canonical and kinetic pictures; below we show that it is the canonical quantities (3) and (4) that correspond to the force and torque on small particles.

Interaction with a small particle.—The most straightforward way to detect the momentum and angular momentum of a wave field is to measure the force and torque it produces on a probe particle [13–22,43–46,48–51,56,61]. Therefore, we consider the interaction of a monochromatic acoustic wave with a small (subwavelength) spherical isotropic particle of the radius a , density ρ_1 and compressibility β_1 , with its center at $\mathbf{r} = \mathbf{r}_0$. We allow the particle to be absorbing; i.e., the parameters $\{\rho_1, \beta_1\}$ are generally complex.

The wave-particle interaction is directly related to the wave scattering problem. For small isotropic particles, the scattered field is conveniently represented by a multipole expansion [62–64], where the small parameter is $ka \ll 1$ ($k = \omega/c$ is the wave number). For electromagnetic waves, the leading term is the dipole one [1–4,24–26], because the monopole cannot radiate transversal waves. In contrast, for longitudinal acoustic waves, the leading terms are the monopole and dipole ones, and these generally have the same order in ka [11,31]. Therefore, a small particle in an acoustic wave field can be approximated by a monopole and dipole, which are induced by the incident field and are interacting with this field (so the interaction is quadratic with respect to the field).

The oscillating monopole and dipole modes of the particle are schematically shown in Fig. 1. The monopole mode is associated with the isotropic compression or expansion of the sphere, while the dipole mode represents

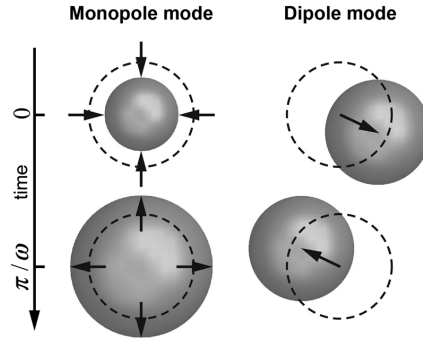


FIG. 1. The monopole and dipole oscillatory modes of a spherical particle. These modes are associated with an isotropic compression or expansion and a linear oscillatory motion of the particle, which are induced by the oscillating scalar pressure p and vector velocity \mathbf{v} fields, respectively.

oscillations of the particle position along certain direction. It is easy to see that these modes can be excited by the oscillating pressure p and velocity \mathbf{v} fields, respectively. Therefore, the induced monopole and dipole moments of the particle can be written as:

$$Q = -i\omega\beta\alpha_m p(\mathbf{r}_0), \quad \mathbf{D} = \alpha_d \mathbf{v}(\mathbf{r}_0), \quad (5)$$

where, following optical terminology, α_m and α_d are the monopole and dipole polarizabilities of the particle, and the prefactor $-i\omega\beta$ in the monopole term is introduced for the convenience in what follows and equal dimensionality of the polarizabilities. Comparing the leading terms of the multipole expansion of the acoustic Mie scattering problem with the standard expressions for the acoustic monopole and dipole radiation [63,64], we find the expressions for the polarizabilities (see the Supplemental Material [65]):

$$\begin{aligned} \alpha_m &= -\frac{4\pi i}{k^3} a_0 \simeq \frac{4\pi}{3} a^3 (\bar{\beta} - 1), \\ \alpha_d &= -\frac{4\pi i}{k^3} 3a_1 \simeq \frac{4\pi}{3} a^3 \frac{3(\bar{\rho} - 1)}{2\bar{\rho} + 1}. \end{aligned} \quad (6)$$

Here, $\bar{\rho} = \rho_1/\rho$ and $\bar{\beta} = \beta_1/\beta$ are the relative density and compressibility of the particle, a_0 and a_1 are the first two Mie scattering coefficients, and we approximated these coefficients by the leading $(ka)^3$ term in $ka \ll 1$ (see the Supplemental Material [65]). Naturally, the monopole and dipole polarizabilities are related to the differences in the compressibilities and mass densities between the particle and the surrounding medium, respectively. These differences induce relative compression and shift of the particle as shown in Fig. 1.

Absorption rate, force, and torque.—The interaction of the induced monopole and dipole moments of the particle with the acoustic field can be described via the minimal-coupling model between the moments (5) (Q, \mathbf{D}) and the

fields (p, \mathbf{v}) . Introducing the proper dimensional coefficients, the complex interaction energy takes the form $W^{\text{int}} = \frac{1}{2}[(i/\omega)Q^*p - \rho\mathbf{D}^* \cdot \mathbf{v}]$. Notably, this energy is precisely equivalent to the energy of the electric dipole \mathbf{D} and charge Q in the electric field $\mathbf{E} = \rho\mathbf{v}$ and the corresponding electric potential $\Phi = i\omega^{-1}p$ ($\mathbf{E} = -\nabla\Phi$).

The interaction can be characterized by the rates of the energy, momentum, and angular momentum transfer between the field and the particle, which are quantified by the absorption rate, radiation force, and radiation torque, respectively [46]. First, the absorption rate is determined by the imaginary part of the interaction energy:

$$\mathcal{A} = \omega \text{Im}(W^{\text{int}}) = 2\omega \left[\text{Im}(\alpha_m)W^{(p)} + \text{Im}(\alpha_d)W^{(v)} \right]. \quad (7)$$

It is naturally proportional to the imaginary parts of the particle polarizabilities (6) (and, hence, of the parameters $\bar{\rho}$ and $\bar{\beta}$) and to the corresponding pressure- and velocity-related energy densities (2) of the field.

Second, the radiation force is associated with the gradient of the real part of the interaction energy and can be written as [3,4,26,28,29,46]:

$$\mathbf{F} = -\frac{1}{2}\text{Re} \left[\frac{i}{\omega} Q^* \nabla p - \rho \mathbf{D}^* \cdot (\nabla) \mathbf{v} \right] = \mathbf{F}^{\text{grad}} + \mathbf{F}^{\text{scat}}. \quad (8)$$

Here the gradient and scattering parts are related to the real and imaginary parts of the particle polarizabilities:

$$\mathbf{F}^{\text{grad}} = \text{Re}(\alpha_m)\nabla W^{(p)} + \text{Re}(\alpha_d)\nabla W^{(v)}, \quad (9)$$

$$\mathbf{F}^{\text{scat}} = 2\omega \left[\text{Im}(\alpha_m)\mathbf{P}^{(p)} + \text{Im}(\alpha_d)\mathbf{P}^{(v)} \right]. \quad (10)$$

These laconic expressions reveal the direct relation between the scattering force (which is associated with the absorption of phonons by the particle) and canonical momentum density (3) of the acoustic field. Importantly, by substituting the polarizabilities (6) into Eqs. (9) and (10), one can check that the gradient force exactly coincides with the force found in earlier calculations for lossless particles [11,31,36,41] ($\mathbf{F}^{\text{scat}} = 0$ in this approximation), while the scattering-force part is equivalent to that found in recent works [35,37] considering viscous fluids. Remarkably, Eqs. (8) and (9) are entirely similar to the expressions for optical radiation forces on small Rayleigh particles or atoms [3,4,24–26,28–30,42–48]. In this manner, the electric- and magnetic-dipole terms in optical equations [28,45–48] (related to the electric and magnetic fields \mathbf{E} and \mathbf{H}) correspond to the monopole and dipole terms in the acoustic equations (related to the pressure and velocity fields p and \mathbf{v}).

Using the above correspondence between the optical and acoustic interactions, we readily find the acoustic torque on a small particle. The isotropic monopole moment cannot induce any torque, and the torque originates solely from the

dipole moment \mathbf{D} of the particle. In analogy with an electric dipole in an electric field [44–46,48,49], we obtain:

$$\mathbf{T} = \frac{1}{2}\text{Re}[\rho\mathbf{D}^* \times \mathbf{v}] = \omega \text{Im}(\alpha_d)\mathbf{S}. \quad (11)$$

The very simple Eq. (11) reveals the direct connection between the spin angular momentum density (4) of the acoustic field and the radiation torque on a small absorptive particle. To the best of our knowledge, this equation has not been derived before. This general connection (entirely similar to the optical case) is very important, because it was implied without rigorous grounds in the very recent experiment measuring acoustic spin [56]. Furthermore, this connection can be seen by comparing very recent numerical simulations of the acoustic torque and analytical calculations of the spin density in the particular case of acoustic Bessel beams [40,58]. Having the simple expression (11), acoustic torques on subwavelength isotropic particles can be readily found analytically in an arbitrary acoustic field.

Equations (7)–(11) are the main results of our work. Even though some of these are equivalent to the previously known expressions (such as gradient force on lossless particles), here the acoustic absorption, forces, and torque are for the first time presented in a unified and physically clear form. All these quantities are determined by the fundamental energy, momentum, and angular-momentum properties (2)–(4) of the field, as well as by the monopole and dipole particle polarizabilities (5) and (6). Note that all the quantities (6)–(11) behave as $\propto (ka)^3$, i.e., proportionally to the volume of the particle. This makes perfect physical sense and allows one to discriminate between various calculations of radiation forces and torques [see, e.g., torques in [33,39] with dependences $\propto (ka)^2$ and $\propto (ka)^5$, respectively]. For larger or lossless [$\text{Im}(\alpha_{m,d}) = 0$] particles, one has to involve higher-order terms in ka (see below).

Example: Forces and torques in an evanescent acoustic field.—To illustrate the above general theory, we consider a single evanescent acoustic wave with the pressure and velocity fields given by [56,57]:

$$p = A e^{ik_z z - \kappa x}, \quad \mathbf{v} = \frac{A}{\omega\rho} \begin{pmatrix} i\kappa \\ 0 \\ k_z \end{pmatrix} e^{ik_z z - \kappa x}. \quad (12)$$

Here, A is a constant amplitude, k_z is the longitudinal propagation constant, and κ is the vertical decay constant. This example is very simple yet generic. On the one hand, the evanescent wave can be treated as a plane wave with the complex wave vector $\mathbf{k} = k_z \bar{\mathbf{z}} + i\kappa \bar{\mathbf{x}}$ (the overbar denotes the unit vectors of the corresponding axes) [45,48] (see Fig. 2), which allows one to use the exactly solvable Mie scattering problem for numerical calculations of forces and torques [82]. On the other hand, the evanescent wave is inhomogeneous, and it carries the intensity gradient ∇W , canonical momentum \mathbf{P} , and spin \mathbf{S} , which exert the gradient force (9), scattering forces (10), and the radiation

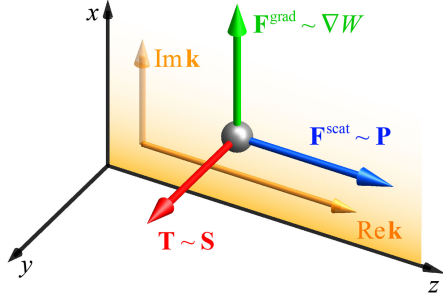


FIG. 2. A small spherical particle in the acoustic evanescent field (12), which can be treated as a plane wave with the complex wave vector $\mathbf{k} = k_z \hat{\mathbf{z}} + i\kappa \hat{\mathbf{x}}$. The gradient and scattering (radiation pressure) forces (9) and (10) are produced by the energy density gradient and canonical momentum (the real part of the wave vector), respectively. The torque (11) is produced by the transverse spin of the evanescent field [45,48,54,56,57].

torque (11) in the three mutually orthogonal directions [45,48,54,56,57] (see Fig. 2).

Figure 3 shows the dependences of these two forces and torque in the field (12) on the dimensionless particle radius ka for the cases of absorptive and lossless particles. We plot analytical results from Eqs. (9)–(11), valid only to leading order, $\propto (ka)^3$, and the exact numerical calculations using the Mie scattering solutions together with the momentum and angular momentum fluxes, similar to the Maxwell stress tensor approach in optics (see the Supplemental Material [65]). Note that the forces and torque are normalized by $F_0 = \pi\beta|A|^2 a^2/2$ and $T_0 = F_0/k$, so the analytical dependences (9)–(11) are linear in Fig. 3. For an absorptive particle, the analytical approximation agrees with the exact calculations for $ka \lesssim 0.3$.

To improve the accuracy of the analytical expressions (9)–(11), one can use the exact expressions for the Mie scattering coefficients a_0 and a_1 in Eq. (6) (see the Supplemental Material [65]). In this case, the monopole and dipole terms include all orders in ka , although the higher-order multipole terms are still neglected. The corresponding refined analytical dependences are shown in Fig. 3 by dashed curves, and these agree with the exact numerical calculation for $ka \lesssim 0.8$.

Note important peculiarities (also known in optics) of the scattering force and torque on lossless particles. First, the scattering (radiation-pressure) force vanishes only in the $(ka)^3$ order but is generally nonzero (see Fig. 3). The higher-order radiation-pressure force originates from the so-called “radiation friction” effect, which is described by small higher-order imaginary parts in the monopole and dipole polarizabilities [29,83,84], and also from the interference between the monopole and dipole fields [29]. Using the Mie coefficients a_0 and a_1 , we find that the higher-order imaginary parts of the polarizabilities can be written as $\tilde{\alpha}_m \simeq \alpha_m + (ik^3/4\pi)\alpha_m^2$ and $\tilde{\alpha}_d \simeq \alpha_d + (ik^3/12\pi)\alpha_d^2$, where

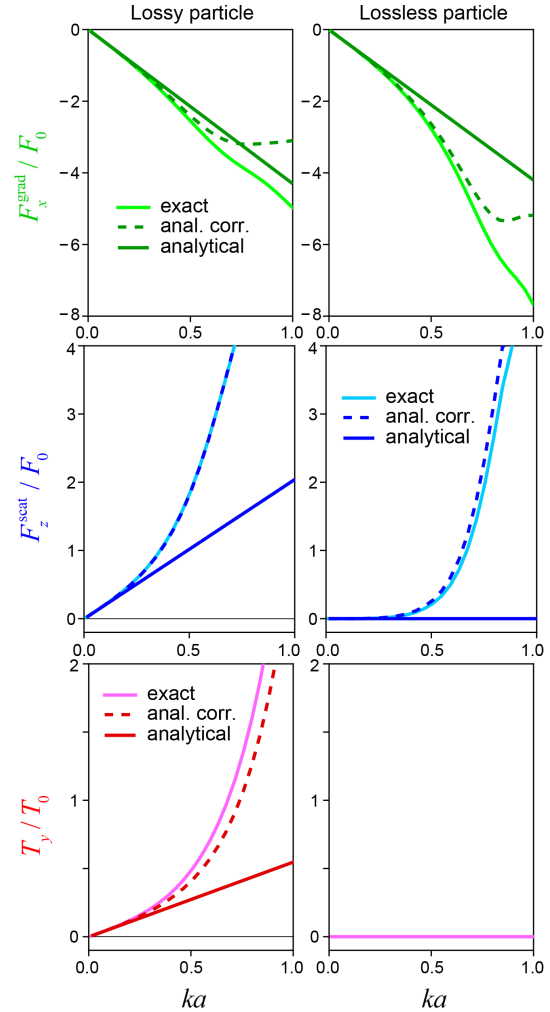


FIG. 3. Exact numerical and approximate analytical calculations of the gradient force, scattering (radiation-pressure) force, and torque on a spherical particle in the acoustic evanescent field (see Fig. 2). The field and particle parameters are these: $k_z/k = 1.34$, $\kappa/k = 0.89$, $\bar{\rho} = 2 + 0.5i$, $\bar{\beta} = 3 + 0.7i$ (the imaginary parts are omitted in the lossless-particle case). See discussion in the text.

$\alpha_{m,d}$ are the leading-order polarizabilities (6) (see the Supplemental Material [65]). Second, the radiation torque vanishes exactly for lossless spherical particles of any radius (Fig. 3). This is also similar to optics, where the radiation-friction effect produces the force but not the torque on the particle [27,49]. Thus, the simplest analytical approximations (6) and (11) coincide with the exact calculations in this case.

Conclusion.—We have presented a general theory of the interaction of a monochromatic acoustic wave field with a

small absorbing spherical particle. Our theory is based on the complex monopole and dipole polarizabilities of the particle, and it provides simple analytical expressions for the absorption rate, radiation forces (including the gradient and scattering forces), and radiation torque. Most importantly, these expressions reveal close connections with the fundamental local properties of the acoustic field: its energy, canonical momentum, and spin angular momentum densities [56–58]. Thus, one can now use acoustic forces and torques to measure the canonical momentum and spin densities of sound waves, and vice versa: use canonical momentum and spin to predict radiation forces and torques. Our work also unifies theoretical approaches to the acoustic and optical field-particle interactions and reveals close parallels between these. This provides a more fundamental understanding and new physical insights into these important problems.

We are grateful to Y. P. Bliokh, A. Y. Bekshaev, and Y. S. Kivshar for fruitful discussions. This work was partially supported by MURI Center for Dynamic Magneto-Optics via the Air Force Office of Scientific Research (AFOSR) (FA9550-14-1-0040), Army Research Office (ARO) (Grant No. W911NF-18-1-0358), Asian Office of Aerospace Research and Development (AOARD) (Grant No. FA2386-18-1-4045), Japan Science and Technology Agency (JST) (Q-LEAP program, and CREST Grant No. JPMJCR1676), Japan Society for the Promotion of Science (JSPS) (JSPS-RFBR Grant No. 17-52-50023 and JSPS-FWO Grant No. VS.059.18N), RIKEN-AIST Challenge Research Fund, the John Templeton Foundation, Russian Foundation for Basic Research (Project No. 19-32-90237), the Foundation for the Advancement of Theoretical Physics and Mathematics “BASIS,” and the Australian Research Council.

- [1] A. Ashkin, History of optical trapping and manipulation of small-neutral particle, atoms, and molecules, *IEEE J. Sel. Top. Quantum Electron.* **6**, 841 (2000).
- [2] D. G. Grier, A revolution in optical manipulation, *Nature* **424**, 810 (2003).
- [3] M. Dienerowitz, M. Mazilu, and K. Dholakia, Optical manipulation of nanoparticles: A review, *J. Nanophoton.* **2**, 021875 (2008).
- [4] S. Sukhov and A. Dogariu, Non-conservative optical forces, *Rep. Prog. Phys.* **80**, 112001 (2017).
- [5] T. Laurell, F. Petersson, and A. Nilsson, Chip integrated strategies for acoustic separation and manipulation of cells and particles, *Chem. Soc. Rev.* **36**, 492 (2007).
- [6] X. Ding, S.-C. S. Lin, B. Kiraly, H. Yue, S. Li, I.-K. Chiang, J. Shi, S. J. Benkovic, and T. J. Huang, On-chip manipulation of single microparticles, cells, and organisms using surface acoustic waves, *Proc. Natl. Acad. Sci. U.S.A.* **109**, 11105 (2012).
- [7] S. Stenholm, The semiclassical theory of laser cooling, *Rev. Mod. Phys.* **58**, 699 (1986).
- [8] S. Chu, The manipulation of neutral particles, *Rev. Mod. Phys.* **70**, 685 (1998).
- [9] W. D. Phillips, Laser cooling and trapping of neutral atoms, *Rev. Mod. Phys.* **70**, 721 (1998).
- [10] M. Aspelmeyer, T. J. Kippenberg, and F. Marquardt, Cavity optomechanics, *Rev. Mod. Phys.* **86**, 1391 (2014).
- [11] H. Bruus, Acoustofluidics 7: The acoustic radiation force on small particles, *Lab Chip* **12**, 1014 (2012).
- [12] X. Ding, P. Li, S.-C. S. Lin, Z. S. Stratton, N. Nama, F. Guo, D. Slotcavage, X. Mao, J. Shi, F. Costanzo, and T. J. Huang, Surface acoustic wave microfluidics, *Lab Chip* **13**, 3626 (2013).
- [13] R. V. Jones, Pressure of radiation, *Nature* **171**, 1089 (1953).
- [14] R. Loudon and C. Baxter, Contributions of John Henry Poynting to the understanding of radiation pressure, *Proc. R. Soc. A* **468**, 1825 (2012).
- [15] I. Brevik, Experiments in phenomenological electrodynamics and the electromagnetic energy-momentum tensor, *Phys. Rep.* **52**, 133 (1979).
- [16] R. N. C. Pfeifer, T. A. Nieminen, N. R. Heckenberg, and H. Rubinsztein-Dunlop, Momentum of an electromagnetic wave in dielectric media, *Rev. Mod. Phys.* **79**, 1197 (2007).
- [17] H. He, M. E. J. Friese, N. R. Heckenberg, and H. Rubinsztein-Dunlop, Direct Observation of Transfer of Angular Momentum to Absorptive Particles from a Laser Beam with a Phase Singularity, *Phys. Rev. Lett.* **75**, 826 (1995).
- [18] A. T. O’Neil, I. MacVicar, L. J. Allen, and M. J. Padgett, Intrinsic and Extrinsic Nature of the Orbital Angular Momentum of a Light Beam, *Phys. Rev. Lett.* **88**, 053601 (2002).
- [19] V. Garcés-Chávez, D. McGloin, M. J. Padgett, W. Dultz, H. Schmitzer, and K. Dholakia, Observation of the Transfer of the Local Angular Momentum Density of a Multiringed Light Beam to an Optically Trapped Particle, *Phys. Rev. Lett.* **91**, 093602 (2003).
- [20] K. Volke-Sepúlveda, A. O. Santillán, and R. R. Boulosa, Transfer of Angular Momentum to Matter from Acoustical Vortices in Free Space, *Phys. Rev. Lett.* **100**, 024302 (2008).
- [21] L. Zhang and P. L. Marston, Angular momentum flux of nonparaxial acoustic vortex beams and torques on axisymmetric objects, *Phys. Rev. E* **84**, 065601(R) (2011).
- [22] C. E. M. Demore, Z. Yang, A. Volovick, S. Cochran, M. P. MacDonald, and G. C. Spalding, Mechanical Evidence of the Orbital Angular Momentum to Energy Ratio of Vortex Beams, *Phys. Rev. Lett.* **108**, 194301 (2012).
- [23] A. Anhäuser, R. Wunenburger, and E. Brasselet, Acoustic Rotational Manipulation Using Orbital Angular Momentum Transfer, *Phys. Rev. Lett.* **109**, 034301 (2012).
- [24] G. A. Askar’yan, Effects of the gradient of a strong electromagnetic beam on electrons and atoms, *Sov. Phys. JETP* **15**, 1088 (1962).
- [25] J. P. Gordon, Radiation forces and momenta in dielectric media, *Phys. Rev. A* **8**, 14 (1973).
- [26] A. Ashkin and J. P. Gordon, Stability of radiation-pressure particle traps: An optical Earnshaw theorem, *Opt. Lett.* **8**, 511 (1983).
- [27] P. L. Marston and J. H. Crichton, Radiation torque on a sphere caused by a circularly-polarized electromagnetic wave, *Phys. Rev. A* **30**, 2508 (1984).

- [28] P. C. Chaumet and M. Nieto-Vesperinas, Time-averaged total force on a dipolar sphere in an electromagnetic field, *Opt. Lett.* **25**, 1065 (2000).
- [29] M. Nieto-Vesperinas, J. J. Sáenz, R. Gómez-Medina, and L. Chantada, Optical forces on small magnetodielectric particles, *Opt. Express* **18**, 11428 (2010).
- [30] D. B. Ruffner and D. G. Grier, Optical Forces and Torques in Nonuniform Beams of Light, *Phys. Rev. Lett.* **108**, 173602 (2012).
- [31] L. P. Gor'kov, On the forces acting on a small particle in an acoustical field in an ideal fluid, *Sov. Phys. Dokl.* **6**, 773 (1962).
- [32] T. Hasegawa, Comparison of two solutions for acoustic radiation pressure on a sphere, *J. Acoust. Soc. Am.* **61**, 1445 (1977).
- [33] F. H. Busse and T. G. Wang, Torque generated by orthogonal acoustic waves—Theory, *J. Acoust. Soc. Am.* **69**, 1634 (1981).
- [34] A. A. Doinikov, Acoustic radiation pressure on a compressible sphere in a viscous fluid, *J. Fluid Mech.* **267**, 1 (1994).
- [35] M. Settnes and H. Bruus, Forces acting on a small particle in an acoustical field in a viscous fluid, *Phys. Rev. E* **85**, 016327 (2012).
- [36] G. T. Silva and H. Bruus, Acoustic interaction forces between small particles in an ideal fluid, *Phys. Rev. E* **90**, 063007 (2014).
- [37] J. T. Karlsen and H. Bruus, Forces acting on a small particle in an acoustical field in a thermoviscous fluid, *Phys. Rev. E* **92**, 043010 (2015).
- [38] L. Zhang and P. L. Marston, Acoustic radiation torque on small objects in viscous fluids and connection with viscous dissipation, *J. Acoust. Soc. Am.* **136**, 2917 (2014).
- [39] G. T. Silva, Acoustic radiation force and torque on an absorbing compressible particle in an inviscid fluid, *J. Acoust. Soc. Am.* **136**, 2405 (2014).
- [40] L. Zhang, Reversals of Orbital Angular Momentum Transfer and Radiation Torque, *Phys. Rev. Applied* **10**, 034039 (2018).
- [41] X. D. Fan and L. Zhang, Trapping Force of Acoustical Bessel Beams on a Sphere and Stable Tractor Beams, *Phys. Rev. Applied* **11**, 014055 (2019).
- [42] M. V. Berry, Optical currents, *J. Opt. A* **11**, 094001 (2009).
- [43] K. Y. Bliokh, A. Y. Bekshaev, A. G. Kofman, and F. Nori, Photon trajectories, anomalous velocities and weak measurements: A classical interpretation, *New J. Phys.* **15**, 073022 (2013).
- [44] A. Canaguier-Durand, A. Cuche, C. Genet, and T. W. Ebbesen, Force and torque on an electric dipole by spinning light fields, *Phys. Rev. A* **88**, 033831 (2013).
- [45] K. Y. Bliokh, A. Y. Bekshaev, and F. Nori, Extraordinary momentum and spin in evanescent waves, *Nat. Commun.* **5**, 3300 (2014).
- [46] K. Y. Bliokh, Y. S. Kivshar, and F. Nori, Magnetoelectric Effects in Local Light-Matter Interactions, *Phys. Rev. Lett.* **113**, 033601 (2014).
- [47] A. Y. Bekshaev, K. Y. Bliokh, and F. Nori, Transverse Spin and Momentum in Two-Wave Interference, *Phys. Rev. X* **5**, 011039 (2015).
- [48] K. Y. Bliokh and F. Nori, Transverse and longitudinal angular momenta of light, *Phys. Rep.* **592**, 1 (2015).
- [49] M. Nieto-Vesperinas, Optical torque: Electromagnetic spin and orbital-angular-momentum conservation laws and their significance, *Phys. Rev. A* **92**, 043843 (2015).
- [50] E. Leader, The photon angular momentum controversy: Resolution of a conflict between laser optics and particle physics, *Phys. Lett. B* **756**, 303 (2016).
- [51] M. Antognozzi, C. R. Bermingham, R. L. Harniman, S. Simpson, J. Senior, R. Hayward, H. Hoerber, M. R. Dennis, A. Y. Bekshaev, K. Y. Bliokh, and F. Nori, Direct measurements of the extraordinary optical momentum and transverse spin-dependent force using a nano-cantilever, *Nat. Phys.* **12**, 731 (2016).
- [52] K. Y. Bliokh, A. Y. Bekshaev, and F. Nori, Dual electromagnetism: Helicity, spin, momentum and angular momentum, *New J. Phys.* **15**, 033026 (2013).
- [53] E. Leader and C. Lorce, The angular momentum controversy: What's it all about and does it matter?, *Phys. Rep.* **541**, 163 (2014).
- [54] A. Aiello, P. Banzer, M. Neugebauer, and G. Leuchs, From transverse angular momentum to photonic wheels, *Nat. Photonics* **9**, 789 (2015).
- [55] Y. Long, J. Ren, and H. Chen, Intrinsic spin of elastic waves, *Proc. Natl. Acad. Sci. U.S.A.* **115**, 9951 (2018).
- [56] C. Shi, R. Zhao, Y. Long, S. Yang, Y. Wang, H. Chen, J. Ren, and X. Zhang, Observation of acoustic spin, *Natl. Sci. Rev.*, **6**, 707 (2019).
- [57] K. Y. Bliokh and F. Nori, Transverse spin and surface waves in acoustic metamaterials, *Phys. Rev. B* **99**, 020301(R) (2019).
- [58] K. Y. Bliokh and F. Nori, Spin and orbital angular momenta of acoustic beams, *Phys. Rev. B* **99**, 174310 (2019).
- [59] L. D. Landau and E. M. Lifshitz, *Fluid Mechanics* (Butterworth-Heinemann, Oxford, 1987).
- [60] R. P. Cameron, S. M. Barnett, and A. M. Yao, Optical helicity, optical spin and related quantities in electromagnetic theory, *New J. Phys.* **14**, 053050 (2012).
- [61] L. Liu, A. Di Donato, V. Ginis, S. Kheifets, A. Amirzhan, and F. Capasso, Three-Dimensional Measurement of the Helicity-Dependent Forces on a Mie Particle, *Phys. Rev. Lett.* **120**, 223901 (2018).
- [62] C. F. Bohren and D. R. Huffman, *Absorption and Scattering of Light by Small Particles* (John Wiley & Sons, New York, 2008).
- [63] E. G. Williams, *Fourier Acoustics: Sound Radiation and Nearfield Acoustical Holography* (Elsevier, San Diego, 1999).
- [64] D. T. Blackstock, *Fundamentals of Physical Acoustics* (John Wiley & Sons, New York, 2001).
- [65] See Supplemental Material at <http://link.aps.org/supplemental/10.1103/PhysRevLett.123.183901> for the derivation of the monopole and dipole polarizabilities using the Mie theory and exact calculations of the acoustic force and torque, which includes Refs. [66–81].
- [66] K. Yosioka and Y. Kawasima, Acoustic radiation pressure on a compressible sphere, *Acta Acust. united Ac.* **5**, 167 (1955).
- [67] W. T. Doyle, Optical properties of a suspension of metal spheres, *Phys. Rev. B* **39**, 9852 (1989).
- [68] L. Jylhä, I. Kolmakov, S. Maslovski, and S. Tretyakov, Modeling of isotropic backward-wave materials composed of resonant spheres, *J. Appl. Phys.* **99**, 043102 (2006).

- [69] A. Moroz, Depolarization field of spheroidal particles, *J. Opt. Soc. Am. B* **26**, 517 (2009).
- [70] A. B. Evlyukhin, C. Reinhardt, A. Seidel, B. S. Luk'yanchuk, and B. N. Chichkov, Optical response features of Si-nanoparticle arrays, *Phys. Rev. B* **82**, 045404 (2010).
- [71] A. B. Evlyukhin, C. Reinhardt, U. Zywietz, and B. N. N. Chichkov, Collective resonances in metal nanoparticle arrays with dipole-quadrupole interactions, *Phys. Rev. B* **85**, 245411 (2012).
- [72] E. C. Le Ru, W. R. C. Somerville, and B. Augu  , Radiative correction in approximate treatments of electromagnetic scattering by point and body scatterers, *Phys. Rev. A* **87**, 012504 (2013).
- [73] P. J. Westervelt, The theory of steady forces caused by sound waves, *J. Acoust. Soc. Am.* **23**, 312 (1951).
- [74] A. J. Livett, E. W. Emery, and S. Leeman, Acoustic radiation pressure, *J. Sound Vib.* **76**, 1 (1981).
- [75] G. Maidanik, Torques due to acoustical radiation pressure, *J. Acoust. Soc. Am.* **30**, 620 (1958).
- [76] L. Zhang and P. L. Marston, Acoustic radiation torque and the conservation of angular momentum (L), *J. Acoust. Soc. Am.* **129**, 1679 (2011).
- [77] G. Maidanik, Acoustical radiation pressure due to incident plane progressive waves on spherical objects, *J. Acoust. Soc. Am.* **29**, 738 (1957).
- [78] F. G. Mitri and Z. E. A. Fellah, New expressions for the radiation force function of spherical targets in stationary and quasi-stationary waves, *Arch. Appl. Mech.* **77**, 1 (2007).
- [79] G. Gouesbet and G. Gr  han, *Generalized Lorenz-Mie Theories* (Springer, Berlin, 2011).
- [80] G. T. Silva, An expression for the radiation force exerted by an acoustic beam with arbitrary wavefront (L), *J. Acoust. Soc. Am.* **130**, 3541 (2011).
- [81] G. T. Silva, T. P. Lobo, and F. G. Mitri, Radiation torque produced by an arbitrary acoustic wave, *Europhys. Lett.* **97**, 54003 (2012).
- [82] A. Y. Bekshaev, K. Y. Bliokh, and F. Nori, Mie scattering and optical forces from evanescent fields: A complex-angle approach, *Opt. Express* **21**, 7082 (2013).
- [83] S. H. Simpson and S. Hanna, Orbital motion of optically trapped particles in Laguerre-Gaussian beams, *J. Opt. Soc. Am. A* **27**, 2061 (2010).
- [84] S. Albaladejo, R. Gomez-Medina, L. S. Froufe-Perez, H. Marinchio, R. Carminati, J. F. Torrado, G. Armelles, A. Garcia-Martin, and J. J. Saenz, Radiative corrections to the polarizability tensor of an electrically small anisotropic dielectric particle, *Opt. Express* **18**, 3556 (2010).



Light-induced rotation of dielectric microparticles around an optical nanofiber

GEORGIY TKACHENKO,^{1,6} IVAN TOFTUL,² CINDY ESPORLAS,¹ AILI MAIMAITI,^{1,3,4}
FAM LE KIEN,¹ VIET GIANG TRUONG,^{1,7} AND SÍLE NIC CHORMAIC^{1,5,8}

¹Okinawa Institute of Science and Technology Graduate University, Onna, Okinawa 904-0495, Japan

²Department of Physics and Engineering, ITMO University, Kronverkskiy prospekt 49197101, Saint-Petersburg, Russia

³Department of Physics, University College Cork, Cork, Ireland

⁴Current address: Department of Physics, Chalmers University of Technology, 412 96 Göteborg, Sweden

⁵Université Grenoble Alpes, CNRS, Grenoble INP, Institut Néel, 38000 Grenoble, France

⁶e-mail: georgiy.tkachenko@oist.jp

⁷e-mail: v.g.truong@oist.jp

⁸e-mail: sile.nicchormaic@oist.jp

Received 1 August 2019; revised 26 November 2019; accepted 9 December 2019 (Doc. ID 374441); published 14 January 2020

Evanescient electromagnetic fields near a waveguide can exert a transverse radiation force on scattering objects. To prove this experimentally, we demonstrate light-induced orbiting of isotropic, dielectric microparticles around an optical nanofiber that guides elliptically polarized, fundamental modes. The orbit frequency is proportional to the helicity of the coupled light. Interestingly, the observed motion is opposite to the energy flow circulation around the fiber. This result verifies the theoretically predicted negative optical torque on a sufficiently large particle in the vicinity of a nanofiber. © 2020 Optical Society of America under the terms of the [OSA Open Access Publishing Agreement](#)

<https://doi.org/10.1364/OPTICA.374441>

Spin angular momentum (SAM) carried by paraxial free-space beams of light can be transferred to a material object, causing it to rotate around its axis (i.e., spin), if the object is absorbing or anisotropic [1]. In contrast, orbital angular momentum (OAM) in beams with optical vortices can even set isotropic, non-absorbing particles into rotation [2,3]. In nonparaxial light, SAM and OAM can couple, leading to, for example, orbiting of isotropic particles trapped by a tightly focused, nonvortex beam [4] and to observable, spin-dependent, transverse shifts of the light itself [5,6]. Symmetry breaking in a system consisting of a scattering object at the interface between two media, under oblique illumination, produces an interesting spin-dependent optomechanical effect [7].

Evanescient electromagnetic fields, which accompany total internal reflection and guiding of light, exhibit even more complicated spin-orbit interactions. In particular, aside from the common axial SAM associated with polarization, such fields exhibit a SAM component perpendicular to the wave vector [8]. In addition, a material object in an evanescent field can experience a transverse spin-dependent force, as demonstrated experimentally by means of a nanocantilever [9] or an optically trapped Mie scattering particle [10] placed near a total internal reflecting glass surface.

The evanescent field around an optical nanofiber [11] guiding a quasi-circularly polarized fundamental mode is also expected to carry significant OAM that is transferable to material objects [12]. In spite of numerous demonstrations of particle trapping, propulsion [13–15], and binding [16,17] in the vicinity of optical nanofibers, orbital motion of particles in such systems has never been reported in the literature. The main reason for this lack of experimental evidence was the uncertainty about the polarization of light at the waist of a nanofiber waveguide. This uncertainty has been lifted only recently [18–20]. In this Letter, we present a clear demonstration of the spin-dependent optical torque by means of light-induced orbiting of isotropic microspheres around a single-mode optical nanofiber.

Let us consider the interaction between a spherical, dielectric particle (of radius R_p) and the evanescent field of a single-mode optical nanofiber (of radius R_f), as sketched in Fig. 1(a). The electric part of an *elliptically* polarized guided mode is

$$\mathcal{E} = \left(\sqrt{1 + \sigma} \mathcal{E}_{p=+1} + e^{i\phi} \sqrt{1 - \sigma} \mathcal{E}_{p=-1} \right) / \sqrt{2}, \quad (1)$$

where $\sigma \in [-1, 1]$ is the helicity parameter [6], $\phi \in [0, 2\pi]$ determines the orientation of the symmetry axes of the polarization ellipse in the xy plane, and $\mathcal{E}_p = (e_r \hat{r} + p e_\phi \hat{\phi} + e_z \hat{z}) e^{i\beta z + i p \varphi}$ is the electric part of the *quasi-circularly* polarized guided mode with a polarization rotation index $p = \sigma/|\sigma| = \pm 1$ [21]. Here, β is the propagation constant, and e_r , e_ϕ , and e_z are the cylindrical components of the mode-profile function of \mathcal{E}_p with $p = +1$. The azimuthal component of the Poynting vector of the elliptically polarized guided mode is $S_\phi = \sigma (e_z h_r^* - e_r h_z^*)/2$, where h_r and h_z are the components of the mode-profile function of the magnetic part, \mathcal{H}_p , of the guided mode with the polarization index $p = +1$. Since the longitudinal field components, e_z and h_z , are nonzero, we have $S_\phi^{(p)} \equiv S_\phi|_{\sigma=p} = p(e_z h_r^* - e_r h_z^*)/2 \neq 0$. It has been shown that $S_\phi^{(p=+1)} > 0$ and $S_\phi^{(p=-1)} < 0$ outside the nanofiber [21].

The light-induced force and torque on any object can be calculated if one knows the exact incident and scattered electromagnetic

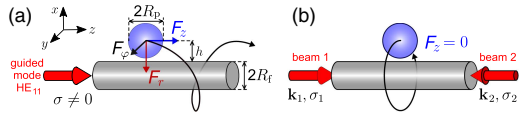


Fig. 1. (a) Isotropic, dielectric particle in the evanescent field of an elliptically polarized, fundamental mode of an optical nanofiber. Due to the azimuthal optical force, F_ϕ , the particle can rotate around the fiber. (b) We eliminate axial motion by using two counterpropagating beams with identical intensity profiles and opposite helicities, $\sigma_1 = -\sigma_2$.

waves. In our problem, the incident wave (here, the evanescent field) is well known [22]. Following the generalized Lorenz–Mie theory, the incident field can be decomposed into vector spherical harmonics, and the scattered field is thus found by application of boundary conditions [23,24]. Thence, the force and torque, respectively, can be found by integration of the linear and angular momenta over a surface enclosing the object. Note that although Lorenz–Mie theory is a generally accepted and fairly accurate semi-analytical approach to optomechanical calculations, it does not take into account multiple rescattering in the light–matter system.

The optical force exerted on a scattering particle near a nanofiber can be decomposed into the axial (F_z), radial (F_r), and azimuthal (F_ϕ) components [21] [see Fig. 1(a)]. Under F_r , the particle is attracted to the fiber surface and stays at $r = \sqrt{x^2 + y^2} \approx (R_f + R_p)$ (the inequality being due to surface roughness and Brownian motion). In this work, we aim at detection of the azimuthal force, F_ϕ , which sets the particle into orbital motion around the fiber. Since Brownian motion breaks mechanical contact between the particle and the fiber, the contribution from light-induced spinning of the particle to its azimuthal motion is expected to be negligible. According to our calculations, F_ϕ is much smaller than the axial force, F_z , which propels the particle towards $z > 0$. In order to prevent F_z from hindering detection of the light-induced rotation, we eliminate the axial motion by launching a second HE₁₁ mode propagating towards $z < 0$ into the nanofiber, with a power equal to that of the initial mode. This is realized experimentally by coupling two non-interfering (due to the lack of spatial coherence) laser beams into the opposite pigtailed of the tapered fiber [see Fig. 1(b)], where $\mathbf{k}_{1,2}$ are the wave vectors.

In principle, the rotation under F_ϕ could be studied if beam 1 were elliptically polarized ($\sigma_1 = \sigma \neq 0$) and beam 2 were linearly polarized ($\sigma_2 = 0$). However, such a beam 2 would produce a mode with an axially asymmetric intensity profile [25], and the particle would tend to stop at the “hot spots,” unless $|\sigma_1| \approx 1$. Since we consider the complete spectrum of σ , we set the polarization of beam 2 to also be elliptical, with $\sigma_2 = -\sigma_1$. In this case, the total azimuthal force is the sum of the contributions from both beams.

Once F_ϕ is known, the orbiting frequency of the particle at equilibrium can be easily calculated from the force balance equation, $F_\phi + F_{fr} = 0$, where F_{fr} is the friction. In our experiments, the particle is immersed in water, which produces a friction of $F_{fr} = -\gamma v$, where v is the linear velocity of the particle’s center, and γ is the drag coefficient. As demonstrated by Marchington *et al.* [26], an appropriate description of the friction for a microsphere in the evanescent field can be obtained using the lubrication correction [27] $\gamma = \gamma_0[(8/15)\ln(h/R_p - 1) - 0.9588]$, where $\gamma_0 = 6\pi\eta R_p$ is the Stokes drag, η is the dynamic viscosity of the fluid ($\eta \approx 1$ mPas for water at room temperature), and the distance

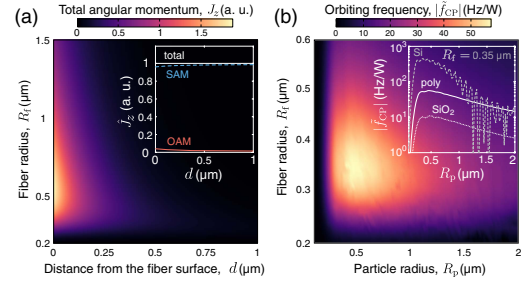


Fig. 2. Simulation results. (a) Density of the total angular momentum of light near a nanofiber (in water) guiding a fundamental mode with $\sigma = 1$. Inset: total angular momentum per photon and its orbital and spin components. (b) Orbiting frequency for a polystyrene particle, as a function of radii of the particle and the fiber. Inset: frequency at the optimum fiber radius ($R_f = 0.35 \mu\text{m}$) for three different particle materials: silicon, polystyrene, and silica.

$h = r - R_f$ [see Fig. 1(a)] depends on the particle surface roughness. We note that the above formula for γ is valid only for large enough particles, $R_p > 0.25 \mu\text{m}$ [27]. The absolute value of the particle rotation frequency around a fiber when both beams are circularly polarized (CP) can thus be expressed as

$$|f_{CP}| = |v|/[2\pi(h + R_f)] = |F_\phi|/[2\pi\gamma(h + R_f)]. \quad (2)$$

As follows from our simulations, in the general case of elliptical polarization (EP), the azimuthal force and the corresponding frequency, f_{EP} , are proportional to $\sigma = \sigma_1$, with opposite signs:

$$f_{EP} = -\sigma |f_{CP}|. \quad (3)$$

This result is consistent with the theoretical findings of Le Kien and Rauschenbeutel [21], for the relevant range of the size parameter, $n_m k R_p$, where n_m is the refractive index of the medium. For convenience, we normalize the rotation frequency by the total optical power, P . That is, we use $\tilde{f}_{CP,EP} = f_{CP,EP}/P$.

Our theoretical findings are summarized in Fig. 2, where J_z is the z component of the total angular momentum carried by the field near an optical nanofiber. In order to better understand the structure of angular momentum, we calculated the SAM and OAM densities [see the inset in Fig. 2(a)] using the canonical expressions [28,29]. Although the majority of J_z comprises the spin part, both components of the total angular momentum can contribute to orbital motion of particles in the vicinity of a nanofiber [30]. As shown in Fig. 2(b), the orbiting frequency is expected to reach about 57 Hz/W for a 1- μm (in diameter) polystyrene particle. As one can see in the inset, the maximum frequency scales with the refractive index: it equals 11 Hz/W for silicon dioxide ($n = 1.45$) and 450 Hz/W for silicon ($n = 3.67$). In practice, one should also consider the Brownian motion, which is inversely proportional to R_p : smaller particles would exhibit longer thermal displacements and therefore a weaker interaction with the evanescent field, which decreases dramatically with the distance from the fiber, d . As a reasonable compromise, we chose to use polystyrene beads with a diameter $2R_p = 3 \mu\text{m}$. Under these conditions, the expected frequency for CP input is $|\tilde{f}_{CP}| \approx 21.2$ Hz/W.

Our experimental setup is sketched in Fig. 3(a). The nanofiber is fabricated by controlled heating and pulling [31] of a step-index single-mode optical fiber (SM980G80 by Thorlabs, Inc.).

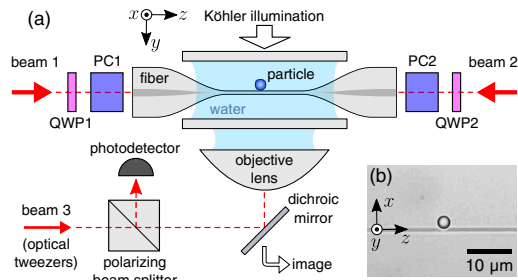


Fig. 3. (a) Experimental setup (not to scale): once the polarization transformations in the tapered fiber are reversed by the polarization compensators, PC1 and PC2, we set the values of σ_1 and $\sigma_2 = -\sigma_1$, by rotating the quarter-wave plates, QWP1 and QWP2. (b) Transmission image of a 3- μm polystyrene particle optically captured at the waist of a nanofiber.

The small tapering angles of 3 mrad provide adiabatic coupling [32,33] between the fundamental modes in the fiber pigtailed and those in the 2-mm-long cylindrical waist region having a radius of $R_f = 0.33 \pm 0.04 \mu\text{m}$ (measured over a set of five nanofibers). The fiber pigtailed are coupled to laser beams 1 and 2 from the same source (Ventus, Laser Quantum Ltd., emission wavelength $\lambda = 1.064 \mu\text{m}$). The initial linear polarization of the beams (along x and y for beams 1 and 2, respectively) is changed into elliptical by means of two quarter-wave plates, QWP1 and QWP2, with their slow axes oriented at equal angles, $\theta_{\text{QWP1}} = \theta_{\text{QWP2}} = \theta$, with respect to x , measured from the point of view of the receiver. This results in $\sigma = \sin 2\theta = -S_3$, where S_3 is the third Stokes parameter in beam 1.

A nanofiber sample is immersed into 0.3 mL of deionized water with 3- μm polystyrene particles (Phosphorex, Inc.) and sandwiched between two glass cover slips separated by 1.5-mm-thick spacers. The sample is imaged by a video camera (DCC3240C by Thorlabs, Inc.) through a water-immersion objective lens (Zeiss Plan-Apochromat, $63\times/1.00\text{w}$) under Köhler illumination [see Fig. 3(b)]. Individual particles are picked up from the bottom slip using an optical tweezers realized by focusing the collimated beam 3 (from the same laser) with the same objective lens. The polarizing beam-splitter cube transmits y -polarized beam 3 and is subsequently used for detection (Si amplified photodetector PDA10A2 by Thorlabs, Inc.) of the laser light escaping from the nanofiber due to scattering by the particle.

Due to uncontrolled bends, twists, or geometrical inhomogeneities, the fiber does not maintain polarization of guided light. In order to control the polarization state at the nanofiber waist, we reverse the unknown polarization transformations for both beams using two free-space compensators, PC1 and PC2. The compensation procedure described elsewhere [20] is based on self-scattering from the waist imaged by a second video camera, replacing the photodetector for this purpose.

Experimental results with $|\sigma| = 1$ are shown in Fig. 4. Orbital motion of the particle around the fiber causes clear quasi-periodical beatings of the measured voltage [see Fig. 4(a)]. The orbiting frequency, \tilde{f}_{CP} , scales linearly with optical power, as summarized in Fig. 4(b) for three different nanofibers. The data were fitted to Eq. (2) with an adjustable drag coefficient, γ_{fit} . The resultant frequency, $\tilde{f}_{\text{CP,fit}} = 19.2 \text{ Hz/W}$, is lower than the expected value

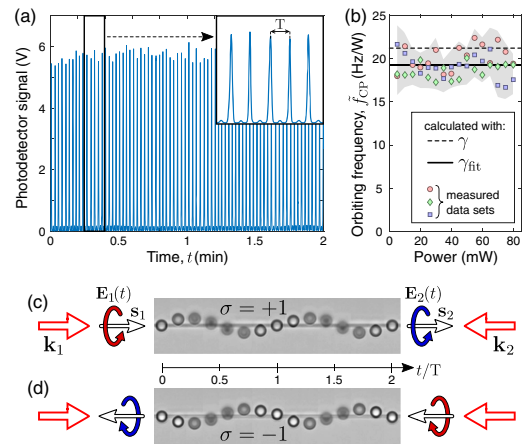


Fig. 4. Experimental results for a CP input ($R = \text{right}$, $L = \text{left}$). (a) Beatings in the detector signal acquired with an optical power of 15 mW in each beam. The zoomed-in view (inset) shows the local period, T . (b) Orbiting frequency versus power in each beam, at $\sigma = +1$. Markers: measured data sets for three samples; gray area: combined standard deviation range. Dashed line: frequency expected for the drag coefficient γ ; solid line: the best fit to the data with γ_{fit} . (c), (d) Time-lapse compilation of images for $\sigma = +1$ (c) and $\sigma = -1$ (d).

by about 9%, a small discrepancy given the complexity of the hydrodynamic problem, a complete solution of which is beyond the scope of this study.

When the sign of σ is reversed, the particle rotates in the opposite direction, with nearly the same period, T , as demonstrated by Visualization 1 and Visualization 2 and the corresponding time-lapse compilations of images in Figs. 4(c) and 4(d), where $\mathbf{s}_{i=1,2} = \sigma_i \mathbf{k}_i / k_i$, and the curved arrows denote the rotation of the electric field vector, \mathbf{E} , in the xy plane for each beam, from the point of view of the receiver. These arrows also indicate the circulation direction of the energy flow around the nanofiber [21].

The results for $\sigma \neq 1$ are presented in Fig. 5, where solid lines show the simulated frequency, $\tilde{f}_{\text{EP}}(\sigma)$, and each error bar is the standard deviation range for at least 20 T duration. For this data set, Eqs. (3) and (2) were applied, without adjustable parameters. As confirmed by Fig. 5(b), the transverse spin-dependent radiation force on the particle is proportional to the SAM projection on the propagation direction, with opposite sign. The observed light-induced rotation is antiparallel to the azimuthal component of the energy flow around the nanofiber [21]. This counterintuitive “negative” radiation torque (OAM-induced) is due to the dominant forward scattering. This is associated with multipolar interference in Mie scattering from large enough particles, $R_p > \lambda / (2\pi n_m) \approx 0.13 \mu\text{m}$. The associated forward scattering of light relates our findings to previous demonstrations of “negative” radiation forces [34–36].

Interestingly, σ influences not only the frequency, but also the particle's trajectory. For CP input ($|\sigma| = 1$), it is close to a circle in the xy plane (see Visualization 1 and Visualization 2). When the polarization is elliptical ($|\sigma| < 1$), the trajectory acquires a figure-of-eight shape, with longer trips along z for smaller $|\sigma|$ (see Visualization 3). This distortion is due to the lack of axial symmetry in the intensity distribution for counterpropagating

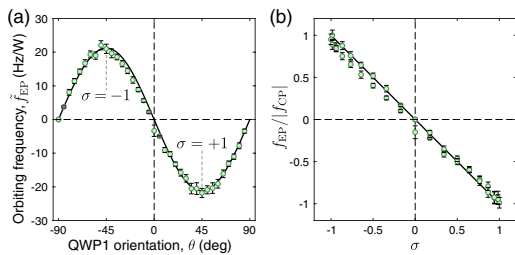


Fig. 5. Experimental results for an EP input and 15-mW power in each beam. (a), (b) Markers: measured orbiting frequency versus QWP1 orientation (a) or the k-projection of SAM in beam 1 (b). Solid lines: simulation using Eq. (3), with $\sigma = \sin 2\theta$.

elliptically polarized modes [25]. Indeed, for $|\sigma|$ close to zero, the intensity maxima for beams 1 and 2 are aligned parallel to the x and y axes, respectively. Hence, the particle is accelerated towards $z > 0$ or $z < 0$ when passing through the xz or yz planes.

Here, we presented a clear experimental demonstration of a transverse, spin-dependent radiation force acting on material objects in evanescent electromagnetic fields. In contrast to previous studies on the subject, we used optical nanofibers, which provide extraordinarily clean experimental conditions, with high visibility and repeatability of measurements. An indispensable prerequisite of this experiment was the complete polarization control of light at the nanofiber waist. In addition to its use for verification of the above fundamental concept, the examined microparticle–nanofiber system could find an application in microfluidics, e.g., as an optically addressed rotary pump.

Funding. Okinawa Institute of Science and Technology Graduate University; Japan Society for the Promotion of Science (P18367); Russian Foundation for Basic Research (19-32-90237).

Acknowledgment. We thank J. M. Ward and K. Karlsson for managing the fiber pulling rig.

REFERENCES

- M. E. J. Friese, T. A. Nieminen, N. R. Heckenberg, and H. Rubinsztein-Dunlop, *Nature* **394**, 348 (1998).
- A. T. O’Neil, I. MacVicar, L. Allen, and M. J. Padgett, *Phys. Rev. Lett.* **88**, 053601 (2002).
- V. Garcés-Chávez, D. McGloin, M. J. Padgett, W. Dultz, H. Schmitzer, and K. Dholakia, *Phys. Rev. Lett.* **91**, 093602 (2003).
- Y. Zhao, J. S. Edgar, G. D. M. Jeffries, D. McGloin, and D. T. Chiu, *Phys. Rev. Lett.* **99**, 073901 (2007).
- N. B. Baranova, A. Y. Savchenko, and B. Y. Zel’dovich, *JETP Lett.* **59**, 232 (1994).
- K. Y. Bliokh, Y. Gorodetski, V. Kleiner, and E. Hasman, *Phys. Rev. Lett.* **101**, 030404 (2008).
- S. Sukhov, V. Kajorndejnukul, R. R. Naraghi, and A. Dogariu, *Nat. Photonics* **9**, 809 (2015).
- K. Y. Bliokh, A. Y. Bekshaev, and F. Nori, *Nat. Commun.* **5**, 3300 (2014).
- M. Antognozzi, C. R. Bermingham, R. L. Harniman, S. Simpson, J. Senior, R. Hayward, H. Hoerber, M. R. Dennis, A. Y. Bekshaev, K. Y. Bliokh, and F. Nori, *Nat. Phys.* **12**, 731 (2016).
- L. Liu, A. Di Donato, V. Ginis, S. Kheifets, A. Amirzhan, and F. Capasso, *Phys. Rev. Lett.* **120**, 223901 (2018).
- L. Tong, F. Zi, X. Guo, and J. Lou, *Opt. Commun.* **285**, 4641 (2012).
- F. Le Kien, V. I. Balykin, and K. Hakuta, *Phys. Rev. A* **73**, 053823 (2006).
- G. Brambilla, G. S. Murugan, J. S. Wilkinson, and D. J. Richardson, *Opt. Lett.* **32**, 3041 (2007).
- L. Xu, Y. Li, and B. Li, *New. J. Phys.* **14**, 033020 (2012).
- A. Maimaiti, V. G. Truong, M. Sergides, I. Gusachenko, and S. Nic Chormaic, *Sci. Rep.* **5**, 9077 (2015).
- M. C. Frawley, I. Gusachenko, V. G. Truong, M. Sergides, and S. Nic Chormaic, *Opt. Express* **22**, 16322 (2014).
- A. Maimaiti, D. Holzmann, V. G. Truong, H. Ritsch, and S. Nic Chormaic, *Sci. Rep.* **6**, 30131 (2016).
- F. Lei, G. Tkachenko, J. M. Ward, and S. Nic Chormaic, *Phys. Rev. Appl.* **11**, 064041 (2019).
- M. Joos, A. Bramati, and Q. Glorieux, *Opt. Express* **27**, 18818 (2019).
- G. Tkachenko, F. Lei, and S. Nic Chormaic, *J. Opt.* **21**, 125604 (2019).
- F. Le Kien and A. Rauschenbeutel, *Phys. Rev. A* **88**, 063845 (2013).
- F. Le Kien, T. Busch, V. G. Truong, and S. Nic Chormaic, *Phys. Rev. A* **96**, 023835 (2017).
- J. P. Barton, D. R. Alexander, and S. A. Schaub, *J. Appl. Phys.* **64**, 1632 (1988).
- E. Almaas and I. Brevik, *J. Opt. Soc. Am. B* **12**, 2429 (1995).
- F. Le Kien, J. Q. Liang, K. Hakuta, and V. I. Balykin, *Opt. Commun.* **242**, 445 (2004).
- R. F. Marchington, M. Mazilu, S. Kuriakose, V. Garcés-Chávez, P. J. Reece, T. F. Krauss, M. Gu, and K. Dholakia, *Opt. Express* **16**, 3712 (2008).
- G. P. Krishnan and D. T. Leighton, *Phys. Fluids* **7**, 2538 (1995).
- K. Y. Bliokh, A. Y. Bekshaev, and F. Nori, *Phys. Rev. Lett.* **119**, 073901 (2017).
- M. F. Picardi, K. Y. Bliokh, F. J. Rodríguez-Fortuño, F. Alpeggiani, and F. Nori, *Optica* **5**, 1016 (2018).
- F. Le Kien, T. Busch, V. G. Truong, and S. Nic Chormaic, *Opt. Express* **27**, 15046 (2019).
- J. M. Ward, A. Maimaiti, V. H. Le, and S. Nic Chormaic, *Rev. Sci. Instrum.* **85**, 111501 (2014).
- J. D. Love, W. M. Henry, W. J. Stewart, R. J. Black, S. Lacroix, and F. Gonthier, *IEEE Proc. J—Optoelectron.* **138**, 343 (1991).
- Y. Jung, G. Brambilla, and D. J. Richardson, *Opt. Express* **16**, 14661 (2008).
- S. Sukhov and A. Dogariu, *Phys. Rev. Lett.* **107**, 203602 (2011).
- J. Chen, J. Ng, Z. Lin, and C. T. Chan, *Nat. Photonics* **5**, 531 (2011).
- C. E. M. Démoré, P. M. Dahl, Z. Yang, P. Glynne-Jones, A. Melzer, S. Cochran, M. P. MacDonald, and G. C. Spalding, *Phys. Rev. Lett.* **112**, 174302 (2014).

Optical binding via surface plasmon polariton interference

Natalia Kostina,¹ Mihail Petrov,¹ Aliaksandra Ivinskaya,¹ Sergey Sukhov,^{2,3} Andrey Bogdanov,¹ Ivan Toftul,¹ Manuel Nieto-Vesperinas,⁴ Pavel Ginzburg,^{1,5} and Alexander Shalin^{1,6}

¹*ITMO University, Department of Nanophotonics and Metamaterials, Saint-Petersburg, 199034, Russia*

²*CREOL, University of Central Florida, Orlando, Florida, 32816-2700, USA*

³*Kotelnikov Institute of Radio Engineering and Electronics of Russian Academy of Science (Ulyanovsk Branch), Ulyanovsk, 432071, Russia*

⁴*Instituto de Ciencia de Materiales de Madrid, Consejo Superior de Investigaciones Científicas, Campus de Cantoblanco, Madrid E-28049, Spain*

⁵*School of Electrical Engineering, Tel Aviv University, Tel Aviv, 6997801, Israel*

⁶*Ulyanovsk State University, Ulyanovsk, 432017, Russia*



(Received 29 May 2018; revised manuscript received 27 December 2018; published 13 March 2019)

Optical binding allows creation of mechanically stable nanoparticle configurations owing to formation of self-consistent optical trapping potentials. While the classical diffraction limit prevents achieving deeply subwavelength arrangements, auxiliary nanostructures enable tailoring optical forces via additional interaction channels. Here, a dimer configuration next to a metal surface was analyzed in detail and the contribution of surface plasmon polariton waves was found to govern the interaction dynamics. It is shown that the interaction channel, mediated by resonant surface waves, enables achieving subwavelength stable dimers. Furthermore, the vectorial structure of surface modes allows binding between two dipole nanoparticles along the direction of their dipole moments, contrary to vacuum binding, where a stable configuration is formed in the direction perpendicular to the polarization of the dipole moments. In addition, the enhancement by one order of magnitude of the optical binding stiffness is predicted owing to the surface plasmon polariton interaction channel. These phenomena pave the way for developing new flexible optical manipulators, allowing for control over a nanoparticle trajectory on subwavelength scales and opening opportunities for optical-induced anisotropic (i.e., with different periods along the field polarization as well as perpendicular to it) organization of particles on a plasmonic substrate.

DOI: [10.1103/PhysRevB.99.125416](https://doi.org/10.1103/PhysRevB.99.125416)

I. INTRODUCTION

Light carries momentum which can influence matter through optical forces, enabling manipulation of micro- and nanoscale objects [1] and even atom ensembles [2]. The methods of optical tweezing [3,4] rely on attraction of small objects to regions of high field intensity. Spatially nonuniform intensity distributions used for positioning microobjects at a predefined pattern can be achieved with a nanostructured environment or by interference of several beams. Yet, since the early years of optical tweezing experiments, it has been discovered that several particles tend to self-organize under homogeneous illumination [5,6]. This effect is referred to as transverse optical binding. The interference between incident and scattered light, owing to its interaction with particles, results in the formation of a set of potential wells defining stable positions of particles. Optical binding has been intensively studied both theoretically [7–11] and experimentally [12–16], including as a prospective method for self-organization of particles. However, the strength of optical binding drops rapidly with nanoparticle size as the scattering is proportional to the nanoparticle radius R as $\sim R^6$. On the other hand, the viscous damping is also reduced for smaller particles, which makes the fluctuations and stochastic processes in liquids to be more influential. As a result, for reliable optical control of subwavelength nanoparticles, strong optical fields are

required. In order to achieve this with available laser intensities, the optical binding can be enhanced by localized plasmon resonances of the nanoparticles [8,17,18]. The localized plasmons can improve trapping efficiency at hot spots of a corrugated metal surface [19,20] or provide particle acceleration against beam direction in plasmonic V-grooves [21]. Three-dimensional structures of plasmonic particles or alternating metal-dielectric layers, such as metamaterials [22–24], can be also employed to trap or manipulate nanoparticles, e.g., for realization of optical pulling forces attracting nanoparticles to a light source [25,26]. In the context of optical binding, flat metal surfaces may be also very relevant. The excitation of propagating surface plasmon polaritons (SPPs) and induced optical thermal forces are responsible for self-organization of micron-sized nanoparticles [27]. Moreover, the direct momentum transfer from SPP to micron-sized particles [28,29] can be used for enhancing the optical forces near planar metallic surfaces, which can be used for sorting and ordering of nanoparticles [15,30,31]. Recently, it was suggested that SPP modes can open the way for manipulating the optical forces acting on nanosized particles by the directional excitation of the propagating SPP modes [32–37].

Here, we propose another mechanism of transverse optical binding via excitation of SPP modes (*SPP binding*) near a metallic planar interface. This mechanism is based on far-field interaction through the interference of SPP waves

and it is different to the formation of resonant nanoparticle molecules due to their near-field interaction [17,18,38,39]. Compared to common transverse binding in a free space (*photon binding*) [40], the proposed approach has several advantages: (i) It can enhance the binding effect for small nanoparticles due to the resonant excitation of SPP modes; (ii) the distance between the bound pair of nanoparticles is defined by the SPP effective wavelength and, thus, can be significantly smaller, surpassing the diffraction limit; and (iii) the binding occurs in the direction of dipole polarization in accordance with the directivity of SPP emission, which differs from the case of a free space binding, where stable configurations are formed in the direction perpendicular to the dipole moments. In this paper, we theoretically show how SPP-based transverse optical binding can bring new features.

II. MODEL AND MAIN EQUATIONS

We consider two identical nanoparticles placed close to a planar metallic interface at coordinates \mathbf{r}_1 and \mathbf{r}_2 in the field of a normally incident plane wave (see Fig. 1). We assume that the nanoparticles have radius R and are made of a dielectric material with permittivity ε . In the dipole approximation, the radius of the nanoparticles R is much smaller than the typical scale of the electric field variations. In this limit, the time-averaged optical force acting on a nanoparticle is given by the expression [41]

$$\mathbf{F} = \frac{1}{2} \text{Re} \sum_i p_i^* \nabla E_i(\mathbf{r}, \omega), \quad (1)$$

where $E_i(\mathbf{r}, \omega)$ is the i th component of a local field.

The dipole moment of a nanoparticle $\mathbf{p}(\mathbf{r})$ is defined as $\mathbf{p}(\mathbf{r}) = \alpha(\omega)\mathbf{E}(\mathbf{r})$, where $\alpha(\omega)$ is the vacuum dipole polarizability corrected with account for retardation effects:

$$\frac{1}{\alpha} = \frac{1}{\alpha_0} - \frac{ik_0^3}{6\pi\varepsilon_0}, \quad \alpha_0 = 4\pi\varepsilon_0 R^3 \frac{\varepsilon - \varepsilon_1}{\varepsilon + 2\varepsilon_1}, \quad (2)$$

where k_0 is the wave vector in a free space, ε_0 is the vacuum permittivity, and α_0 is the static polarizability, assuming the particle is a sphere. The local electric field includes the

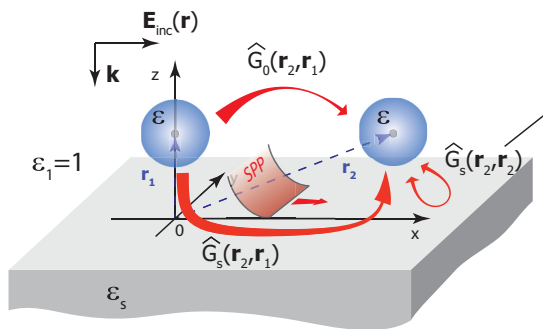


FIG. 1. The scheme of the problem. Nanoparticles with permittivity ε are positioned at equal distances from a surface $z_1 = z_2 = z$. The incident wave is described by the wave vector \mathbf{k} and the electric field $\mathbf{E}_{\text{inc}}(\mathbf{r})$. We assume that the permittivity of the upper half-space is $\varepsilon_1 = 1$ and ε_s is the permittivity of silver substrate.

incident plane wave, the multiply rescattered field between particles via free-space and substrate channels, and the self-induced contribution of each particle through the reflection from the substrate. The local field is given by

$$\mathbf{E}(\mathbf{r}) = \mathbf{E}_0(\mathbf{r}) + \frac{k_0^2}{\varepsilon_0} \widehat{G}(\mathbf{r}, \mathbf{r}_1) \mathbf{p}_1 + \frac{k_0^2}{\varepsilon_0} \widehat{G}(\mathbf{r}, \mathbf{r}_2) \mathbf{p}_2. \quad (3)$$

Here, the first term on the right-hand side \mathbf{E}_0 is the amplitude of the external plane wave $\mathbf{E}_{\text{inc}}(\mathbf{r})$ with the term corresponding to the reflection from the metallic substrate taken into account, while the second and third terms correspond to the field generated by the first and second nanoparticles, respectively. The total Green's function $\widehat{G}(\mathbf{r}, \mathbf{r}_0) = \widehat{G}_0(\mathbf{r}, \mathbf{r}_0) + \widehat{G}_s(\mathbf{r}, \mathbf{r}_0)$ is a sum of the scattered \widehat{G}_s and vacuum \widehat{G}_0 components, respectively [43]. The sum of terms on the right-hand side of Eq. (3) are the fields of the two excited dipoles, resulting in the formation of the interference pattern. The polarizability tensor can be simplified with respect to the self-action Green's function component $\widehat{G}_s(\mathbf{r}_i, \mathbf{r}_i)$:

$$\mathbf{p}_i = \widehat{\alpha}_{i,\text{eff}}^s \left[\mathbf{E}_0(\mathbf{r}_i) + \frac{k_0^2}{\varepsilon_0} \widehat{G}(\mathbf{r}_i, \mathbf{r}_j) \mathbf{p}_j \right], \quad i = 1, 2, j = 2, 1.$$

Here, we have introduced the effective polarizability tensor $\widehat{\alpha}_{i,\text{eff}}^s$ as follows:

$$\widehat{\alpha}_{i,\text{eff}}^s(\mathbf{r}_i, \omega) = \alpha(\omega) \left[\widehat{I} - \alpha(\omega) \frac{k_0^2}{\varepsilon_0} \widehat{G}_s(\mathbf{r}_i, \mathbf{r}_i, \omega) \right]^{-1}, \quad i = 1, 2, \quad (4)$$

if \widehat{I} corresponds to the unitary dyad. This tensor gives a correction of a vacuum polarizability $\alpha(\omega)$ accounting for the nanoparticle self-action through the substrate [33,43]. This tensor is diagonal, as is $\widehat{G}_s(\mathbf{r}_i, \mathbf{r}_i)$ in the case of a flat isotropic substrate [43].

Without loss of generality, we fix the position of the first particle in the origin of the coordinate system at $x_1 = 0$ and $y_1 = 0$ and will consider the force acting on the second particle only. Computing the field at the point of the dipole according to the expression in Eq. (3), one can achieve a system of equations for the dipole moments \mathbf{p}_1 and \mathbf{p}_2 (see Appendix A), and, in the special case of normal incidence of the plane wave, the expression for the dipole moments can be simplified even further:

$$\mathbf{p}_i = \widehat{\alpha}_{i,\text{eff}}^R \mathbf{E}_0(\mathbf{r}_i), \quad (5)$$

$$\begin{aligned} \widehat{\alpha}_{i,\text{eff}}^R(\mathbf{r}_i, \omega) &= \alpha(\omega) \left[\widehat{I} - \alpha(\omega) \frac{k^2}{\varepsilon_0} \widehat{G}_s(\mathbf{r}_i, \mathbf{r}_i, \omega) \right. \\ &\quad \left. - \frac{k^4}{\varepsilon_0^2} \alpha(\omega) \widehat{G}(\mathbf{r}_i, \mathbf{r}_j) \widehat{\alpha}_{j,\text{eff}}^s(\mathbf{r}_j, \omega) \widehat{G}(\mathbf{r}_j, \mathbf{r}_i) \right]^{-1} \\ &\quad \times \left[\widehat{I} + \frac{k^2}{\varepsilon_0} \widehat{G}(\mathbf{r}_i, \mathbf{r}_j) \widehat{\alpha}_{j,\text{eff}}^s(\mathbf{r}_j, \omega) \right], \\ &\quad i = 1, 2 \quad j = 2, 1. \end{aligned} \quad (6)$$

Now, the polarizability $\widehat{\alpha}_{\text{eff}}^R$ (see Appendix A for the details) includes all the interaction channels: (i) the self-action of the nanoparticles through the substrate and (ii) the cross-action of the two nanoparticles via the vacuum and the

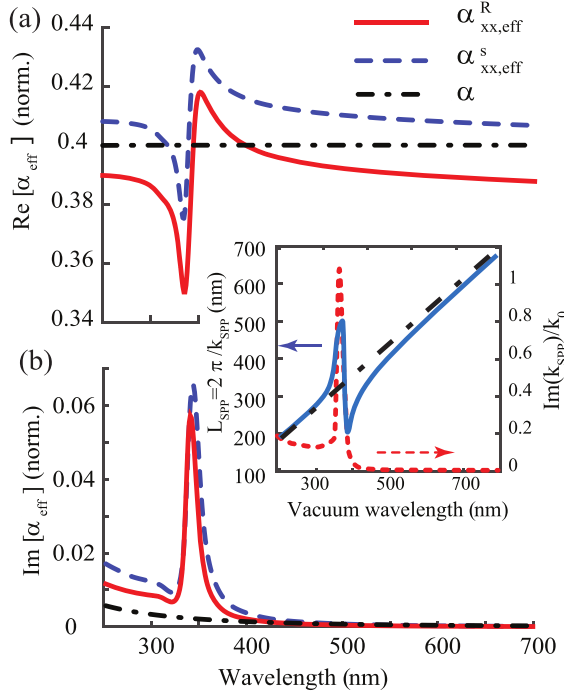


FIG. 2. The spectrum of the real (a) and imaginary (b) parts of the xx components of the effective polarizability tensor $\hat{\alpha}_{\text{eff}}^s$ (blue dashed line) and $\hat{\alpha}_{\text{eff}}^R$ (red solid line) shown along with the vacuum polarizability α (black dash-dotted line). The polarizability is normalized over $4\pi\epsilon_0 R^3$ and calculated for a spherical nanoparticle of radius $R = 15$ nm with $\epsilon = 3$ whose center is located above the surface at $z = 20$ nm. The inset shows the dependence on the vacuum wavelength of the SPP typical period, denoted as $L_{\text{SPP}} = 2\pi/k_{\text{SPP}}$ (upper x axis), and the imaginary part of the SPP wave vector (lower x axis). The dielectric permittivity of the silver substrate ϵ_s was taken from Johnson and Christy [42].

substrate. Moreover, it is worth mentioning that though the effective polarizability tensor $\hat{\alpha}_{\text{eff}}^s$ is diagonal, the tensor $\hat{\alpha}_{\text{eff}}^R$ is nondiagonal, as the presence of the second nanoparticle does not preserve translational symmetry of the system.

The excitation of SPP modes affects both the effective polarizability due to the substrate mediated self-action and the cross action of the nanoparticles. The spectra of the real and imaginary parts of the xx components of $\hat{\alpha}_{\text{eff}}^R$ (solid line) and $\hat{\alpha}_{\text{eff}}^S$ (dashed line) are plotted in Figs. 2(a) and 2(b), respectively, for the case of a silver substrate. The vacuum polarizability α is also shown in this figure with a dash-dotted line. We observe that the effective polarizabilities have a resonance at around 350 nm. From the inset of Fig. 2, one can see that this wavelength corresponds to the SPP resonant excitation for the silver/vacuum interface, which is defined by the condition $\text{Re}[\epsilon_s(\omega)] + 1 = 0$, and also corresponds to the maximal value of the real part of the SPP wavevector $k_{\text{SPP}} = k_0\sqrt{\epsilon_s/(\epsilon_s + 1)}$, where ϵ_s is the permittivity of the silver substrate [42]. In the inset, the effective wavelength of the SPP mode defined as $L_{\text{SPP}} = 2\pi/\text{Re}(k_{\text{SPP}})$ is also shown.

The strong enhancement of the imaginary part of the effective polarizability is a sign of strong rescattering of light into the SPP mode.

III. RESULTS AND DISCUSSION

A. Binding via SPP

By determining the dipole moments of nanoparticles, one can calculate the optical force acting on each nanoparticle using Eq. (1) (see the details in Appendix A). In the following, we will refer to the optical force acting on the second nanoparticle only, fixing the first nanoparticle in the coordinate origin. In order to find the equilibrium positions of the nanoparticle, we plot the dependence of the x component of the optical force as a function of interparticle distance along the x axis as shown in Fig. 3(a). The force is normalized to the optical pressure force acting on the same nanoparticle in vacuum $F_0 = 1/2k|E_0|^2\text{Im}[\alpha(\omega)]$, where $|E_0|$ is the amplitude of the incident plane wave, and the particles' parameters are the same throughout the whole paper: radius $R = 15$ nm and dielectric permittivity $\epsilon = 3$. One can see that the force periodically varies with coordinate, which is due to the interference pattern formed in the vicinity of the metal surface, and the zero-force points show equilibrium positions. These points can be stable along x if the force is restoring (shown with solid circles, i.e., point 1) and unstable otherwise (shown with white filled circles). One should also note that when the nanoparticles approach each other, the force goes to minus infinity until the nanoparticles touch each other. However, this case is out of the scope of the present paper.

To identify the role of plasmons in the interaction force, we have excluded the SPP contribution from the Green's function by integrating over the free space modes only (transverse component of the wave vector is limited by the incident wave vector \mathbf{k} , $k_r < k_1$) in the spectral representation (see Appendix B). One can see that in the absence of SPPs the interaction force becomes one order of magnitude weaker, and the period between stable positions is significantly enlarged, being defined by the vacuum wavelength of photons. Moreover, the equilibrium points shown with blue circles are stable both along the x and y directions, making them globally stable, which does not happen for equilibrium positions along the y coordinate in the case of binding with solely photons. To illustrate this, we plotted the F_y force—see Fig. 3(b)—as a function of the transverse angle ϕ (see the inset in Fig. 3) in the vicinity of points of stable equilibrium. One can see in Fig. 3(c) that the dependence of the binding length on the vacuum wavelength and the period of the SPP wave, which is equal to L_{SPP} . One can see that the binding distance is fully defined by the period of the SPP wave when the excitation condition is fulfilled, thus providing the binding at distances significantly shorter than the vacuum wavelength. This also strongly differs from work of Salary *et al.* [17], where the optical forces between two nanoparticles over a metallic substrate were considered in the regime, where the interaction force is mainly defined by the near-field components.

In order to support the results discussed above, we have performed numerical simulations with the COMSOL MULTIPHYSICS package [see Fig. 3(d), scatter line]; numerical simulation shows good correspondence with the solution

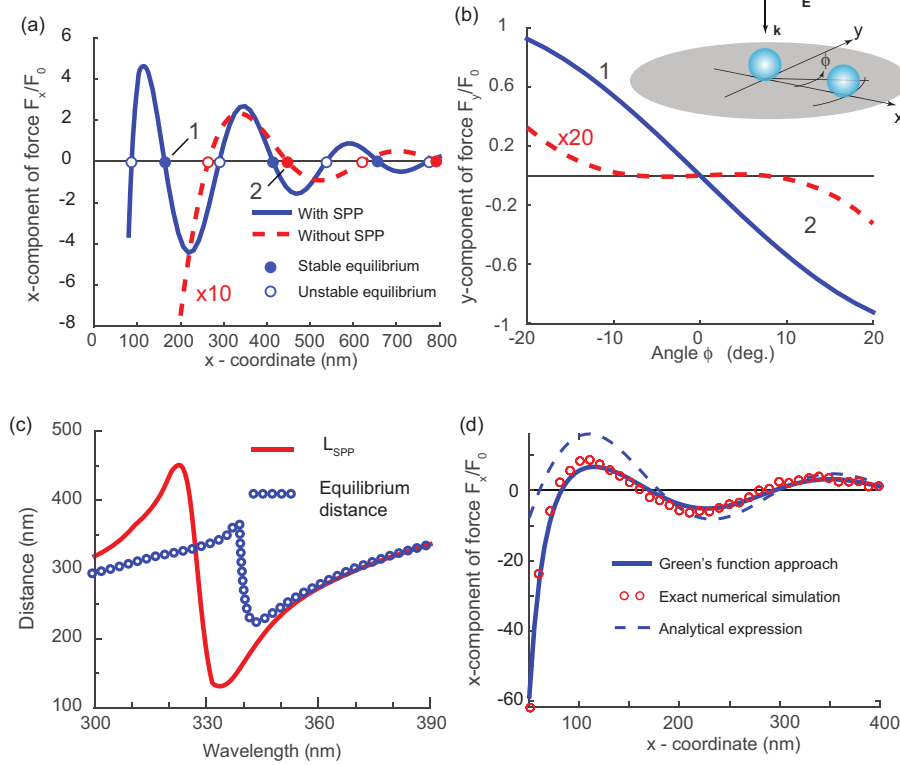


FIG. 3. (a) The x component of optical force plotted along the x axis coinciding with the direction of electric field polarization. The blue solid line denotes the force with account for all interaction channels. The red dashed line is for the interaction through the free space photons only. (b) The y component of the optical force in the direction perpendicular to the x axis, showing the stability of the binding position in the direction transverse to the x axis. The blue solid line and red dashed line correspond to the force calculated with or without account for the SPP interaction channel for the equilibrium positions labeled 1 and 2 in panel (a), respectively. The results are shown for the wavelength $\lambda = 350$ nm. The values of the force for the red dashed lines are multiplied by factors of 10 and 20 in panels (a) and (b), respectively. (c) The distance between the stable equilibrium positions obtained from panel (a) compared with the distance $L = 2\pi/k_{\text{SPP}}$. (d) Comparison of the optical force calculated within Green's function approach as in Fig. 3(a) and calculated numerically with COMSOL MULTYPHYSICS package. The approximate analytical expression given by Eq. (7) for the SPP-induced force is also shown by the dashed line. All the results shown in the figure are computed for $R = 15$ nm and $z = 30$ nm.

obtained with Green's function approach [see Fig. 3(d), solid line]. The particles were illuminated by a plane wave, and the numerical integration of the Maxwell stress tensor over a sphere surrounding a particle was performed. The Green's function approach shows good agreement with numerical results also at distances comparable to the nanoparticle size. One can notice that for our range of distances between the nanoparticles the dipole model gives good agreement with numerical simulations. The higher order multipoles do not contribute to the optical force, as evidenced by our calculations in COMSOL MULTYPHYSICS. It is also in good agreement with a paper by Khlebtsov *et al.* [44]. Moreover, on employing Green's function formalism, we have derived the approximate expression for the contribution of the SPP mode to the optical force (see Appendix C for the details):

$$F_x \approx \pi |p_x|^2 \text{Re} \left[\frac{k_{\text{SPP}}^3 k_{1z}^2 k_{2z}}{k_0^2 (1 - \epsilon_s)} H_1^{(1)}(k_{\text{SPP}} x) \right] \exp[-\text{Im}(k_{1z})z]. \quad (7)$$

Here, $k_{1z} = \sqrt{k_0^2 - k_{\text{SPP}}^2}$ and $k_{2z} = \sqrt{\epsilon_s k_0^2 - k_{\text{SPP}}^2}$ are z components of the SPP wave vector in the upper half-space and in the substrate respectively, $H_1^{(1)}(q)$ is the first-order Hankel function of the first kind, and p_x denotes the x component of the dipole moment of the first or second nanoparticle, as dipole moments for identical nanoparticles are equal. The derived expression illustrates the origin of the SPP mode: the Hankel function describes the SPP mode excited by a dipole and propagating over a flat surface. Its zeros define the equilibrium positions of the nanoparticle. The z component of the wave vector is complex since SPP is a localized wave; thus, the exponent in Eq. (7) shows the decay of the SPP-dipole coupling.

It should be stressed that the transverse binding in a vacuum does not provide stable equilibrium positions along the x axis [40]. This difference of SPP and photon binding can be understood through the difference in the scattering diagrams of SPPs and photons. This is illustrated in Fig. 4 where two-dimensional maps of the x and y force components are plotted.

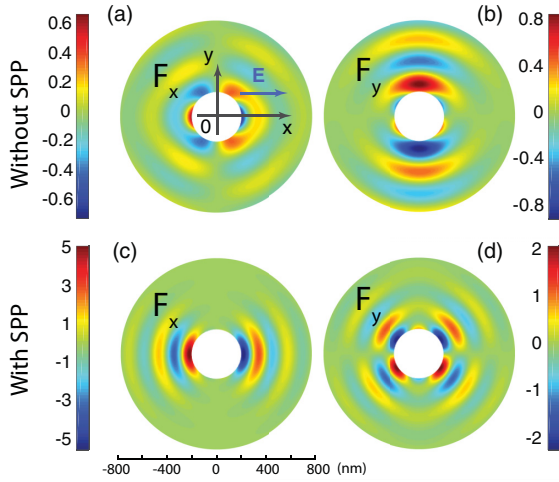


FIG. 4. Two-dimensional maps showing the x and y forces for SPP and photon binding. The different directionality of the scattering pattern is responsible for the different geometry of the stable equilibrium positions. Results are shown for $\lambda = 350$ nm and $z = 25$ nm. The white regions correspond to the high values of the optical force in the vicinity of the first particle, the radius of white regions is around 100 nm; therefore, no equilibrium positions are omitted.

The reshaping of the photon interference [Figs. 4(a) and 4(b)] due to the influence of plasmons [Figs. 4(c) and 4(d)] is clearly seen. The photon binding is well known to have stable configurations perpendicular to the field polarization direction, in accordance with the dipole emission pattern [see Figs. 4(a) and 4(b)]. The SPP binding, on the contrary, has stable configurations along the polarization direction, in which a preferable excitation of SPP modes occurs [see Figs. 4(c) and 4(d)]. It is also worth noting that the amplitudes of the lateral forces are several times higher when SPP modes affect binding.

B. Temporal dynamics of SPP binding

We illustrate the character of SPP binding by calculating the dynamics of the second nanoparticle motion in the force field of the first nanoparticle, which is fixed at the origin of the coordinates. We consider only two-dimensional motion of the nanoparticle, keeping the z coordinate to be constant. The dynamics is obtained through direct solution of the equations of motion under the external optical force with the account for viscous damping. The details are discussed in Appendix D.

Two typical trajectories are shown in Fig. 5 for two different sets of initial coordinates of the second nanoparticle. The particles are illuminated by a plane wave. The color map shows the intensity of nanoparticle attraction to the equilibrium positions along the x axis, i.e., the amplitude projection of the total force \mathbf{F} on the unit vector \mathbf{n} pointing at the nearest equilibrium position. The arrows show the force field, while the lines show the trajectories with color changing from blue to red as time elapses. One can see that the nanoparticle actively tends to set the position along the x axis where the binding force is the strongest.

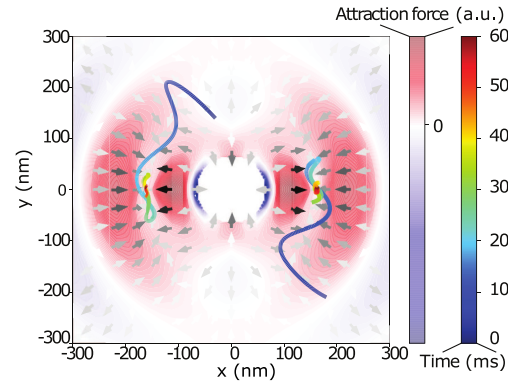


FIG. 5. The dynamics of the second nanoparticle motion. The first nanoparticle is fixed at the origin. The color of the trajectory line denotes the time elapsed since the beginning of motion. The arrows show the force field: darker arrows indicate stronger optical force. The color map at the background shows the force which attracts or repulses the nanoparticle to/from the equilibrium positions at $y = 0$ and $x = \pm 175$ nm. Color represents the projection of the total force \mathbf{F} on the unit vector \mathbf{n} pointing toward the nearest equilibrium position. The intensity of the red color gives the strength of the nanoparticle attraction, while that of the blue shows repulsion of the nanoparticle. The parameters of computation are $R = 15$ nm, $z = 25$ nm, and $\varepsilon = 3$. The laser intensity is taken 5×10^5 W/m², and the dimensionless damping factor is $\gamma = 0.015$, which corresponds to damping in the vacuum with pressure 10^{-6} atm (see Appendix D for details of the simulation method).

C. Stiffness of SPP binding

The important parameter, which characterizes the stability of the equilibrium states, is the stiffness of the trap. At the equilibrium positions, the total optical force is zero, but when shifted from the stable positions the nanoparticles undergo action of a restoring force, which is locally proportional to the amplitude of the displacement $F_x = -\kappa_x \Delta x$, with the parameter κ_x characterizing the stiffness of the system along the x direction. However, this approximation of the restoring force applies only to the gradient component of the optical force. Indeed, we consider the nanoparticles significantly smaller than the wavelength, which results in low and nonresonant polarizabilities so that where $\text{Im}(\alpha_{\text{eff}}) \ll \text{Re}(\alpha_{\text{eff}})$, as $\text{Im}(\alpha_{\text{eff}}) \simeq (R^6/\lambda^3)$, and $R \ll \lambda$ (see Fig. 2). Thus, the radiation force, which is proportional to the imaginary part of the polarizability, can be neglected (see Appendix D).

The stiffness in the considered system strongly depends on the mechanism of the nanoparticle interaction, and, as can be seen from Fig. 3, it is much higher when the plasmon interaction is enabled. We have plotted (see Fig. 6) the spectral dependence of stiffness parameter κ_x calculated at the first equilibrium position, labeled by point 1 in Fig. 3(a). To avoid the dependence of the stiffness on the illumination intensity, we have normalized it to the magnitude $\kappa_0 = F_0/R$, which is the stiffness of a system where the vacuum pressure force F_0 can be restored when the nanoparticle is displaced a distance

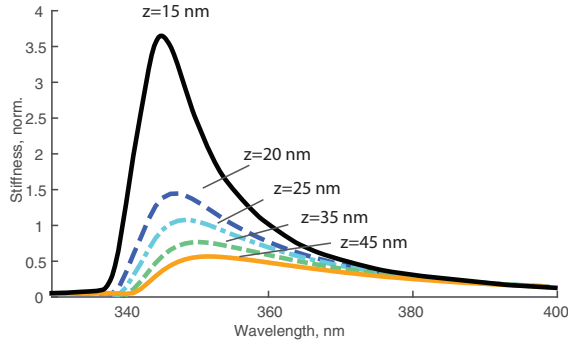


FIG. 6. The stiffness κ_x of the second equilibrium position in units of $\kappa_0 = F_0/R$ as a function of the excitation wavelength. The spectra are shown for different distances z from the nanoparticle center to the surface. The nanoparticle radius $R = 15$ nm.

equal to its radius from its equilibrium position. One can see that the stiffness has a strong resonant behavior, which corresponds to the excitation of SPP modes at wavelengths longer than 350 nm. With the increase of the distance from nanoparticle center to the surface the stiffness rapidly drops, as the coupling with the SPP mode decreases.

One can see from Fig. 6 that the spectral maximum of stiffness depends on the height from the surface. This spectral dependence can be better understood by means of Eq. (7). In the case of negligible losses in the substrate, one can get a simple expression for the stiffness at the first stable equilibrium point, (see Appendix C for more details):

$$\kappa_x \approx \pi |p_x|^2 \frac{(k_{\text{SPP}})^3 |k_{1z}|^2 |k_{2z}|}{k_0^2 (1 - \varepsilon_s)} Y_2(q_1) \exp(-2|k_{1z}|z). \quad (8)$$

Here, $Y_2(q)$ is the cylindrical Webber function of the second order [45], and q_1 is the first positive root of $Y_1(q_1) = 0$, the cylindrical Webber function of the first order. Note that in the regime of SPP excitation without ohmic losses the SPP wave vector can be in a range from k_0 to $+\infty$ when $1 + \varepsilon_s \rightarrow 0$. Then the expression given by Eq. (C11) goes to zero in both limiting cases: $\kappa_x \rightarrow 0$ as $k_{\text{SPP}} \rightarrow 0/\infty$, which implies that the stiffness reaches its maximum at some particular wavelength. This wavelength can be defined for each given distance over the substrate z . The maximal stiffness can be achieved close to the SPP resonance when the SPP wave vector is $\tilde{k} \approx 6/z \gg k_0$. Then, the maximal stiffness at the n th equilibrium position decreases with the distance to the substrate as z^{-6} (see Eq. (C12) in Appendix C):

$$\kappa_{x,n} \sim |p_x|^2 \left(\frac{1}{z}\right)^6 \frac{1}{k_0^2} Y_2(q_{2n+1}), \quad (9)$$

where q_{2n+1} corresponds to the positive roots of $Y_1(q_{2n+1})=0$.

There is a strong dependence of the trap stiffness on the size of the nanoparticles radius and permittivities. With the growth of the particles' radius, the maximal value of the normalized stiffness decreases. The details are given in Appendix F.

D. Conclusion

In this work, we consider transverse optical binding based on surface plasmon polariton interference. We show that two nanoparticles placed in the vicinity of a plasmonic interface can form a stable bound dimer with a binding length defined by the SPP wavelength. This allows formation of the dimers with interparticle distance significantly shorter than the free-space wavelength, thus suppressing the diffraction limit. The binding states are formed along the direction of the incident field polarization, in contrast to photon binding, where the stable bound states are formed perpendicular to the polarization direction. The excitation of SPP modes also enhances the amplitude of the binding forces, resulting in a resonant enhancement of the trap stiffness.

ACKNOWLEDGMENTS

The authors acknowledge the support of the Russian Foundation for Basic Research (Grants No. 16-32-60167, No. 18-02-00414, No. 18-29-20063, and No. 18-52-00005). M.I.P. also acknowledges the support from the BASIS Foundation. A.S. acknowledges the support of the Ministry of Education and Science of the Russian Federation (GOSZADANIE, Grant No. 3.4982.2017/6.7). The force calculations were partially supported by Russian Science Foundation (Grant No. 18-72-10127). M.N.-V. is supported by the Spanish MINECO Grants No. FIS2012-36113-C03-03, No. FIS2014-55563-REDC, and No. FIS2015-69295-C3-1-P.

APPENDIX A: CALCULATION OF A BINDING FORCE

The force $\mathbf{F}_2(\mathbf{r}_2)$ acting on the second nanoparticle is calculated as

$$\mathbf{F}_2(\mathbf{r}_2) = \frac{1}{2} \text{Re} \left[\sum p_{2i}^* (\mathbf{r}_2) \nabla E_i(\mathbf{r}_2) \right]. \quad (A1)$$

The introduction of the effective polarizability parameters significantly simplifies the formula for the electric field $\mathbf{E}(\mathbf{r})$ induced by the dipole moments [see Eq. (3)]. By calculating the field amplitude at the points of the dipoles $\mathbf{E}(\mathbf{r}_1)$ and $\mathbf{E}(\mathbf{r}_2)$, one can get a system of linear equations on the dipole moments:

$$\mathbf{p}_1 = \hat{\alpha}_{1,\text{eff}}^s \mathbf{E}(\mathbf{r}) = \hat{\alpha}_{1,\text{eff}}^s \left[\mathbf{E}_0(\mathbf{r}_1) + \frac{k_0^2}{\varepsilon_0} \hat{G}(\mathbf{r}_1, \mathbf{r}_2) \mathbf{p}_2 \right], \quad (A2)$$

$$\mathbf{p}_2 = \hat{\alpha}_{2,\text{eff}}^s \left[\mathbf{E}_0(\mathbf{r}_2) + \frac{k_0^2}{\varepsilon_0} \hat{G}(\mathbf{r}_2, \mathbf{r}_1) \mathbf{p}_1 \right], \quad (A3)$$

$$\hat{\alpha}_{i,\text{eff}}^s(\mathbf{r}_i, \omega) = \alpha(\omega) \left[\hat{I} - \alpha(\omega) \frac{k_0^2}{\varepsilon_0} \hat{G}_s(\mathbf{r}_i, \mathbf{r}_i, \omega) \right]^{-1}, \quad (A4)$$

$$i = 1, 2.$$

Solving this system, one may get

$$\mathbf{p}_1 = \hat{\alpha}_{1,\text{eff}}^s \left(\mathbf{E}_0(\mathbf{r}_1) + \frac{k_0^2}{\varepsilon_0} \hat{G}(\mathbf{r}_1, \mathbf{r}_2) \times \left\{ \hat{\alpha}_{2,\text{eff}}^s \left[\mathbf{E}_0(\mathbf{r}_2) + \frac{k_0^2}{\varepsilon_0} \hat{G}(\mathbf{r}_2, \mathbf{r}_1) \mathbf{p}_1 \right] \right\} \right), \quad (A5)$$

$$\mathbf{p}_1 = \widehat{\alpha}_{1,\text{eff}}^s \left[\mathbf{E}_0(\mathbf{r}_1) + \frac{k_0^2}{\varepsilon_0} \widehat{G}(\mathbf{r}_1, \mathbf{r}_2) \widehat{\alpha}_{2,\text{eff}}^s \mathbf{E}_0(\mathbf{r}_2) \right] + \frac{k_0^4}{\varepsilon_0^2} \widehat{\alpha}_{1,\text{eff}}^s \widehat{G}(\mathbf{r}_1, \mathbf{r}_2) \widehat{\alpha}_{2,\text{eff}}^s \widehat{G}(\mathbf{r}_2, \mathbf{r}_1) \mathbf{p}_1, \quad (\text{A6})$$

The last expression in Eq. (A5) can be simplified even further, if one renormalizes the effective polarizability tensor with account for nanoparticle cross action:

$$\widehat{\alpha}_{i,\text{eff}}^r(\mathbf{r}_i, \omega) = \alpha_i(\omega) \left[\widehat{I} - \alpha_i(\omega) \frac{k^2}{\varepsilon_0} \widehat{G}_s(\mathbf{r}_i, \mathbf{r}_i, \omega) - \frac{k^4}{\varepsilon_0^2} \alpha_i \widehat{G}(\mathbf{r}_i, \mathbf{r}_j) \widehat{\alpha}_{j,\text{eff}}^s \widehat{G}(\mathbf{r}_j, \mathbf{r}_i) \right]^{-1}, \quad i = 1, 2 \quad j = 2, 1. \quad (\text{A7})$$

Here, the self-action Green's function $\widehat{G}_s(\mathbf{r}_i, \mathbf{r}_i)$ contains the scattered part only, whereas the cross-action part $\widehat{G}(\mathbf{r}_i, \mathbf{r}_j) = \widehat{G}_0(\mathbf{r}_i, \mathbf{r}_j) + \widehat{G}_s(\mathbf{r}_i, \mathbf{r}_j)$ includes both vacuum and scattered parts, determining the cross interaction through vacuum and via substrate respectively. The final expression for the dipole moment will be as follows:

$$\mathbf{p}_i = \widehat{\alpha}_{i,\text{eff}}^r \left[\mathbf{E}_0(\mathbf{r}_i) + \frac{k^2}{\varepsilon_0} \widehat{G}(\mathbf{r}_i, \mathbf{r}_j) \widehat{\alpha}_{j,\text{eff}}^s \mathbf{E}_0(\mathbf{r}_j) \right], \quad i = 1, 2 \quad j = 2, 1 \quad (\text{A8})$$

The case of normal plane-wave incidence on a planar substrate, when the nanoparticles are located at the same height above the surface (see Fig. 1 in the main text) is of a particular interest. In this case, the external electric field \mathbf{E}_0 is equal in the centers of both nanoparticles, and thus the dipole moment has a very simple form:

$$\mathbf{p}_i = \widehat{\alpha}_{i,\text{eff}}^R \mathbf{E}_0(\mathbf{r}_i), \quad (\text{A9})$$

$$\widehat{\alpha}_{i,\text{eff}}^R = \widehat{\alpha}_{i,\text{eff}}^r \left[\widehat{I} + \frac{k^2}{\varepsilon_0} \widehat{G}(\mathbf{r}_i, \mathbf{r}_j) \widehat{\alpha}_{j,\text{eff}}^s \right], \quad i = 1, 2 \quad j = 2, 1. \quad (\text{A10})$$

The optical force component, then, can be calculated as

$$\begin{aligned} F_{2x}(\mathbf{r}_2) &= \frac{1}{2} \text{Re} \left[\sum_{n=x,y,z} p_{2n}^*(\mathbf{r}_2) \partial_{x_2} E_n(\mathbf{r}_2) \right] \\ &= \frac{1}{2} \text{Re} \left\{ \sum_{n=x,y,z} p_{2n}^*(\mathbf{r}_2) \left[\partial_{x_2} E_{0n}(\mathbf{r}_2) + \frac{k_0^2}{\varepsilon_0} \sum_{m=x,y,z} \partial_{x_2} G_{s, nm}(\mathbf{r}_2', \mathbf{r}_2) p_{2m} + \frac{k_0^2}{\varepsilon_0} \sum_{m=x,y,z} \partial_{x_2} G_{nm}(\mathbf{r}_2, \mathbf{r}_1) p_{1m} \right] \right\}. \quad (\text{A11}) \end{aligned}$$

The y and z components can be calculated with the same expression (A11) by substituting the partial derivative with ∂_y and ∂_z respectively.

APPENDIX B: GREEN'S FUNCTION

The Green's function tensor of two half-spaces with permittivities ε_1 (for $z > 0$) and ε_2 (for $z \leq 0$) can be expressed in cylindrical coordinates through [43] (for $z > 0$):

$$\widehat{G}(\rho, \varphi, z > 0) = \frac{ik_1}{8\pi^2} \int_0^\infty \widehat{M}(s, \rho, \varphi) \exp(2is_{z1}\bar{z}) ds, \quad (\text{B1})$$

where k_1 is the wave vector in the upper space, $s = k_r/k_0$ and $s_{z1} = k_{z1}/k_0$ are the radial and z components of the dimensionless wave vector normalized to the wave vector in the free space, and $\bar{z} = zk_0$ is dimensionless coordinate;

$$\begin{aligned} \widehat{M}(s, \rho, \varphi) &= \begin{pmatrix} m_{xx} & m_{xy} & m_{xz} \\ m_{yx} & m_{yy} & m_{yz} \\ m_{zx} & m_{zy} & m_{zz} \end{pmatrix}, \\ m_{xx} &= \frac{s}{s_{z1}} r_s f(s, \rho, \varphi) - s s_{z1} r_p g(s, \rho, \varphi), \\ m_{yy} &= \frac{s}{s_{z1}} r_s g(s, \rho, \varphi) - s s_{z1} r_p f(s, \rho, \varphi), \\ m_{zz} &= 2\pi J_0(s\rho) r_p \frac{s^3}{s_{z1}}, \\ m_{xy} = m_{yx} &= \frac{(r_s + s_{z1}^2 r_p)}{s s_{z1}} h(s, \rho, \varphi), \\ m_{xz} &= -m_{zx} = -s r_p t(s, \rho, \varphi), \\ m_{yz} &= -m_{zy} = -s r_p w(s, \rho, \varphi), \end{aligned} \quad (\text{B2})$$

where the functions $f(s, \rho, \varphi)$, $g(s, \rho, \varphi)$, $h(s, \rho, \varphi)$, $t(s, \rho, \varphi)$, $w(s, \rho, \varphi)$ can be expressed:

$$\begin{aligned} f(s, \rho, \varphi) &= 2\pi \left[\sin^2(\varphi) J_0(s\rho) + \frac{J_1(s\rho)}{s\rho} \cos(2\varphi) \right], \\ g(s, \rho, \varphi) &= 2\pi \left[\cos^2(\varphi) J_0(s\rho) - \frac{J_1(s\rho)}{s\rho} \cos(2\varphi) \right], \\ h(s, \rho, \varphi) &= \pi s^2 J_2(s\rho) \sin(2\varphi), \\ t(s, \rho, \varphi) &= 2\pi i s J_1(s\rho) \cos(\varphi), \\ w(s, \rho, \varphi) &= 2\pi i s J_1(s\rho) \sin(\varphi). \end{aligned} \quad (\text{B3})$$

Here, $J_n(z)$ is the first kind Bessel function of the order n .

APPENDIX C: ANALYTICAL EXPRESSION

Here, we analyze the x component of the optical force acting on the nanoparticles when normal incident light is polarized along the x axis. This is the case considered in Fig. 3. According to Eq. (1), the expression for the force will be as follows:

$$F_x = \frac{1}{2} \text{Re} \left(\sum_i p_i(\mathbf{r})^* \partial_x E_i(\mathbf{r}) \right). \quad (\text{C1})$$

In order to get a simple analytical result showing all the key features of the SPP-assisted force, we will take into account that the effective $\widehat{\alpha}^R$ tensor has diagonal domination, which implies that $\alpha_{ii}^R \gg \alpha_{ij}^R$, $i \neq j$.

The expression in Eq. (C1) can be simplified:

$$F_x = \frac{1}{2} \text{Re} (p_x^* \partial_x E_x^s). \quad (\text{C2})$$

The electrical field generated by the dipole at the point with radius vector \mathbf{r} can be expressed through the Green's function $E_x^s(\mathbf{r}) = 4\pi k_0^2 G_{s,xx}(\mathbf{r}, (0, 0, z)) p_x$.

Then we have an expression for the lateral component of the optical force written in a very simple form:

$$F_x = 2\pi k_0^2 |p_x|^2 \text{Re}[\partial_x G_{s,xx}(\mathbf{r}, (0, 0, z))] \quad (\text{C3})$$

The Green's function is expressed through the integral

$$G_{s,xx}(x, y, z) = G_{s,xx}(\rho, \phi, z) = \frac{ik_1}{8\pi^2} \int_0^\infty m_{xx}(\rho, s) \exp(2is_{1z}\tilde{z}) ds, \quad m_{xx} = sr_s(s) \frac{a_1(\rho, \phi)}{s_{1z}} - ss_{1z}r_p(s)a_2(\rho, \phi),$$

$$a_1 = 2\pi \left[\sin(\phi_0)^2 J_0(s\rho) + \frac{J_1(s\rho)}{s\rho} \cos(2\phi_0) \right], \quad a_2 = 2\pi \left[\cos(\phi_0)^2 J_0(s\rho) - \frac{J_1(s\rho)}{s\rho} \cos(2\phi_0) \right],$$

$$s_{1z} = \sqrt{1 - s^2}, \quad s_{2z} = \sqrt{\varepsilon_2 - s^2}. \quad (\text{C4})$$

Here, we use the same notation as in Appendix B. We are interested only in the component containing r_p term as only it gives rise to SPP response, and also we put $\phi = 0$. Then,

$$G_{s,xx}(\rho, \phi, z) = \frac{ik_1}{8\pi^2} \int_0^\infty m'_{xx}(\rho, s) \exp(2is_{1z}\tilde{z}) ds, \quad m'_{xx} = -ss_{1z}r_p(s)a_2(s, \rho), \quad a_2 = 2\pi \left[J_0(s\rho) - \frac{J_1(s\rho)}{s\rho} \right]. \quad (\text{C5})$$

Next, we have

$$G_{s,xx}(\rho, \phi, z) = -\frac{ik_1}{4\pi} \int_0^\infty ss_{1z}r_p(s) \left[J_0(s\rho) - \frac{J_1(s\rho)}{s\rho} \right] \exp(2is_{1z}\tilde{z}) ds. \quad (\text{C6})$$

With this, we need to compute $\partial_x G_{s,xx}$:

$$\partial_x J_0(s\rho) = k_0 \partial_\rho J_0(s\rho) = -k_0 s J_1(s\rho), \quad \partial_x \frac{J_1(s\rho)}{s\rho} = k_0 s \partial_{s\rho} \frac{J_1(s\rho)}{s\rho} = -k_0 s \frac{J_2(s\rho)}{(s\rho)^2},$$

which gives us

$$\partial_x G_{s,xx}(\rho, 0, z) = \frac{ik_1}{4\pi} k_0 \int_0^\infty s^2 s_{1z} r_p(s) \left[J_1(s\rho) - \frac{J_2(s\rho)}{(s\rho)^2} \right] \exp(2is_{1z}\tilde{z}) ds. \quad (\text{C7})$$

In order to compute the integral with the help of complex analysis, we first continue the integral bounds to $-\infty, +\infty$ using the identity

$$J_n(q) = \frac{1}{2} [H_n^{(1)}(q) - (-1)^n H_n^{(1)}(-q)], \quad \partial_x G_{s,xx}(\rho, 0, z) = \frac{ik_1}{8\pi} k_0 \int_{-\infty}^\infty \underbrace{s^2 s_{1z} r_p(s)}_{I(s)} \left[H_1^{(1)}(s\rho) - \frac{H_2^{(1)}(s\rho)}{(s\rho)^2} \right] \exp(2is_{1z}\tilde{z}) ds. \quad (\text{C8})$$

Now, using Cauchy theorem, we finally evaluate this integral:

$$\partial_x G_{s,xx}(\rho, 0, z) = \frac{ik_1}{8\pi} k_0 2\pi i \text{Res}(I(s))|_{s=\tilde{s}} = -\frac{k_1}{4} k_0 (\tilde{s})^2 \tilde{s}_{1z} \left[H_1^{(1)}(\tilde{s}\rho) - \frac{H_2^{(1)}(\tilde{s}\rho)}{(\tilde{s}\rho)^2} \right] \exp(i\tilde{s}_{1z}\tilde{z}) \text{Res}(r_p(s))|_{s=\tilde{s}}, \quad (\text{C9})$$

where $\text{Res}(r_p(s))|_{s=\tilde{s}}$ stands for residue, and $\tilde{s} = \sqrt{\varepsilon_2 \varepsilon_1 / (\varepsilon_1 + \varepsilon_2)}$ is dimensionless wave vector of SPP mode.

Finally, computing the explicit expression for the residue and substituting the obtained results into Eq. (C3), one can get

$$F_x = \pi |p_x|^2 \text{Re} \left\{ \frac{(\tilde{k})^3 (\tilde{k}_{1z})^2 \tilde{k}_{2z}}{k_0^2 (\varepsilon_1 - \varepsilon_2)} \left[H_1^{(1)}(\tilde{k}x) - \frac{H_2^{(1)}(\tilde{k}x)}{(\tilde{k}x)^2} \right] \exp(2i\tilde{k}_{1z}z) \right\}.$$

Here, we use dimension variables denoting $\tilde{k} = \tilde{s}k_0$, and $\tilde{k}_{z1,2} = \tilde{s}_{z1,2}k_0$. We can go even further, taking into account that $|H_1^{(1)}(\tilde{k}x)| \ll |J_2(\tilde{k}x)/(\tilde{k}x)^2|$:

$$F_x \approx \pi |p_x|^2 \text{Re} \left[\frac{(\tilde{k})^3 (\tilde{k}_{1z})^2 \tilde{k}_{2z}}{k_0^2 (\varepsilon_1 - \varepsilon_2)} H_1^{(1)}(\tilde{k}x) \exp(2i\tilde{k}_{1z}z) \right]. \quad (\text{C10})$$

The case of low losses is of special interest. Then, the final expression for the force can be reduced to

$$F_x = \pi |p_x|^2 \frac{(k^*)^3 |k_{1z}^*|^2 |k_{2z}^*|}{k_0^2 (\varepsilon_1 - \varepsilon_2)} Y_1(k^*r) \exp(-2k_{1z}^*z),$$

where $Y_1(q)$ is the cylindrical Webber function. By expanding this expression around the zeros q_n of the Webber function $Y_1(q) \approx -Y_2(q_n)(q - q_n)$, one can find the expression for the stiffness at the n th equilibrium position along the x axis of the system [see Fig. 3(a)]:

$$\kappa_n \approx \pi |p_x|^2 \frac{(\tilde{k})^3 |\tilde{k}_{1z}|^2 |\tilde{k}_{2z}|}{k_0^2 (\varepsilon_1 - \varepsilon_2)} Y_2(q_{2n-1}) \exp(-2|\tilde{k}_{1z}|z). \quad (\text{C11})$$

Note that in the regime of SPP excitation without ohmic losses the SPP wave vector can be in the range from k_0 to $+\infty$ when $\varepsilon_1 + \varepsilon_2 \rightarrow 0$. With that, the expression Eq. (C11) goes to zero in both limiting cases,

$$\kappa_n \xrightarrow[k \rightarrow 0, \infty]{} 0,$$

which implies that the stiffness reaches its maximum at some particular wavelength. This wavelength can be defined for each given distance over substrate z . The maximal stiffness can be achieved close to SPP resonance when SPP wave vector equals $\tilde{k} \approx 3/z$. Close to the frequency of SPP resonance when $\tilde{k} \rightarrow \infty$, the SPP becomes highly localized close to the interface $|\tilde{k}_z| \gg k_0$. Then, the maximal stiffness can be expressed as

$$\kappa_n \sim |p_x|^2 \left(\frac{3}{z}\right)^6 \frac{1}{k_0^2 \varepsilon_1} Y_2(q_{2n+1}) \exp(-3). \quad (\text{C12})$$

APPENDIX D: DYNAMICS SIMULATION

We write Newton's law for the second particle,

$$m \frac{d^2}{dt^2} \mathbf{r}_2 = \mathbf{F}_2,$$

where \mathbf{F}_2 is given by Eq. (A1). One can rewrite it as

$$\frac{d^2}{dt^2} \mathbf{r}_2 = \frac{1}{2m} \sum_i \text{Re} \left\{ p_{2i}^* \nabla \left[E_{0i} + \frac{k^2}{\varepsilon_0} \sum_j G_{s,ij}(\mathbf{r}_2, \mathbf{r}_2) p_{2j} + \frac{k^2}{\varepsilon_0} \sum_j G_{ij}(\mathbf{r}_2, \mathbf{r}_1) p_{1j} \right] \right\}, \quad i, j = x, y, z, \quad (\text{D1})$$

where $\widehat{G} = \widehat{G}_0 + \widehat{G}_s$. In order to decrease the numerical error in the numerical simulations, we apply the following natural scaling:

$$\begin{aligned} \xi &= \frac{\mathbf{r}}{a}, & \tau &= \frac{t}{T}, & \tilde{\mathbf{E}} &= \frac{\mathbf{E}}{E_0}, & \tilde{G} &= a\widehat{G}, \\ \tilde{\mathbf{k}} &= ak, & \tilde{\mathbf{p}} &= \frac{\mathbf{p}}{4\pi\varepsilon_0 a^3 E_0}, & \tilde{\alpha} &= \frac{\alpha}{4\pi\varepsilon_0 a^3}, \\ T &= \sqrt{\frac{m}{2\pi\varepsilon_0 a E_0^2}}. \end{aligned} \quad (\text{D2})$$

After such substitutions, we have

$$\frac{d^2}{d\tau^2} \xi_2 = \sum_i \text{Re} \left\{ \tilde{p}_{2i}^* \frac{\partial}{\partial \xi} \left[\tilde{E}_{0i} + 4\pi\tilde{k}^2 \sum_j \tilde{G}_{ij}^s(\xi_2, \xi_2) \tilde{p}_{2j} + 4\pi\tilde{k}^2 \sum_j \tilde{G}_{ij}(\xi_2, \xi_1) \tilde{p}_{1j} \right] \right\}. \quad (\text{D3})$$

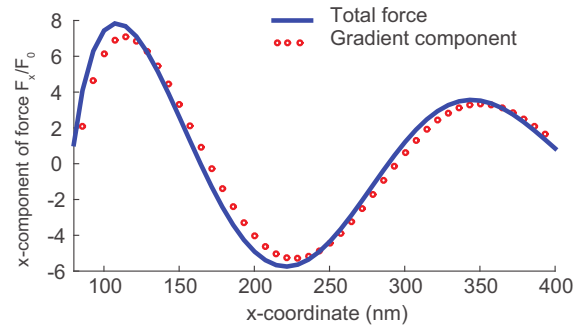


FIG. 7. The total force (blue solid line) and the conservative (red circles) components of the optical force are shown for different wavelengths. The parameters of the calculation are the same as in Fig. 2 of the main text.

We also include the viscosity of the environment by adding the damping factor γ ,

$$\frac{d^2}{d\tau^2} \xi_2 = \tilde{\mathbf{F}}_2(\xi_1, \xi_2) - \gamma \frac{d}{d\tau} \xi_2, \quad (\text{D4})$$

where $\tilde{\mathbf{F}}_2$ is given by the right-hand side of Eq. (D3). Expression (D4) was a target for the numerical simulation. As a good compromise between stability and computational complexity, the Runge-Kutta method of fourth order was applied. Since the motion along the z axis is fixed, we have plane symmetry, which simplifies the force function to $\tilde{\mathbf{F}}_2(\xi_1, \xi_2) = \tilde{\mathbf{F}}_2(\xi_1 - \xi_2)$.

APPENDIX E: CONSERVATIVE VS NONCONSERVATIVE FORCE COMPONENTS

Here, we illustrate the contributions of conservative and nonconservative components of the optical force. The total optical force can be described as $\mathbf{F} = \frac{1}{4} \text{Re}(\widehat{\alpha}_{\text{eff}}) \nabla |E_0|^2 + \frac{1}{2} \text{Im}(\widehat{\alpha}_{\text{eff}}) |E_0|^2 \nabla \varphi$, where φ is the phase of the field. The first term corresponds to the gradient (conservative) force, which is proportional to a real part of particles' polarizability, while the second term corresponds to the scattering (nonconservative) force and is proportional to an imaginary part. By excluding the imaginary part of polarizability one can obtain the conservative force only [43,46,47]. The result is shown in Fig. 7. One can see that for the considered set of the parameters the conservative force strongly dominates over the nonconservative one, which is the difference between the total force and the gradient one.

APPENDIX F: STIFFNESS OF THE OPTICAL TRAP FOR DIFFERENT PARTICLES' PARAMETERS

The stiffness of the optical binding can be significantly influenced by the parameters of bounded particles. As can be seen from Eqs. (C11) and (2), the dielectric permittivity and the radius of the particles can change the value of the polarizability and stiffness. This is illustrated in Fig. 8(a), where the spectral stiffness of the trap is shown for different

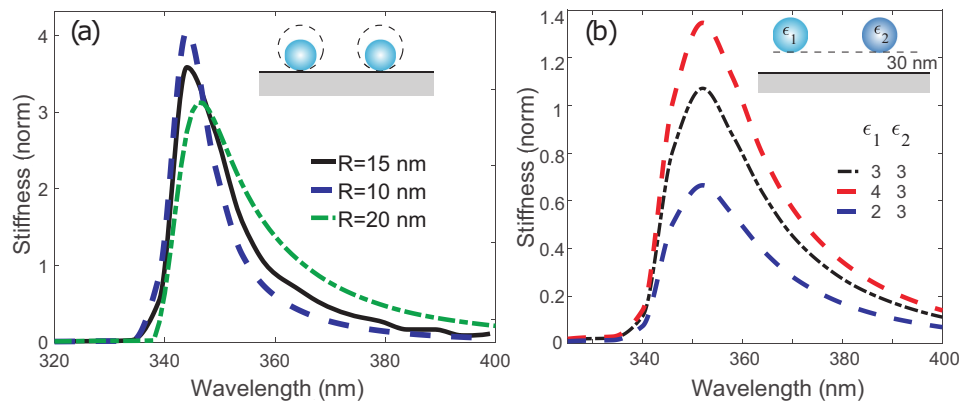


FIG. 8. (a) The stiffness κ_x of the second equilibrium position in units of $\kappa_0 = F_0/R$ as a function of the excitation wavelength. The spectra are shown for different radii R of the nanoparticles. The distance from the surface is zero. (b) The stiffness spectra for nanoparticles made of different materials and $R = 15$ nm.

nanoparticle sizes. We hold the distance between the surface of the particle and the metal interface constant, while varying the nanoparticle size as shown in the inset. The nanoparticle is described by a point dipole placed in the center of the sphere; thus, increasing the radius effectively increases the distance between the dipole and the surface, making the coupling between the dipole and SPP mode weaker. This provides the decrease of the stiffness with the nanoparticle radius increase. Actually, one may note that the absolute value of the stiffness will be increased in the end, as the normalization constant increases with the nanoparticle radius $\kappa_0 \sim R^2$ due to the increase of polarizability of the particle. Similar behavior was observed in case of single particle near plasmonic substrate [33].

The case of nonidentical nanoparticles is of a special interest. We analyzed the stiffness of binding for two nanoparticles of different permittivities. The results are shown in Fig. 8(b), where the spectra of the stiffness parameter are shown for three values of the permittivities. We need to note that in the case of different nanoparticles the system loses symmetry and a constant force acting on the nanoparticle center of mass may appear. To avoid speculating on that, we fix the position of the first nanoparticle at the origin. Lower permittivity results in decrease of maximal stiffness as the intensity of excited SPPs is reduced due to the lower dipole moment, and coupling between the nanoparticles gets weaker. In contrast, the increase of the permittivity gives an increase of binding stiffness.


- [1] O. M. Maragò, P. H. Jones, P. G. Gucciardi, G. Volpe, and A. C. Ferrari, *Nat. Nanotechnol.* **8**, 807 (2013).
- [2] I. Bloch, J. Dalibard, and S. Nascimbène, *Nat. Phys.* **8**, 267 (2012).
- [3] A. Ashkin, *Phys. Rev. Lett.* **24**, 156 (1970).
- [4] V. S. Letokhov, *ZhETF Pisma Redaktsiiu.* **7**, 348 (1968).
- [5] M. M. Burns, J. M. Fournier, and J. A. Golovchenko, *Phys. Rev. Lett.* **63**, 1233 (1989).
- [6] M. M. Burns, J. M. Fournier, and J. A. Golovchenko, *Science (N.Y.)* **249**, 749 (1990).
- [7] F. Depasse and J. M. Vigoureux, *J. Phys. D* **27**, 914 (1994).
- [8] P. C. Chaumet and M. Nieto-Vesperinas, *Phys. Rev. B* **64**, 035422 (2001).
- [9] J. Kesava, P. C. Chaumet, T. Langtry, and A. Rahmani, *J. Nanophoton.* **4**, 041583 (2010).
- [10] M. Mazilu, A. Rudhall, E. M. Wright, and K. Dholakia, *J. Phys.: Condens. Matter* **24**, 464117 (2012).
- [11] S. Sukhov, A. Shalin, D. Haefner, and A. Dogariu, *Opt. Exp.* **23**, 247 (2015).
- [12] R. W. Bowman and M. J. Padgett, *Rep. Prog. Phys. Phys. Society (Great Britain)* **76**, 026401 (2013).
- [13] M.-T. Wei, J. Ng, C. T. Chan, and H. D. Ou-Yang, *Sci. Rep.* **6**, 38883 (2016).
- [14] L. Chvatal, O. Brzobohaty, and P. Zemanek, *Opt. Rev.* **22**, 157 (2015).
- [15] V. Demergis and E. L. Florin, *Nano Lett.* **12**, 5756 (2012).
- [16] S. H. Simpson, P. Zemánek, O. M. Maragò, P. H. Jones, and S. Hanna, *Nano Lett.* **17**, 3485 (2017).
- [17] M. M. Salary and H. Mosallaei, *Phys. Rev. B* **94**, 035410 (2016).
- [18] C. Van Vlack, P. Yao, and S. Hughes, *Phys. Rev. B* **83**, 245404 (2011).
- [19] M. L. Juan, M. Righini, and R. Quidant, *Nat. Photon.* **5**, 349 (2011).
- [20] R. Quidant and C. Girard, *Laser Photon. Rev.* **2**, 47 (2008).
- [21] A. S. Shalin and S. V. Sukhov, *Plasmonics* **8**, 625 (2013).
- [22] A. S. Shalin, P. Ginzburg, A. A. Orlov, I. Iorsh, P. A. Belov, Y. S. Kivshar, and A. V. Zayats, *Phys. Rev. B* **91**, 125426 (2015).
- [23] A. P. Slobozhanyuk, P. Ginzburg, D. A. Powell, I. Iorsh, A. S. Shalin, P. Segovia, A. V. Krasavin, G. A. Wurtz, V. A. Podolskiy, P. A. Belov, and A. V. Zayats, *Phys. Rev. B* **92**, 195127 (2015).

- [24] A. V. Chebykin, A. A. Orlov, A. S. Shalin, A. N. Poddubny, and P. A. Belov, *Phys. Rev. B* **91**, 205126 (2015).
- [25] A. Ivinskaya, N. Kostina, A. Proskurin, M. I. Petrov, A. A. Bogdanov, S. Sukhov, A. A. Krasavin, A. Karabchevsky, A. S. Shalin, and P. Ginzburg, *ACS Photon.* **5**, 4371 (2018).
- [26] A. A. Bogdanov, A. S. Shalin, and P. Ginzburg, *Sci. Rep.* **5**, 15846 (2015).
- [27] V. Garcés-Chávez, R. Quidant, P. J. Reece, G. Badenes, L. Torner, and K. Dholakia, *Phys. Rev. B* **73**, 085417 (2006).
- [28] G. Volpe, R. Quidant, G. Badenes, and D. Petrov, *Phys. Rev. Lett.* **96**, 238101 (2006).
- [29] M. Yuan, L. Cheng, P. Cao, X. Li, X. He, and X. Zhang, *Plasmonics*. **13**, 427 (2018).
- [30] Z. Yan, Y. Bao, U. Manna, R. A. Shah, and N. F. Scherer, *Nano Lett.* **14**, 2436 (2014).
- [31] C. Min, Z. Shen, J. Shen, Y. Zhang, H. Fang, G. Yuan, L. Du, S. Zhu, T. Lei, and X. Yuan, *Nature Commun.* **4**, 2891 (2013).
- [32] S. B. Wang and C. T. Chan, *Nature Commun.* **5**, 3307 (2014).
- [33] M. I. Petrov, S. V. Sukhov, A. A. Bogdanov, A. S. Shalin, and A. Dogariu, *Laser Photon. Rev.* **10**, 116 (2016).
- [34] A. Ivinskaya, M. I. Petrov, A. A. Bogdanov, I. Shishkin, P. Ginzburg, and A. S. Shalin, *Light: Science & Applications* **6**, e16258 (2017).
- [35] S. Sukhov, V. Kajorndejnukul, R. R. Naraghi, and A. Dogariu, *Nature Photon.* **9**, 809 (2015).
- [36] F. J. Rodríguez-Fortuño, N. Engheta, A. Martínez, and A. V. Zayats, *Nat. Commun.* **6**, 8799 (2015).
- [37] S. Scheel, S. Y. Buhmann, C. Clausen, and P. Schneeweiss, *Phys. Rev. A* **92**, 043819 (2015).
- [38] F. J. Valdivia-Valero and M. Nieto-Vesperinas, *Opt. Exp.* **20**, 13368 (2012).
- [39] J. M. Auñón, F. J. Valdivia-Valero, and M. Nieto-Vesperinas, *J. Opt. Soc. Am. A* **31**, 206 (2014).
- [40] K. Dholakia and P. Zemánek, *Rev. Modern Phys.* **82**, 1767 (2010).
- [41] P. C. Chaumet and M. Nieto-Vesperinas, *Opt. Lett.* **25**, 1065 (2000).
- [42] P. B. Johnson and R. W. Christy, *Phys. Rev. B* **6**, 4370 (1972).
- [43] L. Novotny and B. Hecht, *Principles of Nano-optics* (Cambridge University Press, Cambridge, UK, 2012), p. 578.
- [44] B. Khlebtsov, A. Melnikov, V. Zharov, and N. Khlebtsov, *Nanotechnology* **17**, 1437 (2006).
- [45] M. Abramowitz and I. A. Stegun, *Handbook of Mathematical Functions: With Formulas, Graphs, and Mathematical Tables*, Applied Mathematics Series (National Bureau of Standards, Washington, DC, 1964).
- [46] A. S. Ang, S. V. Sukhov, A. Dogariu, and A. S. Shalin, *Sci. Rep.* **7**, 41014 (2017).
- [47] A. S. Ang, A. Karabchevsky, I. V. Minin, O. V. Minin, S. V. Sukhov, and A. S. Shalin, *Sci. Rep.* **8**, 2029 (2018).

Self-Trapped Nanoparticle Binding via Waveguide Mode

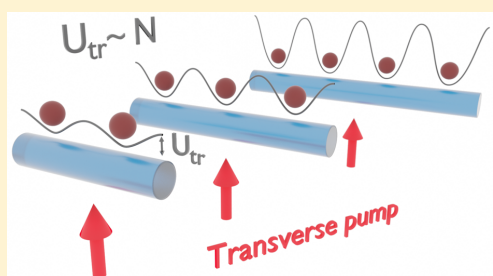
Ivan D. Toftul,*^{ORCID} Danil F. Kornovan, and Mihail I. Petrov

Department of Physics and Engineering, ITMO University, Kronverkskiy prospekt, 49197101 Saint Petersburg, Russia

 Supporting Information

ABSTRACT: In this paper, we study a stable optomechanical system based on a nanoparticle chain coupled to a waveguide mode. Under the plane wave excitation, the nanoparticles form a stable self-organized periodic array along the waveguide axis through the transverse binding effect. We show that, owing to the long-range interaction between the nanoparticles, the trapping potential for each nanoparticle in the chain increases linearly with the system size, making the formation of long chains more favorable. We show that, for an optical nanofiber platform, the binding energy for two nanoparticles is in the range of 9–13 kT, reaching the value of 110 kT when the chain size is increased to 20 nanoparticles. We also suggest the geometry of the two counter-propagating plane waves excitation, which will allow trapping the nanoparticles close to the optical nanofiber, providing efficient interaction between the nanoparticles and the nanofiber.

KEYWORDS: optical binding, self-assembly, one-dimensional interaction, nanofiber, optical force



The optical manipulation provides unique opportunities for controlling micro- and nanoobjects, as well as single atoms, at the remarkable level of precision. This field has passed through ages starting from the early astronomical studies by I. Kepler, to the formulation of electrodynamic grounds in works of J.C. Maxwell,¹ and later, experimental verification by P. N. Lebedev.² The modern age of optical forces and manipulation has started after early works by A. Ashkin,³ where he proposed the basic concept of optical manipulation of microobjects, which later led to a revolution in atomic cooling and trapping.^{4,5} Today, the standard methods of optomechanical control with spatial modulation of electromagnetic field intensity⁶ allows one to manipulate single biomolecules⁷ and sort biological cells.^{8,9} Besides, it can be precise enough to visualize the spin to orbital light momentum conversion.¹⁰ The optical manipulation provides a bridge between classical and quantum physics on the way of cooling of trapped microscale objects down to the temperature of quantized mechanical motion.^{11,12} On the other hand, the quantum physics has already gained a lot due to progress in optical manipulation allowing to trap and study single atoms¹³ or two-dimensional¹⁴ and three-dimensional^{15,16} atomic lattice providing a reliable platform for studying many-body quantum physics.

The majority of the optical trapping and manipulation methods are based on shaping the light field intensity with optical systems such as spatial light modulator which provides formation of the dipole trapping potential. This approach has been effectively used for manipulation of objects in different environment such as air, water, and vacuum. However, an alternative method of large ensembles manipulation and ordering bases on self-assembly approach.¹⁷ The field intensity

pattern forms due to rescattering of the optical fields by the objects resulting in effective dipole–dipole interactions and consequent structuring of large ensembles. A typical example of such effect is transverse optical binding^{18,19} where the nanoparticle can form bounded states under homogeneous illumination. Though the optical dipole–dipole interactions are quite weak, they can be enhanced and modified with auxiliary photonic structures²⁰ such as metamaterials^{21,22} and metasurfaces,²³ plasmonic structures^{24,25} and photonic crystal hollow fibers,²⁶ as well as dielectric nanofibers.²⁷ The latter one represents a versatile platform²⁸ for studying light interaction with nanoparticles^{29,30} and atoms^{31–33} placed close to its surface. Utilization of a single mode long-range dipole–dipole interaction, provided by waveguiding systems, has already been suggested for self-organization of atoms and nanoparticles in waveguiding systems.^{26,34,35}

We propose a particular geometry of the nanoparticle chain placed close to the nanofiber and illuminated by a plane wave propagating in the free space perpendicularly to the fiber axis, as it is shown in Figure 1. Such geometry allows to take the advantage of the transverse optical binding effect.^{19,36} The binding occurs due to the interference of the fields scattered by the nanoparticles, and it has been applied for self-organization of nanoparticle ensembles under the external laser illumination,^{37–39} including the interference of surface plasmon polariton modes.⁴⁰ Recently, a transverse binding has been observed in a large ensemble of dielectric submicron spheres⁴¹

Received: August 12, 2019

Published: December 10, 2019

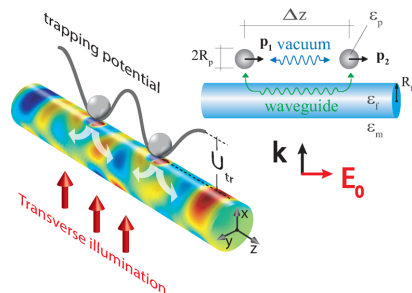


Figure 1. Proposed system configuration, which allows achieving nanoparticles binding close to the nanofiber under transversal plane illumination.

and nanowires^{42,43} with the strong collective interactions through the free-space coupling.

In our work, the nanofiber modes allow for accumulation of long-range interactions between distant nanoparticles, which results in the increasing particles stiffness with the growth of the nanoparticle chain length. Moreover, in the particular geometry of nanofiber binding, we also suggest a method for trapping the nanoparticles in the radial direction close to the fiber surface by using two counter propagating plane waves and taking the advantage of nanofiber lensing effect,⁴⁴ which is based on the refraction of the transverse pump and a sharp focal spot on the other side of the nanofiber. Thus, we suggest the geometry of the system that allows for immediate testing of the reported effect within the particular experimental setup with the use of an optical nanofiber.

RESULTS AND DISCUSSIONS

Binding of Nanoparticles with a Single-Mode Nanofiber.

The force acting on a single dipole particle and averaged over the period of the incident wave is given by^{45,46} $\mathbf{F} = \frac{1}{2} \sum_i \text{Re} \mathbf{p}_i^{*3} \nabla E_{\text{loc},i}$, where the sum is taken over the Cartesian components of the dipole moment \mathbf{p} and local field E_{loc} . The latter one contains the incident plane wave field E_{inc} , the field scattered by the nanofiber E_{sc} , and the field scattered by other nanoparticles E_p . The dipole moment of the n -th particle then is defined through the local field strength $\mathbf{p}_n = \alpha_0 E_{\text{loc}}(\mathbf{r}_n) = \alpha_0 (\mathbf{E}_0(\mathbf{r}_n) + \mathbf{E}_p(\mathbf{r}_n))$, where we defined $\mathbf{E}_0 = \mathbf{E}_{\text{inc}} + \mathbf{E}_{\text{sc}}$ as the external field, and α_0 is the exact dipole polarizability given by the Mie theory⁴⁷ (see Supporting Information, sec. I). The dipole field E_p is the field generated by other nanoparticles and can be expressed via Green's function formalism. For instance, the field generated by the i -th particle at the position of j -th particle has the form $E_{p,ij} = k_0^2 / \epsilon_0 \hat{\mathbf{G}}(\mathbf{r}_i, \mathbf{r}_j) \mathbf{p}_i$ where $\hat{\mathbf{G}} = \hat{\mathbf{G}}_0 + \hat{\mathbf{G}}_s$ is the total Green's tensor that consists of two parts: free-space $\hat{\mathbf{G}}_0$ and scattered $\hat{\mathbf{G}}_s$, which appears due to the presence of the nanofiber (see Supporting Information, sec. II). Here k_0 is the vacuum wavenumber and ϵ_0 is the vacuum permittivity.

The size of nanofiber can be chosen in such a way that it supports only a single guided HE_{11} mode⁴⁸ (SM-single mode regime). In this case, one can expect almost periodical behavior in the interaction strength between the nanoparticles with the interparticle distance Δz . Indeed, in Figure 2a, the optical force between two nanoparticles positioned close to the nanofiber is shown as a function of the distance between them. The contributions of vacuum and nanofiber interaction channels are

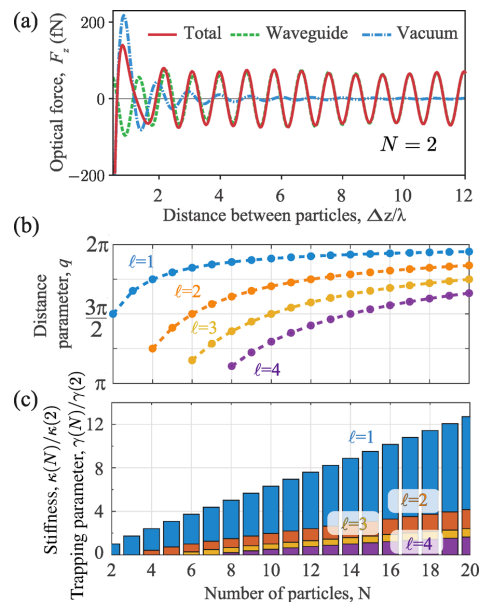


Figure 2. (a) Longitudinal optical force F_z acting on one of two particles as a function of distance along the fiber axis Δz for a single mode (SM) regime (see Figure 1). Red solid line shows optical force considering interaction through both fiber and free space ($\hat{\mathbf{G}}_s + \hat{\mathbf{G}}_0$), green dashed line shows only interaction through the fiber ($\hat{\mathbf{G}}_s$) and blue dash-and-dot line shows only free space interaction ($\hat{\mathbf{G}}_0$). (b) First three branches of the solution for the average distance between the two closest particles $q = \Delta z \beta$ with respect to the number of particles in a chain N . (c) Trapping parameter, which is the fraction of effective potential depth of the trap and thermal energy of the host media kT , and normalized stiffness of the trap with respect to the number of particles in a chain N .

extracted by proper choosing the free-space $\hat{\mathbf{G}}_0$ or scattered $\hat{\mathbf{G}}_s$ part of Green's function. One can see that the force has a well-pronounced periodic character, which allows forming a stable configuration stable system configuration consisting of arbitrary number of particles.^{35,49} Calculation of the optical force between two particles has been also performed using a full numerical model in COMSOL Multiphysics and good agreement with the analytical dipole model was obtained (see Supporting Information, sec. VI, for the details).

In a single mode regime the Green's function of the waveguide can be reduced to $\hat{\mathbf{G}}_s^{\text{wg}}(\mathbf{r}; \mathbf{r}') = \hat{\mathbf{G}}_s^{\text{wg}}(\rho, \varphi; \rho', \varphi') e^{i\beta \Delta z}$, and $\hat{\mathbf{G}}_s^{\text{wg}}(\mathbf{r}; \mathbf{r}')$ is purely imaginary for any waveguiding mode.⁵⁰ Here, we neglect the contribution of leaky and evanescent modes⁴⁸ as they decay significantly at long distances. In the field of a plane wave incident normally to the nanofiber and polarized along the z -axis (TM polarized), as shown in Figure 1, the dipole moments will be aligned preferably along the nanofiber axis, thus, having a dominant z -component of the dipole moment $\mathbf{p}_i \approx \mathbf{n}_z p_i = \mathbf{n}_z \alpha_{\text{eff},zz} E_{0,z}$ (see Supporting Information, sec. III, for the details). TM excitation allows to suppress the vacuum interaction channel as the dipole emission along the nanofiber axis is weak. The force acting on a particle with number n can be estimated as

$$F_n^{\text{SM}} = \frac{|p|^2 k_0^3 \beta}{2\epsilon_0} \text{Im}(g_{zz}) \times \sum_{j \neq n} \cos(\beta |z_n - z_j|) \text{sign}(j - n) \quad (1)$$

Here, N is the total number of particles in the chain, and we introduced the coupling constant $g_{zz}(\rho) = \hat{G}_{s,zz}^{\text{wg}}(\rho, \varphi; \rho, \varphi)/k_0$, which depends only on the radial distance to the nanoparticle center in the geometry shown in Figure 1. The system within the considered approximations has a stable equidistant configuration where separation between the neighboring nanoparticles is constant.⁴⁹ In order to find it, one needs also to estimate the stiffness parameter κ , which determines the strength of the restoring force $F_z = -\kappa(z - z_0)$ acting on a single particle close to the equilibrium position z_0 . This approach is valid as nonconservative part of the binding optical force is negligible. The stable configuration of nanoparticles is observed if the separation distance between the neighboring nanoparticles satisfies two conditions: (i) $F_{n,z} \propto \sum_{j \neq n}^N \cos(q|n - j|) \text{sign}(j - n) = 0$ and (ii) $\kappa_n \propto -\sum_{j \neq n}^N \sin(q|n - j|) > 0$ for all particles. Here $q = \beta \Delta z$ is the distance parameter and Δz is the distance between the neighboring nanoparticles. After taking the sum in eq 1, the first condition provides us with the expression for the equidistant solution $Nq/2 = \pi/2 + \pi(N - l)$, where l is an integer.

The stiffness of the n -th trap $\kappa_n = -\partial_{zz} F_z$ in the chain of N particles can be estimated as follows:

$$\kappa_n^{\text{SM}} = -\frac{|p|^2 k_0^3 \beta^2}{2\epsilon_0} \text{Im}(g_{zz}) \sum_{j \neq n}^N \sin(q|n - j|) \quad (2)$$

and the summation is taken in order to account for the interaction with all nanoparticles in the chain. The stability condition requires that κ_n should be positive for any particle in the chain. The analytical solution of the algebraic system shows that there exists a set of stable configurations. Separation distance q is 2π periodic in a single mode regime, hence, we analyze only fundamental solution which is $0 < q < 2\pi$. The interparticle distance q_1 which corresponds to $l = 1$, has the distance parameter³⁵ $q_1 = 2\pi - \pi/N$ (see blue line in Figure 2b). Moreover, the stiffness parameter $\kappa_n = \kappa(N)$ is the same for any particle in the chain and increases with the growth of total number of particles in the chain as $\kappa(N) \sim \cot(\pi/2N)$, which for $N \gg 1$ provides the linear increase of the stiffness $\kappa(N) \sim N$, as shown in Figure 2c. Other stable equidistant configurations correspond to other values of l and have a larger distance parameter $q = 2\pi - l\pi/N$, $l = 1, 2, \dots$ and $l \leq N/2$, as shown in Figure 2b for $l = 2, 3, 4$. The κ_n values for these solutions also demonstrate the linear growth with N , however, with a smaller slope than for $l = 1$ (see Figure 2c).

Stability of the Trapping. Increase of the stiffness of each nanoparticle's trap basically leads to increased stability of the chain, which can be expressed in terms of the trapping parameter $\gamma_{\text{tr}} = U_{\text{tr}}/kT$, where U_{tr} is the trapping potential separating the stable and unstable positions of each particle in the chain. It can be expressed as $U_{\text{tr}}(N) = \kappa(N) \Delta(\pi/\beta)^2/2$, where π/β is the half distance between particles in the limit $N \gg 1$ and for $l = 1$. The trapping potential for the fundamental configuration, with $l = 1$, then can be estimated in the single mode approximation as follows:

$$\gamma_{\text{tr}}^{\text{SM}}(N) = \frac{\pi^2 k_0^3 |p|^2}{4kT\epsilon_0} \text{Im}(g_{zz}) \cot\left(\frac{\pi}{2N}\right) \propto N \quad \text{for } N \gg 1 \quad (3)$$

This expression is one of the main results of the paper, showing that the stability of the considered system increases linearly with the growth of nanoparticle number in the chain. This basically means that the self-ordering of nanoparticles in

the longer chain will be more preferential and, in fact, is only limited by the width of the exciting laser beam and light intensity as $\gamma_{\text{tr}} \sim |p|^2 \sim |E_0|^2$.

In order to support our analytical results and estimate the achievable values of trapping potential, we used the full model, describing interacting dielectric nanoparticles placed close to a nanofiber. We took into account the plane wave rescattering on the nanofiber, the nanoparticles self-polarization effect due to the nanofiber presence, as well nanoparticle cross-polarization effects. For the set of parameters close to the experimental ones⁵¹ and summarized in Table 1, the calculations give us the

Table 1. Proposed Parameters of the System

parameter	symbol	SM	MM
fiber radius	R_f	300 nm	1000 nm
wavelength	λ_0	1064 nm	
particle radius	R_p	150 nm	
V-number	V	1.860	6.201
distance to the fiber	d	45 nm	50 nm
pump power	P	40 mW/ μm^2	
pump field magnitude	E_0	2.45×10^6 V/m	
permittivity of	media	fiber	particle
	$\epsilon_m = 1$	$\epsilon_f = 1.45^2$	$\epsilon_p = 2.5$

estimation of the binding parameter for two nanoparticles $\gamma(2) \approx 9$ at room temperature, which is a promising value for a potential experimental applications. Moreover, according to Figure 2 in the chain consisting of $N = 20$ nanoparticles in the fundamental configuration one can expect $\gamma(20) \approx 110$, that is, the trapping potential can be 2 orders of magnitude higher than kT .

Nanoparticle Binding in a Multimode Regime. With the increase of nanofiber radius the number of the waveguide modes starts to rapidly increase which significantly changes the picture of nanoparticles interaction. The coupling constants of each mode are depicted in Figure 3a. One can see that the higher modes give the bigger contribution to the coupling constant as their field penetration outside the waveguide is stronger. The simultaneous excitation of different modes provides aperiodic interaction potential between two particles. Our computational model allows for a full modeling of multimode (MM) interaction between the nanoparticles, and the computed optical binding force is shown in Figure 3b for the parameters specified in Table 1. Our estimations of the trapping parameter for MM regime give the value of $\gamma_{\text{tr}}^{\text{MM}}(2) \approx 13$ for the room temperature, which is higher than in a single mode regime due to larger number of modes and their stronger field penetration outside the waveguide.⁵²

Despite the aperiodic interaction, one still can expect the effect of self-induced organization of nanoparticles via transverse binding. In the MM regime, eq 2 will gain another sum over many interaction channels corresponding to different waveguide modes:

$$\kappa_n^{\text{MM}} = -\frac{1}{2} |p|^2 \frac{k_0^3}{\epsilon_0} \times \sum_{\mu=1}^M \beta_{\mu}^2 \text{Im}\{g_{zz}^{\beta_{\mu}}\} \text{Im} \sum_{j=1}^N e^{i\beta_{\mu}|z_n - z_j|} \quad (4)$$

where $\beta_{\mu} = \beta_{\text{HE}_{1\mu}}, \beta_{\text{TM}_{0\mu}}, \dots$ are the propagation constants of the allowed modes (see the dispersion curve in Figure 1 in Supporting Information), and M defines the number of the allowed waveguide modes. The stable configuration of the

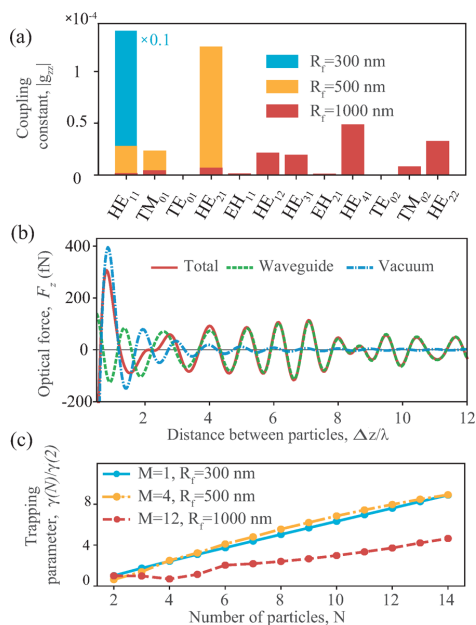


Figure 3. (a) Amplitude of the coupling constant g_c for different modes in single mode and multimode regimes for three different fiber radii: $R_f = 300, 500,$ and 1000 nm. (b) Longitudinal optical force F_z acting on one of the particles as a function of distance between the particles along the fiber axis Δz for multimode regime $R_f = 1000$ nm. (c) The trapping parameter of nanoparticles in a stable equidistant state as a function of the number of particles in multimode regime.

nanoparticle chain can be found through the maximization of eq 4. We applied a numerical optimization algorithm with proper constraints ($K_n > 0, F_{n,z} = 0$ for any n) to identify the nanoparticles configuration and the stiffness of the trap. The optimization procedure started by a configuration of ordered chain separated with the distance $\Delta z \beta_{\max} = 4\pi - \pi/N$, where β_{\max} is the propagation constant corresponding to the dominant mode among all the excited ones (HE_{21} and HE_{41} for $R_f = 500$ and 1000 nm, respectively). The final result after the optimization procedure is the trapping parameter $\langle \gamma \rangle$ averaged over particles presented in Figure 3c. One can see that the system demonstrates the stable configuration, which averaged trapping parameter increases linearly with the size N similar to the SM case.

Radial and Azimuthal Binding of Nanoparticles.

Finally, it is worth speculating about the potential mechanisms of trapping of the nanoparticles close to the nanofiber surface. We have not yet discussed the remaining two degrees of freedom of a nanoparticle: radial and azimuthal. It is known that a particle can easily experience orbital motion around the nanofiber,⁵³ and we need to embrace this motion as well. Illumination of the nanofiber by a plane wave forms an interference pattern in the vicinity of the nanofiber,⁴⁴ which can act as a trapping potential for nanoparticles. However, a single beam illumination also provides a strong optical pressure force acting on nanoparticles, which prevents effective trapping in the radial direction. We suggest a geometry with two counter propagating interfering beams fully compensating the optical pressure force and enabling strong binding of nanoparticles close to the nanofiber

surface. The formed potential trap provides both radial and azimuthal stability of the nanoparticles. In Figure 4a, the field

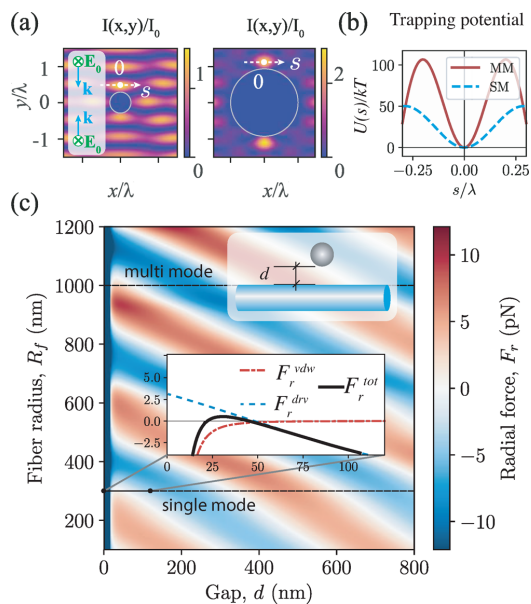


Figure 4. (a) Normalized intensity of the total electric field for two different fiber radii: $R_f = 300$ and 1000 nm. (b) Potential energy of the transverse trap along the x axis normalized by kT . (c) Total radial force as a function of two parameters: the fiber radius R_f and the gap between fiber surface and particle's surface d . Two horizontal dashed black lines correspond to single mode and multimode fiber radii in Table 1. Inset: the force decomposition into optical and van der Waals force. The equilibrium distances for single mode and multimode regimes are $d^{SM} = 45$ nm and $d^{MM} = 50$ nm.

intensity distribution normalized by the intensity of the plane wave is shown around the SM and MM nanofibers providing stability of nanoparticles in the trap in the transverse direction along the s -axis. The trapping parameter cross section is depicted in Figure 4b, demonstrating the values of 50 and 100 for a SM and MM nanofiber, respectively.

The radial stability of the particles is studied in Figure 4c, where the radial force acting on the particle is shown as a function of the fiber-particle gap d and fiber radius R_f . Total radial force also includes the contribution from the van der Waals attractive force⁵⁴ F_r^{vdw} , along with the driving force F_r^{drv} . The white regions in the 2D map correspond to the regions of zero optical force and, thus, the regions of radially stable configurations where the force changes sign from positive to negative with the increase of the gap. The two dashed lines denote the SM and MM nanofiber radii. In Figure 4c, inset, the cross section of the total radial force is shown for SM regime, demonstrating that a stable point at the gap distance of 45 nm can be achieved. Finally, one should note that by adding a phase difference between the up- and down-propagating interfering beams one can gradually modify the radial trapping potential and finely tune the position of the radially stable points (see Supporting Information, sec. V).

CONCLUSION

In this work, we propose that optomechanical systems coupled through a waveguide mode can demonstrate stable configurations, which stability will be increased with growth of the particle numbers in the system. This counterintuitive result is provided by a one-dimensional character of the interaction, providing that under a stochastic self-assembly process, the formation of longer chains will be preferable to the appearance of shorter ones. We suggest the experimental geometry of a nanoparticle chain located close to an optical nanofiber, which provides the trapping potential of 9–13 kT for two dipole nanoparticles at room temperature conditions, reaching the value of 110 kT for a 20 nanoparticles length chain. We also propose an excitation geometry based on two counter-propagating beams, in which one can achieve stable radial and azimuthal trapping locating the nanoparticles chain close to nanofiber, thus, making the proposed effect potentially observable in the experiment. Finally, the result of our paper can be extended to other one-dimensional systems with long-range interaction where the stability of the system will grow with size.

ASSOCIATED CONTENT

Supporting Information

The Supporting Information is available free of charge at <https://pubs.acs.org/doi/10.1021/acsp Photonics.9b01157>.

Additional details about a connection between polarizability and Mie theory, technical details about fiber Green's tensor, the general case of the effective polarizability, fiber dispersion to illustrate different numbers of modes, and a theoretical proposal of the two-beam radial trapping by phase tuning. Last section is devoted to the question of the validity of a dipole approximation supported by the full numerical simulations (PDF)

AUTHOR INFORMATION

Corresponding Author

*E-mail: ivan.toftul@metalab.ifmo.ru.

ORCID

Ivan D. Toftul: 0000-0003-3588-5403

Notes

The authors declare no competing financial interest.

ACKNOWLEDGMENTS

The authors are grateful for the discussions to Prof. Sile Nic Chormaic, Dr. Viet Giang Truong, and Natalia Kostina. M.P. and D.K. have been supported by the Foundation for the Advancement of Theoretical Physics and Mathematics Basis. The reported study was supported by the Ministry of Education and Science of Russian Federation (Project 2.2267.2017/4.6).

REFERENCES

- (1) Maxwell, J. C. *A Treatise on Electricity and Magnetism*; Clarendon Press, 1873.
- (2) Lebedew, P. *Untersuchungen über die Druckkräfte des Lichtes*; Annalen der Physik, 1901.
- (3) Ashkin, A. Acceleration and Trapping of Particles by Radiation Pressure. *Phys. Rev. Lett.* **1970**, *24*, 156–159.
- (4) Minogin, V. G.; Letokhov, V. S. *Laser Light Pressure on Atoms*; CRC Press, 1987.
- (5) Phillips, W. D. Laser cooling and trapping of neutral atoms. *Rev. Mod. Phys.* **1998**, *70*, 721–741.
- (6) Grier, D. G. A revolution in optical manipulation. *Nature* **2003**, *424*, 810–816.
- (7) Neuman, K. C.; Nagy, A. Single-molecule force spectroscopy: optical tweezers, magnetic tweezers and atomic force microscopy. *Nat. Methods* **2008**, *5*, 491–505.
- (8) Atajanov, A.; Zhanov, A.; Yang, S. Sorting and manipulation of biological cells and the prospects for using optical forces. *Micro and Nano Systems Letters* **2018**, *6*, na.
- (9) Wyatt Shields IV, C.; Reyes, C. D.; López, G. P. Microfluidic cell sorting: A review of the advances in the separation of cells from debulking to rare cell isolation. *Lab Chip* **2015**, *15*, 1230–1249.
- (10) Arzola, A. V.; Chvátal, L.; Jákl, P.; Zemánek, P. Spin to orbital light momentum conversion visualized by particle trajectory. *Sci. Rep.* **2019**, *9*, 4127.
- (11) Frimmer, M.; Gieseler, J.; Novotny, L. Cooling Mechanical Oscillators by Coherent Control. *Phys. Rev. Lett.* **2016**, *117*, 163601.
- (12) Tebbenjohanns, F.; Frimmer, M.; Militaru, A.; Jain, V.; Novotny, L. Cold Damping of an Optically Levitated Nanoparticle to Microkelvin Temperatures. *Phys. Rev. Lett.* **2019**, *122*, 223601.
- (13) Kim, M. E.; Chang, T. H.; Fields, B. M.; Chen, C. A.; Hung, C. L. Trapping single atoms on a nanophotonic circuit with configurable tweezer lattices. *Nat. Commun.* **2019**, *10*, na.
- (14) Gross, C.; Bloch, I. Quantum simulations with ultracold atoms in optical lattices. *Science* **2017**, *357*, 995–1001.
- (15) Kumar, A.; Wu, T. Y.; Giraldo, F.; Weiss, D. S. Sorting ultracold atoms in a three-dimensional optical lattice in a realization of Maxwell's demon. *Nature* **2018**, *561*, 83–87.
- (16) Barredo, D.; Lienhard, V.; de Léséleuc, S.; Lahaye, T.; Browaeys, A. Synthetic three-dimensional atomic structures assembled atom by atom. *Nature* **2018**, *561*, 79–82.
- (17) Čížmár, T.; Romero, L. C. D.; Dholakia, K.; Andrews, D. L. Multiple optical trapping and binding: new routes to self-assembly. *J. Phys. B: At., Mol. Opt. Phys.* **2010**, *43*, 102001.
- (18) Forbes, K. A.; Bradshaw, D. S.; Andrews, D. L. Optical binding of nanoparticles. *Nanophotonics* **2019**, *0*, na.
- (19) Dholakia, K.; Zemánek, P. Colloquium: Grippen by light: Optical binding. *Rev. Mod. Phys.* **2010**, *82*, 1767–1791.
- (20) Maragò, O. M.; Jones, P. H.; Gucciardi, P. G.; Volpe, G.; Ferrari, A. C. Optical trapping and manipulation of nanostructures. *Nat. Nanotechnol.* **2013**, *8*, 807–19.
- (21) Bogdanov, A. A.; Shalin, A. S.; Ginzburg, P. Optical forces in nanorod metamaterial. *Sci. Rep.* **2015**, *5*, 15846.
- (22) Kostina, N. A.; Kislov, D. A.; Ivinskaya, A. N.; Proskurin, A.; Redka, D. N.; Novitsky, A.; Ginzburg, P.; Shalin, A. S. Nano-scale tunable optical binding mediated by hyperbolic metamaterials. *ACS Photonics* **2019**, na.
- (23) Ivinskaya, A.; Kostina, N.; Proskurin, A.; Petrov, M. I.; Bogdanov, A. A.; Sukhov, S.; Krasavin, A. V.; Karabchevsky, A.; Shalin, A. S.; Ginzburg, P. Optomechanical Manipulation with Hyperbolic Meta-surfaces. *ACS Photonics* **2018**, *5*, 4371–4377.
- (24) Quidant, R.; Girard, C. Surface-plasmon-based optical manipulation. *Laser Photonics Rev.* **2008**, *2*, 47–57.
- (25) Ivinskaya, A.; Petrov, M. I.; Bogdanov, A. A.; Shishkin, I.; Ginzburg, P.; Shalin, A. S. Plasmon-assisted optical trapping and anti-trapping. *Light: Sci. Appl.* **2017**, *6*, e16258–6.
- (26) Bykov, D. S.; Xie, S.; Zeltner, R.; Machnev, A.; Wong, G. K. L.; Euser, T. G.; Russell, P. S. Long-range optical trapping and binding of microparticles in hollow-core photonic crystal fibre. *Light: Sci. Appl.* **2018**, *7*, 22.
- (27) Frawley, M. C.; Gusachenko, I.; Truong, V. G.; Sergides, M.; Chormaic, S. N. Selective particle trapping and optical binding in the evanescent field of an optical nanofiber. *Opt. Express* **2014**, *22*, 16322.
- (28) Daly, M.; Sergides, M.; Nic Chormaic, S. Optical trapping and manipulation of micrometer and submicrometer particles. *Laser & Photonics Reviews* **2015**, *9*, 309–329.
- (29) Maimaiti, A.; Holzmann, D.; Truong, V. G.; Ritsch, H.; Nic Chormaic, S. Nonlinear force dependence on optically bound micro-particle arrays in the evanescent fields of fundamental and higher order microfiber modes. *Sci. Rep.* **2016**, *6*, 1–10.

- (30) Joos, M.; Ding, C.; Loo, V.; Blanquer, G.; Giacobino, E.; Bramati, A.; Krachmalnicoff, V.; Glorieux, Q. Polarization Control of Linear Dipole Radiation Using an Optical Nanofiber. *Phys. Rev. Appl.* **2018**, *9*, 64035.
- (31) Vetsch, E.; Reitz, D.; Sague, G.; Schmidt, R.; Dawkins, S. T.; Rauschenbeutel, A. Optical Interface Created by Laser-Cooled Atoms Trapped in the Evanescent Field Surrounding an Optical Nanofiber. *Phys. Rev. Lett.* **2010**, *104*, 203603.
- (32) Kornovan, D. F.; Sheremet, A. S.; Petrov, M. I. Collective polaritonic modes in an array of two-level quantum emitters coupled to optical nanofiber. *Phys. Rev. B: Condens. Matter Mater. Phys.* **2016**, *94*, 245416.
- (33) Corzo, N. V.; Raskop, J.; Chandra, A.; Sheremet, A. S.; Gouraud, B.; Laurat, J. Waveguide-coupled single collective excitation of atomic arrays. *Nature* **2019**, *566*, 359–362.
- (34) Chang, D. E.; Cirac, J. I.; Kimble, H. J. Self-organization of atoms along a nanophotonic waveguide. *Phys. Rev. Lett.* **2013**, *110*, 1–6.
- (35) Holzmann, D.; Sonnleitner, M.; Ritsch, H. Self-ordering and collective dynamics of transversely illuminated point-scatterers in a 1D trap. *Eur. Phys. J. D* **2014**, *68*, 352.
- (36) Burns, M. M.; Fournier, J. M.; Golovchenko, J. A. Optical binding. *Phys. Rev. Lett.* **1989**, *63*, 1233–1236.
- (37) Chaumet, P. C.; Nieto-Vesperinas, M. Optical binding of particles with or without the presence of a flat dielectric surface. *Phys. Rev. B: Condens. Matter Mater. Phys.* **2001**, *64*, 035422.
- (38) Chvatal, L.; Brzobohaty, O.; Zemanek, P. Binding of a pair of Au nanoparticles in a wide Gaussian standing wave. *Opt. Rev.* **2015**, *22*, 157–161.
- (39) Demergis, V.; Florin, E. L. Ultrastrong optical binding of metallic nanoparticles. *Nano Lett.* **2012**, *12*, 5756–5760.
- (40) Kostina, N.; Ivinskaya, A.; Sukhov, S.; Bogdanov, A.; Toftul, I.; Nieto-Vesperinas, M.; Ginzburg, P.; Petrov, M. I.; Shalin, A. Optical binding via surface plasmon polariton interference. *Phys. Rev. B: Condens. Matter Mater. Phys.* **2019**, *99*, 125416.
- (41) Brzobohaty, O.; Chvátal, L.; Zemánek, P. Optomechanical properties of optically self-arranged colloidal waveguides. *Opt. Lett.* **2019**, *44*, 707.
- (42) Simpson, S. H.; Zemánek, P.; Maragò, O. M.; Jones, P. H.; Hanna, S. Optical Binding of Nanowires. *Nano Lett.* **2017**, *17*, 3485–3492.
- (43) Donato, M. G.; Brzobohatý, O.; Simpson, S. H.; Irrera, A.; Leonardi, A. A.; Lo Faro, M. J.; Svak, V.; Maragò, O. M.; Zemánek, P. Optical Trapping, Optical Binding, and Rotational Dynamics of Silicon Nanowires in Counter-Propagating Beams. *Nano Lett.* **2019**, *19*, 342–352.
- (44) Le Kien, F.; Hakuta, K. Microtraps for atoms outside a fiber illuminated perpendicular to its axis: Numerical results. *Phys. Rev. A: At., Mol., Opt. Phys.* **2009**, *80*, 1–6.
- (45) Chaumet, P. C.; Nieto-Vesperinas, M. Time averaged total force on a dipolar sphere in an electromagnetic field. *Opt. Lett.* **2000**, *25*, 1065–1067.
- (46) Ranha Neves, A. A.; Cesar, C. L. Analytical calculation of optical forces on spherical particles in optical tweezers: tutorial. *J. Opt. Soc. Am. B* **2019**, *36*, 1525.
- (47) Doyle, W. T. Optical properties of a suspension of metal spheres. *Phys. Rev. B: Condens. Matter Mater. Phys.* **1989**, *39*, 9852.
- (48) Marcuse, D. *Light Transmission Optics*; Van Nostrand Reinhold: New York, 1972.
- (49) Holzmann, D.; Ritsch, H. Tailored long range forces on polarizable particles by collective scattering of broadband radiation. *New J. Phys.* **2016**, *18*, 103041.
- (50) Yao, P. J.; Manga Rao, V.; Hughes, S. On-chip single photon sources using planar photonic crystals and single quantum dots. *Laser & Photonics Reviews* **2010**, *4*, 499–516.
- (51) Nieddu, T.; Gokhroo, V.; Chormaic, S. N. Optical nanofibres and neutral atoms. *J. Opt.* **2016**, *18*, 053001.
- (52) Kumar, R.; Gokhroo, V.; Deasy, K.; Maimaiti, A.; Frawley, M. C.; Phelan, C.; Chormaic, S. N. Interaction of laser-cooled ⁸⁷Rb atoms with higher order modes of an optical nanofibre. *New J. Phys.* **2015**, *17*, 013026.
- (53) Tkachenko, G.; Toftul, I.; Esporlas, C. L.; Maimaiti, A.; Le Kien, F.; Truong, V. G.; Nic Chormaic, S. Light-induced rotation of dielectric microparticles around an optical nanofiber. *arXiv preprint arXiv:1907.13363* **2019**, na.
- (54) Gu, Y.; Li, D. The van der Waals interaction between a spherical particle and a cylinder. *J. Colloid Interface Sci.* **1999**, *217*, 60–69.